LINE OF SIGHT STABILIZATION OF AN OPTICAL INSTRUMENT USING GAINED MAGNETOSTRICTIVE ACTUATORS

by

CHRISTIAAN RUDOLF BESTER

Submitted in partial fulfillment of the requirements for the degree

PHILOSOPHIAE DOCTOR

in the Department of Mechanical and Aeronautical Engineering,

Faculty of Engineering,
Built Environment
and Information Technology

UNIVERSITY OF PRETORIA

FEBRUARY 2003

Abstract

LINE OF SIGHT STABILIZATION OF AN OPTICAL INSTRUMENT USING GAINED MAGNETOSTRICTIVE ACTUATORS

Author: CR Bester
Supervisor: Prof MC van Schoor
Department: Mechanical and Aeronautical Engineering
Degree for which this thesis is submitted: Philosophiae Doctor

Line-of-sight stabilization of an optical instrument using magnetostrictive actuators is described in this study. Various stabilization methods, i.e. gyroscopic, hydraulic, piezoelectric, electrodynamic and magnetostrictive methods, are compared and magnetostrictive stabilization is selected for its relatively large stroke length, low input voltage and wide frequency bandwidth.

The system makes use of two magnetostrictive actuators, one at each end of the optical instrument, mounted between the moving base and instrument. Each actuator is equipped with cylindrical rods of Terfenol-D, a highly magnetostrictive material. Field coils are wound around the rods to produce a strain in the rods, thereby exciting angular motion of the instrument. Actuator stroke length is enhanced by means of a hingeless gain mechanism, rod prestressing and field biasing.

Dynamic characteristics of the system are modelled to facilitate actuator, coil and control system design. A linear, single-degree-of-freedom actuator model, in state-space and transfer function forms, is derived and coupled to a distributed model of the optical instrument, using the Rayleigh-Ritz method. Transfer functions between actuator coil voltages and instrument angular acceleration are derived. Normal mode shapes, natural frequencies and damping factors are predicted.

Design concepts for bias field, prestress, actuator gain and optical instrument support structure, are discussed and the most suitable concepts are selected. The required actuator gain, rod length and diameter, prestress spring stiffness, coil resistance and inductance are calculated. System components are designed in detail and safety of the design is checked.

The actuators are characterized quasi-statically to determine the saturation strain, linear range of operation and DC bias field. The system is dynamically characterized to obtain transfer functions between the coil voltage and instrument angular acceleration. The test setups are described and limitations of the setups are discussed. Test results are processed and discussed. A comparison with the modelled results shows that the model is highly inaccurate. Reasons for inaccuracies are given and updating of the model is motivated.

An updated model is obtained from the experimental results. The model is divided into electrical and mechanical subsystem models. The SDOF actuator models are replaced with 2DOF models (one for each actuator) and coupled to the instrument and base models, using substructure synthesis. The electrical and mechanical subsystem models are subsequently coupled. It is shown that the updated system model is considerably more accurate than the original model.

A linear, suboptimal, disturbance feedforward plus output feedback controller, with output integral feedback, is designed, implemented and tested. An H_2 optimal controller is designed and modified to improve robustness. The controller model is coupled to that of a suboptimal observer. An output integral feedback loop is added to further improve robustness. The controller is implemented in digital filter form. The test apparatus and procedure are described. Test results are processed and discussed. It is shown that the LOS stabilization system achieves 80% of the required isolation, over a frequency bandwidth of 0 Hz to 100 Hz.

A summary of the work done, conclusions that can be drawn from the results, problems encountered and recommendations for future work, are given.

Keywords: Line-of-sight, stabilization, active vibration isolation, magnetostriction, Terfenol-D, actuators, gain mechanisms

Uittreksel

SIGLYNSTABILISASIE VAN 'N OPTIESE INSTRUMENT MET BEHULP VAN MAGNETOSTRIKSIE-AKTUEERDERS MET WINSMEGANISMES

Outeur: CR Bester
Promotor: Prof MC van Schoor
Departement: Meganiese en Lugvaartkundige Ingenieurswese
Graad waarvoor hierdie proefskrif ingedien is: Philosophiae Doctor

Siglynstabilisasie van 'n optiese instrument, m.b.v. magnetostriksie-aktueerders, word in hierdie studie beskryf. Verskeie stabilisasiemetodes, nl. giroskopiese-, hidrouliese-, piezoëlektriese-, elektrodinamiese- en magnetostriksiemetodes, word vergelyk en magnetostriksiestabilisasie word verkies omdat dit 'n relatiewe lang slaglengte, lae insetspanning and wye frekwensieband het.

Die stelsel maak van twee magnetostriksie-aktueerders, een by elke punt van die optiese instrument, wat tussen die bewegende basis en instrument gemonteer is, gebruik. Elke aktueerder bevat silindriese stawe van 'n hoogs magnetostriktiewe materiaal, bekend as Terfenol-D. Klosse is rondom die stawe gewen om 'n veld in die stawe te bewerkstellig, wat 'n vervorming van die stawe teweegbring. Sodoende word hoekbeweging van die optiese instrument opgewek. Aktueerderslaglengte word vergroot deur 'n skarnierlose winsmeganisme, meganiese voorspanning van die stawe en veldvoorspanning.

Die dinamiese karakteristieke van die stelsel word gemodelleer om aktueerder-, klos- en beheerstelselontwerp te vergemaklik. 'n Lineêre, enkelvryheidgraadmodel van die aktueerder word in toestand- en oordragfunksievorm afgelei en m.b.v. die Rayleigh-Ritzmetode aan 'n verspreide massamodel van die optiese instrument gekoppel. Oordragsfunksies tussen die aktueerderklosspannings en hoekversnelling van die optiese instrument word afgelei. Normaalmodusvorme, natuurlike frekwensies en dempingsfaktore word voorspel.

Ontwerpkonsepte vir veldvoorspanning, meganiese voorspanning, aktueerderwinsmeganisme en ondersteuningstruktuur vir die optiese instrument, word bespreek en die mees geskikte konsepte word gekies. Die benodigde aktueerderwins, staaflengte en –diameter, voorspanningveerstyfheid, klosweerstand en –induktansie, word bereken. Detailontwerpe van die stelselkomponente word gedoen en ontwerpveiligheid word ondersoek.

Die aktueerders word kwasi-staties gekarakteriseer om die versadigingspanning, lineêre gebied en GS voorspanningsveld te bepaal. Die stelsel word dinamies gekarakteriseer om oordragsfunksies tussen die klosspanning en hoekversnelling van die instrument te verkry. Die toetsopstellings en beperkinge daarvan word bespreek. Toetsresultate word verwerk en bespreek. 'n Vergelyking tussen die gemodelleerde en gemete resultate toon dat die model hoogs onakkuraat is. Redes vir die onakkuraathede word gegee en modelopdatering word gemotiveer.

'n Opgedateerde model word uit die eksperimentele resultate verkry. Die model word in elektriese en meganiese substelselmodelle opgedeel. Die enkelvryheidsgraadmodelle van die aktueerders word met tweevryheidsgraadmodelle (een vir elke aktueerder) vervang en m.b.v.

substruktuursintese aan die instrument- en basismodelle gekoppel. Die elektriese en meganiese substelselmodelle word daarna gekoppel. Daar word aangetoon dat die opgedateerde model beduidend akkurater as die oorspronklike model is.

'n Lineêre, suboptimale, versteuringvorentoevoer-, plus uitsetterugvoerbeheerder, met uitsetintegraalterugvoer, word ontwerp, geïmplementeer en getoets. 'n H_2-optimale beheerder word ontwerp en gewysig om robuustheid te verbeter. Die beheerdermodel word aan 'n suboptimale waarnemermodel gekoppel. 'n Uitsetintegraalterugvoerlus word bygevoeg om robuustheid verder te verbeter. Die beheerder word as 'n digitale filter geïmplementeer. Die toetsapparaat en –prosedure word beskryf. Toetsresultate word verwerk en bespreek. Daar word aangetoon dat die siglynstabilisasiestelsel 80% van die benodigde isolasie oor 'n frekwensieband van 0 Hz tot 100 Hz lewer.

'n Opsomming van die werk wat gedoen is, gevolgtrekkings wat uit die resultate gemaak kan word, probleme ondervind en aanbevelings t.o.v. toekomstige werk, word gegee.

Sleutelwoorde: Siglyn, stabilisasie, aktiewe vibrasie-isolsie, magnetostriksie, Terfenol-D, aktueerders, winsmeganismes

Acknowledgements

To everybody who helped me through this study. I can compile a list that is much longer than the following, but no shorter.

Firstly, to my Lord and Saviour, the Holy, Almighty God, the Alpha and the Omega, Creator of everything that is, was and will be, for His support throughout my entire life, and especially during this extremely time-consuming and costly job.

My study leader, prof. Tienie van Schoor, for his profound knowledge of Structural Dynamics, and for keeping me on the right track when I was about to derail into the torture chambers of nonlinear, stochastic, multiple degree of freedom vibrations.

Dr Tupper Hyde, who spent his holiday time during his visit to South Africa, to give me useful tips on controller design.

Mr Wynand Avenant and prof. Jasper Steyn, for their financial support.

The friendly staff of Etrema in Ames, Iowa, for their hospitality during my visit there, as well as to the students in the Department of Mechanical Engineering at ISU, Dave, Jon and Toby.

Prof. Stephan Heyns, Gerrit Visser, Danie Smit and Herman Booysen, for lending me their precious laboratory equipment.

Jan Brandt, who made everything I asked him to, and Willie Vos, who drew everything I asked him to.

My friends Andre Ernst and Jacques Cilliers, who tried to train me as an electronics engineer. Thanks for helping me find the correct hardware and software that enabled me to complete the experimental work.

Prof. Jan Visser and prof. Albert Groenwold, who gave me computers to do my calculations and typing on.

My parents, for their relentless prayers, support and understanding, especially when I wanted to take a hammer and stop all vibrations in the laboratory permanently.

Elmi van der Dussen, for her support, even when I was extremely grumpy.

INDEX

INDEX (continued)

INDEX (continued)

INDEX (continued)

INDEX (continued)

INDEX (continued)

INDEX (continued)

INDEX (continued)

List of symbols

a	coefficient
	polynomial coefficient
	length of minor axis of ellipse
A	amplitude
	area
	state-space coefficient matrix
b	coefficient
	length of major axis of ellipse
B	magnetic flux density
	state-space driving matrix
c	damping coefficient
C	coefficient vector
	coupling matrix
	damping matrix
	parameter vector
	programming language
	state-space output matrix
	spring index
C^*	normal mode damping matrix
d	diameter
	disturbance
	wire diameter of a coil spring
d^H	strain constant
d^σ	piezomagnetic cross-coupling constant
D	diameter
	differential (element of a controller)
	distance
	disturbance amplitude
	pitch circle diameter
	state-space transmission matrix
e	error
	error signal
E	error amplitude
	expected value
	global error
	Young's modulus
EI	flexural rigidity
f	frequency
	function
f_n	natural frequency
F	force
	force amplitude vector
g	function
	gravity acceleration (9,81 m/s^2)
G	feedforward transfer function
	gain
	transfer function

List of symbols (continued)

h	function
	height
H	constant height
	magnetic field strength
	output feedback gain
	discrete state-space output matrix
i	imaginary number $\left(\sqrt{-1}\right)$
I	coil current
	integral (element of a controller)
	moment of inertia, second moment of area
	unit matrix
j	imaginary number $\left(\sqrt{-1}\right)$
J	cost function
	discrete state-space transmission matrix
k	constant
	dimensionless constant
	number
	spring stiffness
	stiffness matrix
K	calibration factor
	constant
	correction factor
	coupled modal stiffness matrix
	gain
	linear state feedback gain matrix, linear state feedback gain vector
	stiffness matrix
K^*	normal mode stiffness matrix
l	length
	number
	optical instrument length
L	inductance
	observer driving matrix
L_f	free inductance
L_0	clamped inductance
m	mass
	mass matrix
	number
M	dimensionless constant
	mass matrix
	modal mass matrix
	number
M^*	normal mode mass matrix
n	noise
	number
N	cross-coupling weight
	nonlinearity (in describing function method)
	number

List of symbols (continued)

p	frequency ratio
	load vector
	numerator polynomial coefficient
	pitch
	pole (of a transfer function)
	polynomial coefficient
P	distributed load
	numerator polynomial
	perimeter
	power
	proportional (element of a controller)
	Riccati matrix
	spectral density
q	denominator polynomial coefficient
	normal mode displacement
	number
	polynomial coefficient
Q	denominator polynomial
	modal excitation force
	weight
r	reference input, reference signal
	root, zero (of a transfer function)
R	control weight, input weight
	reference amplitude
	resistance
s	Laplace-domain differential operator
	polynomial coefficient
S	constant
	Riccati matrix
	sensitivity function
t	thickness
	time
T	complimentary sensitivity function
	constant
	couple
	maximum time
	moment
	period
	torque
u	control signal
	input
U	control amplitude
	input amplitude
	matrix of eigenvectors
v	output noise signal

List of symbols (continued)

V	coil voltage
	Laplace-domain amplitude of a function
	voltage
	volume
V_i	input voltage
V_o	output voltage
w	distributed displacement
	process noise signal
	weight
W	distributed displacement amplitude
x	deflection
	displacement
	position
	state variable
	state vector
$\dot{x}$	state derivative vector
$\hat{x}$	estimated state vector
X	state amplitude vector
y	output
	displacement
	stroke length
$\hat{y}$	modelled output
	estimated output
$\ddot{y}$	output acceleration
Y	output amplitude
$\ddot{Y}$	acceleration amplitude
z	zero of a transfer function
	discrete domain differential operator
z^{-1}	discrete domain delay element
Z	impedance

Abbreviations

AC	alternating current
A/D	analogue-to-digital
AR	auto regressive
ARE	algebraic Riccati equation
ARIMA	auto regressive integrated moving average
ARMA	auto regressive moving average
ARMAX	auto regressive integrated moving average with exogenous inputs
ARX	auto regressive with exogenous inputs
AWG	American wire gauge
bei	imaginary part of Kelvin function of { }
ber	real part of Kelvin function of { }
BW	(frequency) bandwidth
cf	coupling factor

List of symbols (continued)

const	constant
CGS	classical Gram-Schmidt
CPU	central processing unit
CSD	cross-spectral density
dB	decibel
D/A	digital-to-analogue
DC	direct current
DE	differential equation
DF	describing function
DFT	Discrete Fourier Transform
DMA	direct memory access
DOF	degree of freedom
DSP	digital signal processing
e.g.	"exempli gratia", for example
foh	first order hold
FD	finite difference method
FE	finite element
FEM	finite element method
FFT	Fast Fourier Transform
FORSE	Frequency domain Observability Range Space Extraction
FRF	frequency response function
HP	high-pass
i.e.	"id est", that is
Im	imaginary part of { }
ITD	Ibrahim time domain
LOS	line of sight
LP	low-pass
LQ	linear quadratic
LQE	linear quadratic estimator
LQG	linear quadratic gaussian
LQR	linear quadratic regulator
LS	least squares
LTF	loop transfer function
LTI	linear time invariant
LTR	loop transfer recovery
LVDT	linear variable displacement transducer
MA	moving average
MDFT	multi-dimensional Fourier Transform
MDOF	multiple degree of freedom
MGS	modified Gram-Schmidt
MIMO	multiple input multiple output
MS	mean-square
NARMAX	nonlinear autoregressive moving average with exogenous inputs
NARX	nonlinear autoregressive with exogenous inputs
ORSE	Observability Range Space Extraction
pf	packing factor
p-p	peak-to-peak
P	proportional (controller)

List of symbols (continued)

PC	personal computer
PCD	pitch circle diameter
PD	proportional-differential (controller)
PDE	partial differential equation
PI	performance index proportional-integral (controller)
PID	proportional-integral-differential (controller)
PSD	power spectral density
RAM	random access memory
Re	real part of { }
R-K	Runge-Kutta
RLS	recursive least squares
RMS	root-mean-square
SDOF	single degree of freedom
SISO	single input single output
sup	supremum
SVD	singular value decomposition
TF	transfer function
TR	transmissibility
zoh	zero order hold

Subscripts

a	active (e.g. in active number of coils in a spring N_a) actuator (e.g. in actuator output y_a)
A	active (e.g. in active system transmissibility TR_A) amplitude (e.g. in field amplitude H_A)
asymm	asymmetric (e.g. in asymmetric assumed mode vector)
b	base (e.g. in base excitation force F_b)
B	bias (e.g. in bias field strength H_B, bias force F_B) bulk modulus (e.g. in fluid spring stiffness due to compressibilty K_B)
c	calibration (e.g. in disturbance accelerometer calibration factor K_{cd}) coil controller (e.g. in controller transfer function G_c) corrected (e.g. in corrected spring wire shear stress τ_c)
ck	index (e.g. *k*-th coil transfer function numerator coefficient)
cl	index (e.g. *l*-th coil transfer function denominator coefficient) closed-loop (e.g. in closed-loop coefficient matrix A_{cl})
cr	critical (e.g. in critical buckling force F_{cr}, critical eddy current frequency f_{cr})
crisscross	indicating relative location between actuator and sensor
d	disturbance (e.g. in driving matrix B_d for disturbance d)
dehyst	dehysterized
distr	distributed (e.g. in distributed density ρ_{distr})
D	damping (e.g. in damping force F_D) differential (e.g. in differential control element)
DC	direct current (e.g. in TR_{DC}, i.e. transmissibility at 0 Hz)

List of symbols (continued)

e	ellipse (e.g. in perimeter of ellipse P_e)
	external (e.g. in external diameter D_e)
	inactive (e.g. in inactive number of coils in a spring N_e)
eff	effective (e.g. effective damping in a coupled electro-mechanical system)
eq	equivalent (e.g. in equivalent density ρ_{eq})
f	free (eg. in free inductance L_f)
	feedforward (e.g. in feedforward gain G_f)
filter	filter (e.g. in filter transfer function G_{filter})
fluid	fluid (e.g. in fluid stiffness k_{fluid})
g	gap (e.g. flux density in the air gap of a magnetic path)
G	gain (e.g. in gain mechanism damping ζ_G)
	gyration (e.g. in radius of gyration r_G)
h	feedback (e.g. in feedback gain G_h)
hyst	hysteresis
i	index (e.g. *i*-th element or mode)
	inner (e.g. in inner coil diameter d_i)
	input (e.g. in input voltage V_i)
I	current (e.g. in force per unit current F_I)
	integral (e.g. in integral feedback control gain H_I)
ii	index (e.g. *ii*-th diagonal element of matrix)
ij	index (e.g. *ij*-th element of matrix)
j	index (e.g. *j*-th element)
k	index (e.g. *k*-th element)
l	index (e.g. *l*-th element)
	number (e.g. in number of coil layers n_l)
loading	indicating driving direction (e.g. loading strain $\varepsilon_{loading}$)
m	magnetic (e.g. in flux density in magnet B_m)
	mean
	mechanical (e.g. in mechanical subsystem transfer function G_m)
M	maximum index, i.e. polynomial order (e.g. in b_M)
max	maximum (e.g. in maximum field H_{max})
min	minimum (e.g. in minimum field amplitude H_{min})
n	index (e.g. *n*-th element)
	natural (e.g. in natural frequency f_n)
	normal mode (e.g. in generalized normal mode displacement q_n)
	number
nc	natural, compressible (e.g. in natural frequency due to compressibility)
ni	natural, incompressible (e.g. in natural frequency due to incompressibility)
N	maximum index , i.e. polynomial order (e.g. in a_N)
o	outer (e.g. in outer coil diameter d_o)
	output (e.g. in output voltage V_o)
p	piston (e.g. in piston cross-sectional area (A_p)
	plant (e.g. in plant transfer function G_p)
	power (e.g. in time where maximum coil power occurs t_p)
P	passive (e.g. in passive system transmissibility TR_P)
parallel	indicating relative location between actuator and sensor

List of symbols (continued)

r	index (e.g. in *r*-th error coefficient e_r)
	reduced-order (e.g. in reduced-order stiffness matrix K_r)
	relative (e.g. in relative displacement y_r)
	rod (e.g. in rod force F_r)
ref	reference (e.g. in volume per unit volume V_{ref})
rigid	rigid body (e.g. in rigid body assumed mode vector)
rotation	indicating degree of freedom (e.g. in rotational transfer function $G_{rotation}$)
row, rows	index (e.g. of a row or rows in a column vector or matrix)
R	resonance (e.g. in resonance magnitude of a transfer function TF_R)
RMS	root-mean-square (e.g. in root-mean-square of output y_{RMS})
s	sample (e.g. in sample time T_s)
	shear (e.g. in spring material shear modulus G_s)
	structure (e.g. in structure assumed mode vector ψ_s)
	system (e.g. in system state vector x_s)
spr	spring (e.g. in spring stiffness k_{spr})
ss	steady-state (e.g. in steady-state Riccati matrix S_{ss})
symm	symmetric (e.g. in symmetric assumed mode vector)
S	static (e.g. in static transfer function magnitude TF_S)
t	total (e.g. in total number of coils of a spring N_t)
translation	indicating degree of freedom (e.g. in translational transfer function $G_{translation}$)
T	Terfenol-D
u	input (e.g. in driving matrix B_u for controllable input u)
unloading	indicating driving direction (e.g. unloading strain $\varepsilon_{unloading}$)
V	voltage (e.g. in input power spectral density P_{vv})
v	voltage (e.g. in time where maximum voltage occurs t_v)
w	wire (e.g. in coil wire thickness)
wc	wire coating (e.g. in coated wire thickness t_{wc})
W	Wahl (e.g. in Wahl shear stress correction factor K_W)
x	state (e.g. in state weight Q_x)
y	output (e.g. in output weight Q_y)
0 (zero)	clamped (e.g. in clamped inductance L_0, clamped permeability μ_0)
	reference value (e.g. in undeformed height of gain mechanism h_0)
	steady-state value
	zero-th value
1,2....	index (e.g. in gains K_1, K_2,....)

Superscripts

i	exponent
iv	fourth partial derivative with respect to spatial coordinate
j	exponent
k	exponent
l	exponent
*	normal (e.g. in normal, or uncoupled modal stiffness matrix K^*)
	optimal (e.g. in optimal output y^*)
T	transpose (of a matrix or vector)
-1	inverse (e.g. of matrix, parameter or variable)

List of symbols (continued)

Greek

α	angle
	dimensionless constant
	real part of eigenvalue
β	dimensionless constant
χ	integration variable
	eddy current loss factor
δ	Dirac delta function
Δ	change in parameter or variable
ε	strain
E	strain amplitude
ϕ	diameter
	magnetic flux
	normal mode shape
	phase angle
Φ	normal mode shape vector
	discrete state-space coefficient matrix
γ	attenuation factor
	dimensionless hysteresis parameter
Γ	discrete state-space driving matrix
η	integration variable
	loss factor
κ	constant
	statistical degrees of freedom
μ	micro
	permeability
μ^{σ}	free permeability
ν	Poissons ratio
φ	phase angle
π	constant (= 3,14159265358979……)
ρ	density
	resistivity
ρA	mass per unit length
σ	stress
$\overline{\sigma}[\ ]$	largest singular value of [ ]
Σ	sum
τ	period
	shear stress
θ	angle
	angular displacement
	dummy variable
	phase angle
$\ddot{\theta}$	angular acceleration
ω	angular frequency
ω_n	angular natural frequency

List of symbols (continued)

Ω	constant frequency imaginary part of eigenvalue
ψ	angle assumed mode shape function
Ψ	assumed mode shape vector
ζ	dimensionless damping factor
Z	dimensionless modal damping matrix

Other

∞	infinity
H_2	type of optimal controller
H_∞	type of optimal controller
$\dot{}$	(dot) derivative with respect to time $\frac{d}{dt}(\ )$
$\ddot{}$	(double dot) 2nd order derivative with respect to time
$'$	(prime) partial derivative with respect to spatial coordinate
$''$	(double prime) 2nd order partial derivative with respect to spatial coordinate
$\bar{}$	(overbar) mean or average value error (e.g. in estimated state vector $\bar{x}$)
^	(hat): approximate value estimated value (of state or output)
$\int$	integral
∂	partial derivative
$\lvert\ \rvert$	absolute value determinant magnitude
$\lVert[\ ]\rVert$	determinant of matrix
( )	function
{ }	vector
[ ]	matrix
2DOF	two degree of freedom

Chapter 1
Introduction

This chapter gives an introduction to the magnetostrictive active line-of-sight (LOS)-stabilization of a vehicle-mounted optical instrument. A formulation of the problem, i.e. the LOS-angular disturbance sensitivity of optical instruments and the wide-band vibration problem in vehicles, is given in section 1.1. Two possible stabilization methods, viz passive and active stabilization, are compared in section 1.2 and the need for active stabilization is pointed out. The performance of hydraulic, electrodynamic, piezo-electric and magnetostrictive actuator types is compared in section 1.3 and the use of magnetostrictive actuation is motivated. Section 1.4 covers a literature survey on magnetostriction and highlights the applicability and limitations of each literature item in solving the stabilization problem. Section 1.5 gives an outline of the rest of the thesis.

1.1 Problem formulation

A moving vehicle is subjected to two sources of vibration, i.e. onboard disturbance systems and the movement of the vehicle over the terrain. The propulsion system is the most dominating source of all the onboard disturbance systems. Each vehicle type is equipped with its own unique type of propulsion system and is thus exposed to a different kind of environment. Vibrations which originate from the propulsion systems of ground vehicles, for instance, can be attributed to moving parts in internal combustion engines, gearboxes and drivelines, while gas turbines and propellers are responsible for vibrations in aircraft and helicopters. Environmentally, or externally induced vibrations are caused by terrain irregularities in road and off-road vehicles, aeroelastic effects in aircraft and hydrodynamic forces in ships.

Vehicle vibrations are transmitted to the vehicle structure, passengers and vehicle systems and may have several undesirable consequences, e.g. the vehicle structure may fail due to fatigue, hydraulic systems may fail due to broken pipes and passengers may experience discomfort and loss of concentration. Furthermore, any fragile onboard equipment such as computers, radios and optical systems, will suffer costly performance losses if exposed to excessive vibration levels. Optical instruments like high resolution imaging television, infrared and laser sensors, periscopes and reconnaissance cameras, are particularly sensitive to vibration environments. A periscope mounted in the turret of an army tank, for example, will not track its target accurately if the mounting base of the periscope vibrates relative to the gun platform. This will lead to incorrect aiming, missed shots and eventually to loss of the tank and its personnel.

Incorrect aiming of an optical instrument can mainly be attributed to an angular disturbance of the mounting base of the instrument. This causes a pitching or yawing rotation of the instrument relative to the desired line of sight (LOS) and results in a pointing error at the target (see figure 1.1). Pitch is more susceptible to external or environmental disturbances.

The pointing error depends on the disturbance angle and the distance between the optical instrument and the target, and can be mathematically expressed as follows:

$$e = \theta D \tag{1.1.1}$$

where e is the pointing error, θ is the disturbance angle and D is the distance between the instrument and the target.

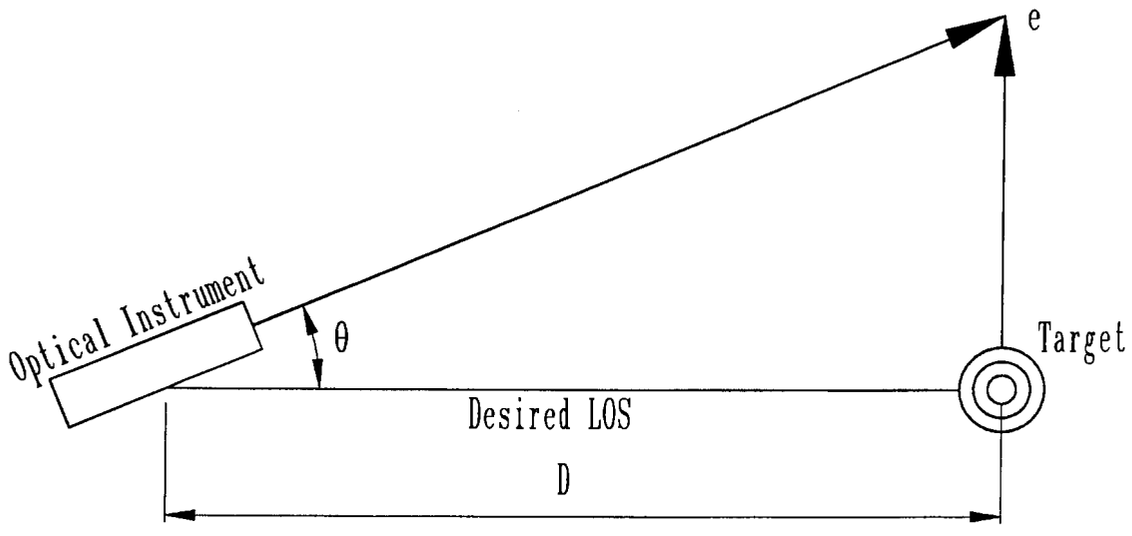

Figure 1.1.1: Line of sight angular disturbances and pointing errors

The pointing error problem is further complicated by the fact that the disturbance angle fluctuates due to vibrations in the mounting base of the optical instrument, and that vehicle vibrations are generally wide-band in nature. The frequency band of aircraft vibrations, for instance, is 15 Hz to 2 kHz, while the frequency band of road vehicle vibrations is 5 Hz to 500 Hz [MIL 810 E, 1988]. Wide-band angular disturbances such as these may cause blurred images, which will make target visibility and recognition extremely difficult.

In order to improve target visibility, it is essential to isolate the instrument from the base vibrations. Although it may be desirable to totally eliminate the LOS error, this may be difficult to achieve due to the high sensitivity of optical instruments. Instead, the effect of the base disturbance must be attenuated to such an extent that the remaining LOS error will minimize target blur. For this reason, minimum LOS errors are usually specified. The specified LOS accuracy for a shipboard electro-optical platform, for example, is less than 0,1 mrad RMS over a frequency band of 0,5 Hz to 200 Hz [Stockum & Carroll, 1984].

The topic of this study is the isolation of a lightweight commercial video camera, mounted on a vibrating platform next to the gun of a tracked vehicle (tank). The isolation system will be specifically designed and implemented to solve the particular problem. A vibration signal with a given frequency spectrum, bandwidth, RMS angular displacement and acceleration, measured on the instrument mounting base of an existing vehicle, will serve as the disturbance. The disturbance will be simulated and excited in a laboratory, where the isolation system will be implemented, tested

and evaluated. The instrument will be represented by a dummy load with the same mass and length.

The objective is to limit the LOS displacement amplitude of the optical instrument to 0,1 mrad peak-to-peak (p-p). The length of the instrument is 250 mm and its mass, together with that of its support structure, is 1,24 kg. The maximum angular displacement of the base is 0,7 mrad p-p and the maximum angular acceleration is 39,48 rad/s^2 p-p. The base RMS angular displacement is 0,181 mrad and the RMS angular acceleration is 9,12 rad/s^2. The frequency band is 2,5 Hz to 500 Hz. The maximum acceleration amplitude occurs at 96 Hz and the maximum displacement amplitude occurs at 24 Hz. The base angular acceleration and displacement signals are shown in figure 1.1.2, and the frequency spectra of the base angular acceleration and displacement are shown in figure 1.1.3.

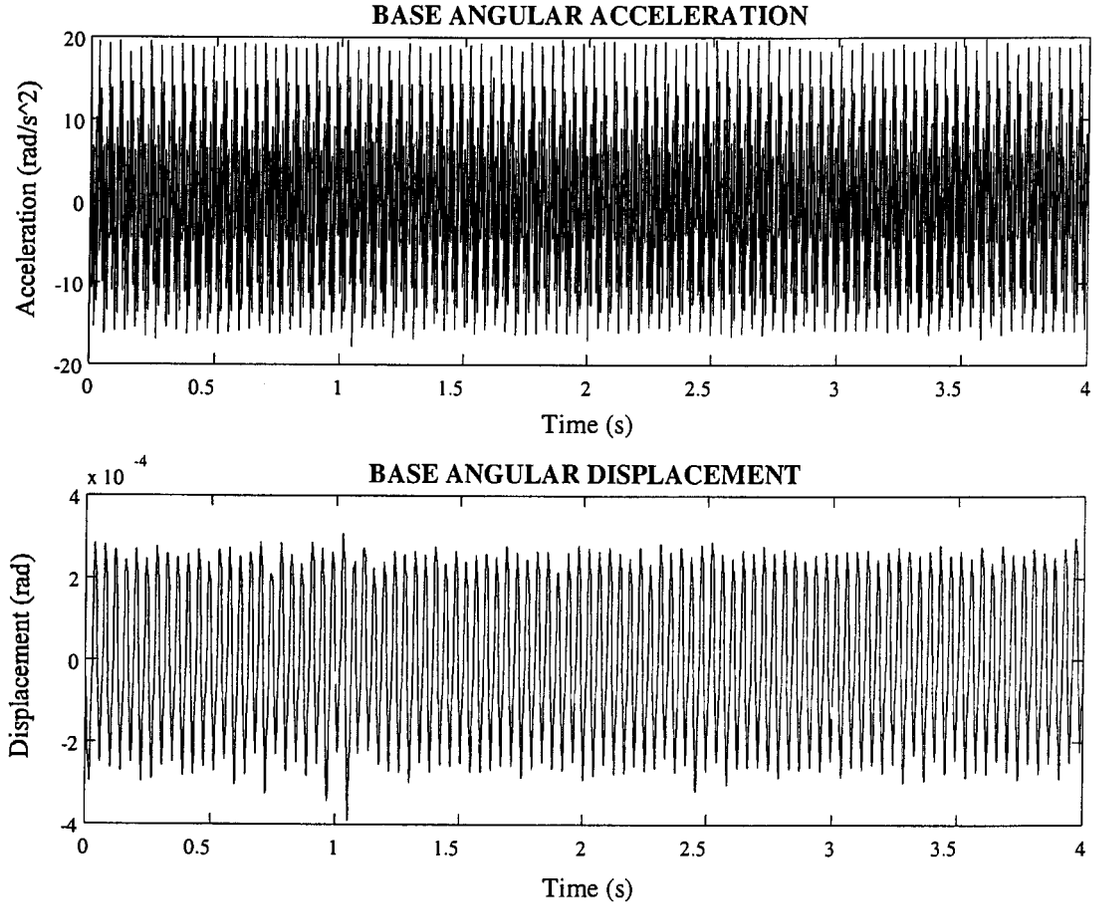

Figure 1.1.2: Base angular acceleration and displacement

It can be seen from figure 1.1.3 that the vibration spectrum is wide-band. This complicates the isolation problem because a limitation is placed on the choice of available stabilization methods, such as passive, semi-active and active vibration isolation. On the one hand, it will be desirable to use an isolator with zero energy consumption, such as a passive isolator, but on the other hand wide-band isolation capabilities are required, which may necessitate an active isolator. The next section will give a more complete comparison between passive and active stabilization systems. It

will be shown by means of mathematical equations and graphs that active isolation is required to stabilize the optical instrument.

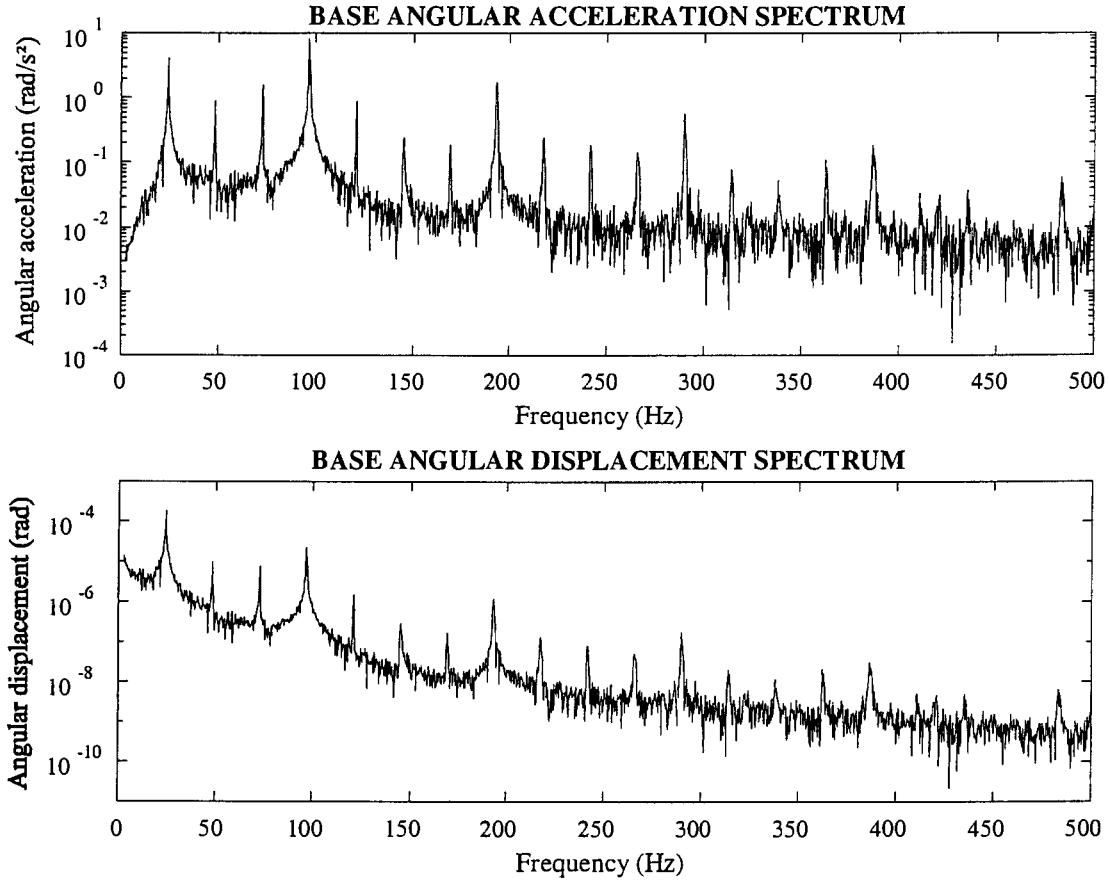

Figure 1.1.3: Base angular acceleration and displacement frequency spectra

1.2 Comparison between passive and active isolation

The previous section gave a background on the vibration sensitivity of vehicle-mounted optical instruments. It was shown that angular disturbances of the mounting base cause pointing errors at the target and that vibration isolation of the instrument is essential to improve target visibility. It was also shown that vehicle vibrations are wide-band in nature, which places a limitation on the choice of a suitable isolator, such as passive, semi-active and active isolators.

This section will discuss three different types of stabilization methods for broadband isolation of the optical instrument, i.e. passive, semi-active and active isolation. The section starts with a basic philosophy of vibration isolation, after which the different methods will be compared by means of mechanical models, equations of motion and damping forces. The performance of each isolation type will be discussed in terms of vibration transmissibility and wide-band isolation ability and the advantages and disadvantages of each method will be pointed out.

Lastly, it will be shown that an active isolation system will be required to reduce the LOS error of the optical instrument to 0,1 mrad p-p over a frequency band of 2,5 Hz to 500 Hz.

The basic philosophy of vibration isolation is to attenuate unwanted disturbances before the disturbances reach the instrument [Crawley & Hall, 1991]. This can be achieved by isolating components at the most suitable locations, e.g. at the source of the disturbance or at major substructure interfaces. In the case of the optical instrument, isolation is essential at locations that have a significant effect on attenuating vibrations in the relevant degree of freedom (DOF). The important DOF in the stabilization of the optical instrument LOS is the pitching rotation DOF, since it directly affects the LOS accuracy of the instrument (see figure 1.1.1). Suitable locations for isolators to reduce pitching motion may for instance be at the front and rear ends of the instrument, where the isolator can exercise a maximum resisting moment to attenuate the rotational motion of the optical instrument, thereby improving visibility of the target.

The ability of an isolator to attenuate vibrations is normally expressed in terms of vibration transmissibility. Transmissibility can be defined as the nondimensional ratio of the response amplitude of a system in steady state harmonic vibration to the excitation amplitude [Harris, 1988]. The ratio may be one of forces, displacements, velocities or accelerations. In the case of the optical instrument, the transmissibility TR can be defined as the ratio of the angular displacement amplitude $\theta(\omega)$ of the instrument, to the angular displacement amplitude $\theta_b(\omega)$ of the base:

$$TR = \frac{\theta(\omega)}{\theta_b(\omega)} \tag{1.2.1}$$

where ω is the angular excitation (or disturbance) frequency in rad/s. A transmissibility of less than one is required for isolation purposes, in other words the angular displacement of the instrument must be less than that of the base. The lower the transmissibility, the better the isolation. If the isolator transmissibility exceeds unity, the base disturbance will be amplified instead of being attenuated. A discussion is provided by Crawley & Hall [1991].

Three isolator types, i.e. passive, semi-active and active isolators can be considered for LOS stabilization of the optical instrument. Firstly, passive isolation works on the principle of attenuating vibrations by means of internal forces, such as isolator stiffness, inertia and damping forces. No external force, with the exception of the base disturbance, acts on the system. The advantages of passive isolation are mechanical simplicity and zero energy consumption, since no external energy sources like hydraulic pumps are required. It is for these reasons that passive isolators have traditionally been the most popular isolator type in use. Unfortunately the absence of an external energy source also creates certain problems, e.g. the transmissibility of the system cannot be altered at high frequencies without affecting static system behaviour. This shortcoming practically rules out the possibility of using passive isolation for broadband disturbance rejection.

Two types of passive vibration isolators can be distinguished, i.e. band-pass filters and low-pass filters. The application of band-pass filters is generally limited to narrow-band vibrations, and therefore cannot be considered suitable for wide-band isolation. Low-pass filters can be used for isolation purposes if the undamped natural frequency of the system is lower than the disturbance

frequency band [Crawley & Hall, 1991]. This can be accomplished by using an isolator with a low spring stiffness.

However, a low spring stiffness may yield an undesirably large static deflection, which cannot be corrected due to the absence of an external force. If, for instance, a low-pass filter is used to isolate an optical instrument against the disturbance shown in figure 1.1.2, a natural frequency of less than 2,5 Hz is required. The spring stiffness required to bring about this natural frequency may be so low that all efforts to stabilize the LOS over a wide frequency band, will result in large static pointing errors which will make the stabilization effort futile. The static error can only be corrected by means of a force that is independent of the natural frequency of the system, such as an active force.

An active isolator makes use of an external energy source to generate forces which oppose the base motion, thereby reducing the vibrations transmitted to the optical element. Examples of active isolators are hydraulic, electrodynamic, piezo-electric, and magnetostrictive actuators. The purpose of active isolation is to modify the passive transmissibility of an isolator in three different ways, i.e. to increase mass, to increase damping near the natural frequency or to reduce the static stiffness of the isolator [Crawley & Hall, 1991]. The advantage of active isolation is the possibility of supplying the correct force to stabilize the optical instrument at any frequency inside the disturbance band, but the main disadvantage is the necessity of an external energy source like hydraulic pressure or electric power. Furthermore, an electronic control system is required to ensure the desired actuator closed loop response. Active isolation is therefore less energy efficient, more bulky and more costly.

The third isolator type, i.e. a semi-active isolator, contains controllable passive damping elements. The control system changes the damping force according to the direction and magnitude of the relative speed between the damper attachment points to ensure the correct damping force at a given frequency. As in the case with passive isolators, the mechanism of removing energy is internal to the system. The advantage is that, except for a small actuator to change the passive damping coefficient, no energy source is required, but the disadvantage is that no energy can be added to the system. No further attention will be paid to semi-active isolation, but instead, the differences between passive and active isolation will be pointed out in the next few paragraphs. The two system types will be compared for damping force, vibration transmissibility and isolation ability.

In order to obtain a better understanding of passive and active system behaviour, consider the two simple single degree of freedom (SDOF) translational systems as shown in figure 1.2.1. The system on the left hand side of figure 1.2.1 consists of a moving base which is attached to a mass m via a linear spring with stiffness k and a viscous damper with damping coefficient c. The absolute displacement of the base is x_b and the absolute displacement of the mass is x. The system on the right hand side of figure 1.2.1 consists of a moving base, which is attached to a mass m via a linear spring with stiffness k. A viscous damper with damping coefficient c connects the mass to an inertial earth via a viscous damper with damping coefficient c. The absolute displacement of the base is x_b and the displacement of the mass is x. The system shown on the left hand side of figure 1.2.1 is a passively damped system (or passive system for short) while the system shown on the right hand side is an active system.

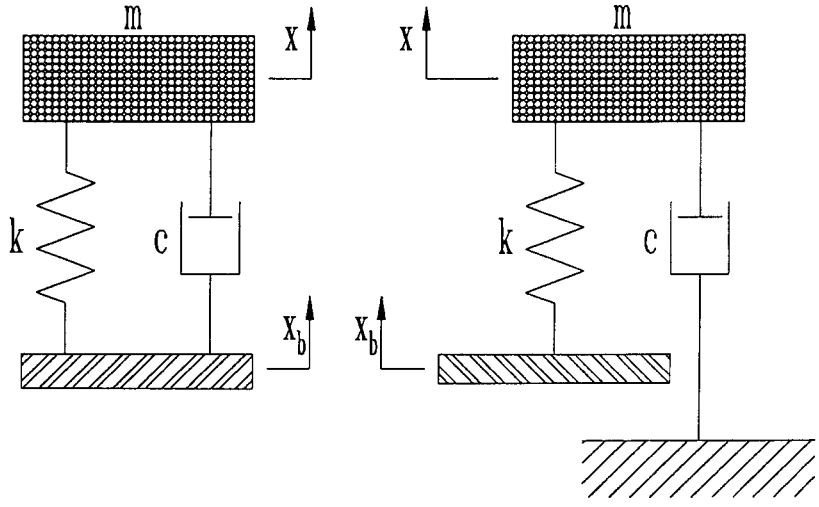

Figure 1.2.1: **Base-excited dynamic system with passive damping (left) and active damping (right)**

The difference between the passive and active systems can best be analyzed by comparing the damper forces of the two systems. The passive damper force F_{DP} is given by the following equation:

$$F_{DP} = c(\dot{x}_b - \dot{x}) \tag{1.2.2a}$$

and the active damper force F_{DA} can be expressed as:

$$F_{DA} = -c\dot{x} \tag{1.2.2b}$$

where $\dot{x}_b$ is the speed of the base and $\dot{x}$ is the speed of the mass.

Equations 1.2.2a and 1.2.2b highlight the important difference between the force characteristics of the two systems. The passive damper force is proportional to the relative speed between the base and the mass, while the active damper force is proportional to the absolute speed of the mass. This difference will inevitably lead to a difference in the vibration transmissibilities of the two systems. The transmissibility TR_P of the passive system in figure 1.2.1 is given by:

$$TR_P = \sqrt{\frac{1+\left(2\xi\frac{\omega}{\omega_n}\right)^2}{\left(1-\left(\frac{\omega}{\omega_n}\right)^2\right)^2+\left(2\xi\frac{\omega}{\omega_n}\right)^2}} \tag{1.2.3a}$$

The transmissibility TR_A of the active system is:

$$TR_A = \frac{1}{\sqrt{\left(1-\left(\frac{\omega}{\omega_n}\right)^2\right)^2 + \left(2\zeta\frac{\omega}{\omega_n}\right)^2}} \qquad \textbf{(1.2.3b)}$$

where ω is the angular frequency of the base disturbance in rad/s, ω_n is the undamped natural angular frequency given by:

$$\omega_n = \sqrt{\frac{k}{m}} \qquad \textbf{(1.2.4)}$$

and ζ is the dimensionless damping ratio:

$$\zeta = \frac{c}{2m\omega_n} \qquad \textbf{(1.2.5)}$$

The transmissibilities of the two systems as given by equations 1.2.3a and 1.2.3b are graphically illustrated in figure 1.2.2. The damping ratios are arbitrarily selected as 5% and 50%, while the undamped natural frequency is 10 Hz and the disturbance frequency band is 1 to 100 Hz.

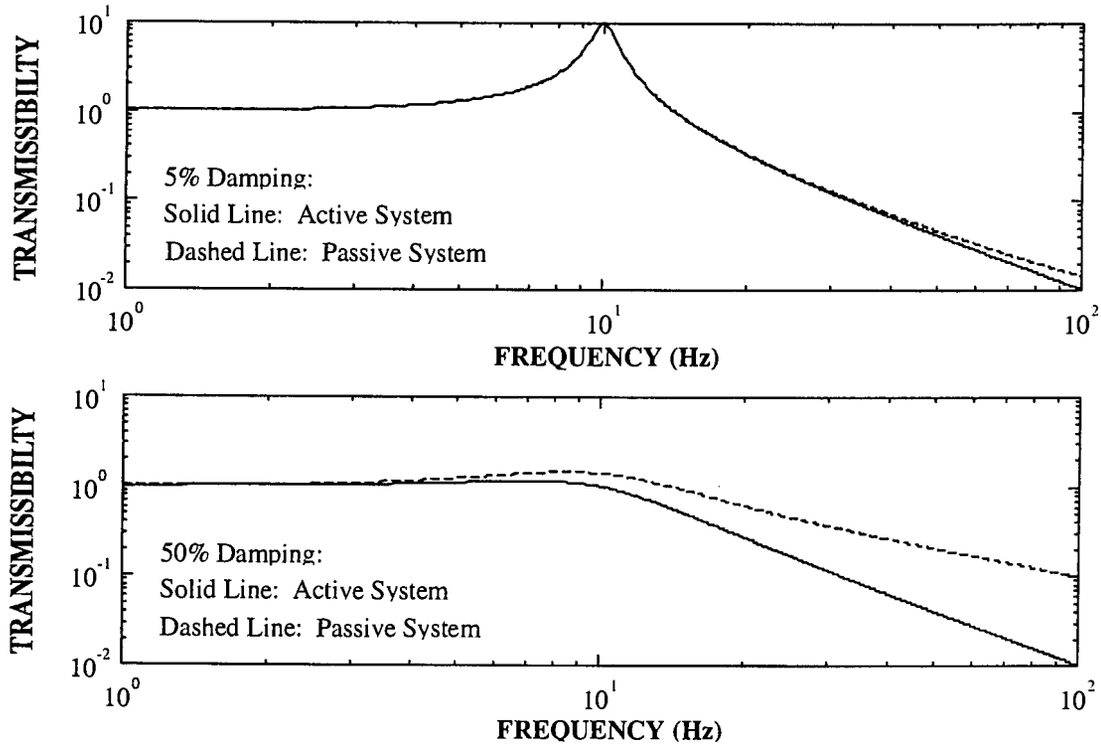

Figure 1.2.2: Passive and active system transmissibilities for a natural frequency of 10 Hz and damping ratios of 5% and 50%

Figure 1.2.2 shows that, in the case of 5% damping, the transmissibilities of the passive and active systems are virtually identical for excitation frequencies from 1 Hz to approximately 30 Hz, but for frequencies above 30 Hz, the transmissibility of the active system is slightly lower. It can therefore be concluded that, at higher frequencies, the active system provides slightly better isolation than the passive system. However, neither system succeeds in lowering the transmissibility peak at resonance (10 Hz).

In the case of 50% damping, there is a significant difference in the transmissibilities of the two systems at frequencies above 3 Hz, and this difference increases with frequency. It can also be seen that the active system gives a lower peak at resonance than the passive system. Furthermore, the active system isolates from 10 Hz upwards, while the passive system only manages to isolate above 14 Hz. Lastly, it can be concluded from figure 1.2.2 that, in order to obtain superior isolation characteristics over a broad frequency band, an active damper with a high damping factor is required.

The above example indicates the differences between passive and active damping. Active damping can be employed to alter the transmissibility of the system, and higher damping factors produce better isolation over a wide frequency band. However, the scope of altering the dynamic behaviour of the system by means of active damping alone is limited because the static transmissibility is constant and cannot be altered to any other desired value (see figure 1.2.2).

Modifying the static transmissibility can for instance be accomplished by applying an external force that is proportional to both the absolute speed and the absolute displacement of the mass, which would necessitate an additional active spring force. The system has the advantage that the transmissibility can be lowered over a wide frequency band without the necessity of a very low isolator spring stiffness. This method is generally applied in active isolation systems. An actuator is used to supply the necessary relative motion between the base and the instrument, thereby adjusting the dynamic characteristics of the system to give the desired isolation.

Judging by the wide-band nature of the disturbance given in figure 1.1.3, passive isolation must be ruled out in favour of active isolation. The latter can be accomplished by various means, i.e. by using hydraulic, electrodynamic, piezo-electric and magnetostrictive actuators. In the next section, four different active isolation methods as possible candidates for LOS stabilization of the optical instrument will be considered and compared. The use of magnetostrictive actuators will be motivated on the basis of performance criteria such as stroke length, frequency response and force output.

1.3 Magnetostrictive active LOS stabilization

It was indicated in the previous section that active vibration isolation is required to stabilize the line of sight of vehicle-mounted optical instruments, which will require actuators powered by an external source. Different types of actuators can be considered for this purpose, such as hydraulic, electrodynamic, piezoelectric and magnetostrictive actuators. Each actuator type works on a different principle and has its own application, advantages and disadvantages. The principles of operation and application of each actuator type will be discussed and compared in this section and

the advantages and disadvantages will be mentioned. The use of magnetostrictive actuators will be motivated for LOS stabilization of the optical instrument.

A hydraulic actuator works on the following principle: A pump supplies hydraulic fluid at a high pressure to an actuator consisting of a cylinder and piston. The fluid exerts a force on the piston and displaces it. The actuator displacement and force are controlled by a hydraulic servovalve which regulates the fluid flow to the cylinder. The actuator performance, expressed in terms of frequency, stroke length and force output, depends on the pump power, the pipe length and diameter, valve inertia, load mass and actuator dimensions such as plunger length and diameter.

An electrodynamic actuator contains a magnetic core and a drive coil wound around the piston of a moving table. A signal generator provides the excitation signal, which is amplified to supply the desired voltage to the coil. The coil induces a magnetic field in the piston and generates a magnetomotive force, which displaces the table. A permanent magnet may be used to provide the magnetic field for excitation forces of up to 200 N, while for higher force requirements an electromagnetic stator assembly is used [Broch, 1984].

Piezoelectric actuators make use of asymmetrical crystalline materials, such as polyvinilidene fluoride (PVDF) and piezoelectric ceramic (PZT), to produce a strain when subjected to an external electric field [Harris, 1988]. For small electrical fields, the strain is proportional to the field, but for larger fields, the strain reaches a saturation point, where an increase in field strength will produce no further increase in strain.

Magnetostrictive actuators require a magnetic field to produce a strain in a ferromagnetic material. The field is supplied by a coil, wound concentrically around a magnetostrictive active rod. When the field is applied, small magnetic domains in the material rotate, causing the rod to expand in the direction of the field [Butler, 1988]. For small fields, the strain is proportional to the field, but when all the domains are aligned, the material becomes magnetically saturated and no further expansion of the rod is possible. However, the saturation strain can be enhanced, by applying a compressive stress to the material. Stresses of up to 65 MPa can be applied [Kvarnsjö, 1993], giving theoretical saturation strains of up to 2000 $\mu\varepsilon$ or 0,2%.

Magnetostrictive materials are mainly rare earth materials, oxides, intermetallic compounds and rapidly quenched amorphous metals. One class of alloys of iron and the rare earth materials terbium (Tb) and dysprosium (Dy) which has become very attractive given its high magnetostriction at room temperatures and above, is $Tb_xDy_{1-x}Fe_{1.9-2}$. This material is better known as Terfenol-D in the commercial market and is currently the most widely used material in magnetostrictive applications. Two versions of Terfenol-D are $Tb_{.27}Dy_{.73}Fe_{1.9-1.95}$ and $Tb_{.3}Dy_{.7}Fe_{1.9-1.95}$, the latter giving higher strains for magnetic field strengths below 1 kOe [Butler, 1988]. The strain versus field strength relationship of $Tb_{.27}Dy_{.73}Fe_{1.9}$ for compressive prestresses of 6,9 MPa to 24,1 MPa is shown in figure 1.3.1.

The range of stroke lengths available from hydraulic actuators is 5,5 μm to 1 m, while that of electrodynamic actuators is 0,3 nm to 20 mm [Broch, 1984]. Magnetostrictive actuator stroke lengths depend on the magnetostrictive strain as well as on the length of the magnetostrictive active rod. A magnetostrictive rod with a length of 100 mm, for instance, can produce a stroke length of 0,2 mm. Piezoelectric actuators deliver strains of 0,02% to 0,06% of their lengths [Van Schoor & Bester, 1992], which is only 10% to 30% of the strains available from magnetostrictive actuators.

Furthermore, piezoelectric actuators may require biasing voltages of up to 300 volts to produce these strains. Magnetostrictive actuators, which may be biased by means of permanent magnets, require 10% or less of the excitation voltage of piezoelectric actuators. However, the high voltage requirement of piezoelectric actuators is not the limiting factor in the choice of a suitable actuator type. (The required voltage increase may for instance be achieved by means of a transformer or a power amplifier). High supply voltages are undesirable in vehicles, mainly due the danger of electrical shock and fires. Therefore, in the interest of safety, supply voltages in vehicle electrical systems are limited to relatively low levels. In the case of military vehicles, for example, the maximum allowable supply voltage is 28 V. Whereas magnetostrictive actuators may meet this safety requirement, piezoelectric actuators may be illegal.

Both magnetostrictive and piezoelectric actuators deliver relatively short stroke lengths compared to those of hydraulic and electrodynamic actuators. Some means of extending the stroke lengths of the former two actuator types is therefore required. Piezoelectric actuators make use of piezostacks to increase the effective actuator length, while magnetostrictive actuators can be equipped with gain mechanisms such as hydraulic or mechanical displacement amplification devices. However, although these measures will give significant improvements, hydraulic and electrodynamic actuators will still deliver far superior stroke lengths.

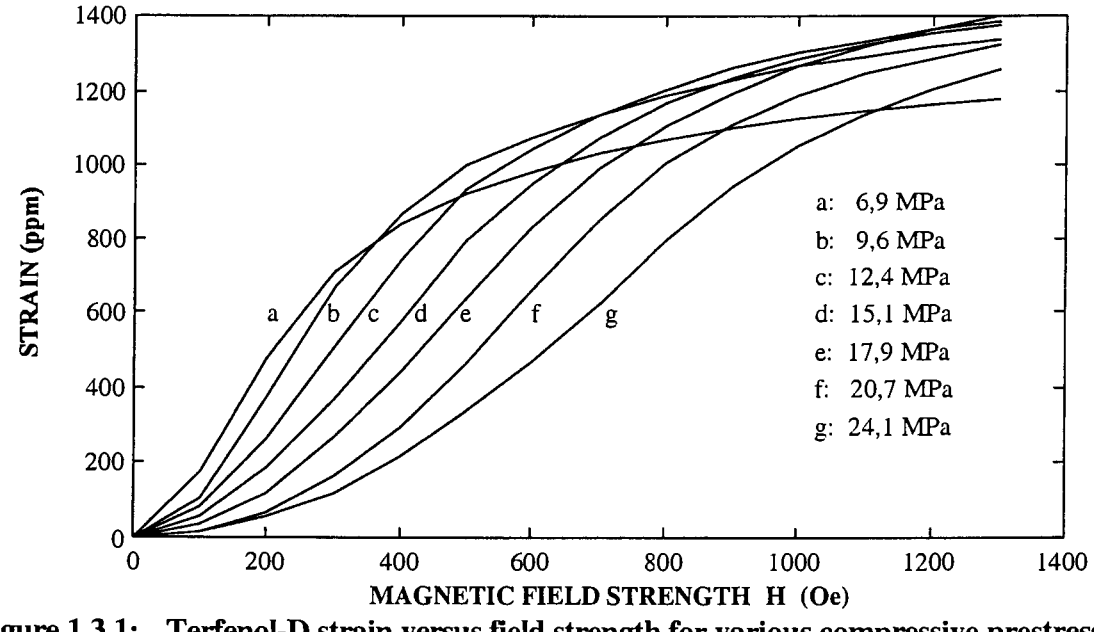

Figure 1.3.1: Terfenol-D strain versus field strength for various compressive prestresses [Butler, 1988]

The frequency range of electrodynamic actuators is 5 Hz to 20 kHz, while hydraulic actuators can be used for frequencies of 0 Hz to 1 kHz [Broch, 1984]. Electrodynamic actuators are generally not recommended for frequencies of lower than 5 Hz because of a danger of coil burnout, while hydraulic actuators are not suitable for frequencies above 70 Hz because hydraulic control valve inertia places a limitation on the reaction speed of the actuator.

The frequency range of magnetostrictive actuators is 0 Hz to 5 kHz, depending on the rod diameter. Larger diameters limit the frequency range due to eddy current losses, but the rods can

be laminated to extend the frequency range [Butler, 1988]. Piezo-electric actuators are capable of very high frequency responses. If the actuator is made up of a single piezofilm, frequencies of up to 1 GHz are attainable, but if piezostacks are used, the increase in actuator mass reduces the natural frequency, thereby narrowing the band significantly. However, frequencies of up to 20 kHz are attainable with piezoelectric actuators.

Another criterion by which the performance of actuators is judged, is output force. Hydraulic, piezoelectric and magnetostrictive actuators are capable of generating larger forces than electrodynamic actuators. Hydraulic actuators rely on the relatively low compressibility of hydraulic fluids to produce a hydrostatic force, while the output forces of piezoelectric and magnetostrictive actuators depend on the cross-sectional area of the actuator, the strain and the elastic modulus of the material.

To summarize the performance capabilities of the different actuator types, figure 1.3.2 gives a simple diagrammatical comparison of the stroke lengths, frequency responses and force outputs of the different actuator types.

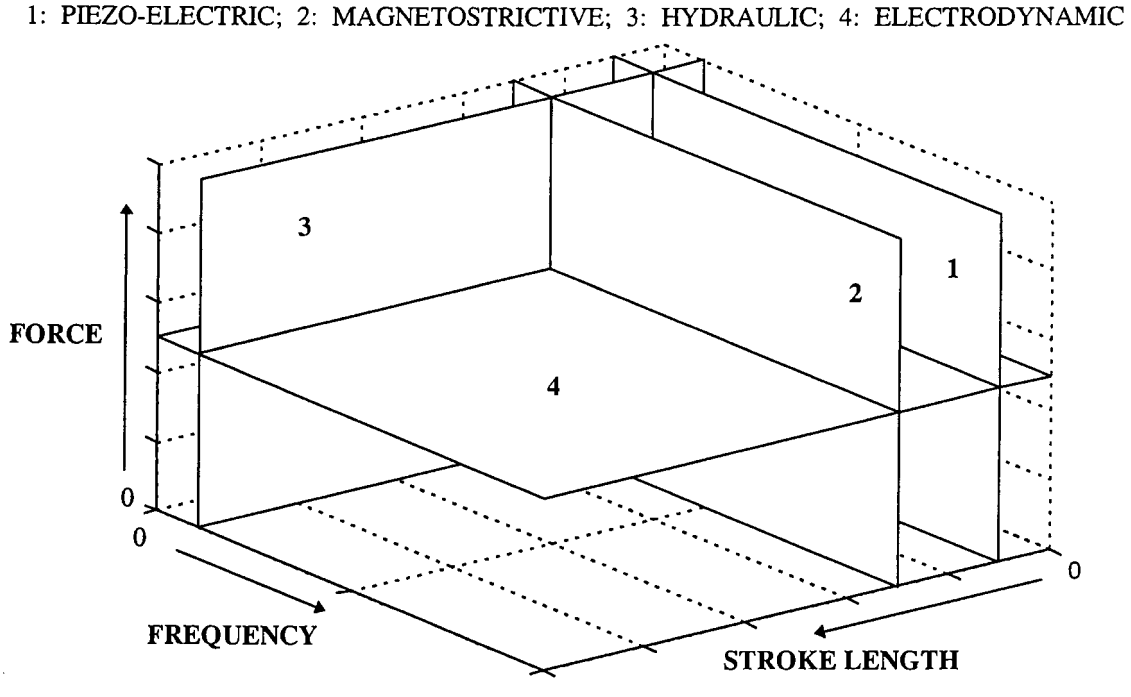

Figure 1.3.2: Comparison of piezoelectric, magnetostrictive, hydraulic and electro-dynamic actuators in terms of stroke length, frequency and force

The information given above can be used to select a suitable actuator type for stabilization of the optical instrument. Firstly, electrodynamic actuators can be ruled out due to their poor low-frequency response. The minimum disturbance frequency is 2,5 Hz (see section 1.1), while the lowest frequency attainable with electrodynamic actuators is 5 Hz.

Secondly, hydraulic actuators are generally not suitable for frequencies above 70 Hz, which are lower than the maximum disturbance frequency, i.e. 500 Hz. Furthermore, hydraulic

actuators require bulky external equipment like pumps, filters, piping and control valves to operate. Due to high pressures, fluid leakage may occur, necessitating periodic replenishment. Periodic flushing and cleaning may also be necessary.

Thirdly, piezoelectric actuators require large amplification (or gain) factors to produce reasonable stroke lengths. A disadvantage of a high gain factor is a reduction in the fundamental natural frequency of the isolation system, which may result in an insufficient isolation bandwidth and an accompanying reduction in actuator stroke at higher frequencies. Furthermore, high gains may cause high stresses in mechanical gain mechanisms. These shortcomings disqualify piezoelectric actuators as a suitable actuator type for LOS stabilization of the optical instrument.

Lastly, magnetostrictive actuators respond over a wide frequency range (0 Hz to 5kHz) and do not require the high excitation voltages of piezoelectric actuators. The stroke length may need amplification, but the gain factor will be smaller than would be required for piezo-electric actuators.

The magnetostrictive gain factor G can be calculated as follows:

$$G = \frac{l\theta}{2\varepsilon_{max} l_T} \tag{1.3.1}$$

where l is the length of the optical instrument, i.e. 250 mm (see section 1.1), θ is the difference between the disturbance angle and the desired LOS angle, i.e. 0,6 mrad, ε_{max} is the maximum magnetostrictive strain and l_T is the active length of the Terfenol-D rod. If the rod length is arbitrarily selected as 35 mm and the maximum allowable strain in the magnetostrictive active rod is 800 $\mu\varepsilon$, which is a conservative value if compared to a theoretical saturation strain of 2000 $\mu\varepsilon$, then the required amplification G, from equation 1.3.1, is 2,7. This is a reasonable gain factor, which can be relatively easily attained.

It can be concluded that magnetostrictive actuators are suitable for LOS stabilization of the optical instrument. The frequency band of the disturbance is within the actuator frequency band and a reasonable gain factor is required to produce the necessary attenuation of the disturbance. In this study, two Terfenol-D actuators will be used to isolate the optical instrument from the base disturbances. The active isolation mechanism is shown in figure 1.3.3.

Figure 1.3.3 shows the vibrating base, the optical element and two actuators, one at each end of the optical element and mounted between the base and the element. Each actuator consists of two Terfenol-D rods, with a coil wound around each rod, a flexible mechanism with a relatively low spring stiffness to act as a mechanical gain mechanism in order to multiply the output displacement of the actuator and, lastly, two coil springs to provide the desired prestress in the rods in order to enhance the saturation strain of the rods. An electronic control system will be used to measure the angular acceleration of the instrument and to control the output force of the actuator accordingly.

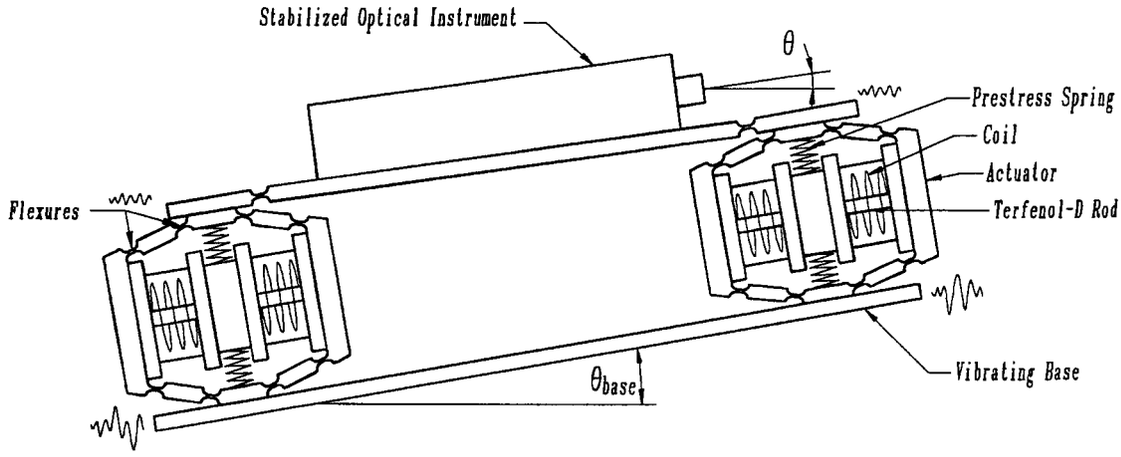

Figure 1.3.3: Magnetostrictive active isolation mechanism

The isolation approach consists of the following four steps: Firstly, a theoretical model, necessary to calculate the desired design input parameters, e.g. actuator size, frequency response and power consumed, is developed. Secondly, the isolators will be built and experimentally validated, and thirdly, the theory will be refined to match the experimental results as closely as needed. Lastly a magnetostrictive system, together with a validated mathematical model, will be demonstrated. To facilitate the work, contributions from related literature by other researchers will be used. The next section is devoted to literature in the field of magnetostriction.

1.4 Magnetostriction literature survey

This section summarizes the relevant work of other researchers in the field of magnetostriction and magnetostrictive applications. The literature survey is done to determine the contribution of these researchers to providing a better understanding of magnetostrictive behaviour, especially as far as the analysis, modelling and design of the magnetostrictive vibration isolation systems are concerned. The applicability of the different literature items to LOS stabilization of the optical instrument will be discussed in short below and the shortcomings will be pointed out.

For the purpose of this study, the available literature in the field of magnetostriction can broadly be classified in two groups, i.e. magnetostrictive material characteristics and magnetostrictive applications. Firstly, literature on material characteristics adresses the dependence of strain and magnetization on the applied field strength, mechanical prestress and temperature, nonlinearities like saturation and hysteresis, mechanical and magnetic biasing and eddy current losses. Secondly, literature on magnetostrictive applications describes, inter alia, vibration and shock isolation, noise cancellation and the design of micropositioners, actuators, resonators and shakers. Literature on magnetostrictive material characterization is discussed in section 1.4.1 and literature on applications in section 1.4.2.

1.4.1 Literature on magnetostrictive material characterization

The characterization, modelling and application of highly magnetostrictive materials are described in the PhD thesis of Kvarnsjö [1993]. A background on the relationship between magnetism and magnetostriction is given in the first chapter. In the second chapter, highly magnetostrictive materials are discussed and special attention is paid to the crystal structure of Terfenol-D, its mechanical properties and temperature dependence of magnetostrictive strain. Static material characterization is done in chapter 3 and linear and nonlinear one-dimensional models are derived in chapter 4. These models are expanded to include multidimensional behaviour and are verified in chapter 5. Chapter 6 is devoted to magnetic circuits, while chapter 7 discusses the application of highly magnetostrictive materials. Conclusions and recommendations on further work are made in chapter 8. A list of 83 references is included. Kvarnsjö's work is particularly useful for the characterization of Terfenol-D and is a valuable tool for the static and dynamic analysis and design of magnetostrictive actuators.

Clark et al [1983] address the influence of stress on magnetostriction and magnetization in rare-earth $Fe_{1.95}$ alloys. Five materials are analyzed over a stress range of 6,9 to 48,3 MPa. It is shown that the shape of the magnetostriction and magnetization curves depend on the relative concentrations of terbium, dysprosium and holmium. Schulze et al [1992] analyze the stress dependence of mechanical coupling, permeability and magnetostriction in $Tb_{0.3}Dy_{0.7}Fe_{1.95}$. The work was done to show how the simultaneous responses of these parameters change with stress and provides guidelines for the design of actuators which retain optimum performance under variable loading.

A finite element analysis of magnetomechanical coupling in magnetostrictive materials is described by Besbes et al [1996]. The finite element method is applied to calculate the magnetic field and mechanical deformation by minimizing the energy functional, which is the sum of the magnetic energy, mechanical energy and work done by external forces. Weak and strong coupling models are discussed in short. The weak coupling model solves the nonlinear magnetic and mechanical equations using an iterative technique, while the strong coupling model solves the nonlinear magnetic and mechanical equations simultaneously using the Newton-Raphson method. Magnetic force is calculated by means of the virtual work principle. The strong coupling model is applied to a simple two-dimensional example and the results are compared with those of the weak coupling model.

A large number of articles on hysteresis modelling of magnetic materials are available. Most of these articles concentrate on Preisach hysteresis models, such as those by Adly et al [1991], Bergqvist & Engdahl [1991], Doong & Mayergoyz [1985], Ossart et al [1995], Restorff et al [1990] and Vajda & Della Torre [1995]. A hysteresis model which makes use of Bessel functions, is presented by Sablik & Jiles [1988], while Rizzoli & Masotti [1995] model the simultaneous effect of hysteresis and saturation using the harmonic balance technique. Leonard et al [1995] describe finite element modelling of hysteresis, while Hall & Flatau [1992] give a much simpler model which makes use of a harmonic function superimposed on the strain curve to include the effect of hysteresis. These models aid in predicting the hysteresis losses during one cycle of static and dynamic excitation.

Clark [1993] investigates the influence of temperatures ranging from 50 K to 250 °C, on the magnetostriction of Terfenol-D and Tb_xDy_{1-x}. Magnetostriction curves are given for two prestresses and for field strengths ranging from 250 Oe to 2000 Oe. It is shown that, for high field

strengths, magnetostriction drops almost linearly with temperature. This article makes the designer aware of the fact that high temperatures must be avoided in magnetostrictive actuators and also quantifies the expected losses.

Sewell and Kuhn [1988] compared different magnetic biasing techniques for Terfenol-D. A magnetic field analysis program utilizing finite element techniques provided solutions that yielded good agreement with measured data. Emphasis was placed on the sensitivity of Terfenol-D to the variation in material properties that can occur under changing conditions of bias field, prestress and drive field. The article provides the designer with different options for magnetic biasing of the magnetostrictive rod.

In a very short article, Butler & Lizza [1987] developed an Eddy current loss factor series for magnetostrictive rods from Kelvin functions of zero order and their derivatives. This model can be used to predict the Eddy current losses for the applicable excitation frequency and rod diameter.

Additional articles on magnetostrictive materials which deserve to be mentioned, discuss magnetostriction in ferromagnetic composites in an elastomer matrix [Bednarck, 1999] and the modelling of large magnetostriction in ferromagnetic shape memory alloys [Likhachev & Ullakko, 2000]. The combination of magnetostrictive characteristics with those of other materials, such as plastics, which display large deformations, and alternative smart materials, which can be used for actuation, are described.

This concludes the discussion of literature on magnetostrictive material characterization. The next section will be devoted to literature on magnetostrictive applications.

1.4.2 Literature on magnetostrictive vibration isolation applications

Five important articles on active vibration and shock isolation are available in the literature. Bryant et al [1993] describe the use of Terfenol with feedback and/or neural network controllers for active vibration control in structures. Tests were performed on a three-legged table, with Terfenol actuators acting as the table legs. The actuators were used to attenuate the vibrations transmitted to the tabletop via the legs. The actuator forces were controlled by a PID controller and a neural network controller. The latter operated on the principle of adaptive back-propagation, which is a fast learning and adaptation algorithm.

Secondly, Hiller et al [1989] describe the attenuation and transformation of vibration through active control of magnetostrictive Terfenol. Experimental results indicate that, if properly controlled, vibration isolation that exhibits significant low-frequency performance and small static deflection can be obtained with magnetostriction.

Reed [1989] reports on the construction of a vibrator using a highly magnetostrictive material. The performance of the vibrator is modelled and verified experimentally. The control system makes use of acceleration feedback to reduce amplification at the mechanical resonance frequency.

In another publication, Reed [1988] describes shock isolation using an active magnetostrictive element. The actuator was modelled and tested and a controller was designed to demonstrate the ability of the actuator to reduce shock levels.

Hall & Flatau [1992] report on the development of a broadband magnetostrictive shaker with a size and mass of only 10% of that of a normal electrodynamic shaker. The frequency band is 300 Hz to 10 kHz and the shaker is capable of producing acceleration amplitudes in excess of 1960 m/s^2 at frequencies greater than 4 kHz with a load mass of 24 gram.

Compact magnetostrictive actuators and linear stepper motors are discussed by Joshi [2000]. Various magnetostrictive materials, together with their saturation strains and Curie temperatures, are listed. Results of strain measurements in TbDyZn (a magnetostrictive alloy) at cryogenic temperatures of 4,2 K and 77 K, are given. A method of obtaining linear motion actuation, by means of a magnetic rod surrounded by an electrical coil, is presented. Applications of linear actuators, such as precision positioning of large adaptive optical surfaces, vibration control, switch and valve operation, are mentioned. Typical response of a small actuator is shown. A digitally controlled, two-mode operation stepper motor with a stroke length of several millimeters, consisting of three magnetostrictive actuators, is discussed and its operation is described.

Certainly one of the most comprehensive publications is the Application Manual for the Design of Etrema Terfenol-D Magnetostrictive Transducers [Butler, 1988]. The manual gives fundamental magnetostrictive relations, like the magnetostrictive coupling coefficient and the eddy current critical frequency, as well as the thermal, mechanical and magnetic properties of Terfenol-D. Design considerations are discussed in full and examples are given for the design of a micropositioner, an actuator, a resonator and an acoustic transducer.

Bond graph models for linear motion magnetostrictive actuators are described by Bryant [1996]. Constitutive equations for strain and magnetic flux density, in terms of field and stress, are given. The Bond graph structure and derivation of the state equations, frequency-domain transfer functions and response, are described. Modelled transfer function spectra are compared with experimentally-determined spectra. Equations for modal vibrations of a magnetostrictive rod are derived in an appendix. The coil voltage to actuator displacement transfer function that is derived, is particularly applicable to this study.

A concise summary of magnetostriction, its principle of operation, modelling of the phenomenon, applications, properties and cost of Terfenol-D are given by Van Schoor et al [1999]. Magnetostrictive actuator modelling techniques are discussed and coil design information is given, together with an SDOF model of an actuator exciting a load mass. Active vibration isolation, passive-active damping and sensor applications are discussed in short. Advantages and disadvantages to be taken into consideration in magnetostrictive actuator design are mentioned.

Additional publications on magnetostrictive applications that also deserve to be mentioned, are the articles on the design and analysis of a self-sensing Terfenol-D actuator [Pratt, 1993], the use of magnetostrictive rods in mechanical applications [Dyberg, 1986], the impedance analysis of an acoustic vibration element [Wakiwaka et al, 1993], the development of a hybrid magnetostrictive and piezo-electric Tonpilz transducer [Butler et al, 1993], the development of an underwater sound transducer [Meeks & Timme, 1977], the silencing of aircraft cabin noise using "antinoise" actuators [Machine Design, April 4, 1994] and magnetostrictive actuation to adjust the shape of an aircraft wing [Ashley, 1998].

The above research provides essential information for the design of a magnetostrictive vibration isolation system. The first five articles in particular cover the control aspect in detail and the models, transfer functions and block diagrams will be necessary aids in the development of a magnetostrictive LOS stabilization system. The Etrema design manual gives indispensible practical and empirical design information, which will be employed in the analysis and design stages of the LOS isolation device. The information given by Van Schoor et al [1999] will serve as a guide to derive the equation of motion and coil current equation of a magnetostrictive actuator. (These equations will be required to investigate the influences of various actuator and coil parameters on actuator performance in the design stage). However, there is one shortcoming in all the articles, namely that no mention is made of any method to stabilize the line of sight of optical instruments.

A current method of sightline stabilization is by means of gyroscopes, as described by Stockum & Carroll [1984]. Gyroscopes make use of gimbals, driven by motors to run at high rotational speeds, to increase the inertia of the system. Unfortunately, gyroscopes are expensive and sensitive instruments, which may not operate smoothly, due to gimbal stiction. The latter phenomenon causes highly nonlinear behaviour, which complicates controller design. The magnetostrictive active LOS stabilization method is a cheaper alternative, which, as will be shown in this study, can be satisfactorily controlled by means of a relatively simple linear controller.

The next section gives a systematic layout of the research and gives an outline of the rest of the thesis.

1.5 Thesis outline

The behaviour of the magnetostrictive active stabilization system is modelled and simulated in chapter 2. The model will serve as a design input and also as an aid in identifying system parameters from experimental test results. The chapter starts with linear and nonlinear models of the magnetostrictive and magnetization characteristics of Terfenol-D, after which a hysteresis model is presented. The equations of motion and coil current equations will subsequently be derived and written in state-space form. A simulation of the behaviour of the actuator will be carried out, which will be followed by a simulation of the behaviour of the system, consisting of the two actuators and optical instrument.

Chapter 3 will be devoted to the design and manufacture of the magnetostrictive actuators, consisting of the Terfenol-D rods, field coils, prestress springs, gain mechanism and support structure of the optical instrument. The information obtained in chapter 2 will serve as design input. Design requirements will be given and design concepts will be generated. The most suitable design concept will be selected. Design calculations will be done for the different system components and safety checks will be included. Design drawings will be made and the actuators and system will be built and assembled.

Experimental evaluation of the stabilization system will be described in chapter 4. The purpose of the tests will be to experimentally determine the system static and dynamic characteristics and to validate and update the model that was developed in chapter 2. The test procedure will be described and test equipment will be discussed. The tests will comprise static and dynamic tests. Static test results will be used to determine the saturation voltages of

the actuators and their linear ranges of operation. Dynamic tests will be carried out to obtain transfer functions between coil input voltage and output angular acceleration of the optical instrument.

Chapter 5 will cover the adjustment of certain model parameters such as natural frequencies, damping factors, input forces and coil current-to-voltage ratios. The purpose will be to generate an improved validated model which can be used with confidence to predict the behaviour of the system and which can be employed to design a suitable controller for the plant. The adjusted parameters will be used to remodel the system behaviour and the results will again be compared with the experimental results.

In chapter 6, a control strategy will be formulated for the plant. Control theory will be discussed, after which optimal and sub-optimal controllers will be designed. Control system stability will be investigated. Control hardware will be described. The controller will be implemented and tested. The test results will be processed, presented and discussed. Isolation system transmissibility will be shown graphically for the disturbance frequency range.

Conclusions which can be derived from the results of this study, will be made in chapter 7 and recommendations will be given about future work in the field of magnetostrictive active stabilization of optical elements.

Chapter 2
Modelling and simulation of magnetostrictive line of sight stabilization system

2.1 Background

In this chapter, the characteristics and behaviour of the magnetostrictive LOS stabilization system, consisting of the two Terfenol-D actuators, the optical instrument and its support structure, are modelled and simulated. The objective of a system model is firstly to obtain a tool for predicting system behaviour before manufacture. The model will give valuable insight into the influence of the linear and nonlinear characteristics of the magnetostrictive active material, i.e. Terfenol-D, on the dynamic properties of the system. Once the material characteristics are known, the linear and nonlinear equations of motion and the coil current equations will be derived. These equations will express the dynamic system behaviour in terms of system parameters such as the Terfenol-D rod diameter and length, actuator displacement gain factor, resistance and inductance of the field coils, mass and damping factors of the actuators and optical instrument.

The model will further be required to write the dynamic equations in state-space form, which is a powerful method of analyzing the coupled mechanical and electrical behaviour of the system. Both linear and nonlinear state-space equations will be derived. In order to facilitate Laplace and frequency domain analysis of the system behaviour, the characteristics will be linearized. The transfer functions (*TF*'s) of the system will subsequently be obtained from the state-space model. A particularly important *TF* which will be derived, is the ratio between the actuator input voltage and instrument angular displacement. In addition, system natural characteristics, such as the natural frequencies, damping factors and resistance to induction ratios of the actuator coils, will be calculated by means of the state-space method. Furthermore, the model will make it possible to simulate system behaviour for arbitrary actuator coil input voltages, like wide-band random voltages.

The model which will be derived in this chapter, will be used in chapter 3 to do a detailed system design. The model will provide a tool to investigate the influences of various design parameters on system performance. The model will for instance be applied to analyze the influence of the number of coil turns and wire thickness on the resistance to inductance ratio of the coil, and also to calculate the effect of different displacement gain factors on the output displacement of the optical instrument.

A further reason for modelling the system characteristics and behaviour, is to obtain a model with which system parameters can be extracted, or identified, from measured data during the experimental evaluation phase. The test data will typically contain measured spectra between coil input voltage and instrument angular acceleration. From these results, natural frequencies and damping factors, as well as coil characteristics will be determined by matching the measured values with the parameters in the model. The extracted parameters will then indicate the degree of accuracy of the initial model, and will also provide an indication of how the model can be adjusted and updated to give a closer representation of the measured behaviour. Identification and updating of the system parameters will be done in chapter 5.

Lastly, the model will be required for control system design purposes. In order to design a suitable controller, *TF* and state-space models of the uncontrolled system (plant) are required to predict the behaviour and characteristics of the controlled system. The models will be applied to determine, inter alia, feedback and feedforward gain matrices. Once the gains are known, behaviour of the controlled system will be simulated and experimentally evaluated. Control system design and testing will be done in chapter 6.

Modelling and simulation of the system characteristics and behaviour will be systematically done in the following sections of this chapter. The magnetostrictive and magnetization characteristics of Terfenol-D will be modelled in sections 2.2 and 2.3. In this study, material characteristics are classified in two groups, i.e. saturation characteristics and hysteresis characteristics. Saturation characteristics will be covered in detail in section 2.2, while section 2.3 will cover hysteresis characteristics.

The equation of motion of a magnetostrictive actuator, in isolation of the rest of the system, will be derived from first principles in section 2.4. This will be done for both linear and nonlinear material properties. For the sake of simplicity, it will be assumed that the actuator has only one degree of freedom. The coil current equation, a differential equation (DE) which expresses the current in the coil wire in terms of the actuator output speed and input voltage, will also be derived from first principles.

In section 2.5, the equation of motion and the coil current equation of the actuator will be coupled to give a single set of dynamic actuator equations in state-space form. The linear and nonlinear state and output equations will be derived in detail. The Laplace and frequency domain transfer functions will be obtained from the linear state-space model.

Natural vibration behaviour of the actuator will be covered in section 2.6. The natural characteristics, i.e. the natural frequency, damping factor and effective resistance to inductance ratio of the coil will be expressed in terms of the eigenvalues of the state-space model and poles of the Laplace-domain transfer function.

Forced behaviour of the actuator will be simulated in section 2.7. Nonlinear behaviour will be simulated first, whereafter the average values of the magnetostrictive parameters will be calculated from the nonlinear solution. These parameters will then be employed to do a linear frequency domain simulation of the actuator behaviour.

In the last section of the chapter, section 2.8, behaviour of the entire system, consisting of the two actuators, the optical instrument and its support structure, will be modelled. The linear actuator model developed in section 2.7, will be coupled to those of the optical instrument and its support structure by means of the Rayleigh-Ritz method. The system state-space model and *TF*'s will be derived. Frequency domain *TF* magnitudes and phase angles will be shown graphically.

2.2 Magnetostrictive and magnetization characteristics of Terfenol-D

This section covers the linear and nonlinear magnetostrictive and magnetization characteristics of Terfenol-D. A background on the sources of nonlinear behaviour in Terfenol-D, i.e. saturation and hysteresis, is given. The nonlinear strain and flux density characteristics are shown graphically, and the influence of stress and field on the saturation properties is discussed. Regression equations are given which closely represent the characteristics. The need for linearization is pointed out and the characteristics are linearized. The linear magnetostrictive and magnetization parameters, i.e. Young's Modulus, the strain constant, piezomagnetic cross-coupling constant and permeability are defined, expressed mathematically and shown graphically. An inverse characteristic, with stress as a function of field, is also presented.

Terfenol-D displays magnetostrictive and magnetization saturation and hysteresis characteristics. When a magnetic field is applied to a Terfenol-D rod, small domains in the material rotate, causing the rod to expand in the direction of the field. For small fields, the strain is proportional to the field, but when all the domains are aligned, the material is magnetically saturated and no further elongation of the rod is possible. A similar phenomenon occurs in the magnetization characteristic of Terfenol-D. When a small field is applied, the increase in magnetic flux density will initially be proportional to the increase in field strength, but when the material becomes magnetically saturated, any further increase in field strength will produce no further increase in flux density.

Magnetostrictive hysteresis in Terfenol-D is explained as follows: If an increasing magnetic field is applied to a demagnetized Terfenol-D rod, the rod will produce an increase in strain. The strain versus field characteristic for the increasing field is known as the loading characteristic. If the field is subsequently removed, the strain will be reduced. However, the rod remains partially magnetized. The characteristic for a decreasing field, or the unloading characteristic, therefore differs from the loading characteristic. If a cyclic field is applied to the rod, an energy loss occurs during every cycle. The magnitude of the loss depends on the initial field and strain, mechanical stress and field strength.

In general, nonlinear systems display phenomena which are not encountered in linear systems, like amplitude-dependent natural frequencies and damping factors, and sub- and superharmonics. As a result, special mathematical techniques are required to describe nonlinear system behaviour, such as the perturbation method, the method of slowly varying amplitude and phase and the describing function method. The mathematical analysis is further complicated if a nonlinearity is discontinuous, because the characteristic is not differentiable at reversal points between loading and unloading characteristics. This type of nonlinearity is appropriately known as a "hard nonlinearity" [Slotine & Li, 1991]. Examples of a hard nonlinearities are hysteresis, backlash, Coulomb friction and dead bands.

Only a few mathematical methods can be applied to analyze the behaviour of systems with hard nonlinearities. One method that is often used for the design of nonlinear control systems, is the describing function (DF) method [Gelb & Vander Velde, 1968]. This method can predict, inter alia, the response of nonlinear systems to sinusoidal inputs. Only the first harmonic component of the system behaviour is taken into account and superharmonics are neglected.

Linear system analysis, on the other hand, is comparatively simple. Characteristics of linear systems, like eigenvalues, eigenvectors, natural frequencies, damping factors and Laplace- and frequency domain transfer functions, are mostly relatively easy to obtain. For this reason, linearization of nonlinear systems is recommended in order to simplify the mathematical analyses.

However, the application of linear system analysis to nonlinear system behaviour may be inadequate. Although linearization may be accurate in a limited working range, it may be inaccurate in the nonlinear or saturation range [Slotine & Li, 1991]. Furthermore, if a control system is designed with parameters obtained from a linear system analysis, poor control performance and system instability may result. In order to design a system which will perform equally well in its linear and nonlinear ranges, it will be necessary to take the effects of nonlinearities into account.

This can be done in more than one way. Firstly, a purely nonlinear analysis can be done where the magnetostrictive and magnetization properties are evaluated at each input field strength. The change in strain per unit change in field strength will not be constant, but will be a function of the momental field. The advantage of this method is that behaviour can be described with a high degree of accuracy. The disadvantage, however, is that the analysis can become extremely complex.

Secondly, the analysis can be carried out by assuming linear behaviour over the excitation range, i.e. the slope of the strain versus field characteristic is assumed constant over the applicable range of behaviour. If the range changes, the slope of the characteristic changes. Nonlinearities are therefore described as range-dependent linearities. This approach is favoured for the advantages it offers in terms of simplified mathematical operations, but may not be as accurate as the nonlinear analysis, due to the fact that sub- and superharmonics are neglected.

In order to analyze and design the system, it is clear from the above paragraphs that both the linear and nonlinear magnetostriction and magnetization characteristics of Terfenol-D are required. These characteristics will enable the designer to obtain the saturation field and proportionality constant between field and strain, to determine to what extent hysteresis will affect actuator performance and to determine whether the input field strength will be sufficient to produce the desired stroke length. The magnetostrictive and magnetization characteristics of Terfenol-D are discussed next.

Strains in magnetostrictive materials are produced by two sources, i.e. a magnetic field and a mechanical stress. A magnetic field rotates the magnetic domains in the material to produce a strain, while a mechanical stress causes an elastic deformation of the material. When both a magnetic field and a mechanical stress are applied, the resultant strain is a combined effect of those of field and stress. Mathematically, strain can be expressed as follows:

$$\varepsilon = \varepsilon(\sigma, H) \qquad \textbf{(2.2.1)}$$

where ε is strain, σ is mechanical stress and H is field strength.

Magnetostriction is also a phenomenon where the combined effect of the application of a mechanical stress and a magnetic field causes a change in magnetic induction (or magnetic flux, magnetization) of a ferromagnetic material [Harris, 1988].

Flux density can therefore, as in the case with material strain, be mathematically expressed as a function of stress and field strength:

$$B = B(\sigma, H) \tag{2.2.2}$$

where B is flux density.

The magnetostrictive and magnetization characteristics will respectively be discussed in sections 2.2.1 and 2.2.2. In both sections, the general nonlinear characteristics will be given first, followed by the linear characteristics. Hysteresis effects on the magnetostrictive and magnetization characteristics will be discussed in section 2.3.

2.2.1 Magnetostrictive characteristics of Terfenol-D

This section covers the linear and nonlinear magnetostrictive characteristics of Terfenol-D. The nonlinear strain characteristics are shown graphically, and the influence of stress and field on the saturation properties is discussed. A two-dimensional regression equation is given which closely represents published characteristics. The characteristics are linearized and the linear magnetostrictive parameters, i.e. Young's Modulus and the strain constant are defined, expressed mathematically and shown graphically. An inverse characteristic, where stress is a function of field, is also presented.

There have been many efforts by researchers to obtain the linear and nonlinear characteristics of Terfenol-D. Consequently, a vast number of applicable data sources exist, such as those by Kvarnsjö [1993], Clark & Savage [1983], Clark et al [1983], Clark et al [1990] and Schulze et al [1992]. Kvarnsjö [1993] gives a complete set of strain versus field strength curves for 10 constant compressive stresses. Clark & Savage [1983] discuss the magnetostriction of rare earth-Fe_2 compounds under compressive stress, while Clark et al [1983] describe the effect of stress on the magnetostriction and magnetization of rare-earth $Fe_{1.95}$ alloys. Schulze et al [1992] analyze the stress-dependence of mechanical coupling, permeability and magnetostriction in $Tb_{0.3}Dy_{0.7}Fe_{1.95}$, while Clark et al [1990] characterize the magnetomechanical coupling in Bridgman-grown $Tb_{0.3}Dy_{0.7}Fe_{1.9}$ at high drive levels.

The magnetostrictive characteristics which will be used in this study, will be obtained from data supplied by Kvarnsjö [1993] and Clark & Savage [1983]. Kvarnsjö [1993] gives a complete set of strain vs mechanical stress and magnetic field curves. The stress range is -65 MPa to -1 MPa and the field strength range is 0 to 2600 Oe (207 kA/m). These strain curves supply a powerful tool for the mathematical analysis of the magnetostrictive characteristics. Two-dimensional interpolation can be applied to the data to obtain functional relationships between stress, field and strain. Furthermore, the mathematical function thus obtained can be differentiated with respect to field and stress to give the strain constant and Young's Modulus respectively.

The data supplied by Clark & Savage is particularly useful for studying the saturation properties of Terfenol-D for various compressive stresses. Although not as complete as the data supplied by Kvarnsjö, the strain curves facilitate the comparison of the saturation characteristics for different stresses. This is accomplished by normalizing the strain curves with respect to stress at zero field strength, in other words, at zero field, the strain is zero for all the stresses. The strain characteristics as supplied by Kvarnsjö [1993] and the normalized strain characteristics as supplied by Clark & Savage [1983] are shown in figure 2.2.1.1 and figure 2.2.1.2 respectively.

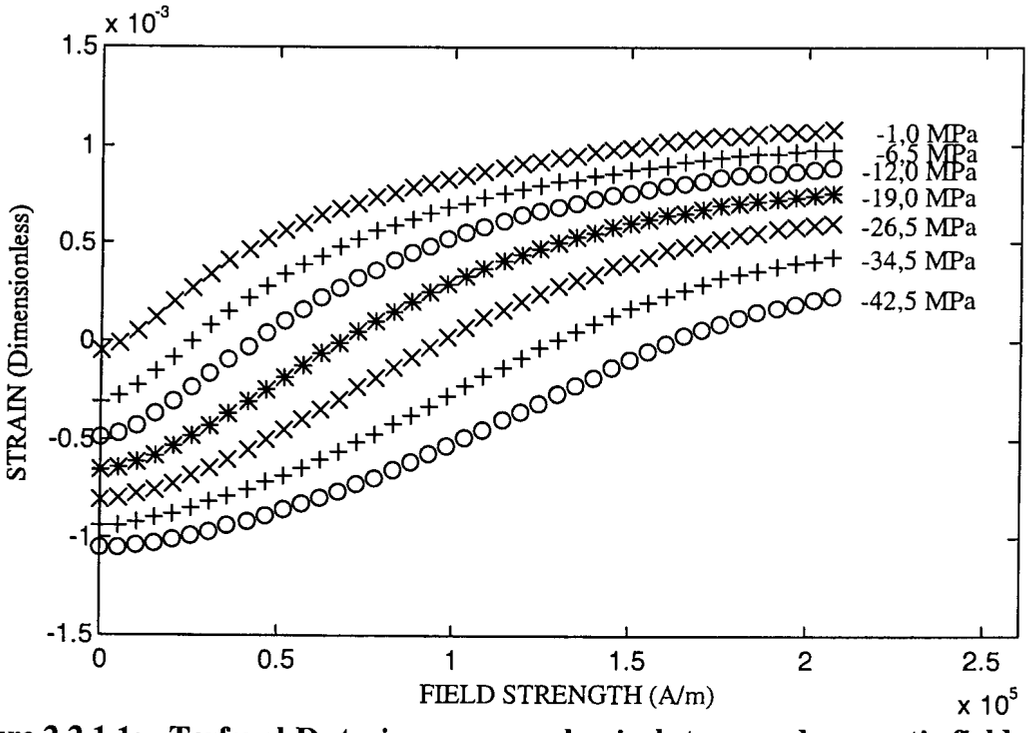

Figure 2.2.1.1: Terfenol-D strain versus mechanical stress and magnetic field strength [Kvarnsjö, 1993]

Figure 2.2.1.1 shows strain versus magnetic field for seven constant compressive stresses. The stresses range from -42,5 MPa to -1 MPa and the field strengths range from 0 to 207 kA/m. It can be seen from figure 2.2.1.1 that strain increases with magnetic field strength and also with mechanical stress. For low compressive stresses, the strain curves initially rise sharply with field, but saturate at relatively low fields and strains. As the compressive stress is increased, the curves do not initially rise as sharply as in the case of low compressive stresses, which implies that higher compressive stresses necessitate larger field strengths to produce the same strain. Also, at higher compressive stresses, the strains saturate at higher field strengths. Although a qualitative analysis of the saturation characteristics of Terfenol-D can be done by means of figure 2.2.1.1, a more complete quantitative analysis can be done by means of figure 2.2.1.2.

Figure 2.2.1.2 shows the normalized strain versus magnetic field for seven constant compressive stresses. The compressive stresses range from 6,9 MPa to 24,1 MPa and the field strengths range from 0 to 1250 Oe (approximately 100 kA/m). The strains at zero field strength are zero for all the stresses. Figure 2.2.1.2 is mainly used to study the magnetostrictive saturation properties of Terfenol-D. It can be seen that, for low stresses, the

strain curves initially rise sharply with field, but saturate at relatively low fields. It can also be seen that the strain curves do not reach sudden saturation points, but that the slopes of the curves gradually drop and eventually decay to zero. The saturation fields and strains are therefore not clearly demarcated.

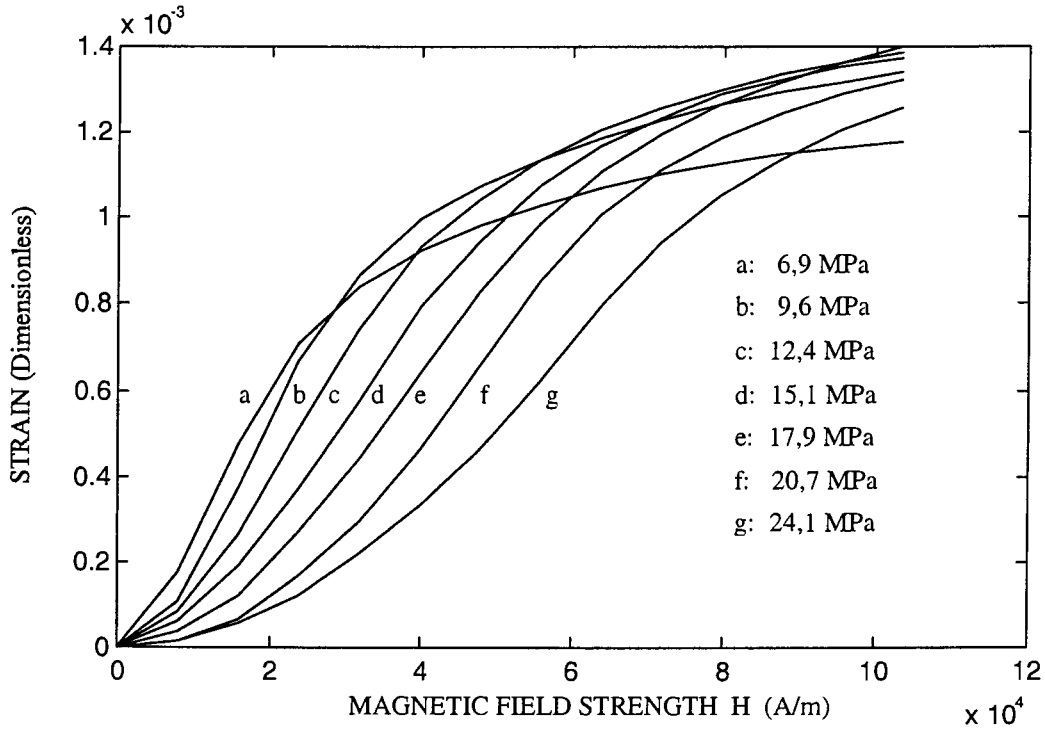

Figure 2.2.1.2: Normalized Terfenol-D strain versus mechanical stress and magnetic field strength [Clark & Savage, 1983]

In order to determine the particular saturation strain and field for a given stress, subjective judgment is needed. Consider, for example, the strain curve for a 6,9 MPa compressive stress (curve a). It can be judged that saturation sets in at 30 kA/m, where the corresponding strain is $0{,}8.10^{-3}$, and that full saturation is reached at a field strength of 100 kA/m, where the strain is $1{,}15.10^{-3}$. As another example, consider the strain curve for a 17,9 MPa compressive stress (curve e). Saturation sets in at 60 kA/m, where the strain is 1.10^{-3}, while at 100 kA/m, where the strain is $1{,}4.10^{-3}$, full saturation has not yet been reached. It can be concluded that the saturation strain can be greatly enhanced by applying higher compressive stresses, but that higher field strengths are required to produce the higher saturation strains. Generally speaking, the higher the compressive stress, the higher the saturation strain. According to Kvarnsjö [1993], a saturation strain of up to 2.10^{-3} is possible with a compressive stress of 65 MPa.

The magnetostrictive strain and saturation characteristics of Terfenol-D have been presented in graphical form in the foregoing paragraphs. The need however also exists for a mathematical function which will express the strain in terms of the mechanical stress and magnetic field. The function will enable the designer of a magnetostrictive actuator and LOS stabilization system to calculate the strain in a Terfenol-D rod for any given stress and field. Furthermore, the function will make it possible to simulate the behaviour of the actuator and system for continuously varying stresses and field strengths. To obtain this function, a

technique is required which will transform the graphical data to a mathematical equation. Such techniques are known in mathematical terms as data regression or data fitting methods.

Several regression techniques can be employed to obtain the desired mathematical function. Firstly, a one-dimensional least-squares nonlinear function can be fitted to the data to obtain strain in terms of field strength for a constant stress. A large number of function types can be used for this purpose, such as polynomial functions, piecewise linear functions and saturating functions. An example of a saturating function for strain in terms of field is given in equation 2.2.1.1:

$$\varepsilon(H)\Big|_{\sigma=const} = \sum_{i=0}^{m} a_i \left[\tanh\left(\frac{\pi H}{H_{sat}} \right) \right]^i \qquad \textbf{(2.2.1.1)}$$

where ε is the strain, H is the field, H_{sat} is the saturation field and σ is the stress. a_i are polynomial constants which depend on the order m of the data fit, as well as on the value of σ. The advantage of this method of data regression is that a high degree of accuracy can be obtaned with a relatively low order of m. The disadvantage is that strain is expressed as a function of field only, and no account is taken of the effect of stress. In order to describe the simultaneous relationship between strain, stress and field, a functional relationship for a_i in terms of stress is required. The one-dimensional nonlinear function is therefore not as simple to apply as was initially intended, and it becomes clear that an alternative technique of data regression will have to be considered.

One such technique is a two-dimensional polynomial data fit. This data regression technique is described in more detail by, inter alia, Hayes [1970]. The method is simpler to apply due to the fact that strain can be expressed as a single function of stress and field. This will facilitate the strain calculation, as well as the derivation of the magnetostrictive constants, i.e. Young's Modulus and the strain constant. The disadvantage of the method is that higher order polynomials are generally required to represent the data fairly accurately. However, this method is preferred to the one-dimensional data fit because of its simplicity of use. The following equation expresses strain as a two dimensional polynomial function of stress and field:

$$\varepsilon(\sigma, H) = \sum_{i=0}^{m} \sum_{j=0}^{n} p_{ij} \sigma^j H^i \qquad \textbf{(2.2.1.2)}$$

where ε is strain, σ is mechanical stress and H is magnetic field strength. m is the order of the polynomial for strain as a function of field and n is the order of the polynomial for strain as a function of stress. p_{ij} are the two-dimensional polynomial coefficients which will give the most accurate approximation to the data for the applicable values of m and n.

Note that in equation 2.2.1.2, stress is of the order of 10^6 Pa, and field is of the order of 10^5 A/m. Products of high order polynomials of stress and field, such as those in equation 2.2.1.2, may therefore be quite large quantities, which may be difficult to calculate and to handle numerically. To avoid the problem of having to deal with unnecessarily large numbers,

it is convenient to scale stress by a factor 10^6 Pa and field by a factor 10^5 A/m, as follows:

$$\varepsilon(\sigma,H)=\sum_{i=0}^{m}\sum_{j=0}^{n}p_{ij}\left(\frac{\sigma}{10^6}\right)^j\left(\frac{H}{10^5}\right)^i \qquad \textbf{(2.2.1.3)}$$

where σ is in Pa and H is in A/m. The order of the polynomial and its influence on the accuracy of the data fit deserve to be mentioned here. Generally, higher values of m and n will give higher accuracy. It was found that values of $m=8$ and $n=4$ gave sufficient accuracy for the strain data supplied by Kvarnsjö [1993]. The values of p_{ij} for $m=8$ and $n=4$ are shown in table 2.2.1.1. The coefficients are truncated after four digits.

Table 2.2.1.1: Two-dimensional polynomial coefficients p_{ij} for strain as a function of mechanical stress and magnetic field

j / *i*	0	1	2	3	4
0	$-1{,}6347.10^{-7}$	$5{,}7158.10^{-5}$	$1{,}7481.10^{-6}$	$3{,}5580.10^{-8}$	$2{,}8999.10^{-10}$
1	$5{,}9733.10^{-4}$	$1{,}2848.10^{-4}$	$1{,}0642.10^{-5}$	$3{,}4613.10^{-7}$	$3{,}7434.10^{-9}$
2	$6{,}2387.10^{-3}$	$-8{,}6155.10^{-4}$	$-1{,}1545.10^{-4}$	$-4{,}1127.10^{-6}$	$-4{,}5506.10^{-8}$
3	$-2{,}0391.10^{-2}$	$1{,}7893.10^{-3}$	$3{,}2207.10^{-4}$	$1{,}2486.10^{-5}$	$1{,}4402.10^{-7}$
4	$3{,}0809.10^{-2}$	$-1{,}9773.10^{-3}$	$-4{,}4307.10^{-4}$	$-1{,}8152.10^{-5}$	$-2{,}1542.10^{-7}$
5	$-2{,}6232.10^{-2}$	$1{,}3023.10^{-3}$	$3{,}4734.10^{-4}$	$1{,}4739.10^{-5}$	$1{,}7806.10^{-7}$
6	$1{,}2855.10^{-2}$	$-5{,}1776.10^{-4}$	$-1{,}5876.10^{-4}$	$-6{,}8867.10^{-6}$	$-8{,}4052.10^{-8}$
7	$-3{,}3814.10^{-3}$	$1{,}1583.10^{-4}$	$3{,}9542.10^{-5}$	$1{,}7379.10^{-6}$	$2{,}1320.10^{-8}$
8	$3{,}6962.10^{-4}$	$-1{,}1295.10^{-5}$	$-4{,}1571.10^{-6}$	$-1{,}8402.10^{-7}$	$-2{,}2615.10^{-9}$

The accuracy of the data fit can be evaluated by comparing the strains calculated with equation 2.2.1.3, with the strains given in figure 2.2.1.1. The strains are calculated for seven compressive stresses in a range of -42,5 MPa to -1 MPa and for a field strength range of 0 to 207 kA/m. The calculated strains and the data as supplied by Kvarnsjö [1993] are shown in figure 2.2.1.3.

Figure 2.2.1.3 shows that, for the tabulated values of p_{ij} in table 2.2.1.1, the strains calculated with equation 2.2.1.3 compare favourably with the data as supplied by Kvarnsjö [1993]. The root mean square (RMS) error of the regression equation is 3,03% for a stress range of -42,5 MPa to -1 MPa and for a field range of 0 to 207 kA/m. It can therefore be concluded that the regression equation closely represents the published data.

Thus far in section 2.2.1, extensive attention has been paid to the nonlinear magnetostriction characteristics of Terfenol-D. The above information can however only be applied to do nonlinear analyses of the behaviour of a magnetostrictive actuator and LOS stabilization system, but is insufficient to analyze linear behaviour. The questions that now arise are: How and to what extent can the magnetostrictive characteristics of Terfenol-D be linearized, and how can the linear magnetostrictive parameters, i.e. Young's Modulus and the strain constant, be calculated. These questions will be answered in the following paragraphs.

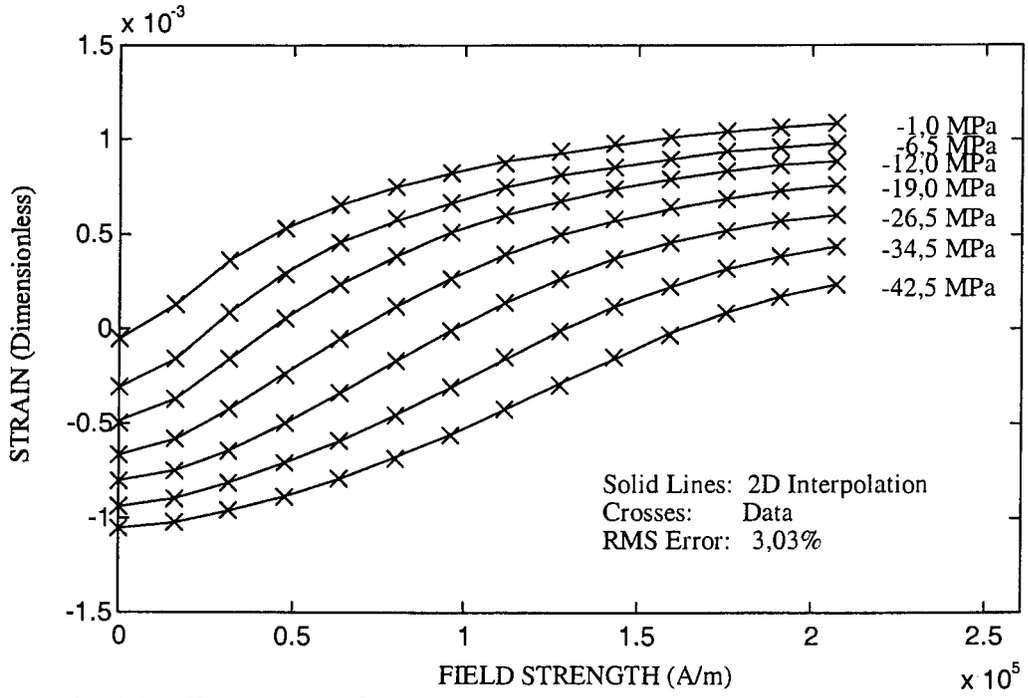

Figure 2.2.1.3: Comparison between calculated Terfenol-D strain and data

Linear magnetostrictive characteristics of Terfenol-D

Equation 2.2.1.3 expressed strain as a nonlinear, two-dimensional polynomial function of stress and field and table 2.2.1.1 gave the polynomial coefficients. The linear characteristics are much simpler in the sense that strain is assumed to be directly proportional to both stress and field. Mathematically, the strain characteristic can be expressed as follows as a linear combination of stress and field:

$$\varepsilon(\sigma, H) = \frac{\sigma}{E} + d^H H \qquad \textbf{(2.2.1.4)}$$

where E is Young's modulus and d^H is the piezomagnetic cross-coupling constant, also known as the magnetostrictive strain constant. The first term on the right hand side of equation 2.2.1.4, i.e. σ/E, describes the linear relationship between strain and stress at a constant field strength, while the second term $d^H H$, gives the linear relationship between strain and field strength at a constant stress.

In order to do a proper analysis of the linear behaviour of a magnetostrictive actuator and LOS stabilization system, mathematical expressions and graphs of Young's Modulus and the strain constant will be required. Mathematical expressions for E and d^H will subsequently be derived and shown graphically.

Young's Modulus can be defined as the change in mechanical stress per unit change in strain, at a constant magnetic field strength. Mathematically, E can be described as the reciprocal of

the partial derivative of strain with respect to stress, at a constant field:

$$E(\sigma,H)=\frac{1}{\left.\frac{\partial\varepsilon(\sigma,H)}{\partial\sigma}\right|_{H=const}}=\frac{10^6}{\sum_{i=0}^{m}\sum_{j=1}^{n}p_{ij}j\left(\frac{\sigma}{10^6}\right)^{j-1}\left(\frac{H}{10^5}\right)^{i}} \qquad \textbf{(2.2.1.5)}$$

where $\varepsilon(\sigma,H)$ is given by equation 2.2.1.2 and p_{ij} are the polynomial coefficients as given by table 2.2.1.2. Young's Modulus versus stress and field is shown graphically in figure 2.2.1.4. The stress range is -26,5 MPa to -1 MPa and the field range is 0 to 100 kA/m.

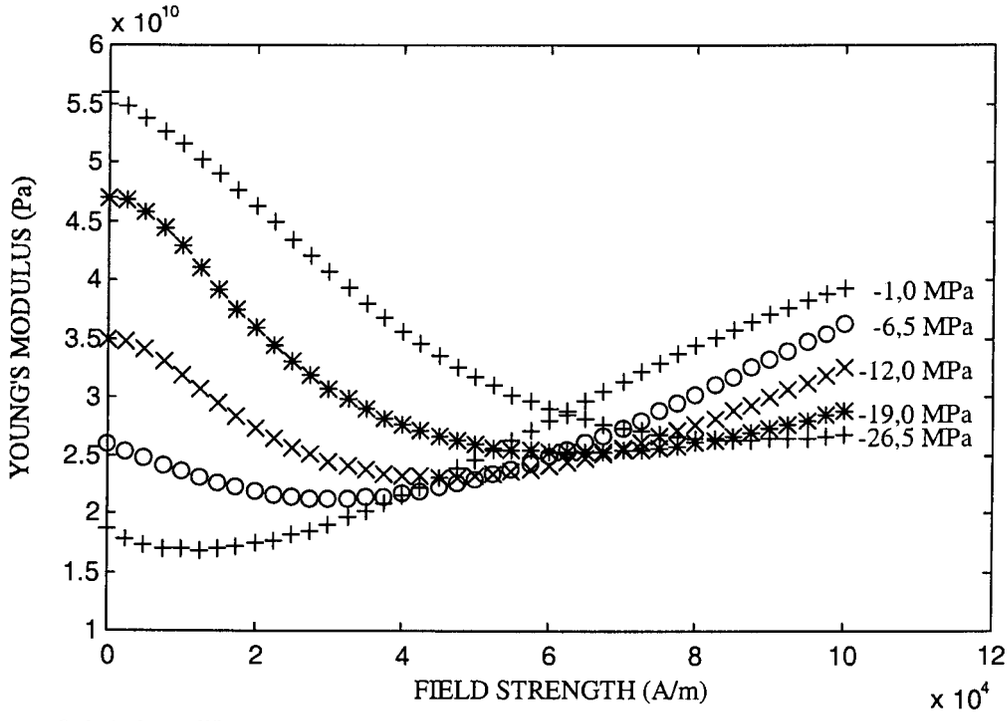

Figure 2.2.1.4: Young's Modulus of Terfenol-D versus mechanical stress and magnetic field strength

The following observations can be made from figure 2.2.1.4: At low field strengths, Young's Modulus increases with a decrease in stress, and the variation in E is relatively high. At zero field strength E varies from approximately 18 GPa for a compressive stress of 1 MPa, to approximately 56 GPa for a compressive stress of 26,5 GPa. As the field increases, the variation in E diminishes. At a field strength of 60 kA/m, the variation in E is at a minimum, i.e. approximately 5 to 6 GPa, and at this field strength it can be assumed that E is relatively independent of stress. As the field is increased beyond 60 kA/m, Young's Modulus increases with an increase in stress, and the variation in E reaches a maximum of approximately 14 GPa at a field of 100 kA/m.

A mathematical expression for Young's Modulus has been obtained by means of partial differentiation of strain with respect to stress. E has been shown graphically for a stress

variation of -26,5 MPa to -1 MPa and a field variation of 0 to 100 kA/m. A similar procedure can be followed to obtain the strain constant in terms of stress and field.

The strain constant d^H can be defined as the change in strain per unit change in magnetic field strength at a constant mechanical stress. Mathematically, d^H can be described as the partial derivative of strain with respect to field at a constant stress:

$$d^H(\sigma,H)=\left.\frac{\partial\varepsilon(\sigma,H)}{\partial H}\right|_{\sigma=const}=10^{-5}\sum_{i=1}^{m}\sum_{j=0}^{n}p_{ij}i\left(\frac{\sigma}{10^6}\right)^j\left(\frac{H}{10^5}\right)^{i-1} \qquad \textbf{(2.2.1.6)}$$

where $\varepsilon(\sigma,H)$ is given by equation 2.2.1.2 and p_{ij} are the polynomial coefficients as given by table 2.2.1.2. The strain constant versus stress and field, according to equation 2.2.1.6, is shown graphically in figure 2.2.1.5. The stress range is -26,5 MPa to -1 MPa and the field range is 0 to 100 kA/m.

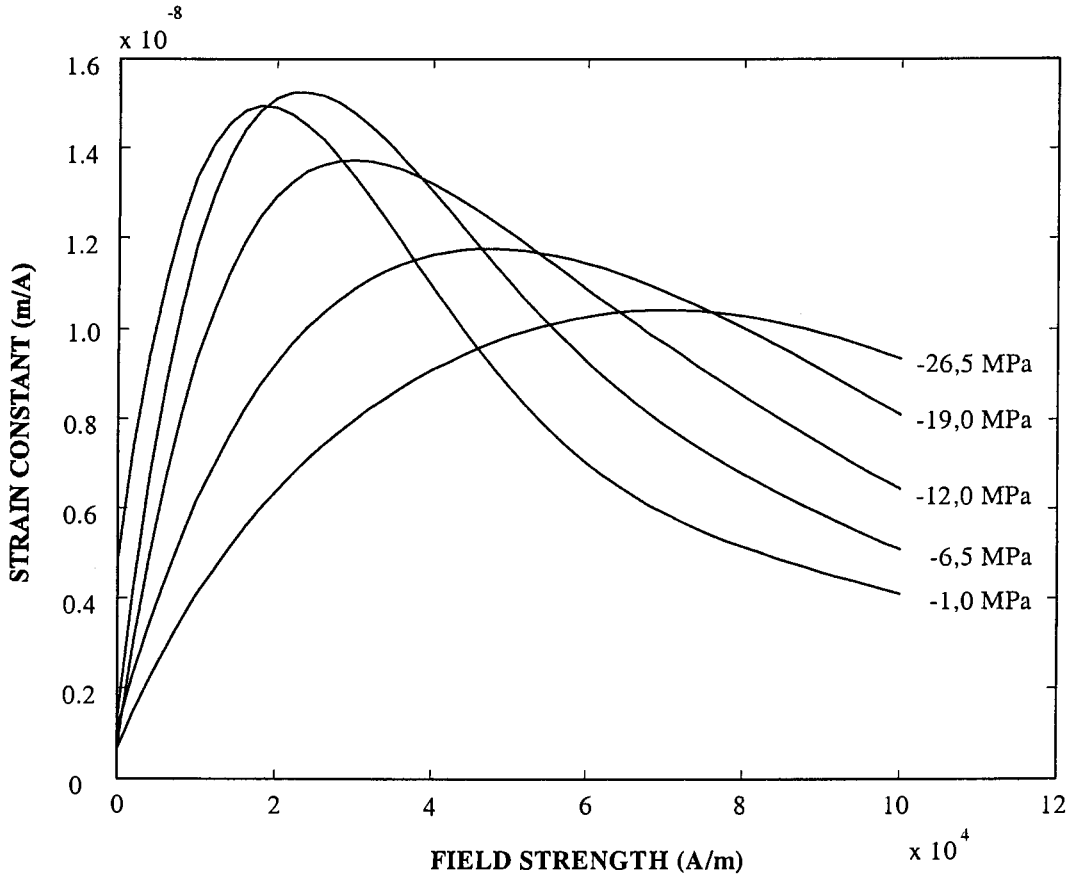

Figure 2.2.1.5: Terfenol-D strain constant versus mechanical stress and magnetic field strength

Figure 2.2.1.5 shows that, for any given constant stress, d^H is initially low, and increases with field until a peak is reached. After the peak, d^H gradually drops off to zero as the material becomes magnetically saturated. The peak value of d^H not only depends on the field, but also

on the stress. The peak value is generally higher for low stresses. Furthermore, for higher stresses, higher field strengths are required to produce the peak value of d^H.

It was shown in equations 2.2.1.5 and 2.2.1.6, as well as in figures 2.2.1.4 and 2.2.1.5, that the linear magnetostrictive parameters, i.e. E and d^H, are dependent on both mechanical stress and magnetic field strength. For small stress and field amplitudes, E and d^H can be assumed constant, but if stresses and field strengths with large amplitudes are applied, the values of E and d^H will vary. In a linear analysis, large amplitude constant values of the linear magnetostrictive parameters are required. It will therefore be necessary to force the changing parameters by means of large amplitude linearization to assume constant values. These values of E and d^H will depend on the reference stress and field, stress amplitude and field amplitude. Large amplitude linearization of the magnetostrictive characteristics of Terfenol-D will be covered in more detail in the next section.

Large amplitude linear magnetostrictive characteristics of Terfenol-D

This section covers the large amplitude linear magnetostrictive characteristics of Terfenol-D. Equations for the large amplitude average values of E and d^H will be given for simultaneous variations in stress and field. It will be shown that the equations can be simplified for the special cases of constant stress and constant field. An example will be done where the average value of d^H and the linear strain versus field characteristic will be calculated. The linear and nonlinear characteristics will be compared and the saturation region will be identified.

A study was carried out by Clark et al [1990] to investigate the influence of different stress and field amplitudes on E and d^H. In the first part of the study, five different field amplitudes were applied, while the compressive stress was held constant. The reference stress and field were 32,3 MPa and 80 kA/m respectively and the field amplitudes were 20, 30, 40, 50 and 60 kA/m. In the second part of the study, five different stress amplitudes were applied, while the field was held constant. The reference stress and field were unchanged from the first part of the study. The stress amplitudes varied from 7,5 MPa to 37,9 MPa in increments of approximately 7,5 MPa. The values of E and d^H were tabulated for each field and stress amplitude. The results of the study are useful for the calculation of E and d^H for large amplitude mechanical and magnetic excitation of Terfenol-D for the given reference stress and field. However, these results are only usable for the abovementioned reference stress and field, and if E and d^H are required for arbitrary reference stresses and fields, the study will have to be repeated.

An alternative method can be applied to determine the large amplitude linear values of E and d^H. The method is analytical, and makes use of the mathematical relationships for E and d^H in equations 2.2.1.5 and 2.2.1.6, as well as the peak-to-peak stresses and fields.

For given peak-to-peak values of stress and field, the average large amplitude values of E and

d^H can be calculated by means of the following equations:

$$\overline{E} = \frac{1}{(\sigma_2 - \sigma_1)(H_2 - H_1)} \int_{\sigma_1}^{\sigma_2} \int_{H_1}^{H_2} E(\sigma, H) dH d\sigma \qquad \textbf{(2.2.1.7a)}$$

$$\overline{d^H} = \frac{1}{(\sigma_2 - \sigma_1)(H_2 - H_1)} \int_{\sigma_1}^{\sigma_2} \int_{H_1}^{H_2} d^H(\sigma, H) dH d\sigma \qquad \textbf{(2.2.1.7b)}$$

where $\overline{E}$ and $\overline{d^H}$ are the average values of E and d^H respectively, σ_2–σ_1 is the peak-to-peak stress and H_2–H_1 is the peak-to-peak field strength. $E(\sigma,H)$ and $d^H(\sigma,H)$ are given by equations 2.2.1.5 and 2.2.1.6 respectively.

The above equations give E and d^H for simultaneous variations in stress and field. The equations can however be simplified if either stress or field is held constant. In the case of a constant stress, for example, the average values of E and d^H for a peak-to-peak field of H_2–H_1 can be calculated as follows:

$$\overline{E}_{\sigma=const} = \frac{1}{H_2 - H_1} \int_{H_1}^{H_2} E(\sigma, H) dH \qquad \textbf{(2.2.1.8a)}$$

$$\overline{d^H}_{\sigma=const} = \frac{1}{H_2 - H_1} \int_{H_1}^{H_2} d^H(\sigma, H) dH \qquad \textbf{(2.2.1.8b)}$$

Equations 2.2.1.8 are useful for the calculation of linear strain versus field characteristics of Terfenol-D at constant stress, and are applicable to any arbitrarily selected reference field, stress and field amplitude. Similar equations to the above can also be derived for the average values of E and d^H, for different stress amplitudes at a constant field strength.

An example of the application of equation 2.2.1.8b will subsequently be done, where the average value of d^H and the linear strain versus field characteristic will be calculated. The linear and nonlinear characteristics will be compared and the saturation region will be identified. To this end, consider the d^H-curve for a 12 MPa compressive stress shown in figure 2.2.1.5. The reference field and field amplitude are arbitrarily selected as 50 kA/m and 32 kA/m respectively. If the integration in equation 2.2.1.8b is carried out, and the numerical value of the peak-to-peak field, i.e. 64 kA/m, is substituted into the resulting equation, the calculated value of $\overline{d^H}$ is $1{,}192.10^{-8}$ m/A. Note that this value of $\overline{d^H}$ is constant, therefore the linear strain characteristic will be a straight line in the strain versus field plane, with a slope of $\overline{d^H}$. The linear strain versus field characteristic, together with the nonlinear characteristic, is shown in figure 2.2.1.6.

The circle in figure 2.2.1.6 indicates the reference point, at a field strength of 50 kA/m and a corresponding strain of 566 $\mu\varepsilon$. For field strengths below 50 kA/m, the slope of the nonlinear strain versus field characteristic curve increases with field, and for field strengths above 50 kA/m, the slope of the curve decreases. In this region, there is a gradual decline in the slope of the curve, which makes it difficult to identify a single point on the curve where the strain saturates. Therefore, subjective judgment of the linear and saturation regions will have

to be made here. By inspection of figure 2.2.1.6, the characteristic for field strengths below 100 kA/m can be considered as the linear region, where the linear characteristic gives reasonable accuracy compared with the nonlinear characteristic. Field strengths above 100 kA/m can be considered as the saturation region. It is clear that, in this region, the linear characteristic becomes highly inaccurate, and is therefore not recommended.

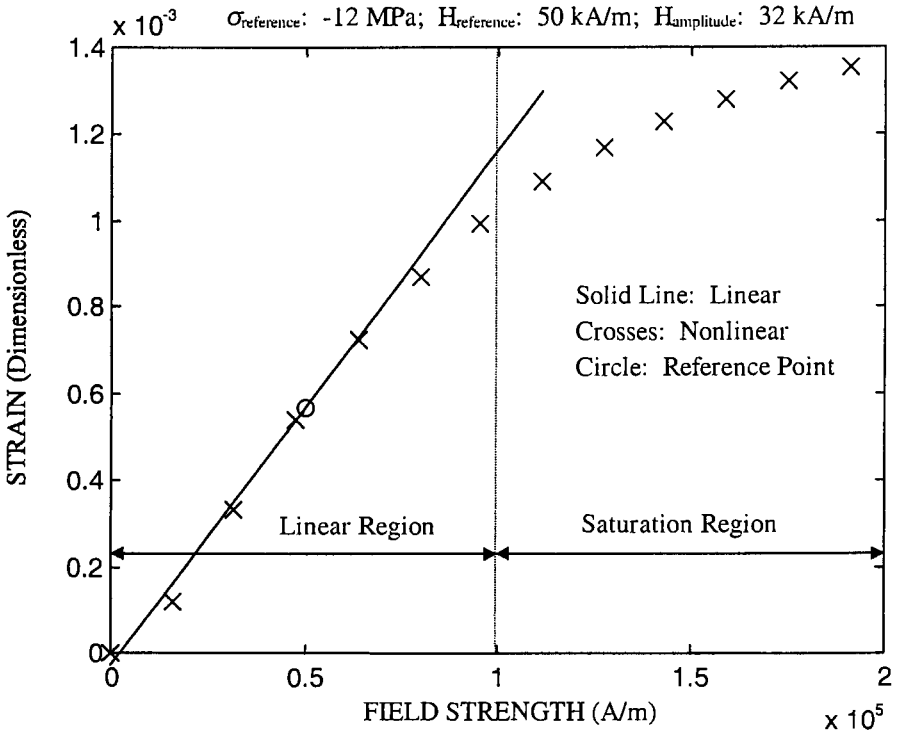

Figure 2.2.1.6: Terfenol-D linear and nonlinear strain versus field characteristics for a constant stress

To summarize, the linear and nonlinear magnetostrictive characteristics were discussed in detail this section. Strain was expressed as a function of stress and field and the characteristics were linearized. Equations for the large amplitude average values of E and d^H were derived. An example was done where $\overline{d^H}$ was calculated for a given reference stress, reference field and field amplitude. The large amplitude linear and nonlinear characteristics were compared graphically and the linear and saturation regions were identified.

The next section will present an alternative magnetostrictive characteristic, with stress as a function of field and strain.

Inverse magnetostrictive characteristic of Terfenol-D

In this short section, an inverse characteristic, where stress is a function of field and strain, will be presented. The inverse characteristic is required because it will be needed to derive the equations of motion of the magnetostrictive actuator and LOS stabilization system in later sections of this chapter. A regression equation will be given to represent the data. Stress will be expressed as a two-dimensional polynomial function of field and strain. The stress characteristic and the data fit will be shown graphically.

The following equation expresses mechanical stress as a two dimensional polynomial function of magnetic field and strain:

$$\sigma = \sigma(\varepsilon, H) = 10^6 \sum_{i=0}^{m} \sum_{j=0}^{n} s_{ij} \left(\frac{\varepsilon}{10^{-3}} \right)^j \left(\frac{H}{10^5} \right)^i \qquad \textbf{(2.2.1.9)}$$

where σ is the stress in Pa, ε is the dimensionless strain and H is the field strength in A/m. The two-dimensional polynomial coefficients s_{ij} for $m = 7$ and $n = 3$ are given in table 2.2.1.2.

Table 2.2.1.2: Two-dimensional polynomial coefficients s_{ij} for mechanical stress as a function of strain and magnetic field

j / *i*	0	1	2	3
0	-0,1334	14,937	-15,741	7,798
1	-8,921	26,12	100,92	32,83
2	-101,9	-3,804	-422,5	-115,9
3	-219,9	-79,86	939,7	103,92
4	-240,9	145,2	-1111,1	35,98
5	142,6	-105,8	703,8	-98,71
6	-43,29	34,22	-223,2	48,45
7	5,297	-4,007	27,70	-7,513

The accuracy of the data fit can be evaluated by comparing the stresses calculated with equation 2.2.1.9 with the data. The stresses are calculated for fourteen field strengths in a range of 0 to 2600 Oe (207 kA/m) and for a strain range of $-1{,}2.10^{-3}$ to $1{,}2.10^{-3}$. The data is obtained by inverting the graphical strain characteristics as supplied by Kvarnsjö [1993], so that stress becomes the dependent variable and field and strain become the independent variables. The RMS error of the data fit is 5,14% for the above field and strain ranges. Figure 2.2.1.7 shows the stresses as calculated with equation 2.2.1.9, together with the data.

Figure 2.2.1.7 shows that, for low field strengths, the stress curves initially rise sharply with strain, but as the strain is increased, the slopes of the curves decrease (see for instance curve a). This type of characteristic is known in mechanical engineering terms as a "softening characteristic". This implies that the required change in stress per unit change in strain decreases. For higher fields (see curve h), the slope of the stress versus strain curve initially decreases with strain until a minimum slope is reached. As the strain is further increased, the slope increases again until a maximum slope is reached at maximum stress. For high field

strengths (see for instance curve n), the slope of the stress versus strain curve increases with strain for all strains. This type of characteristic is known as a "stiffening characteristic".

For low fields, the curves are closely spaced, but as the field increases, the curves are further apart. In the vicinity of the maximum field strength of 2600 Oe, the curves are closely spaced again, which indicates that the strain will not increase significantly with an increase in field. At this field strength, the material is magnetically saturated. This phenomenon was discussed in more detail in previous sections.

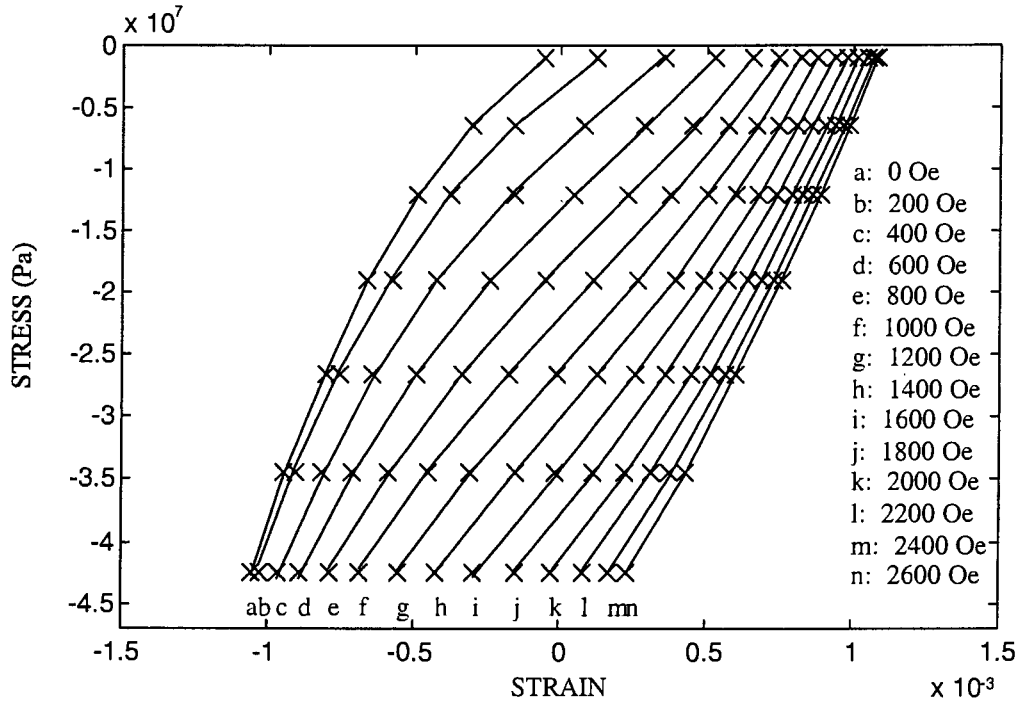

Figure 2.2.1.7: Terfenol-D mechanical stress versus magnetic field and strain: Interpolated two-dimensional polynomial and original data

To summarize section 2.2.1, the magnetostrictive characteristics of Terfenol-D, i.e. the strain, Young's Modulus and the magnetostrictive strain constant were expressed in terms of the mechanical stress and the magnetic field strength. Mathematical equations were obtained by means of least squares fits to data supplied in the literature. The equations were also represented graphically. Section 2.2.2 will cover the magnetization characteristics of Terfenol-D.

2.2.2 Magnetization characteristics of Terfenol-D

This section discusses the linear and nonlinear magnetization characteristics of Terfenol-D. A graph of magnetic flux density versus mechanical stress and magnetic field strength is shown. The influence of stress and field on the saturation flux density is discussed. A two dimensional regression equation is given which closely represents the data. The flux density characteristic is linearized and the linear magnetization parameters, i.e. the piezomagnetic cross-coupling constant d^{σ} and the permeability μ^{σ}, are defined, expressed mathematically and shown graphically.

In section 2.2 magnetostriction was defined as the phenomenon wherein ferromagnetic materials experience an elastic strain when subjected to an external magnetic field. Magnetostriction is also the converse phenomenon in which mechanical stresses cause a change in the magnetic induction, or flux density, of a ferromagnetic material [Harris, 1988]. The magnetization characteristics of all magnetic materials are usually expressed in terms of magnetic flux density versus field strength, but in the case of magnetostrictive materials, flux density is also a function of the applied mechanical stress.

The magnetization characteristics of Terfenol-D are required to calculate the electrical current in the field coil of a magnetostrictive actuator and the magnetic field strength in the active rod, for a given input voltage. The field strength is of particular importance since it produces the magnetostrictive strain in the rod, as well as the actuator force. Once the field strength is known, the strain in the rod can be obtained by means of the magnetostrictive characteristics as given in section 2.2.1.

The magnetization characteristics of Terfenol-D which will be used in this study, are obtained from data supplied by Kvarnsjö [1993]. The flux density of Terfenol-D versus mechanical stress and magnetic field strength for a stress range of -42,5 MPa to -1 MPa and a field range of 0 to 150 kA/m is shown in figure 2.2.2.1.

Figure 2.2.2.1 shows that flux density increases with both stress and field strength. For low field strengths, flux density initially increases sharply, but the increase diminishes as soon as the field exceeds 25 kA/m. Also, the initial increase in flux density is higher for higher stresses. The maximum flux density for the above stress and field range is approximately 1,2 tesla (T).

The flux density curves as shown in figure 2.2.2.1 can be used to do a mathematical analysis of the magnetization characteristics of Terfenol-D. A functional relationship between flux density, stress and field can be obtained by means of two-dimensional interpolation of the data. The mathematical function thus obtained can be differentiated with respect to stress and field to give the piezomagnetic cross-coupling constant d^{σ} and the permeability μ^{σ} respectively. A suitable two-dimensional polynomial equation, which closely represents the data, will subsequently be given, after which d^{σ} and μ^{σ} will be derived.

Flux density can be expressed as follows as a two-dimensional function of stress and field:

$$B(\sigma,H)=\sum_{i=0}^{m}\sum_{j=0}^{n}b_{ij}\left(\frac{\sigma}{10^{6}}\right)^{j}\left(\frac{H}{10^{5}}\right)^{i} \qquad \textbf{(2.2.2.1)}$$

where B is the magnetic flux density in T, σ is the mechanical stress in Pa and H is the magnetic field strength in A/m. Note that the field and stress are scaled by factors of 10^5 A/m and 10^6 Pa respectively. m is the order of the polynomial for flux density as a function of field and n is the order of the polynomial for flux density as a function of stress. b_{ij} are the two-dimensional polynomial coefficients. Values of b_{ij} for $m=8$ and $n=3$ are given in table 2.2.1.1.

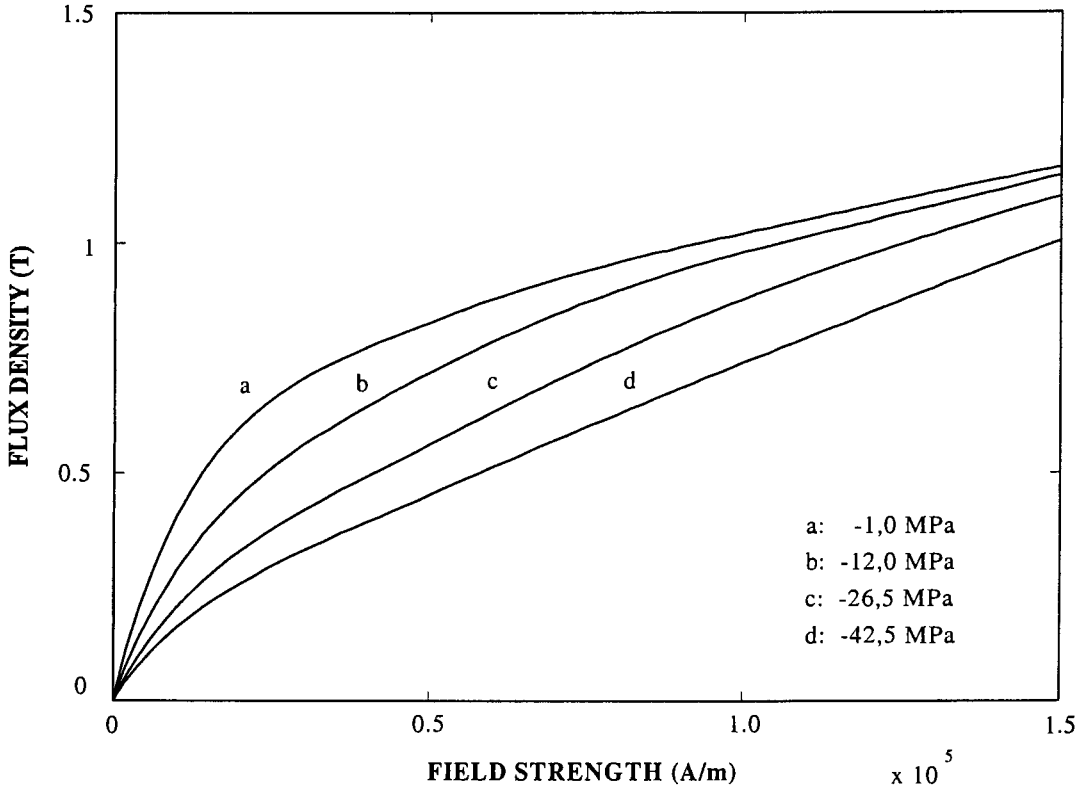

Figure 2.2.2.1: Terfenol-D flux density versus mechanical stress and magnetic field strength [Kvarnsjö, 1993]

The accuracy of the data fit can be evaluated by comparing the flux densities calculated with equation 2.2.2.1 with the flux densities given by Kvarnsjö [1993]. The flux densities are calculated for four compressive stresses in a range of -42,5 MPa to -1 MPa and for a field strength range of 0 to 150 kA/m. The calculated flux densities and the data as supplied by Kvarnsjö [1993] are shown in figure 2.2.2.2.

Table 2.2.2.1: Two-dimensional polynomial coefficients b_{ij} for magnetic flux density as a function of mechanical stress and magnetic field

j / *i*	0	1	2	3
0	$3{,}465.10^{-4}$	$-1{,}535.10^{-5}$	$-1{,}145.10^{-6}$	$-1{,}384.10^{-8}$
1	-5,959	0,2403	$5{,}792.10^{-3}$	$5{,}343.10^{-5}$
2	-21,96	-1,231	$-3{,}54.10^{-2}$	$-3{,}548.10^{-4}$
3	49,44	2,936	$8{,}447.10^{-2}$	$8{,}139.10^{-4}$
4	-67,07	-4,125	-0,1137	$-9{,}994.10^{-4}$
5	55,34	3,575	$9{,}534.10^{-2}$	$7{,}642.10^{-4}$
6	-27,09	1,859	$-4{,}901.10^{-2}$	$-3{,}685.10^{-4}$
7	7,214	0,527	$1{,}394.10^{-2}$	$1{,}013.10^{-4}$
8	-0,8037	$-6{,}227.10^{-2}$	$-1{,}663.10^{-3}$	$-1{,}191.10^{-5}$

Figure 2.2.2.2 shows that, for the values of b_{ij} in table 2.2.1.1, the flux densities calculated with equation 2.2.2.1 compare favourably with the data supplied by Kvarnsjö [1993]. The root mean square error of the regression equation is 0,31% for a stress range of -42,5 MPa to -1 MPa and for a field range of 0 to 150 kA/m.

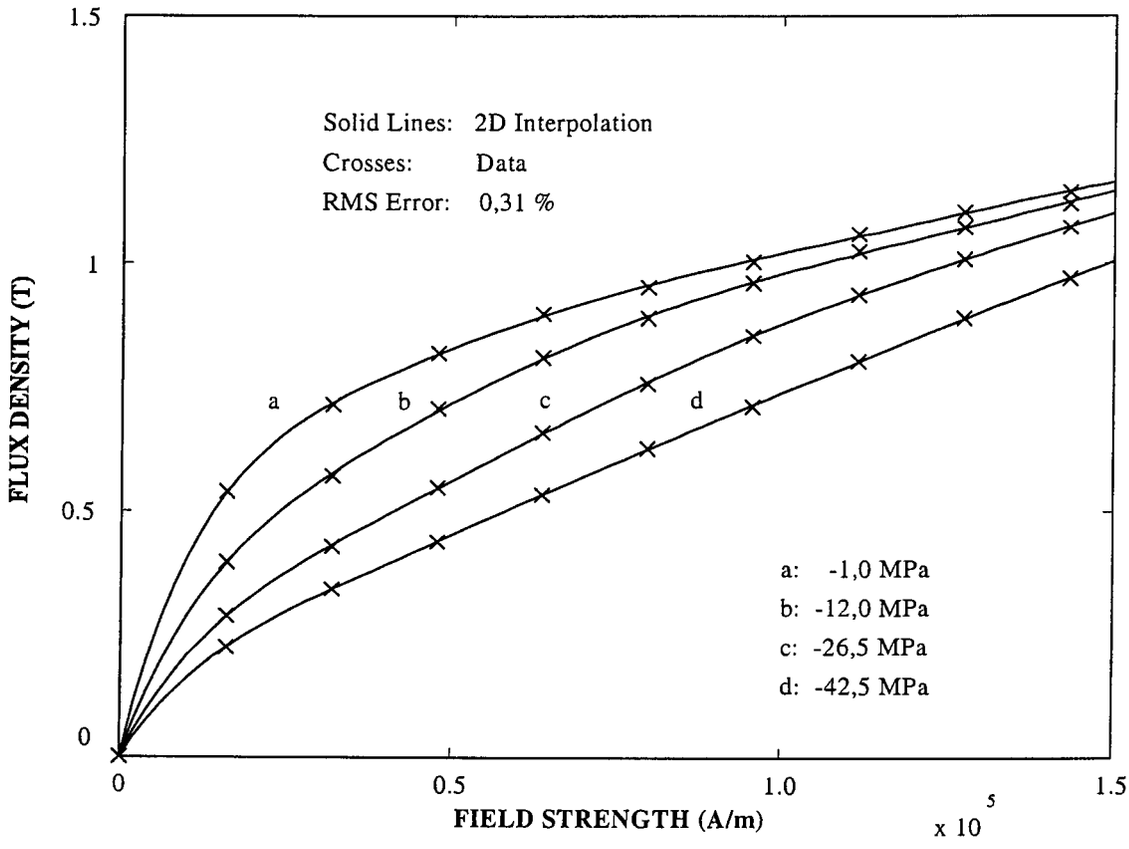

Figure 2.2.2.2: Comparison between calculated Terfenol-D flux density and data

The nonlinear magnetization characteristics of Terfenol-D have been covered in detail in this section. The flux density characteristics have been shown graphically, the saturation properties have been discussed and a regression equation has been given which closely represents the data. Whereas the nonlinear magnetization characteristics are an accurate tool for calculating the coil current of a magnetostrictive actuator and the field in the Terefnol-D rod, the linear characteristics are required to simplify the calculations. The linear magnetization characteristics will be discussed next.

Linear magnetization characteristics of Terfenol-D

Equation 2.2.2.1 expressed the magnetic flux in Terfenol-D as a nonlinear, two-dimensional polynomial function of stress and field. The linear magnetization characteristics of Terfenol-D will be covered in this section. The linear magnetization parameters, i.e the permeability and the piezomagnetic cross-coupling constant, will be derived and shown graphically.

A linear analysis of the magnetization characteristics is simpler than a nonlinear analysis due to the fact that, in the linear case, flux density is assumed to be directly proportional to both stress and field. Mathematically, the flux density can be expressed as follows:

$$B(\sigma, H) = d^{\sigma}\sigma + \mu^{\sigma} H \qquad \textbf{(2.2.2.2)}$$

where d^{σ} is the piezomagnetic cross-coupling constant and μ^{σ} is the permeability. The first term on the right hand side of equation 2.2.2.2, i.e. $d^{\sigma}\sigma$, describes the linear relationship between flux density and stress at a constant field strength, while the second term, $\mu^{\sigma}H$, gives the linear relationship between flux density and field strength at a constant stress.

In order to do a proper analysis of the linear behaviour of a magnetostrictive actuator and LOS stabilization system, the piezomagnetic strain constant and permeability will be required as functions of stress and field. These functions will enable the designer of the plant to calculate d^{σ} and μ^{σ} for any given mechanical stress and magnetic field strength. Mathematical expressions for d^{σ} and μ^{σ} will subsequently be derived and shown graphically.

The piezomagnetic cross-coupling constant can be defined as the change in magnetic flux per unit change in mechanical stress, at a constant magnetic field strength. Mathematically, d^{σ} can be described as the partial derivative of flux density with respect to stress at a constant field, as given by equation 2.2.2.3:

$$d^{\sigma}(\sigma, H) = \left.\frac{\partial B(\sigma, H)}{\partial \sigma}\right|_{H=const} = 10^{-6} \sum_{i=0}^{m} \sum_{j=1}^{n} b_{ij}\, j \left(\frac{\sigma}{10^{6}}\right)^{j-1} \left(\frac{H}{10^{5}}\right)^{i} \qquad \textbf{(2.2.2.3)}$$

where $B(\sigma,H)$ is given by equation 2.2.2.1 and the polynomial coefficients b_{ij} are given in table 2.2.2.1. The cross-coupling constant, according to equation 2.2.2.3, is shown in figure 2.2.2.3. The field range is 0 kA/m to 100 kA/m and the stress range is -1,0 MPa to -26,5 MPa.

Figure 2.2.2.3 shows that, for any given constant stress, d^{σ} is initially low, and increases with field until a peak is reached. After the peak, d^{σ} gradually drops off to zero as the material becomes magnetically saturated. The peak value of d^{σ} not only depends on the field, but also on the stress. The peak value is generally higher for low stresses. Furthermore, for higher stresses, higher field strengths are required to produce the peak value of d^{σ}. Lastly, if figure 2.2.2.3 is compared with figure 2.2.1.5, it can be seen that d^{σ} follows the same trends as d^{H} and that the numerical values of the two parameters are comparable for the same values of stress and field strength.

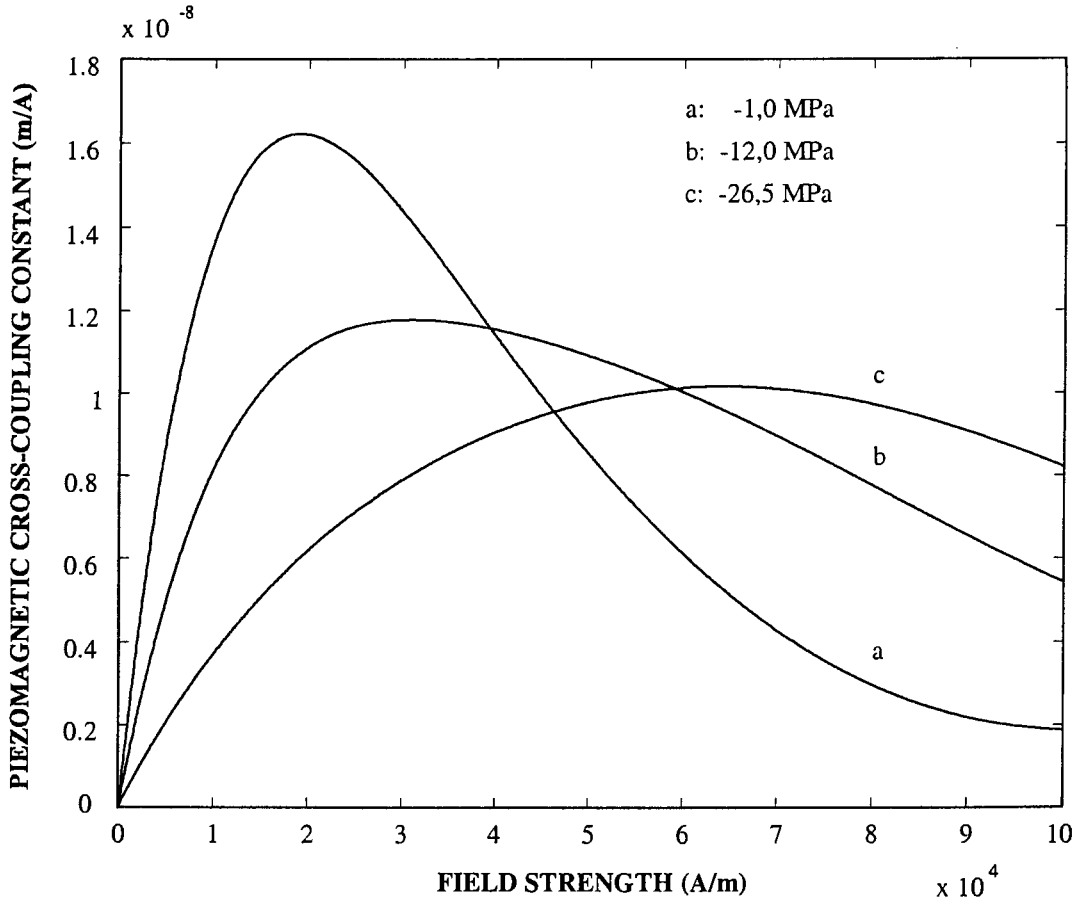

Figure 2.2.2.3: Terfenol-D piezomagnetic cross-coupling constant versus mechanical stress and magnetic field strength

A mathematical expression for the piezomagnetic cross-coupling constant has been obtained by means of partial differentiation of magnetic flux with respect to stress. d^{σ} has been shown graphically for a stress variation of -26,5 MPa to -1 MPa and a field variation of 0 to 100 kA/m. A similar procedure can be followed to obtain the permeability in terms of stress and field.

The permeability μ^{σ} can be defined as the change in magnetic flux per unit change in magnetic field strength, at a constant mechanical stress. Mathematically, μ^{σ} can be described as the partial derivative of flux density with respect to field at a constant stress:

$$\mu^{\sigma}(\sigma,H)=\left.\frac{\partial B(\sigma,H)}{\partial H}\right|_{\sigma=const}=10^{-5}\sum_{i=1}^{m}\sum_{j=0}^{n}b_{ij}i\left(\frac{\sigma}{10^{6}}\right)^{j}\left(\frac{H}{10^{5}}\right)^{i-1} \qquad \textbf{(2.2.2.4)}$$

where $B(\sigma,H)$ is given by equation 2.2.2.1 and the polynomial coefficients b_{ij} are given in table 2.2.2.1. The permeability, according to equation 2.2.2.4, is shown in figure 2.2.2.4. The field range is 0 kA/m to 100 kA/m and the stress range is -1,0 MPa to -26,5 MPa.

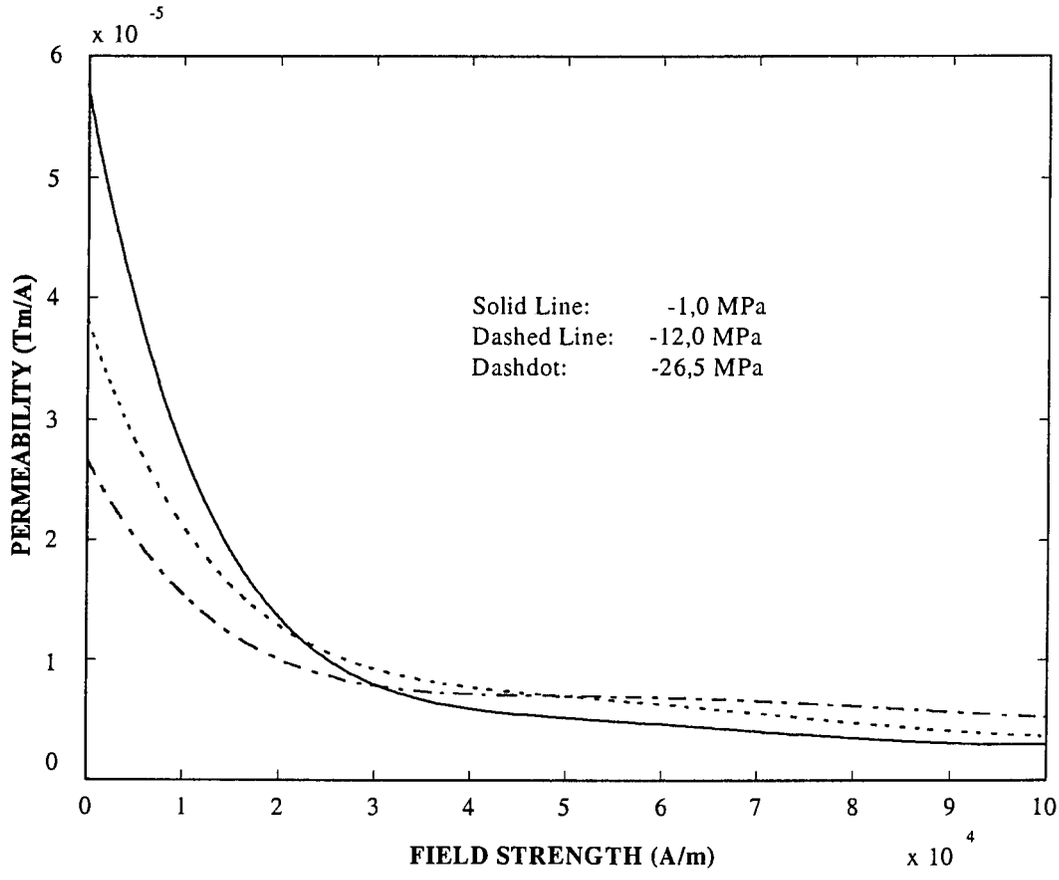

Figure 2.2.2.4: Terfenol-D permeability versus mechanical stress and magnetic field strength

Figure 2.2.2.4 shows that permeability decreases with an increase in field. For field strengths below 25 kA/m, permeability generally increases with stress. For field strengths above 25 kA/m, the material becomes magnetically saturated, permeability is weakly dependent on stress and eventually decays to zero.

It was shown in equations 2.2.2.3 and 2.2.2.4, that the linear magnetization parameters, i.e. d^{σ} and μ^{σ}, are dependent on both mechanical stress and magnetic field strength. For small stress and field amplitudes, d^{σ} and μ^{σ} can be assumed constant, but if large amplitude stresses and field strengths are applied, the values of d^{σ} and μ^{σ} will vary. A similar phenomenon was detected in the magnetostrictive parameters. However, in a linear analysis, large amplitude constant values of the magnetization parameters are required. It will therefore be necessary to force the changing parameters by means of large amplitude linearization to assume constant values. The values of d^{σ} and μ^{σ} will depend on the reference stress and field, the stress amplitude and the field amplitude.

The large amplitude values of d^{σ} and μ^{σ} can be obtained by means of the following equations:

$$\overline{d^{\sigma}} = \frac{1}{(\sigma_2 - \sigma_1)(H_2 - H_1)} \int_{\sigma_1}^{\sigma_2} \int_{H_1}^{H_2} d^{\sigma}(\sigma, H) dH d\sigma \qquad \textbf{(2.2.2.5a)}$$

$$\overline{\mu^{\sigma}} = \frac{1}{(\sigma_2 - \sigma_1)(H_2 - H_1)} \int_{\sigma_1}^{\sigma_2} \int_{H_1}^{H_2} \mu^{\sigma}(\sigma, H) dH d\sigma \qquad \textbf{(2.2.2.5b)}$$

where $\sigma_2 - \sigma_1$ is the peak to peak stress, $H_2 - H_1$ is the peak to peak field and $d^{\sigma}(\sigma,H)$ and $\mu^{\sigma}(\sigma,H)$ are respectively given by equations 2.2.2.3 and 2.2.2.4.

Equations 2.2.2.5 can be simplified if either stress or field is held constant. In the case of a constant stress, for example, equations 2.2.2.5a and 2.2.2.5b reduce to:

$$\overline{d^{\sigma}}_{\sigma=const} = \frac{1}{H_2 - H_1} \int_{H_1}^{H_2} d^{\sigma}(\sigma, H) dH \qquad \textbf{(2.2.2.6a)}$$

$$\overline{\mu^{\sigma}}_{\sigma=const} = \frac{1}{H_2 - H_1} \int_{H_1}^{H_2} \mu^{\sigma}(\sigma, H) dH \qquad \textbf{(2.2.2.6b)}$$

To conclude section 2.2, the linear and nonlinear magnetostrictive and magnetization characteristics of Terfenol-D were covered in detail. It was shown that magnetostrictive strain and magnetic flux saturate at high field strengths. Strain and flux density were expressed mathematically in terms of mechanical stress and magnetic field strength. The expressions were used to derive relationships for the cross-coupling constants, Young's Modulus and permeability. These characteristics are a valuable tool for the analysis of the dynamic behaviour of the Terfenol-D actuators and LOS stabilization system. The characteristics will be used in sections 2.4 to 2.8 to derive the linear and nonlinear equations of motion and coil current equations, the state-space models and transfer functions of the magnetostrictive actuators and system, as well as to simulate their behaviour.

Section 2.2 covered the influence of saturation on the magnetostrictive and magnetization characteristics of Terfenol-D. The effects of hysteresis will be covered in section 2.3.

2.3 The effects of hysteresis on the magnetostrictive and magnetization characteristics of Terfenol-D

This section describes the effects of hysteresis on the magnetostrictive and magnetization characteristics of Terfenol-D. A definition of hysteresis is given. The problems caused by hysteresis are mentioned. A number of magnetostrictive hysteresis models are discussed in short. The effects of hysteresis on the strain constant and permeability are described. A simplified model, which makes use of a hysteresis loss factor and an equivalent viscous damping coefficient, is presented.

When a magnetic material is magnetized with a magnetic field, and the field is subsequently removed, the flux density for the decreasing field will differ from that of the increasing field. The reason is that, during the reversal of the field, the material will not become fully demagnetized, as a portion of the field will remain in the material. This phenomenon is known as magnetic hysteresis. In the case of magnetostrictive materials, not only the flux density characteristic, but also the strain characteristic, exhibits hysteresis. In magnetostrictive hysteresis, the strain characteristic for an increasing field will differ from that of a decreasing field. The characteristic for an increasing field is known as the loading characteristic, while that for the decreasing field is known as the unloading characteristic.

The sequence of the loading and unloading fields has an important effect on the strain history of the material. The latter is determined by, inter alia, the application and usage of the magnetostrictive actuator. For instance, if sensitive equipment such as an optical instrument must be isolated against shock blasts, the field required to cancel the rapidly increasing forces, will be of a transient nature. On the other hand, if the optical instrument is to be isolated against steady-state harmonic base vibrations, the applied field will be cyclic. In the latter case, the loading and unloading curves form a closed loop, called a hysteresis loop. If the optical instrument is subjected to broadband random base vibrations, the required field will not be steady-state harmonic, but will consist of a spectrum of cyclic loadings.

The analysis of the dynamic behaviour of a magnetostrictive actuator and LOS stabilization plant of an optical instrument will necessarily have to make provision for the difference in loading and unloading magnetostrictive and magnetization characteristics. A number of problems arise in such an analysis. The first problem is that for a given excitation field, the strain can have many different values [Restorff et al, 1990]. Contrary to the saturation characteristics considered in section 2.2, the hysteresis strain and flux density cannot be described by single-valued functions of the applied field, as the direction of application of the field, i.e. whether the field is increasing or decreasing, must also be considered. Different characteristics for loading and unloading fields will therefore be required.

A second problem is that the value of magnetostrictive strain constant d^H is lowered if a cyclic excitation field is applied [Kvarnsjö, 1993] and [Pratt, 1993]. It was shown in section 2.2.1 that d^H is the slope of the strain versus magnetic field curve for a constant mechanical stress. However, this is only valid for a "dehysterized" characteristic, where the difference between the loading and unloading characteristics is ignored. Due to the multi-valued nature of hysteresis, the strain constant not only depends on the mechanical stress and magnetic field, but also on the difference between the loading and unloading fields and on the field amplitude.

For a small field amplitude, the hysteresis loop differs from that of a large field amplitude. The large amplitude loop is known as the major loop, while the small amplitude loop is known as the minor loop. Figure 2.3.1 shows an example of a magnetostrictive strain versus field characteristic, including the dehysterized characteristic, the loading and unloading curves, the major and minor hysteresis loops, and the hysteresis and dehysterized strain constants.

Lastly, hysteresis causes energy losses during excitation, necessitating larger field amplitudes to produce the same strain than in the dehysterized case. These energy losses cannot be predicted and must be experimentally measured. Hysteresis therefore also has a damping effect on the dynamic behaviour of the actuator and LOS stabilization plant, as it removes energy from the system. This effect may in some cases be desirable, such as at resonance frequencies where damping is required to suppress unduly high transmitted vibrations.

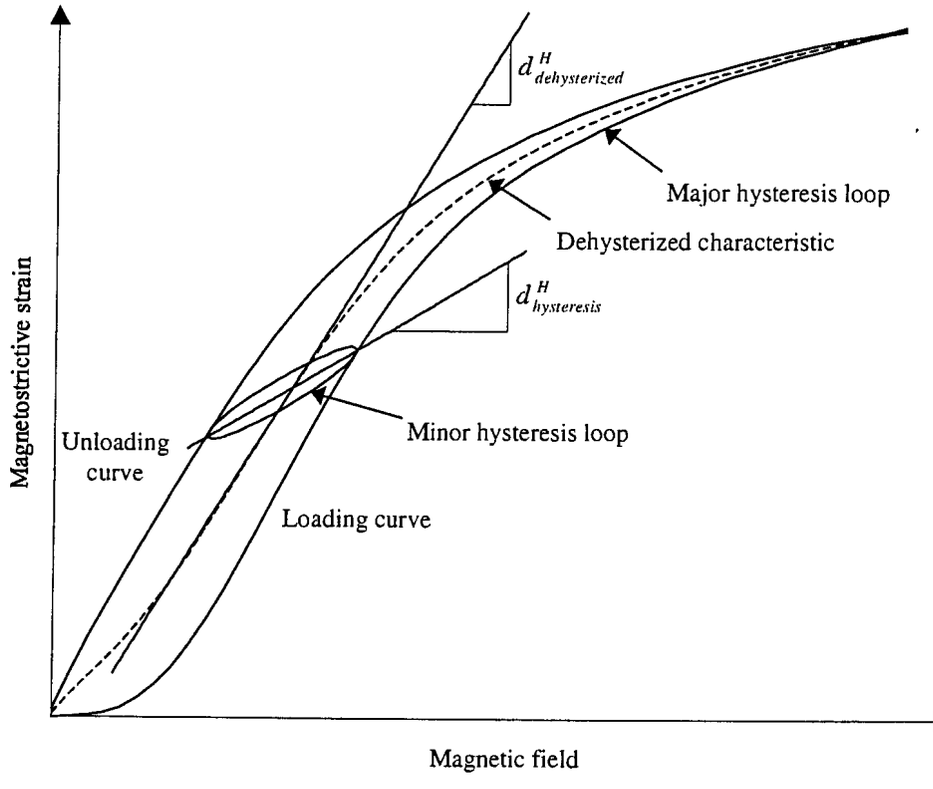

Figure 2.3.1: Hysteresis effects on the magnetostrictive strain versus field characteristic

In order to describe the magnetostrictive and magnetization hysteresis of Terfenol-D, mathematical models will be required to analyze its multi-valued nature, the effect of the lowered strain constant and energy losses. There have been many efforts to obtain mathematical hysteresis models, the most significant of which will be discussed in short in the next paragraphs. The application, advantages and disadvantages of each model will be mentioned. In addition, a linear model, which analyzes the strain constant and damping effect separately, will be presented and discussed in detail.

The Preisach model is arguably the most popular model for magnetic hysteresis. This model was developed in 1935 to describe general magnetic hysteresis, and was later adopted for

magnetostrictive materials by Adly et al [1991], Bergqvist & Engdahl [1991], Doong & Mayergoyz [1985], Ossart et al [1995], Restorff et al [1990] and Vajda & Della Torre [1995]. Other models which have been developed to describe magnetostrictive and magnetic hysteresis, include a Bessel function model [Sablik & Jiles, 1988] and a simplified model which superimposes a harmonic hysteresis function on the strain curve [Hall & Flatau, 1993].

The Preisach model is a general hysteresis model which is applicable to a broad range of phenomena that exhibit hysteresis [Restorff et al, 1990]. The model is widely used because of its computational efficiency. This feature also makes it desirable for the analysis of magnetostriction, where simultaneous changes in field and stress occur. The model takes cross-coupling between the two inputs, i.e. stress and field, into account.

Magnetostrictive and magnetization hysteresis is analyzed by means of an infinite number of generic hysteresis elements which have outputs of only ± 1. The sign is positive for an increasing input and negative for a decreasing input. In order to find the output value, the values of the different elements are summed with a weighting function. The model records a history of the inputs of all the elements in the form of two lists, which contain the local minima and maxima of the input. Since this list can grow without limit, it is truncated whenever a minimum lower than the lowest previous minimum or a maximum higher than the previous maximum is encountered.

The advantage of the Preisach model is that it can be used to predict magnetostrictive and magnetization hysteresis, including minor loops, fairly accurately [Restorff et al, 1990]. However, its application is limited to the time domain, which makes it unsuitable for frequency domain analyses of the behaviour of magnetostrictive actuators.

The Bessel function model [Sablik & Jiles, 1988], describes the simultaneous effects of saturation and hysteresis on the static magnetostrictive and magnetization characteristics of magnetostrictive materials, such as pure iron and Terfenol-D. The strain is expressed as a hyperbolic Bessel function of the effective field, which in turn is described in terms of the magnetization, applied field and its direction of application, stress and permeability.

The model is very powerful as it takes all the nonlinear magnetostrictive and magnetization characteristics into account, but does not provide a simple direct method of obtaining the strain constant. Furthermore, it is not a dynamic model, and can therefore not be used to investigate the effects of frequency on the damping coefficient. The model is more commonly known in the fields of magnetostriction and magnetism as the Jiles-Atherton (JA), or domain wall pinning model.

A model which simplifies the analysis of magnetostrictive hysteresis to a large extent, was developed by Hall & Flatau [1993]. The model describes magnetostrictive strain in terms of flux density for different harmonic coil input currents. The model considers both major and minor hysteresis loops of magnetic flux versus field strength. For major loops, flux density is described in terms of permeability, the maximum and minimum fields, input current, angular excitation frequency and time. A sinusoidal function of field is added to take the flux density saturation properties into account. The flux density hysteresis effects are described by means of a phase angle, which brings about a shift between the loading and unloading characteristics. For the minor loops, a parameter is included which controls the slope at either end of the loop. By setting this parameter to zero, elliptic minor loops are obtained.

The main advantage of the model is that, in contrast with the abovementioned JA model, it is a dynamic model, which takes the effects of the excitation frequency into account. Although the model is considerably simpler than the JA model, it also fails to provide a large amplitude strain constant and damping factor. However, since it was developed for harmonic coil input currents, it is a good starting point in the development of a simplified linear hysteresis model for vibration isolation problems.

The model which will be used in this study, is based on the assumption that all the hysteresis loops can be modelled as ellipses, i.e. the minor as well as the major loops are elliptic loops. This assumption is made in the interest of linearizing the hysteresis characteristics of the actuator and LOS stabilization system. Linearity is of essence in obtaining Laplace- and frequency domain transfer functions and will facilitate in the design of a suitable controller. The use of elliptic hysteresis loops will make it possible to linearize the nonlinear strain versus field strength characteristics, by means of large amplitude range-dependent average strain constants, hysteresis loss factors and viscous damping coefficients.

The effects of hysteresis on the large amplitude strain constant of Terfenol-D, are analyzed next, followed by the derivation of a hysteresis loss factor and a viscous damping coefficient.

The effects of hysteresis on the strain constant of Terfenol-D

The effects of hysteresis on the strain constant of Terfenol-D are modelled in this section. The loading, unloading and dehysterized magnetostrictive strain versus field strength characteristics, for a constant stress, are shown graphically. A mathematical equation is presented which expresses the different strain characteristics in terms of field strength. The hysteresis strain constant $d^H_{hysteresis}$ is defined and expressed mathematically by means of the loading and unloading strain characteristics. A sample calculation of $d^H_{hysteresis}$ is done for a given mechanical stress, reference field and a range of field amplitudes. The hysteresis strain constant is shown graphically and compared with the dehysterized strain constant. The effect of hysteresis on the strain constant are discussed.

The hysteresis characteristics of Terfenol-D, as supplied in graphical form by Kvarnsjö [1993], will be used in this study. For the sake of simplicity, the effects of stress on the hysteresis strain constant will not be discussed here. Instead, the strain constant will be calculated for an arbitrarily selected constant stress, as this method of analysis will also be applicable to other stresses. The loading and unloading strain versus field strength characteristics of Terfenol-D for a selected compressive stress of 12 MPa and a maximum applied field of 207 kA/m are shown in figure 2.3.2, together with the dehysterized characteristic.

A data regression technique will subsequently be used to obtain a mathematical function, which will express the hysteresis strain characteristics, i.e. the loading, unloading and dehysterized strains, in terms of the magnetic field. The function must accurately represent the different characteristics, and must be relatively easy to apply. For the sake of simplicity, it is further desirable to use the same function type for all three the characteristics. In order to distinguish between the loading, unloading and dehysterized characteristics, different numerical values of the function parameters will be used.

A function which satisfies the abovementioned requirements, can be fairly easily obtained by expressing strain ε as a polynomial of function of field strength H:

$$\varepsilon(H)\big|_{\sigma=const} = \sum_{i=0}^{n} p_i \left(\frac{H}{10^5}\right)^i \qquad (2.3.1)$$

where n is the order of the polynomial and p_i are the polynomial coefficients for the respective characteristic cases. Note that in equation 2.3.1, field strength is scaled by a factor of 10^5 A/m to avoid having to deal with unnecessarily large numbers.

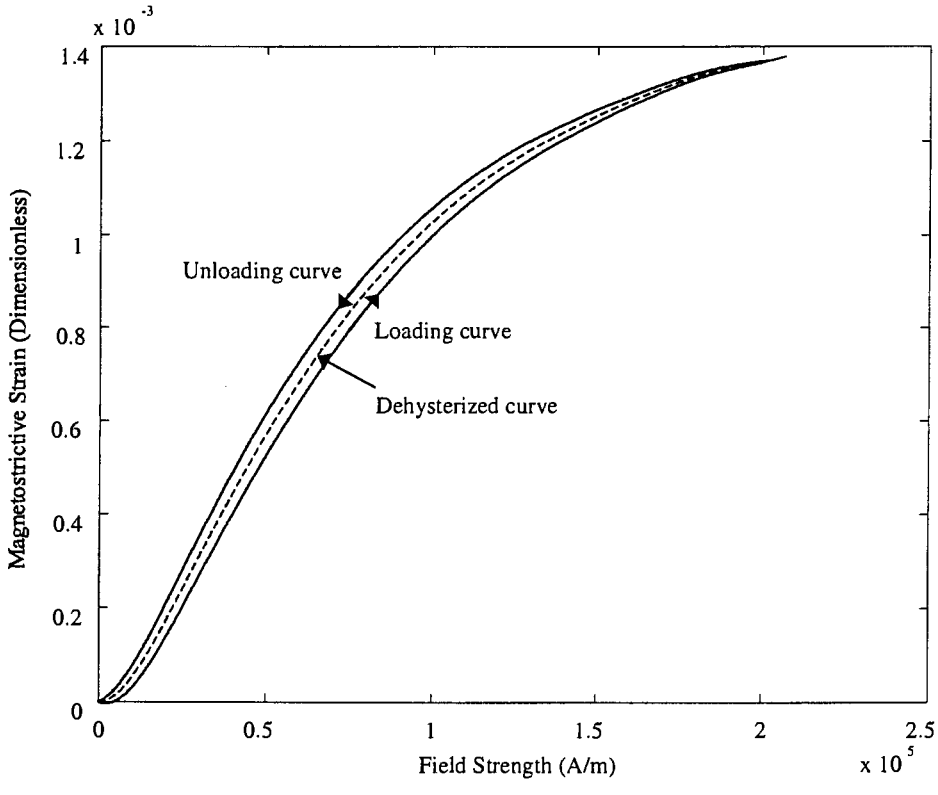

Figure 2.3.2: Loading, unloading and dehysterized strain versus field characteristics of Terfenol-D for a 12 MPa compressive stress [Kvarnsjö, 1993]

The accuracy of the function can be enhanced by using a high order n of the polynomial. However, it was found that sufficient accuracy is obtained if a value of n = 8 is used. The polynomial coefficients p_i for the loading, unloading and dehysterized strain characteristics of Terfenol-D for a compressive stress of 12 MPa are shown in table 2.3.1.

Table 2.3.1: Polynomial coefficients p_i for loading, unloading & dehysterized strain versus field characteristics of Terfenol-D for a 12 MPa compressive stress

Characteristic: i	Loading	Unloading	Dehysterized
0	$-1{,}6324.10^{-7}$	$-1{,}2071.10^{-7}$	$-1{,}4197.10^{-7}$
1	$-3{,}2056.10^{-4}$	$2{,}9977.10^{-4}$	$-1{,}1425.10^{-5}$
2	$8{,}1102.10^{-3}$	$6{,}2320.10^{-3}$	$7{,}1711.10^{-3}$
3	$-1{,}9974.10^{-2}$	$-1{,}6397.10^{-2}$	$-1{,}8185.10^{-2}$
4	$2{,}7567.10^{-2}$	$2{,}2879.10^{-2}$	$2{,}5223.10^{-2}$
5	$-2{,}3164.10^{-2}$	$-1{,}9256.10^{-2}$	$-2{,}1210.10^{-2}$
6	$1{,}1555.10^{-2}$	$9{,}6124.10^{-3}$	$1{,}0584.10^{-2}$
7	$-3{,}1260.10^{-3}$	$-2{,}6032.10^{-3}$	$-2{,}8646.10^{-3}$
8	$3{,}5218.10^{-4}$	$2{,}9357.10^{-4}$	$3{,}2288.10^{-4}$

Having obtained an equation, which expresses the loading and unloading strain versus field strength characteristics of Terfenol-D for a constant stress, the hysteresis strain constant can be defined and calculated. The hysteresis strain constant $d^{H}_{hysteresis}$ is defined as the slope of the major axis of the strain versus field hysteresis loop, and can be calculated by means of the following equation:

$$d^{H}_{hysteresis} = \frac{\varepsilon(H_2)_{loading} - \varepsilon(H_1)_{unloading}}{2\mathrm{H}_A} \qquad \textbf{(2.3.2)}$$

where H_2 is the maximum applied field, H_1 is the minimum applied field and H_A is the field amplitude, given by:

$$\mathrm{H}_A = \frac{H_2 - H_1}{2} \qquad \textbf{(2.3.3)}$$

The strains $\varepsilon(H_1)_{unloading}$ and $\varepsilon(H_2)_{loading}$ are calculated by means of equations 2.3.4a and 2.3.4b:

$$\varepsilon(H_1)_{unloading} = \sum_{i=0}^{8} p_{i\,unloading}\left(\frac{H_1}{10^5}\right)^i \qquad \textbf{(2.3.4a)}$$

$$\varepsilon(H_2)_{loading} = \sum_{i=0}^{8} p_{i\,loading}\left(\frac{H_2}{10^5}\right)^i \qquad \textbf{(2.3.4b)}$$

where the polynomial coefficients p_i for the unloading and loading characteristics are respectively given by the "loading" and "unloading" columns in table 2.3.1. For clarification purposes, the hysteresis loop parameters, i.e. the reference field and strain, minimum and maximum fields and their corresponding strains, field amplitude and hysteresis strain constant, are shown in figure 2.3.3.

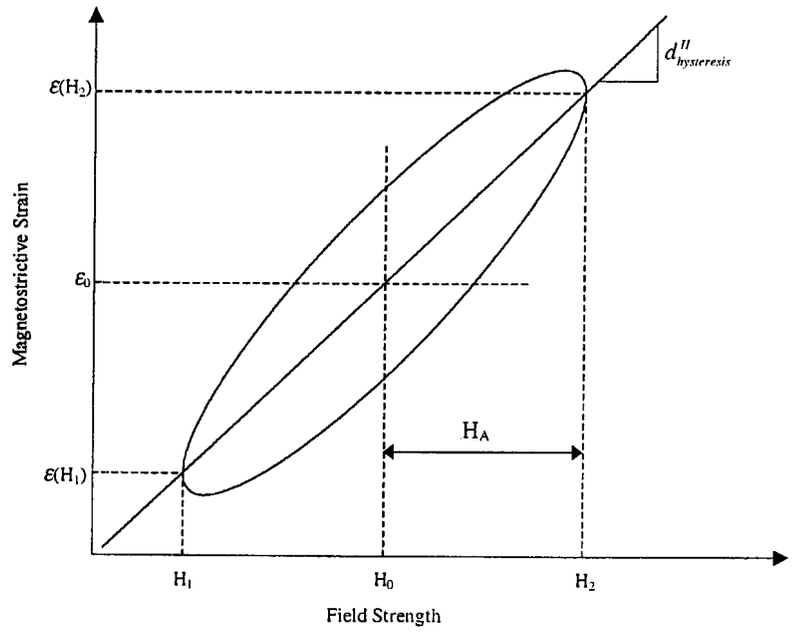

Figure 2.3.3: Magnetostrictive strain versus field strength hysteresis loop parameters and the hysteresis strain constant

Equations 2.3.2 to 2.3.4 provide a simple mathematical tool to calculate the hysteresis strain constant. A graph of the hysteresis strain constant for a stress of 12 MPa, a reference field of 50 kA/m and a field amplitude range of 4 kA/m to 47 kA/m is shown in figure 2.3.4. For comparison purposes, the dehysterized strain constant is also shown.

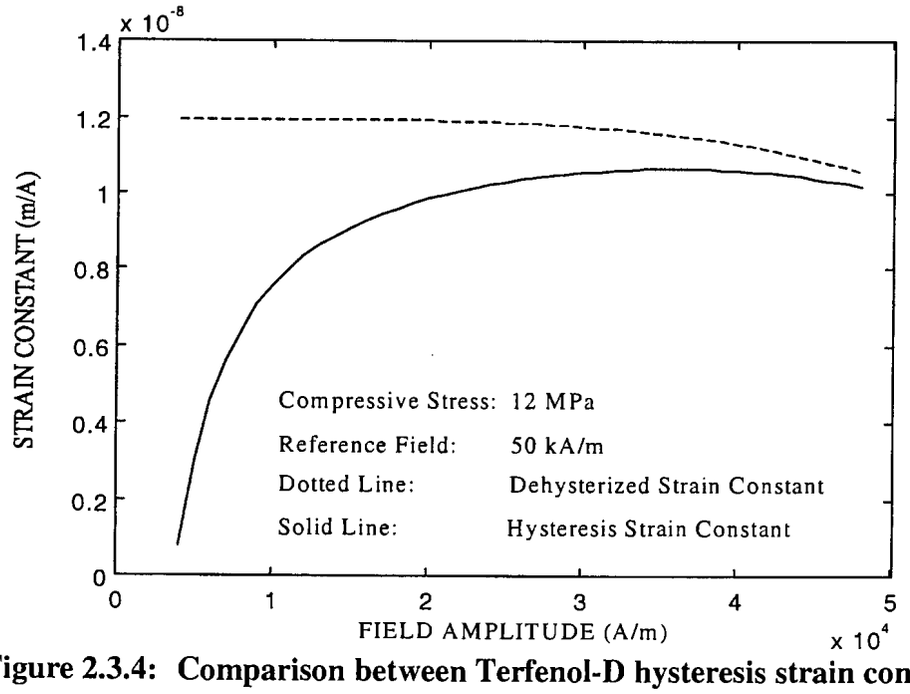

Figure 2.3.4: Comparison between Terfenol-D hysteresis strain constant and dehysterized strain constant for a 48 kA/m field amplitude range

Figure 2.3.4 shows that, for small field amplitudes, the hysteresis strain constant is relatively small in comparison with the dehysterized strain constant. As the field amplitude is increased, the hysteresis strain constant rises rapidly, until a peak is reached at approximately 35 kA/m. For field amplitudes larger than 35 kA/m, the hysteresis strain constant gradually drops and approaches the dehysterized strain constant.

The above example was done to indicate the effect of hysteresis on the strain constant for a given compressive stress, reference field and field amplitude range. Equations 2.3.1 to 2.3.4 are also valid for arbitrary stresses and fields, but the polynomial coefficients in table 2.3.1 are only applicable to a stress of 12 MPa. If the analysis is to be repeated for arbitrary stresses, different tables of polynomial coefficients will have to derived.

This concludes the section on the effects of hysteresis on the strain constant. The next section will be devoted to the hysteresis loss factor and damping coefficient.

Linear magnetostrictive hysteresis loss factor and viscous damping coefficient

This section models the magnetostrictive hysteresis losses of Terfenol-D by means of a linear dimensionless loss factor η and a linear damping coefficient c. An inverse field versus strain characteristic is presented, which is first expressed in dehysterized form, after which a strain rate dependent hysteresis loss term is added. The loss factor is defined in terms of excitation frequency, strain constant, applied field and strain rate. A complex field versus strain characteristic is derived for harmonic excitation and is shown graphically.

A method is presented to calculate η for nonlinear hysteresis loops. The steady-state harmonic damping coefficient is expressed in terms of the loss factor η, stiffness k of the Terfenol-D rod and the angular excitation frequency ω. A damping coefficient for wide-band random excitation is also derived and compared with the harmonic damping coefficient. A sample calculation of η and c is done for a constant stress and a large field amplitude.

An equation for the dehysterized linear strain in terms and the applied magnetic field and mechanical stress was given as follows by equation 2.2.1.4:

$$\varepsilon = \frac{\sigma}{E} + d^H H \tag{2.3.5}$$

where σ is the applied stress, E is Young's Modulus and d^H is the magnetostrictive strain constant. For the purpose of the analysis of the magnetostrictive hysteresis properties, it will be convenient to make use of an inverse characteristic, where the applied field is expressed in terms of strain for a constant stress:

$$H_{dehysterized} = \frac{\varepsilon}{d^H} - \frac{\sigma}{Ed^H} \tag{2.3.6}$$

The above equation describes field in terms of strain and stress in the absence of hysteresis. The equation can be easily extended to accommodate the effects of hysteresis, by adding a hysteresis loss term which contains a dimensionless hysteresis loss factor. The loss factor η

can be defined as the strain loss per cycle at an excitation frequency ω, and can mathematically be expressed as follows:

$$\eta = \frac{\omega d^H H_{loss}}{\dot{\varepsilon}} \tag{2.3.7}$$

where $\dot{\varepsilon}$ is the strain rate. The total field is the dehysterized field plus the hysteresis field loss:

$$H = H_{dehysterized} + H_{loss} \tag{2.3.8}$$

Substitution of equations 2.3.6 and 2.3.7 into equation 2.3.8 gives the following equation for the total magnetic field:

$$H = \frac{1}{d^H}\left(\varepsilon + \frac{\eta}{\omega}\dot{\varepsilon} - \frac{\sigma}{E}\right) \tag{2.3.9}$$

It can be seen from equation 2.3.9, that stress, strain and strain rate are required to obtain the total field. It will however be desirable to express field in terms of stress and strain only, as in the case of the dehysterized field. To this end, the strain rate must be eliminated by expressing it in terms of strain. This is easily accomplished by transforming equation 2.3.9 to the frequency domain, and analyzing the hysteresis characteristics for one cycle of harmonic excitation. The field and strain are then in the following form:

$$H = \mathrm{H}_A e^{j\omega t} \tag{2.3.10a}$$

$$\varepsilon = \mathrm{E}_A e^{j\omega t} \tag{2.3.10b}$$

where H_A is the field amplitude, E_A is the strain amplitude, $j = \sqrt{-1}$ and t is time.

Differentiation of equation 2.3.10b with respect to time, gives:

$$\dot{\varepsilon} = j\omega \mathrm{E}_A e^{j\omega t} = j\omega\varepsilon \tag{2.3.11}$$

Substitution of equation 2.3.11 into equation 2.3.9 gives:

$$H = \frac{1}{d^H}\left[(1 + j\eta)\varepsilon - \frac{\sigma}{E}\right] \tag{2.3.12}$$

Equation 2.3.12 gives the magnetic field strength in terms of mechanical stress and a complex strain.

At this stage of the derivation, it is convenient to analyze the field versus strain characteristic in isolation of the effects of stress. To this end, stress is treated as a constant, in which case field is expressed as follows, in terms of strain:

$$H\big|_{\sigma=const} = \left(\frac{1}{d^H} + j\frac{\eta}{d^H}\right)\varepsilon \tag{2.3.13}$$

Equation 2.3.13 gives the linear hysteresis field versus complex strain relationship at a constant stress. The graphic representation of equation 2.3.13 is an ellipse with a tilted major axis, as shown in figure 2.3.5. The slope of the major axis is $1/d^H$ and the ellipse intersects the field strength axis at a field of $\eta E_A/d^H$. The latter term gives an indication of the additional required field to overcome the losses and to produce the same strain amplitude as in the dehysterized case.

So far in this section it has been assumed that the hysteresis loops are elliptic. The assumption has made it possible to do linear analyses of the magnetostrictive characteristics of Terfenol-D. The assumption is reasonably accurate for minor loops, but in the case of major loops, the loading and unloading curves are distorted (see figure 2.3.2). However, the analysis of the behaviour of a magnetostrictive actuator and LOS stabilization system will be simplified considerably if the characteristics can be linearized. One way of achieving this is to obtain the equivalent elliptic loops of the nonlinear loops. This technique is popular in the field of mechanical engineering, where the force versus speed characteristic of a nonlinear damper, such as a quadratic, Coulomb or hysteretic damper, is expressed in terms of an equivalent viscous damping coefficient [Tse et al, 1978]. Figure 2.3.6 shows a nonlinear magnetostrictive hysteresis loop and its elliptic linear equivalent.

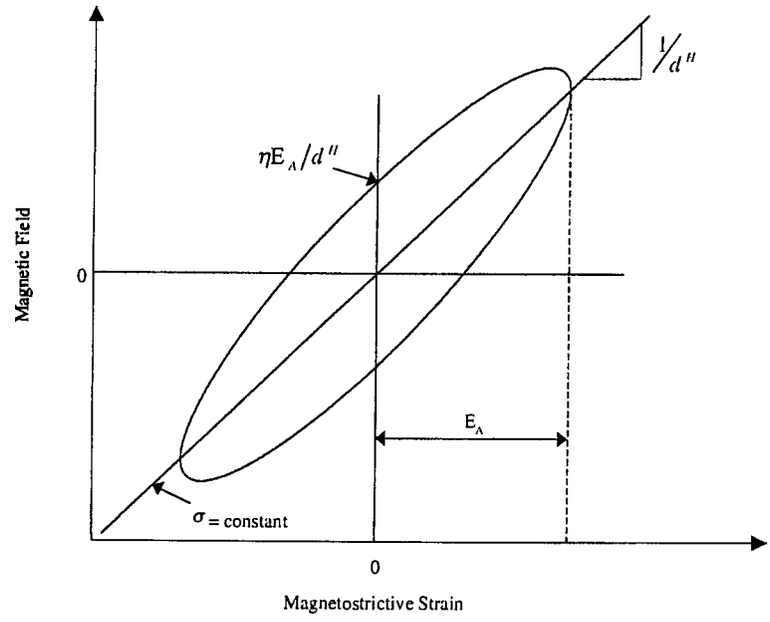

Figure 2.3.5: Magnetic field versus strain for a constant stress

In order to generate the equivalent elliptic loop, the loss factor η must be calculated from the nonlinear magnetostrictive characteristics. The loss factor is the ratio of the dissipated energy to the strain energy for a constant stress, where the dissipated energy is given by the included area of the nonlinear loop.

The loss factor can be obtained by means of the following equation:

$$\eta = \frac{\oint \varepsilon(H)\Big|_{\sigma=const} dH}{\pi \frac{1}{d^H} \mathrm{E}_A^2} \qquad \textbf{(2.3.14)}$$

The hysteresis strain constant d^H can be obtained by means of equations 2.3.2 to 2.3.4.

To summarize, magnetostrictive hysteresis was analyzed by means of a linear hysteresis loss factor in this section. The next section will explain a method to obtain the equivalent linear viscous damping coefficient if the loss factor is known.

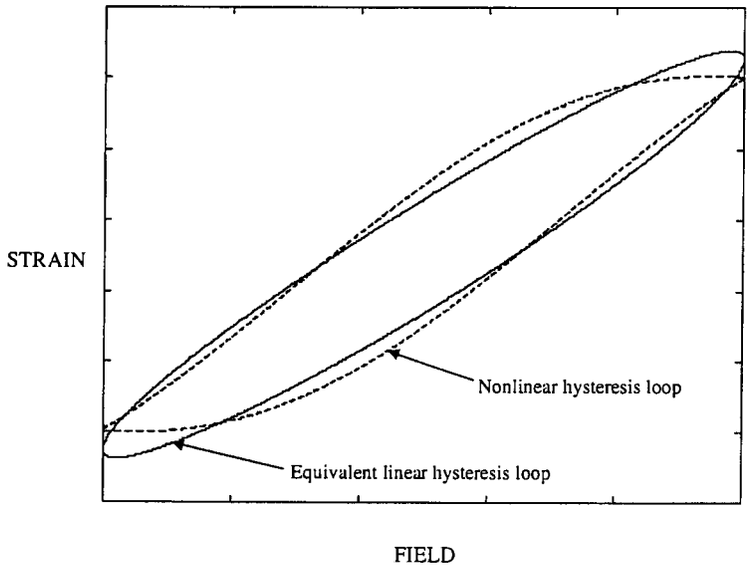

Figure 2.3.6: Nonlinear and equivalent linear magnetostrictive hysteresis loops

Viscous damping coefficient for magnetostrictive hysteresis

This section describes the magnetostrictive hysteresis losses in Terfenol-D in terms of a linear viscous damping coefficient. Mathematical expressions for the steady-state harmonic and wide-band random damping coefficients are given. A sample calculation of the damping coefficient is done for a given constant compressive stress and field amplitude.

The viscous damping coefficient is necessary to derive the linear equations of motion of the actuator and the LOS stabilization system. The equations are similar to that of a mechanical system, and will contain inertia, stiffness, damping and excitation force terms. The damping term is of particular importance in this section. In linear mechanical systems, the damping term may be expressed in a number of ways, e.g. in terms of a constant loss factor, as was done in the previous section, in terms of a viscous damping coefficient and in terms of a dimensionless constant damping factor. In this section, the viscous damping coefficient will be derived.

Whereas the loss factor of Terfenol-D could be expressed in terms of the magnetostrictive characteristics only (see equation 2.3.14), the damping factor also depends on the stiffness k of the Terfenol-D rod and the angular excitation frequency ω. The damping coefficient c can be expressed as follows in terms of k, η and ω:

$$c = \frac{k\eta}{\omega} \tag{2.3.15}$$

where the stiffness k is given by:

$$k = \frac{A_T E}{l_T} \tag{2.3.16}$$

A_T is the rod cross-sectional area, E is Young's Modulus of Terfenol-D and l_T is the rod length.

Closer inspection of equation 2.3.15 reveals that c is directly proportional to stiffness and loss factor, and inversely proportional to excitation frequency. For a constant k and η, the damping coefficient versus frequency characteristic will be a hyperbola. This phenomenon occurs in many hysteretic systems.

Equation 2.3.15 is suitable for the calculation of a damping coefficient at a constant excitation frequency. However, if a magnetostrictive actuator is excited over a wide range of frequencies, as is the case with wide-band random vibrations, c will vary over the frequency range, and will therefore not be constant. Although the analysis of linear systems, which display frequency-dependent damping coefficients, such as rubber isolators, can be carried out with relative ease in the frequency domain, time domain analyses of such systems are complicated. This is mainly due to the fact that the stiffness and damping terms in the equations of motion are time-dependent.

It will therefore be more desirable to obtain a constant c over a wide frequency range, which will facilitate the analysis of the random behaviour of the actuator and LOS stabilization system in both the time domain and the frequency domain. The wide-band average damping coefficient is given by:

$$c = \frac{1}{\Omega_f - \Omega_i} \int_{\Omega_i}^{\Omega_f} c(\omega) d\omega \tag{2.3.17}$$

where Ω_i is the minimum frequency of the disturbance band, Ω_f is the maximum frequency and $c(\omega)$ is given by equation 2.3.15.

Substitution of equation 2.3.15 into equation 2.3.17, gives the following relationship between c, k, η, Ω_f and Ω_i :

$$c = \frac{k\eta}{\Omega_f - \Omega_i} \ln\left(\frac{\Omega_f}{\Omega_i}\right) \tag{2.3.18}$$

The damping coefficient versus frequency relationship for a constant c can be compared with that for a constant η. A graphical comparison is shown in figure 2.3.7.

Equation 2.3.17 can be extended to obtain the damping coefficient if k and η are functions of ω. This may for instance happen in the vicinity of resonance, where the stroke length of the actuator may change dramatically relative to the low frequency stroke length, and due to the nonlinearities which occur at large amplitudes, the values of E and η will change. To accommodate frequency-dependent stiffnesses and loss factors, equation 2.3.17 is modified as follows:

$$c = \frac{1}{\Omega_f - \Omega_i} \int_{\Omega_i}^{\Omega_f} \frac{k(\omega)\eta(\omega)}{\omega} d\omega \qquad \textbf{(2.3.19)}$$

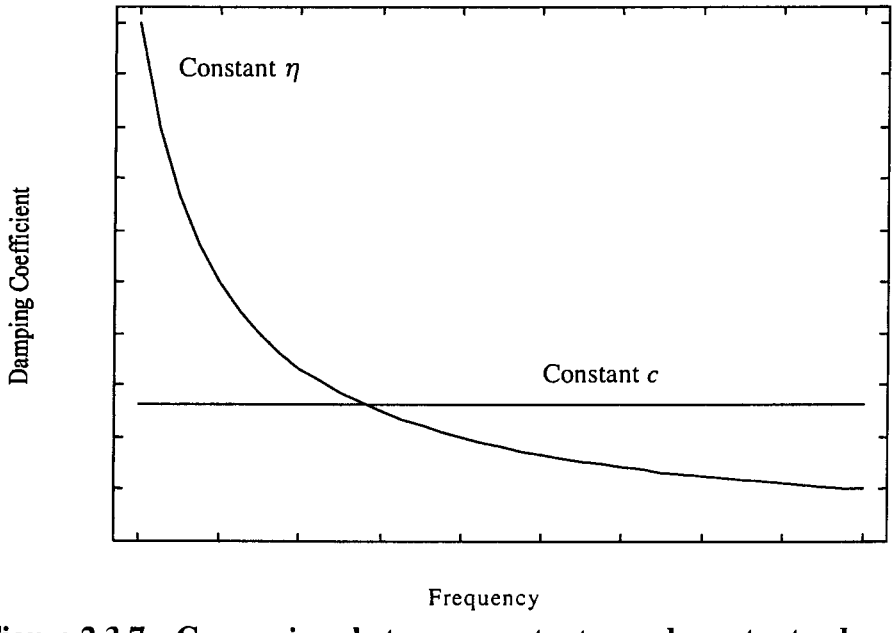

Figure 2.3.7: Comparison between constant η and constant c damping coefficients

A sample calculation of the loss factor and damping coefficient of a Terfenol-D rod is done next. Consider for example a rod with a length of 25 mm and a diameter of 5 mm, excited by a wide-band random (white noise) magnetic field with a reference (DC) value of 103,5 kA/m, a maximum field of 207 kA/m and a minimum value of 0 kA/m. The frequency band of the applied field is 2,5 Hz to 100 Hz. The stress is 12 MPa (compressive).

The parameters required to calculate the damping coefficient, are the large amplitude constant value of Young's Modulus, rod stiffness, strain amplitude, d^H and loss factor. From equations 2.2.1.5 and 2.2.1.8a, $\overline{E} = 36{,}95$ GPa, and from equations 2.3.1 to 2.3.4, $d^H = 6{,}67.10^{-9}$ m/A. By application of equation 2.3.16, k = 29,02 MN/m. The strain amplitude, from equations 2.3.4, is $6{,}9.10^{-4}$. Equation 2.3.14 gives the value of η as 0,0134, and finally, from equation 2.3.18, $c = 2{,}334.10^{3}$ Ns/m.

To summarize, the effects of hysteresis on the magnetostrictive characteristics of Terfenol-D have been discussed in detail in this section. A linear hysteresis loss factor has been defined and viscous damping coefficients have been derived for harmonic and wide-band random excitation.

Before proceeding to the next section, which will cover the effects of hysteresis on the magnetization characteristics of Terfenol-D, it deserves to be mentioned that damping is a phenomenon which is difficult to predict, and is more accurately assessed by means of experimental measurements. Predicted dynamic behaviour of a Terfenol-D actuator and LOS stabilization system will therefore have to be experimentally checked and corrected. The damping model derived above will only serve as a guideline to simulate the actuator and system behaviour in sections 2.7 and 2.8 and will be experimentally determined and corrected in chapters 4 and 5.

The effects of hysteresis on the magnetization characteristics of Terfenol-D

The loading, unloading and dehysterized flux density versus field strength characteristics of Terfenol-D, for a compressive stress of 12 MPa, are shown in figure 2.3.8.

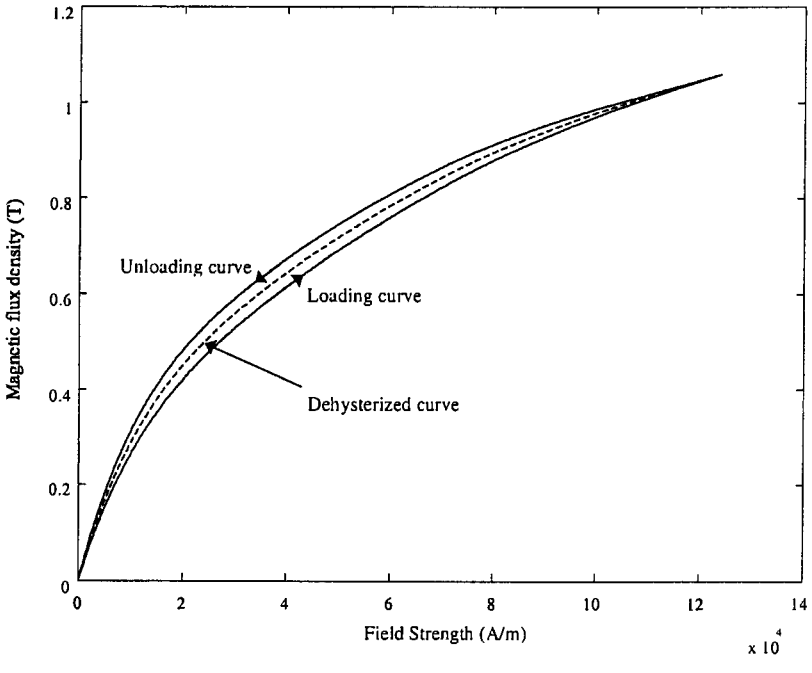

Figure 2.3.8: Loading, unloading and dehysterized flux density versus field strength characteristics of Terfenol-D for a 12 MPa compressive stress [Kvarnsjö, 1993]

Flux density can be expressed mathematically as:

$$B(H)\big|_{\sigma=-12MPa} = \sum_{i=0}^{8} b_i \left(\frac{H}{10^5}\right)^i \qquad \textbf{(2.3.20)}$$

The polynomial coefficients b_i for the loading, unloading and dehysterized flux density characteristics are given in table 2.3.2.

Table 2.3.2: Polynomial coefficients b_i for loading, unloading & dehysterized flux density vs field characteristics of Terfenol-D (12 MPa compressive stress)

Characteristic: i	Loading	Unloading	Dehysterized
0	$3{,}5792.10^{-4}$	$4{,}2134.10^{-4}$	$3{,}8963.10^{-4}$
1	3,4357	4,1987	3,8172
2	-9,8677	-13,49	-11,679
3	20,564	29,362	24,963
4	-26,015	-38,406	-32,210
5	19,742	29,94	24,841
6	-8,795	-13,603	-11,199
7	2,1209	3,3222	2,7216
8	-0,21376	-0,33699	-0,27538

The hysteresis permeability $\mu^{\sigma}_{hysteresis}$ can be calculated by means of the following equation:

$$\mu^{\sigma}_{hysteresis} = \frac{B(H_2)_{loading} - B(H_1)_{unloading}}{2H_A} \qquad \textbf{(2.3.21)}$$

where H_2 is the maximum applied field, H_1 is the minimum field and H_A is field amplitude, given by:

$$H_A = \frac{H_2 - H_1}{2} \qquad \textbf{(2.3.22)}$$

The flux densities $B(H_1)_{unloading}$ and $B(H_2)_{loading}$ are calculated by means of the following equations:

$$B(H_1)_{unloading} = \sum_{i=0}^{8} b_{i\,unloading} \left(\frac{H_1}{10^5}\right)^i \qquad \textbf{(2.3.23a)}$$

$$B(H_2)_{loading} = \sum_{i=0}^{8} b_{i\,loading} \left(\frac{H_2}{10^5}\right)^i \qquad \textbf{(2.3.23b)}$$

where the polynomial coefficients b_i for the unloading and loading characteristics are respectively given by the "loading" and "unloading" columns in table 2.3.2.

Equations 2.3.21 to 2.3.23 provide a simple mathematical tool to calculate the hysteresis permeability. A graph of the hysteresis permeability for a stress of 12 MPa, a reference field of 50 kA/m and a field amplitude range of 4 kA/m to 47 kA/m is shown in figure 2.3.9. For comparison purposes, the dehysterized permeability is also shown.

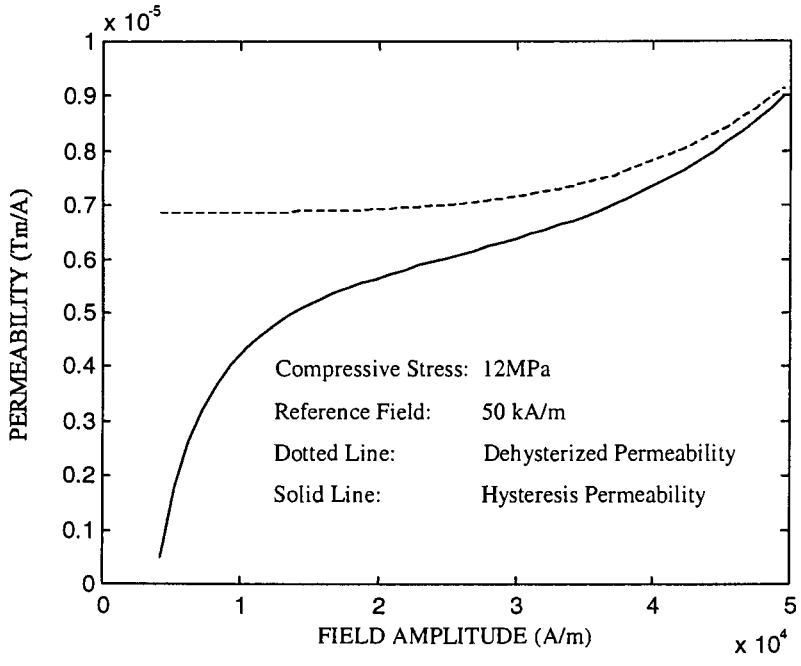

Figure 2.3.9: Comparison between Terfenol-D hysteresis permeability and dehysterized permeability for a 48 kA/m field amplitude range

Figure 2.3.9 shows that, for small field amplitudes, the hysteresis permeability is relatively small in comparison with the dehysterized permeability. As the field amplitude is increased, the hysteresis permeability rises sharply. As the field amplitude approaches the maximum value of 48 kA/m, the hysteresis permeability approaches the dehysterized permeability. It can be seen that hysteresis has a significant effect on the permeability of Terfenol-D, especially at low field amplitudes.

Section 2.3 covered the effects of hysteresis on the magnetostrictive and magnetization characteristics of Terfenol-D. The hysteresis strain constant and permeability, as well as a hysteresis loss factor and damping coefficient, were derived. This concludes the nonlinear characteristics of Terfenol-D. The information given in sections 2.2 and 2.3 will be used in section 2.4 to derive the nonlinear and linear equations of motion and coil current equation of a Terfenol-D actuator.

2.4 Linear and nonlinear equations of motion and coil current equations of a Terfenol-D actuator

The equation of motion and the coil current equation of a Terfenol-D actuator are derived in this section. A diagrammatical representation of the actuator is shown. Assumptions for which the model is valid, are given. The equation of motion is derived for both nonlinear and linear material characteristics. Equations are given for the actuator performance parameters such as displacement, acceleration, strain, stress, force and field strength. A differential equation describing the current in the coil, i.e. the coil current equation, is also derived for both linear and nonlinear material characteristics.

A magnetostrictive actuator is shown diagrammatically in figure 2.4.1. The actuator is mounted on a fixed base and consists of a Terfenol-D rod, a coil, an end cap, a piston and a displacement gain mechanism. The coil induces a field in the rod, which produces a strain and an accompanying compressive force in the rod. The force lifts the piston, whose displacement is amplified by the gain mechanism, thereby extending the stroke length of the actuator. The gain mechanism may operate hydraulically, pneumatically or mechanically. The walls of the actuator serve as magnetic couplers to form a closed circuit for the magnetic flux.

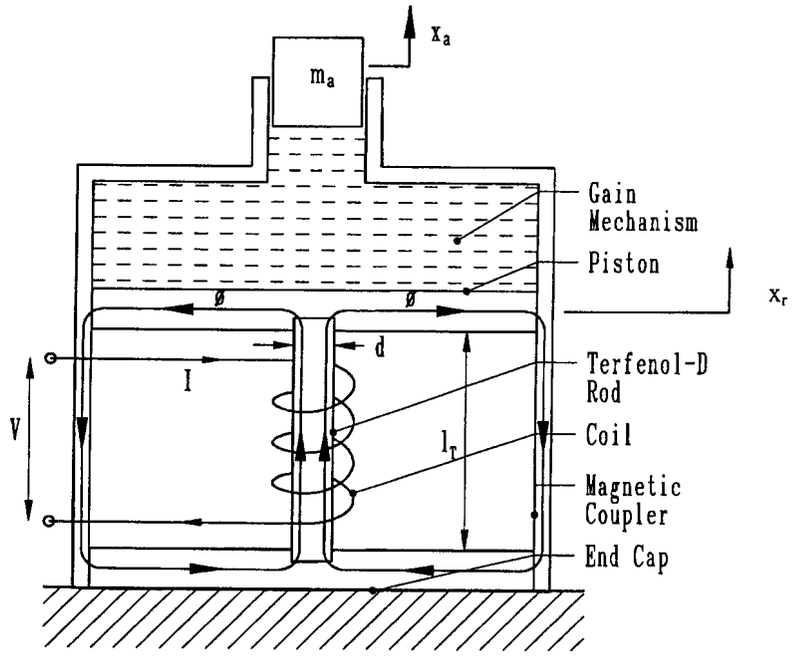

Figure 2.4.1: Diagrammatic representation of a Terfenol-D actuator

The concentrated mass of the actuator is m_a. The displacement of the mass is x_a and the displacement of the piston is x_r. The rod length is l_T and the rod diameter is d. R_c, I and V respectively represent the coil resistance, coil current and input voltage, while the flux in the rod is represented by ϕ.

The equation of motion and the coil current equation of the actuator will be derived from first principles. The equation of motion is a second order differential equation (DE), which

describes the acceleration $\ddot{x}_a$ of the mass in terms of the displacement x_a of the mass and the coil current I. The coil current equation is a first order DE, which describes the rate of change $\dot{I}$ of the coil current in terms of I, $\dot{x}_a$ and the actuator input voltage V.

A number of assumptions are made in order to derive the equations. The first assumption is that the actuator has only one degree of freedom (SDOF). The only displacement parameter that is of importance is the displacement of the mass. Secondly, it is assumed that the end cap and piston are rigid, i.e. there are no displacement losses due to resilience in the actuator. This implies that the elongation of the Terfenol-D rod, times the gain factor, equals the displacement of the mass. Similarly, in the derivation of the coil current equation, infinite permeability of the couplers is assumed, in other words the coupler reluctance, or resistance to magnetic flux, is zero. Lastly, it is assumed that the stiffness of the gain mechanism is zero. The actuator force equals the force produced by the rod, divided by the gain factor.

The nonlinear equation of motion of a Terfenol-D actuator is systematically derived in the next paragraphs. The gain factor is defined in terms of the displacement of the piston and the displacement of the mass. Equations are given for the strain and magnetic field strength in the rod. The stress in the rod is expressed as a nonlinear function of strain and field, which is then used to obtain expressions for the force produced by the rod and the actuator force. A force balance equation is written for the actuator, using Newton's second law. The stress, force produced by the rod, actuator output force and acceleration of the mass are also expressed in terms of the displacement of the mass and the coil current.

The displacement gain factor G of the actuator is defined as the ratio between the displacement of the mass and the elongation x_r of the Terfenol-D rod:

$$G = \frac{x_a}{x_r} \tag{2.4.1}$$

The strain ε in the rod is the displacement of the piston divided by the rod length:

$$\varepsilon = \frac{x_r}{l_T} \tag{2.4.2}$$

It is desirable to eliminate the displacement of the piston from equation 2.4.2, and to express the strain in terms of the displacement of the mass. This is done by substitution of equation 2.4.1 into equation 2.4.2:

$$\varepsilon = \frac{x_a}{G l_T} \tag{2.4.3}$$

The magnetic field H in the rod is given in terms of the coil current I by means of equation 2.4.4:

$$H = \frac{N}{l_T} I \tag{2.4.4}$$

where N is the number of coil turns.

From equation 2.2.1.9, the stress in the rod can be expressed as follows as a function of strain and magnetic field:

$$\sigma = \sigma(\varepsilon, H) \tag{2.4.5}$$

The stress in the rod can be used to derive equations for the force produced by the rod and the actuator output force. The force produced by the rod is the product of the stress in the rod and the cross-sectional area of the rod:

$$F_r = -A_T \sigma \tag{2.4.6}$$

Note the sign convention in equation 2.4.6: A compressive stress in the rod produces a positive force. The actuator output force is the force in the rod divided by the gain factor:

$$F_a = \frac{F_r}{G} \tag{2.4.7}$$

A force balance equation for the actuator is obtained from Newton's second law, i.e. the mass of the actuator times the acceleration of the mass equals the actuator output force:

$$m_a \ddot{x}_a = F_a \tag{2.4.8}$$

From equation 2.4.8, the acceleration of the mass is:

$$\ddot{x}_a = \frac{F_a}{m_a} \tag{2.4.9}$$

The performance parameters of the actuator, i.e. the stress in the rod, force produced by the rod, actuator output force and acceleration of the mass can be obtained from equations 2.4.3 to 2.4.9. It will however be more convenient to express these parameters as functions of displacement of the mass and coil current. This will facilitate the derivation of the equation of motion, coil current equation and state-space equations in section 2.5.

Firstly, the stress in the rod is expressed in terms of displacement and current by substitution of equations 2.4.3 and 2.4.4 into equation 2.4.5:

$$\sigma = \sigma\left(\frac{1}{Gl_T} x_a, \frac{N}{l_T} I\right) \tag{2.4.10}$$

Secondly, the force produced by th of displacement and current by substitution of equation 2.4.10 into equation 2.4.6:

$$F_r = -A_T \sigma\left(\frac{1}{Gl_T}x_a, \frac{N}{l_T}I\right) \tag{2.4.11}$$

Thirdly, the actuator output force is expressed in terms of displacement and current by substitution of equation 2.4.10 into equation 2.4.11:

$$F_a = -\frac{A_T}{G}\sigma\left(\frac{1}{Gl_T}x_a, \frac{N}{l_T}I\right) \tag{2.4.12}$$

Finally, the nonlinear equation of motion is obtained by substitution of equation 2.4.12 into equation 2.4.9:

$$\ddot{x}_a = -\frac{A_T}{m_a G}\sigma\left(\frac{1}{Gl_T}x_a, \frac{N}{l_T}I\right) \tag{2.4.13}$$

Equation 2.4.12 is a nonlinear, second order, ordinary DE which expresses the acceleration of the mass as a function of the displacement of the mass and coil current.

The equation of motion can subsequently be expressed in numerical terms by substitution of equations 2.4.3 and 2.4.4 into equation 2.2.1.9, and by substitution of the resulting equation into equation 2.4.13:

$$\ddot{x}_a = -10^6 \frac{A_T}{m_a G}\sum_{i=0}^{m}\sum_{j=0}^{n} s_{ij}\left(\frac{10^3}{Gl_T}x_a\right)^j\left(\frac{10^{-5}N}{l_T}I\right)^i \tag{2.4.14}$$

where the two-dimensional polynomial coefficients s_{ij} for $m = 7$ and $n = 3$ are given in table 2.2.1.2.

The nonlinear equation of motion of a Terfenol-D actuator has been derived in this section. The strain and stress in the rod, magnetic field, force produced by the rod and actuator output force have also been obtained as nonlinear functions of displacement and coil current. In the next section, the linear equation of motion will be derived using large amplitude constant values of the magnetostrictive parameters, i.e. Young's Modulus and the strain constant.

Linear equation of motion of a Terfenol-D actuator

The linear equation of motion of a Terfenol-D actuator is derived in this section. Average, large amplitude values of the magnetostrictive parameters, i.e. Young's Modulus and the strain constant, are used to express the stress in the rod in terms of the displacement of the mass and the coil current. It will be shown that, in contrast with the nonlinear system, the linear mechanical and magnetostrictive stress terms can be separated. A linear force balance equation is written for the actuator using Newton's second law. The equation of motion,

which gives the acceleration of the mass as a linear combination of the displacement of the mass and the coil current, is derived. The static and dynamic actuator characteristics, i.e. the spring stiffness, natural frequency, damping factor and forcing function are defined and incorporated into the equation of motion. All the terms in the equation of motion are explained.

The linear relationship between strain, mechanical stress and magnetic field, from equation 2.2.1.4, is:

$$\varepsilon = \frac{\sigma}{E} + d^H H \tag{2.4.15}$$

where E and d^H respectively represent the large amplitude average values of Young's Modulus and the strain constant, as given by equations 2.2.1.7a and 2.2.1.7b. From equation 2.4.15, the stress in the rod is expressed as follows as a linear combination of strain and field:

$$\sigma = E\varepsilon - Ed^H H \tag{2.4.16}$$

The first term on the right hand side of equation 2.4.16 is the stress due to the strain, and the second term is the stress due to the applied field. Comparing equations 2.4.16 and 2.4.5 shows that the linear stress equation has an advantage over the nonlinear stress equation, namely that the mechanical and magnetostrictive stress terms can be separated by means of constant factors.

For the purpose of the derivation of the linear equation of motion, it is desirable to express the stress in terms of the displacement of the mass and coil current. This is done by substitution of equations 2.4.3 and 2.4.4 into equation 2.4.16:

$$\sigma = \frac{E}{Gl_T} x_a - \frac{ENd^H}{l_T} I \tag{2.4.17}$$

The above equation will subsequently be used to write the force produced by the rod, the actuator output force and the acceleration of the mass in terms of the displacement of the mass and the coil current. The force produced by the rod is obtained by substitution of equation 2.4.17 into equation 2.4.6:

$$F_r = -\frac{A_T E}{Gl_T} x_a + \frac{A_T ENd^H}{l_T} I \tag{2.4.18}$$

The actuator output force is obtained by substitution of equation 2.4.18 into equation 2.4.7:

$$F_a = -\frac{A_T E}{G^2 l_T} x_a + \frac{A_T ENd^H}{Gl_T} I \tag{2.4.19}$$

The first term on the right hand side of the above equation gives the elastic, or spring force of the actuator, while the second term gives the force supplied by the coil current, or the input

force. The elastic term is negative because it resists the deflection x_a of the spring, while the input force, which forces the mass in the direction of x_a, is positive.

The linear equation of motion is obtained by substitution of equation 2.4.19 into equation 2.4.9:

$$\ddot{x}_a = -\frac{A_T E}{m_a G^2 l_T} x_a + \frac{A_T E N d^H}{m_a G l_T} I \tag{2.4.20}$$

Equation 2.4.20 is a linear, second order, ordinary DE, which gives the acceleration of the mass as a linear combination of the displacement of the mass and the coil current.

Equation 2.4.20 can be simplified by introducing the static and dynamic characteristics of the actuator, i.e. the mass, stiffness, angular natural frequency and input force. To this end, the equation of motion is written as follows:

$$\ddot{x}_a = -\omega_n^2 x_a + \frac{F_I}{m_a} I \tag{2.4.21}$$

where the angular natural frequency ω_n is:

$$\omega_n = \sqrt{\frac{k_a}{m_a}} \tag{2.4.22}$$

and the stiffness k_a is:

$$k_a = \frac{A_T E}{G^2 l_T} \tag{2.4.23}$$

F_I is the ratio of the input force to the input current, given by:

$$F_I = \frac{A_T E N d^H}{G l_T} \tag{2.4.24}$$

Equation 2.4.21 is the undamped linear equation of motion, since it contains no damping terms. Damping is introduced by defining a dimensionless damping factor ζ as:

$$\zeta = \frac{c}{2 m_a \omega_n} \tag{2.4.25}$$

where c is the viscous damping coefficient, which was described in more detail in section 2.3.

The addition of a damping term to equation 2.4.21 alters the equation of motion as follows:

$$\ddot{x}_a = -2\zeta\omega_n\dot{x}_a - \omega_n^2 x_a + \frac{F_l}{m_a} I \tag{2.4.26a}$$

or:

$$\ddot{x}_a + 2\zeta\omega_n\dot{x}_a + \omega_n^2 x_a = \frac{F_l}{m_a} I \tag{2.4.26b}$$

The individual terms in equation 2.4.26b are explained as follows: The first term on the left hand side is the inertia term, the second term is the damping term and the third term is the stiffness term. The term on the right hand side is the forcing term.

The equations for stress, force produced by the rod and actuator output force can be simplified in a similar manner as the equation of motion by introducing the natural frequency, damping factor and input force. The derivation of these equations will not be covered in full here. Instead, only the results will be given.

The stress in the rod, force produced by the rod and actuator output force, in terms of the dynamic characteristics of the actuator, are respectively given by:

$$\sigma = k_a \frac{G}{A_T} x_a + 2\frac{m_a G}{A_T}\zeta\omega_n\dot{x}_a - \frac{G}{A_T} F_l I \tag{2.4.27a}$$

$$F_r = -k_a G x_a - 2m_a G\zeta\omega_n\dot{x}_a + GF_l I \tag{2.4.27b}$$

$$F_a = -k_a x_a - 2m_a\zeta\omega_n\dot{x}_a + F_l I \tag{2.4.27c}$$

To summarize, the linear equation of motion was derived in detail in this section. The coil current equation will subsequently be derived. The nonlinear coil current equation will be derived first, and will be followed by the derivation of the linear coil current equation.

Nonlinear coil current equation of a Terfenol-D actuator

The nonlinear coil current equation of a Terfenol-D actuator is derived in this section. The input voltage of the coil is expressed in terms of the coil current and the rate of change of magnetic flux density. The nonlinear magnetization and magnetostrictive characteristics of Terfenol-D are used to write the coil voltage as a function of the speed of the mass, the coil current and the rate of change of the coil current. Finally, the nonlinear coil current equation is obtained from the coil voltage equation.

The fundamental relationship between the voltage input V to the actuator, the number of coil turns N, the flux density ϕ, the coil resistance R_c and the coil current I is:

$$V = N\dot{\phi} + R_c I \tag{2.4.28}$$

The magnetic flux is the product of the cross-sectional area A_T of the rod and the flux density B:

$$\phi = A_T B \tag{2.4.29}$$

The coil voltage can be expressed in terms of the flux density differentiation of equation 2.4.29 with respect to time, and by substitution of the resulting equation into equation 2.4.28:

$$V = A_T N\dot{B} + R_c I \tag{2.4.30}$$

Equation 2.4.30 expresses the actuator coil input voltage in terms of the flux density rate $\dot{B}$ and the coil current I. The next step is to express the flux rate in terms of the displacement of the mass and the coil current. To this end, the relationship between flux density, stress and field, as given by equation 2.2.2, are used. This relationship is:

$$B = B(\sigma, H) \tag{2.4.31}$$

Differentiation of equation 2.4.31 with respect to time, gives the following equation for the flux density rate $\dot{B}$:

$$\dot{B} = B_\sigma \dot{\sigma} + B_H \dot{H} \tag{2.4.32}$$

where B_σ is the partial derivative of the flux density with respect to mechanical stress at a constant magnetic field strength, which is also d^σ (see section 2.2.2), and B_H is the partial derivative of flux density with respect to field at a constant stress, which is the permeability μ^σ. Equation 2.4.32 can therefore be written as follows:

$$\dot{B} = d^\sigma \dot{\sigma} + \mu^\sigma \dot{H} \tag{2.4.33}$$

where d^σ and μ^σ are functions of stress and field:

$$d^\sigma = d^\sigma(\sigma, H) \tag{2.4.34a}$$
$$\mu^\sigma = \mu^\sigma(\sigma, H) \tag{2.4.34b}$$

The objective of this derivation is to obtain the coil current equation in terms of the same variables as the equation of motion, i.e. x_a and I. To this end, the stress rate and field rate must be eliminated from equation 2.4.33. This is done by differentiation of equation 2.4.16 with respect to time:

$$\dot{\sigma} = E\left(\dot{\varepsilon} - d^H \dot{H}\right) \tag{2.4.35}$$

where, from equations 2.2.1.5 and 2.2.1.6, E and d^H are functions of stress and field:

$$E = E(\sigma, H) \tag{2.4.36a}$$
$$d^H = d^H(\sigma, H) \tag{2.4.36b}$$

The strain rate $\dot{\varepsilon}$ is expressed in terms of the speed of the mass, i.e. $\dot{x}_a$, by differentiation of equation 2.4.3 with respect to time:

$$\dot{\varepsilon} = \frac{\dot{x}_a}{Gl_T} \tag{2.4.37}$$

The field rate $\dot{H}$ is expressed in terms of the rate of change of the coil current, i.e. $\dot{I}$, by differentiation of equation 2.4.4 with respect to time:

$$\dot{H} = \frac{N}{l_T}\dot{I} \tag{2.4.38}$$

After substitution of equations 2.4.37 and 2.4.38 into equation 2.4.35, and subsequent substitution of the resulting equation into equation 2.4.33, the flux density rate becomes:

$$\dot{B} = \frac{Ed^{\sigma}}{Gl_T}\dot{x}_a + \frac{N}{l_T}\left(\mu^{\sigma} - Ed^{\sigma}d^{H}\right)\dot{I} \tag{2.4.39}$$

The actuator coil input voltage is obtained by substitution of equation 2.4.39 into equation 2.4.30:

$$V = \frac{A_T ENd^{\sigma}}{Gl_T}\dot{x}_a + \frac{A_T N^2}{l_T}\left(\mu^{\sigma} - Ed^{\sigma}d^{H}\right)\dot{I} + R_c I \tag{2.4.40}$$

Equation 2.4.40 expresses the coil input voltage in terms of the speed of the mass, the coil current and the rate of change of the coil current. Finally, the coil current equation is obtained by isolating $\dot{I}$ in equation 2.4.40:

$$\dot{I} = \frac{l_T}{A_T N^2\left(\mu^{\sigma} - Ed^{\sigma}d^{H}\right)}\left(-\frac{A_T ENd^{\sigma}}{Gl_T}\dot{x}_a - R_c I + V\right) \tag{2.4.41}$$

Equation 2.4.41 is a nonlinear, first order, ordinary DE which gives the rate of change of the coil current in terms of the speed of the mass, the coil current and the input voltage. The magnetostrictive and magnetization parameters μ^{σ}, E, d^{σ} and d^{H} can be obtained in numerical terms from equations 2.2.1.5, 2.2.1.6, 2.2.2.3 and 2.2.2.4. It must be borne in mind that these equations give the parameters as functions of stress and field, and not as functions of displacement and coil current. However, by substitution of equations 2.4.4 and 2.4.5 into equations 2.4.34 and 2.4.36, the nonlinear functional relationships for the magnetostrictive and

magnetization parameters, in terms of actuator output displacement and coil current, become:

$$\mu^{\sigma} = \mu^{\sigma}\left(\sigma\left(\frac{1}{Gl_T}x_a, \frac{N}{l_T}I\right), \frac{N}{l_T}I\right) \tag{2.4.42a}$$

$$E = E\left(\sigma\left(\frac{1}{Gl_T}x_a, \frac{N}{l_T}I\right), \frac{N}{l_T}I\right) \tag{2.4.42b}$$

$$d^{\sigma} = d^{\sigma}\left(\sigma\left(\frac{1}{Gl_T}x_a, \frac{N}{l_T}I\right), \frac{N}{l_T}I\right) \tag{2.4.42c}$$

$$d^{H} = d^{H}\left(\sigma\left(\frac{1}{Gl_T}x_a, \frac{N}{l_T}I\right), \frac{N}{l_T}I\right) \tag{2.4.42d}$$

To summarize, the nonlinear coil current equation was derived in this section. The linear coil current equation will be derived in the next section. Equation 2.4.40 will form the basis of the derivation.

Linear coil current equation of a Terfenol-D actuator

The linear coil current equation of a Terfenol-D actuator is derived in this section. The average large amplitude constant values of the magnetostrictive and magnetization parameters are used in the derivation. The free inductance, coupling factor and clamped inductance of the coil are defined and employed to simplify the coil current equation. The rate of change of the coil current is written as a linear combination of the speed of the mass, coil current and input voltage.

For the purpose of this derivation, the nonlinear coil voltage equation given by equation 2.4.40 will be used. This equation is repeated here for convenience:

$$V = \frac{A_T E N d^{\sigma}}{Gl_T}\dot{x}_a + \frac{A_T N^2}{l_T}\left(\mu^{\sigma} - E d^{\sigma} d^{H}\right)\dot{I} + R_c I \tag{2.4.43}$$

In the nonlinear case, the magnetostrictive and magnetization parameters μ^{σ}, E, d^{σ} and d^{H} were expressed as functions of displacement and coil current in equations 2.4.42a to 2.4.42d, while in the linear case, these parameters are considered as constants. The linearization technique was covered in more detail in section 2.2.

Equation 2.4.43 is conveniently rewritten as follows in order to introduce the free inductance, the coupling factor and the clamped inductance of the coil into the voltage equation:

$$V = \frac{A_T E N d^{\sigma}}{Gl_T}\dot{x}_a + \frac{A_T N^2 \mu^{\sigma}}{l_T}\left(1 - \frac{E d^{\sigma} d^{H}}{\mu^{\sigma}}\right)\dot{I} + R_c I \tag{2.4.44}$$

The free inductance L_f, coupling factor cf and clamped induction L_0 of the coil are respectively given by:

$$L_f = \frac{A_T N^2 \mu^\sigma}{l_T} \tag{2.4.45}$$

$$cf = \sqrt{\frac{Ed^\sigma d^H}{\mu^\sigma}} \tag{2.4.46}$$

$$L_0 = L_f\left[1-(cf)^2\right] \tag{2.4.47}$$

By substitution of equations 2.4.45 and 2.4.46 into equation 2.4.47 and by substitution of the resulting equation into equation 2.4.44, the coil voltage equation is simplified as follows:

$$\underbrace{V}_{Input} = \underbrace{\frac{A_T ENd^\sigma}{Gl_T}\dot{x}_a}_{\text{"back emf"}} + \underbrace{L_0\dot{I}}_{inductive\ voltage} + \underbrace{R_c I}_{resistive\ voltage} \tag{2.4.48}$$

The first term on the right hand side of equation 2.4.48 gives the coil voltage due to the speed of the mass. This term is known as the "back-emf". The second term gives the coil voltage due to the rate of change of the coil current and is known as the inductive voltage of the coil. The last term gives the coil voltage due to the coil current. This term is the resistive voltage of the coil.

Finally, the linear coil current equation is obtained by isolating $\dot{I}$ in equation 2.4.48:

$$\dot{I} = -\frac{A_T ENd^\sigma}{Gl_T L_0}\dot{x}_a - \frac{R_c}{L_0}I + \frac{1}{L_0}V \tag{2.4.49}$$

To summarize, the linear and nonlinear equations of motion and coil current equations of a Terfenol-D actuator were derived in detail section 2.4. The equation of motion describes the mechanical behaviour of the actuator, while the coil current equation describes the electrical behaviour of the actuator. The two equations therefore describe the behaviour of two separate systems. The equation of motion can only be solved if the coil current is known, while the coil current equation can only be solved if the speed of the mass is known. In order to analyze the behaviour of the actuator as one integrated electromechanical system, the equation of motion and the coil current equation must be coupled into one system of equations. This can be done by means of the state-space method. The state-space equations of the actuator will be derived in section 2.5.

2.5 State-space model and transfer functions of a Terfenol-D actuator

The dynamic equations of the actuator are written in state-space form for the following reasons: Firstly, the equation of motion and the coil current equation can be coupled into one set of dynamic equations. Secondly, transfer functions between the input voltage and all of the actuator outputs, such as the displacement and acceleration of the mass, the rod strain, stress and field, the force producd by the rod and the actuator output force, can be obtained by means of the state-space method.

A third reason for writing the equations in state-space form is to obtain the natural vibration behaviour of the actuator, i.e. actuator behaviour in the absence of any coil voltage input. The actuator eigenvalues and their stability can be evaluated using the state-space method. In the fourth place, the state-space method can be employed to simulate the behaviour of the actuator for any arbitrary input in the time and frequency domains, using either the linear or the nonlinear models. Lastly, the state-space method, inter alia, can be used to design a controller for the LOS stabilization system.

The nonlinear and linear state-space equations, as well as the complex Laplace- and frequency domain *TF*'s of a Terfenol-D actuator, are derived in this section. The section is divided into three parts. The equation of motion and the coil current equation are combined into one set of dynamic actuator equations in section 2.5.1. Both the linear and nonlinear state-space equations are derived. Output equations for the different actuator performance parameters are also given.

The complex Laplace -domain *TF*'s are derived from the linear state and output equations in section 2.5.2. The *TF*'s for all the actuator parameters are given. An open-loop block diagram from the input voltage to the output displacement is shown. The Laplace-domain *TF*'s are transformed to the frequency domain in section 2.5.3. The general complex form of the *TF* is given, after which the magnitude and phase angle of the output displacement to input voltage are given in real form.

2.5.1 State-space model of a Terfenol-D actuator

A method of system representation developed since around 1960, has been the characterization of dynamic systems by means of state equations [Schwarzenbach & Gill, 1986]. The method involves the transformation of one or more sets of DE's with a total order of n into a number n of first order DE's. This requires the introduction of a set of variables, known as the state variables, or states for short, where the number of variables equals the number of DE's.

The state variables are not unique and may be chosen to suit a particular problem. The most suitable states, which describe the behaviour of a Terfenol-D actuator, will be chosen in this section and the state equations will be derived. It will be shown that, for the nonlinear material characteristics, the state derivatives are nonlinear functions of the states and inputs, while for the linear characteristics, the state derivatives are conveniently written as linear combinations of the states and inputs.

In addition to the state equations, a separate set of equations can be written to describe any number of variables, which may be required to analyze the system behaviour, in terms of the states and inputs. These equations are appropriately known as the output equations. A set of output variables will be chosen for the actuator in the following paragraphs, and the linear and nonlinear output equations will be derived. The equation of motion and the coil current equation, which were derived in section 2.4, will form the basis of the derivation of both the state and output equations.

The form of the state and output equations depends on the nature of the system, i.e. whether the system is nonlinear and time-dependent, nonlinear and time-independent, linear and time dependent, or linear and time-independent. The three forms that will be compared in short below, are the general nonlinear and time-dependent form, the nonlinear and time-independent form and the linear and time-independent form. The general nonlinear, time dependent form of the state and output equations is, according to Slotine & Li [1991]:

$$\dot{x} = f(x,u,t) \qquad \textbf{(2.5.1.1a)}$$
$$y = g(x,u,t) \qquad \textbf{(2.5.1.1b)}$$

where x is the state vector, u is the input vector and t denotes time. f is a vector of functions which describes the state derivatives $\dot{x}$ in terms of the states, inputs and time, and g is a vector of functions which describes the outputs in terms of the states, inputs and time.

If the system is time-independent and non-linear, equations 2.5.1.1a and 2.5.1.1b are modified as follows:

$$\dot{x} = f(x,u) \qquad \textbf{(2.5.1.2a)}$$
$$y = g(x,u) \qquad \textbf{(2.5.1.2b)}$$

It can be seen from equations 2.5.1.2a and 2.5.1.2b that the state and output vectors only depend on the states and inputs, and are independent of time.

If the system is time-independent and linear ("LTI"), the state and output equations are:

$$\dot{x} = Ax + Bu \qquad \textbf{(2.5.1.3a)}$$
$$y = Cx + Du \qquad \textbf{(2.5.1.3b)}$$

where A is a constant square matrix which relates the state derivatives to the states, known as the coefficient matrix. B is a constant matrix, which relates the state derivatives to the inputs, known as the driving matrix. C is a constant matrix, which relates the outputs to the states, known as the output matrix. D is a constant matrix, which relates the outputs to the inputs, known as the transmission matrix.

The states must be chosen in such a way that system behaviour can be described by a combination of the states and inputs, such as in equations 2.5.1.2 and 2.5.1.3. A suitable choice of states can for instance be the displacement x_a and speed $\dot{x}_a$ of the actuator mass, as well as the coil current I. This choice is in agreement with the variables chosen for the equation of motion and the coil current equation in section 2.4.

For this choice of states, the state vector can be written as follows:

$$x = \{x_a, \dot{x}_a, I\}^T \tag{2.5.1.4}$$

where the superscript T denotes the transpose of the state matrix.

The input u to the system can be chosen as the actuator coil input voltage V:

$$u = V \tag{2.5.1.5}$$

The outputs are chosen as the displacement x_a of the mass, coil current I, strain ε, field H and stress σ in the rod, the force F_r produced by the rod, the actuator force F_a and the acceleration $\ddot{x}_a$ of the mass:

$$y = \{x_a, I, \varepsilon, H, \sigma, F_r, F_a, \ddot{x}_a\}^T \tag{2.5.1.6}$$

Having chosen the most suitable states and outputs, the nonlinear and linear state and output equations can be derived from the linear and nonlinear equation of motion and the coil current equation. The nonlinear equation of motion was given by equation 2.4.13 and the nonlinear coil current equation was given by equation 2.4.41 and 2.4.42a to 2.4.42d. For the sake of completeness, the equation of motion and the coil current equation will be repeated below. The nonlinear equation of motion is:

$$\ddot{x}_a = -\frac{A_T}{m_a G}\sigma\left(\frac{1}{Gl_T}x_a, \frac{N}{l_T}I\right) \tag{2.5.1.7}$$

where σ is the mechanical stress as a function of displacement and current, as given by equation 2.4.14:

$$\sigma\left(\frac{1}{Gl_T}x_a, \frac{N}{l_T}I\right) = \sum_{i=0}^{m}\sum_{j=0}^{n} s_{ij}\left(\frac{10^3}{Gl_T}x_a\right)^j\left(\frac{10^{-5}N}{l_T}I\right)^j \tag{2.5.1.8}$$

The two-dimensional polynomial coefficients s_{ij} for $m = 7$ and $n = 3$ can be obtained from table 2.2.1.2 in section 2.2.1.

The nonlinear coil current equation, from equation 2.4.41, is:

$$\dot{I} = \frac{l_T}{A_T N^2\left(\mu^\sigma - Ed^\sigma d^H\right)}\left(-\frac{A_T ENd^\sigma}{Gl_T}\dot{x}_a - R_c I + V\right) \tag{2.5.1.9}$$

where the magnetostrictive and magnetization parameters μ^σ, E,d^σ and d^H are functions of the displacement and coil current state variables:

$$\mu^\sigma = \mu^\sigma\left(\sigma\left(\frac{1}{Gl_T}x_a, \frac{N}{l_T}I\right), \frac{N}{l_T}I\right) \quad \textbf{(2.5.1.10a)}$$

$$E = E\left(\sigma\left(\frac{1}{Gl_T}x_a, \frac{N}{l_T}I\right), \frac{N}{l_T}I\right) \quad \textbf{(2.5.1.10b)}$$

$$d^\sigma = d^\sigma\left(\sigma\left(\frac{1}{Gl_T}x_a, \frac{N}{l_T}I\right), \frac{N}{l_T}I\right) \quad \textbf{(2.5.1.10c)}$$

$$d^H = d^H\left(\sigma\left(\frac{1}{Gl_T}x_a, \frac{N}{l_T}I\right), \frac{N}{l_T}I\right) \quad \textbf{(2.5.1.10d)}$$

The nonlinear state equations can now be written in the state-space form as given by equation 2.5.1.2a. This is done by combining the equation of motion (equation 2.5.1.7) and the coil current equation (equation 2.5.1.9) into one vector of functions:

$$\dot{x} = f(x,u) \quad \textbf{(2.5.1.11)}$$

where f is given by:

$$f = \begin{Bmatrix} \dot{x}_a \\ -\frac{A_T}{m_a G}\sigma\left(\frac{1}{Gl_T}x_a, \frac{N}{l_T}I\right) \\ \frac{l_T}{A_T N^2\left(\mu^\sigma - Ed^\sigma d^H\right)}\left(-\frac{A_T ENd^\sigma}{Gl_T}\dot{x}_a - R_c I + V\right) \end{Bmatrix} \quad \textbf{(2.5.1.12)}$$

and the state vector x and input u are respectively given by equations 2.5.1.4 and 2.5.1.5.

The nonlinear output equations are written in the form equation of 2.5.1.2b, by making use of the nonlinear relations which were derived in section 2.4. The actuator output displacement, coil current, strain, field, stress, force produced by the rod, actuator output force and output acceleration, are given in terms of the states and inputs as:

$$y = g(x,u) \quad \textbf{(2.5.1.13)}$$

In equation 2.5.1.13, the output vector y is given by equation 2.5.1.6 and g is given by:

$$g = \begin{Bmatrix} x_a \\ I \\ \frac{1}{Gl_T} x_a \\ \frac{N}{l_T} I \\ \sigma\left(\frac{1}{Gl_T} x_a, \frac{N}{l_T} I\right) \\ -A_T \sigma\left(\frac{1}{Gl_T} x_a, \frac{N}{l_T} I\right) \\ -\frac{A_T}{G} \sigma\left(\frac{1}{Gl_T} x_a, \frac{N}{l_T} I\right) \\ -\frac{A_T}{m_a G} \sigma\left(\frac{1}{Gl_T} x_a, \frac{N}{l_T} I\right) \end{Bmatrix} \qquad \textbf{(2.5.1.14)}$$

An additional output, which is not incorporated in the output vector, is the coil power P. The coil power is omitted because it is not possible to describe P as a linear combination of states and inputs, since P is the product of the input voltage V and the coil current I:

$$P = VI \qquad \textbf{(2.5.1.15)}$$

The nonlinear state and output equations were derived in this section. The linear state and output equations will be derived next.

Linear state and output equations of a Terfenol-D actuator

The damped linear equation of motion of the actuator, (see equation 2.4.26), is:

$$\ddot{x}_a = -\omega_n^2 x_a - 2\zeta\omega_n \dot{x}_a + \frac{F_l}{m_a} I \qquad \textbf{(2.5.1.16)}$$

where F_l is given by equation 2.4.24 as:

$$F_l = \frac{A_T E N d^H}{Gl_T} \qquad \textbf{(2.5.1.17)}$$

The linear coil current equation, as given by equation 2.4.49, is:

$$\dot{I} = -\frac{A_T E N d^\sigma}{Gl_T L_0} \dot{x}_a - \frac{R_c}{L_0} I + \frac{1}{L_0} V \qquad \textbf{(2.5.1.18)}$$

The linear state and output equations are subsequently written in the state-space form as given by equations 2.5.1.3a and 2.5.1.3b:

$$\dot{x} = Ax + Bu \qquad \textbf{(2.5.1.19a)}$$
$$y = Cx + Du \qquad \textbf{(2.5.1.19b)}$$

where A, B, C and D are given by:

$$A = \begin{bmatrix} 0 & 1 & 0 \\ -\omega_n^2 & -2\zeta\omega_n & \dfrac{A_T ENd^H}{Gl_T} \\ 0 & -\dfrac{A_T ENd^\sigma}{Gl_T L_0} & -\dfrac{R_c}{L_0} \end{bmatrix} \qquad \textbf{(2.5.1.20a)}$$

$$B = \frac{1}{L_0}\begin{Bmatrix} 0 \\ 0 \\ 1 \end{Bmatrix} \qquad \textbf{(2.5.1.20b)}$$

$$C = \begin{bmatrix} 1 & 0 & 0 \\ 0 & 0 & 1 \\ \dfrac{1}{Gl_T} & 0 & 0 \\ 0 & 0 & \dfrac{N}{l_T} \\ k_a \dfrac{G}{A_T} & 2\dfrac{m_a G}{A_T}\zeta\omega_n & -\dfrac{ENd^H}{l_T} \\ -k_a G & -2m_a G\zeta\omega_n & \dfrac{A_T ENd^H}{l_T} \\ -k_a & -2m_a\zeta\omega_n & \dfrac{A_T ENd^H}{Gl_T} \\ -\omega_n^2 & -2\zeta\omega_n & \dfrac{A_T ENd^H}{m_a Gl_T} \end{bmatrix} \qquad \textbf{(2.5.1.20c)}$$

$$D = 0 \qquad \textbf{(2.5.1.20d)}$$

and the state vector x and input u are given by equations 2.5.1.4 and 2.5.1.5 respectively.

Equations 2.5.19 and 2.5.20 give the linear state and output equations. The only remaining output, which is not included in the above equations, because it cannot be written as a linear combination of states and inputs, is the coil power P. The coil power is given by:

$$P = VI \qquad \textbf{(2.5.1.21)}$$

To summarize, the nonlinear and linear state and output equations of the actuator were derived in sevtion 2.5.1. The linear state equations can be utilized to derive the complex Laplace domain transfer functions of the actuator, i.e. the ratios of each of the outputs in equation 2.5.1.6, to the input voltage V. This will be done in section 2.5.2.

2.5.2 Complex Laplace-domain transfer functions of a Terfenol-D actuator

The complex Laplace (s)-domain *TF*'s of a Terfenol-D actuator are derived from the linear state space equations obtained in section 2.5.1. The ratio's of the outputs, i.e. the actuator output displacement x_a, coil current I, strain ε, field H and stress σ in the rod, the force F_r produced by the rod, the actuator output force F_a and and the acceleration $\ddot{x}_a$ of the mass, relative to the coil input voltage V, are given in fractional form. The numerators and denominators of the *TF*'s are expressed as polynomial functions of s. The polynomial coefficients of the numerators of all the outputs are given. An open-loop block diagram is included to show the coupling between the mechanical and electrical subsystems.

The transfer functions can be obtained from the state-space model by means of the following equation [Crawley & Hall, 1991]:

$$G(s) = C[sI - A]^{-1} B + D \qquad \textbf{(2.5.2.1)}$$

where $G(s)$ is the transfer function matrix, whose size equals the product of the number of inputs and number of outputs. The derivation of equation 2.5.2.1 is given in appendix A.

Any particular transfer function $G(s)$ can be written in fractional form as:

$$G(s) = \frac{P(s)}{Q(s)} \qquad \textbf{(2.5.2.2)}$$

where $P(s)$ and $Q(s)$ are the numerator and denominator of $G(s)$ respectively.

Equations 2.5.2.1 and 2.5.2.1 can be applied to obtain all the *TF*'s of the actuator, i.e. $X_a(s)/V(s)$, $I(s)/V(s)$, $\varepsilon(s)/V(s)$, $H(s)/V(s)$, $\sigma(s)/V(s)$, $F_r(s)/V(s)$, $F_a(s)/V(s)$ and $\ddot{X}_a(s)/V(s)$.

Two *TF*'s of special importance, which are required for modelling actuator dynamic behaviour and which can also be relatively easily determined experimentally, are $X_a(s)/V(s)$ and $\ddot{X}_a(s)/V(s)$.

$X_a(s)/V(s)$, for instance, is obtained as follows: Substitution of equations 2.1.1.20a and 2.5.1.20b, the first row of the C matrix in equation 2.5.1.20c and equation 2.5.1.20d, into equation 2.5.2.1, gives:

$$\frac{X_a(s)}{V(s)} = \frac{\dfrac{A_T E N d^H}{m_a G l_T L_0}}{s^3 + \left[2\zeta\omega_n + \dfrac{R_c}{L_0}\right]s^2 + \left[\omega_n^2 + \left(\dfrac{A_T EN}{Gl_T}\right)^2 \dfrac{d^\sigma d^H}{m_a L_0} + 2\zeta\omega_n \dfrac{R_c}{L_0}\right]s + \left[\dfrac{R_c}{L_0}\omega_n^2\right]} \tag{2.5.2.3}$$

Similar equations can be derived for the other *TF*'s. For the sake of convenience, the *TF*'s are written in the following general form:

$$G(s) = \frac{P(s)}{Q(s)} = \frac{p_2 s^2 + p_1 s + p_0}{s^3 + q_2 s^2 + q_1 s + q_0} \tag{2.5.2.4}$$

where the polynomial coefficients p_0 to p_2 of the numerator are determined by the particular output and the denominator polynomial coefficients q_0 to q_2 are the same for all the outputs.

The denominator polynomial coefficients q_0 to q_2 are given by:

$$q_0 = \frac{R_c}{L_0}\omega_n^2 \tag{2.5.2.5a}$$

$$q_1 = \omega_n^2 + \left(\frac{A_T EN}{Gl_T}\right)^2 \frac{d^\sigma d^H}{m_a L_0} + 2\zeta\omega_n \frac{R_c}{L_0} \tag{2.5.2.5b}$$

$$q_2 = 2\zeta\omega_n + \frac{R_c}{L_0} \tag{2.5.2.5c}$$

The numerator coefficients for the different outputs are given in table 2.5.2.1.

An open-loop block diagram of the actuator for a coil voltage input and displacement output is shown in figure 2.5.2.1. The block diagram also shows the coupling between the mechanical and electrical subsystems.

This concludes the derivation of the Laplace-domain transfer functions of the actuator. The frequency domain transfer functions will be derived from the Laplace domain transfer functions in section 2.5.3.

Table 2.5.2.1: Numerator polynomial coefficients for the *TF*'s of a Terfenol-D actuator

TF	p_0	p_1	p_2
$\frac{X_a(s)}{V(s)}$	$\frac{A_T ENd^H}{m_a Gl_T L_0}$	0	0
$\frac{I(s)}{V(s)}$	$\frac{\omega_n^2}{L_0}$	$\frac{2\zeta\omega_n}{L_0}$	$\frac{1}{L_0}$
$\frac{\varepsilon(s)}{V(s)}$	$\frac{A_T ENd^H}{m_a L_0 (Gl_T)^2}$	0	0
$\frac{H(s)}{V(s)}$	$\frac{N\omega_n^2}{l_T L_0}$	$\frac{2\zeta\omega_n N}{l_T L_0}$	$\frac{N}{l_T L_0}$
$\frac{\sigma(s)}{V(s)}$	0	0	$\frac{-ENd^H}{l_T L_0}$
$\frac{F_r(s)}{V(s)}$	0	0	$\frac{A_T ENd^H}{l_T L_0}$
$\frac{F_a(s)}{V(s)}$	0	0	$\frac{A_T ENd^H}{Gl_T L_0}$
$\frac{\ddot{X}_a(s)}{V(s)}$	0	0	$\frac{A_T ENd^H}{m_a Gl_T L_0}$

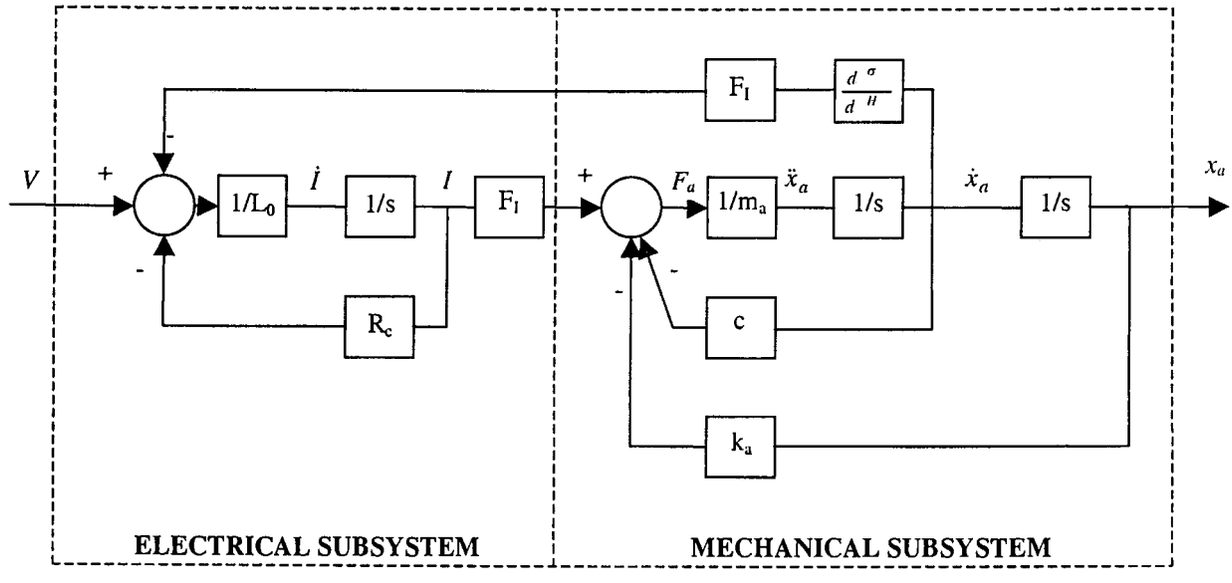

Figure 2.5.2.1: Block diagram of a Terfenol-D actuator

2.5.3 Actuator frequency domain transfer functions

In this section, the linear frequency *(ω)*-domain *TF*'s are obtained from the *s*-domain *TF*'s. Expressions for *ω*-domain *TF*'s are first written in a general complex form, after which the magnitude and phase angle will be expressed as real functions of frequency. It will be shown that all the *TF*'s can be written in the same complex form. The magnitude and phase angle of the actuator output displacement to coil voltage input ratio will be given as real functions of *ω*.

The frequency domain transfer function of the actuator is obtained from the Laplace-domain transfer function by setting $s \equiv j\omega$ in equation 2.5.2.2:

$$G(j\omega) = \frac{P(j\omega)}{Q(j\omega)} \tag{2.5.3.1}$$

where $j = \sqrt{-1}$ and $G(j\omega)$ is a complex function, which can be expressed as follows in terms of a magnitude $G_0(\omega)$ and phase angle $\varphi(\omega)$:

$$G(j\omega) = G_0(\omega) e^{j\varphi(\omega)} \tag{2.5.3.2}$$

The magnitude and phase angle are respectively given by the following real functions of ω:

$$G_0(\omega) = \sqrt{[\mathrm{Re}\{G(j\omega)\}]^2 + [\mathrm{Im}\{G(j\omega)\}]^2} \tag{2.5.3.3a}$$

$$\varphi(\omega) = \tan^{-1}\left[\frac{\mathrm{Im}\{G(j\omega)\}}{\mathrm{Re}\{G(j\omega)\}}\right] \tag{2.5.3.3b}$$

Re{ } and Im{ } are the real and imaginary parts of a complex function and $\tan^{-1}$ is the arctan function.

The general complex form of all the *TF*'s is obtained by substitution of $s \equiv j\omega$ into equation 2.5.2.4:

$$G(j\omega) = \frac{P(j\omega)}{Q(j\omega)} = \frac{(p_0 - p_2\omega^2) + j\omega p_1}{(q_0 - q_2\omega^2) + j\omega(q_1 - \omega^2)} \tag{2.5.3.4}$$

where p_0 to p_2 for the applicable *TF* are given in table 2.5.2.1 and q_0 to q_2 are given in equations 2.5.2.5a to 2.5.2.5c. The complex *TF* between the actuator output displacement and coil input voltage is given by:

$$G(j\omega) = \frac{p_0}{(q_0 - q_2\omega^2) + j\omega(q_1 - \omega^2)} \tag{2.5.3.5}$$

The magnitude and phase angle of the above *TF* are obtained in real form by substitution of equation 2.5.3.5 into equations 2.5.3.3a and 2.5.3.3b respectively:

$$G_0(\omega)=\sqrt{\frac{\left[p_0\left(q_0-q_2\omega^2\right)\right]^2+\left[\omega^3-q_1\omega\right]^2}{\left[q_0-q_2\omega^2\right]^2+\left[q_1-\omega^2\right]^2}} \qquad \textbf{(2.5.3.6a)}$$

$$\varphi(\omega)=\tan^{-1}\left[\frac{\omega^3-q_1\omega}{p_0\left(q_0-q_2\omega^2\right)}\right] \qquad \textbf{(2.5.3.6b)}$$

Equation 2.5.3.6a and 2.5.3.6b give the magnitude and phase angle of the ω-domain *TF* between the actuator output displacement and the coil input voltage. Similar equations can be derived for all the other *TF*'s.

To summarize section 2.5, the nonlinear and linear state and output equations of a Terfenol-D actuator were obtained from the equations of motion and the coil current equation. The linear complex Laplace-domain and frequency domain *TF*'s were also derived. The state-space equations and *TF*'s will be used in section 2.6 to analyze the natural vibration behaviour of the actuator, and in section 2.7 to simulate the forced linear and nonlinear behaviour of the actuator, in the time and frequency domains.

2.6 Natural vibration behaviour of a Terfenol-D actuator

This section describes the natural vibration behaviour of a Terfenol-D actuator. The importance of the analysis of the natural behaviour is mentioned. Two methods of obtaining the natural parameters are explained. The natural parameters are determined from the eigenvalues of the linear state-space model and from the poles of the *TF*'s. A closed form solution of the poles is given. It will be shown that two of the poles are complex conjugates and that the third pole is real. The effective angular natural frequency, damping factor and resistance to inductance ratio of the actuator coil are expressed in terms of the real and imaginary parts of the poles. A method of determining the stability of the poles is given.

It is essential to obtain the natural parameters of the actuator, for a number of reasons. In the first place, it will be important for the actuator designer to know what the maximum allowable load mass can be, before the natural frequency is lowered to such an extent that resonance will occur inside the disturbance band. If the natural frequency is too low, the isolation band of the actuator may not be wide enough to reject the disturbance. Secondly, the damping factor will significantly influence the displacement peak of the actuator at resonance: The higher the damping, the lower the peak. A third reason is that the dynamic displacement of the actuator will be 3 dB lower than the static displacement at a frequency corresponding to the resistance to inductance ratio (R_c/L_0) of the actuator coil. As is the case with the natural frequency, an R_c/L_0-value which exceeds the maximum frequency of the disturbance band, is preferable.

Furthermore, the natural parameters are required to analyze actuator stability. Stability solely depends on the sign of the real parts of the poles. If the real parts of all the poles are negative, the actuator is unconditionally stable. Lastly and most importantly, due to coupling between

the mechanical and electrical subsystems, which was described in more detail in section 2.5, the effective natural frequency, damping factor and resistance to inductance ratio of the coil will differ from those of the separate mechanical and electrical systems.

The natural parameters of the actuator can be determined by two methods, namely by means of the eigenvalues of the coefficient (A)-matrix of the state equations and by means of the poles of the TF, which are also the roots of the denominator $Q(s)$ of the TF. Both methods will be explained in short below. The eigenvalues of the A-matrix will be determined first, after which the poles of the TF will be obtained.

The linear state equation of the actuator, as given by equation 2.5.1.19a, is:

$$\dot{x} = Ax + Bu \tag{2.6.1}$$

where A is the coefficient matrix, x is the state vector, B is the driving matrix and u is the input vector. In the case of natural behaviour, the inputs are zero, therefore:

$$u = 0 \tag{2.6.2}$$

The state-space formulation of the natural behaviour of the actuator is obtained by substitution of equation 2.6.2 into equation 2.6.1:

$$\dot{x} = Ax \tag{2.6.3a}$$

or:

$$\dot{x} - Ax = 0 \tag{2.6.3b}$$

In order to obtain the eigenvalues, equation 2.6.3 must be transformed to the complex Laplace domain. The Laplace-domain equivalent of equation 2.6.3b is:

$$[sI - A]x = 0 \tag{2.6.4}$$

where s is the complex Laplace-domain differential operator and I is a unit matrix with the same size as A. The eigenvalues of A are obtained from equation 2.6.4 by setting the determinant of the $[sI - A]$ matrix equal to zero:

$$|sI - A| = 0 \tag{2.6.5}$$

The s-values for which equation 2.6.5 is valid, represents the eigenvalues. The number of eigenvalues equals the number of states.

Equation 2.6.5 provides a method of obtaining the natural parameters of the actuator by means of the state-space method. An alternative method which can be used, is to determine the poles of the transfer function. This method will be explained next.

The poles α are the roots of the denominator $Q(s)$ of the *TF*, or the values of s for which $Q(s)=0$:

$$\alpha = s\big|_{Q(s)=0} \tag{2.6.6}$$

where $Q(s)$ was given by equation 2.5.2.4 as:

$$Q(s) = s^3 + q_2 s^2 + q_1 s + q_0 \tag{2.6.7}$$

In equation 2.6.7, q_0 to q_2 are the polynomial coefficients of the denominator, which were given by equations 2.5.2.5a to 2.5.2.5c as:

$$q_0 = \frac{R_c}{L_0}\omega_n^2 \tag{2.6.8a}$$

$$q_1 = \omega_n^2 + \left(\frac{A_T EN}{Gl_T}\right)^2 \frac{d^\sigma d^H}{m_a L_0} + 2\zeta\omega_n \frac{R_c}{L_0} \tag{2.6.8b}$$

$$q_2 = 2\zeta\omega_n + \frac{R_c}{L_0} \tag{2.6.8c}$$

Either equation 2.6.5 or equation 2.6.6 can be used to obtain the natural parameters of the actuator, since the eigenvalues of A are equal to the roots of $Q(s)$.

The solutions of equations 2.6.5 and 2.6.6 can be mathematically obtained in closed form, or by means of numerical methods. A closed form solution for the roots α of a third order polynomial, such as in equation 2.6.7, is given by, inter alia, Spiegel [1968]. The poles of the actuator are:

$$\alpha_1 = -\frac{1}{2}(S+T) - \frac{1}{3}q_2 + \frac{1}{2}j\sqrt{3}(S-T) \tag{2.6.9a}$$

$$\alpha_2 = -\frac{1}{2}(S+T) - \frac{1}{3}q_2 - \frac{1}{2}j\sqrt{3}(S-T) \tag{2.6.9b}$$

$$\alpha_3 = S + T - \frac{1}{3}q_2 \tag{2.6.9c}$$

where S and T are given by:

$$S = \sqrt[3]{\frac{9q_1q_2 - 27q_0 - 2q_2^3}{54} + \sqrt{\left(\frac{3q_1 - q_2^2}{9}\right)^3 + \left(\frac{9q_1q_2 - 27q_0 - 2q_2^3}{54}\right)^2}} \tag{2.6.10a}$$

$$T = \sqrt[3]{\frac{9q_1q_2 - 27q_0 - 2q_2^3}{54} - \sqrt{\left(\frac{3q_1 - q_2^2}{9}\right)^3 + \left(\frac{9q_1q_2 - 27q_0 - 2q_2^3}{54}\right)^2}} \tag{2.6.10b}$$

Closer inspection of equations 2.6.9a to 2.6.9c indicates that the first two poles, i.e. α_1 and α_2, are complex conjugates, while α_3 is real.

A compact form of equations 2.6.9a to 2.6.9c is obtained by expressing the poles as follows in terms of the effective natural parameters, i.e. the effective damping factor, natural frequency and resistance to inductance ratio of the coil:

$$\alpha_1 = -\zeta_{eff}\omega_{neff} + j\omega_{neff}\sqrt{1-\zeta_{eff}^2} \tag{2.6.11a}$$

$$\alpha_1 = -\zeta_{eff}\omega_{neff} - j\omega_{neff}\sqrt{1-\zeta_{eff}^2} \tag{2.6.11b}$$

$$\alpha_3 = -\frac{R_c}{L_{0\,eff}} \tag{2.6.11c}$$

where ζ_{eff} is the effective damping factor, ω_{neff} is the effective angular natural frequency and $R_c/L_{0\,eff}$ is the effective resistance to inductance ratio.

The abovementioned natural parameters can be written in terms of the polynomial coefficients of the *TF* denominator by comparing the respective equations for the poles, as given by equations 2.6.9, with those given by equations 2.6.11:

$$\omega_{n\,eff} = \sqrt{S^2 - ST + T^2 + \frac{1}{3}(S+T)q_2 + \frac{1}{9}q_2^2} \tag{2.6.12a}$$

$$\zeta_{eff} = \frac{\frac{1}{2}(S+T) + \frac{1}{3}q_2}{\sqrt{S^2 - ST + T^2 + \frac{1}{3}(S+T)q_2 + \frac{1}{9}q_2^2}} \tag{2.6.12b}$$

$$\frac{R_c}{L_{0\,eff}} = -S - T + \frac{1}{3}q_2 \tag{2.6.12c}$$

where S and T were given by equations 2.6.10a and 2.6.10b.

The last purpose of the analysis of the natural behaviour is to determine the stability of the poles of the *TF*. As was mentioned before, this is done by investigating the sign of the real part of each pole. If the real part of each pole is negative, the actuator is unconditionally stable. If the real part of a pole is positive, that particular pole is unstable. If the real part of a pole is zero, the pole is marginally stable. It can be shown that the effective damping factor, angular natural frequency and resistance to inductance ratio of the actuator are positive, therefore, from equations 2.6.11, the real parts of all the poles are negative. It can be concluded that the linear behaviour of the actuator is unconditionally stable.

To summarize, the linear natural behaviour of a magnetostrictive actuator was analyzed in this section. Forced behaviour will be analyzed in the next section. Time and frequency domain simulations will be done to determine the output displacement, field, strain constant, Young's modulus, piezomagnetic cross-coupling constant and permeability for steady-state harmonic

and random coil input voltages. The state-space model and the frequency domain *TF*'s, which were respectively derived in sections 2.5.1 and 2.5.3, will be used to simulate the behaviour of the actuator.

2.7 Simulation of the characteristics and behaviour of a Terfenol-D actuator

In this section, the characteristics and behaviour of a magnetostrictive actuator are simulated. The results will be used in section 2.8 to calculate the linear LOS stabilization system parameters. Possible techniques for solving the nonlinear equations of motion and coil current equation are discussed and compared, and the most suitable technique is recommended. The solution technique is explained. Simulation and actuator input parameters are given. The simulations are carried out, after which the results are tabled, shown graphically and discussed.

2.7.1 Solution techniques for nonlinear equations of motion

A vast number of techniques exist for solving the equations of motion of nonlinear dynamic systems. These techniques can mainly be classified in two groups, i.e. time-domain techniques and frequency-domain techniques. In time-domain techniques, system parameters such as static (DC) output, rise-time, settling time, maximum displacement and maximum acceleration are obtained. If the system is written in state-space form, the states are also obtained.

In frequency-domain techniques, system parameters such as transfer functions (in magnitude and phase form), DC output, natural frequencies, anti-resonance frequencies and damping factors are obtained. For nonlinear systems, the transfer function dependence on input amplitude is also obtained.

Time-domain techniques include the method of slowly varying amplitude and phase, the perturbation method (also called the method of small parameters) and direct integration methods of the state equations. The latter are mainly the Euler method, Heun's method, 4^{th} and 5^{th} order Runge-Kutta methods, and predictor-corrector methods, such as the Adams-Bashforth and Adams-Moulton methods.

Frequency-domain techniques include, inter alia, the harmonic balance method and the Describing Function (DF) method. In the harmonic balance method, the output of the system to a harmonic input is obtained. Only the fundamental component of the output is retained and higher harmonics in the output are rejected. Using the DF method, the output can be calculated for higher harmonics, but at the cost of additional computational effort. The harmonic balance and DF methods can be considered equivalent if only the fundamental frequency component of the output is considered [Van Schoor, 1989].

Solution techniques considered in this study, are exact methods, the perturbation method, the method of slowly-varying amplitude and phase, statistical linearization, the DF method, Runge-Kutta methods and an iterative harmonic balance technique.

Exact methods

It is possible to obtain exact solutions for only a relatively few second order nonlinear equations of motion [Harris, 1988]. These methods are exact in the sense that the solution is given either in closed-form or in an expression that can be evaluated numerically to any desired degree of accuracy.

Exact solutions for forced vibration of nonlinear systems are virtually nonexistent [Harris, 1988], except if the system can be represented in a stepwise linear manner. Exact methods are discussed in more detail in appendix B.

The perturbation method and the method of slowly varying amplitude and phase

The perturbation method is based on the assumption that the equation of motion of a weakly nonlinear system can be written in the same form as that of a linear system, with an added term accounting for the nonlinearity. The time-domain solution is expressed as a linear series of time functions, whose coefficients are determined recursively. The perturbation method is described in short in appendix C.

The method of slowly varying amplitude and phase is based on the assumption that the solution of the equation of motion can be written as a harmonic function of time, whose amplitude and phase change with time. The method is described in short in appendix D.

Both the perturbation method and the method of slowly varying amplitude and phase can be used to solve the equations of motion of systems with weak nonlinearities. However, for systems with hard nonlinearities, such as Coulomb damping, hysteresis and dead-bands, the methods are, firstly, difficult to apply, and secondly, give highly inaccurate solutions. The behaviour of systems with hard nonlinearities is more easily analyzed with the statistical linearization-, harmonic balance- and DF methods.

The perturbation method and method of slowly varying amplitude and phase, are not easily applied to couple the equations of motion to the coil current equation. State methods, like the Runge-Kutta methods, are better suited for this purpose.

Statistical linearization

Three types of statistical methods for solving nonlinear equations of motion can be distinguished. These are the Fokker-Planck, perturbation and equivalent linearization methods [Atalik & Utku, 1976]. The perturbation method has already been discussed above. The Fokker-Planck method can be used to obtain exact solutions for white-noise inputs. Its disadvantage is that severe restrictions must be imposed on the nonlinearities and on the spectral density of the excitations.

Statistical linearization has a wide range of applicability for solving equations of motion of nonlinear systems under random excitation. The method is an extension of the method of slowly varying amplitude and phase. The method is discussed in appendix E.

The limitation of applying the method to the dynamic analysis of a magnetostrictive actuator, is that the strain characteristic of Terfenol-D is dependent on two variables, i.e. mechanical stress and magnetic field strength (see equation 2.2.1.2). This characteristic makes the statistical linearization method difficult to apply directly. The method can however be applied to obtain the natural frequency, damping factor and coil R_c/L_0 ratio if the time-domain solution of the actuator is known.

The Describing Function (DF) method

In a linear system, the output to a sinusoidal input is also sinusoidal. The output to input ratio is known as the transfer function (*TF*). For a spectrum of frequencies, the output to input ratio is known as the frequency response function (FRF). FRF's are often used for dynamic system modelling, simulation, characterization and control design purposes, because the *TF* at a particular frequency can be expressed in terms of two parameters only, i.e. a magnitude and a phase angle. Linear system analysis can therefore be simplified considerably using FRF's.

In a nonlinear system, the output to a sinusoidal input is non-sinusoidal. Generally, the output will contain more than one frequency component. A nonlinear system therefore cannot be characterized in terms of a transfer function, because its *TF* is undefined. However, if higher harmonics in the output can be neglected (albeit at the cost of accuracy) and only the fundamental component is retained, it is possible to express nonlinear system behaviour in terms of a *TF*. This *TF* is known in dynamics and control engineering as a Describing Function (DF).

In order to analyze a system in terms of its DF, the system must meet certain conditions [Slotine & Li, 1991]. The first is that the nonlinearity must be odd. If the nonlinearity is even, a DC shift will occur in the output. Secondly, the system must contain only one nonlinearity. If the system contains multiple nonlinearities, the nonlinearities must be lumped together, or only the dominant nonlinearity must be considered. Thirdly, the nonlinearity must be time-invariant. This condition is satisfied by a large variety of nonlinearities in practice, such as saturation, hysteresis, backlash and Coulomb friction.

The DF of any nonlinearity, which meets the above requirements, can be derived. A relatively simple method is given by Slotine & Li [1991]. The method is discussed in short in appendix F.

The DF method can also be extended to analyze nonlinear system behaviour to non-harmonic inputs, like two-sinusoid inputs, dual-inputs (e.g. DC plus sinusoid), transient and random inputs. *N* is tabled for a vast range of nonlinearities, for each of the above input types, by Gelb & Vander Velde [1968]. Examples of nonlinearities applicable to the analysis of Terfenol-D characteristics, are saturation and hysteresis. The DF's of these nonlinearities can be found in Gelb & Vander Velde [1968].

The main advantage of the DF method, is that it provides a frequency-domain linearization technique. System characteristics, such as input dependent natural frequency, damping factor and transfer functions, can be easily obtained.

Another advantage of the method is that it can be applied to describe the behaviour of a strongly nonlinear system in a relatively simple way. Hard nonlinearities, such as saturation, hysteresis, Coulomb damping, dead zones and backlash, are easily dealt with.

Depending on the cut-off and excitation frequencies of the system, the first-harmonic approach adopted by the DF method, can be highly accurate. This is particularly true of systems with low-pass filtering characteristics.

The DF method has a number of disadvantages. Firstly, systems which do not display low-pass filtering characteristics, are not necessarily accurately modelled by the DF technique. MDOF systems, for example, may require the inclusion of higher harmonics in the output series expansion for accurate modelling.

Secondly, nonlinearities depending on more than one system parameter, may be difficult to analyze. An example is Terfenol-D, whose strain depends on both field and stress (see equation 2.2.1.2). The problem is aggravated if the output contains a DC component. Terfenol-D, for example, requires a biasing (DC) field and stress to increase the saturation strain (see section 2.2.1).

Runge-Kutta (R-K) methods

In the R-K methods, the states and outputs are obtained in the time domain by direct integration of the state equations. The solution of each state equation is approximated by a polynomial. The order of the polynomial can vary from 1st order to 5th order and higher. The higher the order, the more accurate the solution for the same computational effort [Chapra & Canale, 1985]. For this reason, higher order methods are often preferred to lower order methods. The R-K methods are discussed in detail by Press et al [1992], Burden & Faires [1985], Chapra & Canale [1985], Gerald & Wheatley [1984] and Conte & de Boor [1972]. A 5th order method, also known as Butcher's method, is described mathematically in appendix G.

The advantages of the R-K methods are as follows: If time-domain solutions to nonlinear state equations are required, these methods are often used. The reasons for their popularity are high accuracy and simplicity of use. No prior knowledge of analytical solution methods to DE's is required to apply the R-K methods. All that is required, is relatively simple algebra.

Being state-space solution techniques, the R-K methods allow relatively easy coupling of other state equations to the equations of motion. In the analysis of a magnetostrictive actuator, coupling of the coil current equation to the equation of motion is required. The coil current equation (equation 2.5.1.9), was coupled to the equation of motion (equation 2.5.1.7) in section 2.5, resulting in the state equations 2.5.1.11 and 2.5.1.12.

For wide-band random and harmonic inputs, the R-K methods will give at least one output superharmonic for all frequencies up to half the Nyquist frequency. The lower the ratio between the excitation frequency and the sample frequency, the more superharmonics will be included.

The R-K methods are the only methods capable of describing the two-dimensional magnetostrictive and magnetization characteristics (i.e. stress and field-dependence) of

Terfenol-D in a relatively simple way. Stress and field are calculated using equations 2.4.10 and 2.4.4 respectively, after which the state equations (2.5.1.11 and 2.5.1.12) are solved as described in appendix G.

The R-K methods do also have a number of disadvantages. The first is that no insight into frequency-domain characteristics is provided. The transfer functions, natural frequency, damping factor and coil R_c/L_0 ratio cannot be directly obtained. However, if the time-domain solutions are transformed to the frequency domain, the linear characteristics can be "extracted" using data-fitting techniques. Unfortunately, this method is computationally expensive [Van Schoor, 1989].

For numerically stiff systems, the R-K methods can become numerically unstable if large time steps are used. The problem can be solved either by using smaller time steps, or by using adaptive time stepping. In the latter method, the time step is automatically adjusted according to the changing stiffness of the system. This technique in itself has another disadvantage, namely that the time-domain output will be unequally spaced. If the solution is transformed to the frequency-domain using the Fast Fourier Transform (FFT) technique, inaccurate amplitudes and phases will result. Data interpolation will be required to ensure equally spaced output data.

In the case of hysteretic systems, the state equations may contain discontinuous terms. During a simulation, the state derivative may jump from one level to another within a time-step, resulting in an inaccurate solution. The problem can be solved by adjusting the time increment in such a way that the jump occurs exactly at the end of the time step. This measure may however be clumsy to implement in a numerical solution procedure, since an additional conditional test must be implemented to check whether the jump has occurred.

Being time-domain techniques, the Runge-Kutta methods are initial value dependent. The methods may therefore be potentially dangerous to use if the system of equations is chaotic.

Iterative harmonic balance technique

In the iterative harmonic balance technique, a linear complex transfer function of the actuator is obtained, which takes account of the effects of hysteresis. The procedure is as follows: A number of discrete frequencies are defined in the excitation band. For each frequency, the field amplitude is obtained iteratively. A starting value of the field amplitude is assumed, which is used to calculate Youngs's modulus E, piezomagnetic cross-coupling constant d^{σ}, hysteresis strain constant d^{H}_{hyst}, hysteresis permeability μ^{σ}_{hyst} and equivalent damping coefficient c. The damping factor and R_c/L_0 ratio of the coil are then calculated. These parameters are substituted into the transfer function equations. The coil input voltage and voltage to field transfer function are used to calculate a new value of the field amplitude. The procedure is repeated until the field amplitude converges. The same procedure is applied to all the frequencies in the excitation band.

The iterative harmonic balance method explained above is in essence a DF technique. The advantages and disadvantages of the method are therefore the same as those of the DF method. An additional problem encountered with the harmonic balance method is that

convergence may be difficult to achieve at certain frequencies. At a notch frequency in the voltage amplitude to field *TF*, for instance, the field amplitude may be so low that the hysteresis strain constant and permeability can drop to zero. This will result in infinite values of certain *TF* numerator and polynomial coefficients.

2.7.2 Selection and description of a suitable solution technique for the actuator state equations

The advantages and disadvantages of the different nonlinear system solution techniques were discussed above. The most suitable technique is selected and described in this section. Methods not suitable for solving the state equations are eliminated.

Exact methods can be ruled out because they cannot be used to describe forced behaviour of the Terfenol-D actuator. The perturbation method is unsuitable because a high number of terms are required in the output to describe the discontinuous nature of hysteresis. The same applies to the method of slowly varying amplitude and phase, with the additional difficulty of coupling the coil current equation to the equation of motion.

The statistical linearization method can only be used if the time-domain behaviour of the actuator is known. The difficulty with the method is that the input voltage may contain a DC term to bias the field. Due to this DC offset, using the RMS values of μ^{σ}, E, d^{σ} and d^{H}, will result in inaccurate solutions to the state-space equations. However, fairly accurate results for dehysterized behaviour can be obtained if the average values of these variables, instead of the RMS values, are used.

The R-K methods are ideal for solving the state-space equations in the time-domain, because the dependence of both field and stress can be simultaneously addressed. The R-K methods can however not be considered to describe hysteresis behaviour, due to their inability to handle discontinuities.

The DF and harmonic balance methods can be considered if it can be shown that the magnetostrictive and magnetization parameters are dependent on field alone, instead of both field and stress. Fortunately, this proof can be obtained from the R-K solution.

The following procedure will be used to determine the actuator coil voltage to displacement *TF*. The time-domain solution for dehysterized behaviour will be obtained using the 5^{th} order R-K method. It will be shown that, for dehysterized behaviour, the average values of μ^{σ}, E, d^{σ} and d^{H} do not vary significantly with varying RMS values of input coil voltage. The frequency-domain solution to the state equations, with hysteresis taken into consideration, will be obtained using the iterative harmonic balance method. The *TF*'s for dehysterized behaviour will be compared with those including hysteresis effects. It will be shown that hysteresis has a significant effect on the magnitudes and phases of the *TF*'s.

Description of the iterative harmonic balance method

An algorithm for calculating the actuator parameters and *TF* using the iterative harmonic balance method is described stepwise as follows:

Step I: Specify the parameters of the actuator whose *TF* is required, i.e. mass m_a, displacement gain factor G, Terfenol-D rod length l_T, rod cross-sectional area A_T, coil resistance R_c, number of coil windings N, mechanical prestress σ_0 and coil input voltage amplitude V_A.

Step II: Define the desired frequency in the excitation band. For a wide-band spectrum, start with a low frequency, e.g. 0,01 Hz.

Step III: Estimate the field amplitude. For a starting value, use the following equation:

$$H_A = \frac{N}{l_T} I_A \qquad \textbf{(2.7.2.1)}$$

where H_A and I_A are the field and current amplitude respectively.

I_A is given by:

$$I_A = \frac{V_A}{R_c} \qquad \textbf{(2.7.2.2)}$$

where V_A is the coil input voltage amplitude and R_c is the coil resistance.

Step IV: Using H_A, calculate $\overline{E}$ and $\overline{d^{\sigma}}$ from equations 2.2.1.8a and 2.2.2.6a. Calculate d^{H}_{hyst} from equations 2.3.2 and 2.3.4. From equations 2.3.21 and 2.3.23, calculate μ^{σ}_{hyst}. Using equations 2.4.45 to 2.4.47, calculate L_f, cf and L_0. From equations 2.3.14 to 2.3.16, calculate η, k_a and c. Use equations 2.4.22 and 2.4.25 to calculate ω_n and ζ.

Step V: Substitute the above values of the dynamic parameters into the frequency domain transfer function equation 2.5.3.6a. The coil voltage to field *TF* numerator polynomial coefficients p_0 to p_2 are given in table 2.5.2.1, while the denominator coefficients q_0 to q_2 are given in equations 2.5.2.5a to 2.5.2.5c respectively. Calculate the field amplitude for the given coil voltage input amplitude.

Step VI: Use the new field amplitude and repeat steps IV and V until the field amplitude converges. Methods such as the secant and Newton-Raphson methods may be used to accelerate convergence.

Step VII: Calculate the coil voltage to displacement transfer function magnitude and phase using equations 2.5.3.6a and 2.5.3.6b, with the numerator polynomial coefficient p_0 given in table 2.5.2.1 and the denominator polynomial coefficients q_0 to q_2 given by equations 2.5.2.5a to 2.5.2.5c.

Step VIII: Return to step II and define a new frequency. Repeat steps III to VI until the field converges. Repeat step VII to obtain the *TF* magnitude and phase. Repeat steps I to VIII until the *TF*'s of all the desired frequencies in the excitation band have been solved.

2.7.3 Terfenol-D actuator simulation procedure and results

The simulation procedure and results of a Terfenol-D actuator are covered in this section. The simulations serve two purposes. In the first place, linear actuator characteristics are required to calculate the LOS system characteristics in section 2.8. In the second place, the results of the simulations will be used as inputs to the design of the actuators and LOS stabilization system in chapter 3.

The simulations are done in three steps. Firstly, nonlinear and linear simulations are carried out, using the 5^{th} order Runge-Kutta method, to obtain the dehysterized, nonlinear actuator characteristics. States and outputs are calculated for different coil input voltages. Transfer functions (*TF's*) between coil voltage and actuator displacement are obtained from the simulation results. The procedure and results are given in appendix H.

Secondly, average values of permeability, Young's modulus, piezomagnetic cross-coupling constant and strain constant are calculated from the nonlinear simulation results. These values are used to obtain the linear, dehysterized, characteristics. The characteristics are presented and discussed in appendix J.

Lastly, linear actuator characteristics, which include the effects of hysteresis, are calculated using the iterative harmonic balance technique. The RMS values of the inputs correspond with those of the time-domain simulations. The effects of hysteresis on field amplitude, permeability, strain constant and damping coefficient are calculated (see appendix K). The actuator characteristics are tabled. The actuator stiffness is calculated and the damping factor spectrum is shown graphically.

Actuator and simulation parameters

The actuator parameters required for simulation purposes are the concentrated mass, dimensionless displacement gain factor, Terfenol-D rod length, diameter and cross-sectional area, coil resistance, number of coil windings, coil bias voltage, bias field and bias stress. Mathematical equations, which describe the relationships between these parameters, were derived in section 2.4.

Time-domain simulation parameters are sample frequency, maximum time duration, minimum, maximum and RMS input voltages. Outputs are the actuator states (displacement, speed and coil current), stress and field, as well as the magnetostrictive and magnetization parameters, i.e. permeability, Young's modulus, piezomagnetic cross-coupling constant and strain constant. Nonlinear *TF* spectra are calculated from the input voltage and output displacement. Frequency-domain simulation outputs are field, permeability, strain constant and damping coefficient. Linear *TF* spectra are calculated using these outputs.

The actuator parameters are given in table 2.7.3.1. For the purpose of modelling the characteristics in this chapter, the parameters are fixed. A study will be done in chapter 3 to analyze the effects of varying parameters on actuator characteristics and to select the parameters in such a way as to meet the design criteria.

The sample frequency for time-domain simulations is 2,5 kHz. This frequency is 25 times the maximum frequency of the desired isolation band of the LOS stabilization system, i.e. 100 Hz. The reason for using such a high sample frequency is that the actuator mass is considerably lower than that of the entire system, resulting in a higher natural frequency. Maximum time duration is 40 s, in order to obtain statistically reliable data.

Table 2.7.3.1: Terfenol-D actuator parameters

Actuator parameter	Value
Actuator concentrated mass (m_a)	0,15 kg
Displacement gain factor (G)	5,4
Terfenol-D active rod length (l_T)	35 mm
Rod diameter (d)	6 mm
Rod cross-sectional area (A_T)	$2{,}827.10^{-5}$ m^2
Coil resistance (R_c)	3,2 Ω
Number of coil windings (N)	640
Coil input bias voltage (V_b)	8,75 V
Bias field (H_b)	50 kA/m
Mechanical bias stress (σ_b)	-12 MPa

Wide-band random (white noise) coil voltages are used as inputs for the time-domain simulations. In order to ensure positive field strengths, an input voltage with a minimum of zero and a maximum of 17,5 V (twice the bias voltage) is applied. The RMS value of this input (the full-scale input), is 2,18 V. In order to investigate the effects of nonlinearities, two additional inputs are applied, whose RMS values are 75% and 50% of the RMS value of the full-scale input, i.e. 1,63 V and 1,09 V. Harmonic inputs with the same RMS values as the random inputs are used for the frequency-domain simulations.

Actuator linear characteristics

A summary of the most important actuator characteristics, at 0,01 Hz and resonance, for a 2,18 V RMS input, is given in table 2.7.3.2.

The actuator linear stiffness, from equation 2.4.23, is given by:

$$k_a = \frac{A_T E}{G^2 l_T} \qquad \textbf{(2.7.3.1)}$$

Substitution of the applicable values in tables 2.7.3.1 and 2.7.3.2 into equation 2.7.3.1 gives the actuator stiffness as $6{,}5.10^5$ N/m.

Table 2.7.3.2: Actuator characteristics at 0,01 Hz and resonance for a 2,18 V RMS input

Parameter	0,01 Hz	Resonance (355 Hz)
Field amplitude H_A	17618 A/m	7946 A/m
Permeability μ^σ	$5{,}57.10^{-6}$ Tm/A	$3{,}63.10^{-6}$ Tm/A
Young's modulus E	23,46 GPa	23,46 GPa
Piezomagnetic cross-coupling constant d^σ	$1{,}088.10^{-8}$ m/A	$1{,}088.10^{-8}$ m/A
Strain constant d^H	$9{,}522.10^{-9}$ m/A	$6{,}338.10^{-9}$ m/A
Damping coefficient c	$1{,}31.10^{6}$ Ns/m	24,31 Ns/m
TF magnitude	10,2 μm/V	17,7 μm/V
TF phase	-0,1263 rad	-2,205 rad
Stroke length (17,5 V p-p)	178,5 μm	309,8 μm

The frequency spectrum of the damping coefficient, for a 2,18 V RMS input voltage, is shown in figure 2.7.3.1. The damping coefficient at 0,01 Hz is $1{,}31.10^{6}$ Ns/m. A sharp notch appears between 328 Hz and 332 Hz. At the latter frequency, the damping coefficient is 4,59 Ns/m. For a frequency range of 0,01 Hz to approximately 200 Hz, damping coefficient varies hyperbolically with frequency. In this range, the mathematical relationship between frequency and damping coefficient is:

$$c(f) = \frac{13076}{f} \qquad \textbf{(2.7.3.2)}$$

where f is frequency and c is damping coefficient.

The hyperbolic relationship between damping coefficient and frequency was discussed in section 2.3, where hysteresis models of Terfenol-D were derived (see also equation 2.3.15). On a logarithmic scale, the damping coefficient characteristic between 0,01 Hz and 200 Hz is a straight line, as shown in figure 2.7.3.1.

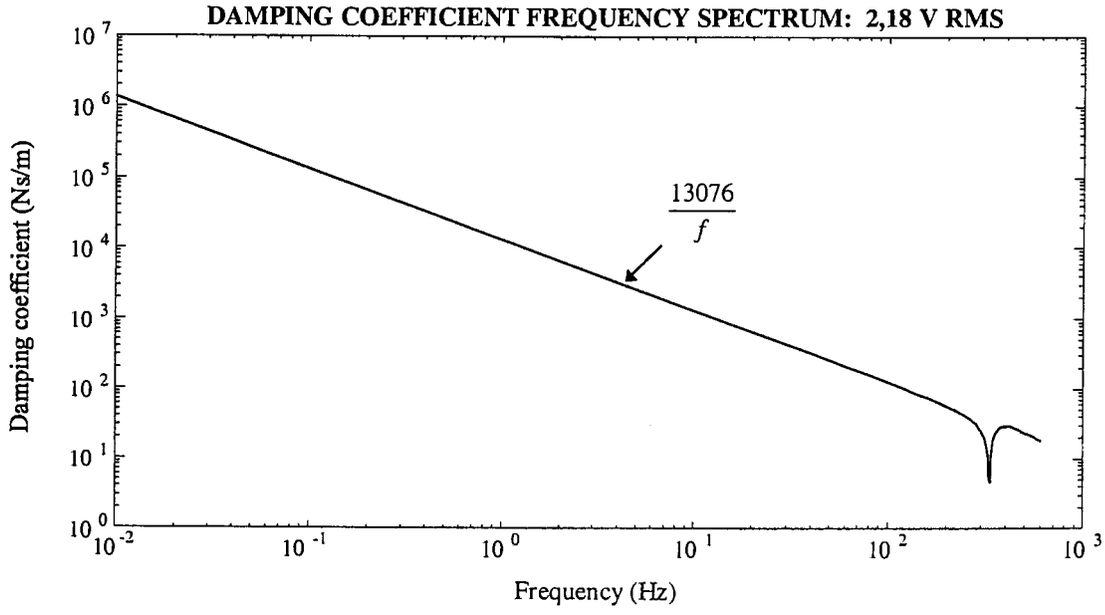

Figure 2.7.3.1: Damping coefficient frequency spectrum for a 2,18 V RMS input

The linear transfer functions, which include the effects of hysteresis, for 2,18 V, 1,63 V and 1,09 V RMS inputs, are shown in figure 2.7.3.2.

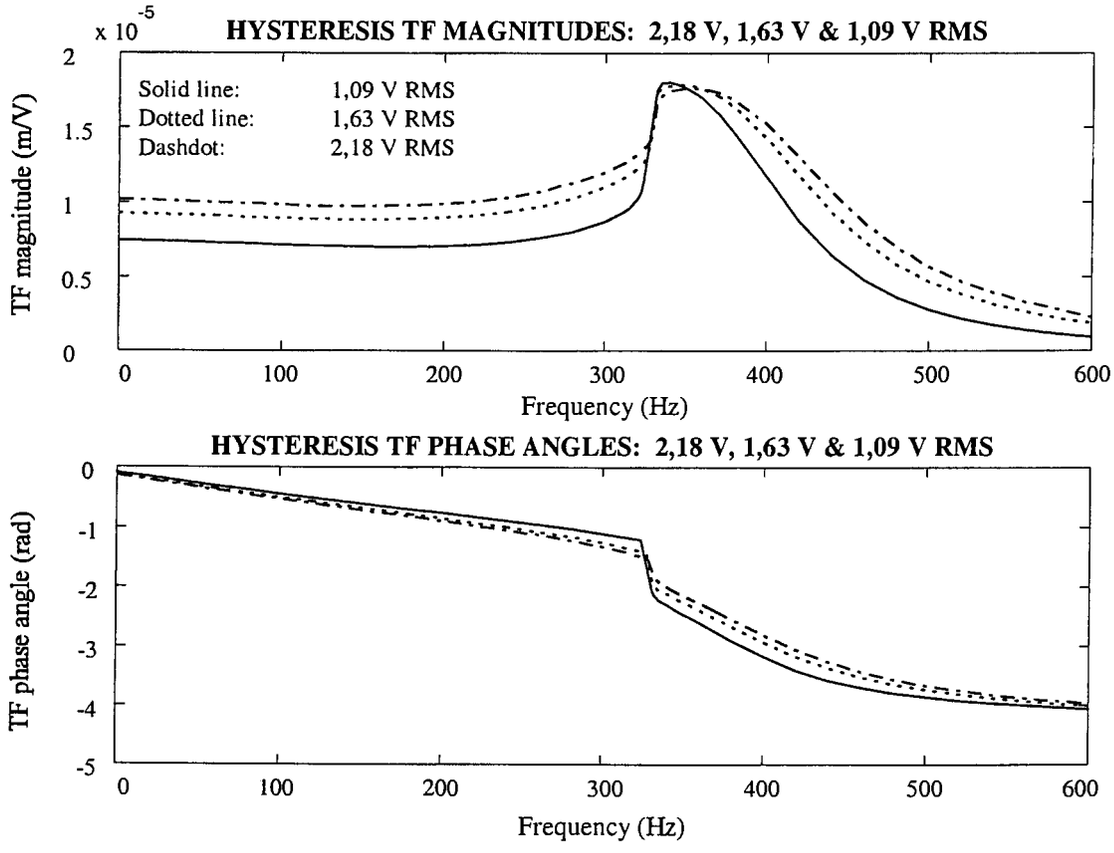

Figure 2.7.3.2: Actuator transfer functions for 2,18 V, 1,63 V and 1,09 V RMS inputs

It can be seen from figure 2.7.3.2 that input voltage magnitude has a significant effect on the characteristics of the Terfenol-D actuator. This can mainly be attributed to the effects of hysteresis. Furthermore, a typical softening characteristic is displayed.

To conclude section 2.7, the hysteresis damping model used in this section was derived from published quasi-static magnetostrictive and magnetization hysteresis loops, as given in section 2.3. These loops are currently the only source available for modelling damping.

High frequency effects on the hysteresis parameters are unknown at this stage. Experimentally measured damping may differ from modelled damping, as will its influence on measured dynamic characteristics. The latter will be experimentally determined in chapter 4, after which the dynamic parameters will be extracted form the test results, using linear identification techniques in chapter 5.

The next section, i.e. section 2.8, will be devoted to the analysis of the characteristics and behaviour of the LOS stabilization system, consisting of two Terfenol-D actuators, the optical instrument and the instrument support structure. The characteristics obtained in section 2.7.3 will be used to model the actuators and system.

2.8 Magnetostrictive LOS stabilization system model

The characteristics of the magnetostrictive LOS stabilization system are modelled in this section. The system consists of the two Terfenol-D actuators, the optical instrument and a support structure for the instrument. The model developed here forms a theoretical basis for open-loop system (plant), to be controlled in chapter 6, as well as to update system dynamic parameters in chapter 5.

A schematic layout of the system is shown and a mathematical model is developed. A beam model is used to analyze the characteristics of the instrument and support structure. Lumped mass, stiffness and damping models are used for the actuators. Actuator hysteresis is modelled using equivalent, linear viscous damping. The equation of motion is derived in modal coordinates.

A number of solution methods for the equation of motion, i.e. the exact separation of variables method, Galerkin, Finite Element (FE), Finite difference (FD) and Rayleigh-Ritz methods, are discussed and compared in short. The Rayleigh-Ritz method is selected as the most suitable solution technique and discussed in detail. Assumed mode shapes are selected and coupled mass, stiffness and damping matrices are obtained using energy methods. An eigenvalue analysis is carried out to obtain the normal mode shapes and natural frequencies.

The equation of motion, in modal form, is coupled to the coil current equation. Transfer functions between the coil input voltages and outputs, i.e. the vertical displacements at the sensor locations and the LOS angle of the system, are derived using state-space techniques. The magnitudes and phases of the frequency-domain transfer functions are shown graphically.

2.8.1 System layout and mathematical model

A schematic layout of the LOS stabilization system is shown in figure 2.8.1.1. The two actuators are mounted at the ends of the structure, between the base and structure. The actuator mass, stiffness, damping coefficient and force are respectively given by m_a, k_a, c_a and F_a. The actuators are soft in the vertical translational direction, but are relatively rigid in the rotational (pitching) direction. In order to allow angular motion of the instrument, the support structure is provided with flexures between the instrument and actuator attachment points.

The optical instrument material is steel. In the interest of saving mass, aluminium is used for the support structure. Aluminium spacers and an aluminium stiffener are provided to prevent bending of the instrument during excitation.

For the purpose of this study, a clamped-clamped beam with actuated supports is used to model the system characteristics and behaviour. Strictly speaking, two beams, each with its own material properties (flexural rigidity and mass per unit length), should be used to separately model the instrument and structure. However, to simplify the model, the assumption is made that the instrument and structure have a common neutral axis. This makes it possible to express the material properties of the individual components in terms of that of a single beam. Due to the presence of notches, spacers and a stiffener, the geometric properties of the beam vary along its length. The beam model is shown in figure 2.8.1.2.

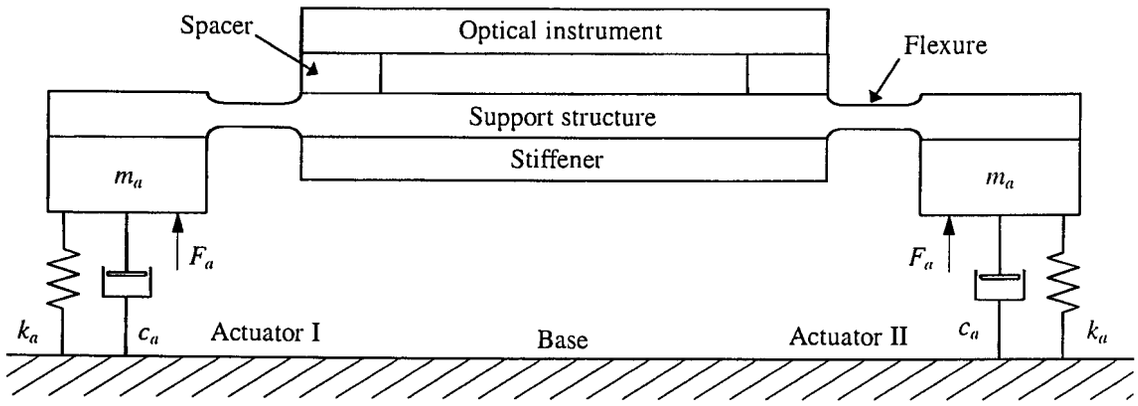

Figure 2.8.1.1: Schematic system layout

The length of the beam is l. The concentrated mass, stiffness, damping coefficient and force of actuator I are given by m_{a1}, k_{a1}, c_{a1} and F_{a1}, while those of actuator II are given by m_{a2}, k_{a2}, c_{a2} and F_{a2}. The output displacements of the two actuators are given by y_{a1} and y_{a2}.

The structural properties of the beam, i.e. density, cross-sectional area, Young's modulus and second moment of area, are respectively given by ρ_s, A_s, E_s and I_s. The properties vary with x, the distance from the left support. The LOS angle of the instrument is given by θ.

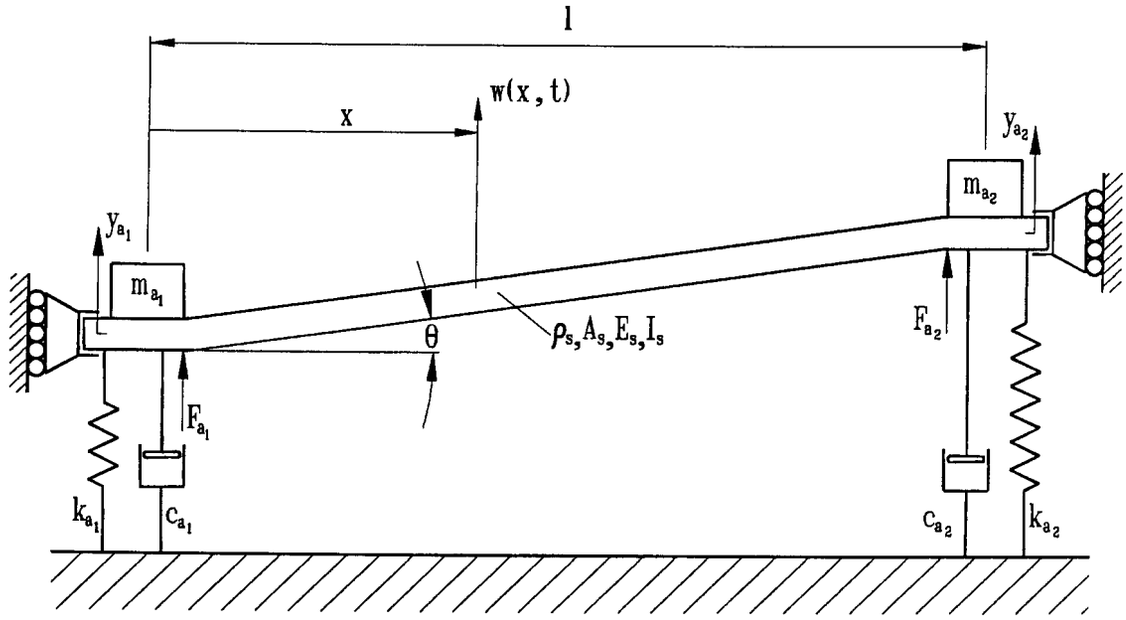

Figure 2.8.1.2: Beam model of optical instrument and support structure

The vertical, or transverse, displacement w at any point x and time t is:

$$w = w(x,t) \qquad \textbf{(2.8.1.1)}$$

The linear equation of motion of the beam is:

$$m\ddot{w} + c\dot{w} + kw = F \tag{2.8.1.2}$$

where m, c and k respectively represent the mass, damping coefficient and stiffness of the beam and the dot indicates differentiation with respect to t.

F is the excitation force at any point x and time t:

$$F = F(x,t) \tag{2.8.1.3}$$

For forces acting at the actuator attachment points only, i.e. at $x = 0$ and $x = l$, F in equation 2.8.1.3 can be written as:

$$F = \delta(0)F_{a1}(t) + \delta(l)F_{a2}(t) \tag{2.8.1.4}$$

where δ is the Dirac delta function, the value of which is one at the actuator attachment points, and zero between the actuators.

For beams with zero damping, the equation of motion is obtained by substitution of $c = 0$ into equation 2.8.1.2:

$$m\ddot{w} + kw = F \tag{2.8.1.5}$$

The equation of motion for an undamped beam, in terms of the material and geometric properties, is

$$\underbrace{\frac{\partial^2}{\partial t^2}(\rho_s A_s w)}_{mass\ \ term} + \underbrace{\frac{\partial^2}{\partial x^2}\left(E_s I_s \frac{\partial^2 w}{\partial x^2}\right)}_{stiffness\ \ term} = P \tag{2.8.1.6}$$

where ρ_s and E_s respectively represent the density and Young's modulus of the beam material at a point x on the beam:

$$E_s = E_s(x) \tag{2.8.1.7a}$$
$$\rho_s = \rho_s(x) \tag{2.8.1.7b}$$

A_s and I_s respectively represent the second moment of inertia and cross-sectional area of the beam at x:

$$I_s = I_s(x) \tag{2.8.1.8a}$$
$$A_s = A_s(x) \tag{2.8.1.8b}$$

The term $\rho_s A_s$ in equation 2.8.1.6 is the mass per unit length of the beam, while $E_s I_s$ is the flexural rigidity. P is the force per unit length, or distributed load acting on the structure at any point x and time t:

$$P = P(x,t) \tag{2.8.1.9}$$

P is the partial derivative of F with respect to x:

$$P = \frac{\partial F}{\partial x} \tag{2.8.1.10}$$

The equation describing static beam behaviour is obtained by omitting the inertia term in equation 2.8.1.6:

$$\frac{\partial^2}{\partial x^2}\left(E_s I_s \frac{\partial^2 w}{\partial x^2}\right) = P \tag{2.8.1.11}$$

For natural behaviour of the beam, the loading vector P in equation 2.8.1.6 is zero, in which case the equation of motion is

$$\underbrace{\frac{\partial^2}{\partial t^2}(\rho_s A_s w)}_{mass\ \ term} + \underbrace{\frac{\partial^2}{\partial x^2}\left(E_s I_s \frac{\partial^2 w}{\partial x^2}\right)}_{stiffness\ \ term} = 0 \tag{2.8.1.12}$$

Equations 2.8.1.6 and 2.8.1.12 must be solved to determine the forced and natural behaviour of the system. Possible solution methods are discussed in section 2.8.2, after which the most suitable method is selected and described in section 2.8.3.

2.8.2 Solution methods for beam equations of motion

The available methods of solving beam transverse equations of motion can broadly be divided into two groups, namely analytical methods and numerical methods [Rao, 1989]. A diagram, which classifies the methods of analysis, from Rao [1989], is shown in figure 2.8.2.1.

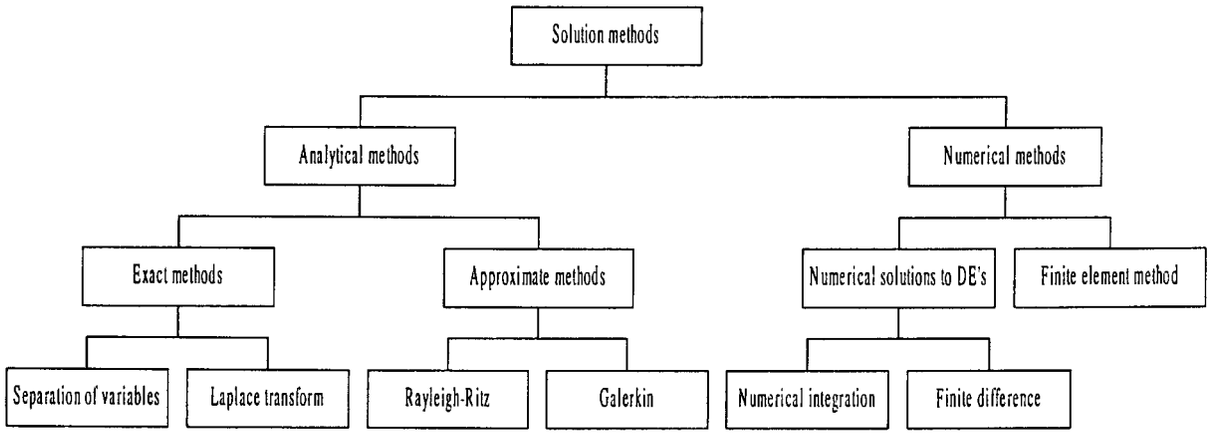

Figure 2.8.2.1: Solution methods for beam transverse equations of motion

Analytical methods include exact and approximate methods. Exact methods are, inter alia, the Laplace transform method and the separation of variables method, while the Rayleigh-Ritz and

Galerkin methods are approximate analytical methods. Two types of numerical methods exist, such as numerical solution of the equation of motion and the Finite Element Method (FEM). Two methods can be used to obtain numerical solutions of the equation of motion, i.e. numerical integration and the Finite Difference (FD) method.

A number of the methods, i.e. the exact separation of variables, Finite Difference, Finite Element, Galerkin and Rayleigh-Ritz methods are summarized by Rao [1989]. A short summary of the most important methods is given in the next few paragraphs.

Exact separation of variables method

The separation of variables method entails the separation of time and spatial variables in continuous systems such as beams, plates, shafts and rods, thereby simplifying system analysis. Parameters such as displacement, speed, acceleration, shear force and bending moment are written as products of separated spatial and time functions. The spatial functions for displacement, for instance, are typically the normal, or uncoupled, mode shapes, while the time functions are the modal amplitudes. In lateral beam vibrations, the normal mode shapes are one-dimensional functions of the spatial parameter x, while the amplitudes are functions of the time parameter t.

Consider equation 2.8.1.6. For constant E_s, I_s, ρ_s and A_s, the beam equation of motion is:

$$\underbrace{\rho_s A_s \frac{\partial^2 w}{\partial t^2}}_{\text{mass term}} + \underbrace{E_s I_s \frac{\partial^4 w}{\partial x^4}}_{\text{stiffness term}} = P \qquad \textbf{(2.8.2.1)}$$

Using separation of variables, the exact solution to equation 2.8.2.1 is expressed as:

$$w(x,t) = \sum_{i=1}^{\infty} \phi_i(x) q_i(t) \qquad \textbf{(2.8.2.2)}$$

where $\phi_i(x)$ is the i-th normal mode shape of the beam at a position x on the beam and $q_i(t)$ is the i-th modal amplitude at time t. The i-th normal mode shape is given by (see appendix L):

$$\phi_i(x) = A_i \cos \beta_i x + B_i \sin \beta_i x + C_i \cosh \beta_i x + D_i \sinh \beta_i x \qquad \textbf{(2.8.2.3)}$$

where A_i, B_i, C_i and D_i are constants determined by the boundary values and β_i is the i-th eigenvalue, given by:

$$\beta_i = \left(\frac{\rho_s A_s}{E_s I_s} \omega_i^2 \right)^{\frac{1}{4}} \qquad \textbf{(2.8.2.4)}$$

The values of β_i depend on the beam supports. Tabulated values of β_i for different beam support configurations, such as cantilever, simply-supported, clamped-clamped and clamped-free beams, are given by Harris [1988], Thomson [1993] and Tse et al [1978]. In most of these references, only the first four to six eigenvalues are given.

The advantage of the separation of variables method is its simplicity of use in continuous systems with constant material and geometric properties. The method is well-established in vibration theory and therefore forms the theoretical basis of most vibration analysis methods for continuous systems. The method allows the separation of spatial and time variables, thereby reducing the degree of mathematical complication. A single normal mode can for instance be analyzed in isolation of all the other modes. Furthermore, system displacement is simply obtained by adding the individual modal displacements.

However, for systems with varying material and geometric properties, application of the method becomes complicated. Secondly, the behaviour of an infinite number of modes may be difficult to describe mathematically. Thirdly, while relatively simple solutions exist for input forces such as impulse, step, ramp and steady-state harmonic functions, this may not be the case for wide-band random excitation. Alternative methods, such as the Rayleigh-Ritz, Galerkin, FD and FE methods must therefore be considered. These methods are described in short below.

The Rayleigh-Ritz method

The Rayleigh-Ritz method is an approximate method, which makes use of a finite number of assumed modes, to describe continuous system behaviour. The assumed mode shapes are combined linearly to form the normal mode shapes. The assumed mode shapes are selected in such a way as to satisfy all the boundary values of the problem. For the clamped-clamped beam with actuated supports, as used in this study, beam end displacements are equal to the actuator output displacements, while the beam end slopes are zero.

The stiffness, damping and inertia matrices of the assumed modes are calculated using energy methods. An eigenvalue problem is solved to determine the eigenvectors and eigenvalues. The normal mode shapes are the products of the assumed mode shapes and the eigenvectors.

The use of a finite number of modes implies that the resulting eigenvalues and normal mode shapes will not be exact. Generally, the higher the number of assumed modes, the more accurate the approximation will be, and vice versa. A practical rule is that, if n number of natural frequencies is required with an acceptable degree of accuracy, $2n$ number of assumed modes must be used [Clough & Penzien, 1982].

The advantages of the method are firstly that system behaviour can be expressed in terms of a finite number of modes. Secondly, material and geometrical properties need not be uniform. Thirdly, the relative contribution of each assumed mode to the normal modes can be obtained from the eigenvectors.

However, the method is not easily applied to systems with a large number of discontinuities, such as stepped beams. This type of system is more easily analyzed using the finite element method. The analysis of discontinuous structures using the Rayleigh-Ritz method, may require the division of the beam into piecewise continuous substructures. The displacement of each substructure is expressed in terms of its own modes, known as component modes. The displacement, slope, bending moment and shear force of each component must match those of its neighbouring components at the boundaries. This method is known as the component mode synthesis method, or substructure synthesis method. More detail about the method is

provided by Béliveau & Souci [1985], Benfield & Hruda [1971], Craig & Bampton [1968], Hintz [1975], Klein & Dowell [1974], Kubomura [1982], Kubomura [1987], Meirovitch [1990], Rubin [1975] and Thomson [1993].

The Galerkin method

Similar to the Rayleigh-Ritz method, a finite number of assumed modes are used which satisfy the boundary values of the beam. Due to the limited number of assumed modes, an error, or residual term, results in the equation of motion. The error is minimized by integrating the product of each mode shape and the residual term over the length of the beam and setting the result equal to zero. For n number of assumed modes, an n x n coefficient matrix is obtained in terms of the eigenvalues. The latter are calculated by setting the determinant of the coefficient matrix equal to zero. The resulting modes are orthogonal and modal superposition can be applied. The Galerkin method is described in more detail by Rao [1989].

The difference between the Rayleigh-Ritz and Galerkin methods is that the Galerkin method is a weighted residual method, while the Rayleigh-Ritz method is an energy method. The latter is fundamentally a better approach, therefore the Rayleigh-Ritz method is preferred to the Galerkin method for the purpose of this study.

The Finite Difference method

Contrary to the Rayleigh-Ritz and Galerkin methods, the FD method does not make use of assumed mode shapes to model continuous system behaviour. In the FD method, the stiffness and mass are defined at m number of discrete nodes along the beam. The partial derivatives of w with respect to x and t, in equation 2.8.2.1, are obtained by numerical differentiation. The central difference method is normally used for differentiation of w with respect to x. Boundary values are taken into account by adding discrete points left of actuator I and right of actuator II. The partial derivatives of w with respect to t can be obtained by either the forward difference method or the backward difference method.

The advantages of the method are that a finite number of nodes and time steps can be used to describe beam behaviour, thereby simplifying the problem. The disadvantages are firstly that the size of the eigenvalue problem is m, which can be large if a large number of nodes are used. Reducing m to decrease the size of the problem, can result in highly inaccurate eigenvalues. Secondly, while the method is relatively easily applied to solve the equation of motion of a uniform beam (equation 2.8.2.1), analyzing the behaviour of non-uniform beams, as described by equations 2.8.1.6 to 2.8.1.8, may be highly complicated.

The FD method is not as often used in vibration analyses as the Rayleigh-Ritz method and the FE method. An application of the FD method is the analysis of nonlinear, coupled three-dimensional fluid vibrations in tanks of arbitrary geometry [Van Schoor, 1989]. Application of the FD method to the analysis of vibrations in one-dimensional continuous systems, e.g. transverse vibrations in beams, is explained in more detail by Rao [1989]. Mathematical theory of the FD method is provided by Burden & Faires [1985], Chapra & Canale [1985], Conte & de Boor [1972] and Gerald & Wheatley [1984].

The Finite Element Method (FEM)

In the finite element method, the beam is divided into a finite, or discrete number of elements along the length of the beam. Four cubic displacement shape functions are written for each element. The shape functions are expressed in terms of the translational and rotational degrees-of-freedom (DOF's) at the element ends. The element mass (m_e) and stiffness (k_e) matrices are calculated using energy methods. The sizes of m_e and k_e are 4 x 4 each. The loading vector F for each shape function is obtained by integrating the product of the distributed loading vector and the shape function over its length, resulting in a 4 x 1 element loading vector. The FEM is in essence a Rayleigh-Ritz method applied to a beam element.

The m_e and k_e matrices of all the elements are assembled in order to obtain mass and stiffness matrices for the entire beam. This is done by prescribing equal element displacements at interfaces between neighbouring elements. Known DOF's of the beam are eliminated. In this study, the known DOF's are the beam end slopes, which are zero. Once the beam mass and stiffness matrices are known, an eigenvalue analysis is carried out to determine the normal mode shapes and natural frequencies.

The advantage of using FEM to solve a beam equation of motion is that the mass and stiffness matrices are sparse, thereby facilitating the eigenvalue analysis. Secondly, no prior knowledge is required to select the assumed modes. Thirdly, for a beam with a large number of discontinuities and varying material properties, FEM is easily applied to determine the natural and forced behaviour. A further advantage is that the same element shape functions can be used for all beam vibration problems. Contrary to the Rayleigh-Ritz method, a new set of shape functions is not required to solve a new problem.

A disadvantage of the FE method is that the size of the eigenvalue problem increases quadratically with the number of elements. Normally, for high accuracy, a large number of elements are required. The main disadvantage, however, is that no physical insight is provided by the method, since an element shape function does not give a global picture of what the normal mode shapes will eventually look like. The Rayleigh-Ritz method has a clear advantage in this regard, since the solution is defined in terms of the (global) assumed modes, which are used to calculate the normal modes. If the assumed mode shapes are carefully selected, only a small number of modes are required, resulting in a small eigenvalue problem.

Selection of the Rayleigh-Ritz method

In this section, the different methods discussed above are compared and the inapplicable methods are eliminated. The Rayleigh-Ritz method is selected as the most appropriate method to solve the beam equations of motion.

The exact method is extremely difficult to apply to the analysis of beams with varying geometry, and can therefore be eliminated. The Galerkin method, being a weighted residual method, is fundamentally not as good as the Rayleigh-Ritz method, which is an energy method. The Rayleigh-Ritz method is therefore preferred to the Galerkin method for this application. The disadvantage of the FD method is that a large number of nodes are required for a beam with varying geometry, resulting in a large eigenvalue problem. The FE method has the same disadvantage, i.e. a large eigenvalue problem for a beam with varying geometry.

The FE method is mainly ruled out because it fails to give physically interpretable normal mode shapes in terms of element shape functions.

Irrespective of its disadvantages, the Rayleigh-Ritz method is the most appropriate method for solving the equation of motion of the LOS stabilization system. Using physical insight, the assumed mode shapes can be carefully selected to satisfy the boundary values and to deal with discontinuities. The Rayleigh-Ritz method is discussed in detail in section 2.8.3.

2.8.3 Detailed discussion of the Rayleigh-Ritz method

The undamped equation of motion for natural behaviour of the beam shown in figure 2.8.1.2 is:

$$m\ddot{w}(x,t)+kw(x,t)=0 \qquad \textbf{(2.8.3.1)}$$

The displacement $w(x,t)$ is determined by the superposition of n number of normal, uncoupled modes:

$$w(x,t)=\sum_{i=1}^{n}\phi_i(x)q_i(t) \qquad \textbf{(2.8.3.2)}$$

where $\phi_i(x)$ is the i-th normal mode shape of the beam at a position x, $q_i(t)$ is the i-th modal amplitude at time t and n is the number of modes.

Equation 2.8.3.2 is written concisely in matrix form as:

$$w=\Phi q \qquad \textbf{(2.8.3.3)}$$

where Φ is the 1 x n row vector of normal mode shapes:

$$\Phi=\begin{Bmatrix}\phi_1(x) & \phi_2(x) & \cdots & \phi_i(x) & \phi_j(x) & \cdots & \phi_n(x)\end{Bmatrix} \qquad \textbf{(2.8.3.4)}$$

and q is the n x 1 column vector of normal mode amplitudes:

$$q=\begin{Bmatrix}q_1(t) & q_2(t) & \cdots & q_i(t) & q_j(t) & \cdots & q_n(t)\end{Bmatrix}^T \qquad \textbf{(2.8.3.5)}$$

The normal mode shapes $\phi_i(x)$ are currently unknown. In order to obtain the solution to equation 2.8.3.1, n number of assumed modes shapes $\psi_i(x)$ are chosen which satisfy the boundary conditions of the beam. The assumed mode shape vector Ψ is given by:

$$\Psi=\begin{Bmatrix}\psi_1(x) & \psi_2(x) & \cdots & \psi_i(x) & \psi_j(x) & \cdots & \psi_n(x)\end{Bmatrix} \qquad \textbf{(2.8.3.6)}$$

The size of Ψ is the same as that of Φ, i.e. 1 x n.

The boundary conditions of the beam shown in figure 2.8.1.2 are the same as those of a clamped-clamped beam with moving supports. For this type of beam, the boundary values are as follows: Beam displacement at x = 0 is equal to the output displacement of the left

The boundary conditions of the beam shown in figure 2.8.1.2 are the same as those of a clamped-clamped beam with moving supports. For this type of beam, the boundary values are as follows: Beam displacement at $x = 0$ is equal to the output displacement of the left actuator, while beam displacement at $x = l$ is equal to the output displacement of the right actuator. The slopes of the beam at both ends are zero.

Mathematically, these boundary conditions can be expressed as:

$$w(x_{a1},t) = y_{a1} \qquad \textbf{(2.8.3.7a)}$$
$$w(x_{a2},t) = y_{a2} \qquad \textbf{(2.8.3.7b)}$$
$$w'(0,t) = 0 \qquad \textbf{(2.8.3.7c)}$$
$$w'(l,t) = 0 \qquad \textbf{(2.8.3.7d)}$$

where x_{a1} and x_{a2} are the attachment points of the two actuators and y_{a1} and y_{a2} are the actuator output displacements. For actuators attached at the beam ends, equations 2.8.3.7a to 2.8.3.7d become:

$$w(0,t) = y_{a1} \qquad \textbf{(2.8.3.8a)}$$
$$w(l,t) = y_{a2} \qquad \textbf{(2.8.3.8b)}$$
$$w'(0,t) = 0 \qquad \textbf{(2.8.3.8c)}$$
$$w'(l,t) = 0 \qquad \textbf{(2.8.3.8d)}$$

Assumed mode shapes which satisfy the boundary conditions of the beam under discussion, are:

$$\psi_i(x) = \cos\left(\frac{i\pi x}{l}\right) \qquad \textbf{(2.8.3.9)}$$

The advantages of using the above mode shapes is that they are infinitely differentiable and easy to generate. The disadvantage is that an extremely high number of modes (larger than 100) are required to accurately describe flexure bending. The reason is that the flexures are situated close to the beam ends (see figure 2.8.1.1).

An alternative set of assumed modes, which describe flexure bending with a limited number of modes, can be used. The modes include five symmetric bending modes and four asymmetric bending modes, as well as a purely translational rigid body mode. The symmetric and asymmetric bending mode shapes are shown in figures 2.8.3.1 and 2.8.3.2 respectively. The disadvantage of using these mode shapes is that differentiation with respect to x, to obtain inflections, may be tedious, especially if polynomials are used to generate the mode shapes.

Note from figure 2.8.3.2, that two of the asymmetric mode shapes are almost identical. The two mode shapes differ only in the flexure, where quadratic bending is used for the one mode and quartic bending for the other. Both these modes are rigid between the flexures.

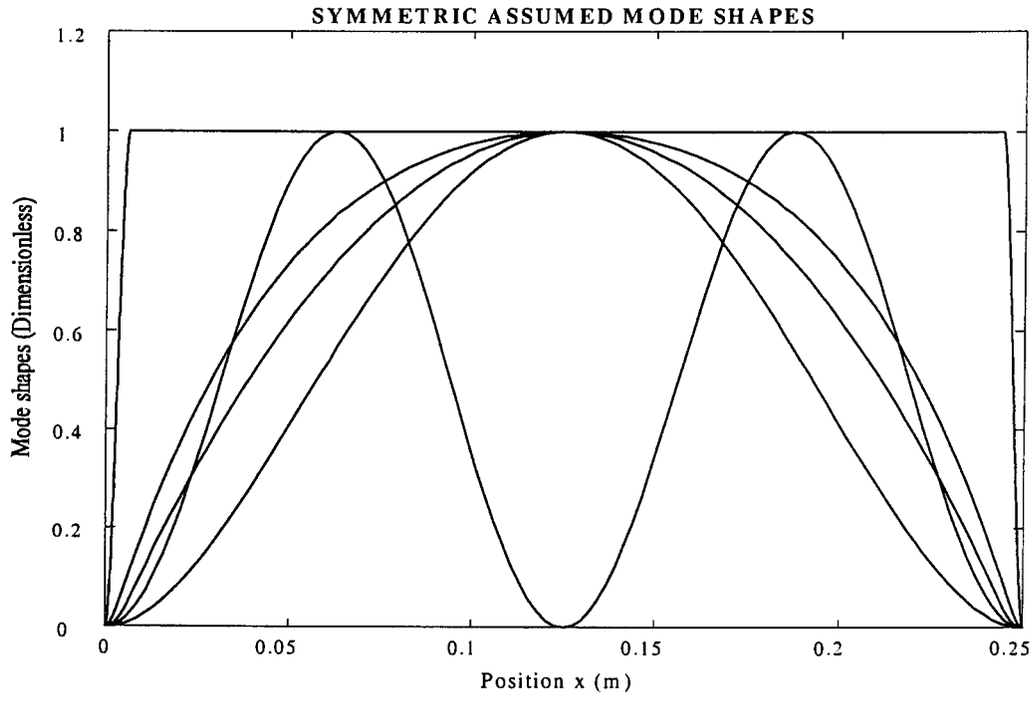

Figure 2.8.3.1: Symmetric assumed mode shapes for beam model

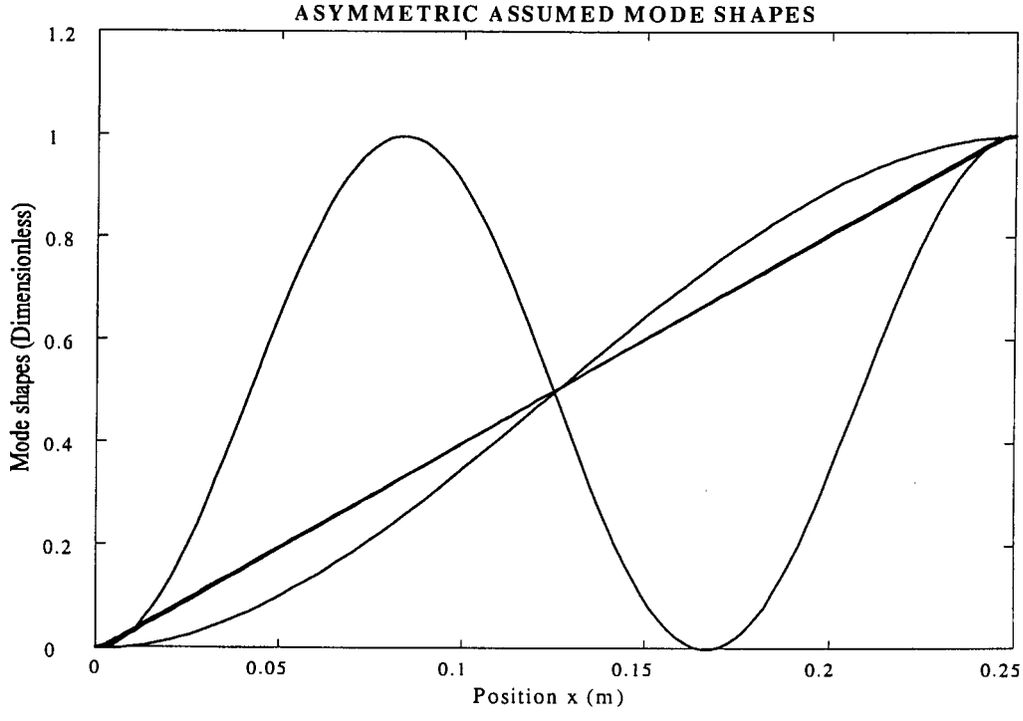

Figure 2.8.3.2: Asymmetric assumed mode shapes for beam model

The modal distributed mass and stiffness matrices of the beam, for the assumed modes, are:

$$M_b = \int_{x=0}^{x=l} \rho_s(x) A_s(x) \psi_i(x) \psi_j(x) dx \qquad \textbf{(2.8.3.10a)}$$

$$K_b = \int_{x=0}^{x=l} E_s(x) I_s(x) \psi_i''(x) \psi_j''(x) dx \qquad \textbf{(2.8.3.10b)}$$

where ψ_i and ψ_j are the i-th and j-th assumed mode shapes respectively and the prime denotes partial differentiation with respect to x.

M_b is the distributed mass matrix and K_b is the distributed stiffness matrix.

If the assumed mode shapes ψ are equal to the normal mode shapes ϕ, M_b and K_b will be diagonal matrices and the modes will be uncoupled. Generally, assumed modes of a beam with varying geometric and material properties will be coupled, therefore M_b and K_b will not be diagonal. If all the elements of the stiffness matrix are non-zero, the beam is said to be statically, or elastically coupled. If all the elements of the mass matrix are non-zero, the beam is dynamically, or inertia coupled.

An imbalance mass is usually required to bring about both static and dynamic coupling. In practice, static and dynamic coupling is obtained if the stiffnesses of the two actuators differ slightly and if a sensor is placed close to one actuator.

The concentrated masses and stiffnesses of the actuators can be included in the model. The contribution of the actuators to the modal mass and stiffness matrices is:

$$M_a = \Psi^T(x_a) m_a \Psi(x_a) \qquad \textbf{(2.8.3.11a)}$$

$$K_a = \Psi^T(x_a) k_a \Psi(x_a) \qquad \textbf{(2.8.3.11b)}$$

where m_a and k_a are the actuator masses and stiffnesses respectively and $\Psi(x_a)$ is the assumed mode vector at the actuator attachment points x_a.

The modal mass matrix is the sum of the distributed mass and the concentrated mass, while the modal stiffness matrix is the sum of the distributed stiffness and the concentrated stiffness:

$$M = M_b + M_a \qquad \textbf{(2.8.3.12a)}$$

$$K = K_b + K_a \qquad \textbf{(2.8.3.12b)}$$

The natural frequencies and normal mode shapes of the beam are determined by solving the following eigenvalue equation:

$$(K - M\Omega^2)U = 0 \qquad \textbf{(2.8.3.13)}$$

where Ω^2 is a diagonal matrix containing the eigenvalues and U is a square matrix containing the eigenvectors. The eigenvalues are the values of Ω^2 for which

$$\left|K - M\Omega^2\right| = 0 \qquad \textbf{(2.8.3.14)}$$

The natural frequency f_i of the i-th normal mode is:

$$f_i = \frac{1}{2\pi}\Omega_{ii} \qquad \textbf{(2.8.3.15)}$$

where Ω_{ii} is the i-th diagonal element of the matrix Ω containing the natural frequencies of the beam.

The normal mode shapes are the product of the assumed mode shape vector and U:

$$\Phi = \Psi U \qquad \textbf{(2.8.3.16)}$$

The mode shapes obtained by means of equation 2.8.3.16 are real.

The uncoupled, normal mode mass and stiffness matrices are:

$$M^* = U^T M U \qquad \textbf{(2.8.3.17a)}$$
$$K^* = U^T K U \qquad \textbf{(2.8.3.17b)}$$

The equation of motion of the beam, in terms of the uncoupled, normal coordinates $\{q\}$, are:

$$M^*\ddot{q} + K^* q = 0 \qquad \textbf{(2.8.3.18)}$$

Equation 2.8.3.18 gives the undamped beam equation of motion. The equation of motion of a damped beam is also required, because the two Terfenol-D actuators, which serve as beam supports, are hysteretically damped (see section 2.7). Hysteresis damping can be modelled by means of equivalent viscous damping (see section 2.3). The inclusion of viscous damping in the Rayleigh-Ritz model is discussed in the next section, after which hysteresis damping is expressed in terms of equivalent viscous damping.

Inclusion of viscous damping in the Rayleigh-Ritz model of the beam

The equation of motion for natural behaviour of a viscous damped beam, in normal coordinates, is:

$$M^*\ddot{q} + C^*\dot{q} + K^* q = 0 \qquad \textbf{(2.8.3.19)}$$

where C^* is the uncoupled damping matrix, given by:

$$C^* = \int_{x=0}^{x=l} c(x)\phi_i(x)\phi_j(x)dx \qquad \textbf{(2.8.3.20)}$$

C^* is also known as the orthogonal, classical, modal or proportional damping matrix [Craig, 1981].

For uncoupled damped modes, it is required that C^* be a diagonal matrix. To make this possible, the normal mode shapes must simultaneously uncouple the mass, stiffness and damping matrices. Uncoupling of the mass and stiffness matrices was achieved by solving the

undamped eigenvalue problem as given in equation 2.8.3.13. The mode shapes thus obtained do however not give a diagonal damping matrix. If the undamped mode shapes are substituted into equation 2.8.3.20, C^* will contain non-zero, off-diagonal terms, resulting in coupled mode shapes.

A diagonal C^* matrix can be obtained in a number of ways. The first is to use Rayleigh damping, which is a particular form of proportional damping. In Rayleigh damping, the damping matrix C is directly proportional to both the coupled mass and stiffness matrices:

$$C = \alpha M + \beta K \tag{2.8.3.21}$$

where M and K are respectively given by equations 2.8.3.10a and 2.8.3.10b. C is the coupled damping matrix, given by:

$$C = \int_{x=0}^{x=l} c(x)\psi_i(x)\psi_j(x)dx \tag{2.8.3.22}$$

α and β are determined from known damping factors of the first two normal mode shapes. The damping factors of the higher modes are then expressed in terms of α and β. Rayleigh damping is described in more detail by Craig [1981].

The advantage of using Rayleigh-damping is that a diagonal damping matrix is easily obtained. The disadvantage is that the uncoupled modal damping factors must be known in advance. In this chapter, the uncoupled damping matrix is unknown and must be derived from actuator damping parameters.

The second method gives proportional damping with specified damping factors for a given number of modes [Craig, 1981]. The damping matrix C, from Craig [1981], is:

$$C = \left(M\Phi M^{*-1}\right)C^*\left(M^{*-1}\Phi^T M\right) \tag{2.8.3.23}$$

Determining the damping matrix using equation 2.8.3.23 is even simpler than using Rayleigh damping, if the uncoupled modal damping matrix C^* is known in advance. However, as with Rayleigh-damping, C^* is unknown for the beam vibration problem under discussion.

The third, and preferred method, is to write equation 2.8.3.19 in state variable form and to obtain the eigenvalues of the coefficient matrix, which contain the uncoupled damping factors. The assumption made here is that damping does not change the undamped normal mode shapes. This assumption is only acceptable for low damping, which gives an insignificant shift in natural frequency (for example, a damping factor of 10% lowers the natural frequency by as little as 0,5%).

The state variable form of equation 2.8.3.19 is:

$$\begin{Bmatrix} \dot{q} \\ \ddot{q} \end{Bmatrix} = -\begin{bmatrix} M^* & 0 \\ C^* & M^* \end{bmatrix}^{-1}\begin{bmatrix} 0 & -M^* \\ K^* & 0 \end{bmatrix}\begin{Bmatrix} q \\ \dot{q} \end{Bmatrix} \tag{2.8.3.24}$$

where M^*, K^* and C^* are respectively given by equations 2.8.3.17a, 2.8.3.17b and 2.8.3.20. In equation 2.8.3.24, M^* and K^* are diagonal, but C^* is not.

The eigenvalues are determined by solving the $2n$ x $2n$ eigenvalue problem:

$$|sI - A| = 0 \tag{2.8.3.25}$$

where A is the coefficient matrix given by:

$$A = \begin{bmatrix} M^* & 0 \\ C^* & M^* \end{bmatrix}^{-1} \begin{bmatrix} 0 & -M^* \\ K^* & 0 \end{bmatrix} \tag{2.8.3.26}$$

The i-th eigenvalue s_i is given by:

$$s_i = -\alpha_i \pm j\Omega_{di} \tag{2.8.3.27}$$

where α_i is the real part of the i-th eigenvalue and Ω_{di} is the imaginary part, which is the i-th damped natural frequency:

$$\alpha_i = \zeta_i \Omega_{ii} \tag{2.8.3.28a}$$

$$\Omega_{di} = \Omega_{ii}\left(1 - \zeta_i^2\right)^{\frac{1}{2}} \tag{2.8.3.28b}$$

The i-th modal damping factor ζ_i is

$$\zeta_i = \frac{\alpha_i}{\left(\alpha_i^2 + \Omega_{di}^2\right)^{\frac{1}{2}}} \tag{2.8.3.29}$$

The i-th diagonal element of the uncoupled C^* matrix is given by:

$$C_{ii}^* = 2\zeta_i M_{ii}^* \Omega_{ii} \tag{2.8.3.30}$$

The procedure described above gives the normal, uncoupled viscous damping matrix. The matrix can also be derived for a beam excited by actuators with hysteresis damping. This is done in short in the following section.

Rayleigh-Ritz model of beam excited by actuators with hysteresis damping

It was shown in section 2.7 that the Terfenol-D actuators display hysteresis damping. These hysteresis effects must be included in the model, since the transfer function between the coil input voltages and the LOS angle of the optical instrument are damping-dependent. The most convenient way of including hysteresis in the model is to derive a diagonal, linear viscous damping matrix for the beam, the elements of which are the natural mode damping coefficients.

The assumption made here is that all the damping in the system is provided by the actuators. Since material and joint damping in the beam are unknown in the modelling stage, these effects will be excluded here. In chapter 4, the transfer functions of the system will be measured,

after which the damping factors, including all the damping effects, will be extracted in chapter 5.

Recall from equation 2.3.15 that the relationship between the actuator viscous damping coefficient c_a, stiffness k_a, dimensionless loss factor η_a and frequency ω is:

$$c_a = \frac{k_a \eta_a}{\omega} \tag{2.8.3.31}$$

Rewriting equation 2.8.3.31 gives:

$$\omega c_a = k_a \eta_a \tag{2.8.3.32}$$

where ωc_a is the dynamic dissipative stiffness of the actuator. For hysteresis damping, the term $k_a \eta_a$ is constant for all frequencies, since c_a varies hyperbolically with frequency (see also figure 2.3.7).

The modal dissipative stiffness of the beam, in terms of that of the actuators, is given by:

$$\Omega C^* = \Phi^T(x_a) k_a \eta_a \Phi(x_a) \tag{2.8.3.33}$$

where C^* is the coupled n x n modal matrix and Ω is a diagonal matrix containing the undamped angular natural frequencies of the beam. $\Phi(x_a)$ is the undamped normal mode vector at the actuator attachment points.

In order to uncouple the damping matrix, the equation of motion 2.8.3.19 is first premultiplied by Ω:

$$\Omega M^* \ddot{q} + \Omega C^* \dot{q} + \Omega K^* q = 0 \tag{2.8.3.34}$$

Equation 2.8.3.34 is subsequently written in state-variable form as:

$$\begin{Bmatrix} \dot{q} \\ \ddot{q} \end{Bmatrix} = -\begin{bmatrix} \Omega M^* & 0 \\ \Omega C^* & \Omega M^* \end{bmatrix}^{-1} \begin{bmatrix} 0 & -\Omega M^* \\ \Omega K^* & 0 \end{bmatrix} \begin{Bmatrix} q \\ \dot{q} \end{Bmatrix} \tag{2.8.3.35}$$

where ΩC^* is given by equation 2.8.3.33.

The eigenvalues of the beam are the values of s for which:

$$|sI - A| = 0 \tag{2.8.3.36}$$

where A is the coefficient matrix:

$$A = \begin{bmatrix} \Omega M^* & 0 \\ \Omega C^* & M^* \end{bmatrix}^{-1} \begin{bmatrix} 0 & -\Omega M^* \\ \Omega K^* & 0 \end{bmatrix} \tag{2.8.3.37}$$

From the eigenvalues, the uncoupled damping coefficients can be obtained using the procedure set out in equations 2.8.3.27 to 2.8.3.30.

The Rayleigh-Ritz model developed in section 2.8.3 will be used in section 2.8.4 to obtain the natural frequencies and normal mode shapes of the system.

2.8.4 Natural frequencies, normal mode shapes and modal damping factors

The natural frequencies, normal mode shapes and modal damping factors of the system are calculated in this section. The actuator parameters are given, together with the beam mass per unit length and flexural rigidity. The first ten natural frequencies are calculated and tabled and the first four normal mode shapes are shown. The mode shapes and natural frequencies are discussed. Modal damping factors and coefficients for the first three natural frequencies are calculated.

The Terfenol-D actuator parameters, from section 2.7.3, are given in table 2.8.4.1. The mass per unit length and structural rigidity of the optical instrument, support structure and stiffener are shown in figures 2.8.4.1 and 2.8.4.2 respectively.

Table 2.8.4.1: Terfenol-D actuator parameters

Parameter	Symbol	Value
Concentrated mass	m_a	0,15 kg
Stiffness	k_a	$6{,}5.10^5$ N/m
Dynamic dissipative stiffness	$k_a\eta_a$	13076.2π N/m

It can be seen from figure 2.8.4.2 that the flexural rigidity between the instrument attachment points is approximately 10^6 times of that in the middle of the flexures. It can therefore be expected that the natural frequencies, where flexure bending dominates, will be considerably lower than those where bending between the flexures dominates.

The coupled mass and stiffness matrices are calculated from equations 2.8.3.10 to 2.8.3.12. The assumed modes are as given in section 2.8.3. Only dynamic coupling is considered. The eigenvalue problem, as given in equation 2.8.3.13, is solved for Ω and U. The undamped natural frequencies and normal mode shapes are calculated from equations 2.8.3.15 and 2.8.3.16 respectively. The calculated natural frequencies for the first ten normal modes are given in Table 2.8.4.2.

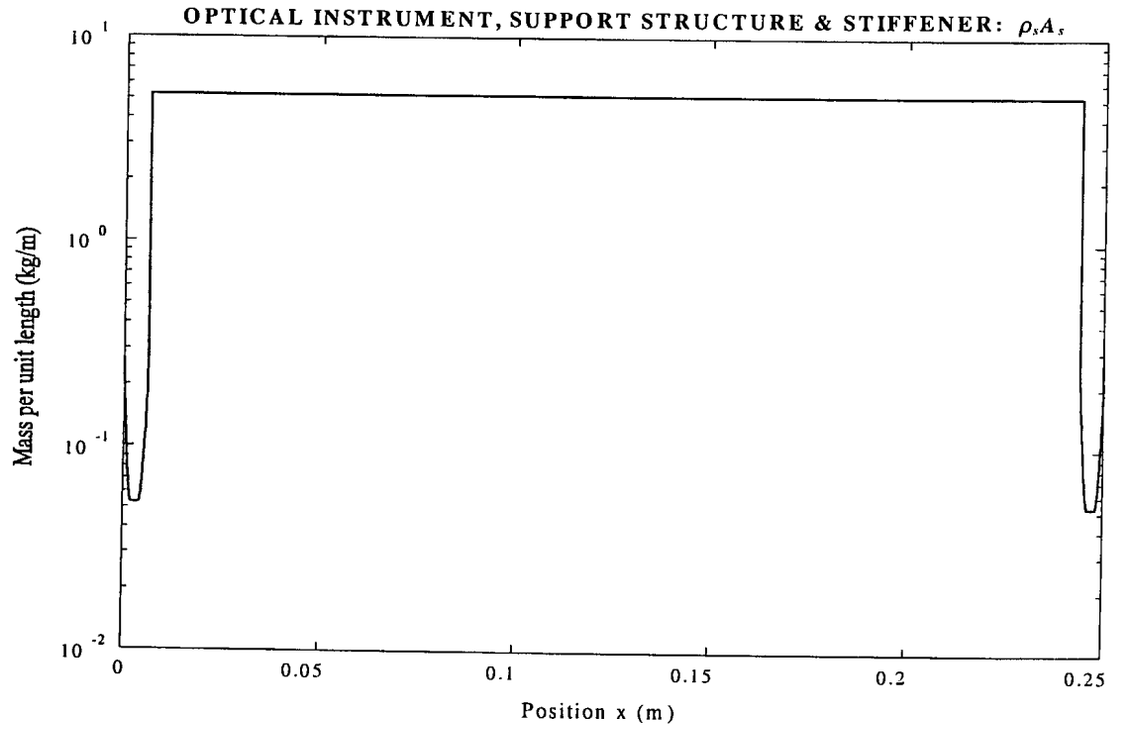

Figure 2.8.4.1: **Mass per unit length of optical instrument, support structure and stiffener**

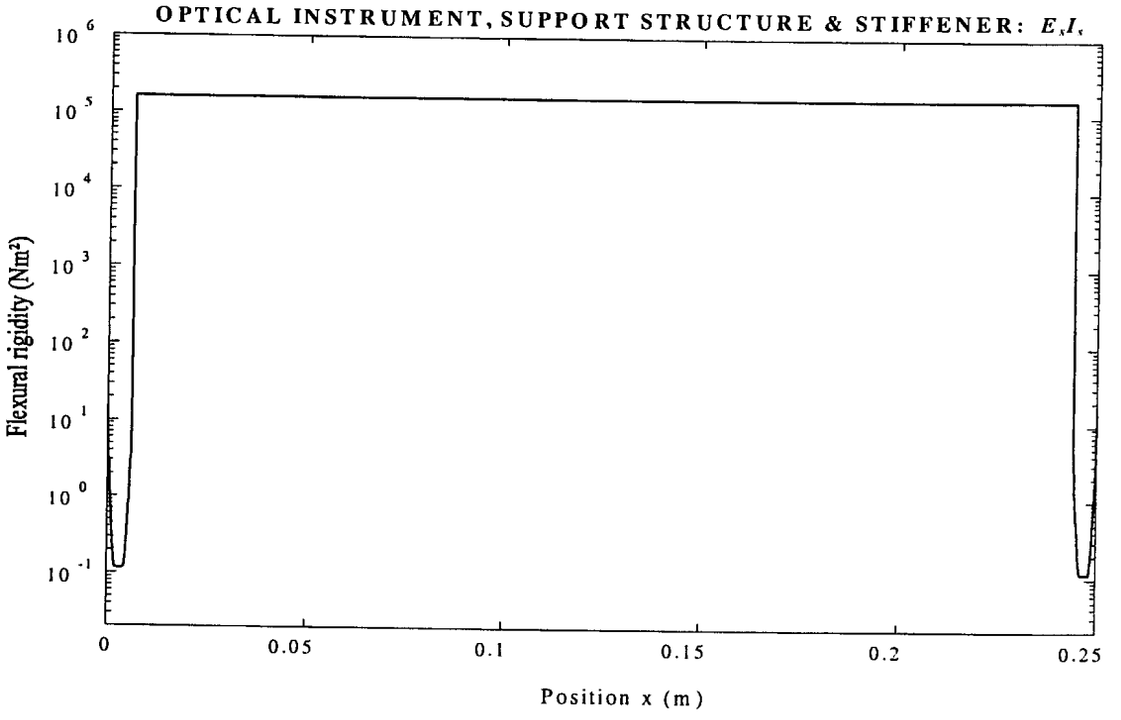

Figure 2.8.4.2: **Flexural rigidity of optical instrument, support structure and stiffener**

Table 2.8.4.2: Natural frequencies for first ten normal modes

Mode number	Natural frequency (Hz)
1	145,81
2	218,97
3	4 625,2
4	6 266,3
5	12 242
6	30 847
7	59 881
8	156 860
9	259 300
10	710 430

Modal stiffness and mass are calculated from equations 2.8.3.17a and 2.8.3.17b. Modal dissipative stiffness is calculated from equation 2.8.3.33. The state coefficient matrix, as given by equation 2.8.3.37, is calculated and the eigenvalue problem in equation 2.8.3.36 is solved. Modal damping factors and coefficients are calculated from equations 2.8.3.29 and 2.8.3.30. The normal mode mass, stiffness and damping matrices, for the first three normal modes, are given below, while the damping factors are shown in table 2.8.4.3.

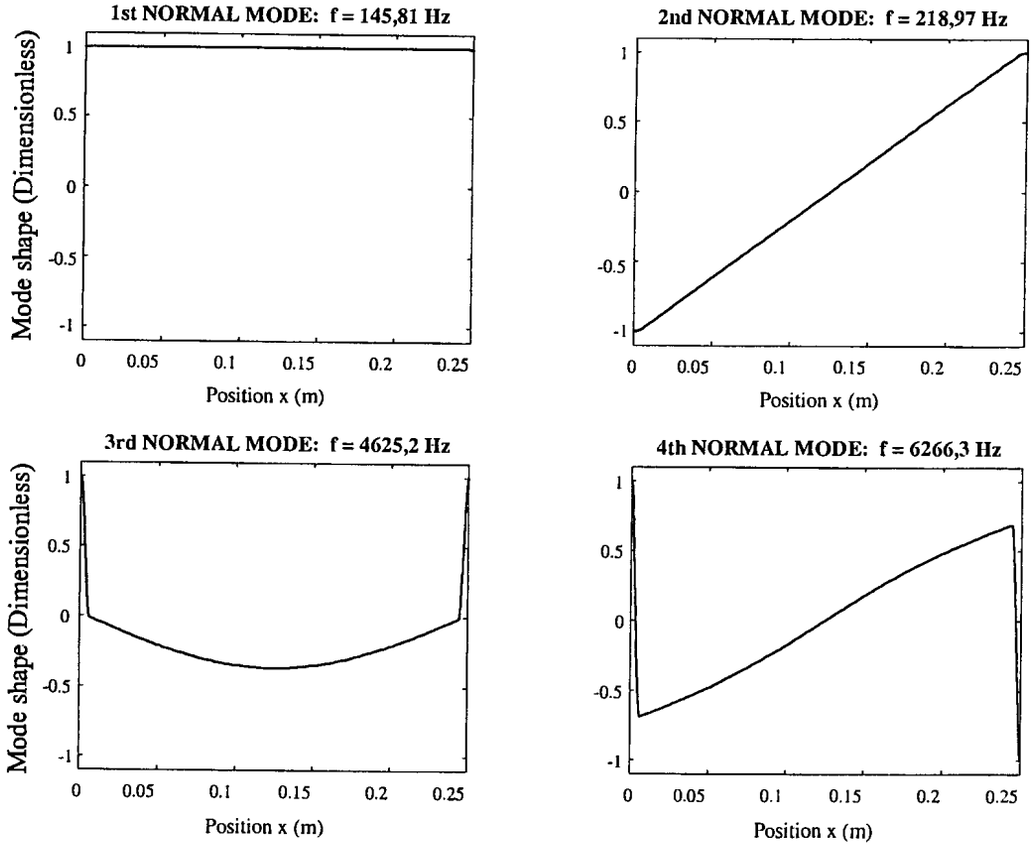

Figure 2.8.4.3: First four normal mode shapes of support structure

The normal mode mass, stiffness and damping matrices are:

$$M^* = \begin{bmatrix} 1{,}538 & 0 & 0 \\ 0 & 0{,}699 & 0 \\ 0 & 0 & 0{,}387 \end{bmatrix} kg \qquad \textbf{(2.8.4.1a)}$$

$$K^* = \begin{bmatrix} 1{,}291.10^6 & 0 & 0 \\ 0 & 1{,}323.10^6 & 0 \\ 0 & 0 & 3{,}269.10^8 \end{bmatrix} N/m \qquad \textbf{(2.8.4.1b)}$$

$$C^* = \begin{bmatrix} 177{,}43 & 0 & 0 \\ 0 & 119{,}43 & 0 \\ 0 & 0 & 5{,}65 \end{bmatrix} Ns/m \qquad \textbf{(2.8.4.1c)}$$

Table 2.8.4.3: Damping factors for first three normal modes

Mode number	Natural frequency (Hz)	Damping factor (%)
1	145,81	6,3
2	218,97	6,21
3	4625,2	0,025

It can be seen from table 2.8.4.3 that the damping factors are relatively low. The assumption made in section 2.8.3 that normal mode damping can be analyzed using the undamped normal modes, without significant distortion of the mode shapes, is therefore valid.

2.8.5 Forced behaviour of the LOS stabilization system

The forced linear equation of motion of the system, from equation 2.8.3.19, is:

$$M^*\ddot{q} + C^*\dot{q} + K^*q = Q \qquad \textbf{(2.8.5.1)}$$

where M^*, C^* and K^* are normal mode mass, damping and stiffness matrices respectively and Q is the modal excitation force vector, given by:

$$Q = \int_{x=0}^{x=l} \Phi^T(x) F(x,t) dx \qquad \textbf{(2.8.5.2)}$$

F is the distributed force vector as given by equation 2.8.1.3.

In more concise matrix form, equation 2.8.5.2 can be written as:

$$Q = \Phi^T F \tag{2.8.5.3}$$

The system state-space equations for forced behaviour are fully derived in appendix M. The equations are written in the following familiar form:

$$\dot{x} = Ax + Bu \tag{2.8.5.4a}$$
$$y = Cx + Du \tag{2.8.5.4b}$$

where:

$$x = \left\{ \{q\} \quad \{\dot{q}\} \quad \{I_1 \quad I_2\}^T \right\}^T \tag{2.8.5.5a}$$
$$u = \{V_1 \quad V_2\}^T \tag{2.8.5.5b}$$
$$y = \{w_1 \quad w_2 \quad \theta\}^T \tag{2.8.5.5c}$$

$$A = \begin{bmatrix} 0 & I & 0 \\ -\Omega^2 & -2Z\Omega & \dfrac{A_T E N d^H}{G l_T} M^{*-1} \left[\Phi^T(0) \quad \Phi^T(l) \right] \\ 0 & -\dfrac{A_T E N d^\sigma}{G l_T L_0} \begin{bmatrix} \Phi(0) \\ \Phi(l) \end{bmatrix} & -\dfrac{R_c}{L_0} \begin{bmatrix} 1 & 0 \\ 0 & 1 \end{bmatrix} \end{bmatrix} \tag{2.8.5.6a}$$

$$B = \begin{bmatrix} 0 & 0 \\ 0 & 0 \\ \dfrac{1}{L_0} \begin{bmatrix} 1 & 0 \\ 0 & 1 \end{bmatrix} \end{bmatrix} \tag{2.8.5.6b}$$

$$C = \begin{bmatrix} \{\Phi(x_1)\} & \{0\} & \{0 \quad 0\} \\ \{\Phi(x_2)\} & \{0\} & \{0 \quad 0\} \\ \left\{ \dfrac{1}{l} \left(\Phi(x_2) - \Phi(x_1) \right) \right\} & \{0\} & \{0 \quad 0\} \end{bmatrix} \tag{2.8.5.6c}$$

$$D = \{0 \quad 0\} \tag{2.8.5.6d}$$

The system transfer functions, which are the ratios between the outputs and inputs, are obtained by means of equation 2.5.2.1. The transfer function $G_{kl}(s)$ for the k-th input and l-th output, is:

$$G_{kl}(s) = \frac{y_l}{u_k} = C_{row\,l}\left[sI - A\right]^{-1} B_{column\,k} + D_{column\,k} \qquad \textbf{(2.8.5.7)}$$

The desired transfer functions of the system, for the inputs and outputs in equations 2.8.5.5b and 2.8.5.5c, are:

$$G_{11}(s) = \frac{W_1(s)}{V_1(s)} \qquad \textbf{(2.8.5.8a)}$$

$$G_{12}(s) = \frac{W_2(s)}{V_1(s)} \qquad \textbf{(2.8.5.8b)}$$

$$G_{13}(s) = \frac{\Theta(s)}{V_1(s)} \qquad \textbf{(2.8.5.8c)}$$

$$G_{23}(s) = \frac{\Theta(s)}{V_2(s)} \qquad \textbf{(2.8.5.8d)}$$

where $W_k(s)$ and $V_l(s)$ respectively represent the Laplace-transform of the k-th displacement output and l-th coil voltage input, while $\Theta(s)$ is the Laplace-transformed LOS output angle of the optical instrument.

For the sake of convenience, G_{11} is called the "parallel" *TF*, i.e. the *TF* for an input at actuator I and an output at instrument attachment point I. Assuming equal actuator characteristics, the same *TF* will be obtained for an input at actuator II and an output at instrument attachment point II, i.e.:

$$G_{22}(s) = G_{11}(s) \qquad \textbf{(2.8.5.9)}$$

G_{12} is called the "crisscross" *TF*, i.e. for an input at actuator I and an output at instrument attachment point II. G_{21}, for an input at actuator II and an output at instrument attachment point I, is:

$$G_{21}(s) = G_{12}(s) \qquad \textbf{(2.8.5.10)}$$

The above *TF*'s, in terms of the state and output matrices, are:

$$G_{11}(s) = C_{row\,1}\left[sI - A\right]^{-1} B_{column\,1} \qquad \textbf{(2.8.5.11a)}$$

$$G_{12}(s) = C_{row\,2}\left[sI - A\right]^{-1} B_{column\,1} \qquad \textbf{(2.8.5.11b)}$$

$$G_{13}(s) = C_{row\,3}\left[sI - A\right]^{-1} B_{column\,1} \qquad \textbf{(2.8.5.11c)}$$

$$G_{23}(s) = C_{row\,3}\left[sI - A\right]^{-1} B_{column\,2} \qquad \textbf{(2.8.5.11d)}$$

The transfer functions G_{11}, G_{12} and G_{23} are calculated below. The positions of the actuators are at the beam ends, i.e. at $x = 0$ and $x = l$. Positions of the instrument attachment points are:

$$x_1 = 0{,}006\ m \qquad \textbf{(2.8.5.12a)}$$

$$x_2 = 0{,}244\ m \qquad \textbf{(2.8.5.12b)}$$

The first three normal modes are used. The natural frequencies and damping factors are as in table 2.8.4.3. The normal mode mass matrix is as given in equation 2.8.4.1a. The values of d^H, μ^σ and L_0 are obtained from the actuator simulation results as given in section 2.7.3, for a frequency corresponding to the second normal mode of the undamped system, i.e. 218,97 Hz. This is the first natural frequency for angular excitation of the optical instrument (see figure 2.8.4.3). At this frequency, d^H and μ^σ are $8{,}14.10^{-9}$ m/A and $4{,}71.10^{-6}$ Tm/A respectively, while L_0 is $8{,}7.10^{-4}$ H.

The Terfenol-D piezomagnetic cross-coupling constant d^σ and Young's modulus E, from section 2.7.3, are $1{,}09.10^{-8}$ m/A and 23,46 GPa respectively. The rest of the actuator parameters, i.e. l_T, A_T, N, R_c, are as given in table 2.7.3.1.

The *TF's* are obtained by application of equations 2.8.5.11a, 2.8.5.11b and 2.8.5.11d. The *TF's* are of the form:

$$G_{kl}(s) = \frac{P(s)}{Q(s)} = \frac{\sum_{i=0}^{i=5} p_i s^i}{\sum_{j=0}^{j=8} q_j s^j} \qquad \textbf{(2.8.5.13)}$$

Note that, as was the case with the actuator model developed in section 2.5, the relative degree-of-freedom of the *TF*, i.e. the difference between the numerator and denominator polynomial orders is 3. The coefficients for the different *TF's* are given in table 2.8.5.1. The denominator coefficients are the same for all the *TF's*.

Table 2.8.5.1: *TF* numerator and denominator polynomial coefficients

Transfer function:	G_{11}	G_{12}	G_{23}
p_0	$1{,}5675.10^{23}$	$2{,}9397.10^{21}$	$6{,}1524.10^{23}$
p_1	$9{,}3771.10^{19}$	$-2{,}2232.10^{18}$	$3{,}8398.10^{20}$
p_2	$1{,}3882.10^{17}$	$-5{,}0367.10^{16}$	$7{,}5677.10^{17}$
p_3	$3{,}6558.10^{13}$	$-1{,}3525.10^{13}$	$2{,}0033.10^{14}$
p_4	$1{,}6154.10^{8}$	$-6{,}3107.10^{7}$	$8{,}9857.10^{8}$
p_5	$4{,}2246.10^{4}$	$-1{,}6733.10^{5}$	$2{,}3591.10^{5}$
q_0	$1{,}8162.10^{28}$	$1{,}8162.10^{28}$	$1{,}8162.10^{28}$
q_1	$2{,}1747.10^{25}$	$2{,}1747.10^{25}$	$2{,}1747.10^{25}$
q_2	$3{,}8878.10^{22}$	$3{,}8878.10^{22}$	$3{,}8878.10^{22}$
q_3	$2{,}7594.10^{19}$	$2{,}7594.10^{19}$	$2{,}7594.10^{19}$
q_4	$1{,}7394.10^{16}$	$1{,}7394.10^{16}$	$1{,}7394.10^{16}$
q_5	$6{,}4991.10^{12}$	$6{,}4991.10^{12}$	$6{,}4991.10^{12}$
q_6	$8{,}6782.10^{8}$	$8{,}6782.10^{8}$	$8{,}6782.10^{8}$
q_7	7658,7	7658,7	7658,7
q_8	1	1	1

The frequency-domain transfer functions are obtained by substitution of s with $j\omega$ in equations 2.8.5.11a to 2.8.5.11d. As is the case with the actuator transfer functions (see section 2.7), the system ω-domain transfer functions are complex, with frequency-dependent magnitudes and phase angles. The "parallel", "crisscross" and optical instrument LOS angle transfer functions, for a frequency band of 0 Hz to 400 Hz, are shown graphically in figures 2.8.5.1 to 2.8.5.3.

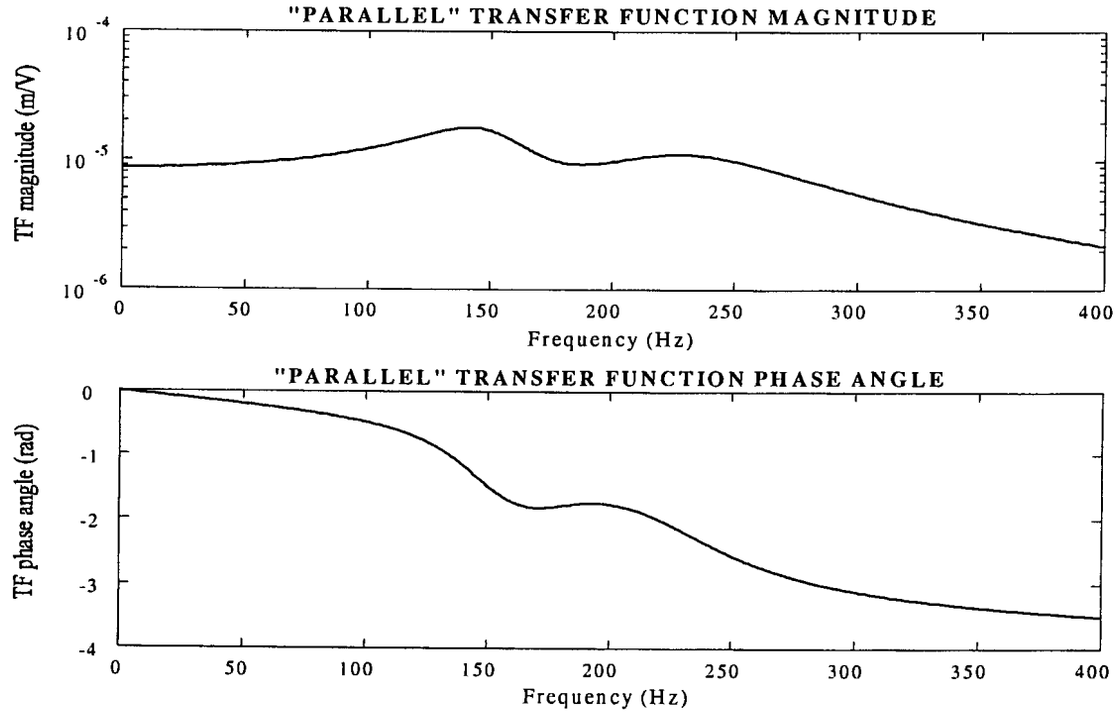

Figure 2.8.5.1: System *TF* magnitude for "parallel" excitation and measurement

A special case arises if the coil input voltages V_1 and V_2 are 180° out-of-phase, i.e.:

$$V_2 = -V_1 \qquad \textbf{(2.8.5.14)}$$

In this case, the magnitude of the transfer function G_{23} is twice that shown in figure 2.8.5.3. The excited DOF is purely rotational and no translation is possible.

This concludes the simulation of the LOS stabilization system. The *TF's* derived and calculated above, will be used as design inputs in chapter 3 and will be experimentally measured in chapter 4. Thereafter, in chapter 5, the state-space and *TF* parameters will be extracted from the measured *TF's* and the model will be updated.

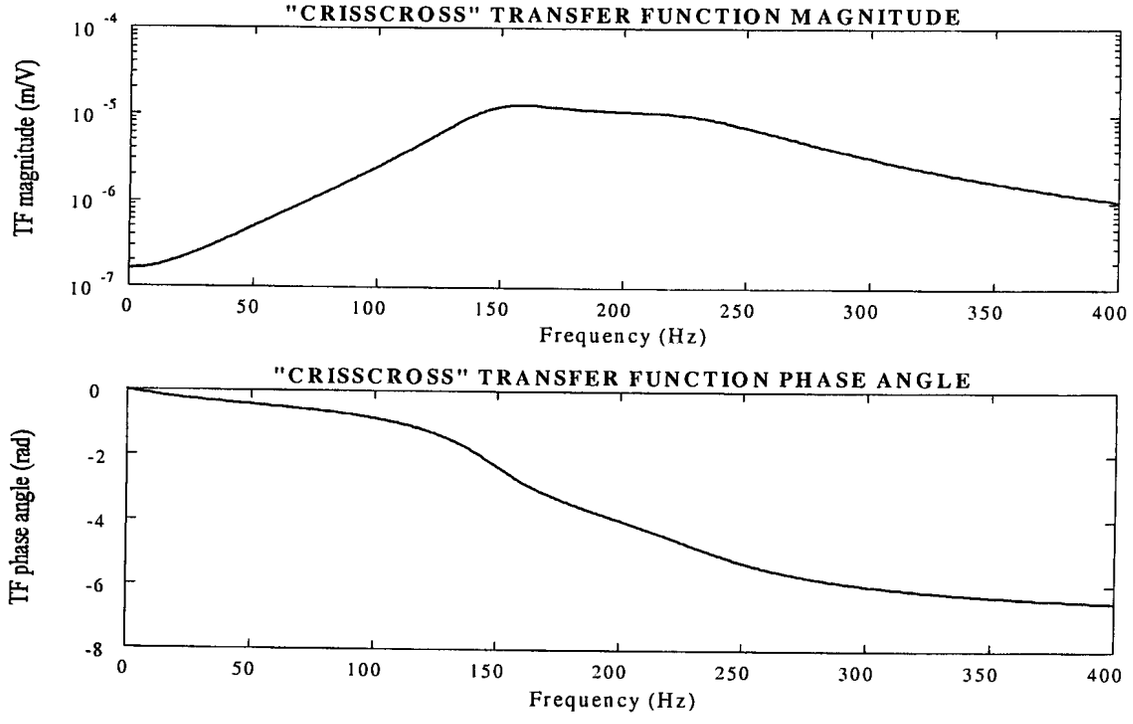

Figure 2.8.5.2: System *TF* magnitude for "crisscross" excitation and measurement

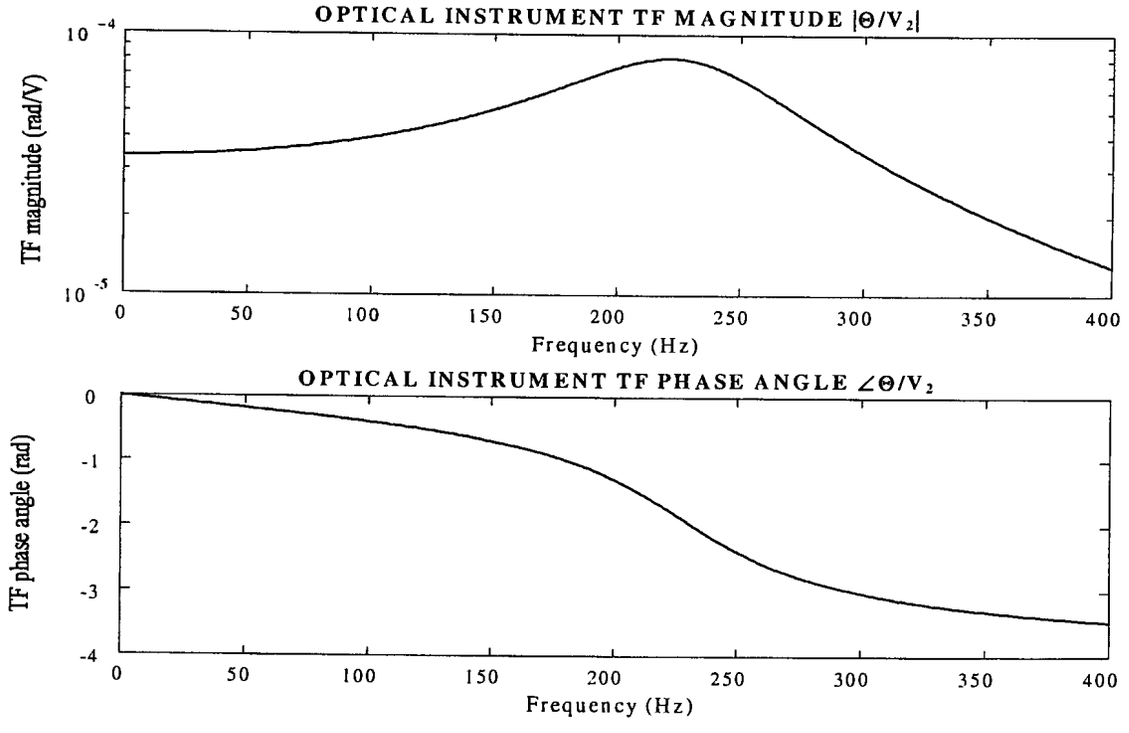

Figure 2.8.5.3: System LOS angle per unit input voltage

2.9 Summary of chapter 2 and preview of chapter 3

The magnetostrictive and magnetization characteristics of Terfenol-D were modelled in section 2.2. The characteristics were linearized and the strain constant, Young's modulus, piezomagnetic cross-coupling constant and permeability were derived from graphs published in literature. The effects of hysteresis on the strain constant and permeability were investigated in section 2.3. It was shown that hysteresis has a significant influence on both these parameters.

A Terfenol-D actuator was modelled in section 2.4. The nonlinear and linear equations of motion and coil current equations were expressed in terms of the magnetostrictive, magnetization, actuator and coil dynamic parameters. The equations of motion were coupled to the coil current equation in section 2.5, where an actuator state-space model was developed. Linear s- and ω-domain transfer functions were derived from the state-space model. The natural vibration behaviour of an actuator was covered in section 2.6 and the coupling effects of the coil current equation and the equation of motion on the eigenvalues, were indicated.

Actuator behaviour was simulated in section 2.7. The linear dynamic parameters were calculated for different input levels. A beam model was developed for the optical instrument and its support structure in section 2.8, which was coupled to the linear actuator model. An uncoupled modal equation of motion was derived. The natural frequencies and mode shapes of the system were calculated, using the Rayleigh-Ritz method, and shown graphically. The coil current equations were coupled to the equation of motion in state-space and the system transfer functions were obtained in the s- and ω-domains.

In chapter 3, the theory developed in chapter 2, together with the base disturbance parameters, will be used as inputs to design the Terfenol-D actuators and LOS stabilization system. The parameters required to reject the disturbance, such as actuator stroke length, system natural frequency, bandwidth, coil resistance to inductance ratio and input voltage, will be determined.

Chapter 3
Design and manufacture of magnetostrictive LOS stabilization system

3.1 Background

The design and manufacture of the magnetostrictive LOS stabilization system, consisting of two Terfenol-D actuators and a support structure for the optical instrument, are described in this chapter. The design inputs are given, i.e. the maximum allowable LOS angle, the frequency band and spectrum of the disturbance, the mass of the optical instrument and the maximum available voltage of the power source. These inputs are used to determine the required system performance parameters, namely the actuator stroke length and displacement gain factor, mechanical prestress in the Terfenol-D rods, system natural frequency, coil resistance to inductance ratio, bias voltage and amplitude.

Once the performance parameters have been determined, design concepts are generated, evaluated and compared. The principle of operation, performance parameters, advantages and disadvantages of each concept are discussed. The most suitable concept, on which the design will be based, is selected. A detailed design of the system and its components follows, including the necessary mathematical equations, graphs, component parameters, material specifications and assembly and detail drawings. In order to ensure system safety and reliability, a number of critical parameters, such as the buckling force and buckling frequency of the rods and critical eddy current frequency, are checked. The manufacturing and assembly procedures of the system are described.

The actuator and system design and manufacture are covered in detail in the following sections: Section 3.2 gives the design inputs, which are employed in section 3.3 to determine the system performance parameters. The design concepts are generated and compared in section 3.4 and the most suitable concept is selected. A detailed design of the actuators and system follows in section 3.5. Detail and assembly drawings are given in section 3.6. The design checks are covered in section 3.7 and 3.8. Section 3.9 describes the manufacturing procedure, and finally, chapter 3 is summarized and chapter 4 is previewed in section 3.10.

3.2 Magnetostrictive actuator and system design input parameters

This section gives the design input parameters of the actuators and system. The maximum allowable LOS angle, frequency band and spectrum of the disturbance, the mass of the optical instrument and its support structure, and the available voltage of the power source, are given. These parameters are required to calculate the system performance factors, such as the actuator stroke length and output force, system natural frequency, resistance to inductance ratio of the coils and the system bandwidth.

The different inputs influence the design as follows: The maximum allowable LOS angle and base angular disturbance determine the actuator output stroke length. The angular acceleration of the base and the mass of the optical instrument determine the required actuator

output force. The disturbance frequency bandwidth determines the resistance to inductance ratio of the coils, natural frequency and stabilization system bandwidth. The available voltage of the power source determines the maximum coil input voltage.

The base disturbance angular acceleration and displacement frequency spectra are shown in figure 3.2.1.

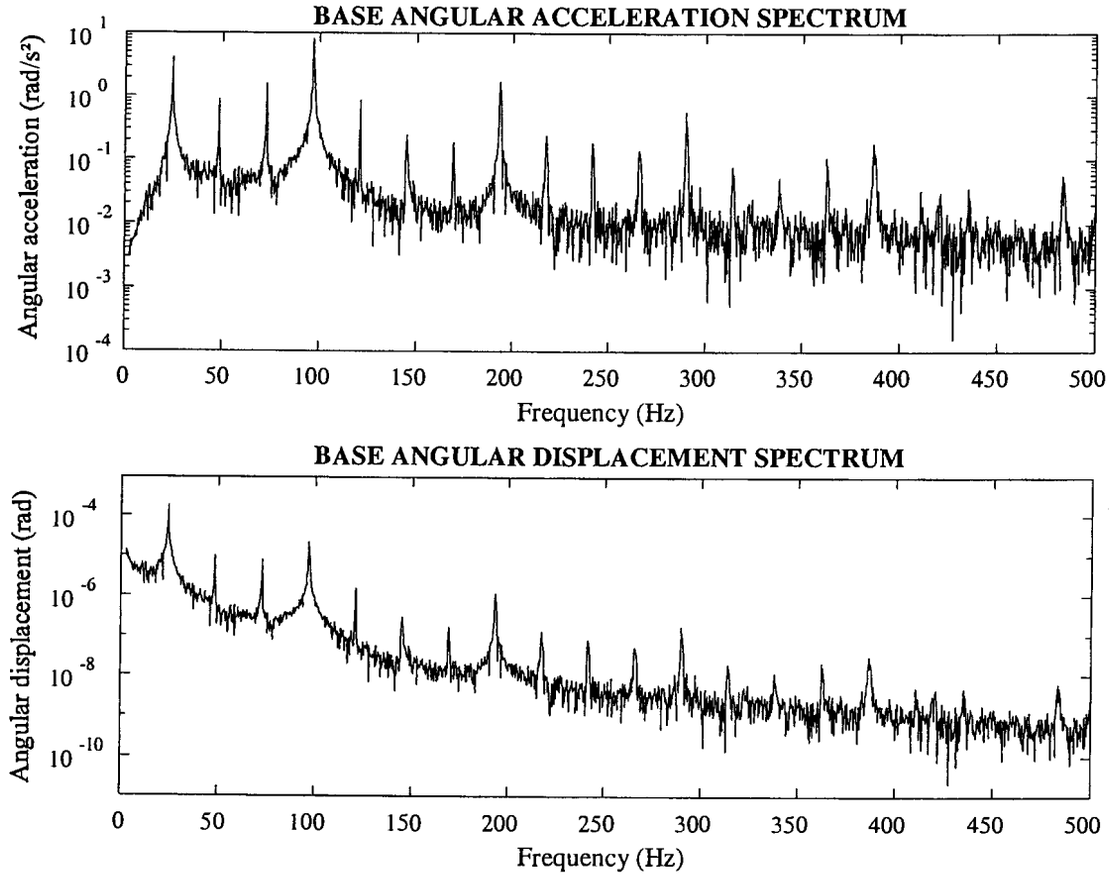

Figure 3.2.1: Base angular acceleration and displacement frequency spectra

The maximum allowable LOS angular displacement and acceleration of the optical instrument are 0,1 mrad peak-to-peak (p-p) and 5,37 rad/s^2 respectively. The maximum and RMS angular displacements of the disturbance are 0,7 mrad p-p and 1,81.10^{-4} rad respectively, while the maximum and RMS angular accelerations of the disturbance are 39,48 rad/s^2 p-p and 9,12 rad/s^2 respectively. The attenuation factor, which is the ratio of the difference between the base and instrument angular displacements, to the base angular displacement, is 85%.

The crest factor, or peak-to-RMS ratio of the disturbance displacement, is 2,17. The base disturbance bandwidth is 2,5 Hz to 500 Hz. The dominant frequency of the base angular acceleration signal is 96,75 Hz, while that of the base angular displacement is 24 Hz. The mass of the optical instrument and its support structure is 1,24 kg. The maximum available voltage of the source is 28 V.

The disturbance bandwidth deserv detail here. The purpose of the LOS stabilization system is to limit the instrument angular displacement to a value of 0,1 mrad, which is considerably lower than that of the disturbance, i.e. 0,7 mrad. This poses a problem, as the LOS angle of the instrument will be difficult to measure accurately due to output noise, which is aggravated by the presence of high frequencies in the disturbance signal. A sample frequency of five to ten times the maximum disturbance frequency is normally required for accurate measurement. For the disturbance under consideration, the maximum frequency is 500 Hz (see figure 3.2.1), therefore a sample frequency of 2,5 kHz to 5 kHz will be required.

In order to limit the influence of noise, it will be desirable to reduce the sample frequency to a more convenient value of 1 kHz. However, this measure will imply that disturbance frequencies above 100 Hz will have to be ignored and that the energy in the signal above 100 Hz will be unaccounted for. Since the bulk of the energy (91%) is concentrated below 100 Hz, limiting the disturbance band to 100 Hz is justifiable. Therefore, in this study, the maximum disturbance frequency will be limited to 100 Hz.

For the sake of completeness, all the actuator and system design input parameters are summarized in table 3.2.1.

Table 3.2.1: Magnetostrictive actuator and system design input parameters

Maximum allowable LOS angular displacement	0,1 mrad p-p
Maximum allowable LOS angular acceleration	5,37 rad/s^2 p-p
Maximum angular displacement of base disturbance	0,7 mrad p-p
Maximum angular acceleration of base disturbance	39,48 rad/s^2 p-p
RMS angular displacement of base disturbance	0,181 mrad
RMS angular acceleration of base disturbance	9,12 rad/s^2
Base disturbance displacement crest factor	2,17
Attenuation factor	85%
Percentage energy in disturbance below 100 Hz	91%
Base disturbance bandwidth	2,5 Hz to 100 Hz
Dominant base angular acceleration frequency	96,75 Hz
Dominant base angular displacement frequency	24 Hz
Length of optical instrument	250 mm
Mass of optical instrument and support structure	1,24 kg
Available voltage of power source	28 V

In the next section, the above design input parameters will be used to determine the actuator and system performance criteria.

3.3 Terfenol-D LOS stabilization system performance parameters

The system performance parameters required to reject the base disturbance, are determined in this section. These parameters will be used in section 3.5 to do a detailed system design. The parameters are the actuator stroke length and output force, coil resistance to inductance ratio and system natural frequency and bandwidth. The system design inputs, which were given in section 3.2, are used to calculate the performance parameters.

The actuator stroke length is determined from the maximum disturbance angle, maximum allowable LOS angle of the optical instrument and instrument length. The actuator output force is determined from the actuator displacements. The system frequency bandwidth, natural frequency and coil resistance-to-inductance ratio are determined from the disturbance frequency bandwidth.

Actuator stroke length

A sketch of the base and instrument angular displacements, and actuator stroke lengths and forces, is shown in figure 3.3.1. The instrument length is l. The angular displacement of the base is given by θ_b, while that of the instrument is given by θ. The stroke lengths of actuators I and II are respectively given by y_{a1} and y_{a2}. The force outputs of actuators I and II are F_{a1} and F_{a2} respectively. The moment acting on the instrument, due the actuator forces, is T.

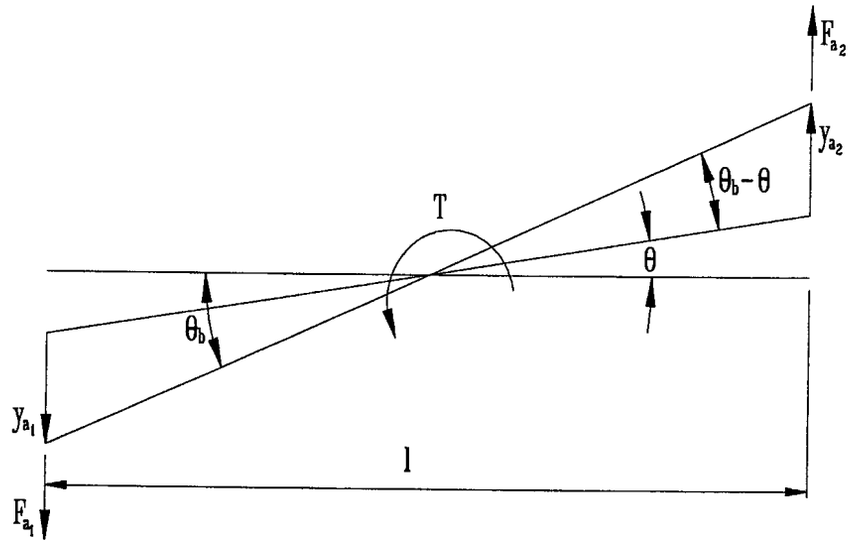

Figure 3.3.1: Base and instrument displacements and actuator stroke lengths and forces

The actuator stroke lengths y_{a1} and y_{a2} can be expressed as follows in terms of l, θ_b and θ:

$$y_{a1} = y_{a2} = \frac{l}{2}(\theta_b - \theta) \qquad \textbf{(3.3.1)}$$

The numerical values of l, θ_b and θ, from table 3.2.1, are:

$$l = 0{,}25 \text{ m} \quad \textbf{(3.3.2a)}$$

$$\theta_b = 0{,}7.10^{-3} \text{ rad} \quad \textbf{(3.3.2b)}$$

$$\theta = 0{,}1.10^{-3} \text{ rad} \quad \textbf{(3.3.2c)}$$

By substitution of Equations 3.3.2a to 3.3.2c into equation 3.3.1, the required stroke lengths of the two actuators are:

$$y_{a1} = y_{a2} = 75.10^{-6} \text{ m} \quad \textbf{(3.3.3)}$$

Actuator force

From Newton's 2nd law, actuator force can be expressed as follows:

$$F_a = \frac{m\omega^2 y_a}{2} \quad \textbf{(3.3.4)}$$

where F_a is peak-to-peak output force per actuator, m is system concentrated mass, ω is excitation frequency and y_a is actuator stroke length. The concentrated mass depends on the particular normal mode of the support structure and optical instrument that has to be excited. For angular motion, m is the modal mass of the first angular normal mode, i.e. 0,699 kg (see equation 2.8.4.1a):

$$m = M_{22} = 0{,}699 \text{ kg} \quad \textbf{(3.3.5)}$$

The excitation frequency is the maximum frequency of the disturbance band, i.e. 628,3 rad/s (corresponding to a frequency of 100 Hz - see table 3.2.1):

$$\omega = 628 \text{ rad/s} \quad \textbf{(3.3.6)}$$

From equation 3.3.3, y_a is 75.10^{-6} m. Substitution of equations 3.3.3, 3.3.5 and 3.3.6 into equation 3.3.4, gives:

$$F_a = 10{,}35 \text{ N} \quad \textbf{(3.3.7)}$$

Note that the actuator force given in equation 3.3.7 is the *external* force required by each actuator and does not include Terfenol-D rod or displacement gain mechanism stiffness. Rod and gain mechanism stiffness will be included in the detailed design in section 3.5.1.

System bandwidth

The disturbance rejection bandwidth (BW) of the system can be defined as the frequency where the magnitude of the TF is 70,7% of its DC value [Kuo, 1982]. The rejection BW thus defined is also known as the -3dB bandwidth. In order to reject the disturbance over the entire disturbance band, the BW must be at least as wide as the disturbance band. In section 3.2, the disturbance band was given as 100 Hz, therefore a disturbance rejection band of at least 100 Hz is required.

The rejection band depends on a number of system parameters, such as the natural frequencies, damping factors and coil R_o/L_o ratios. In an SDOF system, if the coupling effects of the coils are ignored, the –3dB bandwidth (BW) only depends on the natural frequency and damping factor. The bandwidth of an SDOF system, in terms of f_n and ζ, is:

$$BW = f_n g(\zeta) \tag{3.3.8}$$

where $g(\zeta)$ is:

$$g(\zeta) = \left[\left(1-2\zeta^2\right)+\sqrt{4\zeta^4-4\zeta^2+2}\right]^{0,5} \tag{3.3.9}$$

$g(\zeta)$ for damping factors of 0 to 1, from Kuo [1982], is given in table 3.3.1.

Table 3.3.1: $g(\zeta)$ for ζ ranging from 0 to 1 [Kuo, 1982]

Damping factor ζ	$g(\zeta)$
0,0	1,5538
0,1	1,5428
0,2	1,5096
0,3	1,4537
0,4	1,3745
0,5	1,2720
0,6	1,1482
0,7	1,0100
0,8	0,8709
0,9	0,7461
1,0	0,6436

From equation 3.3.8, it can be seen that BW is directly proportional to f_n, while, from table 3.3.1, it can be seen that BW decreases with an increase in ζ. It can further be seen that BW is strongly dependent on ζ. As damping is a parameter which is difficult to design into a system without any experimentally determined values, it is necessary to adopt a safe strategy in the system design.

One approach is to use the damping factor which will give the narrowest bandwidth, i.e. $\zeta = 1$. For this value of ζ, the value of g, from table 3.3.1, is 0,6436, and the bandwidth, from equation 3.3.8, is $0{,}6436 f_n$. For a desired system bandwidth of 100 Hz, the required natural

frequency, for $\zeta = 1$, is 155 Hz. However, if this approach is taken in the design of an actuator, the stiffness will be too high and excessive coil power may be required to give the desired stroke length.

Another approach is to ignore the influence of damping on the *BW* altogether and to use a *BW* of $\sqrt{2}$ times the natural frequency. At this frequency, the *TF* magnitude is equal to the DC magnitude and is damping independent. By taking this approach, the natural frequency required to give a bandwidth of 100 Hz, is 70,7 Hz. Note that this natural frequency gives a narrower bandwidth than the –3dB bandwidth, since the transfer function magnitude is 100% of that at DC, and not 70,7% as is the case with the –3dB bandwidth.

The above approaches can be successfully applied to the design of SDOF systems. However, the system under consideration is MDOF (see section 2.8), which requires a different design approach. The *TF* of an MDOF system may display an anti-resonance frequency, which is slightly larger than the lowest natural frequency. Depending on damping, the *TF* magnitude may show a sharp drop at frequencies above resonance, in which case the bandwidth may, for all practical purposes, be limited to the lowest natural frequency. As an example, consider a system whose zeroes z and poles p are:

$$z = -5 \pm j.628$$
$$p = \begin{Bmatrix} -5 \pm j.600 \\ -500 \pm j.1571 \\ -628 \end{Bmatrix} \qquad \textbf{(3.3.10)}$$

The magnitude and phase of the system are shown in figure 3.3.2. The lowest natural frequency is 95,4 Hz, while the anti-resonance frequency is 100,1 Hz. The bandwidth is 97,8 Hz, which is only 2,5% higher than the lowest natural frequency.

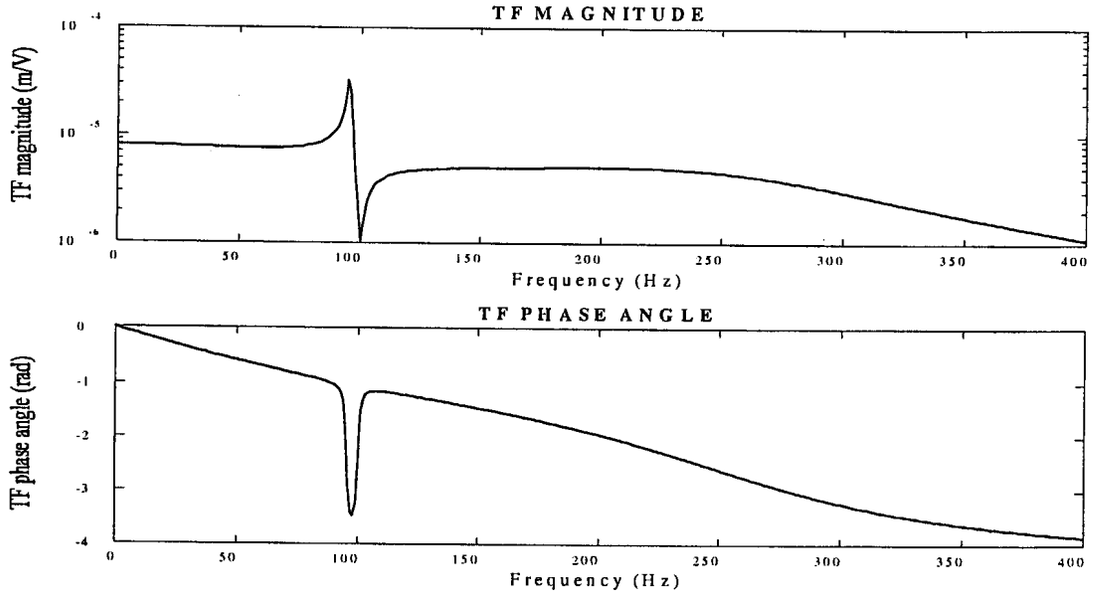

Figure 3.3.2: Transfer function of an MDOF system with a bandwidth close to f_n

Although the simulated *TF* of the system does not display an anti-resonance frequency (see figure 2.8.5.3), the dynamic and magnetostrictive parameters used in the simulations may differ from the true parameters. The differences may be attributed to phenomena such as hysteresis. The true parameters will be obtained from measured *TF's* in chapter 5. Until the true parameters are known, it will be assumed that the system may have an anti-resonance frequency close to the natural frequency. As a safety precaution, the system will be designed to have a natural frequency of at least 100 Hz. If the system has an anti-resonance frequency close to the natural frequency, it will be outside the isolation bandwidth.

Coil resistance to inductance ratio

The coil resistance to inductance ratio (R_c/L_0) determines the real poles of the system *TF* (see sections 2.4, 2.5 and 2.8). In order to ensure a bandwidth of at least 100 Hz, the real poles (and R_c/L_0 ratio) must be at least 100 Hz. If the R_c/L_0 ratio is lower than 100 Hz, the field versus coil voltage *TF* may drop below -3dB inside the disturbance band. This may result in insufficient isolation at the higher end of the band and may require excessive coil power to correct. In this design, in order to ensure a *BW* of at least 100 Hz, a coil R_c/L_0 ratio of at least 100 Hz is required.

Summary of required system parameters

For the sake of completeness, the required system performance parameters, as discussed above, are summarized in table 3.3.2.

Table 3.3.2: LOS stabilization system performance parameters

Performance parameter	Parameter value
Actuator stroke length	75.10^{-6} m
Actuator output force	10,35 N
Disturbance rejection bandwidth	2,5 Hz to 100 Hz
System natural frequency	≥ 100 Hz
Coil resistance to inductance ratio	≥ 100 Hz

The above parameters will be used in section 3.5 to do a detailed design of the actuators and system. Before that can be done, it is necessary to suggest and compare a number of possible design concepts in section 3.4. The concepts are discussed and evaluated and the most suitable concept is selected.

3.4 Magnetostrictive LOS stabilization system design concepts

This section discusses the possible system design concepts. The need for a displacement gain mechanism, magnetic biasing and mechanical biasing is motivated. A number methods to achieve the desired actuator gain, bias field and bias stress in the Terfenol-D rod are presented. The different concepts are compared on the basis of principle of operation, effective range of operation, advantages and disadvantages. Mathematical equations, graphs and tables are supplied to explain the principle of operation of each concept. The most suitable concepts are motivated and selected. These concepts are incorporated into an actuator and system design concept.

The stroke length of a magnetostrictive actuator depends on the strain in the active rod and the rod length. The maximum strain in the rod depends on the saturation strain of the particular material at a given prestress. Terfenol-D, which is a highly magnetostrictive material, can produce "giant" magnetostrictive strains of up to 2000 $\mu\varepsilon$. However, this strain is attainable at the cost of high compressive prestresses and large field strengths, which are not desirable for design purposes. Large field strengths are inefficient in terms of energy consumption, while high compressive stresses may be unpractical to achieve and may lead to rod buckling.

The other factor which determines the actuator stroke length, i.e. the rod length, is unfortunately also limited. In order to produce feasible actuator stroke lengths, a rod with an unrealistic length may be required, which will lead to an actuator of unpractical proportions. Furthermore, as is the case with high compressive prestresses, unduly long rods will also be prone to buckling. It is therefore clear that both the strain in the rod and the rod length limit the actuator stroke length to practically achievable values.

One method of achieving an actuator with the desired stroke length, is to implement a displacement gain mechanism, which "multiplies" the elongation of the rod with a dimensionless displacement gain factor. The gain mechanism may operate on pneumatic, hydraulic or purely mechanical principles. The advantage of a displacement gain mechanism is an increase in stroke length without the need of high fields or stresses. The actuator can be operated more efficiently in the linear range of its strain versus field characteristic, without having to force the field into the saturation range.

Unfortunately, there is also a disadvantage to the use of a gain mechanism, namely that the actuator output force is decreased by a factor equal to the displacement gain factor (see equation 2.4.7). Irrespective of this disadvantage, each of the actuators which will be used in this study will be equipped with a gain mechanism, since it is the only practical means of obtaining the desired stroke length.

In section 2.2 it was shown that Terfenol-D would produce a positive strain if subjected to a positive field. Terfenol-D will however, like other magnetostrictive materials, also produce a positive strain if a negative field is induced, as shown in figure 3.4.1. This characteristic is known as a symmetric characteristic. The disadvantage of a symmetric characteristic is that the strain amplitude is smaller for a given field amplitude than is the case with an asymmetric characteristic. This point is explained in the following example.

Consider the Terfenol-D strain versus field characteristic shown in figure 3.4.1. For a field with a zero mean (point a) and an amplitude of 40 kA/m, the maximum field is 40 kA/m and the minimum field is –40 kA/m. The strain which corresponds with the maximum field is 800 $\mu\varepsilon$ (point b). The strain which corresponds with the minimum field is also 800 $\mu\varepsilon$ (point c). It can be seen that the maximum available strain for a field with an amplitude of 40 kA/m and a zero mean, is 800 $\mu\varepsilon$. The strain versus field characteristic in the above example is symmetric.

Next, consider a field with a mean of 40 kA/m (point b), with the same amplitude as before, i.e. 40 kA/m. The maximum field will be 80 kA/m and the minimum field will be 0 kA/m. The minimum strain will be zero (point a), while the maximum strain will be 1300 $\mu\varepsilon$ (point d). This strain versus field characteristic is asymmetric. It is clear from figure 3.4.1 that the maximum strain in the asymmetric case is approximately 63% higher than in the symmetric case.

The above technique of improving the maximum strain is known as magnetic biasing. Due to the advantage illustrated in the above example, magnetic biasing will be applied in this study to obtain the maximum available strain in the Terfenol-D rod.

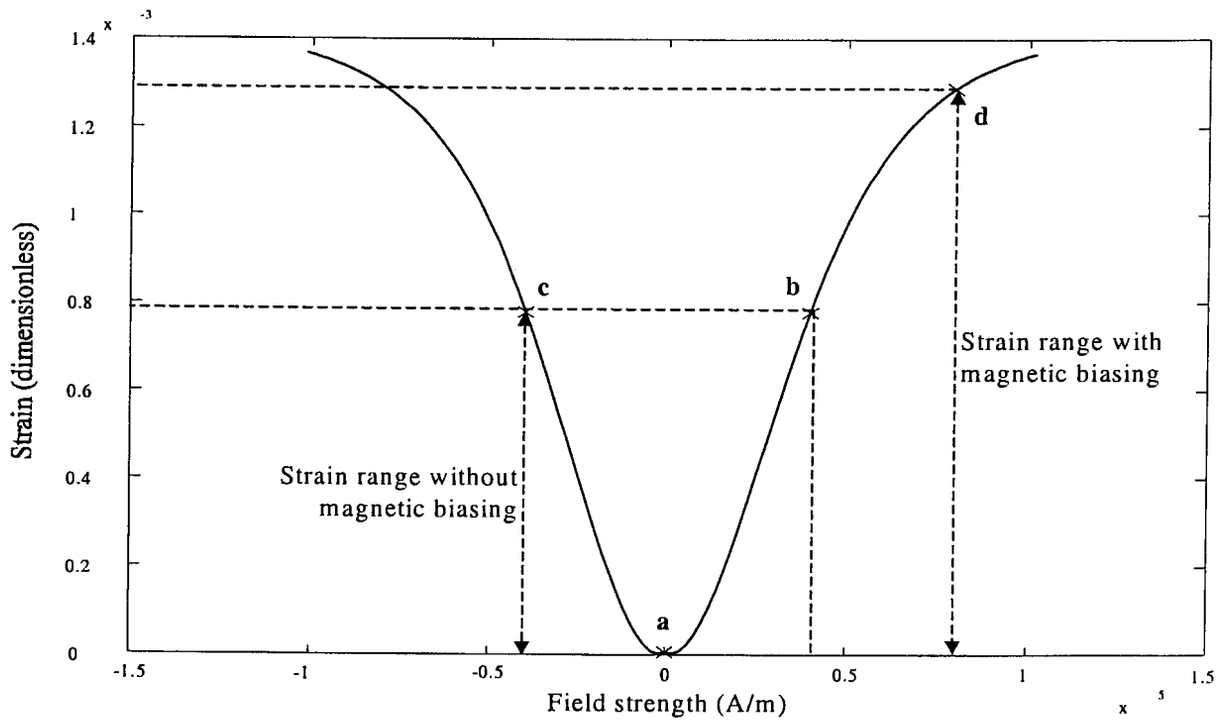

Figure 3.4.1: Magnetostrictive strain versus magnetic field strength for two bias fields

Mechanical biasing, or prestressing, of a Terfenol-D rod is required for two reasons. In the first place, larger saturation strains can be achieved. Figure 3.4.2 illustrates the effect of two compressive prestresses, i.e. 6,9 MPa and 17,9 MPa, on the magnetostrictive strain of Terfenol-D. At a field strength of 100 kA/m, the strain for a prestress of 6,9 MPa is approximately 1200 $\mu\varepsilon$, while for a prestress of 17,9 MPa, the strain is approximately

1400 $\mu\varepsilon$. It can be seen that a prestress can be used to good effect to increase the magnetostrictive strain in the rod. Secondly, Terfenol-D is soft in tension and must therefore always be under compression. The tensile strength of Terfenol-D is only 28 MPa, while the compressive strength is 700 MPa [Butler, 1988].

There are however, also disadvantages in prestressing the rod. The first is that higher compressive prestresses require larger field strengths to produce the same strain. For instance, to produce a strain of 750 $\mu\varepsilon$ at a prestress of 6,9 MPa, a field strength of approximately 20 kA/m is required, while a field strength of approximately 45 kA/m is required to produce the same strain at a prestress of 17,9 MPa (see figure 3.4.2). This problem can be solved by means of magnetic biasing, where, for instance, a permanent magnet is used to provide the desired bias field.

The second disadvantage, which has already been mentioned, is the danger of buckling. Buckling can be avoided by applying moderate prestresses, which do not exceed the buckling load of the rod, but at the same time, are ample to significantly increase the saturation strain. Mechanical biasing will be used in this study to improve the saturation strain of the rod.

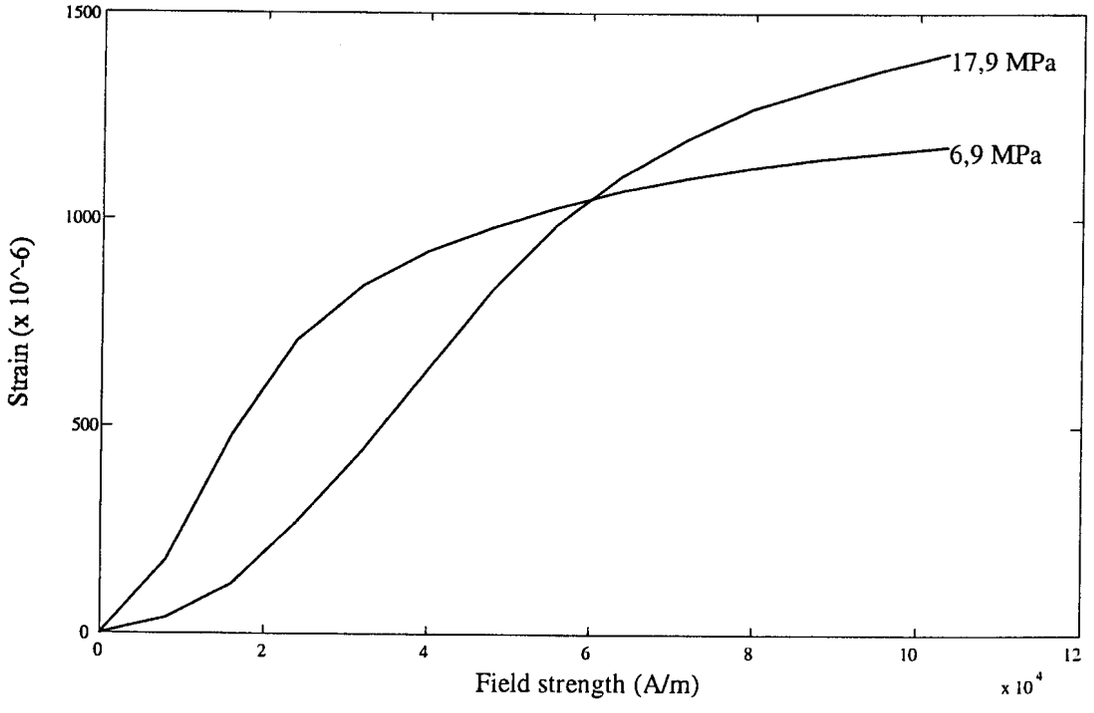

Figure 3.4.2: Terfenol-D strain versus field strength for two compressive prestresses

Section 3.4 is organized as follows: In section 3.4.1, different methods that can be used to obtain the desired actuator gain, are discussed. Bias field and bias stress concepts are covered in sections 3.4.2 and 3.4.3 respectively. The actuator and LOS stabilization system design concepts are presented in section 3.4.4.

3.4.1 Actuator gain concepts

Four methods of achieving the desired actuator displacement gain factor are presented in this section. The first method, which is also the simplest, works on the principle of resonance. A mechanical spring connects the actuator with the optical instrument. If the actuator is operated at frequencies in the vicinity of the natural frequency of the mechanism, a considerable displacement gain can be achieved.

A second method of increasing the output displacement of the actuator, is to make use of a hydraulic gain mechanism. The optical instrument is supported by a hydraulic piston with a cross-sectional area which is smaller than that of the Terfenol-D rod. During excitation, the displacement of the piston will be larger than that of the rod, thereby extending the output displacement of the actuator. The gain factor equals the ratio of the rod area to the piston area.

A third method of obtaining a displacement gain is to utilize the change in dimensions of a structure with unique geometric properties, such as an elliptical structure. The Terfenol-D rod is mounted along the major axis of the ellipse. During excitation, the length of the major axis will increase and the length of the minor axis will decrease. The gain factor is the ratio of the decrease in the length of the minor axis to the increase in the length of the major axis.

The fourth and last gain concept works on the same principle as the elliptical structure mentioned above, but the elliptical shape is replaced with an octagonal shape. The sides of the octagon are relatively hard in comparison with the corners, which act as flexures. During excitation, the corners deflect and allow the dimensions of the octagon to change. The length of the structure is increased while the height is decreased. The gain factor is the ratio of the decrease in height of the octagon, to the increase in length. The four concepts will be discussed in more detail in the following paragraphs.

Resonance spring gain mechanism

A mechanical model of a resonance spring gain mechanism is shown in figure 3.4.1.1. m_s is the concentrated mass of the optical instrument and its support structure, while m_a is the concentrated mass of the actuator. x_b represents the base disturbance displacement, while x_a is the displacement of the actuator mass, which is also the deformation of the Terfenol-D rod. x_s is the displacement of the instrument. k_a is the stiffness of the actuator, and F_m is the magnetostrictive force in the rod. k_{spr} is the stiffness of the gain spring and c represents the damping coefficient of the gain mechanism.

The principle of operation of the mechanism is as follows: The force F_m acts on the mass m_a, whose displacement x_a is resisted by the elastic stiffness k_a of the rod. The displacement of the mass is transmitted to the optical instrument through the spring k_{spr}. At low excitation frequencies, the instrument displacement will not be significantly larger than that of the mass. As the frequency is increased, x_s will exceed x_a, and the effect will increase with frequency.

The maximum amplification, or gain, will be achieved in the vicinity of the natural frequency of the system. At frequencies above the natural frequency, the gain will start to decrease and

eventually, at high frequencies, the displacement of the instrument will be smaller than that of the mass. This method is more effective if the damping is low.

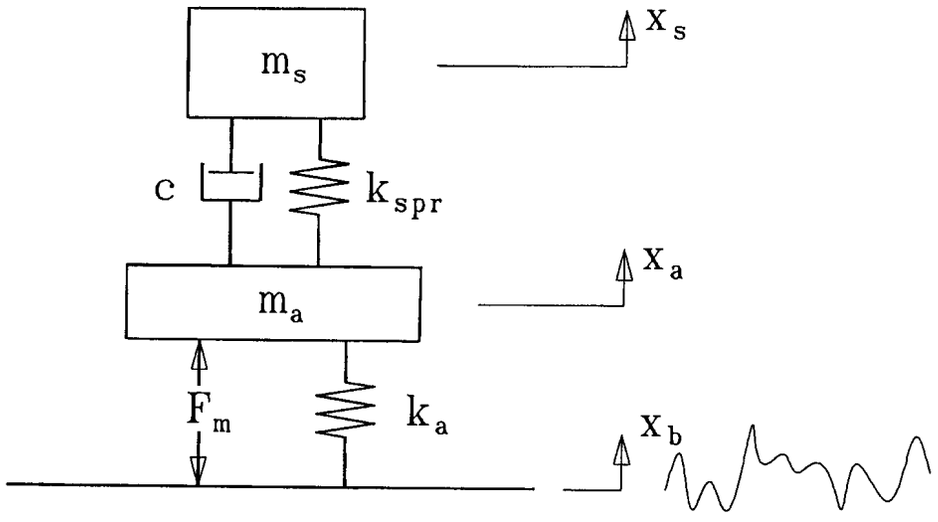

Figure 3.4.1.1: Resonance spring gain mechanism

The displacement gain factor is the ratio of the displacement x_s, of the mass to the displacement x_a, of the rod:

$$G = \frac{x_s}{x_a} \tag{3.4.1.1}$$

G can be derived in terms of the mechanical properties of the gain mechanism and the excitation frequency. The assumption is made that the natural frequency of the gain mechanism and instrument is significantly lower than that of the Terfenol-D rod and actuator mass:

$$\frac{k_{spr}}{m_s} << \frac{k_a}{m_a} \tag{3.4.1.2}$$

The derivation is not done here, but can be found in standard textbooks on vibration theory, such as Tse et al [1978]. The gain factor is given by:

$$G = \sqrt{\frac{1+\left(2\zeta_G \frac{\omega}{\omega_G}\right)^2}{\left(1-\left(\frac{\omega}{\omega_G}\right)^2\right)^2 + \left(2\zeta_G \frac{\omega}{\omega_G}\right)^2}} \tag{3.4.1.3}$$

where ω is the angular excitation frequency and ζ_G is the damping factor of the gain

mechanism:

$$\zeta_G = \frac{c}{2\sqrt{k_{spr} m_s}} \qquad \textbf{(3.4.1.4a)}$$

ω_G is the natural frequency of the gain mechanism:

$$\omega_G = \sqrt{\frac{k_{spr}}{m_s}} \qquad \textbf{(3.4.1.4b)}$$

The gain factor is shown graphically in figure 3.4.1.2. The frequency-dependence of the gain, natural frequency, desired gain and gain band are indicated on the graph.

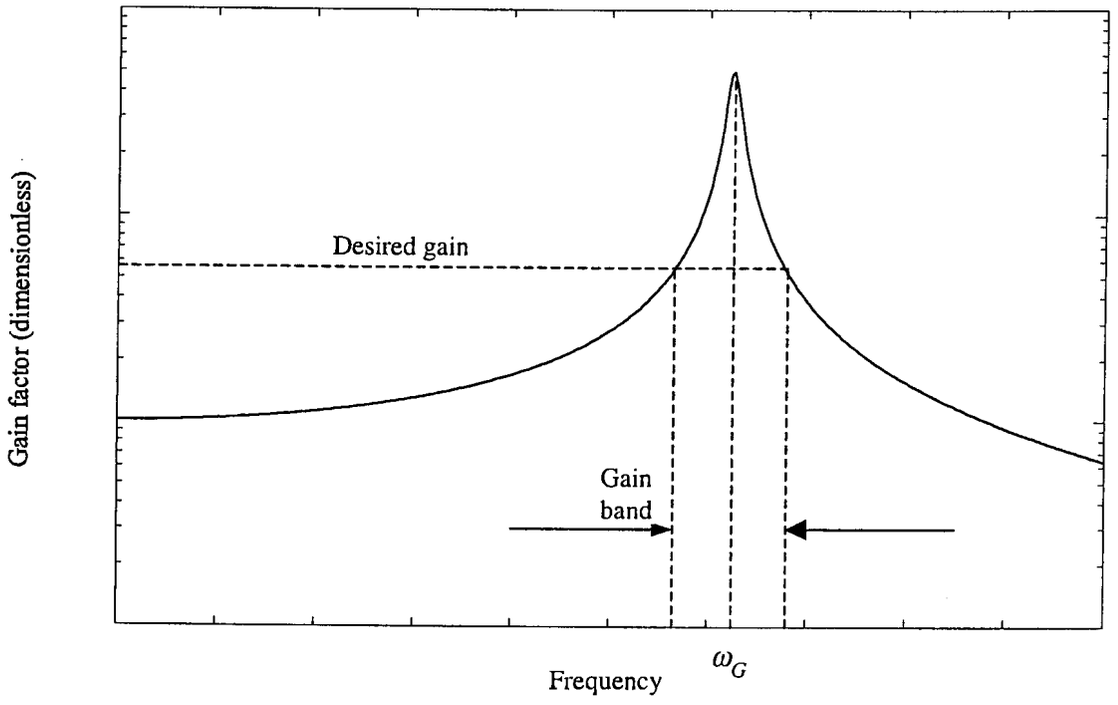

Figure 3.4.1.2: Resonance spring displacement gain factor versus frequency

The advantage of the resonance gain mechanism is its simplicity. This is due to the fact that only a spring is needed to accomplish a gain. However, the disadvantage is that a significant gain can only be achieved in the vicinity of the natural frequency, in a relatively narrow frequency band. This type of gain mechanism is very limited and cannot be used in the stabilization system of the optical instrument, since the disturbance is wide-band (2,5 Hz to 100 Hz - see section 3.2). A second disadvantage is that the gain is not constant, which will complicate closed-loop control of the line of sight of the optical instrument.

Due to these shortcomings, the resonance gain mechanism concept will have to be ruled out and alternative mechanisms, which are independent of the excitation frequency, will have to be considered. One such mechanism is a hydraulic gain mechanism, which will be discussed next.

Hydraulic gain mechanism

The principle of operation of a hydraulic gain mechanism is described in this section. A mathematical expression for the displacement gain factor is derived in terms of the dimensional parameters of the actuator. The effect of fluid compressibility on actuator stiffness, natural frequency and the output displacement to input coil voltage transfer function is given. The advantages and disadvantages of a hydraulic gain mechanism are mentioned.

A hydraulically gained actuator is shown in figure 3.4.1.3. The actuator consists of a Terfenol-D rod, a piston, which supports the mass of the optical instrument, and hydraulic fluid, which fills the space between the rod and the piston. The actuator is mounted on a moving base. The cross-sectional area of the rod is A and that of the piston is A_p. The piston cross-sectional area is smaller than the rod cross-sectional area. The displacement of the rod is x_a and that of the optical instrument is x_s. The base displacement is x_b.

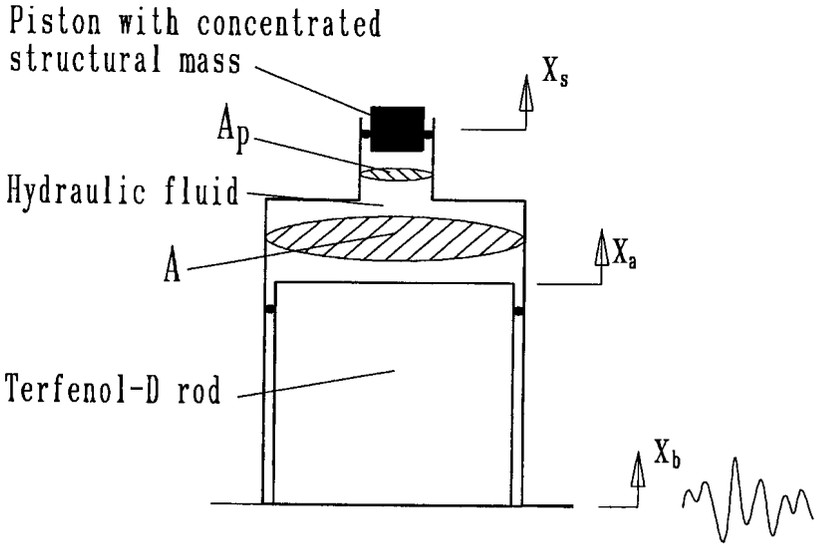

Figure 3.4.1.3: Actuator with hydraulic gain mechanism

The hydraulic gain mechanism works as follows: During excitation, a strain is produced in the rod, which displaces the hydraulic fluid and lifts the piston. The piston displacement is larger than that of the rod, thereby extending the output displacement or stroke length of the actuator. The displacement gain factor depends on cross-sectional area of the rod and the cross-sectional area of the piston. A mathematical expression for the gain factor is derived below.

The volume of fluid v_r displaced during excitation is the product of the rod cross-sectional area and the rod displacement:

$$v_r = Ax_a \tag{3.4.1.5}$$

The volume of fluid v_p which displaces the piston is the product of the piston cross-sectional area and the piston displacement:

$$v_p = A_p x_s \tag{3.4.1.6}$$

Assuming incompressibilty of the hydraulic fluid, the volume of fluid displaced by the rod equals the volume of fluid which displaces the piston:

$$v_p = v_r \tag{3.4.1.7}$$

Substitution of equations 3.4.1.5 and 3.4.1.6 into equation 3.4.1.7 gives:

$$Ax_a = A_p x_s \tag{3.4.1.8}$$

The displacement gain factor is the ratio of the piston displacement to the rod displacement:

$$G = \frac{x_s}{x_a} \tag{3.4.1.9}$$

By substitution of equation 3.4.1.8 into equation 3.4.1.9, the gain factor can be expressed as the ratio of the rod cross-sectional area to the piston cross-sectional area:

$$G = \frac{A}{A_p} \tag{3.4.1.10}$$

It is clear from equation 3.4.1.10 that the gain factor only depends on the cross-sectional areas of the rod and piston. Since both these areas are constant, the gain factor is also constant. If the hydraulic gain mechanism is compared with the resonance gain mechanism, it can be seen that the most important advantage of the hydraulic gain mechanism is a displacement gain factor which is independent of the excitation frequency, and whose operation does not depend on resonance.

In the derivation of equation 3.4.1.10, the assumption was made that the hydraulic fluid is incompressible. However, all hydraulic fluids exhibit a certain degree of compressibility, which will "soften" the actuator by introducing a resilience between the rod and the piston. This resilience will reduce the natural frequency of the actuator and will therefore alter the voltage input to displacement output transfer function (*TF*) of the actuator. The compressibility effect will differ from fluid to fluid, and will increase if the excitation is of such a nature that evaporation, or cavitation, of the fluid takes place.

Fluid compressibility is normally described by means of a bulk modulus [Schwarzenbach & Gill, 1986] and [Ashby & Pinches, 1989]. The bulk modulus can in turn be used to obtain an equivalent spring stiffness of the fluid, which facilitates the derivation of the *TF*. The bulk

modulus is defined below, and the equivalent stiffness, *TF* and actuator natural frequency are given. The *TF* of a compressible fluid is compared with that of an incompressible fluid. The derivation of the *TF* will not be done here, but is given in appendix N.

The bulk modulus can be defined as the ratio of the change in pressure, to the change in volume per unit volume:

$$K_B = \frac{\Delta P}{\left(\frac{\Delta V}{V}\right)} \tag{3.4.1.11}$$

where K_B is the bulk modulus, ΔP is the change in pressure, V is volume and ΔV is the change in volume.

The equivalent fluid stiffness k_{fluid} is given by:

$$k_{fluid} = \frac{A^2 K_B}{V_{ref}} \tag{3.4.1.12}$$

where V_{ref} is the reference volume.

The complex Laplace-domain *TF* of the actuator is:

$$\frac{X_s(s)}{V(s)} = \frac{\frac{\alpha}{\beta}\frac{AENd^H}{m_s(G-1)l_T L_0}}{s^3 + \frac{1}{\beta}\frac{R_c}{L_0}s^2 + \left[\alpha\frac{AE}{m_s G(G-1)l_T} + \frac{\alpha^2}{\beta}\left(\frac{AEN}{l_T}\right)^2 \frac{d^\sigma d^H}{m_s G(G-1)L_0}\right]s + \frac{\alpha}{\beta}\frac{AE}{m_s G(G-1)l_T}\frac{R_c}{L_0}} \tag{3.4.1.13}$$

where E is Young's Modulus of Terfenol-D, N is the number of coil turns, m_s is the concentrated mass of the optical instrument and its support structure, l_T is the length of the Terfenol-D rod, L_0 is the clamped coil inductance, R_c is the coil resistance, d^H is the strain constant and d^σ is the piezomagnetic cross-coupling constant. α and β are dimensionless parameters given by:

$$\alpha = \frac{k_{fluid}}{k_{fluid} + \frac{AE}{l_T}} \tag{3.4.1.14a}$$

$$\beta = 1 + \left(1 - \frac{k_{fluid}}{k_{fluid} + \frac{AE}{l_T}}\right)\frac{AENd^H}{l_T}\frac{Nd^\sigma}{L_0} \tag{3.4.1.14b}$$

For the sake of conciseness, the *TF* can be written in the following general form:

$$TF = \frac{P(s)}{Q(s)} = \frac{p_2 s^2 + p_1 s + p_0}{s^3 + q_2 s^2 + q_1 s + q_0} \qquad \textbf{(3.4.1.15)}$$

where the polynomial coefficients of $P(s)$ and $Q(s)$ are given in table 3.4.1.1. For comparison purposes, the polynomial coefficients for an incompressible hydraulic gain mechanism are also given.

Table 3.4.1.1: *TF* polynomial coefficients for magnetostrictive actuator with compressible and incompressible hydraulic gain mechanisms

Gain mechanism:	**Incompressible**	**Compressible**
Coefficient		
p_0	$\frac{AENd^H}{m_s(G-1)l_T L_0}$	$\frac{\alpha}{\beta}\frac{AENd^H}{m_s(G-1)l_T L_0}$
p_1	0	0
p_2	0	0
q_0	$\frac{AE}{m_s G(G-1)l_T}\frac{R_c}{L_0}$	$\frac{\alpha}{\beta}\frac{AE}{m_s G(G-1)l_T}\frac{R_c}{L_0}$
q_1	$\frac{AE}{m_s G(G-1)l_T}+\left(\frac{AEN}{l_T}\right)^2\frac{d^\sigma d^H}{m_s G(G-1)L_0}$	$\alpha\frac{AE}{m_s G(G-1)l_T}+\frac{\alpha^2}{\beta}\left(\frac{AEN}{l_T}\right)^2\frac{d^\sigma d^H}{m_s G(G-1)L_0}$
q_2	$\frac{R_c}{L_0}$	$\frac{1}{\beta}\frac{R_c}{L_0}$

The natural frequency ω_{nc} of a Terfenol-D actuator with a compressible hydraulic gain mechanism is:

$$\omega_{nc} = \sqrt{\alpha\frac{AE}{m_s G(G-1)l_T}} \qquad \textbf{(3.4.1.16a)}$$

whereas the natural frequency ω_{ni} of an actuator with an incompressible hydraulic gain mechanism is:

$$\omega_{ni} = \sqrt{\frac{AE}{m_s G(G-1)l_T}} \qquad \textbf{(3.4.1.16b)}$$

If equations 3.4.1.16a and 3.4.1.16b are compared, it can be seen that the compressibility of the fluid reduces the natural frequency with a factor $\sqrt{\alpha}$.

The advantage of a hydraulic gain mechanism, i.e. a constant factor gain over a wide frequency range, has already been mentioned. The disadvantages are as follows: In the first place, proper sealing at the contact surface between the cylinder and piston is essential.

Improper sealing may cause leaks, resulting in fluid losses and infiltration of air into the fluid chamber. The presence of air in the fluid will significantly reduce actuator output. Furthermore, maintenance will have to be done periodically to check the condition of the seals. The actuator will therefore have to be dismantled from time to time, resulting in lost operation time.

The hydraulic gain mechanism will not be considered for the magnetostrictive actuators used in this study. A gain mechanism which is not plagued by fluid leaks, sealing problems or costly maintenance, will be discussed in the next section. The gain mechanism makes use of the change in dimensions of an elliptical structure, mounted around the Terfenol-D rod.

Elliptical gain mechanism

A gain mechanism in the form of an elliptically-shaped structure is described in this section. Its principle of operation is explained. The gain factor is derived in terms of the elongation of the Terfenol-D rod and the lengths of the major and minor axes of the ellipse. The application, advantages and disadvantages of this type of gain mechanism are mentioned in short.

An elliptical gain mechanism is shown in figure 3.4.1.4. An elliptical structure is horizontally mounted on a moving base with a vertical displacement of x_b. The optical instrument is attached to the top of the structure, and the Terfenol-D actuator is mounted along the major axis of the ellipse. The mass and displacement of the instrument are m_s and x_s respectively. The length of the major axis of the ellipse is b, while that of the minor axis is a. The elongation of the Terfenol-D rod is $2\Delta b$ and the output displacement of the mechanism is $2\Delta a$.

The principle of operation of the mechanism is as follows: During excitation, the major axis of the ellipse is extended to a length $b+\Delta b$, while at the same time, the minor axis is shortened to a length of $a-\Delta a$. Due to the fact that the minor axis is shorter than the major axis, Δa is larger than Δb. The gain factor G is the ratio of Δa to Δb, and depends on the dimensional properties of the undeformed shape, i.e. a and b. An increase in the ratio of b to a leads to an increase in G. In order to obtain the gain factor for a gain mechanism with given dimensional properties, an equation which relates G to a and b is sought. This relationship is derived in appendix P.

A number of assumptions must be made in the derivation. Firstly, it is assumed that during excitation, the gain mechanism is not distorted, in other words the profile always stays elliptical. A second assumption is that the strain in the structure of the gain mechanism is zero, therefore the perimeter of the ellipse stays constant.

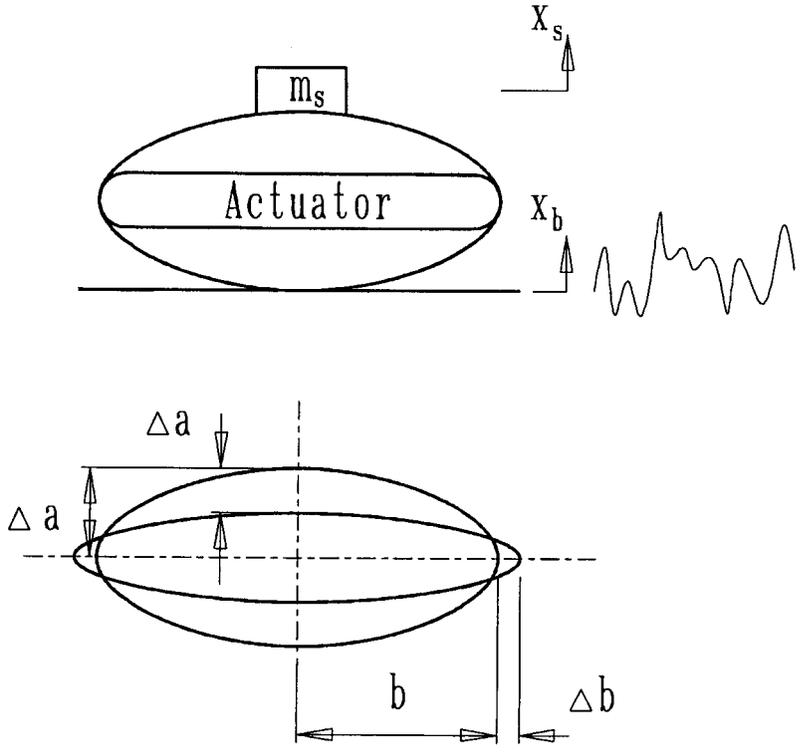

Figure 3.4.1.4: Elliptical gain mechanism

The gain factor is given by:

$$G = \frac{a - \sqrt{a^2 - 2b\Delta b + (\Delta b)^2}}{\Delta b} \qquad \textbf{(3.4.1.17)}$$

It can be seen from equation 3.4.1.17 that the gain factor depends on the dimensions a and b of the undeformed elliptical structure, as well as on the elongation Δb of the Terfenol-D rod. As was the case with the hydraulic actuator, which was discussed in the previous section, the gain factor is independent of excitation frequency. The elliptical gain mechanism has further advantages over the hydraulic gain mechanism, namely that it does not require periodic maintenance it is not plagued by fluid leaks.

One disadvantage of the elliptical structure, however, is that the elliptical shape is difficult to manufacture. Furthermore, it may be difficult to attach the gain mechanism to the optical instrument and to the base. In order to facilitate attachment of the gain mechanism, it will have to be flattened to a certain extent at the top and bottom.

The application of this method of obtaining a displacement gain also deserves mentioning. The method is mainly used by the Swedish Navy for underwater detection at high frequency. The gain factor is enhanced by exciting the structure at resonance, and the resulting gain is the combined effect of the geometric gain factor of the ellipse and the resonance spring gain described before.

This method of accomplishing an actuator displacement gain will not be considered any further in this study because of the manufacturing and installation problems described above. In order to overcome these problems, an octagonal flexural gain mechanism which operates on the same principle as the elliptical structure, but which is easier to manufacture, is recommended. This gain concept is discussed next.

Octagonal flexural gain mechanism

The principle of operation of an octagonal flexural gain mechanism is described in this section. The displacement gain factor is expressed in terms of the geometric properties of the mechanism by means of two methods, i.e. an exact method and an approximate method. The exact method expresses the gain in terms of the Terfenol-D rod length, strain in the rod, and the length and initial slope angle of the slanted sides of the octagon. The approximate method expresses the gain in terms of the initial angle of the slanted sides only.

The gain factor versus initial slope angle is shown graphically. The advantages and disadvantages of the octagonal flexural gain mechanism are discussed, and this method of accomplishing a displacement gain is selected for the LOS stabilization of the optical instrument.

A Terfenol-D actuator with an octagonal flexural gain mechanism is shown in figure 3.4.1.5. The mechanism consists of two horizontal beams, one at the top and one at the bottom, two vertical beams at the ends of the rod and four slanted beams which connect the horizontal beams with the vertical beams. During excitation, the eight corners of the mechanism, which are relatively soft in comparison with the beams, act as flexures to allow simultaneous changes in the length and height of the octagon. The horizontal beam at the bottom serves to attach the actuator to the base, while the horizontal beam at the top serves to attach the actuator to the optical instrument.

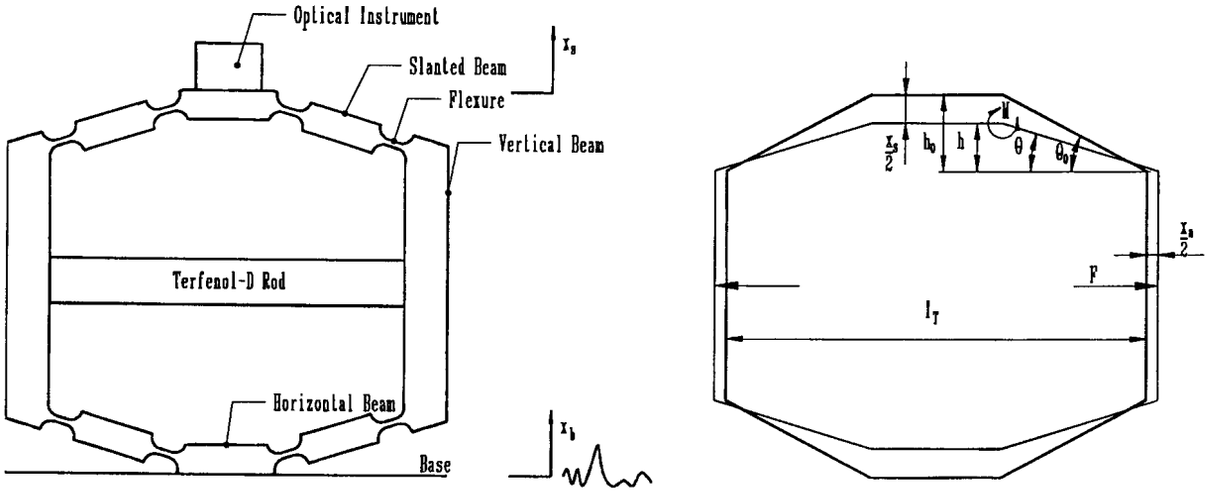

Figure 3.4.1.5: Octagonal flexural gain mechanism

The initial length of the Terfenol-D rod is l_T. The length of each slanted beam is r and the initial slope angle and height of the beam are θ_0 and h_0 respectively. The principle of operation of the gain mechanism is as follows: During excitation, a strain ε is produced in the rod, which generates a force F in the rod and extends the length of the mechanism by x_a. The force causes a bending moment M in the flexures, which tilts the slanted beam from an initial slope angle of θ_0 to a final slope angle of θ. The height of the slanted beam is reduced from an initial height h_0 to a final height h, which causes a vertical displacement x_s at the optical instrument. A displacement gain is brought about if x_s exceeds x_a.

An exact equation, which expresses the gain in terms of ε, l_T, r and θ_0, is derived in appendix Q. An alternative approximate equation, which expresses the gain in terms of θ_0 only, is also derived in the appendix. The gain factors obtained with the two methods are compared and it is shown that the gain depends strongly on θ_0, while ε, l_T and r have an insignificant effect.

The exact equation for the gain factor, in terms of r, θ_0, ε and l_T, is:

$$G = 2\frac{r\sin\theta_0 - \sqrt{r^2 - \left(r\cos\theta_0 + \frac{\varepsilon l_T}{2}\right)^2}}{\varepsilon l_T} \qquad \textbf{(3.4.1.18)}$$

The approximate equation for the gain factor, in terms of θ_0, is:

$$G = \cot\theta_0 \qquad \textbf{(3.4.1.19)}$$

The approximate gain factor is acceptably accurate for initial angles ranging from 5° to 35°, i.e. for gains ranging from 1,7 to 11,4 (see appendix Q). It can be concluded that, for the above range of θ_0, the gain depends strongly on θ_0, but is relatively insensitive to l_T, ε and r. The approximate gain factor, for slanted beam angles ranging from 5° to 30°, is shown in figure 3.4.1.6.

It has been shown above that the desired gain can be achieved by means of an octagonal flexural gain mechanism. The gain can be expressed in terms of the geometric properties of the octagon, using simple mathematical equations. As was the case with the elliptical structure discussed in the previous section, the gain factor is independent of the excitation frequency, as long as the system is not excited in the vicinity of one of its natural frequencies. This mechanism can therefore be designed to give an almost constant gain over a wide frequency band.

The octagonal gain mechanism is not plagued by the problems associated with the manufacture and installation of the ellipse because the sides are straight, thereby facilitating attachment of the actuator to the instrument and base. Due to the advantages just mentioned, the above method of achieving the desired gain will be employed in the design of the two Terfenol-D actuators.

However, there are also disadvantages that deserve to be addressed. One disadvantage is that the mechanism can only transmit and amplify motion through bending at the flexures. The latter will have to be very soft in order not to absorb too much actuator power. To this end, the flexures will have to be relatively thin, which could weaken the structure and lead to failure. Special attention will be paid to this problem during the detail design stage, which will be discussed in section 3.5.

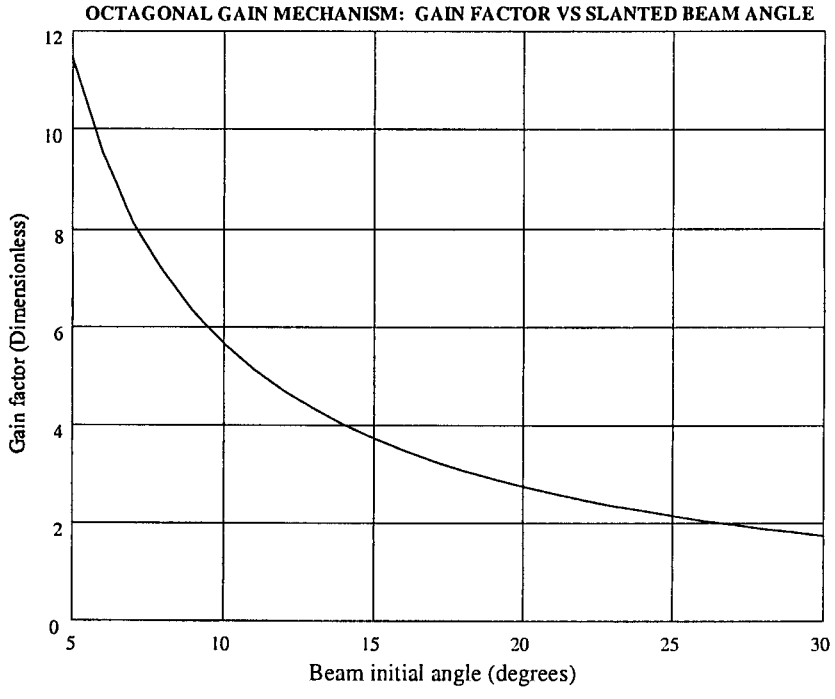

Figure 3.4.1.6: Gain factor versus initial angle of the slanted beam

This concludes the actuator gain mechanism concepts. Different concepts of achieving bias fields are discussed in section 3.4.2.

3.4.2 Magnetic biasing concepts

Two methods can be used to accomplish magnetic biasing. In the first method, a permanent magnet is used to induce a permanent bias field in the rod. This method is appropriately known as permanent magnet biasing. In the second method, an external current or voltage source is connected to the coil, to induce a field in the rod. The DC field is not permanent and will only be applied as long as the source is connected to the coil. This method is known as electromagnetic biasing. The two biasing methods will be discussed in short below.

Permanent magnet field biasing

Permanent magnet field biasing of a Terfenol-D rod is described in this section. The concept is shown diagrammatically. The principle of operation of permanent magnet biasing and its effect on dynamic excitation of the coil are explained. A number of permanent magnet materials are mentioned and their compositions and coercivities are tabled. The design philosophy of permanent magnet biasing is discussed and the necessary design equations are derived. The advantages and disadvantages of permanent magnet biasing are given.

A permanent magnet biasing concept is shown schematically in figure 3.4.2.1. A field coil is mounted concentrically around a Terfenol-D rod. The coil is connected to an AC voltage source, which induces an AC field in the rod. A permanent magnet, which induces a DC field

in the rod, is mounted concentrically around the coil. End caps are mounted at the rod ends to close the path of magnetic flux through the rod (see also figure 2.4.1). An air gap exists between the magnet and end caps. The force produced by the rod, due to the field, is F_r.

The DC field induced by the magnet biases the field in the rod. When the AC field is superimposed on the bias field, a fluctuating strain, with a displaced DC component, is produced. A positive strain results if a positive field is applied, while a negative strain results if a negative field is applied. This is known as the so-called "two-way effect" (see also figure 3.4.1).

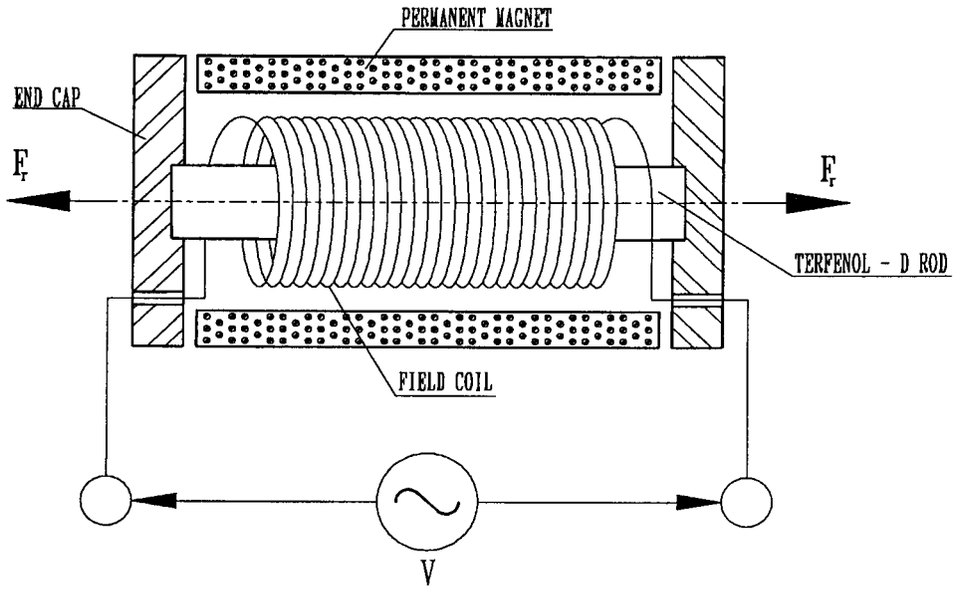

Figure 3.4.2.1: Permanent magnet field biasing of a Terfenol-D rod

The maximum field H_{max} is given by:

$$H_{max} = H_b + H_A \tag{3.4.2.1}$$

where H_b is the bias field and H_A is the amplitude of the AC component of the field.

The minimum field H_{min} is given by:

$$H_{min} = H_b - H_A \tag{3.4.2.2}$$

In order to ensure positive fields during excitation, the bias field must be equal to or larger than the field amplitude.

The maximum strain is the strain that corresponds with the maximum field at a given constant mechanical stress, i.e.:

$$\varepsilon_{max} = \varepsilon(H_b + H_A)\big|_{\sigma=const} \tag{3.4.2.3}$$

The minimum strain is the strain that corresponds with the minimum field at a given constant stress:

$$\varepsilon_{\min} = \varepsilon(H_b - H_A)\big|_{\sigma=const} \qquad \textbf{(3.4.2.4)}$$

As an example, consider a field with a bias component of 50 kA/m and a harmonic AC component of 50 kA/m excited at a frequency of 1 Hz. The stress is –12 MPa. The field is shown graphically in figure 3.4.2.2. The maximum field is 100 kA/m, while the minimum field is 0 kA/m. The maximum strain, from equation 2.3.1 and table 2.3.1 (for the dehysterized characteristic), is 1003 $\mu\varepsilon$, while the minimum strain is 0 $\mu\varepsilon$.

If the permanent magnet is removed and only the AC field is applied, the bias field will be zero. Irrespective of the direction of the field, a positive strain will result (the so-called "one-way effect"). This will considerably reduce the strain in the rod, and consequently, also the actuator output stroke length. Repeating the analysis for the above example, with $H_b = 0$ in equations 3.4.2.3 and 3.4.2.4, the maximum and minimum fields will be 50 kA/m and –50 kA/m respectively. The maximum strain of 572 $\mu\varepsilon$ will occur at both 50 kA/m and –50 kA/m, while the minimum strain will be 0 $\mu\varepsilon$. The maximum strain, if compared with that achieved with a bias field of 50 kA/m, is approximately 43% lower.

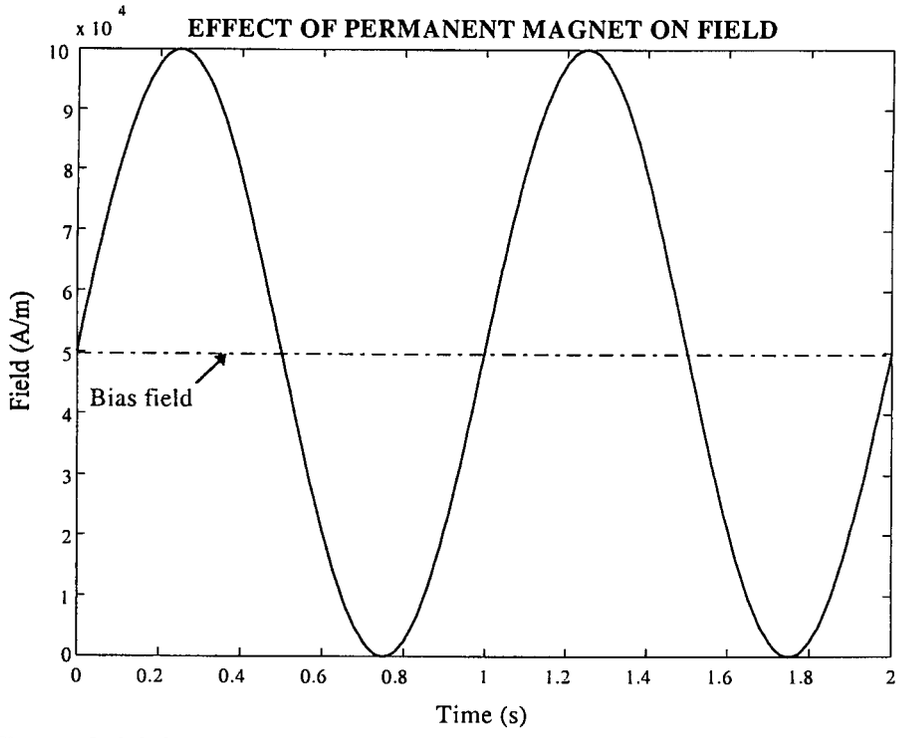

Figure 3.4.2.2: Effect of permanent magnet on field strength

Permanent magnets are generally made of hard magnetic materials with high intrinsic coercivities. The coercivity of a magnetic material is its ability to resist demagnetization. Traditionally, magnetic materials with coercivities above 10 kA/m have been known as hard magnetic materials [Jiles, 1991].

However, modern permanent magnet materials display coercivities two orders of magnitude larger than this. Samarium-cobalt, with a coercivity of 696 kA/m, has been a very popular permanent magnet material since 1967. More recently, in 1984, neodymium-iron-boron was introduced, with a coercivity of almost twice that of samarium-cobalt. The coercivities of various permanent magnet materials and their composition, from Jiles [1991], are given in table 3.4.2.1.

Table 3.4.2.1 Compositions and coercivities of various permanent magnet materials [Jiles, 1991]

Material	Composition	Coercivity (kA/m)
Steel	99% Fe,1% C	4,00
36 Co Steel	36% Co, 3,75% W, 5,75% Cr, 0,8% C	18,25
Alnico 2	12% Al, 26% Ni, 3% Cu, 63% Fe	52,00
Alnico 5	8% Al, 15% Ni, 24% Co, 3% Cu, 50% Fe	57,60
Alnico DG	8% Al, 15% Ni, 24% Co, 3% Cu, 50% Fe	56,00
Ba Ferrite	$BaO_6Fe_2O_3$	192,00
PtCo	77% Pt, 23% Co	344,00
Remalloy	12% Co, 17% Mo, 71% Fe	18,40
Vicalloy	13% V, 52% Co, 35% Fe	36,00
Samarium-cobalt	$SmCo_5$	696,00
Neodymium-iron-boron	$Nd_2Fe_{14}B$	1120,00

The goal of permanent magnet design is to obtain the magnet volume, which will give the desired bias field in the rod. The magnet volume V_m, in terms of the bias field, rod, magnet and air gap parameters, from appendix R, is given by:

$$V_m = \frac{B_T(H_b)A_T}{B_m H_m}\left(H_b l_T - \frac{B_T(H_b)A_T l_g}{\mu_0 A_g}\right) \qquad \textbf{(3.4.2.5)}$$

For a cylindrical magnet, the volume, in terms of the dimensional parameters, is:

$$V_m = \frac{\pi}{4}\left(d_o^2 - d_i^2\right)l_m \qquad \textbf{(3.4.2.6)}$$

where d_i and d_o are the magnet inner and outer diameters respectively.

Equations 3.4.2.5 and 3.4.2.6 provide the most important design equations for permanent magnet biasing of the Terfenol-D rod. In equation 3.4.2.5, the term B_mH_m is known as the magnet energy. Magnets are normally designed in such a way that the product of B_mH_m is a maximum [McCaig & Clegg, 1987].

The advantage of permanent magnet biasing is a considerable reduction in the required coil current, coil input voltage and power. The field supplied by the external source only requires an AC component, while the DC component is supplied by the permanent magnet.

However, there are also disadvantages to this method of magnetic biasing. The permanent magnet may become demagnetized if exposed to high fields and high temperatures. Even if used at relatively low temperatures, demagnetization may occur with time. The process can be retarded by using a permanent magnet with a high coercivity, but these materials are relatively expensive. Due to the high cost, permanent magnet biasing will not be considered in this study. An alternative magnetic biasing method, i.e. electromagnetic biasing, will be discussed in the next section.

Electromagnetic field biasing

This section discusses magnetic biasing of a Terfenol-D rod by means of an electromagnetic field. The concept is shown and the principle of operation is discussed. Equations for the coil current, voltage and power are given in terms of the bias field, field amplitude and excitation frequency. The power requirement of electromagnetic biasing is compared with that of permanent magnet biasing. The advantages and disadvantages of electromagnetic biasing are discussed. Electromagnetic biasing is motivated and selected as the most suitable magnetic biasing concept for this study.

An electromagnetic field biasing concept is shown in figure 3.4.2.3. A Terfenol-D rod is mounted concentrically inside a field coil, which is connected to an external voltage source with a voltage V. The end caps act as couplers to close the magnetic flux path (see also figure 2.4.1). The voltage source induces a field, which contains both the AC and bias (DC) fields, in the rod. The bias field is only present as long as the external source is connected to the coil. The force produced by the rod, due to the applied field, is F_r.

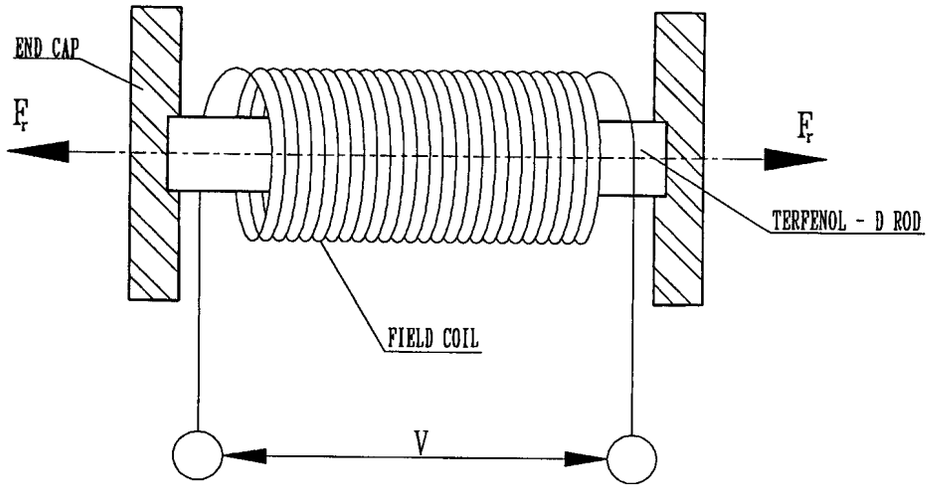

Figure 3.4.2.3: Electromagnetic field biasing of a Terfenol-D rod

The coil input current required to give the desired field in the rod, from equation 2.4.4, is:

$$I = \frac{l_T}{N} H \tag{3.4.2.7}$$

where I is the coil current, l_T is the rod length, N is the number of coil turns and H is the strength of the magnetic field in the rod. The coil impedance Z is given by:

$$Z = \sqrt{R_c^2 + \omega^2 L_0^2} \tag{3.4.2.8}$$

where R_c is the coil resistance, L_0 is the clamped inductance of the coil and ω is the angular excitation frequency. The voltage V supplied to the coil is the product of the coil impedance Z and the coil current I:

$$V = ZI \tag{3.4.2.9}$$

Substitution of equations 3.4.2.7 and 3.4.2.8 into equation 3.4.2.9 gives the coil voltage as follows in terms of the field:

$$V = \frac{l_T}{N} \sqrt{R_c^2 + \omega^2 L_0^2} H \tag{3.4.2.10}$$

The coil power is the product of the coil voltage and the coil current:

$$P = VI \tag{3.4.2.11}$$

The maximum coil current, voltage and power, from appendix S, are expressed as follows:

$$I_{\max} = \frac{l_T}{N}(H_b + H_A) \tag{3.4.2.12a}$$

$$V_{\max} = \frac{l_T}{N} \sqrt{R_c^2 + \omega^2 L_0^2}(H_b + H_A) \tag{3.4.2.12b}$$

$$P_{\max} = \left(\frac{l_T}{N}\right)^2 \sqrt{R_c^2 + \omega^2 L_0^2}(H_b + H_A)^2 \tag{3.4.2.12c}$$

Equations 3.4.2.12 give the relationships between the most important coil performance parameters for electromagnetic field biasing.

Equations 3.4.2.12 can also be used to compare the performance of a permanent magnet biased field with that of an electromagnetically biased field.

For permanent magnet biasing, the DC component of the field induced by the coil is zero, in

which case equations 3.4.2.12 become:

$$I_{\max} = \frac{l_T}{N} H_A \tag{3.4.2.13a}$$

$$V_{\max} = \frac{l_T}{N} \sqrt{R_c^2 + \omega^2 L_0^2}\, H_A \tag{3.4.2.13b}$$

$$P_{\max} = \left(\frac{l_T}{N}\right)^2 \sqrt{R_c^2 + \omega^2 L_0^2}\, H_A^2 \tag{3.4.2.13c}$$

The difference $\Delta P_{\max}$ between the maximum coil power for an electromagnetically biased field and that for a permanent magnet biased field, by subtracting equation 3.4.2.13c from equation 3.4.2.12c, is:

$$\Delta P_{\max} = \left(\frac{l_T}{N}\right)^2 \sqrt{R_c^2 + \omega^2 L_0^2}\left(H_b^2 + 2H_b H_A\right) \tag{3.4.2.14}$$

It can be seen from equation 3.4.2.14 that the difference between the maximum coil power for electromagnetic field biasing and that for permanent magnet field biasing, increases with bias field.

The advantage of electromagnetic field biasing is a substantial saving in the cost of a permanent magnet. As was mentioned in the previous section, the cost of permanent magnet materials, such as samarium cobalt, is high. Another advantage of electromagnetic biasing is simplicity of construction of the actuator. Both DC and AC components of the field are supplied by the coil, therefore a permanent magnet is not required and can be omitted. This further reduces actuator size and mass.

The disadvantage of electromagnetic field biasing is power consumption, as indicated in equation 3.4.2.14. Although an initial cost saving can be effected by using electromagnetic biasing, the running cost of this biasing method will be higher. However, since the aim of this study is to build and test a technology demonstrator, the high initial cost of a permanent magnet cannot be justified, therefore electromagnetic biasing will be used.

This concludes the discussion on magnetic biasing. A number of mechanical biasing techniques will be investigated in section 3.4.3 and the most suitable concept will be motivated and selected.

3.4.3 Mechanical biasing concepts

Mechanical biasing, or prestressing, of a Terfenol-D rod, is discussed in this section. A motivation for mechanical biasing is given, and the principle of operation is explained. Two methods of achieving mechanical biasing, i.e. by means of Belleville springs and coil springs, are discussed. The parameters which determine the characteristics of each spring type are mentioned, and the force versus deflection characteristic of each spring type is given mathematically and graphically. The advantages and disadvantages of each spring type are discussed and the use of coil springs is motivated.

It was shown in section 3.4 that a Terfenol-D rod subjected to a compressive prestress, will give higher saturation strains than an unstressed rod. The advantage of applying a compressive prestress to the rod is a larger rod strain and therefore a longer actuator stroke length for the same peak-to-peak magnetic field.

Mechanical prestressing of a Terfenol-D rod is shown schematically in figure 3.4.3.1. A prestress is brought about by a compressive force F_b acting at the ends of the rod. The end caps aid in distributing the stress uniformly over the rod cross-sectional area, denoted by A_T.

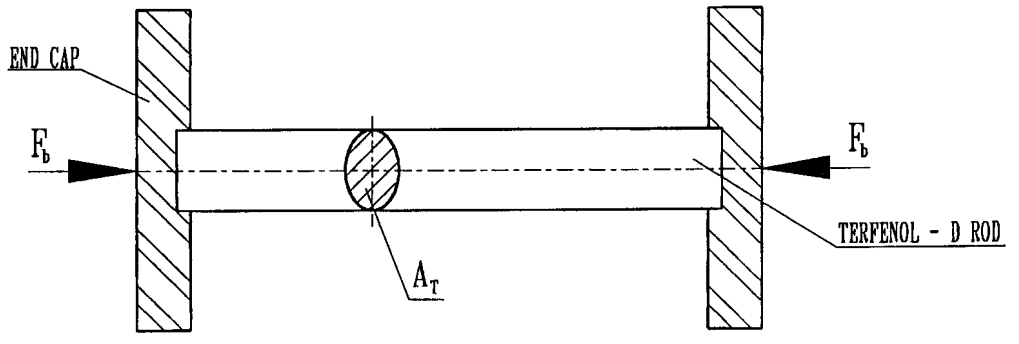

Figure 3.4.3.1: Mechanical prestressing of a Terfenol-D rod

The prestress σ_b is the ratio of the spring force F_b to the cross-sectional area A_T of the rod:

$$\sigma_b = \frac{F_b}{A_T} \qquad \textbf{(3.4.3.1)}$$

Practically, a prestress can be accomplished by using a mechanical spring, which exerts a force on the rod via an end cap (see figure 3.4.3.2). The prestress depends on the force versus deflection characteristic of the spring, initial spring deflection and rod cross-sectional area. In order to provide a relatively constant prestress during excitation, the initial deflection of the spring must be relatively large in comparison with the magnetostrictive deformation of the rod.

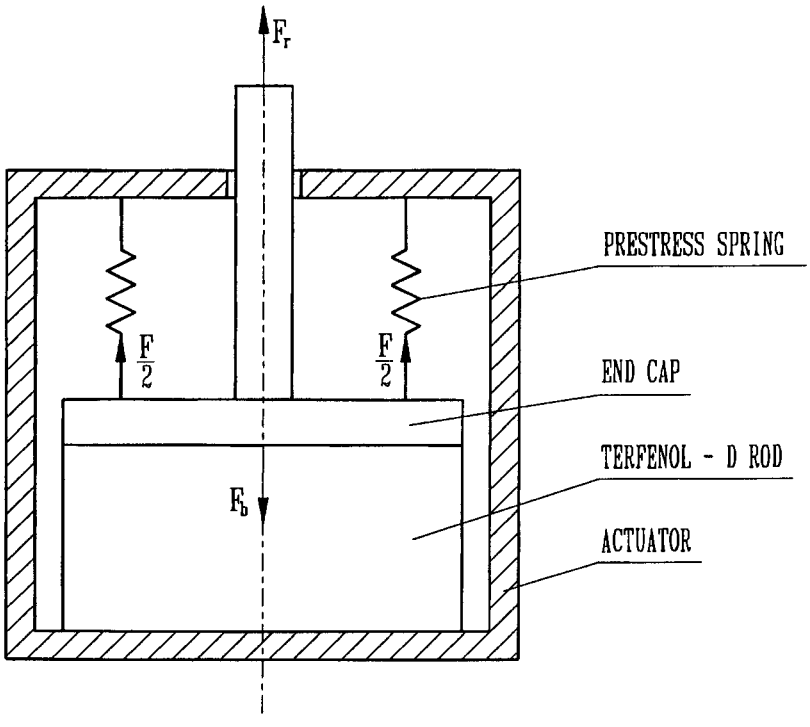

Figure 3.4.3.2: Prestressing by means of a mechanical spring

The spring force F is a function of the initial deflection x_i of the spring:

$$F = F(x_i) \tag{3.4.3.2}$$

The bias force acting on the rod is equal to the spring force:

$$F_b = F \tag{3.4.3.3}$$

Rod prestress can be enhanced by gaining the spring force. This can for instance be accomplished by using a displacement gain mechanism, as was discussed in section 3.4.1. The advantage is that the desired prestress can be achieved by using a relatively soft spring. For a gain factor of G, rod prestress, in terms of spring force, is given by:

$$F_b = GF \tag{3.4.3.4}$$

Two spring types, which can be considered for mechanical biasing, are Belleville springs (or Belleville washers) and coil springs. The two spring types are discussed in short below. The dimensional parameters, force versus deflection characteristics, advantages and disadvantages of each spring type are given. Belleville washers are discussed first, followed by a discussion of coil springs.

Mechanical biasing with Belleville springs

A Belleville spring is shown in figure 3.4.3.3. The spring has the shape of a shallow conical disc, or washer, with a hole in the centre. The conical angle is α. The outer diameter of the washer is D_e and the diameter of the hole is D_i. The thickness of the spring is t, the free height is h and the total height is H. The applied axial compressive force is F and the spring deflection is x.

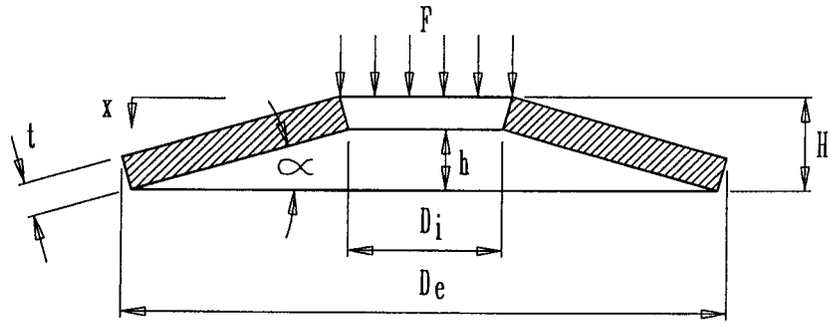

Figure 3.4.3.3: Diagrammatic representation of a Belleville spring

The force versus deflection characteristic is given as follows by Roark & Young [1983]:

$$F = \frac{4E}{\left(1-\nu^2\right)MD_i^{\,2}}\left[\left(h-x\right)\left(h-\frac{x}{2}\right)t+t^3\right]x \qquad \textbf{(3.4.3.5)}$$

where E and ν are Young's modulus and Poissons' ratio of the spring material and M is a dimensionless constant which depends on the ratio of the outer diameter of the spring to the hole diameter. M can be conveniently described by the following approximate empirical equation, which was obtained by interpolation from data supplied by Roark & Young [1983]:

$$M \approx 0{,}8196 - \frac{0{,}8516}{\left(D_e/D_i\right)^{2{,}7}} \qquad \textbf{(3.4.3.6)}$$

As can be seen from equation 3.4.3.5, spring force is a cubic function of deflection. The parameters E, ν, M and D_i are constant for a given spring, while t, h and x are variables, which determine the shape of the characteristic. The influence of t and h on the characteristics of two Belleville washers is illustrated in figure 3.4.3.4. Both springs have an outer diameter of 10 mm, a hole diameter of 3,2 mm and a thickness of 0,3 mm. The free height to thickness ratio of the first spring is 1,435 and that of the second spring is 1,167. The maximum deflection is 1 mm in both cases.

A high degree of nonlinearity is displayed by both spring characteristics. The differences in the two characteristics are the following: The force curve of spring I initially rises more sharply than that of spring II. However, for deflections between 0,3 mm and 0,6 mm, the force curve of spring I displays a region of zero gradient, or constant force, while the slope of the force curve of spring II shows an increasing trend. For deflections larger than 0,5 mm, the

compressive force of spring II exceeds that of spring I. At the maximum deflection of 1 mm, the maximum compressive force of spring I is 460 N, while that of spring II is 660 N.

Figure 3.4.3.4 highlights the most important advantage of a Belleville spring, i.e. that a constant force versus deflection characteristic can be obtained over a reasonably wide deflection range by proper selection of the *h/t* ratio. This feature makes the spring particularly desirable for maintaining a constant prestress in the Terfenol-D rod.

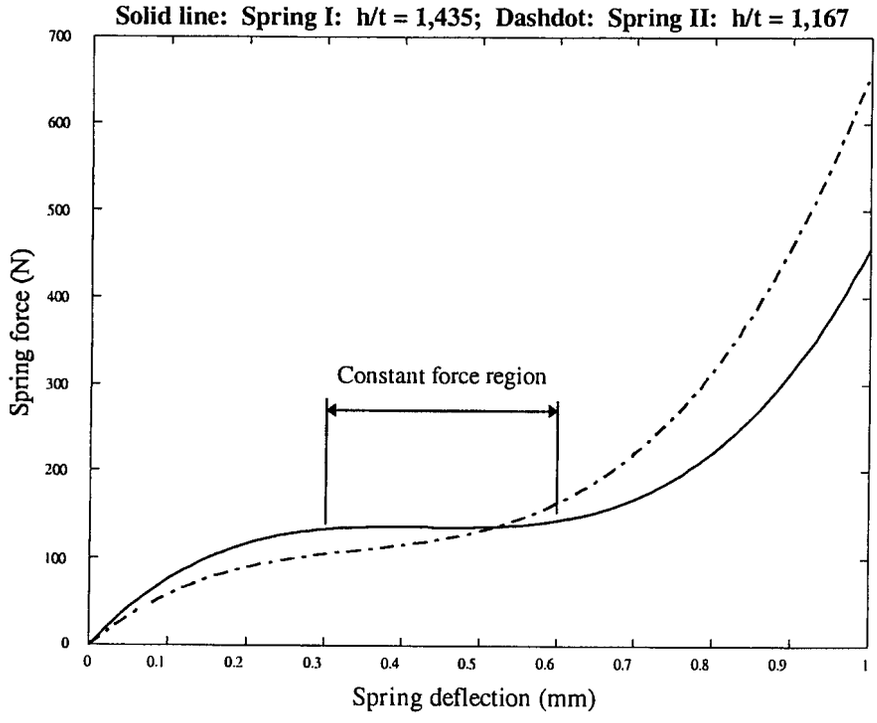

Figure 3.4.3.4: Spring force versus deflection characteristics of two Belleville springs

Belleville springs have a number of disadvantages: In the first place, due to their low height, Belleville springs are relatively stiff in comparison with other spring types. In order to reduce stiffness, a number of springs must be stacked. This leads to another problem, i.e. that during dynamic excitation, friction forces act at contact surfaces between the springs, which may cause hysteresis losses in the actuator output displacement. The problem can be overcome by lubricating the springs, but this will have to be done periodically in order to replenish the lubricant and to keep the springs clean.

A second disadvantage of using a conical spring for this application, is its nonlinearity. It was shown in chapter 2 that, due to magnetostrictive and magnetization saturation and hysteresis, Terfenol-D is a material which displays a high degree of nonlinearity in its static and dynamic behaviour. During characterization tests, it may be difficult to isolate material nonlinearities from spring nonlinearities. Lastly, depending on the *h/t* ratio, Belleville springs may become unstable at large deflections and may snap through.

For the abovementioned reasons, Belleville springs will not be considered for mechanical biasing. Coil springs are a feasible alternative. The characteristics, advantages and disadvantages of a coil spring will be discussed next.

Mechanical biasing with coil springs

Mechanical biasing of a Terfenol-D rod by means of a coil spring is described in this section. The spring parameters are given and the spring stiffness and spring wire shear stress are described in terms of the material and dimensional properties. The advantages and disadvantages of this spring type are mentioned. The coil spring is selected as the most suitable spring for mechanical biasing of the rod.

A diagrammatical representation of a coil spring is shown in figure 3.4.3.5. The outer diameter of the spring is D_e and the pitch circle diameter (PCD) is D. The change in the PCD during compression is ΔD. The free length is l_f and the compressed length is l_c. The wire diameter is d. The applied compressive force is F and the deflection is x.

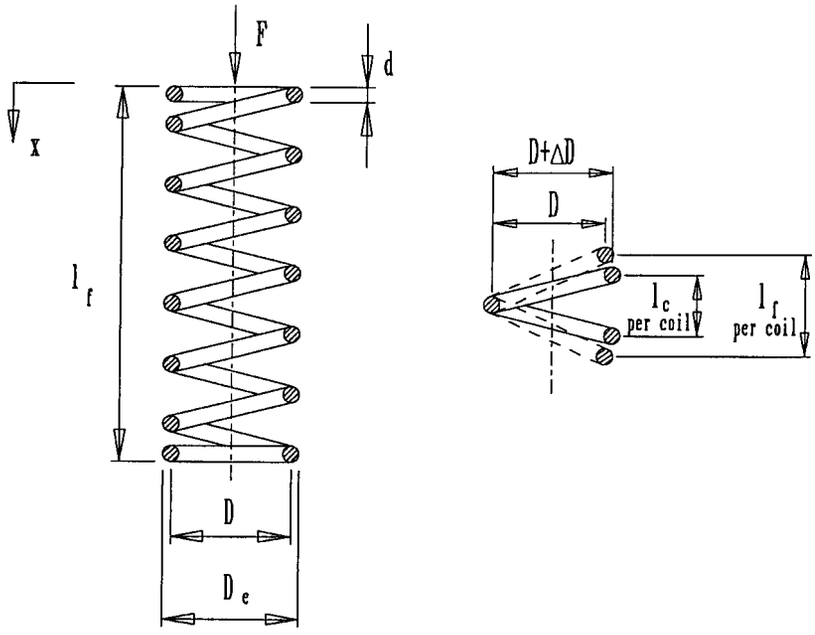

Figure 3.4.3.5: Diagrammatical representation of a coil spring

Two important coil spring parameters are the spring stiffness and spring wire shear stress. Equations for the spring characteristic and shear stress in terms of the spring material properties, dimensional parameters and type of coil ends, will be given in the following paragraphs. It will be shown that the characteristic of a coil spring is weakly nonlinear, but can, for this application, be assumed as linear.

Spring free length l_f can be expressed as follows in terms of the wire diameter d, total number of coils N_t and maximum deflection x_{max}:

$$l_f = dN_t + x_{max} \tag{3.4.3.7}$$

Rod prestress σ_b in terms of rod cross-sectional area A_T and compressive force in the rod F_b, is given by equation 3.4.3.1. F_b, in terms of spring force F and gain factor G, is given by equation 3.4.3.4. F, in terms of spring deflection x, is given by equation 3.4.3.2. For a spring with a linear characteristic, F is given by:

$$F = kx \tag{3.4.3.8}$$

where k is the spring stiffness, given as follows by the SAE Spring Design Manual [1990]:

$$k = \frac{G_s d^4}{8D^3 N_a} \tag{3.4.3.9}$$

In equation 3.4.3.9, G_s is the spring material shear stress modulus and N_a is the number of active coils. The latter is determined by the total number of coils N_t, and the type of spring end. The relationship between N_t and N_a is:

$$N_a = N_t - N_e \tag{3.4.3.10}$$

where N_e is the number of inactive coils. Values of N_e for different spring ends, from Shigley [1977], are given in table 3.4.3.1.

Table 3.4.3.1: N_e for different spring end types [Shigley, 1977]

Type of spring end	N_e
Plain end	0,5
Plain and ground end	1,0
Squared end	1,0
Squared and ground end	2,0

It can be seen from equation 3.4.3.9 that k is directly proportional to G_s, directly proportional to d^4, inversely proportional to D^3 and inversely proportional to N_a. Since these parameters are constant for a given spring, the stiffness is also constant.

Equations 3.4.3.8 to 3.4.3.10 are valid for a linear spring characteristic. However, a coil spring displays a weakly nonlinear characteristic, which can be attributed to a change in coil diameter during compression (see figure 3.4.3.5). The relative change in diameter $\Delta D/D$ can be described as a function of the spring pitch p, spring diameter D, wire diameter d and a dimensionless factor α which accounts for the degree of constraint from unwinding during

compression:

$$\frac{\Delta D}{D} = \alpha f(p, d, D) \tag{3.4.3.11}$$

For a spring which is constrained from unwinding, α and f are respectively given as:

$$\alpha = 0{,}05 \tag{3.4.3.12a}$$

$$f = \frac{p^2 - d^2}{D^2} \tag{3.4.3.12b}$$

where p is the pitch, given by:

$$p = \frac{l_f}{N_t} \tag{3.4.3.13}$$

When one or both ends of the spring are free to unwind without friction, α and f are given by:

$$\alpha = 0{,}1 \tag{3.4.3.14a}$$

$$f = \frac{p^2 - 0{,}8pd - 0{,}2d^2}{D^2} \tag{3.4.3.14b}$$

Equations 3.4.3.12 and 3.4.3.14 are valid for a spring whose deflection corresponds with the maximum spring deflection. However, due to the relatively small elongation of the Terfenol-D rod, the spring deflection and accompanying change in diameter will be insignificant. For this application, spring stiffness can therefore be considered as constant.

Apart from spring stiffness, another important parameter, which must be considered in the selection of a suitable spring type for mechanical biasing of the Terfenol-D rod, is stress. If a compressive force is applied to a coil spring, the coil wire is subjected to a shear stress. The shear stress depends on the spring PCD, wire diameter, applied force and spring index.

The shear stress τ_c is given by:

$$\tau_c = K_w \tau \tag{3.4.3.15}$$

where τ is given by:

$$\tau = \frac{8}{\pi}\frac{FD}{d^3} \tag{3.4.3.16}$$

K_w is the Wahl shear stress correction factor, given by:

$$K_w = \frac{4C-1}{4C-4} + \frac{0{,}615}{C} \qquad \textbf{(3.4.3.17)}$$

where C is the spring index, which is the ratio of the PCD to the wire diameter:

$$C = \frac{D}{d} \qquad \textbf{(3.4.3.18)}$$

Combination of equations 3.4.3.15 to 3.4.3.18, gives the shear stress as follows in terms of applied force, spring PCD and wire diameter:

$$\tau_c = \frac{D}{d}\left[\frac{4\left(\frac{D}{d}\right)-1}{4\left(\frac{D}{d}\right)-4} + \frac{0{,}615}{\left(\frac{D}{d}\right)}\right]\frac{8F}{\pi d^2} \qquad \textbf{(3.4.3.19)}$$

The main advantage of using a coil spring for mechanical biasing is its almost constant spring stiffness, as discussed above. A further advantage is that coil springs needn't be stacked to give the correct stiffness, as is required with Belleville springs. The problem of mechanical hysteresis can therefore be eliminated. Coil springs can be designed to give the desired stiffness by selecting the correct PCD, wire thickness and number of active coils (see equation 3.4.3.9).

The disadvantages of coil springs are twofold. In the first place, coil springs operate at high shear stresses, even during normal use. If exposed to high loads for long periods, coil springs tend to yield slowly and fail to maintain a constant force.

Secondly, coil springs may buckle under large compressive forces. This problem can however be overcome by a using a spring with a low free length to PCD ratio and by making use of fixed ends, instead of hinged ends. According to the SAE Spring Design Manual [1990], a free length to PCD (l_f/D) ratio of less than 5,2 is required for unconditional buckling stability of a spring with fixed ends. By comparison, a coil spring with hinged ends will be unconditionally stable if the free length to PCD ratio is less than 2,6.

In spite of the shortcomings of coil springs, this spring type is preferred to Belleville springs for mechanical biasing of the Terfenol-D rods. The advantages of coil springs outweigh the disadvantages. Spring life can be extended by designing more conservatively in order to reduce shear stresses, while the buckling problem is easily solved using a relatively low l_f/D ratio.

The concepts discussed in sections 3.4.1 to 3.4.3 can be combined to create a design concept for the actuators and LOS stabilization system. Section 3.4.4 will cover the actuator and system design concept.

3.4.4 Terfenol-D actuator and LOS stabilization system design concept

The Terfenol-D actuator and LOS stabilization system design concepts are described in this section. The Terfenol-D rods, gain mechanism, coils and prestress springs are combined into a unit to generate an actuator design concept. The concept is shown diagrammatically. A design concept for the support structure is also shown. The actuator and support structure concepts are combined to generate a system design concept.

An actuator design concept is shown in figure 3.4.4.1. The actuator consists of two Terfenol-D rods, a coil wound around each rod, two springs, four end caps, a gain mechanism, two bolts and nuts and a centrepiece. The coils induce a field in the rods, while the springs provide mechanical biasing in the form of compressive prestressing of the rods. The gain mechanism extends the elongation of the rods to provide the desired actuator stroke length, and also acts as a magnetic coupler to close the path of magnetic flux through the rods. The end caps serve as mechanical couplings between the rods and the gain mechanism, and locate the rods relative to the gain mechanism.

The bolts act as an additional measure to adjust the prestress in the rods and to complement the springs. The nuts lock the bolts to the gain mechanism to take up any free play in the actuator. The centrepiece provides a support for the rods and prestress springs.

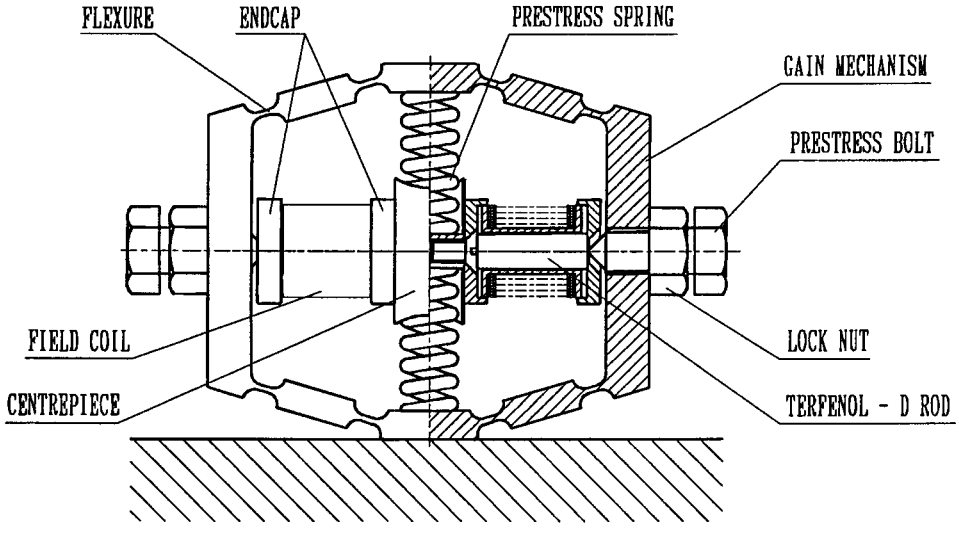

Figure 3.4.4.1: Terfenol-D actuator design concept

The actuator concept described above is used to generate a concept for the LOS stabilization system. The system is shown diagrammatically in figure 3.4.4.2. The system consists of two actuators, the optical instrument and its support structure. The support structure is soft at the actuator attachment points to allow easy bending, thereby making angular motion of the optical instrument possible. The actuators are mounted at the ends of the support structure to achieve the highest possible angular moment on the optical instrument.

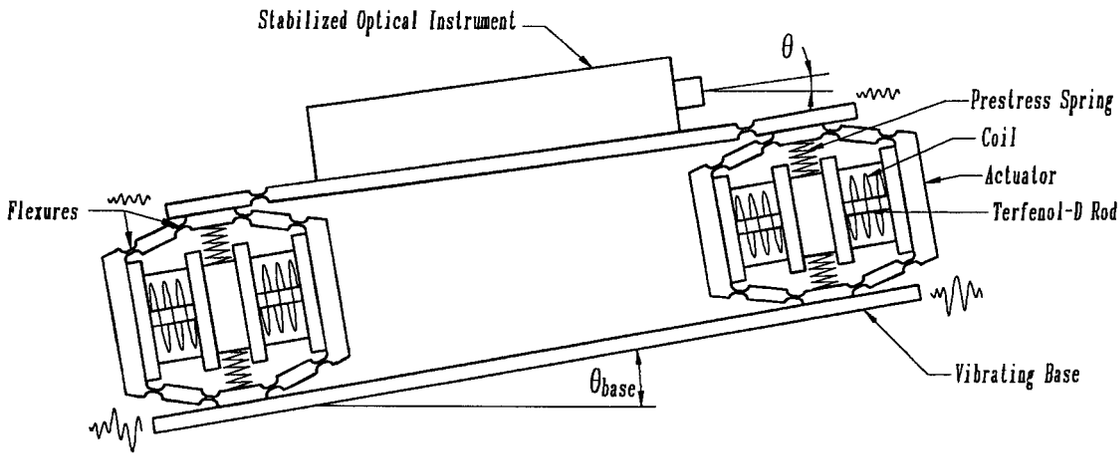

Figure 3.4.4.2: Terfenol-D LOS stabilization system design concept

This concludes the design concepts. A detailed design of the system and all its components will be done in section 3.5. The concept generated in this section will form the basis of the design.

3.5 Detailed design of the Terfenol-D actuators and stabilization system

A detailed design of the Terfenol-D actuators and optical instrument support structure is done in this section. The Terfenol-D rod length and diameter, rod strain and elongation, actuator displacement gain factor, gain mechanism stiffness and maximum stress are determined. The finite element method is used to determine the design parameters of the gain mechansim and support structure. The field coils and prestress springs are designed. Design theory is given and practical design aspects are addressed. Design parameters and geometries are calculated, tabled and shown graphically.

Gain mechanism design, including the calculation of the Terfenol-D rod length and diameter, rod elongation and strain, actuator displacement gain factor, gain mechanism stiffness and maximum stress are determined in section 3.5.1. The field coils and prestress springs are designed in sections 3.5.2 and 3.5.3 respectively. The support structure is designed in section 3.5.4.

3.5.1 Detailed design of the Terfenol-D actuators

Design of the Terfenol-D actuators is described in detail in this section. The required Terfenol-D rod length, diameter and cross-sectional area are calculated. The necessary mathematical equations are given and practical aspects to be taken into account, are discussed. Suitable actuator gain factor and rod length are selected, using the simulated and required stroke lengths and rod strain. Rod diameter is calculated from the strain, gain factor and required output force. Gain mechanism geometry, maximum mechanism stress, mechanism stiffness and mechanism deflection profile are determined. A first order calculation of the

required slanted beam angle is done, followed by a more comprehensive finite element calculation. Actuator parameters are tabled.

Rod length, diameter and actuator gain factor

The mathematical relationship between actuator output stroke length, displacement gain factor and rod elongation, is:

$$y_a = Gx_r \tag{3.5.1.1}$$

where y_a is output stroke length, G is gain factor and x_r is rod elongation. Rod elongation is the product of the strain in the rod and rod length:

$$x_r = \varepsilon l_T \tag{3.5.1.2}$$

where ε is rodstrain and l_T is rod length. Substitution of equation 3.5.1.2 into equation 3.5.1.1 gives the actuator output displacement in terms of the gain factor, rod length and strain in the rod:

$$y_a = Gl_T\varepsilon \tag{3.5.1.3}$$

from which:

$$Gl_T = \frac{y_a}{\varepsilon} \tag{3.5.1.4}$$

Equation 3.5.1.4 will be used to determine the gain factor and strain.

Comparison between simulated and required stroke length and strain

The simulated (quasi-static) stroke length, from table 2.7.3.2, is:

$$y_{a\max} = 178{,}5\,\mu m \tag{3.5.1.5}$$

The maximum strain corresponding to the above actuator stroke length is:

$$\varepsilon_{\max} = 944\,\mu\varepsilon \tag{3.5.1.6}$$

The stroke length and strain obtained with the simulations can be compared with those required to reject the disturbance. The required stroke length, from table 3.3.2, is:

$$y_a = 75\mu m \tag{3.5.1.7}$$

If equations 3.5.1.5 and 3.5.1.7 are compared, it can be seen that the required stroke length is considerably shorter (approximately 60%) than the simulated stroke length. The latter was

obtained with a gain factor of 5,4, which was arbitrarily selected for the simulations (see table 2.7.3.1).

The simulated value of the maximum rod strain, i.e. 944 $\mu\varepsilon$, is acceptable since it is in the linear region of the strain versus field characteristic (see figure 3.4.1). For this strain, saturation nonlinearities can, for all practical purposes, be neglected. A maximum strain of 944 $\mu\varepsilon$ is therefore a feasible value and will be used in the design calculations that follow. If a higher maximum strain is allowed, magnetostrictive saturation may be encountered. On the other hand, if strain is limited to a lower value, excessive rod length may be required. This may lead to rod buckling, especially if compressive prestresses are applied to enhance saturation strain.

Practical aspects to be considered in the selection of rod length and gain

Practical factors to be taken into account in selecting a suitable rod length and gain are as follows. From equation 3.5.1.4, it can be seen that, the shorter the rod, the higher the required gain for the same stroke length and strain. Higher gains have the advantage that lower coil input voltages are required to produce the desired actuator stroke length. However, higher gains lower the natural frequency (see equations 2.4.22 and 2.4.23). If the natural frequency is too low, the system isolation band may be too narrow to reject the disturbance.

Another disadvantage of a high gain is that it may be practically impossible to achieve. The reason is as follows: In order to make a high gain possible, a low slanted beam angle is required (see figure 3.4.1.6). A lower limit must however be placed on the slanted beam angle. If the angle is decreased below a certain value, which depends on the gain and flexure geometry, rod length and strain, the flexures will start to stretch, instead of bend. This will have an adverse effect on actuator output displacement.

For the purpose of assembling the actuators, the rods must be recessed in the end caps. The recessed parts of the rods are not exposed to the magnetic field and do not contribute to the actuator force. Additional rod length, known as the passive length, is required for this purpose. Furthermore, spools are required for winding the coils around the rods. Spool end thickness will inevitably add to the passive length. The danger of excessive passive length is that it may contribute to rod buckling and must therefore be limited as much as is practically possible.

Gain mechanism stiffness must be taken into account. In the simulations described in chapter 2, an ideal gain mechanism, i.e. with zero stiffness, was assumed. However, it is to be expected that the flexures of the octagonal gain mechanism (see figure 3.4.1.5) will not be ideal, i.e. their stiffness will not be zero. Flexure stiffness will add to actuator stiffness. Since actuator output displacement is inversely proportional to stiffness for the same field strength, output displacement will be reduced. In order to compensate for the reduction in displacement, the gain factor must be increased.

A last factor to be taken into account, is the cost of Terfenol-D rods. The manufacturer of the Tefenol-D rods, i.e. Etrema, prices rods per 25 mm length. To save cost, rod lengths must preferably be limited to 25 mm each.

Rod length and gain factor selection procedure

The procedure for obtaining rod length and gain factor is as follows: The values of y_a and ε_{max} in equations 3.5.1.6 and 3.5.1.7 are substituted into equation 3.5.1.4. A number of feasible rod lengths are arbitrarily selected, for which the corresponding gains are calculated. A rod length, with its corresponding gain, is subsequently decided upon. The resulting gain is adjusted to allow for gain mechanism stiffness. Rod length is adjusted to allow for recessing of rod ends in the end caps. (Passive length required for coil spool thickness will be addressed in the detailed coil design in section 3.5.2).

Substitution of equations 3.5.1.6 and 3.5.1.7 into equation 3.5.1.4 gives:

$$Gl_T = 0{,}0794 \text{ m} \qquad \textbf{(3.5.1.8)}$$

A number of arbitrarily selected rod lengths and corresponding gain factors, which satisfy equation 3.5.1.8, are given in table 3.5.1.1.

Table 3.5.1.1: Gain factors for selected rod lengths

Rod length l_T (m)	Gain factor G (Dimensionless)
0,025	3,18
0,030	2,65
0,035	2,27
0,040	1,99
0,045	1,76

A rod length of 35 mm, or 0,035 m, was used in the simulations in sections 2.7 and 2.8. For this rod length, the corresponding gain factor, from table 3.5.1.1, is 2,27. This gain factor will however be insufficient, since the effect of gain mechanism stiffness is not taken into account. To accommodate the reduction in output displacement, the gain factor must be increased. The percentage increase will depend on the ratio of gain mechanism stiffness to rod stiffness. Gain mechanism stiffness is unknown at this stage. It is assumed that the ratio of gain mechanism stiffness to rod stiffness will be approximately 20%. Consequently, the gain factor as given in table 3.5.1.1 is increased by approximately 20%, i.e. from 2,27 to 2,7. Therefore, the gain G is 2,7:

$$G = 2{,}7 \qquad \textbf{(3.5.1.9)}$$

Rod elongation x_r, from equation 3.5.1.1, for a gain factor of 2,7 and an actuator output displacement of 75.10^{-6} m, is:

$$x_r = 27{,}8.10^{-6} \text{ m} \qquad \textbf{(3.5.1.10)}$$

Passive rod length can be limited to 0,75 mm per rod end. The total length of the two rods, recessing included, is therefore 38 mm:

$$l_T = 38 \text{ mm} \tag{3.5.1.11}$$

The length l_r per rod, for two rods, is 19 mm:

$$l_r = 19 \text{ mm} \tag{3.5.1.12}$$

Selection of rod diameter and calculation of rod cross-sectional area

The relationship between actuator output force F_a, rod cross-sectional area A_T, rod strain ε and Youngs modulus E, is given by:

$$F_a = \frac{A_T E \varepsilon}{G} \tag{3.5.1.13}$$

from which A_T is obtained as:

$$A_T = \frac{G F_a}{E \varepsilon} \tag{3.5.1.14}$$

Young' modulus of Terfenol-D can vary from 16 GPa to 56 GPa (see figure 2.2.1.4). The average value of E, from table 2.7.3.2, is 23,46 GPa. It can be seen from equation 3.5.1.14 that the lowest E-value will give the highest cross-sectional area for the same strain, force and gain factor. In the interest of design safety, the lowest E-value, i.e. 16 GPa, is used to calculate A_T. For a gain factor of 2,7 (from equation 3.5.1.9), actuator force of 10,35 N (from table 3.3.2), Young's modulus of 16 GPa and strain of 944 $\mu\varepsilon$ (from equation 3.5.1.6), the rod cross-sectional area is:

$$A_T = 1{,}85.10^{-6} \text{ m}^2 \tag{3.5.1.15}$$

Rod cross-sectional area, in terms of rod diameter, is given by:

$$A_T = \frac{\pi}{4} d_T^2 \tag{3.5.1.16}$$

From equation 3.5.1.16, rod diameter is obtained as follows in terms of cross-sectional area:

$$d_T = \sqrt{\frac{4A_T}{\pi}} \tag{3.5.1.17}$$

The rod diameter d_T, which will give the required cross-sectional area in equation 3.5.1.15, is:

$$d_T = 1{,}53 \text{ mm} \tag{3.5.1.18}$$

The rod diameter in equation 3.5.1.18 is the minimum diameter that will give the required actuator output force. However, rods with this diameter are not produced by the manufacturer, Etrema. The smallest rod diameter produced, is 5 mm. During the time of actuator manufacture, the only available rod diameter was 6 mm. Therefore, the diameter of the Terfenol-D rods used in the actuators, is 6 mm:

$$d_T = 6 \text{ mm} \tag{3.5.1.19}$$

The cross-sectional area of the 6 mm rods, from equation 3.5.1.16, is:

$$A_T = 2{,}827.10^{-5} \text{ m}^2 \tag{3.5.1.20}$$

Actuator output force, for the above rod cross-sectional area, a strain of 944 $\mu\varepsilon$, Young's modulus of 16 GPa and gain of 2,7, from equation 3.5.1.13, is:

$$F_a = 158{,}2 \text{ N} \tag{3.5.1.21}$$

It can be seen that the actuator force is approximately 15 times higher than required (see equation 3.3.7). This is due to the fact that the rod diameter is approximately 4 times the required diameter.

Calculation of gain mechanism deflection, stiffness, stress and geometry

A concept of an octagonal gain mechanism was shown in figure 3.4.1.5. The gain mechanism geometry, deflection, stiffness and stresses are calculated in this section. To facilitate the calculation procedure, a mechanical model of the gain mechanism is used. The calculations are done in two stages. A 1st order calculation of the slanted beam angle is done, using a simple beam and hinge model. The assumptions made in the calculation are given. Shortcomings of the method are mentioned and the use of a more accurate and sophisticated finite element (FE) method is motivated. Calculation of the slanted beam angle is repeated using the FE method. The 1st order calculation of the slanted beam angle is used as an aid to determine gain mechanism geometry. Stresses and gain mechanism stiffness are calculated.

In order to do a first order calculation of the slanted beam angle, a simplified quarter model of the gain mechanism is used. The model consists of three beams, i.e. a horizontal beam, slanted beam and vertical beam, connected with hinges. The assumption is made that the beams are rigid and the hinges are frictionless.

The quarter model is shown in figure 3.5.1.1. The slanted beam length is r and its initial horizontal slope angle, before deflection, is θ_0. The force in the rod if F_r, the rod length is l and its elongation is x_r. The actuator output deflection is y_a.

The gain factor G is the ratio between y_a and x_r:

$$G = \frac{y_a}{x_r} \tag{3.5.1.22}$$

The relationship between the initial slanted beam angle and displacement gain factor is given by the following equation (see also equation 3.4.1.19):

$$G = \cot\theta_0 \tag{3.5.1.23}$$

For a given value of G, θ_0 can be obtained from equation 3.5.1.23 as:

$$\theta_0 = \cot^{-1}(G) \tag{3.5.1.24}$$

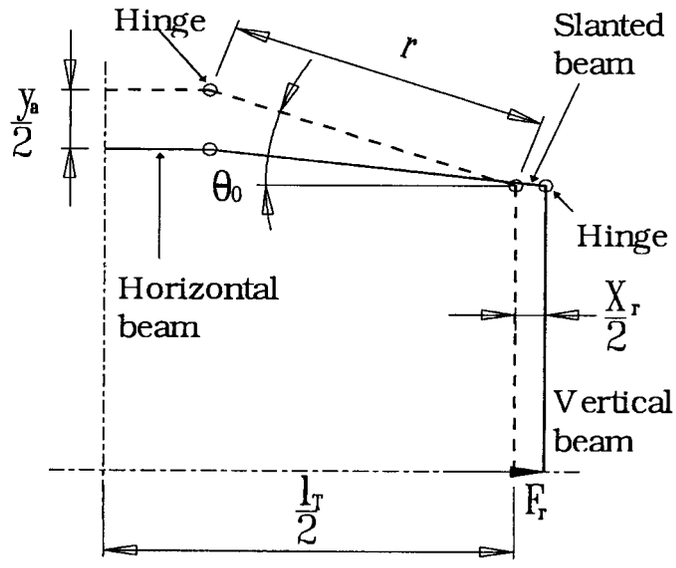

Figure 3.5.1.1: Octagonal gain mechanism beam and hinge quarter model

For a given gain factor of 2,7, the required slanted beam angle, from equation 3.5.1.24, is:

$$\theta_0 = 20{,}3° \tag{3.5.1.25}$$

The assumptions for which equation 3.5.1.25 is valid, are not realistic, since it is practically impossible to obtain zero flexure thickness and infinite beam thickness between flexures. A practically implementable gain mechanism will have beams and flexures with finite thickness, the flexures being considerably thinner than the beams. Consequently, the mechanism will bend in the flexures and slightly in the beams.

The bending profile is mathematically complicated to evaluate, since it will not only depend on mechanism geometry, but also on mechanism forces and displacements. The prestress spring force and rod elongation will cause stresses in the mechanism. These stresses will be higher in the flexures than in the beams. Furthermore, stress concentrations will be present at connecting points between flexures and beams. The 1st order method used above cannot be used to calculate stresses. A more powerful method, which takes the effects of geometry, forces and stress concentrations into account, is required. The finite element method (FEM) is used for this purpose. FEM calculation of the gain mechanism parameters is discussed below.

FEM calculation of gain, gain mechanism deflection profile, stiffness and stresses

The displacement gain factor, gain mechanism deflection profile, stiffness and maximum stress are calculated in this section, using the FE method. The method is applied iteratively to calculate the above parameters. In order to limit computational complexity, the analysis is carried out on a quarter model of the mechanism.

The method is applied as follows. An initial gain mechanism geometry is generated using the slanted beam angle obtained in equation 3.5.1.25. An element grid is generated. Mechanism boundary values are specified and material properties are given. Prestress spring and rod forces are applied and the deflection profile is calculated. The gain factor, which is the ratio between output displacement and rod end displacement, is calculated. Gain stiffness, which is the ratio between rod force and rod end displacement, is calculated. Maximum stress is calculated.

Calculated values of gain factor, mechanism stiffness and stresses are analyzed. If the stiffness is too high, flexure length is increased. If the gain factor is too low, the slanted beam angle is decreased. If stresses are too high, either flexure width or notch radius is increased. The procedure is repeated until the calculated parameters correspond with the required parameters.

Final gain mechanism geometry is shown in figure 3.5.1.2. The length of the slanted beam is 24,66 mm and its horizontal slope angle is 17°. The lengths and widths of the flexures are 2 mm and 1 mm respectively. The notch radii are 2 mm each. The thickness of the mechanism is 20 mm (not shown). Horizontal beam length is 14 mm and its width is 5mm. Vertical beam length and width are 46,87 mm and 7,5 mm respectively.

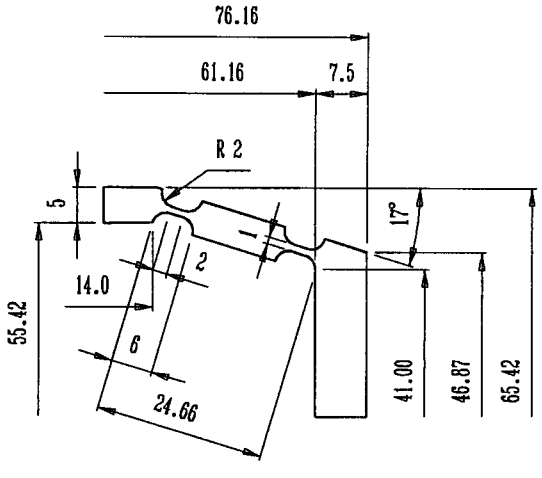

Figure 3.5.1.2: Gain mechanism quarter model geometry

The element grid is shown in figure 3.5.1.3. The number of elements, per quarter of the gain mechanism, is 624. Two-dimensional quadrangular elements are used. Mechanism boundary values are as shown in figure 3.5.1.3. Material is mild steel, with a Young's modulus of 210 GPa and a Poissons ratio of 0,29.

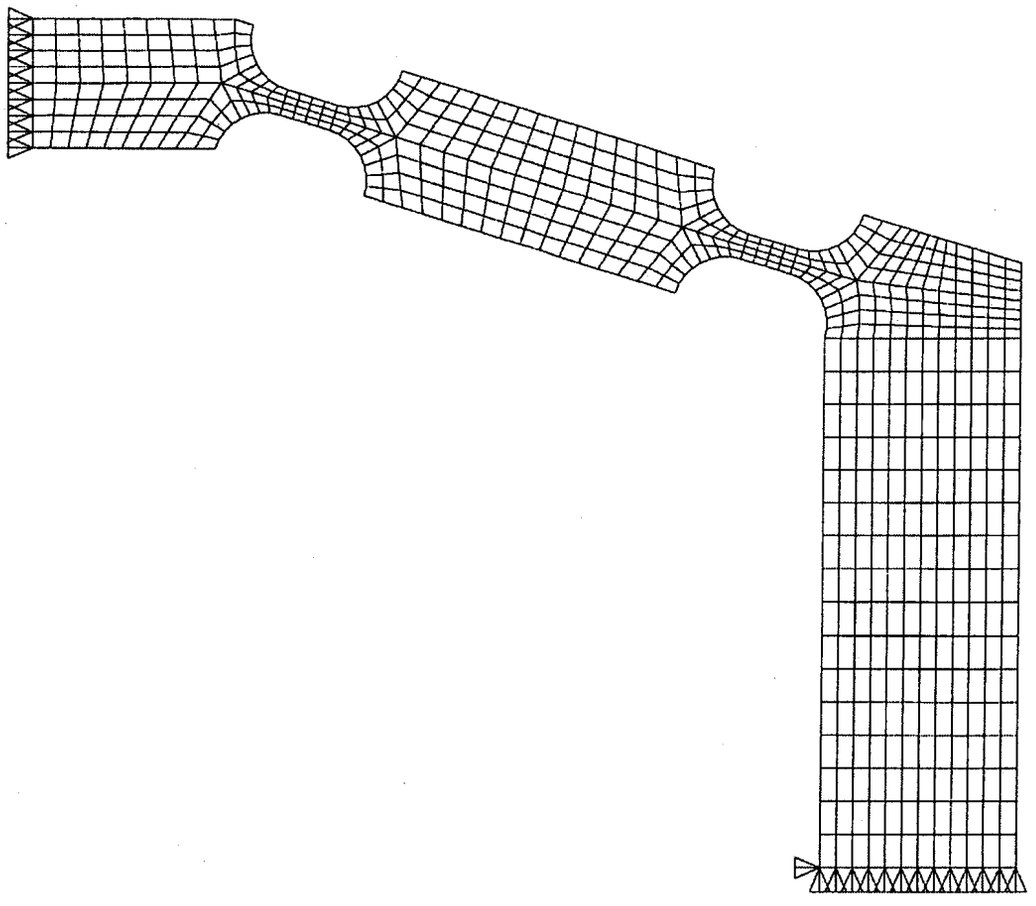

Figure 3.5.1.3: Gain mechanism quarter model finite element grid

The input forces and displacements applied to the gain mechanism are the prestress spring force and rod elongation. Spring force F is given by:

$$F = \frac{\sigma_b A_T}{G} \qquad \textbf{(3.5.1.26)}$$

where σ_b is the prestress, A_T is the rod cross-sectional area and G is the gain. For a gain of 2,7, rod cross-sectional area of $2{,}827.10^{-5}m^2$ and compressive prestress of 12 MPa, F is 125,66 N. The force acting on the quarter model is half the spring force:

$$\frac{F}{2} = 62{,}83 \text{ N} \qquad \textbf{(3.5.1.27)}$$

Rod elongation x_r, from equation 3.5.1.10 is $27{,}8.10^{-6}$ m. For the quarter model, the maximum horizontal displacement is half the rod elongation:

$$\frac{x_r}{2} = 13{,}9.10^{-6} \text{ m} \qquad \textbf{(3.5.1.28)}$$

A linear analysis is carried out to obtain the deflection shape, gain factor, maximum stress and gain stiffness. Gain mechanism stiffness is calculated as a percentage of rod stiffness. Both prestress spring force and rod elongation inputs are applied to calculate maximum stress, while only rod elongation is applied to calculate gain factor.

The deflection profile of the quarter model is shown in figure 3.5.1.4. The calculated parameters are given in table 3.5.1.2. For the sake of completeness, all the actuator parameters determined in section 3.5.1, are included.

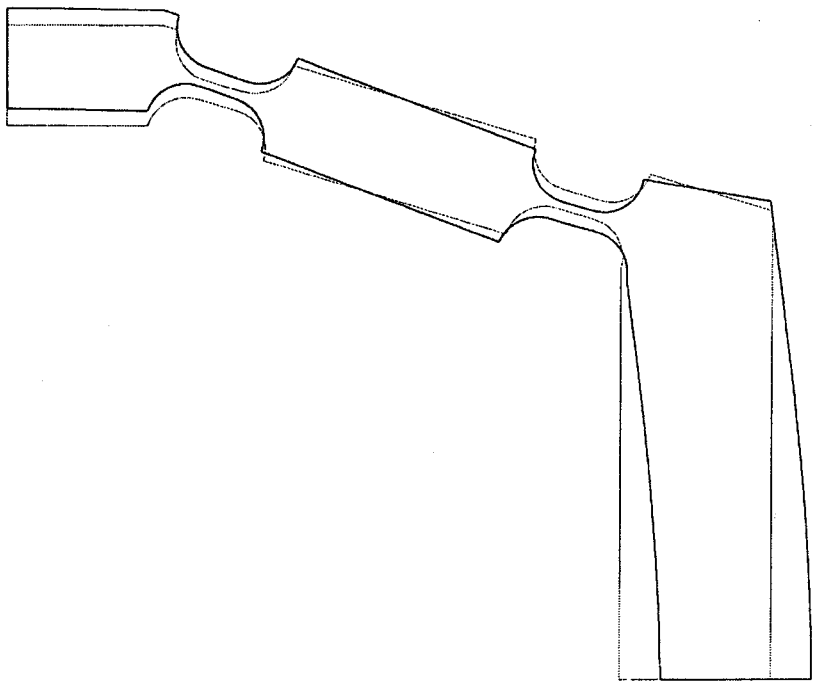

Figure 3.5.1.4: Gain mechanism deflection profile

Table 3.5.1.2: Terfenol-D actuator parameters

Parameter	Value
Terfenol-D rod length (total)	38 mm
Rod length (per rod)	19 mm
Rod diameter	6 mm
Rod cross-sectional area	$2{,}827.10^{-5}$ m^2
Rod elongation (total)	27,8 μm
Rod stiffness	$17{,}46.10^{6}$ N/m
Actuator stroke length	75 μm
Actuator gain factor	2,7
Actuator output force	158,2 N
Mechanism slanted beam angle	17°
Mechanism maximum stress	80,95 MPa
Mechanism stiffness	$3{,}28.10^{6}$ N/m
Ratio of mechanism stiffness to rod stiffness	18,8%

This concludes the gain mechanism design. Field coil design is covered in section 3.5.2.

3.5.2 Detailed design of field coils

The design of the field coils is described in detail in this section. Design input parameters are given, followed by all the required mathematical relationships. Practical design aspects are discussed. Coil parameters are calculated and tabled. Coil current, voltage and power versus frequency are shown graphically.

The given coil parameters are the Terfenol-D rod diameter, length and strain, actuator output force and stroke length, E, d^{σ}, d^{H} and μ^{σ} of Terfenol-D, coil bandwidth and maximum available input voltage. The input parameters, from sections 2.7, 2.8, 3.3 and 3.5.1 are summarized in table 3.5.2.1.

A parameter which is of particular importance in coil design, is μ^{σ}, since it, inter alia, determines the R_c/L_0 ratio. The higher μ^{σ}, the lower R_c/L_0. The value of μ^{σ} obtained from the simulations is 4,71 μTm/A (see section 2.8.5). This value of μ^{σ} includes the effects of hysteresis. This value is however considerably lower than the value of 11,6 μTm/A given by Butler [1988]. It is unknown whether the latter value includes hysteresis effects, but it is a safer value to use for design purposes, since it will give a lower R_c/L_0 ratio. In the interest of coil design safety, a μ^{σ} value of 11,6 μTm/A will be used.

Table 3.5.2.1: Coil design input parameters

Parameter	Value
Rod diameter	6 mm
Rod length (total)	38 mm
Actuator output force	158,2 N
Actuator stroke length	75 μm
Rod strain	944 $\mu\varepsilon$
Coil bandwidth	≥ 100 Hz
E of Terfenol-D	23,46 GPa
d^{σ} of Terfenol-D	$1{,}09.10^{-8}$ m/A
d^{H} of Terfenol-D	$8{,}14.10^{-9}$ m/A
μ^{σ} of Terfenol-D	$1{,}16.10^{-5}$ Tm/A
Maximum available coil voltage	28 V

Mathematical relationships required for coil design

The number of coil turns per layer n_c depends on the active rod length l_a and coated wire thickness d_{wc}. The relationship between n_c, l_a and d_{wc} is:

$$l_a = n_c d_{wc} \tag{3.5.2.1}$$

The coated wire thickness is the thickness of the bare copper wire plus the thickness of the coating:

$$d_{wc} = d_w + 2t_c \tag{3.5.2.2}$$

where d_w is the thickness of the bare wire and t_c is the coating thickness.

The number of coil turns N is given by:

$$N = n_c n_l \tag{3.5.2.3}$$

where n_c is the number of turns per layer and n_l is the number of layers.

The coil wire length l_c is given by:

$$l_c = \pi N D_c \tag{3.5.2.4}$$

where D_c is the arithmetic mean of the coil inner and outer diameters d_i and d_o:

$$D_c = \frac{d_i + d_o}{2} \tag{3.5.2.5}$$

The difference between the inner and outer diameters, in terms of n_l and d_{wc}, is:

$$d_o - d_i = 2n_l d_{wc} \tag{3.5.2.6}$$

The coil packing factor *pf*, which is the ratio of the packed volume of the coil, to the available volume, is given by:

$$pf = \frac{\pi N d_{wc}^2}{2(d_o - d_i)l_a} \tag{3.5.2.7}$$

The wire cross-sectional area A_w is:

$$A_w = \frac{\pi}{4} d_w^2 \tag{3.5.2.8}$$

The coil resistance R_c is given by:

$$R_c = \frac{\rho_c l_c}{A_w} \tag{3.5.2.9}$$

where ρ_c is the wire material resistivity.

R_c can be written as follows in terms of ρ_c, N, D_c and A_w:

$$R_c = \pi \frac{\rho_c N D_c}{A_w} \tag{3.5.2.10}$$

The rod cross-sectional area A_T is:

$$A_T = \frac{\pi}{4} d_T^2 \tag{3.5.2.11}$$

where d_T is the rod diameter.

The free inductance L_f is:

$$L_f = \frac{\mu^\sigma A_T N^2}{l_a} \tag{3.5.2.12}$$

where μ^σ is the free permeability of Terfenol-D.

The clamped inductance L_0 is:

$$L_0 = L_f\left[1-(cf)^2\right] \tag{3.5.2.13}$$

where cf is the coupling factor given by:

$$cf = \sqrt{\frac{Ed^{\sigma}d^{H}}{\mu^{\sigma}}} \tag{3.5.2.14}$$

L_0, in terms of the rod, coil and Terfenol-D magnetostrictive and magnetization parameters, is:

$$L_0 = \frac{\mu^{\sigma}A_T N^2}{l_a}\left(1-\frac{Ed^{\sigma}d^{H}}{\mu^{\sigma}}\right) \tag{3.5.2.15}$$

The −3dB bandwidth BW of the coil is given by:

$$BW = \frac{1}{2\pi}\frac{R_c}{L_0} \tag{3.5.2.16}$$

where R_c/L_0 is the coil resistance to inductance ratio.

The frequency-dependent coil impedance Z_c is:

$$Z_c = \sqrt{R_c^2 + \omega^2 L_0^2} \tag{3.5.2.17}$$

where ω is the angular frequency, given in terms of frequency f as:

$$\omega = 2\pi f \tag{3.5.2.18}$$

The coil phase angle φ between voltage and current is:

$$\varphi = \tan^{-1}\left(\frac{\omega L_0}{R_c}\right) \tag{3.5.2.19}$$

The field H, current I, voltage V and power P, for a biased harmonic field, are respectively given by:

$$H = H_b + H_A \sin \omega t \tag{3.5.2.20a}$$

$$I = \frac{l_a}{N}\left(H_b + H_A \sin \omega t\right) \tag{3.5.2.20b}$$

$$V = \frac{l_a}{N}\left[R_c H_b + Z_c H_A \sin\left(\omega t + \varphi\right)\right] \tag{3.5.2.20c}$$

$$P = \left(\frac{l_a}{N}\right)^2 \left[R_c H_b + Z_c H_A \sin\left(\omega t + \varphi\right)\right]\left[H_b + H_A \sin \omega t\right] \tag{3.5.2.20d}$$

The maximum field H_{max}, from equation 3.4.2.1, is:

$$H_{max} = H_b + H_A \tag{3.5.2.21}$$

The maximum current I_{max} is:

$$I_{max} = \frac{l_a}{N}\left(H_b + H_A\right) \tag{3.5.2.22}$$

The maximum input voltage V_{max} is:

$$V_{max} = \frac{l_a}{N}\left[R_c H_b + Z_c H_A \sin\left(\omega t_v + \varphi\right)\right] \tag{3.5.2.23}$$

where t_v is given by:

$$t_v = \frac{1}{\omega}\left[\left(2n+1\right)\frac{\pi}{2} - \varphi\right]; \quad n = 0, 2, 4, \ldots \tag{3.5.2.24}$$

The maximum power P_{max} is:

$$P_{max} = \left(\frac{l_a}{N}\right)^2 \left[R_c H_b + Z_c H_A \sin\left(\omega t_p + \varphi\right)\right]\left[H_b + H_A \sin \omega t_p\right] \tag{3.5.2.25}$$

where t_p is given by the roots of the following equation:

$$\frac{\cos \omega t_p}{Z_c \cos\left(\omega t_p + \varphi\right)} + \frac{H_b + H_A \sin \omega t_p}{R_c H_b + Z_c H_A \sin\left(\omega t_p + \varphi\right)} = 0 \tag{3.5.2.26}$$

Values of t_p which give minima of P are rejected.

The maximum rod strain ε_{max} is:

$$\varepsilon_{max} = \varepsilon(H_b) + d^H H_A \tag{3.5.2.27}$$

The minimum rod strain ε_{min} is:

$$\varepsilon_{min} = \varepsilon(H_b) - d^H H_A \tag{3.5.2.28}$$

The actuator static force F_a is:

$$F_a = \frac{A_T E}{G}(\varepsilon_{max} - \varepsilon_{min}) \tag{3.5.2.29}$$

The actuator static stroke length y_a is:

$$y_a = Gl_a(\varepsilon_{max} - \varepsilon_{min}) \tag{3.5.2.30}$$

Equations 3.5.2.1 to 3.5.2.30 give the most important equations required to calculate the coil parameters. Before the calculations can be done, a number practical coil aspects, which will have a significant influence on the design, are addressed. This is done in the next section.

Practical coil design aspects

Practical aspects to be considered in coil design, include factors such as passive rod length, space consumed by spools, packing methods and their influence on space utilization and magnetic saturation, the influence of coil impedance on amplifier output power, the influence of number of windings on coil frequency bandwidth, available wire diameters and insulation coating thickness. Each of these aspects, together with their respective influences on coil design, will be discussed in short below.

In order to allow ample space for coil spools and recessing of the rods in the end caps, the active rod length will be shorter than the total rod length. If 20% of the rod length is allowed for spools and recessing, 80% of the total rod length will be usable. From table 3.5.2.1, the total rod length is 38 mm. The usable, or active rod length, is therefore 30,4 mm.

The coil inner diameter must exceed the rod diameter, plus the spool thickness and free space between the spool and rod, to prevent sticking of the rod. The assumption is made that spool thickness and free space will take up no more than 40% of the rod diameter. The rod diameter, from table 3.5.2.1, is 6 mm. The coil inner diameter is therefore selected as 8,4 mm.

Coil packing methods include parallel and staggered packing. The two packing methods are shown diagrammatically in figures 3.5.2.1 and 3.5.2.2.

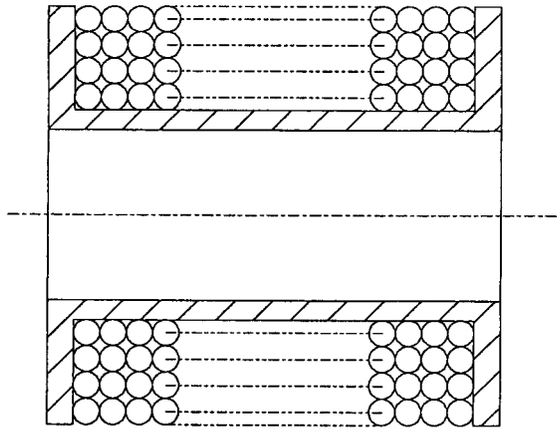

Figure 3.5.2.1: Parallel packing of a field coil

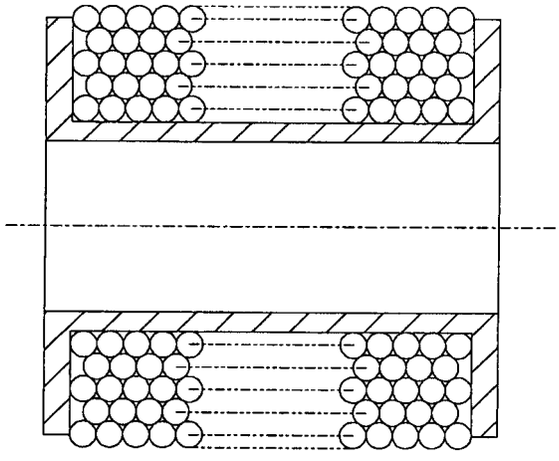

Figure 3.5.2.2: Staggered packing of a field coil

It can be seen from the above figures, that staggered packing gives better utilization of available coil space than parallel packing. However, a coil with staggered packing is more difficult to wind than a coil with parallel packing. During winding, a constant stress must be maintained in the wire, else the coil may deform as shown in figure 3.5.2.3. The consequence is that the centre of the Terfenol-D rod may be exposed to a larger field than the ends and may therefore magnetically saturate at relatively low coil currents. To avoid uneven fields, parallel packing will be used for the field coils in this study.

An important factor to be considered in coil design, is coil impedance. The coil impedance must be matched to that of the output circuit of an amplifier, which will be used to amplify the signal generator output voltage. If the impedance is too low, coil current and power will be excessive, resulting in clipping of the voltage signal and possible amplifier damage.

Amplifier output circuits are normally matched to electromagnetic field coils, such as audio loudspeaker coils, with impedances of 4Ω or 8Ω. For the same field and active rod length, an 8Ω coil will consume less power than a 4Ω coil. The impedance of the coils used in this study, will be 4Ω per actuator (at an excitation frequency of 100 Hz). The reason is that the field

biasing method that will be used in this study, is electromagnetic (see section 3.4.2). For electromagnetic biasing, both the bias and AC components of the field must be supplied by the power source. However, for future production models, field biasing will be done with permanent magnets, in which case only the AC component of the field will be required, thereby significantly reducing input power.

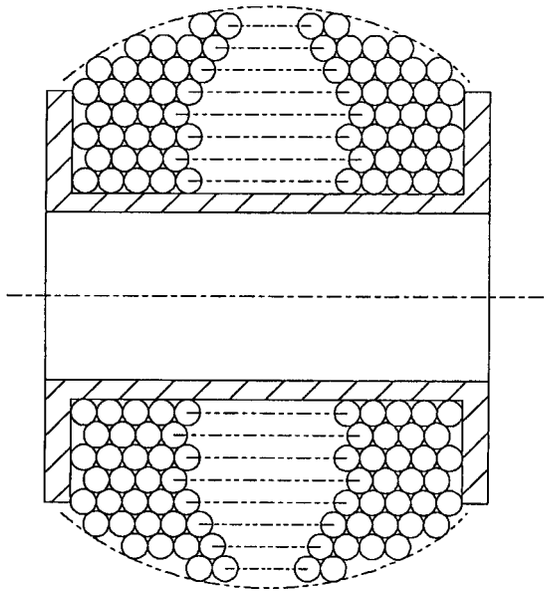

Figure 3.5.2.3: Possible coil deformation with staggered packing

Another important coil design parameter is the resistance to inductance ratio (R_c/L_0), which determines coil bandwidth (see equation 3.5.2.16). An R_c/L_0 ratio of at least 100 Hz is required to ensure that the coil produce sufficient field in the rod over the entire isolation bendwidth. As a safety precaution, the R_c/L_0 ratio is chosen 50% higher than the maximum frequency of the isolation band, i.e. 150 Hz. This is done to allow for possible variations in dynamic and material parameters, e.g. permeability, which is difficult to model, due to phenomena such as hysteresis (see section 2.3).

Impedance and resistance to inductance ratio are determined by the following factors (see equations 3.5.2.10, 3.5.2.15 and 3.5.2.17: ρ_c, N, D_c, A_w, l_a, μ^σ, E, d^σ and d^H. The active rod length l_a and the magnetostrictive and magnetization parameters μ^σ, E, d^σ and d^H have already been determined. Parameters which remain to be determined, are wire resistivity and cross-sectional area, number of windings and coil diameter.

Coil wire resistivity depends on the wire material. Copper, with a resistivity of $1{,}7.10^{-8}$ Ωm [Bartkowiak, 1973] and [Sears & Zemansky, 1975] is often used in electromagnetic field coils and will also be used in this study.

Wire cross-sectional area depends on the wire diameter. A vast number of wire diameters can be considered, three of which are 0,511 mm (for AWG 24), 0,644 mm (for AWG 22), and 0,4 mm (for "API 2"). The cross-sectional areas of the different wires are given in table 3.5.2.2. The wire with the smallest cross-sectional area, i.e. "API 2", is selected, since it will

give the highest R_c/L_0 ratio for the same length. The insulation coating thickness of "API 2" is 0,035 mm.

Table 3.5.2.2: Coil wire diameters and cross-sectional areas

Wire	Diameter (mm)	Cross-sectional area (mm^2)
"API 2"	0,4	0,126
AWG 24	0,511	0,205
AWG 22	0,644	0,326

For the selected wire diameter, the number of windings, which will give the required impedance and R_c/L_0 ratio, is calculated. From the number of windings, the coil PCD, inner and outer diameters can be determined. To systematize the design, a stepwise procedure, using equations 3.5.2.1 to 3.5.2.30, is given below.

Coil design procedure

A stepwise design procedure to calculate the required coil parameters, is as follows:

Step I: For the selected d_w, A_w is calculated, using equation 3.5.2.8.

Step II: For E, d^H, d^σ and μ^σ, as given in table 3.5.2.1, cf is calculated, using equation 3.5.2.14.

Step III: For a BW of 150 Hz and Z_c of 4 Ω at 100 Hz, equations 3.5.2.16 and 3.5.2.17 are simultaneously solved for R_c and L_0.

Step IV: With L_0 and cf, L_f is calculated, using equation 3.5.2.13.

Step V: With L_f, μ^σ and A_T, N is calculated, using equation 3.5.2.12.

Step VI: With R_c, ρ_c and A_w, l_c is calculated, using equation 3.5.2.9.

Step VII: With l_c and N, D_c is calculated using equation 3.5.2.4.

Step VIII: With l_a, d_w and t_c, n_c is calculated, using equations 3.5.2.1 and 3.5.2.2.

Step IX: With N and n_c, n_l is calculated, using equation 3.5.2.3.

Step X: With n_l, d_{wc} and D_c, equations 3.5.2.5 and 3.5.2.6 are simultaneously solved for d_i and d_o.

Step XI: With N, d_{wc}, d_i, d_o and l_a, pf is calculated, using equation 3.5.2.7.

Step XII: With H_b and H_A, I, V and P are calculated for a number of frequencies in the band ranging from 0 Hz to 333 Hz, using equations 3.5.2.22 to 3.5.2.26.

Step XIII: Actuator output force F_a is checked, using equation 3.5.2.29. F_a must be at least 158,2 N.

Step XIV: Actuator output displacement y_a is checked, using equation 3.5.2.30. y_a must be at least 75 μm.

Step XV: Coil input voltage V is checked: It must be smaller than the maximum available source voltage of 28 V.

Coil parameters

The coil parameters are calculated using the procedure set out in steps I to XV. The parameters are given in table 3.5.2.3. It can be seen from table 3.5.2.3 that the bias voltage of 8,8 V compares favourably with the bias voltage of 8,75 V used for the simulations (see table 2.7.3.1). The bias field of 56,13 kA/m is approximately 12% larger than the bias field used for the simulations. The actuator output force is 47% higher than required. This is due to the fact that the value of Young's modulus of Terfenol-D used for the coil design (23,46 GPa) is 47% higher than the value used for the gain mechanism design (16 GPa).

Table 3.5.2.3: Magnetostrictive actuator coil parameters

Parameter	Value
Inner diameter	8,4 mm
Outer diameter	16,2 mm
Pitch circle diameter (PCD)	12,3 mm
Number of spools per actuator	2
Coil length per spool (50% of rod active length)	15,2 mm
Total wire length	24,4 m
Wire diameter, excluding coating	0,4 mm
Wire coating thickness	0,035 mm
Wire material resistivity	$1{,}7.10^{-8}$ Ωm
Number of windings per layer, per spool	35
Number of layers per spool	9, plus 10 windings
Total number of windings	640
Packing factor	78,5%
Free inductance	4,27 mH
Clamped inductance	3,50 mH
Coupling factor	42%
Resistance to (clamped) inductance ratio	150 Hz
Resistance	3,3 Ω
Impedance at 100 Hz	4,0 Ω
Bias field	56,13 kA/m
Field amplitude (constant)	56,13 kA/m
Maximum field	112,3 kA/m
Bias current	2,67 A
Current amplitude	2,67 A
Maximum current	5,33 A
Bias voltage	8,8 V
Maximum static Terfenol-D rod strain	944 $\mu\varepsilon$
Actuator static force (p-p)	232 N
Actuator static stroke length	75 μm

Coil current, voltage and power versus frequency curves, are shown in figure 3.5.2.4. For comparison purposes, the curves for electromagnetic and permanent field biasing are shown on the same scale.

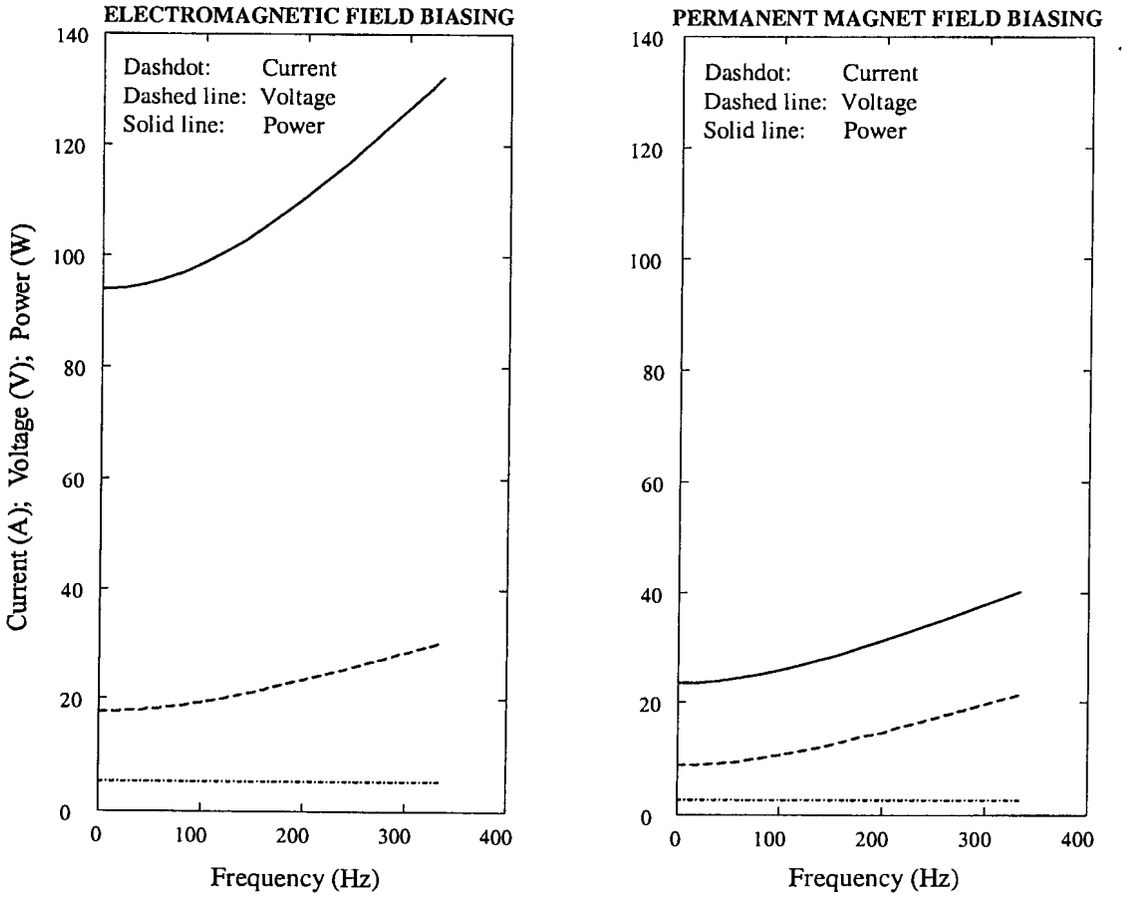

Figure 3.5.2.4: Coil current, voltage and power

Current, voltage and power at 0,01 Hz (quasi-static), 100 Hz (maximum frequency of disturbance band), 150 Hz (coil cutoff frequency) and 333 Hz (system cutoff frequency) are given in table 3.5.2.4.

From figure 3.5.2.4 and table 3.5.2.4, it can be seen that biasing method has a significant influence on current, voltage and power. Electromagnetic field biasing consumes significantly more power than permanent magnet biasing. However, irrespective of its high power consumption, electromagnetic biasing will be used in this study to avoid the high cost of permanent magnets.

Table 3.5.2.4: Current, voltage and power for two biasing methods

Frequency (Hz):		**0,01**	**100**	**150**	**333**
Comment:		Quasi-static	Disturbance BW	Coil BW	System BW
Electromagnetic biasing:	Current (A)	5,33	5,33	5,33	5,33
	Voltage (V)	17,6	19,4	21,2	30,2
	Power (W)	93,8	98,7	104,1	132,3
Permanent magnet biasing:	Current (A)	2,67	2,67	2,67	2,67
	Voltage (V)	8,8	10,6	12,4	21,4
	Power (W)	23,5	25,8	28,3	40,3

This concludes the detailed design of the field coils. A detailed design of the prestress springs follows in section 3.5.3.

3.5.3 Detailed design of prestress springs

A detailed design of the mechanical bias (prestress) springs is done in this section. Spring design input parameters, i.e. required Terfenol-D rod prestress, rod cross-sectional area, actuator gain factor, available space and wire material shear modulus are given. A stepwise design procedure, using the equations given in section 3.4.3, is presented. The spring parameters are calculated and tabled.

The spring design input parameters are given in table 3.5.3.1.

Table 3.5.3.1: Prestress spring design input parameters

Parameter	**Symbol**	**Value**
Terfenol-D rod compressive prestress	σ_b	12 MPa
Rod cross-sectional area	A_T	$2{,}83.10^{-5}$ m^2
Actuator gain factor	G	2,7
Available space (compressed length)	l_c	20,8 mm
Wire shear stress modulus (for steel)	G_s	79,3 GPa

A stepwise spring design procedure is as follows:

Step I: A spring diameter (D) and wire thickness (d) are arbitrarily selected. A number of available wire diameters, from 0,15 mm to 5,39 mm, are considered. For this spring, a diameter of 7,6 mm and wire thickness of 2,3 mm, are selected.

Step II: A nominal spring deflection x of 1,4 mm (approximately 20 times actuator output displacement) is selected. The maximum deflection x_{max} is selected as 3 times nominal deflection, i.e. 4,2 mm.

Step III: The spring end type, i.e. squared and ground (this end type simplifies spring attachment), is selected. From table 3.4.3.1, N_e for this end type is 2,0.

Step IV: With σ_b and A_T known, F_b is calculated, using equation 3.4.3.1.

Step V: With F_b and G known, F is calculated, using equation 3.4.3.4.

Step VI: With F and x known, k is calculated, using equation 3.4.3.8.

Step VII: With G_s, D, d and k known, N_a is calculated, using equation 3.4.3.9.

Step VIII: With N_a and N_e known, N_t is calculated, using equation 3.4.3.10.

Step IX: With d, N_t and x_{max} known, l_f is calculated, using equation 3.4.3.7.

Step X: With l_f and N_t known, p is calculated, using equation 3.4.3.13.

Step XI: With l_f and D known, l_f/D is calculated.

Step XII: With p, D and d known, $\Delta D/D$ is calculated, using equations 3.4.3.11 and 3.4.3.12.

Step XIII: With D and d known, C is calculated, using equation 3.4.3.18.

Step XIV: With C known, K_w is calculated, using equation 3.4.3.17.

Step XV: With D, d and F known, τ_c is calculated, using equation 3.4.3.19.

Spring parameters are calculated using the procedure as set out in steps I to XV above. The parameters are summarized in table 3.5.3.2.

Table 3.5.3.2: Actuator prestress spring design parameters

Number of springs per actuator	2
Type of spring	Coil spring
Spring force (per spring)	125,6 N
Spring stiffness (per spring)	90 kN/m
Spring nominal deflection	1,4 mm
Total number of coils per spring	9
Number of active coils per spring	7
Spring mean diameter (PCD)	7,6 mm
Wire diameter	2,3 mm
Spring index	3,3
Spring solid length	20,8 mm
Spring free length	25 mm
Spring pitch	2,76 mm
Spring maximum outer diameter	9,6 mm
Wahl shear stress correction factor	1,51
Wire shear stress	302 MPa
Spring free length to PCD ratio	3,3
Type of spring end	Squared and ground
End condition	Fixed
	Constrained from unwinding

This concludes the detailed design of the coil springs and of the actuator. Design of the support structure is described in the next section.

3.5.4 Support structure design

Support structure design is described in this section. Structure geometry is shown. The finite element method is used to calculate the deflection profile and maximum Von Mises stress. Material properties and the input displacement at an actuator attachment point are given. The finite element grid and deflection profile are shown. It is shown that the maximum Von Mises stress is relatively low.

The support structure geometry is shown in figure 3.5.4.1 and its finite element grid is shown in figure 3.5.4.2. A total number of 624 two-dimensional quadrangular elements are used. A fine grid, as shown in figure 3.5.4.3, is used for the flexures.

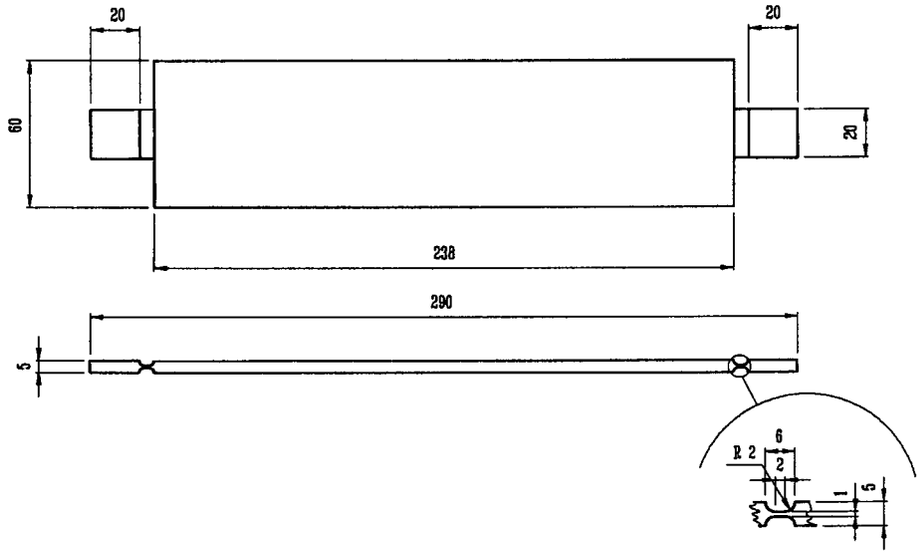

Figure 3.5.4.1: Support structure geometry

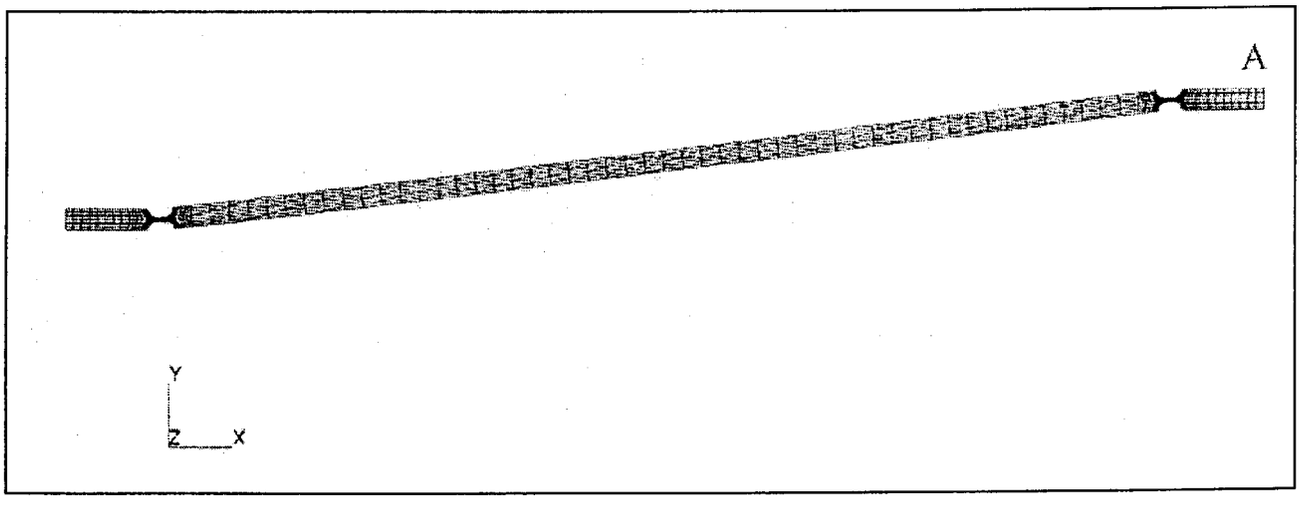

Figure 3.5.4.2: Support structure finite element grid

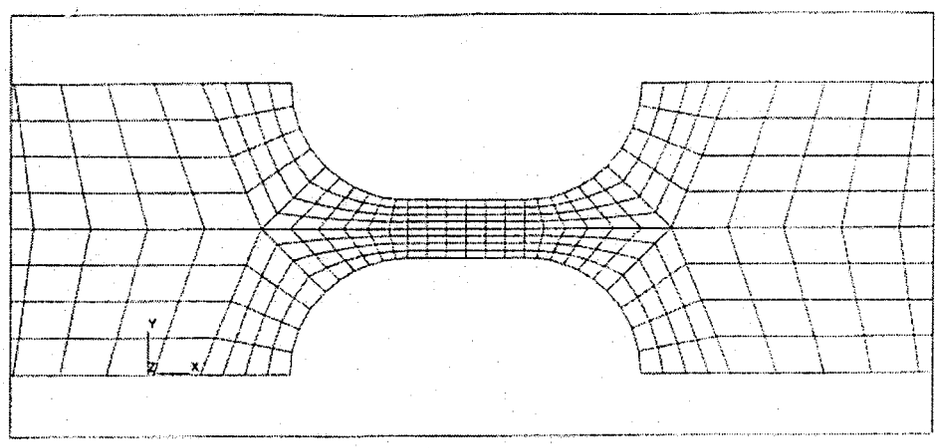

Figure 3.5.4.3: Flexure finite element grid

Support structure material is aluminium grade 7075, which has a Young's modulus of 71 GPa and Poissons ratio of 0,33. The maximum deflection of the structure, which is twice the displacement of a single actuator, i.e. 150 μm, occurs at the right hand actuator attachment point (point A in figure 3.5.4.2). The maximum calculated Von Mises stress, which occurs at the centre of the flexure, is 16,3 MPa. This stress is relatively low. The structure deflection profile is shown on the finite element grid in figure 3.5.4.2.

This concludes the design calculations, practical design aspects and design parameters of the most important system components. Detailed and assembly drawings are shown in the next section.

3.6 System assembly drawing and component detail drawings

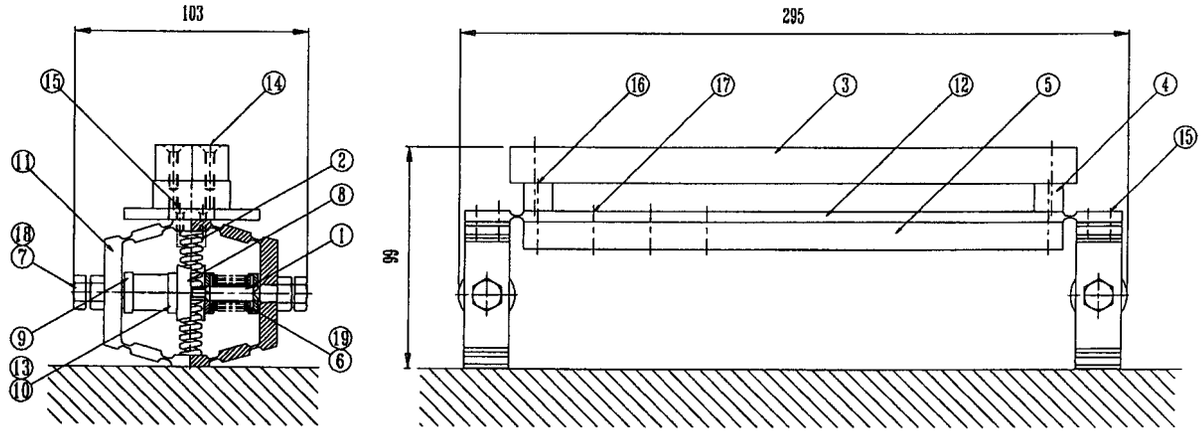

ITEM	QUANTITY	DESCRIPTION	MATERIAL
19	AR	SPOOL WIRE ϕ 0.4	COPPER
18	4	LOCK NUT	EN8
17	4	CSK HEAD SCREW M4 X 15	EN8
16	2	CSK HEAD SCREW M4 X 25	EN8
15	6	CSK HEAD SCREW M4 X 10	EN8
14	4	CSK HEAD SCREW M4 X 20	EN8
13	4	CSK HEAD SCREW M4 X 6	EN8
12	1	SUPPORT STRUCTURE	ALUMINIUM 7075
11	2	GAIN MECHANISM	EN8
10	4	ENDCAP 1	EN8
9	4	ENDCAP	EN8
8	2	CENTREPIECE	EN8
7	4	PRESTRESS BOLT	HIGH TENSILE STEEL
6	4	COIL SPOOL	TEFLON
5	1	STIFFENER	ALUMINIUM
4	2	SPACER	ALUMINIUM
3	1	DUMMY LOAD	EN8
2	4	COMPRESSION PRESTRESS SPRING	SPRING STEEL
1	4	ROD	TEKTRONIX-D

OPTICAL INSTRUMENT LOS STABILIZATION SYSTEM

Figure 3.6.1: System assembly drawing

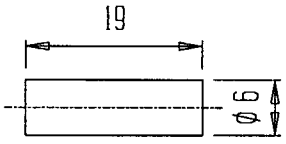

ITEM 1
ROD
MATL.: TERFENOL - D

Figure 3.6.2: Item 1: Terfenol-D rod

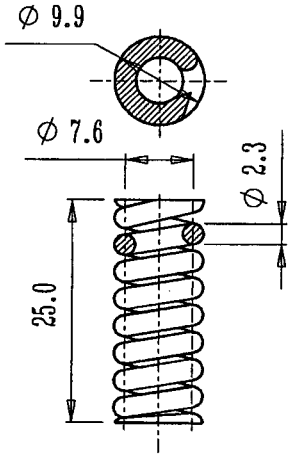

ITEM 2
PRESTRESS SPRING
MATL.: SPRING STEEL

Figure 3.6.3: Item 2: Prestress spring

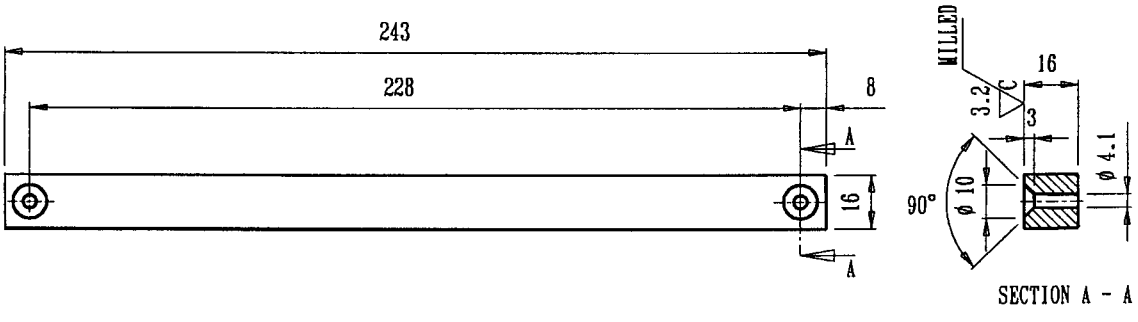

ITEM 3
DUMMY LOAD
MATL.: EN8

Figure 3.6.4: Item 3: Dummy load

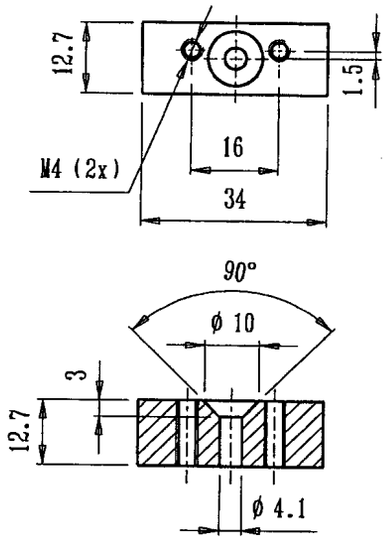

ITEM 4
SPACER
MATL.: ALUMINIUM

Figure 3.6.5: Item 4: Spacer

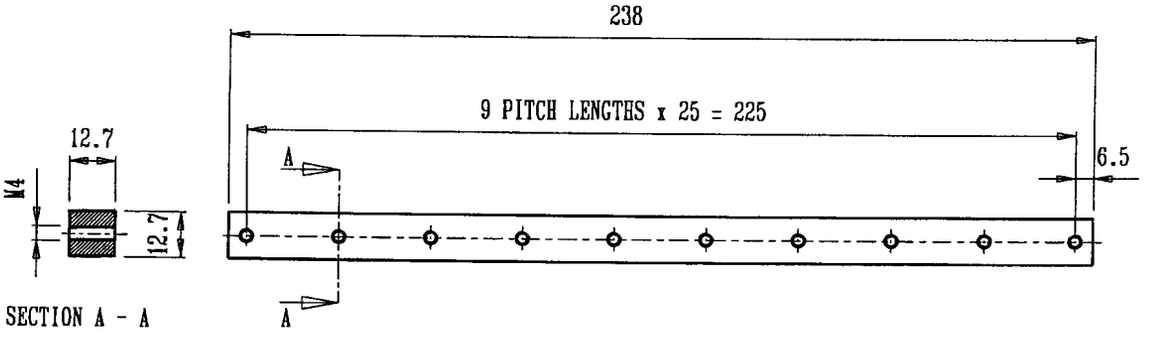

ITEM 5
STIFFENER
MATL.: ALUMINIUM

Figure 3.6.6: Item 5: Stiffener

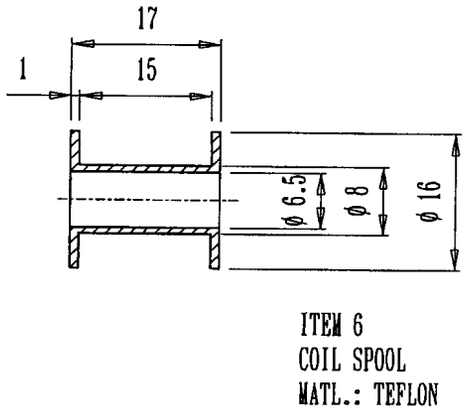

Figure 3.6.7: Item 6: Coil spool

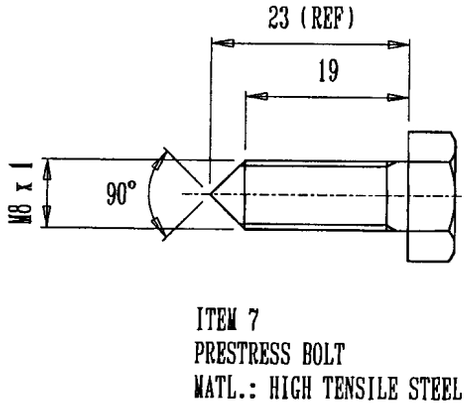

Figure 3.6.8: Item 7: Prestress bolt

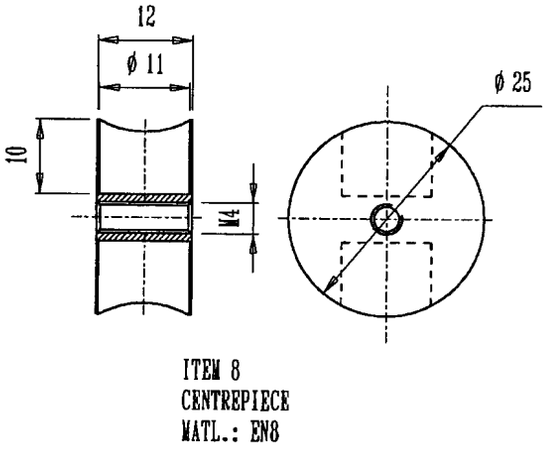

Figure 3.6.9: Item 8: Centrepiece

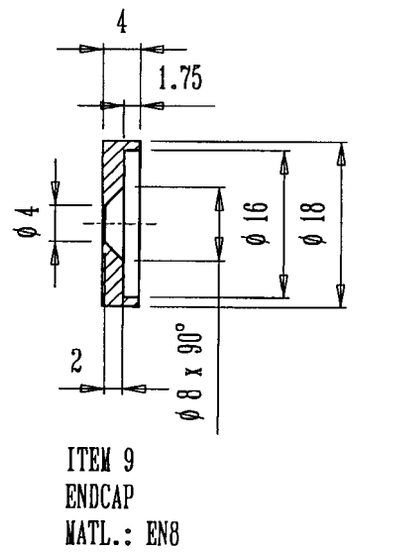

Figure 3.6.10: Item 9: Endcap

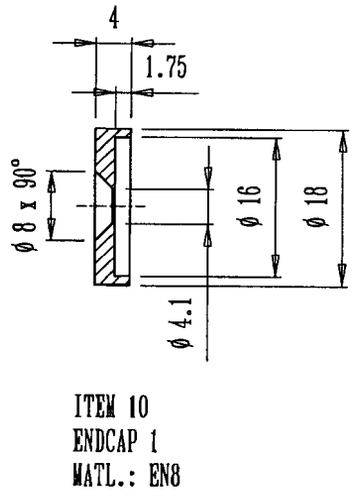

Figure 3.6.11: Item 10: Endcap 1

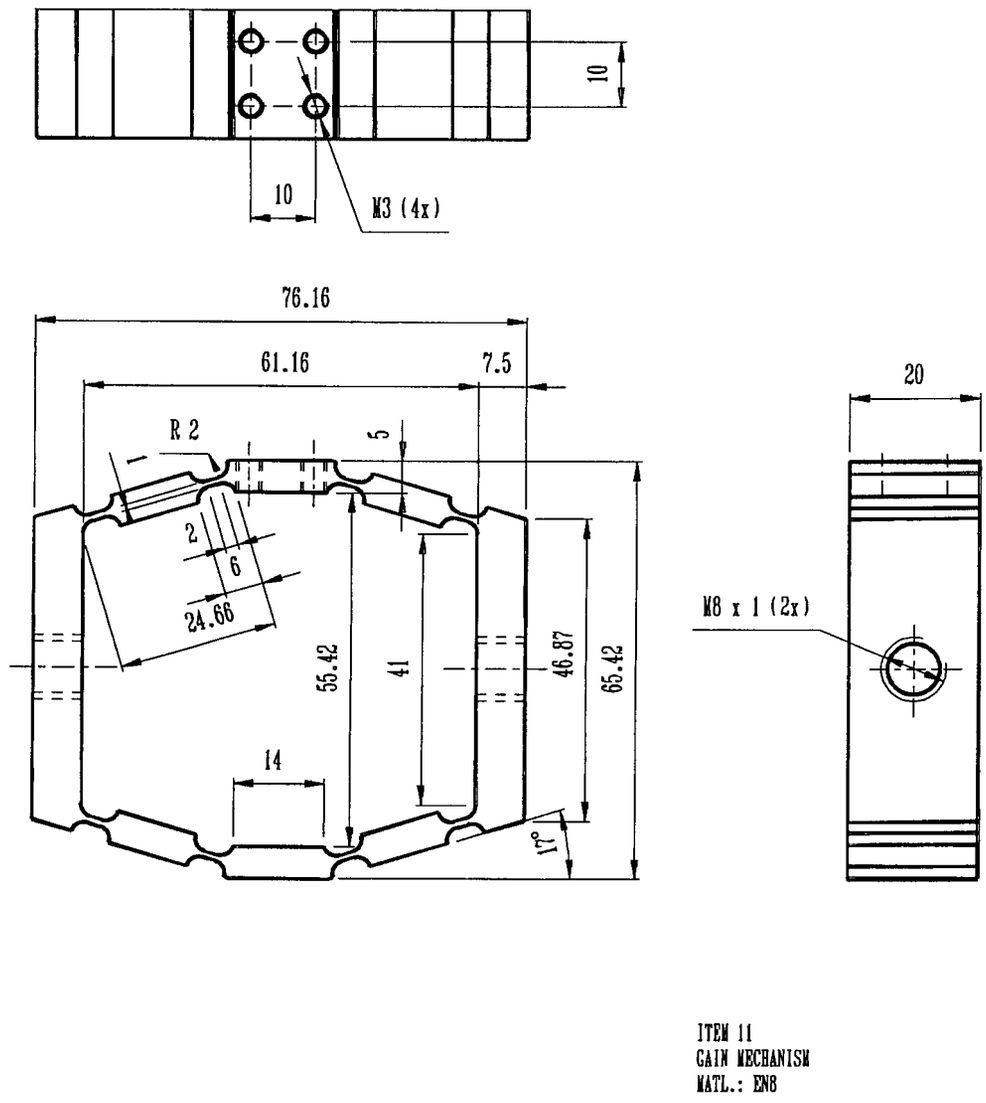

Figure 3.6.12: Item 11: Gain mechanism

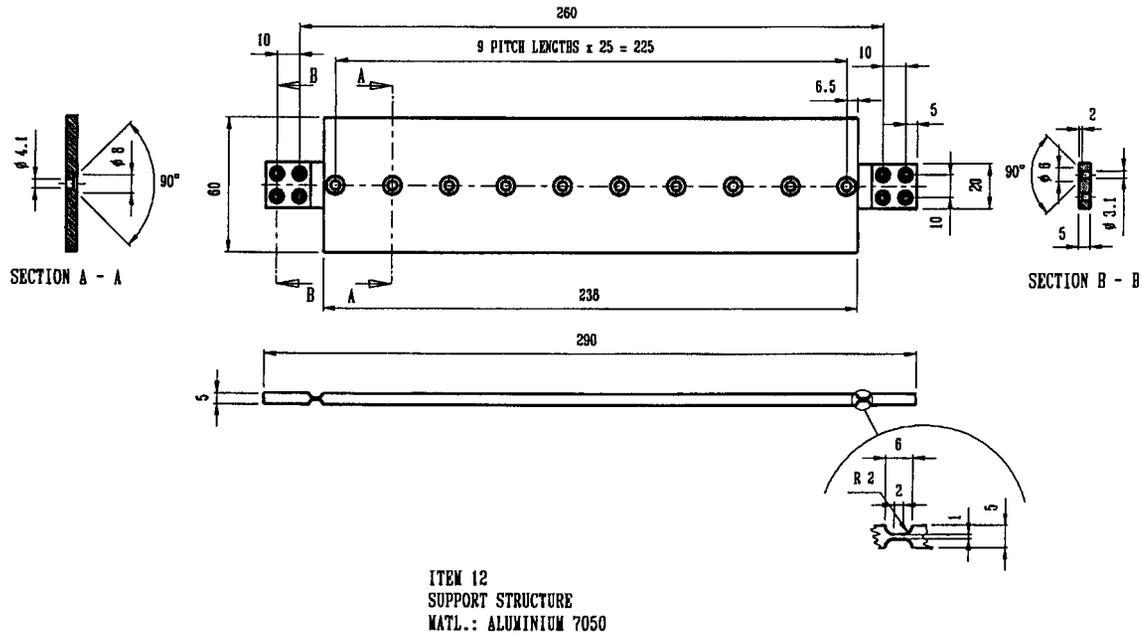

Figure 3.6.13: Item 12: Support structure

3.7 Design safety checks

A number of design safety checks are described in this section. The checks are required to ensure that the actuator and system design is safe. The checks comprise investigations into static and dynamic buckling of the Terfenol-D rods. Buckling criteria are defined. The static buckling load on the rods is calculated and compared with the crtical compressive load. The natural frequency of the rods is calculated and compared with the maximum frequency of the disturbance band. Static buckling is investigated in section 3.7.1, while dynamic buckling is investigated in section 3.7.2.

3.7.1 Static buckling of the Terfenol-D rods

It was mentioned in section 2.2 that the saturation strain of Terfenol-D can be greatly enhanced by subjecting the material to a compressive prestress. The prestress is also known as the bias stress. Generally, the larger the prestress, the larger the saturation strain. The practical implication of applying a prestress is that the desired elongation of a Terfenol-D rod with a given length can be obtained with smaller magnetic field amplitudes, thereby reducing the energy input into the coil.

The disadvantage, however, is that excessively large prestresses can cause the rods to buckle. The designer of a Terfenol-D actuator must therefore ensure that the prestress is sufficient to produce the desired saturation strain, but at the same time, the stress must be brought about by a compressive load which will not exceed the critical buckling load of the rod.

The static compressive and buckling loads of the rods are calculated in this section. A conservative approach is followed in the calculation of the loads. The factors which influence the buckling load

are discussed. It will be shown that the compressive load is well below the critical buckling load and that the actuator design is safe as far as static buckling of the rods is concerned.

Consider a Terfenol-D rod which is subjected to a static compressive load, as shown in figure 3.7.1.1. The compressive load is F_b. The cross-sectional area of the rod is given by A_T. The load is distributed over the entire cross-sectional area of the rod by means of two end caps, one at each end of the rod.

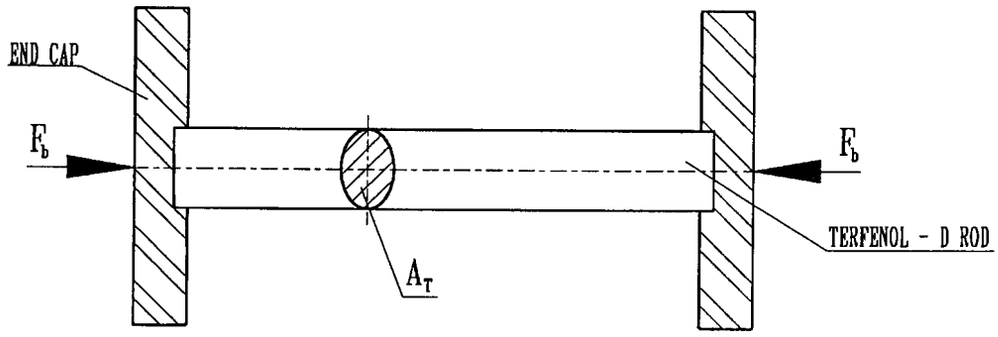

Figure 3.7.1.1 Compressive load acting on a Terfenol-D rod

The maximum compressive load acting on the rod is the product of the maximum stress in the rod and the cross-sectional area of the rod:

$$F_b = \sigma_{max} A_T \qquad \textbf{(3.7.1.1)}$$

where σ_{max} the maximum stress. The maximum stress is the sum of the compressive prestress and the stress amplitude:

$$\sigma_{max} = \sigma_b + \sigma_A \qquad \textbf{(3.7.1.2)}$$

where σ_b is the compressive prestress and σ_A is the stress amplitude. The stress amplitude is limited by the prestress: Since the tensile strength of Terfenol-D is relatively low in comparison with its compressive stress [Butler, 1988], it is essential to maintain a compressive stress in the rod under all circumstances. Therefore, the maximum allowable stress amplitude is equal to the prestress:

$$\sigma_A = \sigma_b \qquad \textbf{(3.7.1.3)}$$

Substitution of equation 3.7.1.3 into equation 3.7.1.2 gives:

$$\sigma_{max} = 2\sigma_b \qquad \textbf{(3.7.1.4)}$$

Finally, the compressive load on the rod is obtained in terms of the prestress by substitution of equation 3.7.1.4 into equation 3.7.1.1:

$$F_b = 2\sigma_b A_T \qquad \textbf{(3.7.1.5)}$$

The critical load F_{cr} is given as follows by Shigley [1977]:

$$F_{cr} = A_T \frac{n\pi^2 E}{(l_T/r_G)^2} \tag{3.7.1.6}$$

where n is the end condition constant of the rod, E is Young's modulus of Terfenol-D and r_G is the radius of gyration of the rod cross-section. Equation 3.7.1.6 is also known as the Euler equation, or the Euler column formula [Shigley, 1977].

For a rod with a round cross-section, as is used in this study, the radius of gyration is:

$$r_G = \frac{d_T}{4} \tag{3.7.1.7}$$

where d_T is the rod diameter. Substitution of equation 3.7.1.7 into equation 3.7.1.6 gives the critical load as follows in terms of the rod diameter:

$$F_{cr} = A_T \frac{n\pi^2 E}{(4l_T/d_T)^2} \tag{3.7.1.8}$$

The rod end condition constant n depends on the attachment method of the rods. Possible end conditions which can be considered for this analysis include fixed-free, rounded-rounded, fixed-rounded and fixed-fixed conditions. Theoretical values of n vary from 0,25 for fixed-free columns to 4 for fixed-fixed columns. However, practice has shown that, in the cases of fixed-rounded and fixed-fixed columns, it is difficult, if not impossible, to fix the column ends in such a way that the theoretical values apply. Instead, a more realistic practical value of 1,2 is recommended for both these cases. For the sake of completeness, the theoretical and recommended values of n for the abovementioned four rod end conditions, from Shigley [1977], are given in table 3.7.1.1.

Table 3.7.1.1: Theoretical and recommended n-values for different rod end conditions [Shigley, 1977]

End condition	Theoretical value of n	Recommended value of n
Fixed-free	0,25	0,25
Rounded-rounded	1,00	1,00
Fixed-rounded	2,00	1,20
Fixed-fixed	4,00	1,20

The applicable end condition for the Terfenol-D rod is a debatable point. If it is assumed that the rod is fully supported by the actuator structure, the buckling analysis can be based on fixed-fixed ends, in which case the recommended end condition constant will be 1,2. If, however, cognisance is taken of the fact that during compression, the rod may not be perfectly straight and the load surfaces at the ends of the rod may not be parallel, the assumption can be made that a fixed-free end condition applies, for which n is 0,25. The latter end condition will yield a lower critical load, resulting in a more conservative design. For the purpose of this analysis, an end condition constant of 0,25 will be used.

The compressive load on the rod and the critical buckling load are subsequently calculated and compared. Numerical values for the rod length, diameter and cross-sectional area, the prestress, Young's modulus and end condition constant are obtained from previous sections and substituted into the applicable equations. From section 3.5, the total rod length is 0,038 m, the rod diameter is 0,006 m and the rod cross-sectional area is $2{,}827.10^{-5}$ m^2:

$$l_T = 0{,}038 \text{ m} \quad \textbf{(3.7.1.9a)}$$

$$d_T = 0{,}006 \text{ m} \quad \textbf{(3.7.1.9b)}$$

$$A_T = 2{,}827.10^{5} \text{ m}^2 \quad \textbf{(3.7.1.9c)}$$

The prestress, from section 2.7, is 12.10^6 Pa:

$$\sigma_b = 12.10^6 \text{ Pa} \quad \textbf{(3.7.1.10)}$$

Young's modulus can vary from approximately 16 GPa to 56 GPa (see section 2.2, figure 2.2.1.4). Taking a conservative approach, the lowest value of 16 GPa is used:

$$E = 16.10^9 \text{ Pa} \quad \textbf{(3.7.1.11)}$$

The end condition constant, from the above discussion, is 0,25:

$$n = 0{,}25 \quad \textbf{(3.7.1.12)}$$

By subsitution of equations 3.7.1.9c and 3.7.1.10 into equation 3.7.1.5, the maximum compressive load is:

$$F_b = 339{,}3 \text{ N} \quad \textbf{(3.7.1.13)}$$

By substitution of equations 3.7.1.9a to 3.7.1.9c, 3.7.1.11 and 3.7.1.12 into equation 3.7.1.8, the critical buckling load of the rod is:

$$F_{cr} = 1739 \text{ N} \quad \textbf{(3.7.1.14)}$$

By comparison of equations 3.7.1.13 and 3.7.1.14, the maximum compressive load on the rod is considerably lower than the critical buckling load. The conclusion can therefore be drawn that the actuator design is safe as far as static buckling of the rods is concerned.

This concludes the static buckling analysis of the Terfenol-D rods. A dynamic buckling analysis is carried out in the next section.

3.7.2 Dynamic buckling of the Terfenol-D rods

The possibility of dynamic buckling of the Terfenol-D rods is investigated in this section. A buckling criterion is defined. The rods are modelled as transversely vibrating beams with distributed mass and stiffness. The centerpiece, end caps and coils are modelled as a concentrated mass, attached at the centre of the beam. The concentrated mass is included in the beam mass by means of an equivalent density of the rod material. Two beam end conditions, i.e. clamped-clamped and simply supported, are considered. In order to ensure a conservative design, buckling is investigated for the end condition which gives the lowest fundamental natural frequency.

The effect of compressive prestress on the natural frequency of the rods is added. The fundamental natural frequency is calculated and compared with the maximum frequency of the disturbance band. It is shown that the fundamental natural frequency is significantly higher than the maximum disturbance frequency.

Static buckling of the rods was investigated in the previous section. It was shown that buckling would occur if the applied static load exceeded the critical buckling load. The dynamic buckling analysis of the rods differs from the static buckling analysis in the sense that, during dynamic excitation, the rods can buckle due to transverse resonance, as well as the axial compressive forces acting on the rods. Resonance will normally occur at the transverse natural frequencies of the rods. The fundamental natural frequency is of particular importance in the investigation.

The natural frequency depends on the distributed stiffness and inertia of the rods, concentrated mass of the coils, compressive prestress in the rods and rigidity of the joints between the rods and end caps. For the purpose of the dynamic buckling analysis, it is necessary to model the rods, coils and centrepiece with equivalent mechanical elements. The rods are modelled as a transversely vibrating beam and the coils and centrepiece are modelled as a concentrated mass attached at the beam centre. Two rod end models are considered, i.e. simply supported ends and clamped-clamped ends. Prestress is modelled by means of an axial load acting at the beam ends.

In order to design conservatively, the end condition which gives the lower fundamental natural frequency, will be used in the model. Since beams with simply-supported ends have lower natural frequencies than beams with clamped-clamped ends for the same stiffness and mass distributions, the simply-supported beam end model will be used.

The fundamental natural frequency of a simply-supported beam with a concentrated mass at the centre, and which is subjected to an axial force acting at the beam ends, is derived in appendix T. The frequency is given by:

$$f_1 = \frac{1}{2\pi}\sqrt{\left(\frac{\pi}{l_T}\right)^4 \frac{EI}{\rho\left(1+2m_c/\rho A_T l_T\right)A_T} - \left(\frac{\pi}{l_T}\right)^2 \frac{F_b}{\rho\left(1+2m_c/\rho A_T l_T\right)A_T}} \qquad \textbf{(3.7.2.1)}$$

Calculation of the fundamental transverse natural frequency of the rods is done by substitution of numerical values for the rod length, Young's Modulus and density of the rod material, cross-sectional area and second moment of area of the rod, concentrated mass of the coils, centrepiece and end cap, as well as the compressive force acting on the rod, into equation 3.7.2.1.

The density of the beam material, i.e. Terfenol-D, is 9250 kg/m^3 [Butler, 1988]:

$$\rho = 9250 \text{ kg/m}^3 \quad \textbf{(3.7.2.2)}$$

The calculated mass of the coils is 16 g each, while those of the centrepiece and end caps are 34 g and 12 g each:

$$m_{coil} = 0{,}016 \text{ kg} \quad \textbf{(3.7.2.3a)}$$
$$m_{centrepiece} = 0{,}034 \text{ kg} \quad \textbf{(3.7.2.3b)}$$
$$m_{end\,cap} = 0{,}012 \text{ kg} \quad \textbf{(3.7.2.3c)}$$

The concentrated mass attached at the centre of the beam, is the sum of the masses of the two coils, centrepiece and two end caps:

$$m_c = 2m_{coil} + m_{centrepiece} + 2m_{end\,cap} \quad \textbf{(3.7.2.4)}$$

By substitution of equations 3.7.2.3 into equation 3.7.2.4, m_c is:

$$m_c = 0{,}09 \text{ kg} \quad \textbf{(3.7.2.5)}$$

The beam length, diameter and cross-sectional area are 38 mm, 6 mm and 2,827.10^{-5} m^2 respectively:

$$l_T = 0{,}038 \text{ m} \quad \textbf{(3.7.2.6a)}$$
$$d_T = 0{,}006 \text{ m} \quad \textbf{(3.7.2.6b)}$$
$$A_T = 2{,}827.10^{-5} \text{ m}^2 \quad \textbf{(3.7.2.6c)}$$

Young's modulus of the beam material, i.e. Terfenol-D, is 16 GPa (see equation 3.7.1.11):

$$E = 16.10^9 \text{ Pa} \quad \textbf{(3.7.2.7)}$$

The second moment of area of the beam cross-section is:

$$I = \frac{\pi d_T^4}{64} \quad \textbf{(3.7.2.8)}$$

Substitution of equation 3.7.2.6b into equation 3.7.2.8 gives the second moment of area of the rods as:

$$I = 6{,}362.10^{-11} \text{ m}^4 \quad \textbf{(3.7.2.9)}$$

The maximum axial compressive force acting on the beam is 339,3 N (see equation 3.7.1.13):

$$F_b = 339{,}3 \text{ N} \qquad \textbf{(3.7.2.10)}$$

The fundamental natural frequency of the beam is obtained by substitution of equations 3.7.2.2, 3.7.2.5, 3.7.2.6a, 3.7.2.6c, 3.7.2.7, 3.7.2.8 and 3.7.2.10, into equation 3.7.2.1:

$$f_1 = 478{,}8 \text{ Hz} \qquad \textbf{(3.7.2.11)}$$

If the effect of the compressive force is neglected, the fundamental natural frequency is:

$$f_1 = 490{,}9 \text{ Hz} \qquad \textbf{(3.7.2.12)}$$

If equations 3.7.2.11 and 3.7.2.12 are compared, it can be seen that the axial force reduces the fundamental natural frequency by approximately 2,5%.

From equation 3.7.2.11, the fundamental transverse natural frequency of the rods is 478,8 Hz. The maximum frequency of the disturbance band is 100 Hz. Seeing that the natural frequency is considerably higher than the maximum frequency of the disturbance band, it can be concluded that the rods will not buckle during dynamic excitation.

In the next section, the effects of eddy currents on inductance losses in the rods will be investigated.

3.8 Investigation of eddy current losses in the Terfenol-D Rods

The effects of eddy current losses in the Terfenol-D rods are investigated in this section. The investigation is motivated. The complex eddy current loss factor is defined and expressed in terms of Kelvin functions of the crtical frequency ratio. Series expansions for the loss factor are also given. The critical eddy current frequency is expressed in terms of the material resistivity, rod diameter and clamped permeability. In the interest of simplifying the design, an equation which gives the critical frequency in terms of the rod diameter only, is presented and shown graphically. This equation is used to indicate that the critical frequency is well above the maximum frequency of the disturbance.

When a dynamic field is induced in the Terfenol-D rods, a circulating eddy current is caused in the rods. The eddy current produces a magnetic field which opposes the induced field, thereby reducing the effective permeability and inductance [Butler, 1988]. Eddy current losses become significant when the actuator is operated at frequencies above the critical eddy current frequency. The losses are expressed in terms of a dimensionless loss factor, called the eddy current loss factor. The critical frequency depends on the resistivity and clamped permeability of Terfenol-D, as well as on the rod diameter. The effective permeability, critical frequency and eddy current loss factor are discussed in short below.

The effective permeability is the product of the clamped permeability and the loss factor:

$$\mu_{eff} = \chi \mu_0 \tag{3.8.1}$$

where μ_{eff} is the effective permeability, χ is the eddy current loss factor and μ_0 is the clamped permeability.

The clamped permeability can be expressed mathematically as:

$$\mu_0 = \mu^{\sigma}\left[1-(cf)^2\right] \tag{3.8.2}$$

where μ^{σ} is the free permeability and cf is the coupling factor.

Free permeability is the partial derivative of the magnetic flux density with respect to the applied magnetic field at a constant mechanical stress (see equation 2.2.2.4):

$$\mu^{\sigma} = \left.\frac{\partial B(\sigma, H)}{\partial H}\right|_{\sigma=const} \tag{3.8.3}$$

where B is flux density, σ is stress and H is field strength.

The coupling factor, from equation 3.5.2.14, is given by:

$$cf = \sqrt{\frac{Ed^{\sigma}d^{H}}{\mu^{\sigma}}} \tag{3.8.4}$$

where E is Young's modulus, d^{σ} is the piezomagnetic cross-coupling constant and d^{H} is the strain constant.

The critical frequency f_{cr}, according to Butler [1988], is:

$$f_{cr} = \frac{2\rho_T}{\pi \mu_0 {d_T}^2} \tag{3.8.5}$$

where ρ_T is the resistivity and d_T is the rod diameter. The resistivity and clamped permeability are material properties, while the diameter is a property of the rod. It can be seen from equation 3.8.5 that the critical frequency is directly proportional to resistivity, inversely proportional to clamped permeability and inversely proportional to diameter squared.

The frequency ratio p is the dimensionless ratio of the excitation frequency to the critical eddy current frequency:

$$p = \frac{f}{f_{cr}} \tag{3.8.6}$$

The eddy current loss factor is a complex dimensionless factor given by:

$$\chi = \chi_r - j\chi_i \tag{3.8.7}$$

where χ_r and χ_i respectively represent the real part and imaginary part of the loss factor. χ_r and χ_i can be expressed as follows in terms of ber and bei Kelvin functions of the frequency ratio and their derivatives [Butler & Lizza, 1987]:

$$\chi_r = \frac{2}{\sqrt{p}} \frac{\left(ber\sqrt{p}\right)\left(bei'\sqrt{p}\right) - \left(bei\sqrt{p}\right)\left(ber'\sqrt{p}\right)}{ber^2\sqrt{p} + bei^2\sqrt{p}} \tag{3.8.8a}$$

$$\chi_i = \frac{2}{\sqrt{p}} \frac{\left(ber\sqrt{p}\right)\left(ber'\sqrt{p}\right) + \left(bei\sqrt{p}\right)\left(bei'\sqrt{p}\right)}{ber^2\sqrt{p} + bei^2\sqrt{p}} \tag{3.8.8b}$$

where the prime denotes differentiation with respect to p.

For design purposes, especially as far as the selection of a suitable rod diameter is concerned, equations 3.8.8 may be difficult to apply. The reason is that the ber and bei functions of p and their derivatives are relatively complicated to evaluate.

In order to facilitate the evaluation of the functions, Butler & Lizza [1987] developed the following infinite series expansions for χ_r and χ_i:

$$\chi_r = \sum_{q=0}^{\infty} \frac{(p/4)^{2q}}{\left[(q!)^2(2q+1)!\right]} \Bigg/ \sum_{q=0}^{\infty} \frac{(p/4)^{2q}}{\left[(q!)^2(2q)!\right]} \tag{3.8.9a}$$

$$\chi_i = \frac{2}{p} \sum_{q=0}^{\infty} \frac{(p/4)^{2q}\,2q}{\left[(q!)^2(2q)!\right]} \Bigg/ \sum_{q=0}^{\infty} \frac{(p/4)^{2q}}{\left[(q!)^2(2q)!\right]} \tag{3.8.9b}$$

Equations 3.8.9a and 3.8.9b provide a simple calculation method for the real and imaginary parts of the complex loss factor in terms of the frequency ratio. Although the series are infinite, truncation of the series can be applied, albeit at the cost of accuracy. Accuracy will depend on the frequency ratio and the number of terms retained in the series expansion.

Equation 3.8.5 expresses the critical frequency in terms of the resistivity, clamped permeability and rod diameter. For design purposes, calculation of the critical frequency can be simplifed by expressing it in terms of the rod diameter only. This is done by substitution of known numerical values of the material parameters, i.e. the resistivity and clamped permeability, into equation 3.8.5. The resistivity of Terfenol-D is given as follows by Butler & Lizza [1987] and Butler [1988]:

$$\rho_T = 600.10^{-9}\ \Omega\text{m} \tag{3.8.10}$$

The clamped permeability is given by Butler [1988] as:

$$\mu_0 = 5{,}56.10^{-6} \text{ Tm/A} \tag{3.8.11}$$

By substitution of equations 3.8.10 and 3.8.11 into equation 3.8.5, the following empirical equation for the critical frequency in terms of the rod diameter results:

$$f_{cr} = \frac{0{,}06871}{d_T^2} \tag{3.8.12}$$

where d_T is the rod diameter in metres.

For the rod diameter in millimetres, equation 3.8.12 becomes:

$$f_{cr} = \frac{68710}{d_T^2} \tag{3.8.13}$$

Equation 3.8.13 shows that the critical frequency is inversely proportional to the diameter squared. Therefore, the larger the diameter, the lower the critical frequency. A similar equation, in Imperial units, has been derived by Butler [1988]. For the purpose of convenience, a graphical depiction of equation 3.8.13 is shown in figure 3.8.1. The high-loss and low-loss regions are indicated on the graph.

The critical eddy current frequency for the rod diameter used in this study can now be calculated and compared with the maximum frequency of the disturbance band. The rod diameter, from section 3.5, is 6 mm:

$$d_T = 6 \text{ mm} \tag{3.8.14}$$

By substitution of equation 3.8.14 into equation 3.8.13, the critical frequency is:

$$f_{cr} = 1909 \text{ Hz} \tag{3.8.15}$$

The maximum frequency of the disturbance band is 100 Hz (see table 3.2.1). If this frequency is compared with f_{cr}, it can be seen that the critical frequency is well above the disturbance band. The conclusion that can be drawn from the above analysis is that eddy current losses are insignificant in the disturbance band, and can be ignored in this study. As far as eddy current losses are concerned, the selected rod diameter of 6 mm is therefore suitable for installation in the actuators.

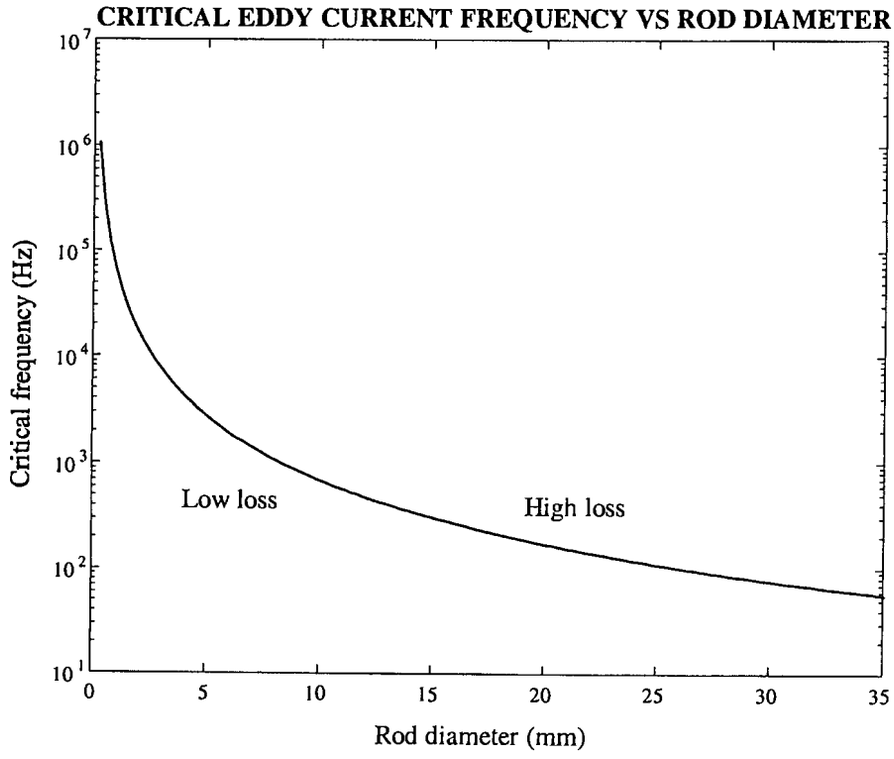

Figure 3.8.1: Terfenol-D critical eddy current frequency versus rod diameter [Butler, 1988]

In the next section, manufacturing and assembly procedures of the actuators and LOS stabilization system are described.

3.9 Terfenol-D actuator and system manufacturing and assembly procedures

A description of the actuator and support structure manufacturing procedures is given in this section. Assembly procedures of the actuators and system are described in short.

The four Terfenol-D rods are bought from the manufacturer, i.e. Etrema Products Inc., Ames Iowa. The actuator gain mechanisms are manufactured from 20 mm thick mild steel sheets. The holes for the prestress bolts are drilled and tapped, after which the mechanisms are cut out, using the wire erosion technique. The mild steel centrepiece and end caps are turned on a lathe. Prestress bolts are tapered on a lathe to aid in locating the end caps. The prestress springs are manufactured from spring steel by a spring manufacturer. Teflon spools for the field coils are turned on a lathe, after which coil wire is wound around the spools on a lathe. Epoxy is used to bond the turns and layers toggether. The coil wire length and number of turns are checked and coil resistance is measured.

The inner end caps are attached to the centrepieces with screws. The two rods of each actuator are placed inside the coils and centred inside the recesses in the end caps. The rods, coils, end caps and centrepiece are placed inside the gain mechanisms and centred. The

prestress bolts and nuts are fastened lightly and the prestress springs are fitted. (At this stage rod prestress is uncontrolled, since it cannot be measured. Prestress adjustment will be described in more detail in chapter 4).

The support structure for the optical instument is milled from 7075 high strength, aircraft quality aluminium. A numerically controlled milling machine is used. The stiffener is milled from commercial quality aluminium. The stiffener is clamped to the support structure and the holes for the connecting screws are drilled. The "dummy" load representing the optical instrument is milled from mild steel strips. The spacers between the support structure and "dummy" load are milled from commercial quality aluminium. The spacers are clamped between the support structure and "dummy" load and the holes for the connecting screws are drilled.

The support structure, stiffener, spacers and dummy load are assembled using screw joints. The actuators are attached to the support structure with screw joints. Assembly drawings of the actuator and system are shown in section 3.6.

3.10 Summary of chapter 3 and preview of chapter 4

The design and manufacture of the Terfenol-D actuators and the LOS stabilization system were discussed in detail in chapter 3. The design inputs were given and were used to obtain the actuator and system performance parameters. A number of design concepts were generated and compared and the most suitable concepts for a gain mechanism, magnetic field biasing and mechanical biasing were selected. These concepts were incorporated into an actuator design concept and a system design concept. A detailed design of all the actuator and system components was done. The design was checked for static and dynamic buckling of the rods and eddy current losses. The manufacturing and assembly procedures of the actuators and system were described.

Experimental testing of the actuators and system will be covered in chapter 4. The purpose of the tests is twofold: In the first place, the system characteristics, such as the stroke length of the actuators and system bandwidth must be measured to establish whether the design meets the requirements. Secondly, the accuracy of the model developed in chapter 2, must be evaluated. The modelled dynamic characteristics will be compared with the experimentally measured characteristics. Differences between modelled and measured characteristics will be explained and recommendations towards updating of the model will be made.

The following aspects of the experimental tests are covered in chapter 4. The test specimens, i.e. the two Terfenol-D actuators and LOS stabilization system, are discussed in short. The modelled characteristics, as well as the design parameters and dimensions of the system, are used to write a test specification. The test setup and apparatus are discussed and the tests are designed. The test procedures for the quasi-static and dynamic tests are spelt out. Post-processing of the test results is done. The test results are compared with the modelled results and reasons for differences between the modelled and experimental results are given.

Chapter 4
Experimental testing of magnetostrictive LOS stabilization system

4.1 Background

Experimental testing of the magnetostrictive LOS stabilization system is described in this chapter. The tests are motivated and the goals of the tests are spelt out. Performance, mass and dimensional parameters of the test samples, i.e. the two actuators, optical instument and its support structure, are given. These parameters are used to prescribe the test equipment and to design the test signals. The test setups and equipment are described. The tests are designed and carried out. Processing of the results is done. The results are presented, discussed and compared with the modelled results obtained in chapter 2.

Experimental tests are carried out for the following reasons: The test results will firstly indicate whether the degree of complexity of the model developed in chapter 2, was sufficient. In the second place, a measure of accuracy of the modelled Terfenol-D material and system characteristics will be provided. Thirdly, experimentally determined characteristics will be required in chapter 5 to update and improve model accuracy. The fourth and most important reason, is that an experimentally verified model will be required in chapter 6 to design a controller.

Two types of tests, i.e. quasi-static and dynamic tests, are carried out. A quasi-static test is done on each actuator in order to determine its stroke length and the ratio between its output displacement and input voltage. The voltage where this ratio is a maximum, is used as the bias voltage for the dynamic tests. Dynamic tests are carried out on the system to obtain the transfer function between coil input voltage and instrument angular acceleration. From this *TF*, other important system characteristics, such as resonance and antiresonance frequencies, are obtained.

The experimental tests are systematically covered in the following sections. The test specimens, i.e. the two actuators, optical instrument and its support structure, are discussed in short in section 4.2. The test setup and equipment are described in section 4.3, followed by the test design and test procedure in section 4.4. Section 4.5 covers the test results. Processing of the test data is described in section 4.5.1. *TF* spectra are calculated and shown in section 4.5.2. A discussion of the dynamic test results is given in section 4.5.3. The experimental and modelled results are compared, reasons for the differences are discussed and the need for an updated model is given in section 4.5.4. A summary of chapter 4 and a preview of chapter 5 are given in section 4.6.

4.2 Technical details of the test specimens

Technical details of the test specimens are given in this section. The details are required for two purposes. Firstly, the performance requirements of the test equipment, such as signal generator frequency bandwidth, measurement ranges of the displacement transducer and accelerometers, and power output of the amplifier, must be determined. Secondly, the technical details will serve as design inputs for the quasi-static and dynamic test signals.

For the purpose of this study, three specimens are considered, i.e. the two actuators, which will be individually tested quasi-statically, and the entire system, which will be tested dynamically. All the appropriate specimen parameters are tabled and dimensions are shown schematically.

The dimensional parameters are the length, width and height of the test specimens. The performance characteristics are: Actuator stroke length, maximum *translational* acceleration at each end of the optical instrument, frequency bandwidth and coil resistance, voltage, current and power. Note that the *translational* acceleration at the ends of the optical instrument is given, rather than the *angular* acceleration. The reasons are twofold. In the first place, it is easier to measure translational acceleration and to divide it by the instrument length in order to obtain its angular acceleration, than to directly measure angular acceleration. Secondly, this method of measurement will facilitate a direct comparison with the modelled characteristics obtained in section 2.8 and to update the model, as will be discussed in chapter 5.

Actuator and system dimensions are obtained from sections 3.5 and 3.6, while the performance parameters are obtained from sections 2.7, 2.8 and 3.2. Figures 4.2.1 and 4.2.2 respectively show the dimensions of the actuators and LOS stabilization system. The technical and performance parameters are summarized in table 4.2.1.

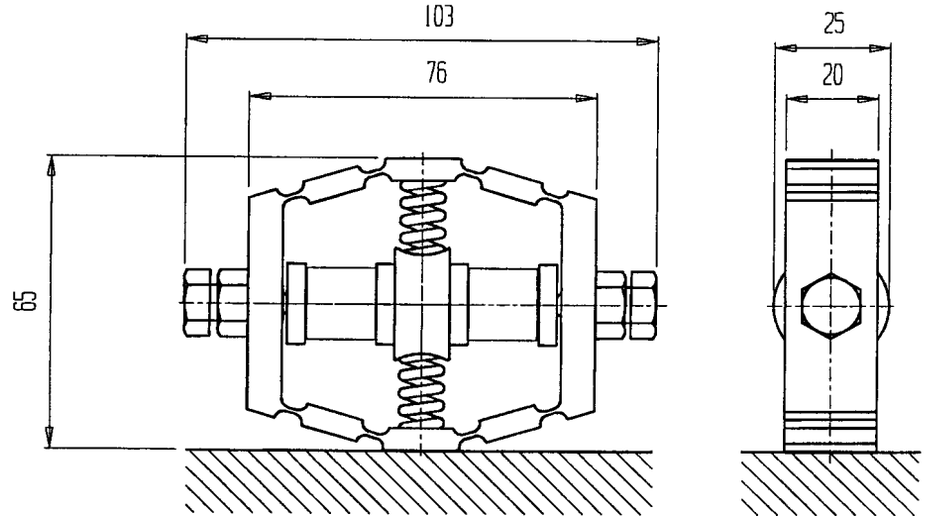

Figure 4.2.1: Terfenol-D actuator dimensions

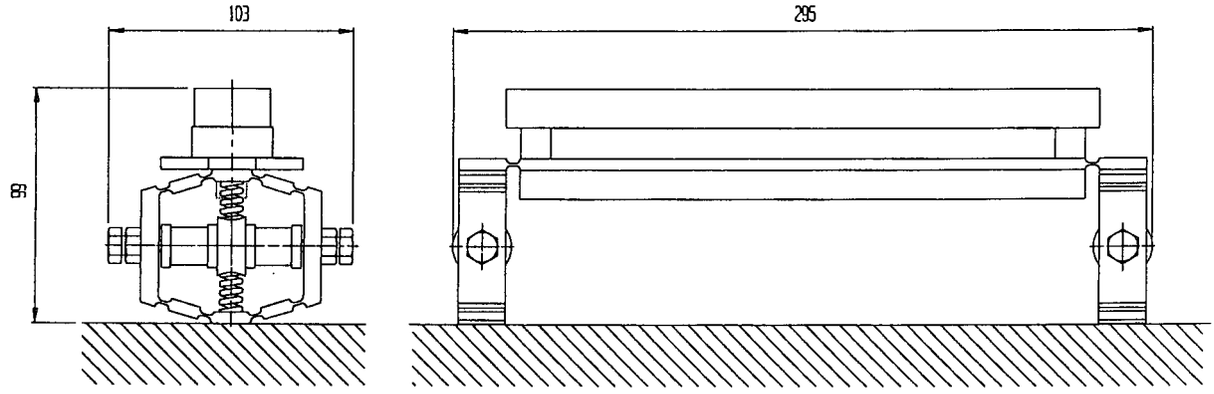

Figure 4.2.2: LOS stabilization system dimensions

Table 4.2.1: Actuator and system test parameters

Parameter	Value
System length	0,295 m
System width	0,103 m
System height	0,099 m
Actuator length	0,103 m
Actuator width	0,025 m
Actuator height	0,065 m
Actuator stroke length	75.10^{-6} m
Translational acceleration at actuator	4,26 m/s^2
Coil static resistance per actuator	3,2 Ω
Coil voltage input per actuator	17,5 V (p-p)
Coil current per actuator	5,47 A (p-p)
Coil power per actuator	98,7 W

One performance parameter that is not shown in the table, is the system frequency bandwidth (333 Hz). The reason is that this bandwidth is considerably higher than the disturbance bandwidth of 2,5 Hz to 100 Hz. The latter bandwidth, instead of the former, will be used to design the dynamic test signals.

The parameters given in this section, will be used to in section 4.3 to determine the technical requirements of the test equipment and to design the quasi-static and dynamic test signals in section 4.4.

4.3 Test setups and equipment

The test setups and equipment are described in this section. The equipment consists of a personal computer, digital signal processing equipment, test bench, sensors, signal analyzer and power amplifiers. The test bench provides a base for attachment of the LOS stabilization system and sensors. A personal computer (PC) is used to generate the test input signals in digital form. The PC contains a digital signal processing (DSP) card, which converts the signals to analogue form. A power amplifier is used to drive the actuator coils.

Two types of sensors are used to measure the outputs, i.e. displacement transducers, to measure actuator and system quasi-static displacements, and accelerometers, to measure base and system accelerations. A voltage divider is used to facilitate measurement of the input signal. A signal analyzer captures the coil input voltage and sensor output signals. The PC is used for post-processing of the test results.

The test setups are described in section 4.3.1, followed by a discussion on the signal generation equipment in section 4.3.2. The sensors, signal acquisition and processing equipment are discussed in section 4.3.3.

4.3.1 Test setups

Test setups for the quasi-static and dynamic tests are shown and discussed in this section. Two dynamic test setups are considered, i.e. an ideal setup and an available setup. The ideal setup makes simultaneous characterization of the system possible for all the known inputs. However, this setup is not feasible, since all the required equipment is not available. An alternative setup, which makes use of available equipment, is used instead. The limitations of this setup are mentioned and discussed.

The actuator quasi-static test setup is shown in figure 4.3.1.1. The actuator is attached to a fixed base. The input signal is coil voltage (V) and the output signal is actuator displacement. An inductive (eddy current) displacement transducer, mounted on a fixed base, is used for measuring actuator displacement.

The reason for attaching the actuators to a fixed base is that the quasi-static tests are mainly done to determine the most suitable coil bias voltages to be used in the dynamic tests. The effect of base motion is not of importance for this purpose.

The dynamic test setup is designed to facilitate controller design and testing in chapter 6. The controlled system will be excited by two inputs, i.e. the coil voltage (controllable input) and the base acceleration (uncontrollable input or disturbance). The controllable input must be commanded in such a way that its behaviour will cancel the uncontrollable input behaviour. In order to determine the latter behaviour, the system is attached to an elastically-mounted base, connected to an external shaker. The shaker will be used in chapter 6 to excite the base.

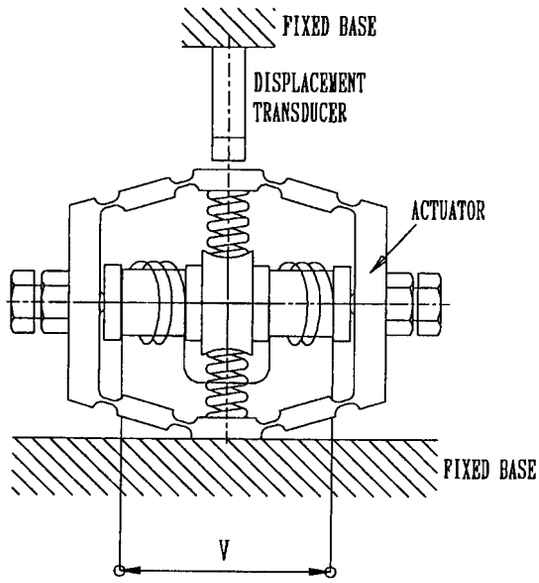

Figure 4.3.1.1: Actuator quasi-static test setup

An ideal dynamic test setup is shown in figure 4.3.1.2. Each actuator is attached to a moving base, in the form of a rigid beam. Each base is suspended by a spring, guided by a linear bearing and connected to an electrodynamic shaker by means of a string (also known as a stinger). The two actuator coils are excited 180 °out-of-phase to excite angular motion of the optical instrument. Accelerometers are mounted at each end of the optical instrument and on each moving base (i.e. four accelerometers in total). The advantage of this test setup is that it makes simultaneous measurement of all the *TF*'s of the system possible, provided the test equipment is available.

However, the equipment required for the above setup, is not available. Available equipment is limited to the following: The test bench contains only one moving base and only one shaker is available. Furthermore, the signal analyzer used to capture measured data has only two analogue input channels, therefore only one coil voltage and one acceleration can be measured during a test.

It is therefore necessary to simplify the setup by making use of available equipment. Such a setup is shown in figure 4.3.1.3. Actuator 1 is attached to a fixed base, while actuator 2 is attached to an elastically-mounted base. The coil of actuator 2 is excited by a voltage signal, while that of actuator 1 has an open circuit. The coil voltage signal and one accelerometer signal are measured during a test. The test is conducted as many times as the number of accelerometers.

The advantage of this setup is its simplicity in comparison with the ideal setup. The disadvantage is that separate tests must be done to obtain the various *TF*'s of the system. With this setup, tests will necessarily take longer to conduct than with the ideal setup. This setup will however be used, due to the problem with availability of test equipment.

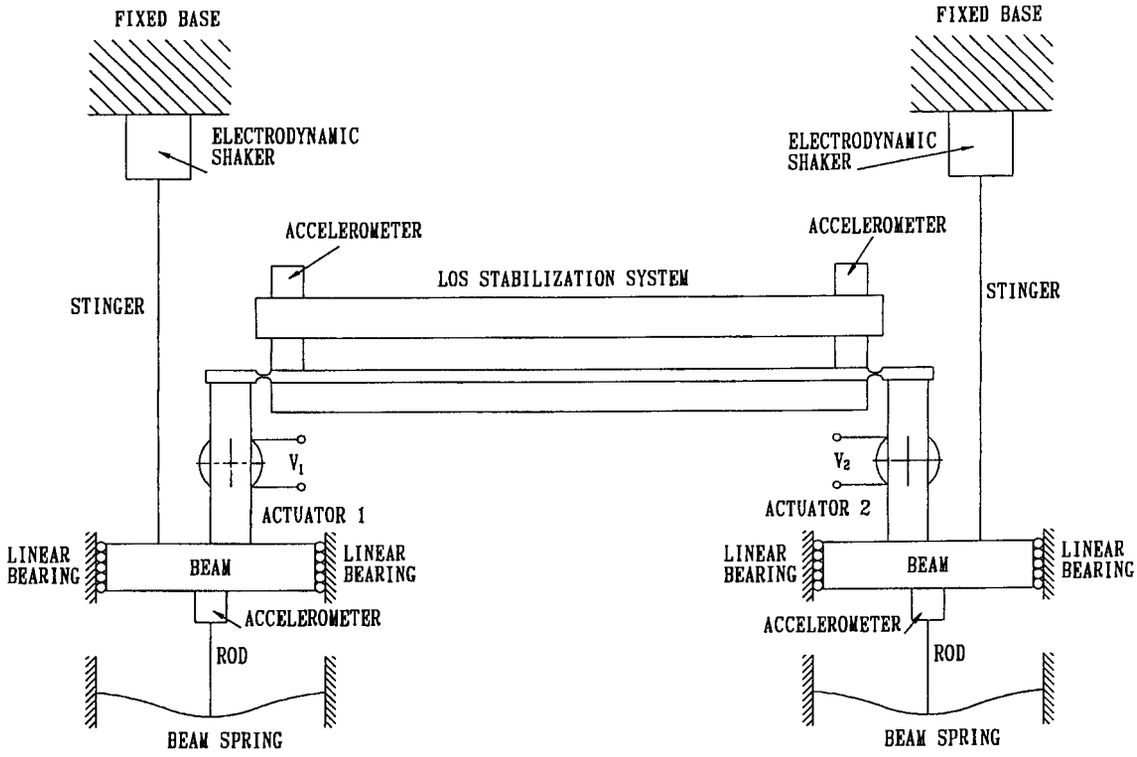

Figure 4.3.1.2: Ideal dynamic test setup

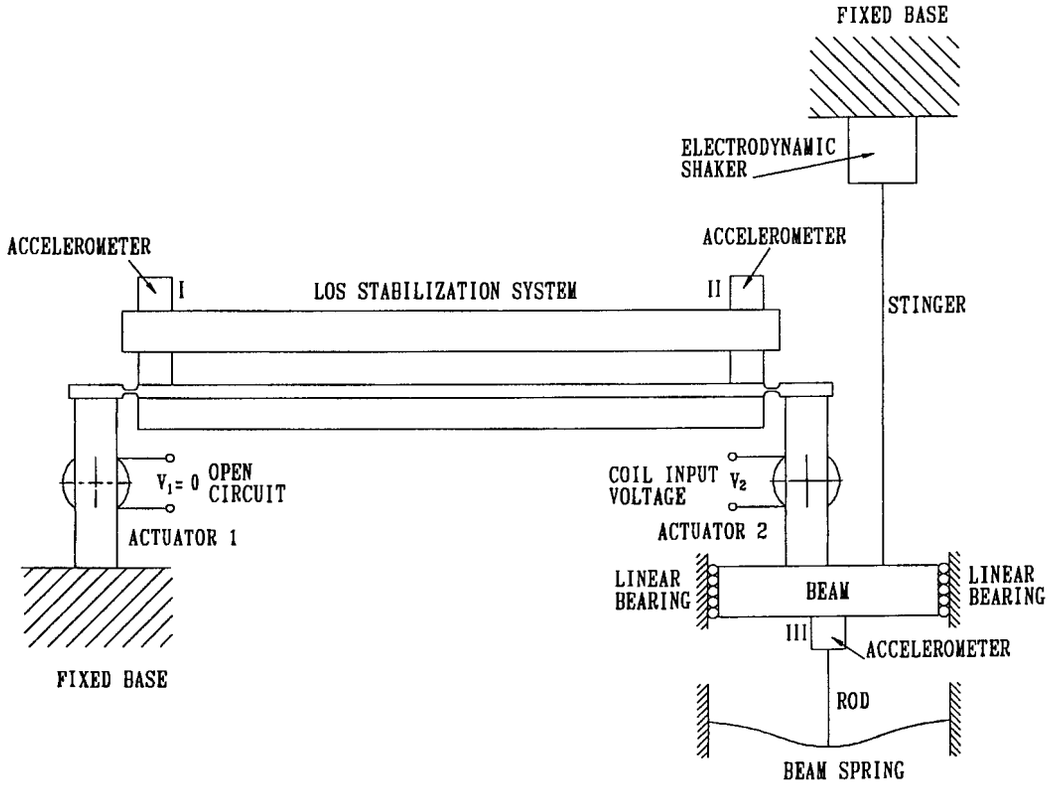

Figure 4.3.1.3: Available dynamic test setup

The system is excited by applying a voltage signal to the coil of actuator 2. The voltage and accelerometer signals are captured and processed to obtain system *TF*'s. The signal generation equipment is discussed in the next section.

4.3.2 Signal generation equipment

The test signal generation equipment is shown schematically in figure 4.3.2.1. The signals are generated in Simulink, which is a Matlab real-time simulation environment. Using Simulink, the following basic time-domain input signals can be generated: Constant, step, delayed step, sine, sine sweep, square wave, sawtooth, random and band-limited white-noise.

Arbitrary signals can be obtained in a number of ways. The signals can either be imported from Matlab or from external files. Alternatively, the abovementioned basic signals can be combined to build the required signal. For instance, a signal can be added to, subtracted from, multiplied with, or multiplexed with another signal. Furthermore, a signal can, inter alia, be clipped, rate-limited, integrated, differentiated, filtered and resampled.

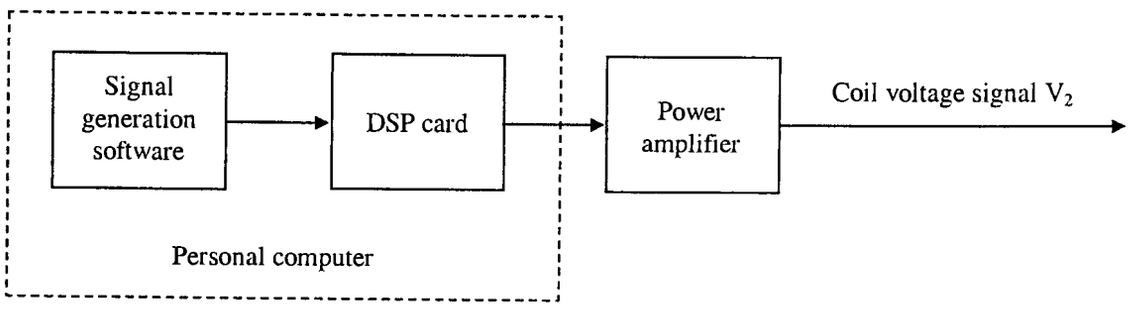

Figure 4.3.2.1: Test signal generation equipment

A signal can be generated and viewed in real time. For this purpose, algorithms such as the linear, Euler, Heun, 3rd order Runge-Kutta, 5th order Runge-Kutta, Adams, Gear and Adams/Gear algorithms are supplied. Sample frequencies can be arbitrarily selected and adaptive time-stepping is possible.

Digital signal processing card

The DSP card is a floating point card manufactured by dSpace. It is provided with a built-in processor, the clock of which runs at 40 MHz. The card has the facility to directly code a Simulink-generated signal in the C-programming language, as well as to compile the signal to an object file.

Execution speed of the compiled signal is determined by the clock speed of the card only, and not by that of the PC's central processing unit. Adaptive time-stepping is not available for

coding. Sampling frequency is strongly dependent on the number of operations executed per time step.

The card gain, i.e. the ratio between the amplitude of the simulated signal and that of the card output signal, is 10. The card has four digital-to-analogue (D/A) channels and four analogue-to-digital (A/D) channels.

Power amplifier

An MB Dynamics SS 250 power amplifier is available for the tests. The amplifier is matched to an electrodynamic shaker normally used for modal testing of structures. Amplifier frequency bandwidth, according to the manufacturer, is 0 Hz to 30 kHz. Output power is controlled by a rheostat. Maximum power output is 750 W and automatic clipping takes place in case of overloading. For the purpose of this study, a bandwidth of 100 Hz and a power output of 98,7 W are required.

An important amplifier characteristic applicable to this study is its input to output transfer function. Since the amplifier will be used to power the actuator coils during control, a minimum phase shift of the commanded signal will be required. To determine the phase shift, *TF*'s were measured for random input signals with three different power levels. The signals were low-pass filtered at 100 Hz. Power levels were -8,94 dB, -10,88 dB and -13,21 dB, relative to maximum power output. A sample frequency of 1280 Hz was used. Measured *TF* spectra are shown in figure 4.3.2.2. The maximum phase shift at 100 Hz is 0,14°, which can be considered negligible for all practical purposes.

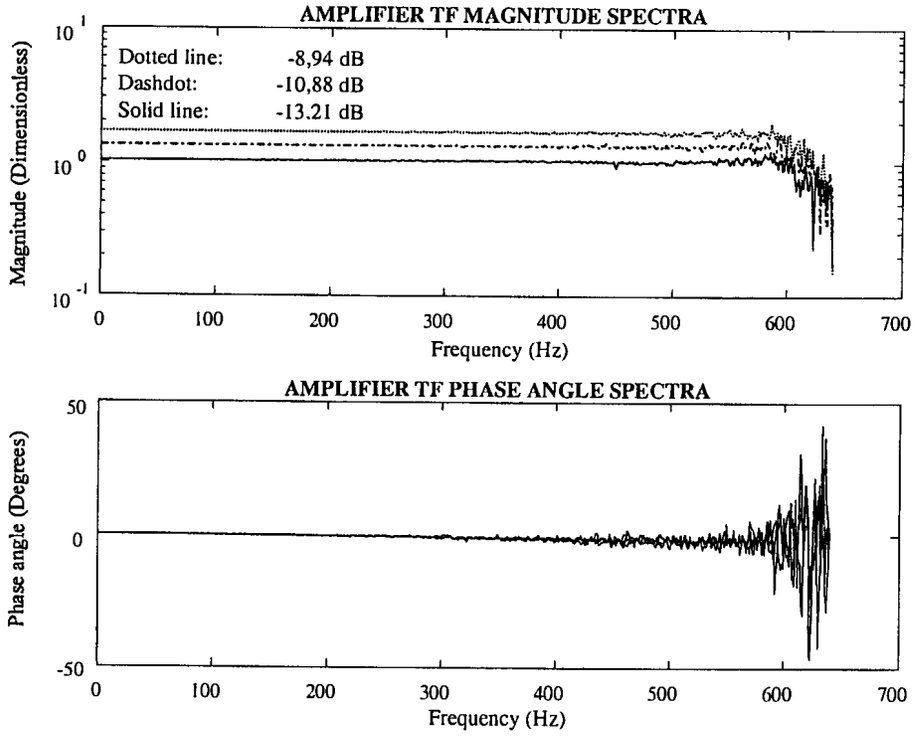

Figure 4.3.2.2: Amplifier transfer function spectra for three power output levels

4.3.3 Signal measuring, acquisition and analyzing equipment

The sensors, sensor amplifiers and signal analyzer are described in this section. A schematic layout of the equipment is shown. Sensor types and manufacturers, calibration factors, ranges and amplifier gains are given. The displacement transducer is described first, followed by the accelerometers and signal analyzer.

A schematic layout of the signal measurement, acquisition and analyzing equipment is shown in figure 4.3.3.1. The type of sensor used depends on the type of test: A displacement transducer is used for the quasi-static tests, while accelerometers are used for the dynamic tests. The sensor output signal is amplified in order to capture it with the signal analyzer.

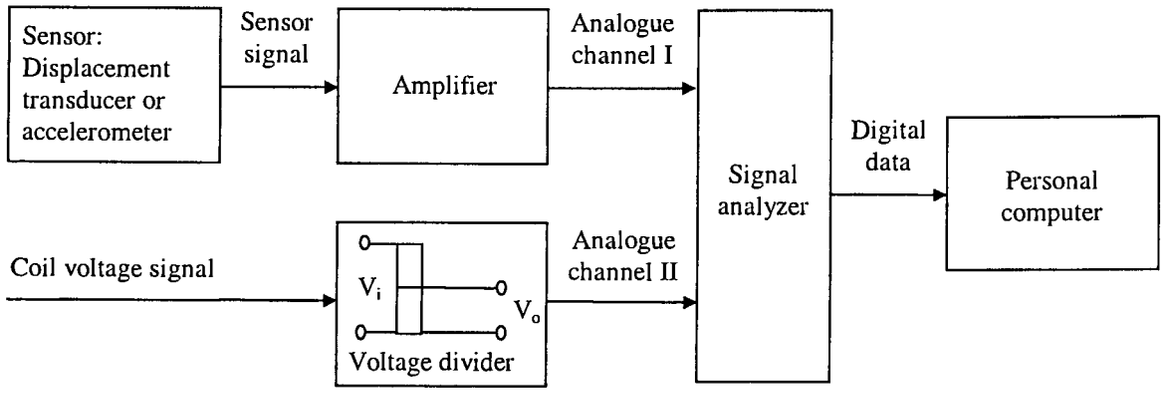

Figure 4.3.3.1: Signal measurement, acquisition and analyzing equipment layout

The signal analyzer has two analogue input channels. The two channels are respectively used for capturing the sensor output and coil input voltage signals. The amplitude of the latter signal (17,5 V as simulated- see sections 2.7 and 2.8) exceeds the input range of the analyzer (± 10 V) and is therefore reduced to a measurable level by means of a voltage divider. The divider gain is 0,25.

Captured data can be processed in real-time, using the analyzer, or can be off-loaded to the computer for post-processing. The latter option is preferred, since the available analyzer can only process two signal characteristics at a time. If, for instance, the *TF* between two signals is required in magnitude and phase format, other characteristics, such as time traces, PSD's, CSD's and coherence spectra, cannot be obtained during the same test. In order to obtain these characteristics, the tests must be repeated.

Computer post-processing, on the other hand, can be relatively easily done using signal processing software. Overlaps can be adjusted and frequency resolution can be changed without repeating the tests. In this study, the signal analyzer is only used to capture and view the data, whereafter the signal processing is done on the computer.

Displacement transducer

An inductive (eddy current) transducer, manufactured by SKF, is used for the displacement measurements. The transducer measures the distance between its tip and a magnetic material placed close to its tip. A gap is normally left between the transducer and the actuator to protect the transducer tip from damage. Due to this gap, the measured output has a DC offset, which has to be subtracted from the measured output to obtain actuator displacement. The transducer output is in volts and its calibration factor is 125 μm/V. A 24V DC driver, type CMSS665, by the same manufacturer, powers the transducer.

Accelerometers

Two accelerometers, manufactured by Setra, are available for the characterization tests. Accelerometer ranges are 15 g and 30 g respectively. Nominal natural frequencies, as claimed by the manufacturer, are 800 Hz for the 15 g accelerometer and 1150 Hz for the 30 g accelerometer. Claimed ± 3 dB flat response ranges are 0 Hz to 400 Hz and 0 Hz to 700 Hz for the 15 g and 30 g accelerometers respectively. The lower cutoff frequencies were checked and found to be 5 Hz, instead of 0 Hz, for both accelerometers. The accelerometers do however respond below 5 Hz, but response is outside the ± 3 dB range. Experimentally determined calibration factors of the two accelerometers are 29,32 mV/g for the 15 g accelerometer and 46 mV/g for the 30 g accelerometer.

Signal analyzer

A Diagnostic Instruments type PL 202 signal analyzer is used for data acquisition purposes. The analyzer has two analogue input channels. The maximum signal input range is ± 10 V per channel. Any input outside this range is clipped. Single-capture or continuous acquisition is possible.

Frequency bandwidth ranges from 25 Hz to 40 kHz. Acquisition time ranges from 2,5 ms to 64 s, depending on the bandwidth and number of data points. The latter is adjustable from 256 to 4096 in fixed steps. A manually selectable anti-alias filter is provided.

The following signal characteristics can be obtained in real time: Frequency spectrum, PSD, time trace, difference between time traces of the two measured signals, FRF, coherence, octave bands and 1/3 octave bands. Real-time averaging of data, including RMS calculation, is possible. Four window types are provided, i.e. exponential (for pulse-type inputs), Hanning, flat top and rectangular.

Automatic or manual screen ranging can be selected. The latter is logarithmically adjustable in fixed steps from 10 mV to 10 V. Axis display formats include real and imaginary, logarithmic, linear magnitude, logarithmic magnitude and phase.

Captured data can be stored in files. The files can be recalled, reviewed, erased, copied and off-loaded, for instance to a personal computer, through a standard RS 232 port. Software for data off-loading is provided by the manufacturer.

4.4 Test design and procedure

The quasi-static and dynamic test design and procedures are described in this section. Quasi-static test signal generation is discussed in section 4.4.1, followed by a description of the quasi-static test execution in section 4.4.2. In section 4.4.3, quasi-static test data processing is described and the test results are shown and discussed. The most suitable coil bias voltage for the dynamic tests is calculated in section 4.4.4. Dynamic test signal selection, design and generation are described in section 4.4.5, followed by a description of the dynamic test execution in section 4.4.6.

4.4.1 Quasi-static test signal generation

Truncated ramp voltage signals are used as inputs for the quasi-static tests. The desired signal characteristics are: A low rate-of-rise to prevent the excitation of dynamic behaviour such as overshoot, sufficient amplitude to excite the actuator over its entire voltage and displacement ranges, and a relatively short time duration to minimize the risk of coil overheating.

The maximum voltage applied to the coil depends on the coil resistance and amplifier output power. For an amplifier power of 400 W (approximately 53% of full amplifier power, see section 4.2) and static coil resistance of 3,2 Ω (see section 3.5.2), a voltage of 36 V is achievable. To prevent coil overheating, the signal time duration is limited to 4 s. The rate-of-rise of the ramp is 250 V/s.

The signal generation block diagram is shown in figure 4.4.1.1. The signal is generated in Simulink, using the available input functions. The truncated ramp input is constructed from two rate-limited step inputs. The first step, with a height of H, is applied at time t = 0. The ramp is terminated by adding a delayed, rate-limited step with height -H, to the first step. The resulting signal is shown in figure 4.4.1.1.

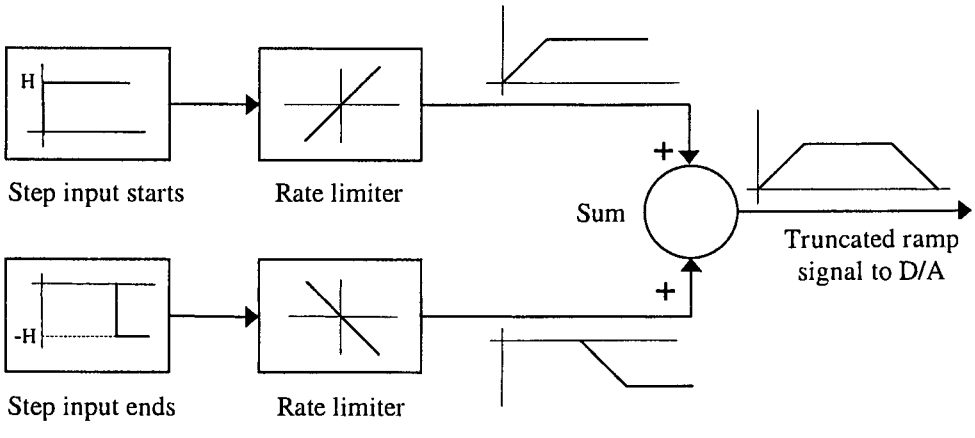

Figure 4.4.1.1: Block diagram for quasi-static signal generation

Analogue-to-digital conversion of the signal is done by means of the DSP card. The card has a gain of 10 and its maximum output voltage is 10 V (see section 4.3.2). The card characteristics must be compensated for in the Simulink model. Failure to do so may lead to

clipping of the signal. To prevent this, the height H and rate-of-rise of the signal are respectively adjusted to 0,96 V and 6,7 V/s. The signal is coded in the C-programming language, compiled to an object file and viewed on the analyzer display screen.

4.4.2: Quasi-static test execution

The two actuators are tested separately. The test procedure is as follows. A voltage divider with a gain of 0,25 is connected in parallel with the coil in order to facilitate input voltage measurement. The displacement transducer is attached on a fixed base above the actuator, as shown in figure 4.3.1.1. A gap is left between the actuator and the transducer tip. The transducer is connected to its driver. The DSP card output is connected to the input of the power amplifier, whose output is connected to the actuator coil (see figure 4.3.2.1). The amplifier gain is adjusted to give the required coil voltage.

The test signal is applied to the actuator coil. The voltage across the divider and the transducer output voltage, are measured and captured using the signal analyzer. Captured data is transferred to a personal computer for processing. The input and output signals are multiplied with their respective calibration and gain factors. (The transducer calibration factor is 125 μm/V - see section 4.3.3, while the coil voltage gain is the inverse of the divider gain, i.e. 4 V/V). It is important to note that the actuator will give a negative displacement for a positive coil voltage. This is due to the geometry of the octagonal displacement gain mechanism (see figure 3.4.1.5) The actuator output signal is therefore multiplied with an additional gain factor of –1.

Output displacement versus input voltage curves of the two actuators are plotted. The characteristics of the two actuators are compared. If the characteristics display unduly large differences, adjustments are made to the actuators and the tests are repeated.

A possible cause for differences between the actuator characteristics is Terfenol-D rod prestress. Prestress can be easily adjusted, either by changing the torque in the prestress bolts, or by replacing the prestress springs. However, measuring rod prestress is not as simple. Due to space limitations, measuring equipment, such as load cells and strain gauges, cannot be placed inside the actuators. Rod prestress is therefore adjusted iteratively. The characteristic of the actuator with the highest output displacement is used as reference. The rod prestress of the other actuator is adjusted and the test is repeated. The characteristics are compared again and the process is repeated until sufficient correspondence between the characteristics is obtained. The test results are displayed and discussed in section 4.4.3.

4.4.3 Quasi-static test results and discussion of results

Output displacement versus input voltage characteristics of the two actuators are shown in figure 4.4.3.1. Voltage and displacement ranges are 40 V and 120 μm respectively. The loading and unloading curves are indicated, together with the required actuator stroke length of 75 μm.

The maximum output displacements, for a 36 V coil input, are 110 μm for actuator I and 113 μm for actuator II. The percentage difference between the maximum output displacements, relative to that of actuator I, is 2,7%. From the loading curves, it can be seen that the required stroke lengths of actuators I and II are produced with input voltages of 13,2 V and 12,3 V respectively.

The linear and saturation ranges are not clearly demarcated. In section 2.2, it was mentioned that subjective judgment is required to determine the transition point between the ranges. From figure 4.4.3.1, it can be judged that the linear ranges of the two actuators end at the required stroke length of 75 μm.

A dead zone of 2,5 V appears in each loading curve. During loading from a state of 0 V and 0 μm displacement, displacement initially remains at 0 μm, but increases as soon as the voltage reaches 2,5 V. The dead zone is a result of magnetostrictive hysteresis, which was discussed in more detail in section 2.3. In short, the closer the spacing between the loading and unloading curves, the less significant the effects of hysteresis. From figure 4.4.3.1, it can be seen that, at lower voltages, spacing between the curves is wider than at higher voltages.

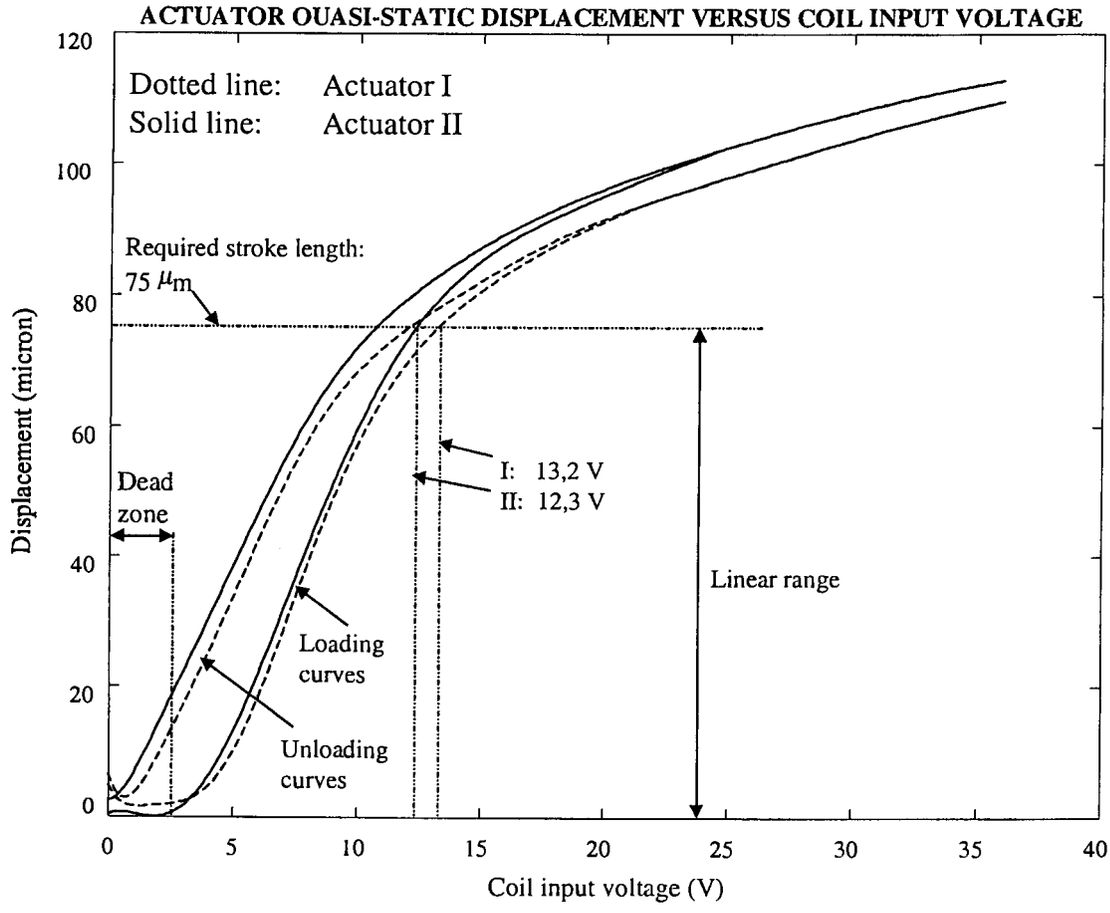

Figure 4.4.3.1: Actuator quasi-static displacement versus coil input voltage

The differences between the characteristics of the two actuators remain, even after adjustment of the rod prestress, using the iterative method described above. The following reasons can be given for the differences: Firstly, during actuator assembly, fitting the prestress springs may have caused slight twisting of the flexures. The flexures are relatively soft and can be easily damaged.

Secondly, the magnetostrictive characteristics of the rods may differ slightly. The rod manufacturer, Etrema, does however include a measured quasi-static (strain versus field) characteristic with each rod upon delivery. Differences in rod characteristics are therefore known before actuator assembly.

The quasi-static characteristics shown in figure 4.4.3.1 are not expressed in terms of rod strain and induced magnetic field. The reason is that, for the purpose of analyzing actuator and system performance, parameters such as output displacement, stroke length and input voltage, are more important. These parameters are also directly measurable.

However, in the interest of facilitating future designs and for updating the model, it is necessary to determine the rod strain. If gain mechanism stiffness and passive rod length are neglected and equal strains in the two rods are assumed, the maximum strain achieved with actuator II, is 1100 $\mu\varepsilon$. If passive rod length and gain mechanism stiffness (3,28 MN/m – as calculated by means of the FE method in section 3.5.1) are included, the maximum strain in the rods of actuator II is 1410 $\mu\varepsilon$. The maximum linear strain, which occurs at a stroke length of 75 μm, is 944 $\mu\varepsilon$ (see also section 3.5.1).

From the quasi-static test results, the most suitable bias voltage for the dynamic tests is determined. This is done in section 4.4.4.

4.4.4 Calculation of bias voltage for dynamic tests

The following procedure is followed to calculate the bias voltage. The first step is to obtain the dehysterized displacement versus coil voltage characteristic for each actuator. The dehysterized characteristic is the average of the loading and unloading curves (this definition was adopted in section 2.3, where the hysteresis effect on the strain versus field characteristics was studied):

$$x_{dehysterized}(V) = \frac{1}{2}\left\{x_{loading}(V) + x_{unloading}(V)\right\} \qquad \textbf{(4.4.4.1)}$$

where V is coil input voltage and x is output displacement.

Equation 4.4.4.1 is differentiated numerically with respect to coil voltage to obtain the displacement derivatives, or gradients, of the dehysterized characteristics. The curves of displacement derivative versus coil voltage of the two actuators are shown in figure 4.4.4.1.

It can be seen from figure 4.4.4.1 that the *shapes* of the displacement derivative curves resemble those of the modelled dehysterized strain constant curve (see figure 2.2.1.5). For low coil voltages, the gradients are low. The gradients increase with an increase in voltage

and reach a peak. The maximum displacement gradient of actuator I is 9,3 μm/V at 6,7 V, while that of actuator II is 8,8 μm/V at 6,4 V. For further increases in coil voltage, the gradients decay to zero in the saturation region.

Theoretically, the voltage where the gradient peaks, can be selected as the bias voltage. For this bias voltage, coil voltage will range from 0 V to approximately twice the bias voltage. (Actuator I, for example, produces a stroke length of 75 μm at 13,2 V, while the theoretical bias voltage is 6,7 V). However, it is undesirable to extend the voltage range below 2,5 V, since hysteresis losses are more significant at lower voltages (see discussion in section 4.4.3).

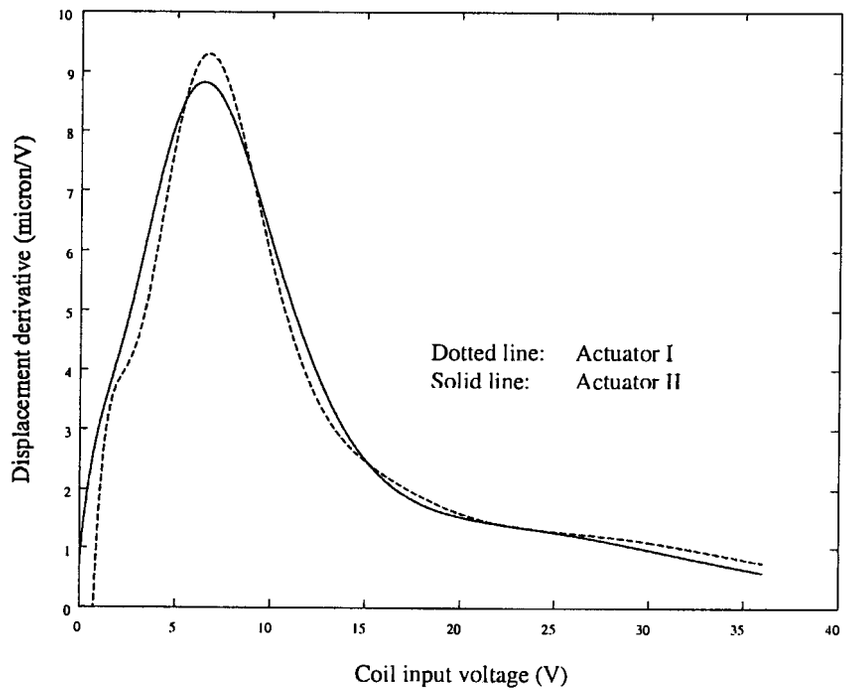

Figure 4.4.4.1: Displacement derivatives versus coil voltage of the two actuators

In order to limit hysteresis losses, it is necessary to increase the coil voltages. The required increase is unknown at this stage. The coil voltages are therefore arbitrarily raised by 2,5 V (the dead zone voltage), resulting in bias voltages of 9,1 V and 8,75 V for actuators I and II respectively. These voltages respectively differ by only 3,4% and 0,5% from the design bias voltage of 8,8 V (see table 3.5.2.3).

The disadvantage of increasing the coil voltage is that the maximum voltage is moved into the saturation region. The maximum voltage of actuator I, for instance, will be 15,7 V, an increase of approximately 20%. The problem can, to a large extent, be solved with permanent magnet biasing.

4.4.5 Dynamic test signal selection, design and generation

The selection, design and generation of the dynamic test signals are described in this section. A number of signal types are considered and a suitable test signal type is selected. Signal parameters, such as duration, amplitude and bandwidth are determined and tabulated. A block diagram for dynamic signal generation is shown.

Dynamic test signal types and selection of the most suitable signal type

Signal types to be considered for dynamic characterization purposes, are steady-state harmonic, stepped-sine, sine-sweep, wide-band random (white noise) and transient type signals. A short description of each input signal type, from Ewins [1991], is given below. The application, advantages and disadvantages of each signal type are discussed in short. The most suitable dynamic test signal type is selected.

Steady-state harmonic inputs are mainly applied to obtain the *TF* magnitude and phase of a system at a single frequency. If the *TF*'s are required at more than one frequency, a characterization test must be carried out at each frequency of interest. Wide-band, high-resolution characterization of systems using harmonic inputs is therefore not recommended.

Stepped-sine inputs can be used for system characterization over a limited bandwidth. A harmonic input is applied, preferably at the lowest or highest frequency in the band. The frequency is fixed for a sufficiently long period to ensure that steady-state conditions are attained before measurements are made. The frequency is adjusted stepwise and the procedure is repeated. The test is stopped when measurements have been made at all the frequencies in the band. Input amplitude is held constant with time.

Sine sweep inputs are in a sense similar to stepped-sine inputs, but the frequency is varied continuously, instead of stepwise. A harmonic input is applied at the lowest or highest frequency in the band. The frequency is varied slowly to ensure that steady-state conditions are attained before making measurements. Frequency can be varied linearly or logarithmically with time. Input amplitude is held constant with time. Sine sweep tests are not recommended for combinations of short test times, wide frequency bands and high resolutions. Under these circumstances, steady-state conditions are difficult to attain.

Random inputs are often used for wide-band characterization of systems. A special type of random input is the so-called "white noise" signal, with an approximately constant amplitude spectrum and a random phase. During testing, the signal time trace is recorded in samples of equal duration. The amplitude spectra of the individual samples are averaged. Sequential or overlap averaging can be performed. For a given bandwidth, data reliability is improved with an increase in sample duration and number of samples.

Data reliability is indicated by the "statistical degrees of freedom" κ, given by the following equation:

$$\kappa = 2mT\ BW \qquad \textbf{(4.4.5.1)}$$

where m is the number of samples, T is the sample duration and BW is the frequency bandwidth. The higher κ, the more reliable the data. As an example, Ewins [1991] recommends a κ-value of 10 for an 80% probability that the estimated spectrum is within 50% of the true spectrum at any given frequency. For an 80% probalility that the estimated spectrum is within 18% of the true spectrum, κ should approach 100.

Transient inputs are mainly applied to obtain the pulse- or impact behaviour of a system. Input time duration is relatively short in comparison with the lowest natural period of the system. The input amplitude spectrum normally decays exponentially with frequency. This type of test is not suitable for wide-band characterization where constant amplitudes are required over the frequency spectrum.

In this study, wide band random inputs are used for dynamic system characterization. Harmonic excitation is ruled out because the disturbance frequency band is too wide to conduct a test at each frequency (0 to 100 Hz, with a resolution of 1/3 Hz). Stepped-sine and sine-sweep inputs are undesirable, since steady-state conditions will be difficult to attain in a short test time. Lastly, transient tests will give unwanted exponentially decaying amplitude spectra.

Dynamic test input signal design

The dynamic test input signal parameters are bias voltage, voltage amplitude, voltage RMS-to-peak ratio, frequency bandwidth, time duration and sample frequency. The peak-to-peak voltages, for a quasi-static stroke length of 75 μm, are 13,2 V for actuator I and 12,3 V for actuator II. The amplitude is 50% of the peak-to-peak voltage, i.e. 6,6 V for actuator I and 6,25 V for actuator II. The bias voltages are 9,1 V for actuator I and 8,75 V for actuator II.

It was mentioned in section 4.3 that, due to a problem with availability of test equipment, it is possible to excite the coil of one actuator only. In the interest of safety, the bias voltage and voltage amplitude are selected to correspond with those of the actuator with the maximum peak-to-peak voltage, i.e. 9,1 V and 6,6 V respectively. The corresponding minimum and maximum voltages are 2,5 V and 15,7 V respectively.

Test signal bandwidth is mainly determined by the disturbance bandwidth. As was motivated in the previous section, a wide-band, white noise, random signal is used for system characterization. However, this signal contains frequencies well above the disturbance bandwidth. The signal must therefore be low-pass filtered above 100 Hz. In order to prevent filter interference in the disturbance band, the signal is filtered at a 30% higher frequency, i.e. at 130 Hz. A 4^{th} order filter is used for this purpose. High-pass filtering of the signal is not desirable, since the signal must be DC-biased. Test signal bandwidth is therefore 0 Hz to 130 Hz.

As an unwritten rule, sampling frequency should be in the order of five to ten times the maximum disturbance frequency, i.e. 500 Hz to 1 kHz. The DSP card, however, allows the use of significantly higher sampling frequencies. To make full use of its performance, the test signal is sampled at 2 kHz, which is 20 times that of the maximum disturbance frequency.

The crest factor of a signal is the inverse of its RMS-to-peak ratio. The disturbance crest factor is 2,17 (see table 3.2.1), i.e. its RMS-to-peak ratio is 0,46. Using the same crest factor, the required RMS voltage of the test signal, for an amplitude of 6,6 V, is 3,03 V. The RMS-to-peak ratio of a wide-band random signal is normally in the order of 0,25. In order to obtain a 0,46 RMS-to-peak ratio, the random signal is gained to raise the peak and then clipped. Due to the high sampling rate, clipping of the signal does not occur inside the 0-100 Hz disturbance band.

The reliability of test signal data is determined by the bandwidth, number of test samples and sample duration (see equation 4.4.5.1). In this study, test signal duration is limited to 3,2 s per sample. The number of samples is arbitrarily selected as 37. The total test duration is the product of the number of samples and duration per sample, i.e. 118 s. For a bandwidth of 100 Hz, the statistical degrees of freedom κ, from equation 4.4.5.1, is 23680. This value of κ is 237 times the value of 100, as recommended by Ewins [1991], for an 80% probability that the measured value is within 18% of the true value. The dynamic test signal parameters are summarized in table 4.4.5.1.

Table 4.4.5.1: Dynamic test signal parameters

Bias voltage	9,1 V
Voltage amplitude	6,6 V
Maximum voltage	15,7 V
Minimum voltage	2,5 V
RMS voltage	3,03 V
Crest factor	2,17
Frequency bandwidth	0 Hz to 130 Hz
Sampling frequency	2 kHz
Total duration	118 s
Number of test samples	37
Duration per sample	3,2 s

Dynamic test signal generation

As with the quasi-static signals, the signals are generated in Simulink. A signal generation block diagram is shown in figure 4.4.5.1. The signals are constructed from standard Simulink input functions, i.e. step and random functions. Every time the test signal is applied, a new random signal, with the same frequency band, RMS and peak values, is generated.

Gradual application of the input signal is desirable to prevent the excitation of unwanted transients. To this end, the random signal is multiplied with a truncated ramp function. The ramp function is created from two rate-limited step functions, as described in section 4.4.1.

The signal is low-pass filtered at 130 Hz, i.e. 30% above the maximum frequency of the disturbance band. Gains and saturation elements are used to adjust the amplitude and crest factor. The bias voltage is created using the same method as in section 4.4.1 and added to the random function.

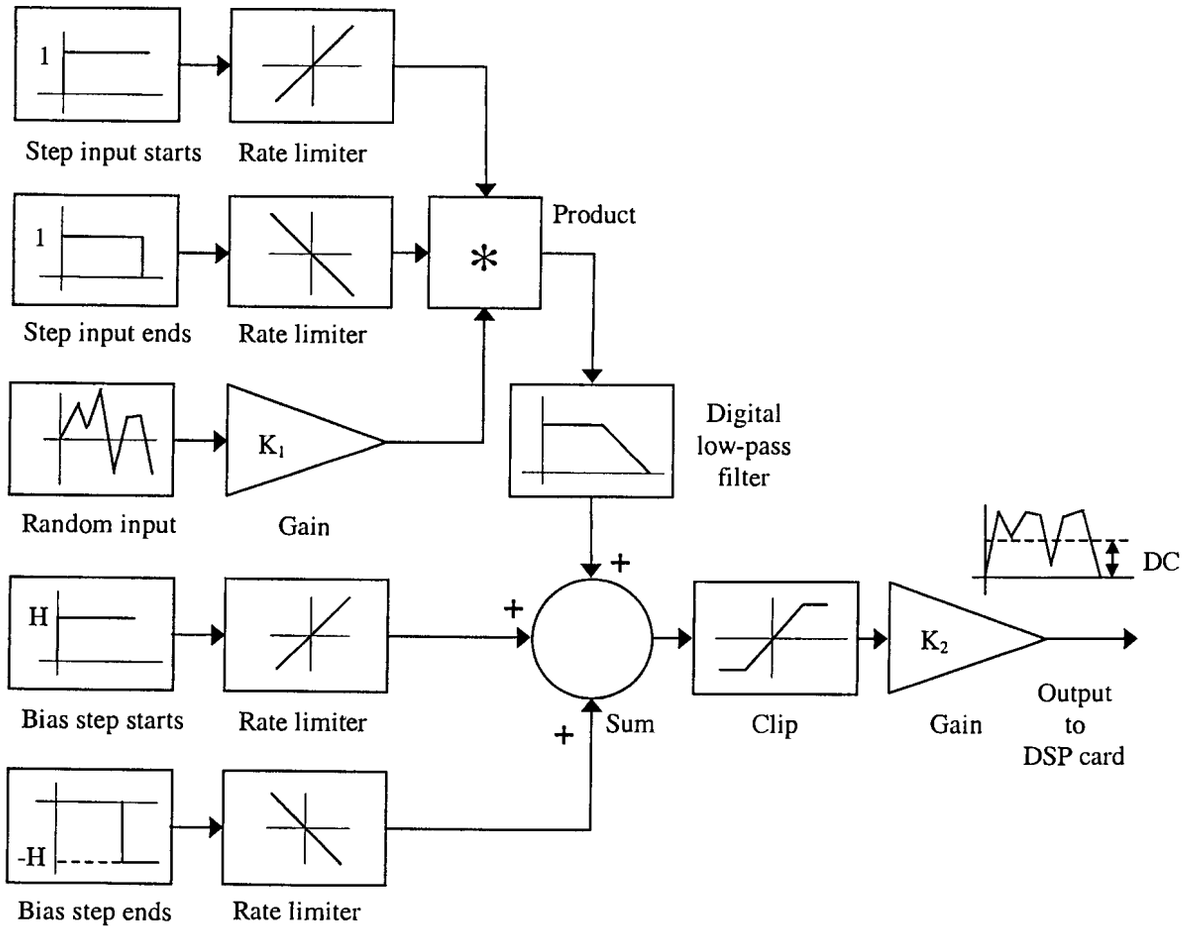

Figure 4.4.5.1: Block diagram for dynamic signal generation

The test signal is simulated and viewed using the Simulink scope. It is then divided by the DSP card gain factor (see section 4.4.1 for the procedure), coded in C and compiled to an object file. It is captured and viewed using the signal analyzer.

4.4.6 Dynamic test execution

A voltage divider with a gain of 0,25 is connected in parallel with the coil. Accelerometers are attached at the measurement positions (see figure 4.3.1.3). The DSP card output is connected to the input of the power amplifier, whose output is connected to the actuator coil. The amplifier output power is adjusted to –8,94 dB, relative to maximum power. The test signal is applied to the actuator. The coil voltage signal and one accelerometer signal are captured using the signal analyzer. A signal analyzer sampling frequency of 1280 Hz is used. This is

12,8 times the maximum frequency of the disturbance band and 8,8 times the predicted first natural frequency (see table 2.8.4.2).

A new test signal is generated and the test is repeated until all 37 tests have been completed. Total test time is 118 s. Captured data of each test is viewed on the signal analyzer screen. The data is stored in a file and transferred to the PC for processing. The tests are repeated for the other accelerometer positions. In total, 111 tests are conducted, i.e. 37 per accelerometer.

4.5 Dynamic test results

The dynamic test results are processed, presented and discussed in this section. The data processing method is explained. Transfer function magnitudes and phase spectra are calculated and shown graphically. Frequency domain characteristics, such as resonance and anti-resonance frequencies, are indicated. The dynamic test results are discussed and compared with the modelled results. It is shown that the modelled results currently compare poorly with the experimental results. Reasons for differences between experimental and modelled results are given.

Dynamic test data processing is explained in section 4.5.1. *TF* magnitude and phase angle spectra are shown in section 4.5.2. Resonance and anti-resonance frequencies are indicated. The dynamic test results are discussed in section 4.5.3. A comparison between the experimental and modelled results is drawn in section 4.5.4 and reasons for differences are given.

4.5.1 Dynamic test data processing

The data is processed in Matlab, using the signal processing toolbox. Each measured signal is multiplied with its calibration factor. The voltage signal is multiplied with the inverse of the voltage divider gain, i.e. 4 V/V. The accelerometer calibration factors are converted from mV/g to $m/s^2/V$ and multiplied with the accelerometer output signals.

The accelerations and coil input voltage are used to calculate the *TF* between coil input voltage and rotational (angular) acceleration of the instrument. The *TF* between coil input voltage and translational acceleration is also calculated. Although this *TF* does not influence LOS accuracy of the instrument, it is a valuable tool to identify the modes of excitation of the instrument. The three accelerations at the accelerometer positions, together with the rotational and translational accelerations, are shown diagrammatically in figure 4.5.1.1.

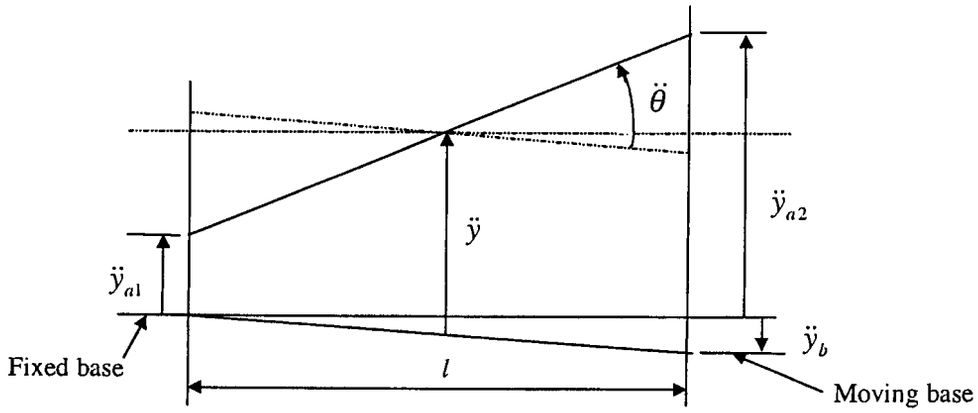

Figure 4.5.1.1: Diagram indicating measured, rotational and translational accelerations

In figure 4.5.1.1, $\ddot{y}_{a1}$ is the acceleration at accelerometer I (see figure 4.3.1.3), $\ddot{y}_{a2}$ is the acceleration at accelerometer II and $\ddot{y}_b$ is the acceleration at accelerometer III, i.e. the base acceleration. Note that $\ddot{y}_b$ is positive downward, since the accelerometer is mounted upside down under the beam. $\ddot{\theta}$ is the instrument rotational (angular) acceleration and $\ddot{y}$ is the translational acceleration of the instrument centre of mass. l is the instrument length.

TF spectra between the output accelerations and input voltage are calculated using the following equation, from Ewins [1991]:

$$G(\omega) = \frac{P_{\ddot{y}u}(\omega)}{P_{uu}(\omega)} \qquad \textbf{(4.5.1.1)}$$

where $P_{\ddot{y}u}(\omega)$ is the cross-spectral density (CSD) between input voltage and output acceleration and $P_{uu}(\omega)$ is the input voltage power spectral density (PSD).

Using equation 4.5.1.1, the following spectra are calculated: $\ddot{y}_{a1}/V$, $\ddot{y}_{a2}/V$ and $\ddot{y}_b/V$. Data overlapping is done to smooth the spectra. The number of overlaps is 256 per test, for 37 tests per accelerometer. For 256 overlaps, a test duration of 3,2 s and sampling frequency of 1280 Hz, the frequency resolution is 1/3 Hz.

The averages $G_{a1}(\omega)$, $G_{a2}(\omega)$ and $G_b(\omega)$ of the test spectra are calculated using the following equations:

$$G_{a1}(\omega) = \frac{1}{37}\sum_{i=1}^{37}\left(\frac{P_{\ddot{y}_{a1}V}}{P_{VV}}\right)_i \qquad \textbf{(4.5.1.2a)}$$

$$G_{a2}(\omega) = \frac{1}{37}\sum_{i=1}^{37}\left(\frac{P_{\ddot{y}_{a2}V}}{P_{VV}}\right)_i \qquad \textbf{(4.5.1.2b)}$$

$$G_b(\omega) = \frac{1}{37}\sum_{i=1}^{37}\left(\frac{P_{\ddot{y}_bV}}{P_{VV}}\right)_i \qquad \textbf{(4.5.1.2c)}$$

where i is the test number.

The transfer function $G_{parallel}$ for parallel excitation, i.e. excitation at actuator II and measurements at accelerometers II and III, is calculated using the following equations:

$$G_{parallel}(\omega) = G_{a2}(\omega) + G_b(\omega) \tag{4.5.1.3}$$

The sign of $G_b(\omega)$ is positive, in agreement with the sign convention in figure 4.5.1.1.

The transfer function $G_{crisscross}$ for crisscross excitation, i.e. excitation at actuator II and measurement at accelerometer I, is given by:

$$G_{crisscross}(\omega) = G_{a1}(\omega) \tag{4.5.1.4}$$

The *TF* between coil input voltage and optical instrument rotational acceleration is the difference between the parallel and crisscross accelerations, divided by the instrument length:

$$G_{rotation} = \frac{\ddot{\theta}}{V} = \frac{1}{l}\left(G_{parallel} - G_{crisscross}\right) \tag{4.5.1.5}$$

The *TF* between coil input voltage and instrument translational acceleration is the average of the parallel and crisscross *TF*'s:

$$G_{translation} = \frac{\ddot{y}}{V} = \frac{1}{2}\left(G_{parallel} + G_{crisscross}\right) \tag{4.5.1.6}$$

The parallel, crisscross, rotational and translational *TF* magnitude and phase spectra are calculated from equations 4.5.1.3 to 4.5.1.6 respectively. The spectra are shown graphically in section 4.5.2.

4.5.2 Transfer function spectra

TF magnitude and phase spectra for parallel and crisscross excitations, for a frequency band of 0 Hz to 500 Hz, are shown in figure 4.5.2.1. The figure also shows the disturbance bandwidth (*BW*) and input filter frequencies.

TF magnitude and phase spectra for rotational motion of the optical instrument are shown in figure 4.5.2.2. For the purpose of clarity, the resonance and anti-resonance frequencies for rotational motion, together with the magnitudes and phases at these frequencies, are given in table 4.5.2.1. *TF* magnitude and phase spectra for translational motion are shown in figure 4.5.2.3.

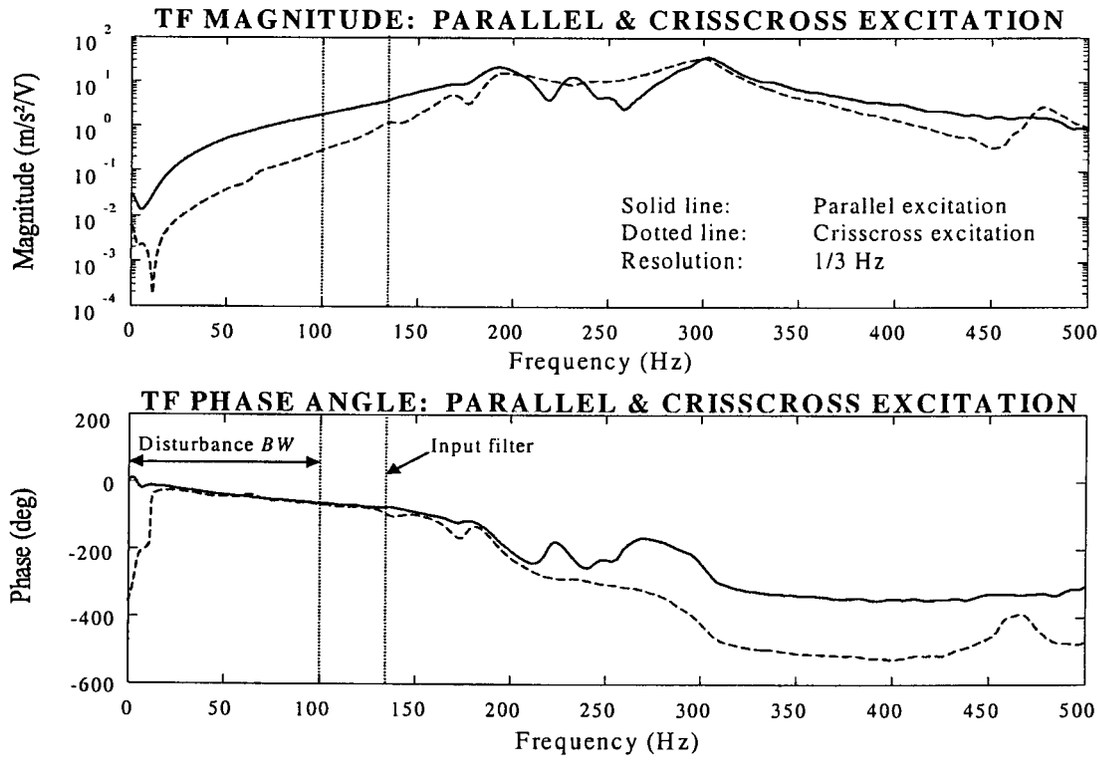

Figure 4.5.2.1: Parallel and crisscross excitation transfer function frequency spectra

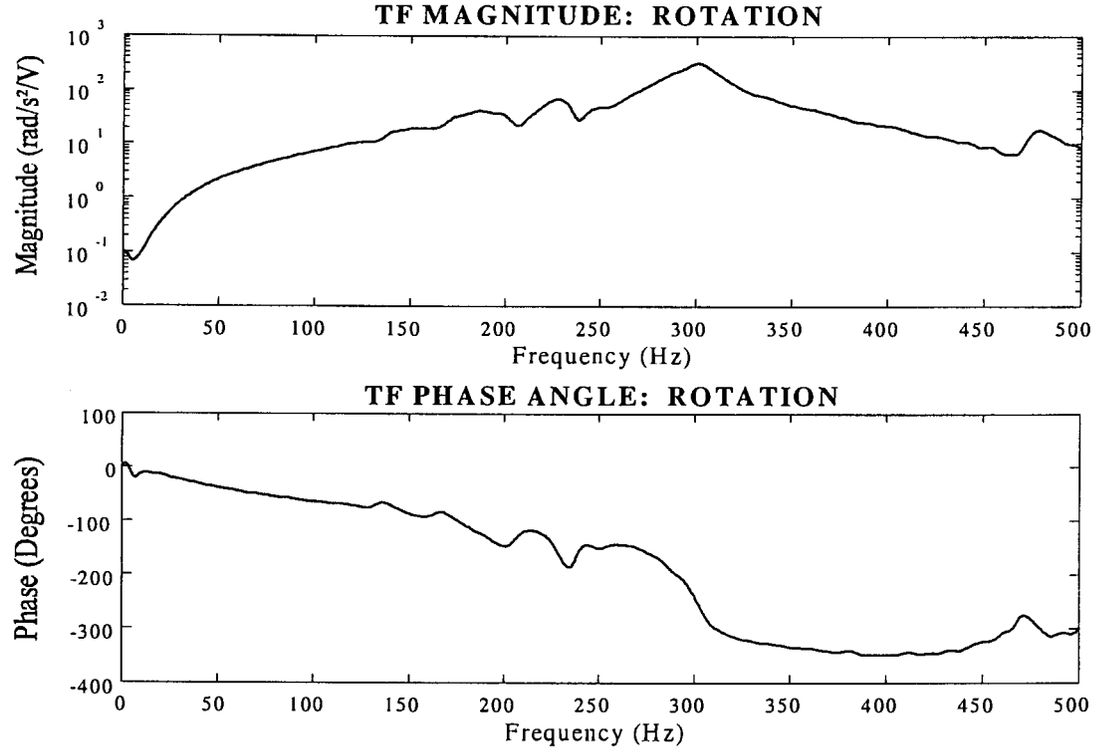

Figure 4.5.2.2: Transfer function magnitude and phase spectra for rotation

Table 4.5.2.1: Resonance and anti-resonance frequencies, magnitudes & phases for rotation

Frequency (Hz)	Resonance	Anti-resonance	Magnitude (rad/s²/V)	Phase (°)
186,3	✓	×	40,47	-128,0
206,7	×	✓	22,21	-130,4
227,3	✓	×	67,98	-153,9
238,7	×	✓	28,19	-162,0
247,0	✓	×	45,42	-147,2
254,3	×	✓	48,14	-146,3
301,0	✓	×	320,5	-246,8
466,0	×	✓	6,53	-297,2
478,3	✓	×	18,11	-294,4

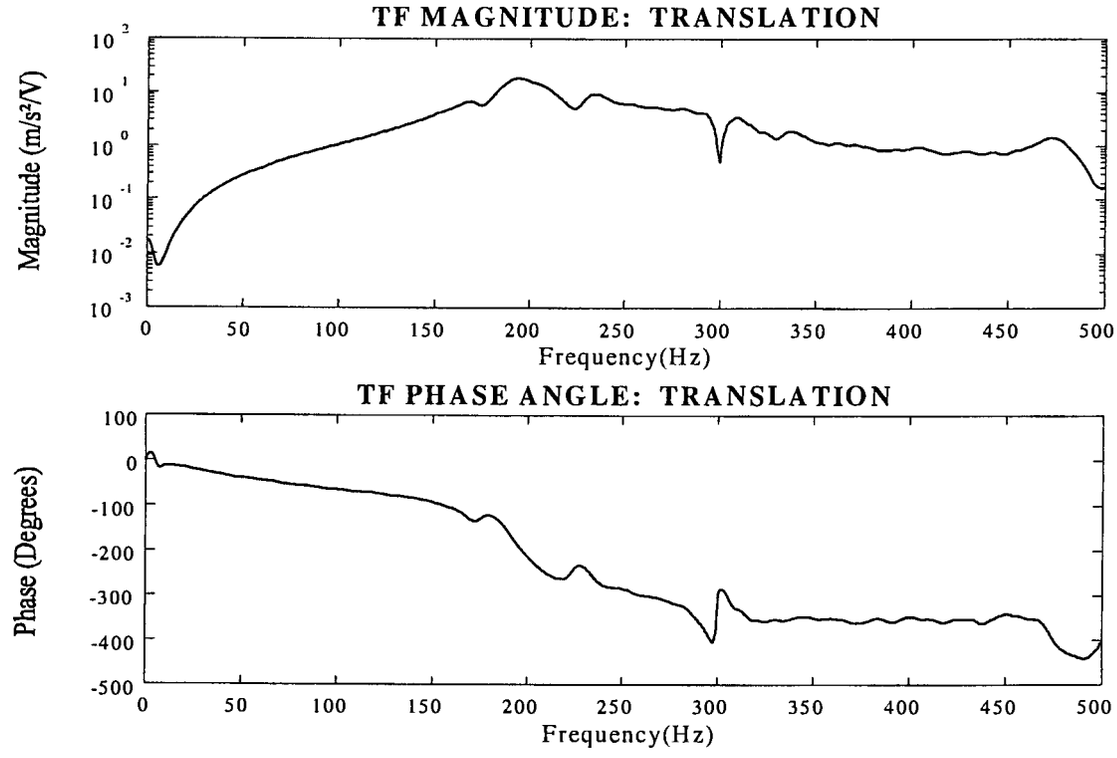

Figure 4.5.2.3: Transfer function magnitude and phase spectra for translation

4.5.3 Discussion of dynamic test results

Magnitude and phase of the rotational DOF at the end of the disturbance band, i.e. at 100 Hz, are 7,21 rad/s²/V and -63,1° respectively. All the resonance and anti-resonance frequencies are well above the disturbance band. Dominant rotational resonance frequencies are 227,3 Hz and 301 Hz. The magnitude peak at 478,3 Hz is due to base resonance. This peak also appears in the translational *TF* magnitude. An anti-resonance frequency, i.e. at 5 Hz, is

noticable in the magnitude graph in figure 4.5.2.2. This is not a system anti-resonance frequency, but rather a notch in the accelerometer transfer function.

From figure 4.5.2.3, it can be judged that the peak at 186,3 Hz, is a dominant translational resonance frequency. At this frequency, a peak also appears in the rotational *TF* spectrum. This may be attributed to different actuator stiffnesses. At 238,7 Hz, a slight peak appears in the translational *TF* magnitude, while at 301 Hz, a notch occurs in the translational magnitude, where the dominant rotational resonance frequency occurs.

It can be seen from figures 4.5.2.1 to 4.5.2.3, that the phase angles gradually drop with an increase in frequency from 0 Hz. This phenomenon also appeared in the modelled *TF* (see figure 2.8.5.3). The phase drop can be attributed to coil inductance.

The -3 dB bandwidth of the coil cannot be directly obtained from the *TF* spectra. The reason is that the system consists of two coupled (mechanical and electrical) subsystems. The coil bandwidth can however be calculated after separating the electrical characteristic of the coil (I/V-spectrum) from the mechanical characteristic. This will be done in chapter 5.

4.5.4 Comparison between experimental and modelled results

The modelled and experimentally determined input voltage to output acceleration *TF*'s, for parallel and crisscross excitation, are shown in figures 4.5.4.1 and 4.5.4.2 respectively. Modelled spectra are obtained from coil input voltage to output displacement characteristics as simulated in section 2.8.5. The modelled *TF*'s are multiplied with $-\omega^2$ to obtain voltage to angular acceleration *TF*'s. Figure 4.5.4.3 shows the modelled and experimentally determined input voltage to output angular acceleration *TF*'s.

It is clear from the abovementioned three figures that correspondence between the modelled and experimental results is poor. It can be deduced that the model is currently highly inaccurate and must therefore be improved before a controller can be designed.

Possible reasons for differences between the modelled and experimental results are as follows: Firstly, in chapter 2, an ideal SDOF model was used for each actuator. It is however obvious from this section that the experimental *TF* spectra display more resonant frequencies than the modelled spectra. This can be attributed to actuator dynamics, i.e. each actuator behaves like an excited structure, with more than one degree of freedom.

Furthermore, natural frequencies depend on a number of other factors, such as Young's modulus of the Terfenol-D rods, system distributed and concentrated mass, strain constant, gain mechanism stiffness and gain factor. Parameters such as Young's modulus and the strain constant are prestress-dependent (see section 2.2). The problems of determining prestress were discussed in more detail in sections 4.4.2 and 4.4.3.

In the third place, actuator output (displacement or acceleration) must be multiplied by -1, since a positive Terfenol-D rod elongation produces a negative actuator output displacement (see figure 3.4.1.5). The model developed in chapter 2 did not take this characteristic into

consideration, which partly explains the large differences between modelled and measured phase spectra.

Lastly, a hysteresis damping model, which was derived from quasi-static hysteresis loops published in the literature, was used in chapter 2 (see section 2.3). An effort was made to derive a dynamic damping model from the hysteresis loops. However, it was mentioned in section 2.3 that experimentally measured results are required to obtain an accurate damping model. Updating of the damping model will be explained in chapter 5, where a modal damping model will be described.

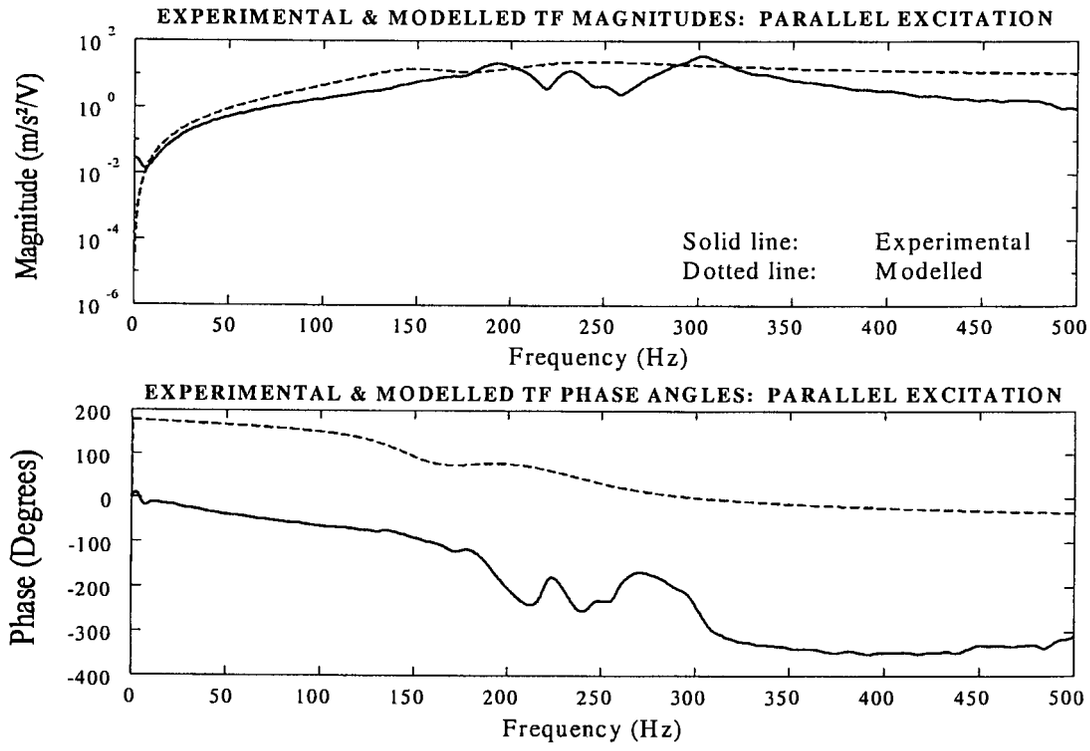

Figure 4.5.4.1: **Experimental and modelled *TF* magnitude and phase spectra for parallel excitation**

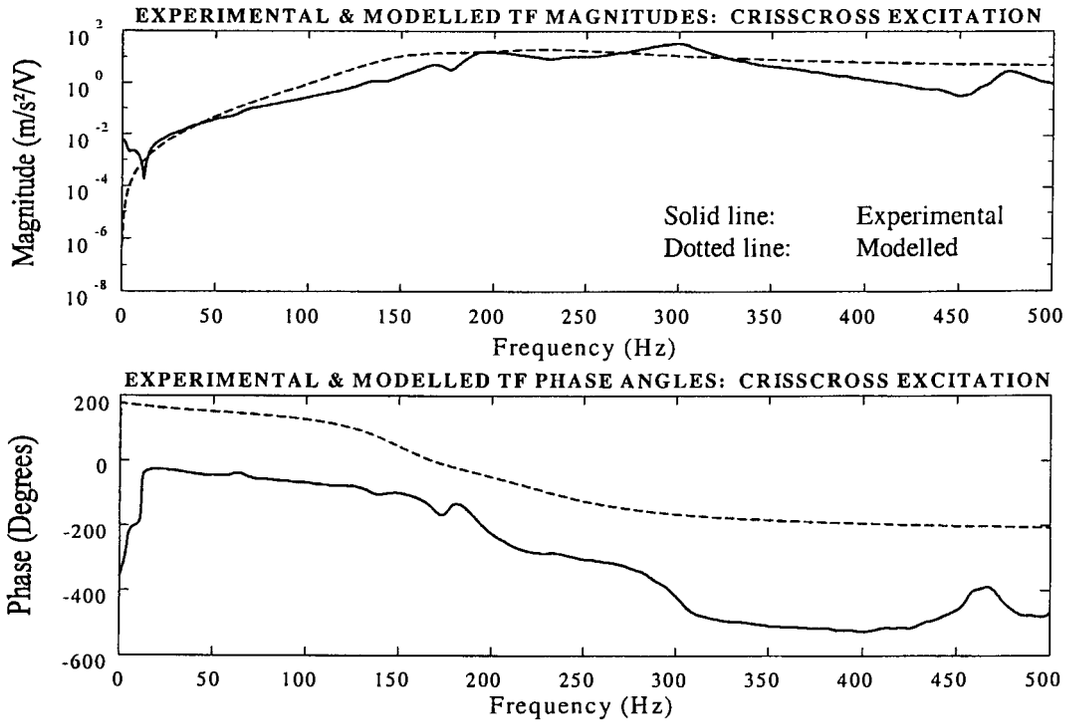

Figure 4.5.4.2: **Experimental and modelled *TF* magnitude and phase spectra for crisscross excitation**

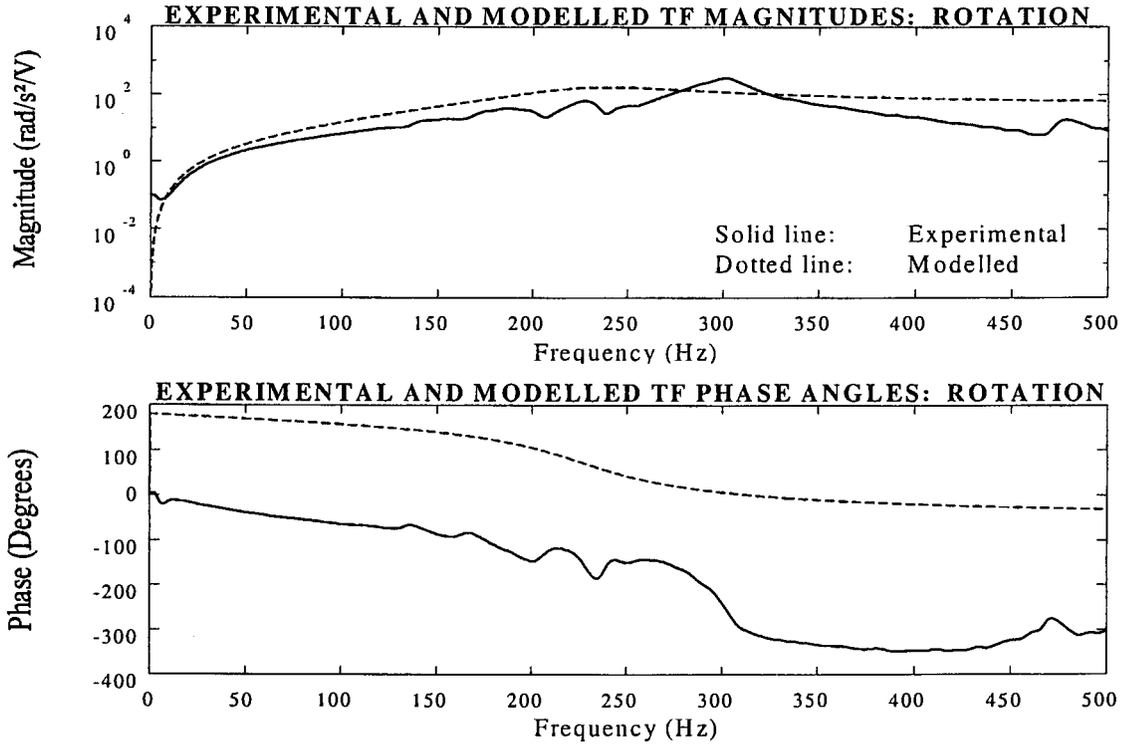

Figure 4.5.4.3: **Experimental and modelled *TF* magnitude and phase spectra for angular motion (rotation)**

4.6 Summary of chapter 4 and preview of chapter 5

The Terfenol-D actuator and LOS stabilization system characteristics were determined experimentally in this chapter. The actuators were tested quasi-statically. The system, consisting of the two actuators, optical instrument and its support structure, was tested dynamically. The purpose of the quasi-static tests was to determine the actuator linear ranges, maximum stroke length, input voltages required to produce the stroke length and bias voltage for the dynamic tests. The dynamic tests were carried out to obtain system frequency-domain *TF*'s between coil voltage and instrument angular acceleration, as well as resonance and anti-resonance frequencies. These characteristics are required to update the model and to design a controller.

The test specimens were discussed in short. Quasi-static and dynamic test setups and equipment were described and shown diagrammatically. The tests were carried out and the measured signals were processed. The results were shown graphically and discussed. It was shown that all the resonance and anti-resonance frequencies are well above the disturbance bendwidth. The dynamic test results were compared with the modelled results. Reasons for differences between the modelled and measured results were given. It was shown that the model is inaccurate and must therefore be updated to represent the measured results more accurately. Model updating will be described in chapter 5.

The model updating procedure is as follows: A 2DOF discrete model is developed for each actuator and an SDOF model of the elastically mounted base is included. The distributed model of the optical instrument is left unchanged. The electrical and mechanical subsystems are analyzed separately. The actuator, base and optical instrument equations of motion are coupled using component mode synthesis. The *TF* spectra are recalculated and compared with the experimentally determined spectra. It will be shown that the accuracy of this model is sufficient.

Chapter 5
Identification of system parameters and updating of system model

5.1 Background

In this chapter, two model updating approaches are considered. The first approach is direct identification from measured transfer function spectra, by using system identification theory. The second approach is updating of a physical model, by means of iterative parameter adjustment.

A motivation for updating the model is given and the procedure is explained. System identification theory is discussed and a suitable identification technique is selected. The selected technique is described in detail.

An updated *TF* model is obtained from the experimentally determined *TF* magnitude and phase spectra, by means of linear frequency domain identification. The *TF* is presented in numerator and denominator polynomial form. *TF* spectra of the updated model are compared with the experimentally determined *TF* spectra. It is shown that the model is sufficiently accurate. This identification technique generally gives high accuracy without a thorough knowledge of the system and is relatively quick and easy to apply.

The limitations of the *TF* model are, firstly, that no physical insight is provided into certain system characteristics, such as normal modes, modal forcing functions, coupling between mechanical and electrical subsystems, or the effects of base motion on system transmissibility. Secondly, depending on the order of the approximation model, an overdetermined system may be required to ensure high accuracy. Although the model may closely approximate the experimental data, excessive computational effort may be required to model noise, instead of system characteristics.

In order to overcome the abovementioned limitations of the *TF* model, a physical model is also derived. The model parameters are selected and adjusted until the calculated *TF* magnitude and phase spectra closely match the experimentally determined *TF* spectra. The advantage of a physical model is that it can be derived from first principles and that all the characteristics can be related to physical system parameters, such as mass, stiffness, damping and input force. The disadvantage is that the model updating procedure may be tedious.

The physical model is subsequently separated into two models, i.e. one for the electrical subsystem (coil) and one for the mechanical subsystem. Reasons for separating the models are given and the difficulties of identifying the electrical and mechanical subsystem models are mentioned. A method of analyzing the models separately is described. The coil model is presented in canonical state-space and *TF* forms. Coil *TF* magnitude and phase spectra are shown and the *TF* poles and zeroes are discussed. The relationship between coil current and modal excitation force is given.

The equations of motion of the mechanical subsystem, which consists of the two actuators, elastically mounted base and the optical instrument and support structure, are derived.

Different methods of coupling the component equations of motion are discussed. The component mode synthesis method is selected as the most suitable method for this purpose. The undamped natural frequencies and normal mode shapes are calculated. Modal damping and forcing terms are added. The latter terms are obtained from the coil model. The overall system *TF* spectra are calculated and compared with the experimentally determined *TF* spectra. It is shown that the model is sufficiently accurate.

The system open-loop transmissibility (*TR*), i.e. the base angular acceleration to optical instrument angular acceleration transfer function, is obtained by means of the physical model. The open-loop transmissibility will be required in chapter 6 to design a controller.

Motivation for updating the system model

It was shown in section 4.5 that the modelled and experimentally determined system *TF*'s differed considerably. The following reasons were mentioned. In the first place, the experimental *TF* spectra displayed more resonant frequencies than the modelled spectra. This was attributed to the fact that the SDOF actuator models were insufficient and that MDOF actuator models would be required to accurately describe system characteristics.

Secondly, due to the geometry of the gain mechanisms, a positive rod elongation would produce a negative actuator displacement (see figure 3.4.1.5). The model developed in chapter 2 did not take this characteristic into consideration, which partly explains the large differences between modelled and measured phase spectra. The problem can however be solved relatively easily, by multiplying the output with -1.

Lastly, in chapter 2, damping was modelled by means of a hysteresis damping model, which was derived from quasi-static hysteresis loops published in the literature (see section 2.3). Since the system is required to operate over a wide frequency range, a quasi-static damping model would necessarily be inaccurate. The damping model can be improved by making use of viscous modal damping.

Layout of this chapter

Model updating is systematically described in the following sections. Identification theory is discussed in short in section 5.2. A classification of identification techniques is given. Linear and nonlinear system identification techniques are respectively mentioned in sections 5.2.1 and 5.2.2. A suitable identification technique is selected in section 5.2.3, followed by a discussion of linear least-squares frequency domain identification in section 5.2.4.

In section 5.3, an updated frequency domain *TF* model is obtained from the measured spectra by means of a least-squares data fit. Model order is determined iteratively. The model parameters, i.e. the numerator and denominator polynomial coefficients, are given and the *TF* poles and zeroes are calculated. The updated model *TF* is compared with the experimentally determined *TF*.

Identification of the coil characteristics is covered in section 5.4. Separation of the coil and mechanical subsystem models is motivated and described in section 5.4.1. The coil model is presented in section 5.4.2.

The undamped equations of motion of the mechanical subsystem, for natural behaviour, are derived in section 5.5, using the component mode synthesis method. Damping and forcing terms are added in section 5.6. The latter terms are obtained from the coil model. Updated system state-space and *TF* models are derived. The updated model *TF* magnitude and phase spectra are compared with the experimentally determined *TF* spectra and it is shown that accuracy of the updated model is acceptable. The *TF* poles and zeroes are calculated and a pole-zero diagram is shown. The *TF*'s of the individual mode shapes are calculated and the dominating mode is identified. The system bandwidth is calculated. The open-loop transmissibility is calculated by means of the physical model.

A summary of chapter 5 and a preview of chapter 6 are given in section 5.7.

5.2 System identification theory

System identification theory is summarized in this section. A broad classification of identification model types is given. Linear and nonlinear, as well as time and frequency domain identification models and techniques are discussed in short. A suitable identification technique is selected for this study and described.

Linear time-domain and frequency-domain identification models and techniques are mentioned in section 5.2.1. In section 5.2.2, nonlinear time- and frequency domain identification models and techniques are mentioned. The most suitable identification technique is selected in section 5.2.3, followed by a detailed discussion of the technique in section 5.2.4.

The process of constructing models and estimating unknown system parameters from experimental data, is called system identification [Franklin et al, 1990]. A broad classification of estimation methods is given by Schoukens & Pintelon [1991]. The methods are classified in three categories, i.e. nature of the selected model, application of the model and stochastic characteristics of the measurements. A classification of identification methods is summarized in table 5.2.1.

Table 5.2.1: Classification of system identification methods [Schoukens & Pintelon, 1991]

Category	
Selected model:	Parametric versus nonparametric Time domain versus frequency domain Linear-in-the-parameters versus nonlinear-in-the-parameters
Application:	Time invariant systems versus time varying systems Linear systems versus nonlinear systems
Stochastic characteristics:	Noise on the input and output versus noise on the input only versus noise on the output only

A category which can be added to the above, is on-line (real-time) versus off-line (classical) identification. On-line and off-line identification are discussed in more detail by Sinha & Kuszta [1983]. The determination of frequency spectra, e.g. those shown in section 4.5, can be done on-line, using modern signal analyzers. Extraction of model parameters, such as natural frequencies, damping factors and modal amplitudes, is mostly done off-line.

Parametric actuator and LOS stabilization system models were developed in chapter 2. The state-space and *TF* models were derived in terms of the Terfenol-D magnetostrictive and magnetization parameters and the actuator, coil and system dynamic parameters (see sections 2.4 to 2.8). Nonparametric models were obtained from the experimental test results in chapter 4, where the actuator and system *TF*'s were represented by their respective spectra (see figure 4.5.2.2). Time domain simulations of the actuator behaviour were done in chapter 2 (see section 2.7.3), while the system frequency domain *TF's* were derived from the complex Laplace domain *TF's* in section 2.8.5.

A distinction is made between a linear system and a linear-in-the-parameters system. A model is called linear-in-the-parameters if there is a linear relationship between its parameters and its output [Franklin et al, 1990]. The actuator and system frequency domain *TF's* are nonlinear-in-the-parameters. Consider for instance the modelled SDOF actuator frequency domain output equation, which, from equation 2.5.3.5, can be written as:

$$Y(j\omega) = \frac{p_0}{\left(q_0 - q_2\omega^2\right) + j\omega\left(q_1 - \omega^2\right)} U(j\omega) \qquad \textbf{(5.2.1)}$$

where ω is the angular excitation frequency, $U(j\omega)$ and $Y(j\omega)$ are the complex frequency domain coil voltage input and actuator displacement output respectively. The parameters p_0, q_0, q_1 and q_2 are the *TF* numerator and denominator polynomial coefficients. It can be seen from the above equation that $Y(j\omega)$ is a nonlinear function of the *parameters*.

A system is linear if there is a linear relationship between its input and output. In equation 5.2.1, the ratio of the output $Y(j\omega)$ to the input $U(j\omega)$ at any given frequency ω, is linear.

5.2.1 Linear system identification models and techniques

The objective of linear identification is to obtain a system model in transfer function or state-space form, from measured data. Linear identification models and techniques include the following: The ARMA method for discrete time-domain identification of linear systems, time-domain models from free-decay response, identification models for time-varying systems, regression techniques to determine model coefficients, Laplace- and frequency-domain *TF* models from discrete time-domain models, frequency-domain models from measured *TF* spectra and state-space identification of linear systems. The abovementioned models are not discussed here. A summary of each of the methods is given in appendix U.

5.2.2 Nonlinear system identification models and techniques

Techniques for determining the parameters of nonlinear systems from measured data can broadly be classified as time-domain techniques, frequency-domain techniques, force-state component identification and identification using neural networks. The methods are summarized in appendix U.

5.2.3 Selection of a suitable identification technique

For the purpose of this study, the system models that will be identified, will mainly be parametric, time invariant, linear, frequency *(ω)* domain *TF* and state-space models. Time-varying, nonlinear and time-domain models will not be considered.

The reasons are, firstly, that the models developed in chapter 2 are state-space and frequency-domain *TF* models. These models will serve as a guide for updating the system model from experimentally-determined *TF* spectra. A second reason is that *TF* and state-space models are mostly used for the design of classical and optimal controllers. Adaptive controllers, which adjust control parameters in real time using learning algorithms, are an exception. Adaptive controllers will not be considered in this study. A third reason is that experimentally-determined spectra already exist. These spectra were obtained during the test phase, as described in chapter 4. The last reason is that ω-domain spectra give physical insight into dynamic characteristics, such as magnitude, phase angle, number of DOF's, resonance and anti-resonance frequencies, DC gains and frequency bandwidths.

The disadvantages are firstly that ω-domain models are nonlinear-in-the-parameters, as discussed before. Secondly, processing is almost always done off-line. Real-time determination of *TF* polynomial coefficients is not possible with the currently available equipment. Thirdly, during conversion from a *TF* model to a state-space model, a canonical model almost always results. The canonical model states do not necessarily correspond with the selected model states. The latter must be obtained by a similarity transform. Lastly, frequency-domain identification requires longer data records than time-domain identification [Liu & Miller, 1995].

In this chapter, the coil voltage to angular acceleration *TF* of the optical instrument is obtained from measured spectra in the frequency-domain, using the Gauss-Newton technique. A physical system model is also derived. The coil and mechanical subsystem models are separated and a canonical coil model is developed.

Actuator characteristics are modelled by means of 2DOF discrete models, instead of the SDOF models used in chapter 2. Substructure synthesis is used to couple the actuator, optical instrument and base models. The actuator and base stiffnesses are adjusted until the modelled *TF* spectra match the experimentally determined natural frequencies with an acceptable degree of accuracy. The normal mode shapes of the optical instrument are subsequently calculated. The mechanical subsystem model is coupled to the coil model in state-space. The system *TF* magnitude and phase spectra are calculated and compared with the experimentally determined spectra. The coil back-emf is not modelled.

5.2.4 Least-Squares method for frequency-domain identification

The frequency domain *TF* model which approximates the measured spectra, can be written as follows in complex form:

$$\hat{G}(j\omega)=\frac{\hat{P}(j\omega)}{\hat{Q}(j\omega)} \tag{5.2.4.1}$$

where $\hat{G}(j\omega)$ is the approximate *TF* and $\hat{P}(j\omega)$ and $\hat{Q}(j\omega)$ respectively represent the numerator and denominator of $\hat{G}(j\omega)$. $\hat{P}(j\omega)$ and $\hat{Q}(j\omega)$ are polynomials in $j\omega$:

$$\hat{P}(j\omega)=\sum_{k=0}^{M} p_k (j\omega)^k \tag{5.2.4.2a}$$

$$\hat{Q}(j\omega)=\sum_{l=0}^{N} q_l (j\omega)^l \tag{5.2.4.2b}$$

where M is the order of the numerator polynomial and N is the order of the denominator polynomial. p_k and q_l are the numerator and denominator polynomial coefficients respectively. For the sake of convenience, the polynomial coefficients are written as follows in vector form:

$$\{C_p\}=\{p_0, p_1, \cdots, p_M\}^T \tag{5.2.4.3a}$$

$$\{C_q\}=\{q_0, q_1, \cdots, q_N\}^T \tag{5.2.4.3b}$$

where $\{C_p\}$ and $\{C_q\}$ are the numerator and denominator polynomial coefficient vectors respectively. These two vectors are combined as follows in one coefficient, or parameter, vector $\{C\}$:

$$\{C\}=\{\{C_p\},\ \{C_q\}\}^T=\{p_0, p_1, \cdots, p_M,\ \ q_0, q_1, \cdots, q_N\}^T \tag{5.2.4.4}$$

It is desirable to obtain a model which is proper, i.e. a model whose numerator order is less than or equal to the denominator order:

$$M \le N \tag{5.2.4.5}$$

In order to ensure a high degree of accuracy, large values of M and N are required. However, the larger M and N, the more computationally intensive the identification procedure becomes. Furthermore, in a physical system model, such as an equation of motion, M and N are determined by the number of normal modes.

The purpose of the model is to represent the experimentally-determined *TF* spectra as accurately as possible. The difference between the modelled *TF* and experimentally-determined *TF* is known as the estimation error and is given by:

$$e = G - \hat{G} \tag{5.2.4.6}$$

where e is the error, $\hat{G}$ is the modelled *TF* and G is the experimentally determined *TF*. G is known at discrete frequencies (see section 4.5), thus the error can only be evaluated at these frequencies.

The error e_r at the r-th frequency is:

$$e_r = G_r - \hat{G}_r \tag{5.2.4.7}$$

where $\hat{G}_r$ and G_r are the approximate *TF* and measured *TF* at the r-th frequency, given by:

$$\hat{G}_r = \hat{G}(j\omega_r) \tag{5.2.4.8a}$$
$$G_r = G(j\omega_r) \tag{5.2.4.8b}$$

It can be seen from equations 5.2.4.7 and 5.2.4.8, it can be seen that the error varies with frequency. As a globally accurate model is required, the error squared is summed and minimized over the frequency band.

The global error is given by the following equation:

$$E = \sum_{r=1}^{N} |e_r|^2 \tag{5.2.4.9}$$

where E is the global error of the model and N is the number of discrete frequencies.

Both $\hat{G}$ and G are complex (see equations 5.2.4.8). The global error can therefore be expressed as the sum of the error of the real term squared plus the error of the imaginary term squared [Schoukens & Pintelon, 1991]:

$$E = \sum_{r=1}^{N} \left[\left(\mathrm{Re}\{G_r\} - \mathrm{Re}\{\hat{G}_r\} \right)^2 + \left(\mathrm{Im}\{G_r\} - \mathrm{Im}\{\hat{G}_r\} \right)^2 \right] \tag{5.2.4.10}$$

E is a nonlinear function of the polynomial coefficient vector C:

$$E = E(C) \tag{5.2.4.11}$$

For the global error to be a minimum, the partial derivative of the error with respect to the model parameters, must be zero:

$$\frac{\partial E}{\partial C_l} = 0, \quad l = 1, 2, \cdots, M + N + 2 \qquad \textbf{(5.2.4.12)}$$

where C_l is the l-th element of the model parameter vector, given by equation 5.2.4.4. The coefficients which will minimize E, must be determined. Methods for solving LS problems are discussed next.

Methods for solving least-squares problems

Least-squares (LS) problems can, inter alia, be classified as linear and nonlinear problems. The following linear LS solution techniques are described by Chen et al [1989]: Gaussian elimination, Cholesky decomposition, classical and modified Gram-Schmidt methods, Householder transformation, Givens method and singular value decomposition (SVD). These techniques are applicable to linear-in-the-parameters systems.

Frequency-domain models are nonlinear-in-the-parameters (see equation 5.2.1). The following nonlinear LS solution techniques, for nonlinear-in-the-parameters systems, are described by Schoukens & Pintelon [1991]: The gradient method, Newton-Raphson algorithm, Gauss-Newton algorithm and the method of Levenberg-Marquardt. Methods to obtain linear-in-the-parameters models for frequency-domain identification purposes are described by Schoukens & Pintelon [1991]. These methods have however become obsolete due to the rapid development of computers.

The main drawback of the gradient method is its slow convergence. Speed of convergence can be improved using the Newton-Raphson method, which gives quadratic convergence. However, to make this possible, 2nd order derivatives must be calculated, which may be time-consuming. Furthermore, the Newton-Raphson method does not gurarantee convergence.

The problem of calculating 2nd order derivatives can be avoided by using the Gauss-Newton method. For most problems the Gauss-Newton method demands less computation time per iteration step than the Newton-Raphson algorithm. In the neighbourhood of the solution, the Newton-Raphson method will generally converge faster than the Gauss-Newton method. However, the convergence region of the Gauss-Newton method is larger than that of the Newton-Raphson method. As with the Newton-Raphson method, the Gauss-Newton method does not guarantee convergence.

A method which assures unconditional convergence, at least to a local minimum, is the Levenberg-Marquardt method. The method is a combination between the gradient and Gauss-Newton methods.

The Gauss-Newton method is well-established for nonlinear-in-the-parameter LS identification. This method is also used in this study to obtain the *TF* numerator and denominator coefficients from experimentally-determined *TF* frequency spectra. The method is described in appendix V.

5.3 Updated system *TF* model from least-squares data fit

In this section, an approximate transfer function is obtained by doing a least-squares data fit to the experimentally determined frequency domain spectra. The *TF* is written in numerator and denominator polynomial form and the polynomial coefficients are tabled. The approximate *TF* magnitude and phase spectra are shown graphically and compared with the experimentally determined spectra. The poles and zeroes are tabled.

The approximate frequency domain transfer function $\hat{G}(j\omega)$ is written in the following form:

$$\hat{G}(j\omega) = \frac{\hat{P}(j\omega)}{\hat{Q}(j\omega)} \tag{5.3.1}$$

$\hat{P}(j\omega)$ and $\hat{Q}(j\omega)$ respectively represent the *TF* numerator and denominator polynomials in $j\omega$, given by:

$$\hat{P}(j\omega) = \sum_{k=0}^{M} p_k (j\omega)^k \tag{5.3.2a}$$

$$\hat{Q}(j\omega) = \sum_{l=0}^{N} q_l (j\omega)^l \tag{5.3.2b}$$

where p_k and q_l are the k-th numerator and l-th denominator polynomial coefficients respectively. M and N are the numerator and denominator polynomial orders respectively.

M and N are determined iteratively. Initial values of M and N are determined from the number of resonance and anti-resonance frequencies of the experimentally determined *TF* (see table 4.5.2.1). A pole is added to model the coil *TF*. The total number of poles is therefore 2 per resonance frequency, plus one coil pole. The number of zeroes is 2 per anti-resonance frequency. Two zeroes, in the origin of the complex plane, are added. The notch, which appears at approximately 5 Hz in the *TF* spectra (see figure 4.5.2.2), is not accounted for, since it is assumed that it is an accelerometer characteristic, rather than a system characteristic (see also section 4.3.3).

Five resonance and four anti-resonance frequencies are listed in table 4.5.2.1. Applying the method set out above, M and N are:

$$M = 10 \tag{5.3.3a}$$
$$N = 11 \tag{5.3.3b}$$

The difference between M and N is the relative degree of freedom of the *TF*, given by:

$$M - N = 1 \tag{5.3.4}$$

With the above values of M and N, the Gauss-Newton method is used to fit an approximate transfer function $\hat{G}(j\omega)$, to the experimental spectra. The numerator and denominator polynomial coefficients are obtained from the data fit.

$\hat{G}(j\omega)$ is calculated using equations 5.3.2. The magnitude and phase of $\hat{G}(j\omega)$ are calculated and compared with the experimental spectra. If the accuracy of the fit is poor, M and N are each increased by 2. The process is repeated until the poles and zeroes coincide. Coinciding poles and zeroes are then eliminated. After two iterations, the following values of M and N result:

$$M = 14 \qquad \textbf{(5.3.5a)}$$
$$N = 15 \qquad \textbf{(5.3.5b)}$$

The *TF* numerator and denominator polynomial coefficients p_k and q_l, which minimize the LS error for the above values of M and N, are given in table 5.3.1.

Table 5.3.1: Polynomial numerator and denominator coefficients

Coefficient	Value
p_0	0
p_1	0
p_2	$-1{,}0667.10^{43}$
p_3	$-6{,}9076.10^{39}$
p_4	$-2{,}6194.10^{37}$
p_5	$-1{,}5266.10^{34}$
p_6	$-2{,}3520.10^{31}$
p_7	$-1{,}2339.10^{28}$
p_8	$-9{,}4729.10^{24}$
p_9	$-4{,}5154.10^{21}$
p_{10}	$-1{,}6358.10^{18}$
p_{11}	$-7{,}3367.10^{14}$
p_{12}	$-8{,}0479.10^{10}$
p_{13}	$-4{,}0799.10^{7}$
p_{14}	$1{,}7934.10^{3}$
q_0	$4{,}3672.10^{47}$
q_1	$1{,}3445.10^{45}$
q_2	$2{,}1924.10^{42}$
q_3	$4{,}1830.10^{39}$
q_4	$3{,}9207.10^{36}$
q_5	$5{,}2226.10^{33}$
q_6	$3{,}4152.10^{30}$
q_7	$3{,}3812.10^{27}$
q_8	$1{,}5984.10^{24}$
q_9	$1{,}2220.10^{21}$
q_{10}	$4{,}0475.10^{17}$
q_{11}	$2{,}4539.10^{14}$
q_{12}	$5{,}1186.10^{10}$
q_{13}	$2{,}5149.10^{7}$
q_{14}	$2{,}4468.10^{3}$
q_{15}	1

The magnitude and phase spectra of the approximate transfer function $\hat{G}(j\omega)$, together with the experimentally determined spectra, are shown in figure 5.3.1. The poles and zeroes of $\hat{G}(j\omega)$ are given in table 5.3.2.

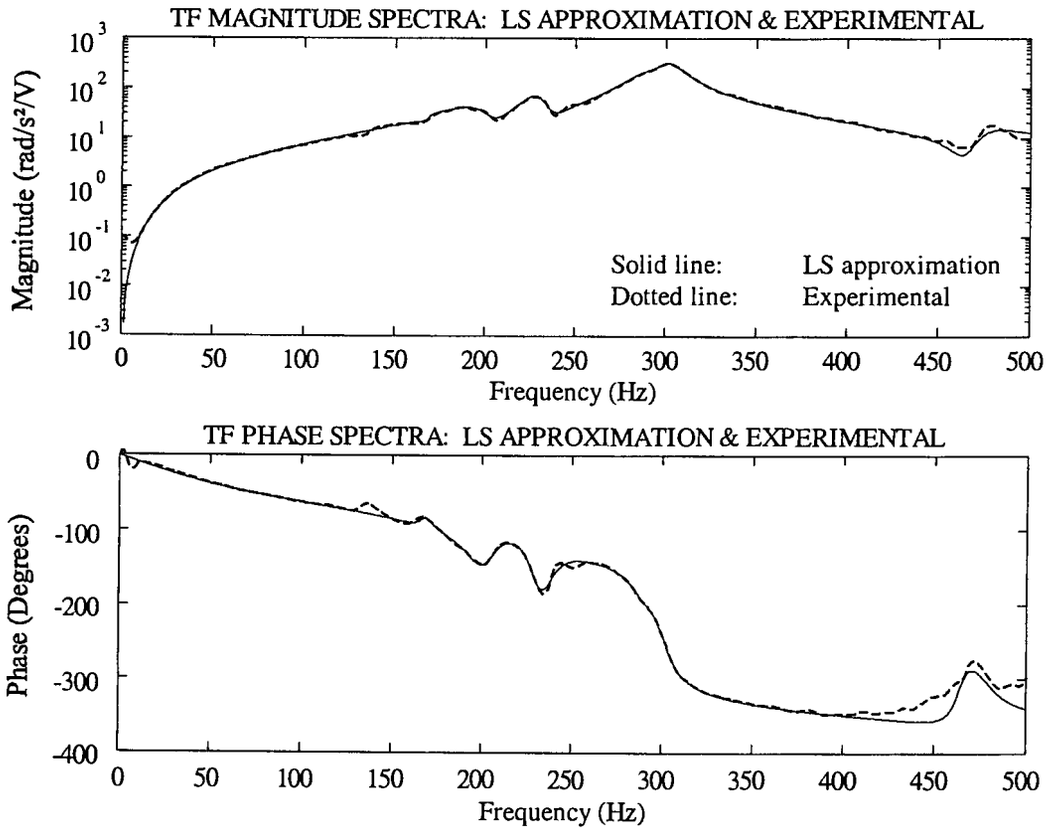

Figure 5.3.1: LS approximation and experimentally determined TF spectra

It can be seen from figure 5.3.1 that the accuracy of the magnitude spectrum is acceptable for a frequency band of 10 Hz to 430 Hz. For frequencies below 10 Hz, inaccuracies are caused by the two zeroes in the origin of the complex plane. A more accurate low-frequency model can for instance be obtained by detailed accelerometer modelling. Accuracy of the phase spectrum is acceptable for a frequency band of 10 Hz to 350 Hz. The phase is slightly inaccurate at 130 Hz and 240 Hz.

Table 5.3.2: Transfer function poles and zeroes:

Frequency (Hz)	Damping factor (%)	Pole	Zero	Type	Sign of real part
0		×	✓	Real	
0		×	✓	Real	
68,74		✓	×	Real	Negative
167,5	2,29	×	✓	Complex conjugate pair	Negative
168,4	2,48	✓	×	Complex conjugate pair	Negative
197,3	6,48	✓	×	Complex conjugate pair	Negative
205,2	3,96	×	✓	Complex conjugate pair	Negative
228,6	2,69	✓	×	Complex conjugate pair	Negative
237,0	3,21	×	✓	Complex conjugate pair	Negative
263,2	40,76	✓	×	Complex conjugate pair	Negative
287,7	3,25	✓	×	Complex conjugate pair	Negative
291,0	3,53	×	✓	Complex conjugate pair	Negative
301,2	2,61	✓	×	Complex conjugate pair	Negative
323,7		×	✓	Real	Negative
463,7	1,29	×	✓	Complex conjugate pair	Negative
474,7	2,68	✓	×	Complex conjugate pair	Negative
4016,1		×	✓	Real	Positive

All the poles and zeroes but one, are inside the test band of 0,33 Hz to 500 Hz. The zero at 4016 Hz is well above the test band. The real pole at 69 Hz is inside the isolation bandwidth of the system, i.e. 2,5 Hz to 100 Hz. The real parts of all the poles are negative. The real parts of all the zeroes, except for the two zeroes in the origin of the complex plane and the zero at 4016 Hz, are negative. The sign of the latter zero indicates that $\hat{G}(j\omega)$ is non-minimum phase.

5.4 Identification of coil characteristics

The system spectra shown in figures 4.5.2.1 to 4.5.2.3 are spectra of a system which consists of two coupled subsystems, i.e. electrical and mechanical subsystems. The electrical subsystem consists of the coils, while the mechanical subsystem consists of the actuators, elastically-mounted base, optical instument and its support structure. The coil input is the supply voltage V and the output is current I. The mechanical subsystem input is actuator force and the output is the optical instrument angular acceleration $\ddot{\theta}$. Actuator force is related to coil current by the equation:

$$F = F_I I \qquad \textbf{(5.4.1)}$$

where F_I is force per unit current.

A block diagram of the system is shown in figure 5.4.1. The two subsystems and the subsystem coupling element are also shown.

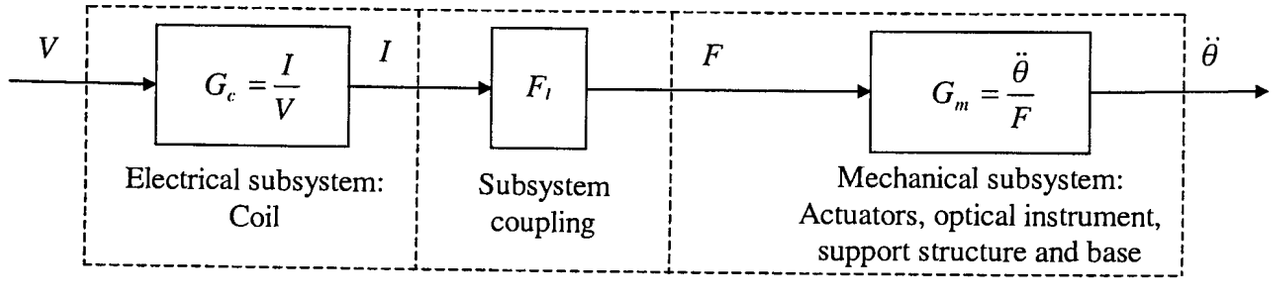

Figure 5.4.1: System block diagram

The system *TF* is given by:

$$G = G_c F_I G_m \tag{5.4.2}$$

where G_c is the coil transfer function and G_m is the mechanical subsystem transfer function.

5.4.1 Separation of electrical and mechanical subsystem models

It is convenient to separate the coil and mechanical subsystem characteristics, since this measure will make it possible to obtain the coil *TF*, true normal mode shapes, natural frequencies, damping factors and forces. One method of directly obtaining the coil characteristics, would be to measure voltage and current during the test phase and to calculate the coil *TF*, i.e. *I/V*. A signal analyzer with three analogue input channels, i.e. one for each of the voltage, current and acceleration signals, would be required for this purpose. Alternatively, an additional set of tests could be done to measure the coil current, using the available signal analyzer.

Obtaining the mechanical subsystem *TF*, in isolation of the electrical characteristics, would be more difficult, since both output angular acceleration and input force would be required for this purpose. Firstly, angular acceleration cannot be measured directly. Angular acceleration can however be calculated from measured vertical accelerations, as was explained in section 4.5. Secondly, force could not be measured directly, since the sensors required for this purpose are load cells, which would not fit between the actuators and support structure. A relatively flat, washer-type, load cell would be a welcome solution to the problem. Although this type of load cell is currently under development, it is not ready for use in this study.

An alternative identification method is to obtain the coil and mechanical subsystem *TF*'s from the system *TF*. To make this technique possible, a number of assumptions must be made. It is firstly assumed that all the peaks and notches in the *TF* spectra are mechanical subsystem characteristics, with the peaks occuring at resonance frequencies and the notches occuring at anti-resonance frequencies. It is further assumed that coil damping is high. A consequence of this assumption is that the coil *TF* will not display sharp resonance peaks.

A frequency domain *TF* of the system is obtained from an LS data fit, using the Gauss-Newton method (see appendix V). The resonance and anti-resonance frequencies are identified and their corresponding poles and zeroes are calculated. Using the poles and zeroes, the

mechanical subsystem *TF* is derived. The quotient of the system *TF* and the mechanical subsystem *TF* gives the coil *TF*.

An advantage of this identification technique is that the subsystem *TF*'*s* can be relatively easily determined. Furthermore, the mechanical subsystem *TF* can be written in modal form and the dominating mode can be identified. The disadvantage, however, is that the back-emf cannot be obtained using this technique.

5.4.2 Coil model

The coil *TF* is the ratio between current I and voltage V. The complex frequency domain transfer function $G_c(j\omega)$ is given by:

$$G_c(j\omega) = \frac{I(j\omega)}{V(j\omega)} = \frac{\sum_{ck=0}^{M_C} p_{ck}(j\omega)^{ck}}{\sum_{cl=0}^{N_C} q_{cl}(j\omega)^{cl}} \qquad \textbf{(5.4.2.1)}$$

where p_{ck} and q_{cl} are the k-th numerator and l-th denominator polynomial coefficients respectively. The coefficicents for $M_c = 2$ and $N_c = 3$ are given in table 5.4.2.1. The *TF* magnitude and phase spectra are shown in figure 5.4.2.1.

Table 5.4.2.1: Coil *TF* numerator and denominator polynomial coefficients

Coefficient:	$p_{c0}(\text{x}10^8)$	$p_{c1}(\text{x}10^5)$	$p_{c2}(\text{x}10^1)$	$q_{c0}(\text{x}10^9)$	$q_{c1}(\text{x}10^6)$	$q_{c2}(\text{x}10^3)$	$q_{c3}(\text{x}10^0)$
Value:	4,1629	1,0574	1,3316	1,3321	3,4874	1,8168	1

The coil Laplace-domain *TF* is obtained by substitution of $j\omega$ with s in equation 5.4.2.1:

$$G_c(s) = \frac{\sum_{ck=0}^{M_C} p_{ck} s^{ck}}{\sum_{cl=0}^{N_C} q_{cl} s^{cl}} \qquad \textbf{(5.4.2.2)}$$

where the p_{ck} and q_{cl} coefficients are equal to those in equation 5.4.2.1.

The coil *TF* has two complex conjugate zeroes, one real pole and two complex conjugate poles. The undamped frequency and damping ratio of the zeroes are 889,9 Hz and 71,01 % respectively. The frequency of the zeroes is above the maximum frequency of the measurenent band (500 Hz). The frequency of the real pole is 74,19 Hz. The undamped frequency and damping ratio of the poles are 269,1 Hz and 39,95% respectively. The real parts of all the coil poles and zeroes are negative.

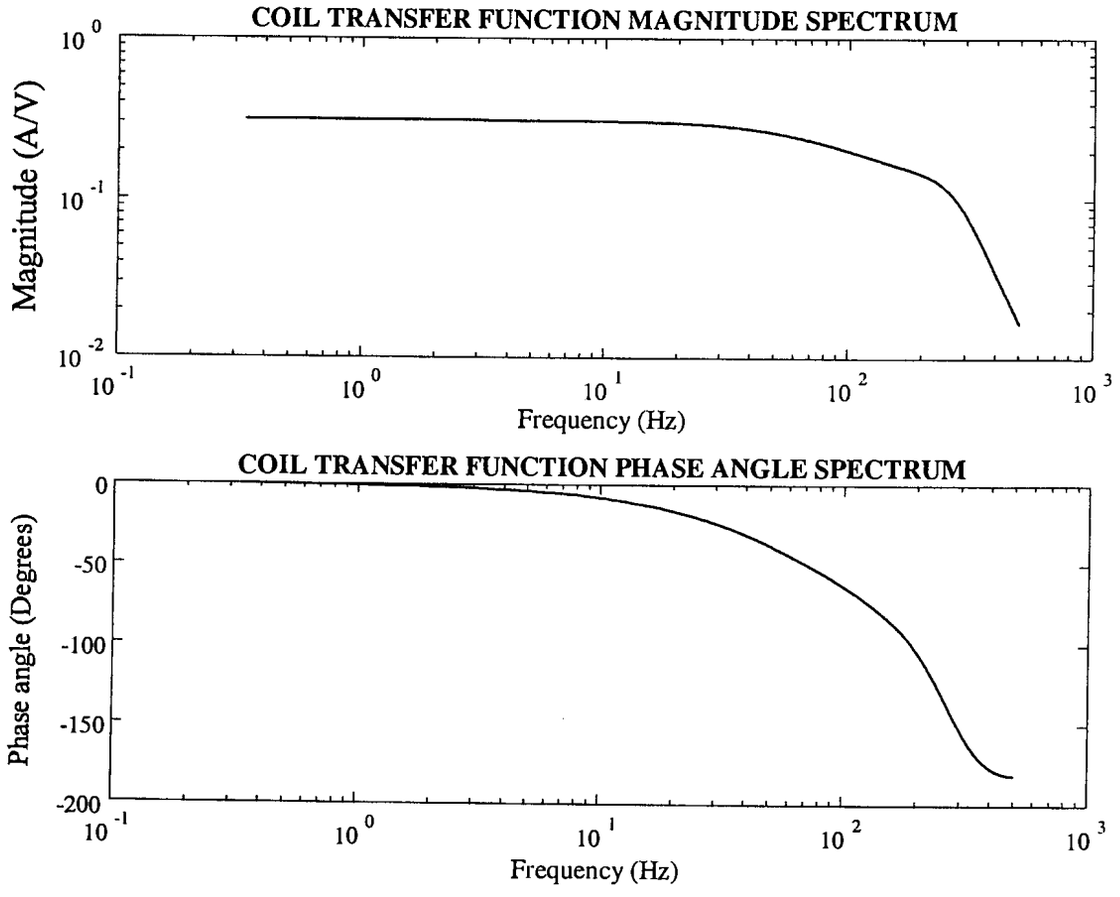

Figure 5.4.2.1: Coil transfer function magnitude and phase spectra

The coil *TF* at DC is the ratio of p_0/q_0, which is equal to the inverse of the coil resistance of 3,2 Ω, i.e. 0,3125 A/V. The coil *TF* magnitude at 100 Hz is 3,69 dB lower than the DC magnitude. The -3 dB bandwidth of the coil is 84 Hz. The coil bandwidth is lower than the required bandwidth of 100 Hz and the design bandwidth of 150 Hz (see section 3.5.2). This can mainly be attributed to the presence of the real pole at 74 Hz. It will however be shown in section 5.6, that, due to the presence of mechanical subsystem poles above 100 Hz, the overall system bandwidth is 199 Hz, which exceeds the required bandwidth by 99 Hz. The complex poles and zeroes of the coil *TF* are well above the disturbance bandwidth of 100 Hz.

The coil state-space model is given by:

$$\dot{x}_c = A_c x_c + B_c V \qquad \textbf{(5.4.2.3a)}$$
$$I = C_c x_c + D_c V \qquad \textbf{(5.4.2.3b)}$$

where x_c is the coil state vector and A_c, B_c, C_c and D_c are the coil state and output matrices, given by:

$$A_c = \begin{bmatrix} 0 & 1 & 0 \\ 0 & 0 & 1 \\ -q_{c0} & -q_{c1} & -q_{c2} \end{bmatrix} \qquad \textbf{(5.4.2.4a)}$$

$$B_c = \{0 \quad 0 \quad 1\}^T \qquad \textbf{(5.4.2.4b)}$$

$$C_c = \{p_{c0} \quad p_{c1} \quad p_{c2}\} \qquad \textbf{(5.4.2.4c)}$$

$$D_c = 0 \qquad \textbf{(5.4.2.4d)}$$

Actuator force, in terms of the state vector and input, is obtained by substitution of equation 5.4.2.3b into equation 5.4.1:

$$F = F_I C_c x_c + F_I D_c V \qquad \textbf{(5.4.2.5)}$$

The individual modal forces Q_i are given by:

$$Q_i = \phi_i^T F_{I_i} \left(C_c x_c + D_c V \right) \qquad \textbf{(5.4.2.6)}$$

where ϕ_i is the i-th normal mode shape vector and F_{I_i} is the i-th normal mode input force per unit coil current. Equation 5.4.2.6 will be used in section 5.6 to describe the modal forcing terms.

5.5 Mechanical subsystem model using component mode synthesis

It was shown in section 4.5.4 that the system model derived in chapter 2 is inadequate, due to the fact that simple SDOF models were used to describe actuator behaviour. It was also mentioned in chapter 4 that a dynamic model would be required to describe motion of the elastically-mounted base. In this section, each actuator will be modelled with a 2DOF discrete spring-mass model. The original distributed mass and stiffness model developed for the optical instrument and support structure in section 2.8, is retained. An SDOF model is added to represent the base.

The total number of DOF's required to update the model is 15, i.e. 2 for each actuator, 10 for the optical instrument and support structure, and one for the base. This number of DOF's exceeds the number of DOF's used in the original model by five (see section 2.8).

The increase in DOF's does not pose any problems for updating the model. A number of modelling techniques that can be considered for this purpose, are the Rayleigh-Ritz method, Newton's 2nd law, FEM, the mechanical impedance method and component mode synthesis. The main shortcoming of the Rayleigh-Ritz method, for this application, is that coupling of discrete and distributed models may be difficult. This is also a drawback of Newtons's 2nd law, which is clumsy in defining boundary values between discrete and continuous subsystems. Another limitation, which is of secondary importance, is that displacement of an internal DOF of a particular component may be difficult to obtain.

The mechanical impedance method is relatively easy to apply, but gives twice the required number of eigenvalues, since the resulting system DE is 4th order per DOF. Lastly, unless the system is enlarged significantly, no real need exists to use FEM. The only method that is powerful, yet simple enough for this purpose, is component mode synthesis. This method deals with the coupling of component equations of motion using modal displacement vectors. A coupling matrix is used to express boundary values in terms of component modal displacements. System mass and stiffness matrices are derived using energy methods. Normal mode shapes and natural frequencies are obtained from a Rayleigh-Ritz type eigenvalue analysis.

The component mode shapes used in the analysis, may either be component normal modes or component assumed modes. If normal modes are used, boundary values between substructures will not necessarily be satisfied. Additional coupling modes may be required for this purpose. Coupling modes include constraint modes, rigid body modes, attachment modes and inertia relief attachment modes. A description of these modes is given by Craig [1981]. If, on the other hand, assumed modes are used, the modes can be initially selected to satisfy all the boundary values. This method, as explained by Thomson [1993], is also used is in this study. Mode shapes which satisfy the boundary values, will be selected below.

More detail about substructure synthesis is provided by Meirovitch [1990], Kubomura [1987], Béliveau & Souci [1985], Kubomura [1982], Craig [1981], Hintz [1975], Rubin [1975], Klein & Dowell [1974], Benfield & Hruda [1971] and Craig & Bampton [1968].

The system, with its components, is shown shematically in figure 5.5.1. Discrete spring-mass models of the two actuators and base are shown in figure 5.5.2.

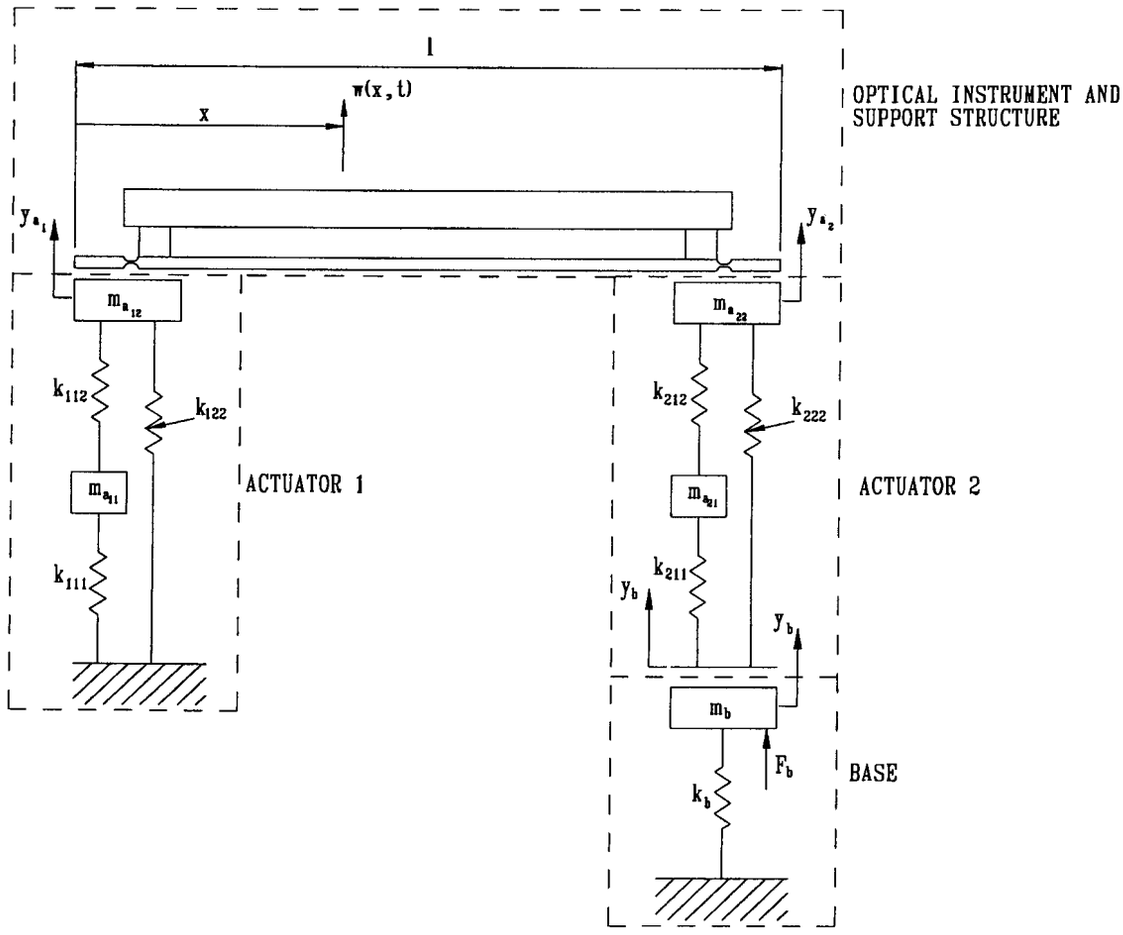

Figure 5.5.1: System model, with substructures

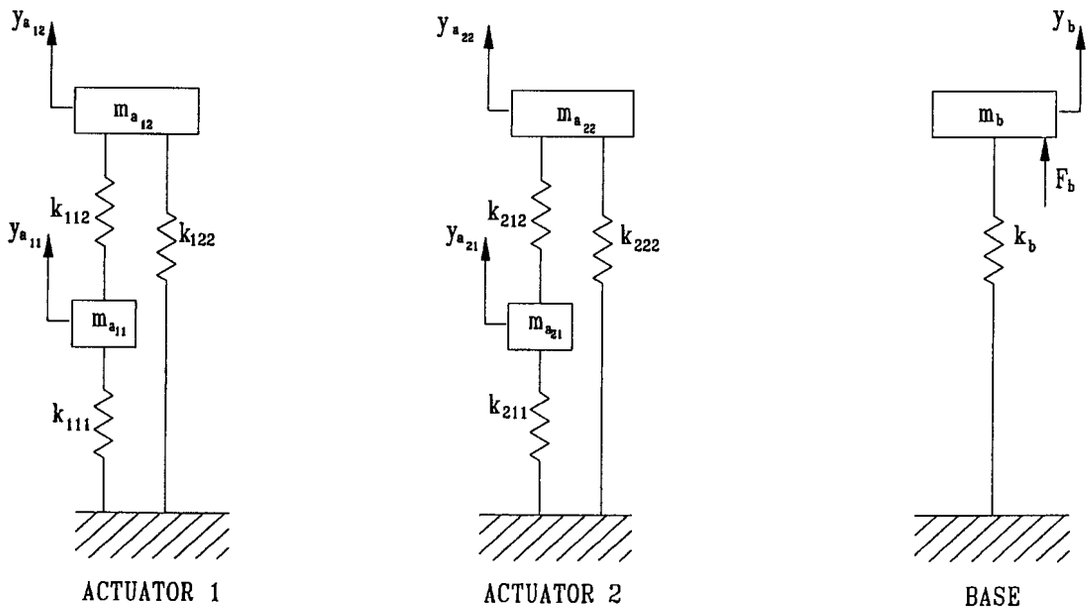

Figure 5.5.2: Actuator and base discrete models

System equation of motion in terms of component displacements

The equation of motion of a linear mechanical system is:

$$m\ddot{y} + c\dot{y} + ky = F \tag{5.5.1}$$

where m, c, k, y and F respectively represent mass, damping, stiffness, displacement and force. F and y are functions of time t:

$$y = y(t) \tag{5.5.2a}$$
$$F = F(t) \tag{5.5.2b}$$

The system described in this section, consists of the actuators, the optical instrument and its support structure, and the elastically-mounted base. Discrete models are used for the actuators and base, while a distribured model is used for the instrument and support structure.

The system equation of motion is firstly derived for natural motion of an undamped system. This is done in order to obtain real normal mode shapes. The assumption is made that damping does not change the mode shapes. This technique was also used in section 2.8. Damping and forcing terms will be added in section 5.6.

The system equation of motion is written in the following general form:

$$m\ddot{y} + ky = 0 \tag{5.5.3}$$

where m and k are the system mass and stiffness matrices. m and k contain component mass and stiffness matrices on the diagonal, as well as off-diagonal matrices which describe coupling between adjacent components. y is the system displacement vector, given by:

$$y = \left\{ \{y_{a1}\},\quad w(x),\quad \{y_{a2}\},\quad y_b \right\}^T \tag{5.5.4}$$

where $\{y_{a1}\}$ and $\{y_{a2}\}$ are the displacement vectors of actuators I and II respectively, $w(x)$ is the distributed displacement of the optical instrument and support structure and y_b is the base displacement.

System modal analysis

The system displacement vector y is determined by the superposition of r number of normal modes:

$$y = \sum_{i=1}^{r} \phi_i q_i(t) \tag{5.5.5}$$

where ϕ_i is the i-th normal mode shape and q_i is the i-th normal mode displacement as a function of time. The number of normal modes r depends on the total number of component

modes n_t and the number of constraint equations. The constraint equations describe motion at boundaries between adjacent components.

Equation 5.5.5 is written concisely in matrix form as:

$$y = \Phi q_n \tag{5.5.6}$$

where Φ is the system normal mode shape matrix and q_n is the modal displacement vector. Φ is given by:

$$\Phi = \begin{bmatrix} [\Phi_1] \\ \{\Phi_s(x)\} \\ [\Phi_2] \\ \{\Phi_b\} \end{bmatrix} \tag{5.5.7}$$

where $[\Phi_1]$ is the 2 x r normal mode shape matrix of actuator I, $\{\Phi_s(x)\}$ is the 1 x r normal mode shape vector, as a function of x, of the optical instrument, $[\Phi_2]$ is the 2 x r normal mode shape matrix of actuator II and Φ_b is the 1 x r normal mode vector of the base. The size of Φ is 6 x r. The elements of Φ are derived later.

The system modal equation of motion, for undamped natural motion, is:

$$M^* \ddot{q}_n + K^* q_n = 0 \tag{5.5.8}$$

where M^* and K^* are the diagonal modal mass and stiffness matrices of the system. The sizes of M^* and K^* are n_t-r each.

The normal mode shapes and mass and stiffness matrices are currently unknown. In order to solve equation 5.5.3, a number of mode shapes must be assumed for each component. The component assumed mode shapes are given in the next section.

Component assumed mode shapes

Assumed mode shapes for each component are given in this section. As opposed to the Rayleigh-Ritz method, which requires that all the assumed mode satisfy the boundary values, the component mode synthesis method only requires that the *combination* of assumed modes of each component satisfy the boundary values [Thomson, 1993].

The boundary values are:

$$w_s(0) = y_{a12} \tag{5.5.9a}$$

$$w_s(l) = y_{a22} + y_b \tag{5.5.9b}$$

$$w_s'(0) = 0 \tag{5.5.9c}$$

$$w_s'(l) = 0 \tag{5.5.9d}$$

The assumed mode shapes ψ_{a1} and ψ_{a2} of actuators I and II are:

$$\psi_{a1} = \begin{bmatrix} 1 & 1 \\ 1 & -1 \end{bmatrix} \tag{5.5.10a}$$

$$\psi_{a2} = \begin{bmatrix} 1 & 1 \\ 1 & -1 \end{bmatrix} \tag{5.5.10b}$$

The sizes of ψ_{a1} and ψ_{a2} are 2 x 2 each.

Three types of assumed modes were used for the optical instrument and support structure in section 2.8.3, i.e. symmetric bending modes (see figure 5.5.3), asymmetric bending modes (see figure 5.5.4) and a rigid body mode, with unity displacement along the length of the instrument.

The assumed mode vector of the instrument and structure can be written as:

$$\psi_s(x) = \left\{ \{\psi_{symm}(x)\} \quad \{\psi_{asymm}(x)\} \quad \psi_{rigid}(x) \right\} \tag{5.5.11}$$

where ψ_{symm} and ψ_{asymm} are the symmetric and asymmetric assumed mode vectors and ψ_{rigid} is the rigid body mode of the following form:

$$\psi_{rigid}(x) = 1 \tag{5.5.12}$$

The size of $\psi_s(x)$ is 1 x 10.

The assumed mode ψ_b of the base is:

$$\psi_b = 1 \tag{5.5.13}$$

ψ_b is a 1 x 1 scalar.

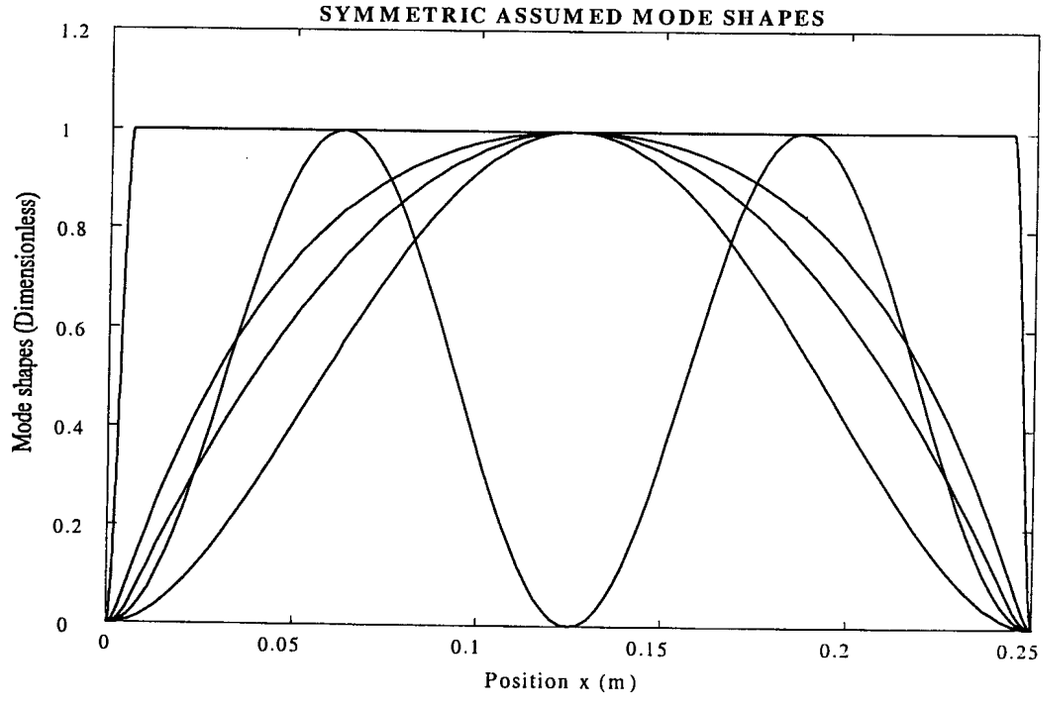

Figure 5.5.3: Symmetric assumed mode shapes for the optical instrument and support structure

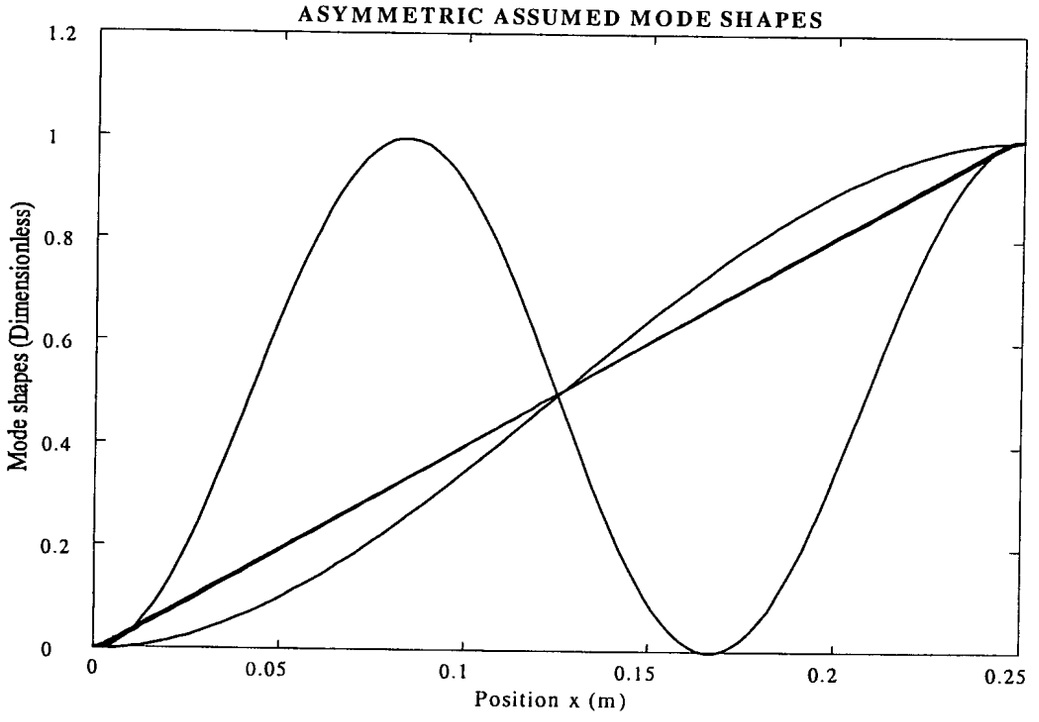

Figure 5.5.4: Asymmetric assumed mode shapes for the optical instrument and support structure

The system assumed mode matrix ψ is compiled from the component assumed modes as follows:

$$\psi = \begin{bmatrix} [\psi_{a1}] & & & \\ & \{\psi_s(x)\} & & \\ & & [\psi_{a2}] & \\ & & & \psi_b \end{bmatrix} \tag{5.5.14}$$

The size of ψ is 6 x 15.

Component displacements in terms of assumed mode displacements

The actuator displacements, in terms of their assumed mode shapes and modal displacements, are:

$$y_{a1} = \psi_{a1} q_{a1} \tag{5.5.15a}$$
$$y_{a2} = \psi_{a2} q_{a2} \tag{5.5.15b}$$

where y_{a1} and y_{a2} are given by:

$$y_{a1} = \{y_{a11}, \quad y_{a12}\}^T \tag{5.5.16a}$$
$$y_{a2} = \{y_{a21}, \quad y_{a22}\}^T \tag{5.5.16b}$$

The actuator modal displacement vectors are given by:

$$q_{a1} = \{q_{a11}, \quad q_{a12}\}^T \tag{5.5.17a}$$
$$q_{a2} = \{q_{a21}, \quad q_{a22}\}^T \tag{5.5.17b}$$

The displacement of the optical instrument, in terms of its assumed mode shapes and modal displacements, is:

$$w(x) = \psi_s(x) q_s \tag{5.5.18}$$

where $w(x)$ is the vertical translational displacement of the instrument, as a function of x, and q_s is its modal displacement vector, given by:

$$q_s = \{q_{s1}, \quad q_{s2}, \quad \cdots, \quad q_{s10}\}^T \tag{5.5.19}$$

The displacement of the base, in terms of its assumed mode shape and modal displacement, is:

$$y_b = q_b \tag{5.5.20}$$

Component modal mass and stiffness matrices

The modal mass matrices M_{a1} and M_{a2} of actuators I and II are:

$$M_{a1} = \psi_{a1}^{T} m_{a1} \psi_{a1} \quad \textbf{(5.5.21a)}$$

$$M_{a2} = \psi_{a2}^{T} m_{a2} \psi_{a2} \quad \textbf{(5.5.21b)}$$

where ψ_{a1} and ψ_{a2} are given in equations 5.5.10. m_{a1} and m_{a2} are the mass matrices of actuators I and II respectively, for the displacement coordinate systems y_{a1} and y_{a2} given in equations 5.5.16. m_{a1} and m_{a2} are given by:

$$m_{a1} = \begin{bmatrix} m_{a11} & 0 \\ 0 & m_{a12} \end{bmatrix} \quad \textbf{(5.5.22a)}$$

$$m_{a2} = \begin{bmatrix} m_{a21} & 0 \\ 0 & m_{a22} \end{bmatrix} \quad \textbf{(5.5.22b)}$$

Since each actuator is modelled as a 2DOF discrete system (see figure 5.5.2), m_{a1} and m_{a2} are diagonal matrices. The sizes of M_{a1} and M_{a2} are 2 x 2 each.

The modal stiffness matrices K_{a1} and K_{a2} of actuators I and II are:

$$K_{a1} = \psi_{a1}^{T} k_{a1} \psi_{a1} \quad \textbf{(5.5.23a)}$$

$$K_{a2} = \psi_{a2}^{T} k_{a2} \psi_{a2} \quad \textbf{(5.5.23b)}$$

where k_{a1} and k_{a2} are the stiffness matrices of actuators I and II respectively, for the displacement coordinate systems y_{a1} and y_{a2} given in equations 5.5.16. k_{a1} and k_{a2} can be derived as:

$$k_{a1} = \begin{bmatrix} (k_{111} + k_{112}) & -k_{112} \\ -k_{112} & (k_{112} + k_{122}) \end{bmatrix} \quad \textbf{(5.5.24a)}$$

$$k_{a2} = \begin{bmatrix} (k_{211} + k_{212}) & -k_{212} \\ -k_{212} & (k_{212} + k_{222}) \end{bmatrix} \quad \textbf{(5.5.24b)}$$

The sizes of K_{a1} and K_{a2} are 2 x 2 each.

The modal mass and stiffness matrices of the optical instrument and support structure, from

equations 2.8.3.10, are:

$$M_s = \int_{x=0}^{x=l} \rho_s(x) A_s(x) \psi_{si}(x) \psi_{sj}(x) dx \qquad \textbf{(5.5.25a)}$$

$$K_s = \int_{x=0}^{x=l} E_s(x) I_s(x) \psi''_{si}(x) \psi''_{sj}(x) dx \qquad \textbf{(5.5.25b)}$$

where $\psi_s(x)$ are the assumed mode shapes of the optical instrument and support structure as shown in figures 5.5.3 and 5.5.4. The mass per unit length $\rho_s A_s$ and flexural rigidity $E_s I_s$, as functions of x, are shown in figures 2.8.4.1 and 2.8.4.2. The sizes of M_b and K_b are 10 x 10 each.

The modal mass and stiffness matrices of the base are:

$$M_b = \psi_b^T m_b \psi_b \qquad \textbf{(5.5.26a)}$$

$$K_b = \psi_b^T k_b \psi_b \qquad \textbf{(5.5.26b)}$$

M_b and K_b are 1 x 1 scalars.

System modal equation of motion

The modal equation of motion of the system is:

$$M\ddot{q} + Kq = 0 \qquad \textbf{(5.5.27)}$$

where M and K are the system modal mass and stiffness matrices respectively, given by:

$$M = \begin{bmatrix} [M_{a1}] & [0] & \cdots & [0] \\ [0] & [M_s] & \ddots & \vdots \\ \vdots & \ddots & [M_{a2}] & [0] \\ [0] & \cdots & [0] & [M_b] \end{bmatrix} \qquad \textbf{(5.5.28a)}$$

$$K = \begin{bmatrix} [K_{a1}] & [0] & \cdots & [0] \\ [0] & [K_s] & \ddots & \vdots \\ \vdots & \ddots & [K_{a2}] & [0] \\ [0] & \cdots & [0] & [K_b] \end{bmatrix} \qquad \textbf{(5.5.28b)}$$

M and K respectively contain the component modal mass and stiffness matrices in square blocks, of different sizes, on the diagonal. Off-diagonal submatrices of M and K are zero. The sizes of M and K are 15 x 15 each.

The system displacement vector q is:

$$q = \left\{ \{q_{a1}\} \quad \{q_s\} \quad \{q_{a2}\} \quad q_b \right\}^T \tag{5.5.29}$$

The size of q is the sum of the sizes of the different component modal displacement vectors, i.e. 15 x 1. The modal displacement vectors q_{a1}, q_{a2}, q_s and q_b are currently uncoupled. Modal coupling is done in the next section.

System coupled modal displacements

The displacement at the boundary between actuator I and the support structure, i.e. at $x = 0$, is:

$$w_s(0) = y_{a12} \tag{5.5.30}$$

The displacement at the boundary between actuator II and the support structure, i.e. at $x = l$, is the sum of the base displacement and the deflection of actuator II:

$$w_s(l) = y_{a22} + y_b \tag{5.5.31}$$

Combination of equations 5.5.10, 5.5.15 to 5.5.18, 5.5.30 and 5.5.31, gives:

$$\psi_s(0) q_s = q_{a11} - q_{a12} \tag{5.5.32a}$$
$$\psi_s(l) q_s = q_{a21} - q_{a22} + q_b \tag{5.5.32b}$$

or:

$$q_{a12} = q_{a11} - \psi_s(0) q_s \tag{5.5.33a}$$
$$q_{a22} = q_{a21} - \psi_s(l) q_s + q_b \tag{5.5.33b}$$

Equations 5.5.33a and 5.5.33b are combined and written as follows in matrix form:

$$\begin{Bmatrix} q_{a12} \\ q_{a22} \end{Bmatrix} = \begin{bmatrix} 1 & 0 & -\psi_s(0) & 0 \\ 0 & 1 & -\psi_s(l) & 1 \end{bmatrix} \begin{Bmatrix} q_{a11} \\ q_{a21} \\ q_s \\ q_b \end{Bmatrix} \tag{5.5.34}$$

Substitution of equation 5.5.34 into equation 5.5.29, gives the system modal displacements as:

$$\begin{Bmatrix} \begin{Bmatrix} q_{a11} \\ q_{a12} \end{Bmatrix} \\ --- \\ \{q_s\} \\ --- \\ \begin{Bmatrix} q_{a21} \\ q_{a22} \end{Bmatrix} \\ --- \\ q_b \end{Bmatrix} = \begin{bmatrix} 1 & \{0\} & 0 & 0 \\ 1 & -\{\psi_s(0)\} & 0 & 0 \\ \{0\} & [I] & \{0\} & \{0\} \\ 0 & \{0\} & 1 & 0 \\ 0 & -\{\psi_s(l)\} & 1 & 1 \\ 0 & \{0\} & 0 & 1 \end{bmatrix} \begin{Bmatrix} q_{a11} \\ \{q_s\} \\ q_{a21} \\ q_b \end{Bmatrix} \tag{5.5.35}$$

Equation 5.5.35 is written in matrix notation as:

$$q = Cq_r \tag{5.5.36}$$

where q is the uncoupled system modal displacement vector given by equation 5.5.29 and q_r is the reduced modal displacement vector, given by:

$$q_r = \{q_{a11} \quad \{q_s\} \quad q_{a21} \quad q_b\}^T \tag{5.5.37}$$

C is the coupling matrix, given by:

$$C = \begin{bmatrix} 1 & \{0\} & 0 & 0 \\ 1 & -\{\psi_s(0)\} & 0 & 0 \\ \{0\} & [I] & \{0\} & \{0\} \\ 0 & \{0\} & 1 & 0 \\ 0 & -\{\psi_s(l)\} & 1 & 1 \\ 0 & \{0\} & 0 & 1 \end{bmatrix} \tag{5.5.38}$$

The sizesof q and q_r are 15 x 1 and 13 x 1 respectively. The size of C is 15 x 13.

System coupled modal equation of motion

The uncoupled modal equation of motion of the system is given in equation 5.5.27. Substitution of the coupling equation 5.5.36 into equation 5.5.27, gives:

$$MC\ddot{q}_r + KCq_r = 0 \qquad \textbf{(5.5.39)}$$

Premultiplication of equation 5.5.39 with C^T gives:

$$M_r\ddot{q}_r + K_r q_r = 0 \qquad \textbf{(5.5.40)}$$

where M_r and K_r are the reduced-order mass and stiffness matrices, respectively given by:

$$M_r = C^T MC \qquad \textbf{(5.5.41a)}$$
$$K_r = C^T KC \qquad \textbf{(5.5.41b)}$$

The sizes of M_r and K_r are 13 x 13 each. The off-diagonal elements of M_r and K_r are non-zero and the reduced coordinate equation of motion (5.5.40), is coupled. The normal mode shapes, natural frequencies, mass and stiffness matrices of the system are derived next.

Normal mode shapes, natural frequencies, mass and stiffness matrices

The reduced coordinate vector q_r can be expressed as follows in terms of the eigenvector U and the normal mode displacement vector q_n:

$$q_r = Uq_n \qquad \textbf{(5.5.42)}$$

The sizes of U and q_n are 13 x 13 and 13 x 1 respectively.

Substitution of equation 5.5.42 into equation 5.5.40 and premultiplication of the resulting equation with U^T gives:

$$U^T M_r U\ddot{q}_n + U^T K_r U q_n = 0 \qquad \textbf{(5.5.43)}$$

For natural motion

$$\ddot{q}_n = -\Omega^2 q_n, \qquad \textbf{(5.5.44)}$$

where Ω^2 the 13 x 13 diagonal eigenvalue matrix.

Substitution of equation 5.5.44 into equation 5.5.43 and simplification of the resulting equation, gives:

$$\left(K_r - M_r\Omega^2\right)Uq_n = 0 \qquad \textbf{(5.5.45)}$$

The eigenvalues are the values of Ω^2 for which:

$$\left|K_r - M_r\Omega^2\right| = 0 \tag{5.5.46}$$

The natural frequency f_i of the i-th normal mode is:

$$f_i = \frac{1}{2\pi}\Omega_{ii} \tag{5.5.47}$$

The uncoupled, normal mode mass and stiffness matrices, from equations 5.5.8 and 5.5.43, are:

$$M^* = U^T M_r U \tag{5.5.48a}$$
$$K^* = U^T K_r U \tag{5.5.48b}$$

The sizes of M^* and K^* are 13 x 13 each.

The normal mode shape matrix Φ is given by:

$$\Phi = \psi C U \tag{5.5.49}$$

where ψ and C are respectively given by equations 5.5.14 and 5.5.38 and U is the eigenvector. The size of Φ is 6 x 13.

The component normal mode shapes are given by:

$$\begin{bmatrix} [\Phi_1] \\ \{\Phi_s(x)\} \\ [\Phi_2] \\ \{\Phi_b\} \end{bmatrix} = \begin{bmatrix} [\psi_{a1}][C_{rows\,1,2}] \\ \{\psi_s(x)\}[C_{rows\,3-12}] \\ [\psi_{a2}][C_{rows\,13,14}] \\ \psi_b\{C_{row\,15}\} \end{bmatrix} U \tag{5.5.50}$$

The system displacement vector, in terms of the normal mode matrix and modal displacement vector, is given by:

$$y = \Phi q_n \tag{5.5.51}$$

y is a 6 x 1 vector.

Component displacements are given by:

$$\begin{Bmatrix} y_{a1} \\ w(x) \\ y_{a2} \\ y_b \end{Bmatrix} = \begin{bmatrix} [\Phi_1] \\ \{\Phi_s(x)\} \\ [\Phi_2] \\ \{\Phi_b\} \end{bmatrix} q_n \qquad \textbf{(5.5.52)}$$

The first five natural frequencies of the system were experimentally determined in section 4.5. The first five natural frequencies and mode shapes of the system will be calculated in the next section, using the equations derived in this section. The stiffnesses and masses of the actuators and base will be selected and adjusted until the calculated natural frequencies correspond sufficiently accurately with the experimentally determined natural frequencies. The equation of motion will be written in state-space form and coupled to the coil state equations. The state equations will be converted to *TF* form, *TF* spectra will be calculated and compared with the experimentally determined spectra.

5.6 Updated system model

An updated system model is presented in this section. The actuators are modelled by means of 2DOF discrete models, instead of the SDOF models developed in chapter 2. An additional SDOF model is included to represent the elastically mounted base. The distributed mass and stiffness model of the optical instrument and support structure, as developed in chapter 2, is left unchanged.

The updating procedure is as follows: Model parameters are selected and adjusted until the calculated natural frequencies closely match the experimentally determined natural frequencies. The model parameters are the actuator, optical instrument and base stiffnesses and masses. Damping is initially ignored in order to obtain real mode shapes. The component mode synthesis method, as described in section 5.5, is used to calculate the normal mode shapes of the optical instrument and support structure. Once the mode shapes have been determined, modal damping and excitation forces are added.

Modal equations of motion are derived and written in state-space form. From the state-space equations, the system transfer function between input voltage and instrument angular acceleration is obtained. As with the masses and stiffness, damping and force parameters are adjusted until the calculated system *TF* closely matches the experimentally determined *TF*. The modelled *TF* is compared with the experimentally determined *TF* and it is shown that the updated model is sufficiently accurate.

A system block diagram is included to show the coil and mechanical subsystem models and to indicate coupling between the subsystems. The modal *TF*'s are calculated and the dominating mode is indicated. A pole-zero diagram of the *TF* is shown. The system bandwidth is calculated and it is shown that it exceeds the required bandwidth.

Base motion and its effect on system behaviour are also analyzed in order to obtain the open-loop transmissibility (*TR*) of the system. (The *TR* is the ratio of instrument angular acceleration to base angular acceleration). The *TR*, together with the system transfer function, is required for control system design purposes, which will be described in chapter 6.

Updated natural frequencies and normal mode shapes

The normal mode shapes and natural frequencies are calculated by means of the component mode synthesis method, described in section 5.5. The actuator and base masses and stiffnesses are selected and the natural frequencies are calculated. The latter are compared with the experimentally determined natural frequencies and, if the comparison is poor, the masses and stiffnesses are updated until the model gives sufficiently accurate natural frequencies. The resulting masses and stiffnesses are given in table 5.6.1.

These masses and stiffnesses, together with the assumed mode shapes, as given in section 5.5, are substituted into equations 5.5.21 to 5.5.28 to obtain the component modal mass and stiffness matrices *M* and *K*. The assumed mode shapes are substituted into equation 5.5.38 to obtain the coupling matrix *C*. The coupled mass and stiffness matrices are calculated using equations 5.5.41. The eigenvector *U* and natural frequencies f_i are obtained by solving the eigenvalue problem, the solution of which is given in equations 5.5.45 to 5.5.47. The normal mode shapes are obtained by application of equation 5.5.50.

Table 5.6.1: Updated actuator and base stiffnesses and masses

Component	Parameter	Symbol	Value
Actuator I	Stiffness	k_{111}	$7{,}34.10^5$ N/m
	Stiffness	k_{112}	$9{,}9672.10^4$ N/m
	Stiffness	k_{122}	$1{,}0972.10^6$ N/m
	Displacement gain	G_1	2,7
	Mass (ungained)	m_{a11}/G_1	0,1482 kg
	Mass (ungained)	m_{a12}/G_1	0,0456 kg
	Mass (gained)	m_{a11}	0,4 kg
	Mass (gained)	m_{a12}	0,1231 kg
Actuator II	Stiffness	k_{211}	$8{,}7327.10^5$ N/m
	Stiffness	k_{212}	$1{,}1761.10^5$ N/m
	Stiffness	k_{222}	$1{,}0863.10^6$ N/m
	Displacement gain	G_2	2,7
	Mass (ungained)	m_{a21}/G_2	0,1482 kg
	Mass (ungained)	m_{a22}/G_2	0,0456 kg
	Mass (gained)	m_{a21}	0,4 kg
	Mass (gained)	m_{a22}	0,1231 kg
Base	Stiffness	k_b	$7{,}1559.10^7$ N/m
	Mass	m_b	8 kg

The first five normal mode shapes of the optical instrument and support structure, together with their corresponding natural frequencies, are shown in figure 5.6.1. Each mode shape is normalized with respect to the maximum displacement of the particular mode. A short discussion of the mode shapes follows.

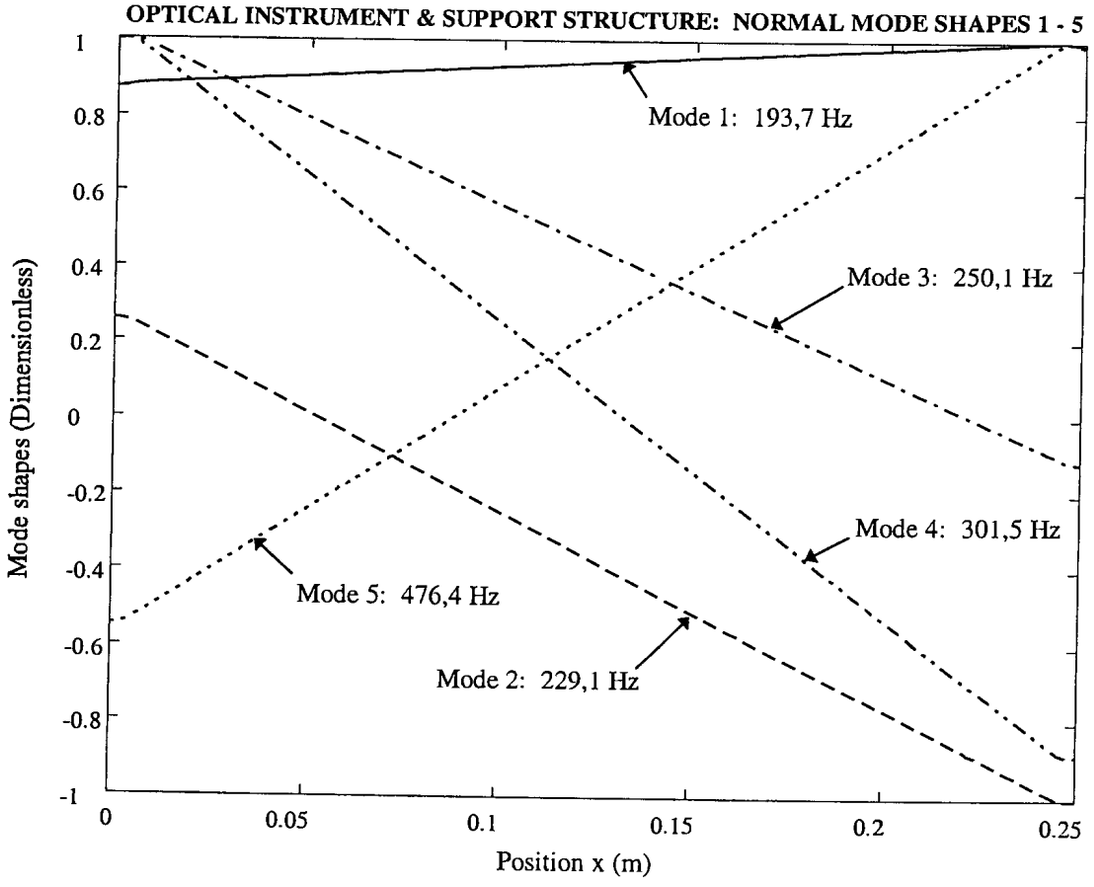

Figure 5.6.1: First five mode shapes of the optical instrument and support structure

It can be seen from figure 5.6.1 that translational motion dominates in the 1st mode. The modal displacements at the ends of the support structure, i.e. at x = 0 and x = 0,25 m, differ by approximately 10%. The mode shape is not entirely translational, which can be attributed to unequal actuator stiffnesses, as shown in table 5.6.1. (A possible cause of the unequal stiffnesses is slight distortion of the actuator flexures during assembly). It can further be seen from figure 5.6.1, that rotational motion dominates in the 4th mode. The modal displacement at x = 0 is approximately equal to that at x = 0,25 m, but of opposite sign.

An almost constant displacement separates the 2nd and 3rd mode shapes. A possible explanation is that, at 229 Hz and 250 Hz, the two actuators behave like dynamic absorbers. At 229 Hz, actuator I *passively* cancels the motion at x = 0, with the result that the support structure displacement is relatively small at that position. Similarly, at 250 Hz, actuator II cancels the support structure motion at x = 0,25 m. Note that the 2nd and 3rd mode shapes, as shown in figure 5.6.1, did not appear in the original mode shapes calculated in section 2.8.

The 5th normal mode shape results from the elastically mounted base. This mode is not closely coupled to the other four normal modes.

The 1st to 4th natural frequencies of the updated model differ from the experimentally determined frequencies by 3,9%, 0,79%, 1,2% and 0,17% respectively (see also table 4.5.2.1). Accuracy of the model will be further improved in the next section, when damping and forcing terms are added and the mechanical subsystem model is coupled to the coil model.

The 6th to 13th normal mode shapes are not shown. These mode shapes occur at frequencies ranging from 5 kHz to 710 kHz. Since the acquisition frequency of the signal analyzer used in the experimental tests was 1280 Hz (see section 4.4.6), the model can only be updated for frequencies up to the Nyquist frequency, i.e. 640 Hz.

Updated system state-space and transfer function model

The system modal equations of motion are given by:

$$M^*\ddot{q}_n + C^*\dot{q}_n + K^*q_n = \Phi_s^T F_I I \tag{5.6.1}$$

where M^*, C^* and K^* respectively represent the modal mass, modal damping coefficient and modal stiffness. Φ_s is the optical instrument normal mode shape vector, I is the coil current and F_I is the force per unit current. The current is given by equations 5.4.2.3 and 5.4.2.4.

Premultiplication of equation 5.6.1 with M^{*-1} and simplification of the resulting equation gives:

$$\ddot{q}_n + 2Z\Omega\dot{q}_n + \Omega^2 q_n = M^{*-1}Q \tag{5.6.2}$$

where Z is the modal damping matrix, Ω is the modal natural frequency matrix and Q is the modal force input vector, given by:

$$Q = \Phi_s^T F_I I \tag{5.6.3}$$

Z and Ω are diagonal matrices, whose sizes correspond with the number of normal modes in a given frequency band. For the first five normal modes, Z and Ω are 5 x 5 square matrices each. Q is a 5 x 1 vector.

The optical instrument angular acceleration, in terms of the modal accelerations, is:

$$\ddot{\theta} = \frac{\Phi_s(x_2) - \Phi_s(x_1)}{x_2 - x_1}\ddot{q}_n \tag{5.6.4}$$

where x_1 and x_2 respectively represent the longitudinal coordinates of the accelerometer attachment points.

Equations 5.6.2 and 5.6.4 are written as follows in state-space form:

$$\begin{Bmatrix}\dot{q}_n\\ \ddot{q}_n\end{Bmatrix}=\begin{bmatrix}[0] & [I]\\ -\Omega^2 & -2Z\Omega\end{bmatrix}\begin{Bmatrix}q_n\\ \dot{q}_n\end{Bmatrix}+\begin{bmatrix}[0]\\ M^{*-1}\end{bmatrix}Q \tag{5.6.5a}$$

$$\ddot{\theta}=\frac{\Phi_s(x_2)-\Phi_s(x_1)}{x_2-x_1}\begin{bmatrix}-\Omega^2 & -2Z\Omega\end{bmatrix}\begin{Bmatrix}q_n\\ \dot{q}_n\end{Bmatrix}+\frac{\Phi_s(x_2)-\Phi_s(x_1)}{x_2-x_1}M^{*-1}Q \tag{5.6.5b}$$

Combination of equations 5.4.2.3 to 5.4.2.5, 5.6.3 and 5.6.5 results in the following state equation for the coupled system:

$$\begin{Bmatrix}\dot{q}_n\\ \ddot{q}_n\\ \dot{x}_c\end{Bmatrix}=\begin{bmatrix}[0] & [I] & [0]\\ -\Omega^2 & -2Z\Omega & M^{*-1}\Phi_s^T F_l C_c\\ [0] & [0] & A_c\end{bmatrix}\begin{Bmatrix}q_n\\ \dot{q}_n\\ x_c\end{Bmatrix}+\begin{bmatrix}\{0\}\\ \{0\}\\ B_c\end{bmatrix}V \tag{5.6.6}$$

where A_c, B_c and C_c are the coil state and output matrices given in equations 5.4.2.4. Numerical values of the coil state matrix elements are given in table 5.4.2.1.

The system output equation is given by:

$$\ddot{\theta}=\frac{\Phi_s(x_2)-\Phi_s(x_1)}{x_2-x_1}\begin{bmatrix}-\Omega^2 & -2Z\Omega & M^{*-1}\Phi_s^T F_l C_c\end{bmatrix}\begin{Bmatrix}q_n\\ \dot{q}_n\\ x_c\end{Bmatrix} \tag{5.6.7}$$

The system state and output equations are written as follows:

$$\begin{aligned}\dot{x}&=Ax+B_V V\\ y&=Cx+D_V V\end{aligned} \tag{5.6.8}$$

where A, B_V, C and D_V are respectively given by:

$$A=\begin{bmatrix}[0] & [I] & [0]\\ -\Omega^2 & -2Z\Omega & M^{*-1}\Phi_s^T F_l C_c\\ [0] & [0] & A_c\end{bmatrix} \tag{5.6.9a}$$

$$B_V=\begin{bmatrix}\{0\} & \{0\} & B_c\end{bmatrix}^T \tag{5.6.9b}$$

$$C=\frac{\Phi_s(x_2)-\Phi_s(x_1)}{x_2-x_1}\begin{bmatrix}-\Omega^2 & -2Z\Omega & M^{*-1}\Phi_s^T F_l C_c\end{bmatrix} \tag{5.6.9c}$$

$$D_V=0 \tag{5.6.9d}$$

The sizes of the A, B_V, C and D_V matrices are 13 x 13, 13 x 1, 1 x 13 and 1 x 1 respectively. Note that the order of the system is lower than that of the frequency domain TF described in section 5.3.

The undamped angular natural frequencies (Ω), damping factors (Z) and input forces per unit current per unit mass $\left(M^{*-1}\Phi_s^T F_I\right)$ of the first five normal modes are given in table 5.6.2.

Table 5.6.2: Modal frequency, damping factor and force per unit mass per unit current

Mode number	f_n (Hz)	Ω (rad/s)	Z (%)	$M^{*-1}\Phi_s{}^T F_I$ (N/kg/A)
1	193,62	1216,6	4,00	35,242
2	230,17	1446,2	1,75	-7,9059
3	250,10	1571,4	3,55	-2,9391
4	299,11	1879,4	3,04	-103,72
5	476,37	2993,1	1,20	65,347

The signs of the $M^{*-1}\Phi_s^T F_I$ terms for the 2nd to 4th modes differ from those of the 1st and 5th modes. The reason is that the signs of the displacements of the 2nd to 4th modes at the attachment point of actuator II, i.e. at x = 0,25 m, differ from those of the 1st and 5th modes (see figure 5.6.1).

The transfer function between input voltage and output angular acceleration is obtained by substitution of equations 5.6.9 into equation 2.5.2.1. The transfer function $G(s)$, in numerator and denominator polynomial form, is:

$$G(s) = \frac{\sum_{k=0}^{M} p_k s^k}{\sum_{l=0}^{N} q_l s^l} \qquad \textbf{(5.6.10)}$$

The TF numerator and denominator polynomial coefficients are given in table 5.6.3.

A block diagram of the system is shown in figure 5.6.2. The electrical and mechanical subsystems, subsystem inputs and outputs, subsystem coupling, modal excitation forces, accelerations, velocities and displacements, as well as system output angular acceleration, are indicated.

In figure 5.6.2, V is the coil input voltage, G_c is the coil transfer function, I is the coil current, F_I is the force per unit current, Φ_s is the normal mode shape vector and Q is the modal excitation force. M^*, C^* and K^* respectively represent the modal mass, modal damping coefficient and modal stiffness. $\ddot{\theta}$ is the angular acceleration of the optical instrument, s is the complex Laplace domain differential operator, x_1 and x_2 are the longitudinal coordinates of the accelerometer attachment points.

Table 5.6.3: *TF* numerator & denominator polynomial coefficients

Coefficient	Value
p_0	0
p_1	0
p_2	$-8{,}4062.10^{36}$
p_3	$-3{,}3157.10^{33}$
p_4	$-1{,}4211.10^{31}$
p_5	$-4{,}8225.10^{27}$
p_6	$-8{,}4473.10^{24}$
p_7	$-2{,}4310.10^{21}$
p_8	$-2{,}0674.10^{18}$
p_9	$-4{,}8705.10^{14}$
p_{10}	$-1{,}7883.10^{11}$
p_{11}	$-3{,}0275.10^{7}$
p_{12}	$-3{,}6572.10^{3}$
q_0	$3{,}2766.10^{41}$
q_1	$9{,}1519.10^{38}$
q_2	$1{,}2393.10^{36}$
q_3	$2{,}0897.10^{33}$
q_4	$1{,}6119.10^{30}$
q_5	$1{,}8762.10^{27}$
q_6	$9{,}8145.10^{23}$
q_7	$8{,}4358.10^{20}$
q_8	$3{,}0026.10^{17}$
q_9	$1{,}9869.10^{14}$
q_{10}	$4{,}3527.10^{10}$
q_{11}	$2{,}2966.10^{7}$
q_{12}	$2{,}2632.10^{3}$
q_{13}	1

The updated model *TF* magnitude and phase spectra, for a frequency band of 0 Hz to 500 Hz, are shown in figure 5.6.3. A comparison between the updated model *TF* spectra and the experimentally determined spectra is shown in figure 5.6.4. A pole-zero diagram of the updated model *TF* is shown in figure 5.6.5. The poles and zeroes are respectively indicated by crosses and circles. All the real parts of the poles and zeroes are negative, indicating that the updated system model is stable and minimum phase.

The input voltage to angular acceleration *TF*'s of the individual normal modes are shown in figure 5.6.6. From the figure, it can be seen that the 4th mode is the dominating mode in the frequency range of 0 Hz to 500 Hz. The relative contributions of the 1st and 2nd modes are approximately one order below that of the 4th mode, while those of the 3rd and 5th modes are approximately two orders below that of the 4th mode.

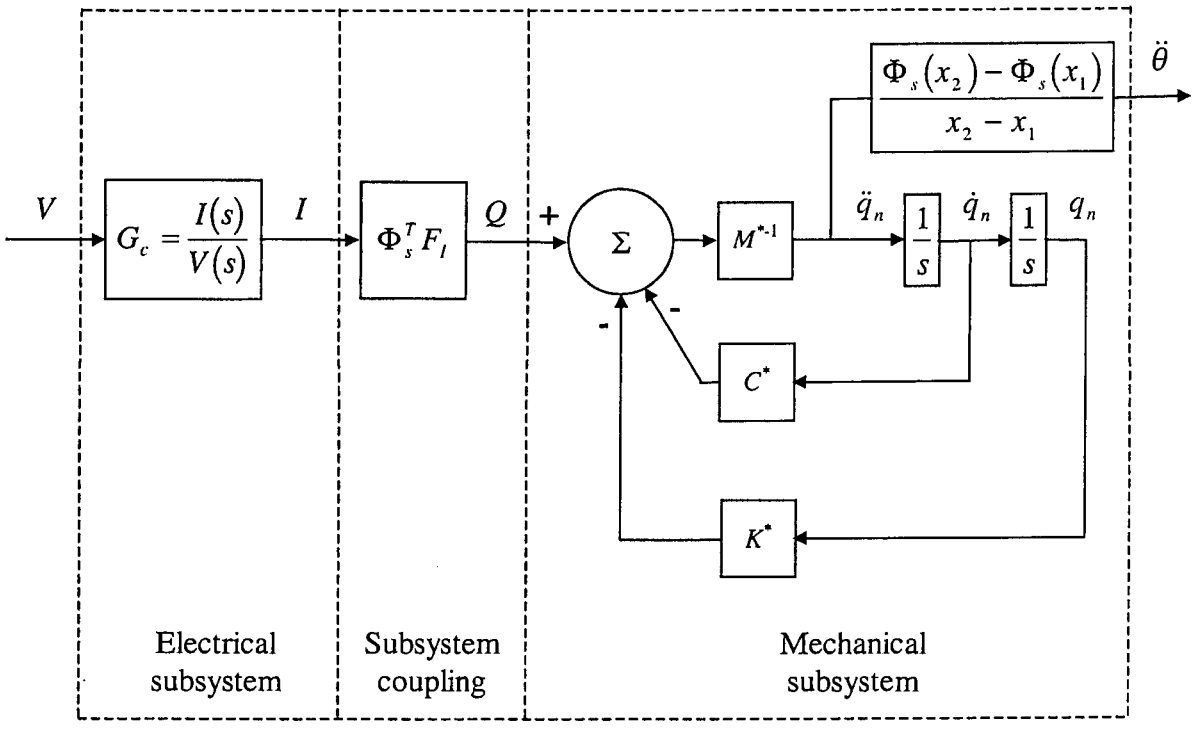

Figure 5.6.2: Updated system model block diagram

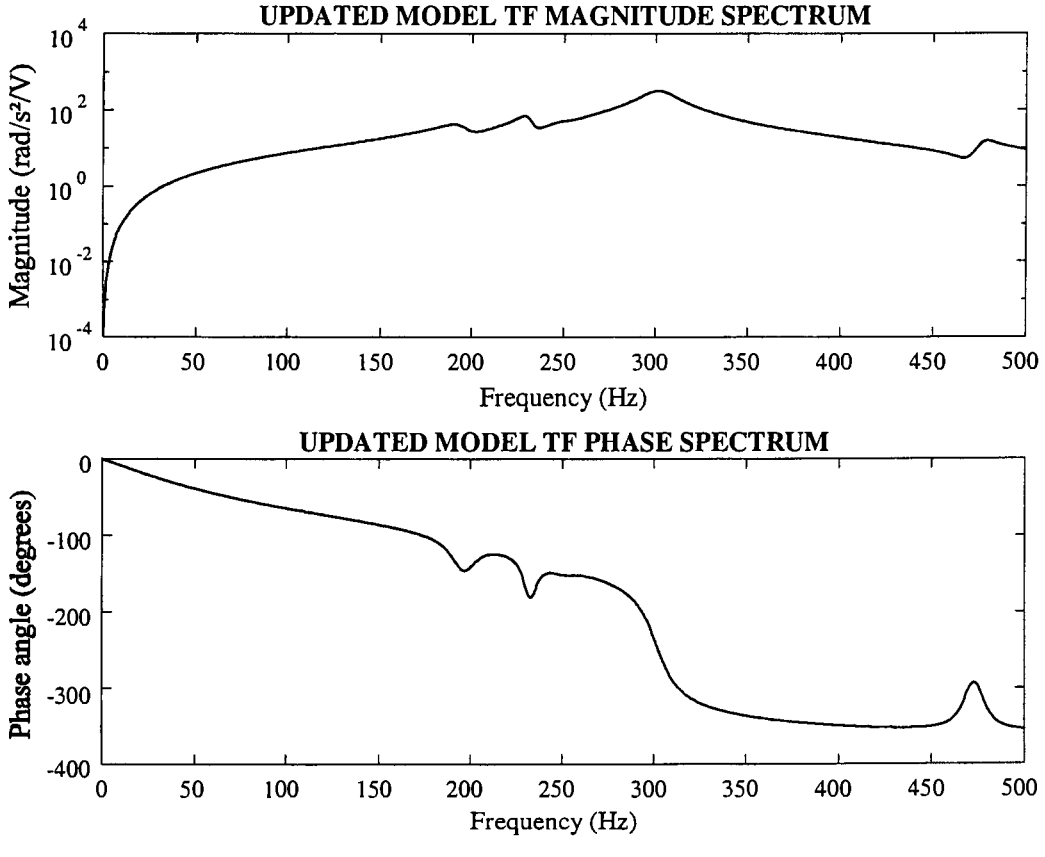

Figure 5.6.3: Updated model *TF* spectra

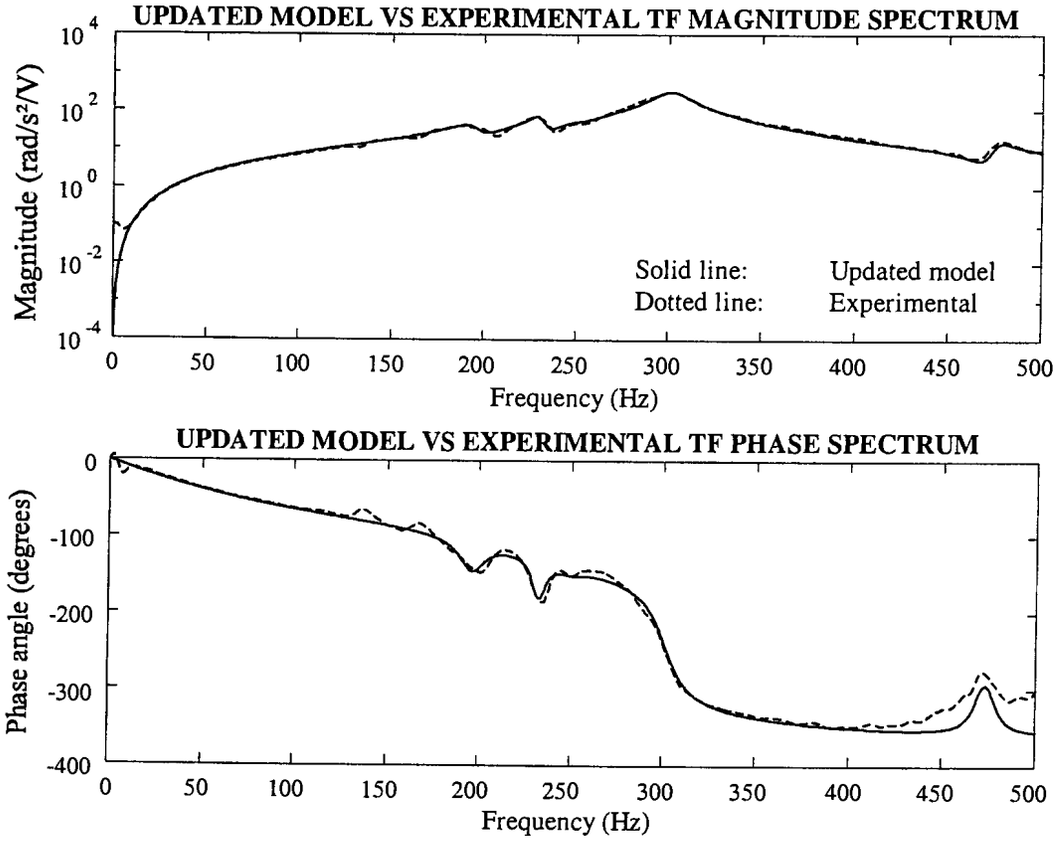

Figure 5.6.4: Comparison between updated model *TF* and experimental *TF* spectra

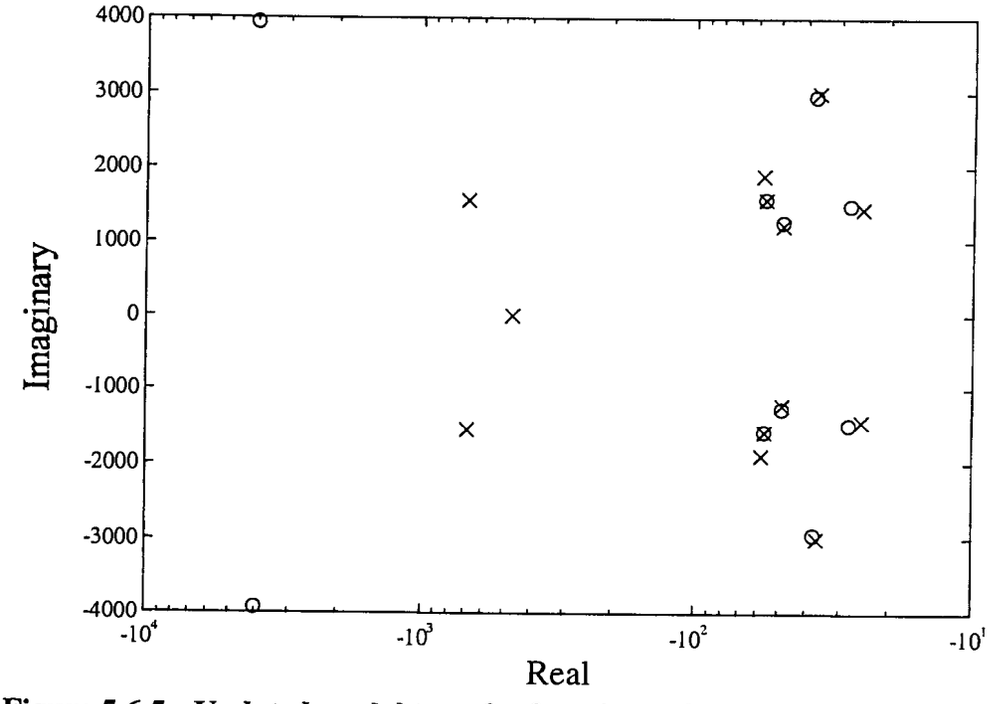

Figure 5.6.5: Updated model transfer function pole-zero diagram

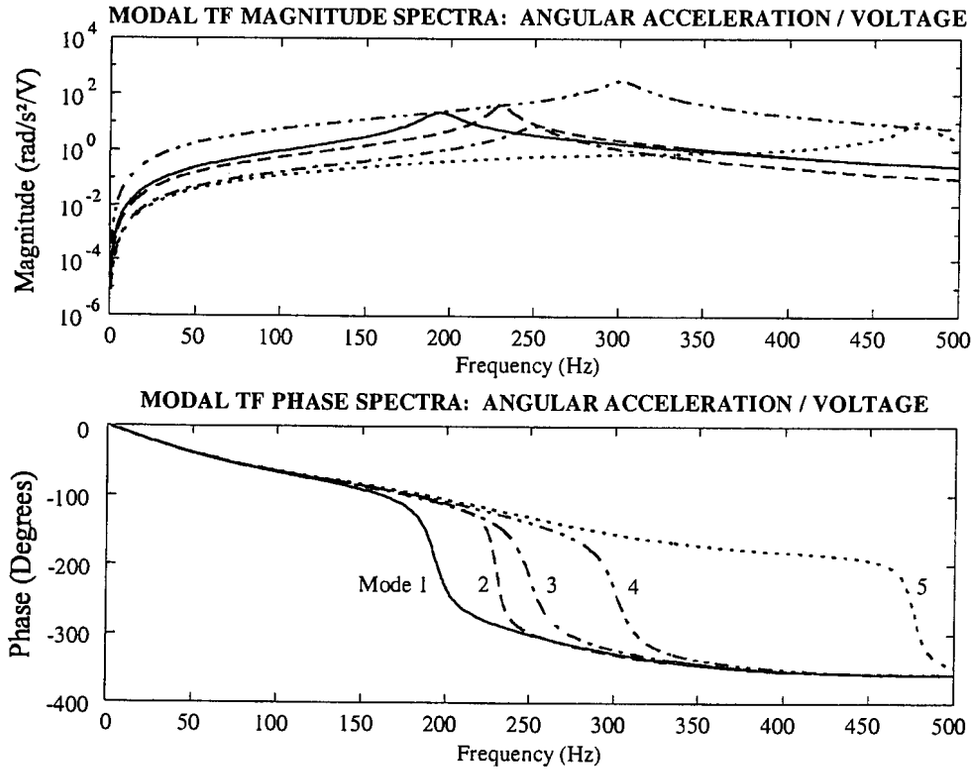

Figure 5.6.6: Modal transfer function spectra

In order to determine the system isolation bandwidth (BW), the coil voltage to instrument angular *displacement TF* is analyzed, instead of the voltage to angular *acceleration TF*. The *TF* magnitude is shown in figure 5.6.7, together with the -3 dB and disturbance bandwidths.

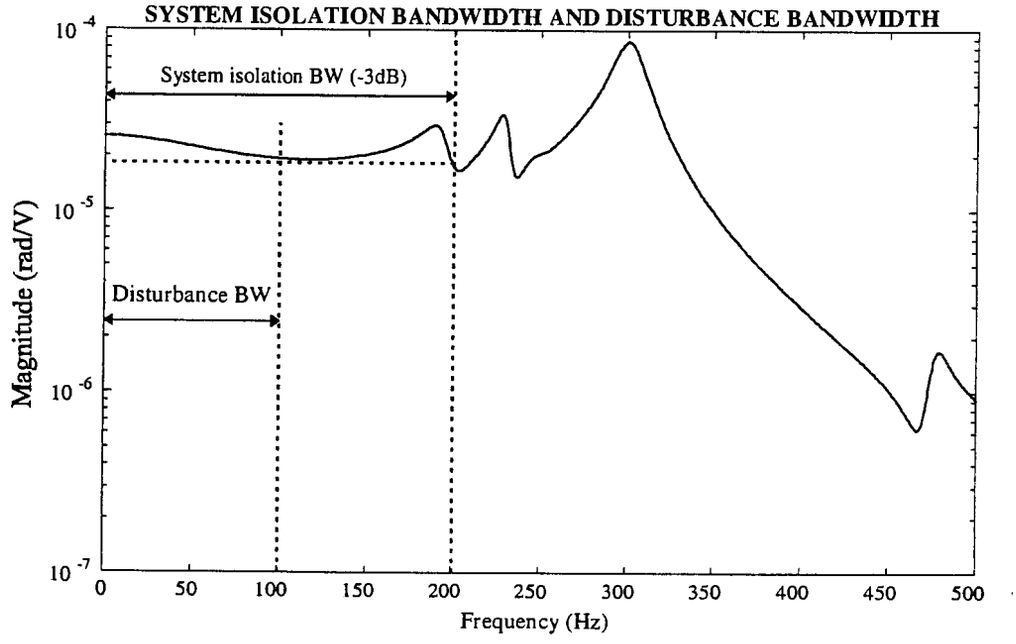

Figure 5.6.7: System isolation bandwidth and disturbance bandwidth

The *TF* magnitude at 0 Hz is $2{,}57.10^{-5}$ rad/V. The lowest frequency where the magnitude is 3 dB below this value, i.e. $1{,}81.10^{-5}$ rad/V, is 199 Hz. This frequency is almost double the maximum frequency of the disturbance, i.e. 100 Hz. It can therefore be concluded that the system isolation bandwidth is sufficient, despite the fact that the coil bandwidth is only 84 Hz (see section 5.4.2).

System base to output transmissibility

System transmissibility (*TR*) can be expressed in terms of a number of transfer functions, such as the input force to output force *TF*, base angular displacement to output angular displacement *TF* (θ/θ_b), base angular velocity to output angular velocity *TF* ($\dot{\theta}/\dot{\theta}_b$) and base angular acceleration to output angular acceleration *TF* ($\ddot{\theta}/\ddot{\theta}_b$). The most appropriate transfer function, is mainly determined by the sensors used for system characterization and control.

Accelerometers were used for dynamic system characterization in chapter 4. The measured vertical accelerations were subsequently used to calculate the base and output angular accelerations (see section 4.5.1). Accelerometers will also be used as sensors during testing of the control system, which will be described in more detail chapter 6. It is therefore appropriate to express the *TR* as the transfer function between base angular acceleration and output angular acceleration ($\ddot{\theta}/\ddot{\theta}_b$).

The transmissibility is required in terms of system characteristics, such as state and output parameters, natural frequencies, damping factors and normal mode shapes. A derivation of the *TR* is given in appendix W. In order to simplify the derivation, an assumption is made that the *TR* is independent of sensor dynamics. The consequence of this assumption is that the transfer functions, θ/θ_b, $\dot{\theta}/\dot{\theta}_b$ and $\ddot{\theta}/\ddot{\theta}_b$, are equal over a wide frequency bandwidth. This makes it possible to derive the transfer function θ/θ_b and set it equal to $\ddot{\theta}/\ddot{\theta}_b$:

$$TR = \frac{\ddot{\theta}}{\ddot{\theta}_b} = \frac{-\omega^2\theta}{-\omega^2\theta_b} = \frac{\theta}{\theta_b} \qquad \textbf{(5.6.11)}$$

The component mode synthesis method, which was described in detail section 5.5, is used to determine the *TR*. The *TR* is determined independently of any coil voltage input, and therefore does not contain any coil parameters. A state-space model is obtained for the mechanical subsystem, which is subsequently written in *TF* form.

The modal equation of motion (see appendix W), is:

$$\ddot{q}_n + 2Z\Omega\dot{q}_n + \Omega^2 q_n = M^{*-1}Q \qquad \textbf{(5.6.12)}$$

where Q is the modal force vector (see appendix W).

The modal state and output equations are written as follows:

$$\dot{x} = A_b x + B_b \theta_b \tag{5.6.13a}$$

$$\theta = C_b x + D_b \theta_b \tag{5.6.13b}$$

The state vector x is:

$$x = \begin{Bmatrix} q_n \\ \dot{q}_n \end{Bmatrix} \tag{5.6.14}$$

A_b, B_b, C_b and D_b are respectively given by:

$$A_b = \begin{bmatrix} 0 & I \\ -\Omega^2 & -2Z\Omega \end{bmatrix} \tag{5.6.15a}$$

$$B_b = \begin{Bmatrix} \{0\} \\ M^{*-1} U^T C^T \begin{Bmatrix} \{0\} \\ \{0\} \\ l\psi_{a2}^T \begin{Bmatrix} k_{211} \\ k_{222} \end{Bmatrix} \end{Bmatrix} \end{Bmatrix} \tag{5.6.15b}$$

$$C_b = \begin{Bmatrix} \dfrac{\Phi_s(x_2) - \Phi_s(x_1)}{x_2 - x_1} & \{0\} \end{Bmatrix} \tag{5.6.15c}$$

$$D_b = 0 \tag{5.6.15d}$$

The sizes of A_b, B_b, C_b and D_b are 24 x 24, 24 x 1, 1 x 24 and 1 x 1 respectively (see appendix W).

Combination of equations 5.6.13 to 5.6.15 gives:

$$\begin{Bmatrix}\dot{q}_n\\ \ddot{q}_n\end{Bmatrix}=\begin{bmatrix}0 & I\\ -\Omega^2 & -2Z\Omega\end{bmatrix}\begin{Bmatrix}q_n\\ \dot{q}_n\end{Bmatrix}+\begin{Bmatrix}\{0\}\\ M^{*-1}U^TC^T\begin{Bmatrix}\{0\}\\ \{0\}\\ l\psi_{a2}^T\begin{Bmatrix}k_{211}\\ k_{222}\end{Bmatrix}\end{Bmatrix}\end{Bmatrix}\theta_b \qquad \textbf{(5.6.16a)}$$

$$\theta=\begin{bmatrix}\dfrac{\Phi_s(x_2)-\Phi_s(x_1)}{x_2-x_1} & \{0\}\end{bmatrix}\begin{Bmatrix}q_n\\ \dot{q}_n\end{Bmatrix} \qquad \textbf{(5.6.16b)}$$

The system transmissibility is the *TF* between θ_b and θ is given by:

$$\frac{\theta}{\theta_b}=C_b\left[sI-A_b\right]^{-1}B_b \qquad \textbf{(5.6.17)}$$

By application of equation 5.6.11, the *TR*, which is also the *TF* between $\ddot{\theta}_b$ and $\ddot{\theta}$, is given by:

$$\frac{\ddot{\theta}}{\ddot{\theta}_b}=C_b\left[sI-A_b\right]^{-1}B_b \qquad \textbf{(5.6.18)}$$

The number of state equations, for the selected number of actuator and optical instrument assumed modes, is 24. The system as described by equations 5.6.16, has 24 eigenvalues in complex conjugate pairs. However, many of the eigenvalues occur at high frequencies, well above the bandwidth, and have no significant effect on system performance inside the band. States corresponding with these frequencies, can therefore be eliminated. This was also done for the coil voltage input, where, apart from the three coil states, only the first ten mechanical subsystem states were retained. For the base input, the 5th and 10th states (corresponding with the 5th normal mode) are eliminated, while the 1st to 4th and 6th to 9th states (corresponding with the first four normal modes) are retained.

The transmissibility magnitude and phase spectra , for a frequency bandwidth of 0 to 500 Hz, are shown in figure 5.6.8.

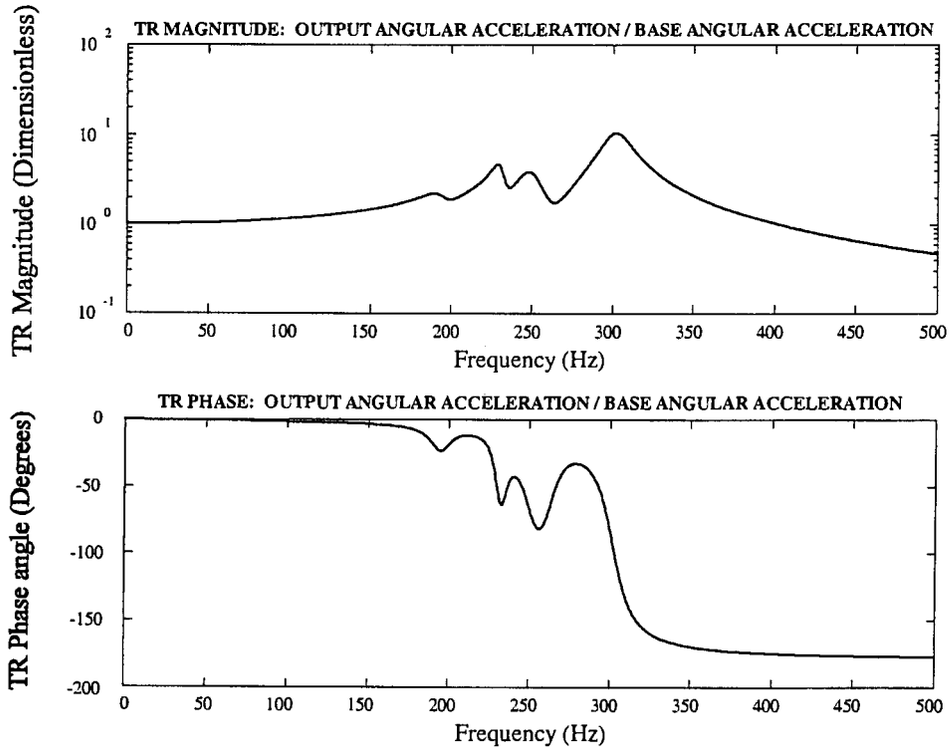

Figure 5.6.8: System base to output transmissibility spectra

Two-input state-space model for control system analysis and design purposes

The state-space model of the system currently consists of two separate state models, one for the coil voltage input, given by equations 5.6.6 to 5.6.9, and one for the base angular acceleration input, given by equations 5.6.13 to 5.6.18. For the purpose of analyzing and designing the control system, it is convenient to combine the two state models into a single state model, with two simultaneous inputs, i.e. coil voltage and base angular acceleration. The coil voltage is the controllable input, while the base motion is the uncontrollable input, or disturbance. The state and output equations, for these two inputs, are:

$$\dot{x} = Ax + B\begin{Bmatrix} V \\ \ddot{\theta}_b \end{Bmatrix} \qquad \textbf{(5.6.19a)}$$

$$\ddot{\theta} = Cx + D\begin{Bmatrix} V \\ \ddot{\theta}_b \end{Bmatrix} \qquad \textbf{(5.6.19b)}$$

The state vector, from equation 5.6.6, is:

$$x = \begin{Bmatrix} q_n \\ \dot{q}_n \\ x_c \end{Bmatrix} \qquad \textbf{(5.6.20)}$$

A is the system coefficient matrix, given in equation 5.6.9a:

$$A = \begin{bmatrix} [0] & [I] & [0] \\ -\Omega^2 & -2Z\Omega & M^{*-1}\Phi_s^T F_l C_c \\ [0] & [0] & A_c \end{bmatrix} \tag{5.6.21}$$

The first ten rows and columns of A correspond with A_b in equation equation 5.6.15a.

B is a matrix with two vector columns:

$$B = [B_V \quad B_{\ddot{\theta}b}] \tag{5.6.22}$$

B_V is given by equation 5.6.9b:

$$B_V = \begin{Bmatrix} \{0\} \\ \{0\} \\ B_c \end{Bmatrix} \tag{5.6.23a}$$

For the first four normal modes $B_{\ddot{\theta}b}$ is given by:

$$B_{\ddot{\theta}b} = \begin{Bmatrix} \{B_b\}_{rows\,1-4} \\ 0 \\ \{B_b\}_{rows\,13-16} \\ 0 \\ \begin{Bmatrix} 0 \\ 0 \\ 0 \end{Bmatrix} \end{Bmatrix} \tag{5.6.23b}$$

C is the output matrix given in equation 5.6.9c:

$$C = \frac{\Phi_s(x_2) - \Phi_s(x_1)}{x_2 - x_1}\begin{bmatrix} -\Omega^2 & -2Z\Omega & M^{*-1}\Phi_s^T F_l C_c \end{bmatrix} \tag{5.6.24}$$

D is a row vector with two zero elements:

$$D = \{0 \quad 0\} \tag{5.6.25}$$

Note that the C-matrix in equation 5.6.24 corresponds with the C-matrix in equation 5.6.9c. However, this C-matrix does not correspond with C_b in equation 5.6.15c. In order to obtain a C-matrix, which is valid for both inputs, the elements of $B_{\ddot{\theta}b}$ are modified as explained in short in the following paragraphs. A more complete explanation is provided in appendix W.

The procedure is as follows: Equations 5.6.16 are written in canonical form, whereby uncoupled state and output equations for each normal mode are obtained. Each modal state equation is then written as follows in *TF* form, using equation 5.6.11:

$$\left(\frac{\ddot{\theta}}{\ddot{\theta}_b}\right)_i = \left(\frac{\theta}{\theta_b}\right)_i = C_i\left[sI - A_i\right]^{-1} B_i \qquad \textbf{(5.6.26)}$$

where the subscript i denotes the i-th normal mode. The sizes of A_i, B_i, C_i and D_i are respectively 2 x 2, 2 x 1, 1 x 2 and 1 x 1.

For the i-th mode, equation 5.6.26 can be expressed as follows in numerator and denominator polynomial form:

$$\left(\frac{\ddot{\theta}}{\ddot{\theta}_b}\right)_i = \left(\frac{p_1 s + p_0}{s^2 + q_1 s + q_0}\right)_i \qquad \textbf{(5.6.27)}$$

where the numerator and denominator polynomial coefficients are given by:

$$p_{0i} = \left(-A_{11}B_2C_2 + A_{12}B_2C_1 + A_{21}B_1C_2 - A_{22}B_1C_1\right)_i \qquad \textbf{(5.6.28a)}$$

$$p_{1i} = \left(B_1C_1 + B_2C_2\right)_i \qquad \textbf{(5.6.28b)}$$

$$q_{0i} = \left(A_{11}A_{22} - A_{12}A_{21}\right)_i \qquad \textbf{(5.6.28c)}$$

$$q_{1i} = \left(-A_{11} - A_{22}\right)_i \qquad \textbf{(5.6.28d)}$$

Equations 5.6.9 are subsequently written in canonical form to obtain an uncoupled state and output equation for each of the first four normal modes. The modal state equation for the i-th mode is then written as follows, in the *TF* form of equation 5.6.26:

$$\left(\frac{\ddot{\theta}}{V}\right)_i = C_i\left[sI - A_i\right]^{-1} B_i \qquad \textbf{(5.6.29)}$$

From equations 5.6.28a and 5.6.28b, B_{1i} and B_{2i} for the i-th mode are determined as follows:

$$\begin{Bmatrix} B_1 \\ B_2 \end{Bmatrix}_i = \begin{bmatrix} C_1 & C_2 \\ A_{21}C_2 - A_{22}C_1 & A_{12}C_1 - A_{11}C_2 \end{bmatrix}_i^{-1} \begin{Bmatrix} p_1 \\ p_0 \end{Bmatrix}_i \qquad \textbf{(5.6.30)}$$

where C_1 and C_2 are the elements of C_i in equation 5.6.29.

The resulting $B_{\ddot{\theta}b}$ -vector, is:

$$B_{\ddot{\theta}_b} = \left\{(B_1)_{i=1} \quad (B_1)_{i=2} \quad (B_1)_{i=3} \quad (B_1)_{i=4} \quad 0 \quad (B_2)_{i=1} \quad (B_2)_{i=2} \quad (B_2)_{i=3} \quad (B_2)_{i=4} \quad 0 \quad 0 \quad 0 \quad 0\right\}^T \qquad \textbf{(5.6.31)}$$

Equations 5.6.19 therefore become:

$$\begin{Bmatrix} \dot{q}_n \\ \ddot{q}_n \\ \dot{x}_c \end{Bmatrix} = \begin{bmatrix} [0] & [I] & [0] \\ -\Omega^2 & -2Z\Omega & M^{*-1}\Phi_s^T F_l C_c \\ [0] & [0] & A_c \end{bmatrix} \begin{Bmatrix} q_n \\ \dot{q}_n \\ x_c \end{Bmatrix} + \begin{bmatrix} B_V & B_{\ddot{\theta}b} \end{bmatrix} \begin{Bmatrix} V \\ \ddot{\theta}_b \end{Bmatrix} \qquad \textbf{(5.6.32a)}$$

$$\ddot{\theta} = \frac{\Phi_s(x_2) - \Phi_s(x_1)}{x_2 - x_1} \begin{bmatrix} -\Omega^2 & -2Z\Omega & M^{*-1}\Phi_s^T F_l C_c \end{bmatrix} \begin{Bmatrix} q_n \\ \dot{q}_n \\ x_c \end{Bmatrix} \qquad \textbf{(5.6.32b)}$$

Equations 5.6.32 will be used to design a suitable control system. Controller design, testing and implementing will be discussed in more detail in chapter 6.

5.7 Summary of chapter 5 and preview of chapter 6

Updating of the system model was described in this chapter. Model updating was motivated in section 5.1 and an updating procedure was given. Identification theory was discussed in short in section 5.2 and linear least-squares frequency domain identification was selected as the most suitable technique for this study.

In section 5.3, an updated *TF* model was obtained from the experimentally determined *TF* spectra, using the Gauss-Newton method. The order of the model was determined iteratively. The *TF* numerator and denominator polynomial coefficients were determined by means of a least-squares data fit to the experimentally determined spectra. The *TF* magnitude and phase spectra were calculated and compared with the measured spectra. It was shown that the accuracy of the updated model was sufficient. The poles and zeroes of the updated *TF* were calculated. It was shown that all the poles and zeroes, with the exception of one zero, have negative real parts and are inside the test band.

Separation of the coil and mechanical subsystem models was motivated in section 5.4 and the procedure was described. The coil *TF* model was separated from the system *TF* and written in canonical state-space form. 2DOF actuator models were developed in section 5.5 to replace the original SDOF models. The distributed mass and stiffness model developed for the optical instrument and support structure in section 2.8 was retained. An SDOF model was included to represent the elastically mounted base. Coupling of the actuator, base and optical instrument models by means of component mode synthesis was explained.

In section 5.6, a physical model was developed to aid in updating the natural frequencies and normal mode shapes. The model parameters were selected and adjusted until the modelled natural frequencies matched the exprimentally-determined frequencies. The normal mode shapes were calculated and modal damping and -force terms were added. A system state model was derived and written in *TF* form. The *TF* spectra were calculated and compared with the experimentally-determined *TF* spectra. *TF* poles and zeroes were calculated and it was shown that all the poles and zeroes have negative real parts. System open-loop transmissibility was obtained and shown graphically. A two-input state-space model was subsequently derived, with coil voltage and base angular acceleration as inputs.

Controller design, implementation and testing will be described in chapter 6. Various controller types will be discussed in section 6.2, followed by a discussion on disturbance attenuation methods in section 6.3. The controller design will be described in detail in section 6.4. The experimental test setup and test equipment will be discussed in section 6.5, followed by the test execution procedure in section 6.6. Test results will be presented and discussed in section 6.7. Chapter 6 will be summarized in section 6.8.

Chapter 6
Design, implementation and testing of a controller for the LOS stabilization system

6.1 Background

Control system design, implementation and testing are described in this chapter. General control theory is given as a background. Various controller types, i.e. feedforward, output and state feedback controllers, linear and nonlinear controllers, tracking controllers, regulators and optimal controllers, are discussed in short.

Principles of disturbance attenuation are discussed in more detail. The attenuation factor is defined and the nature of the disturbance is discussed. Requirements for disturbance and noise attenuation are given. An attenuation method for a known disturbance entering a system at a given point, is described. A short summary of optimal control, in terms of H_2 and H_∞ optimal criteria, is given. Other modern disturbance attenuation techniques, such as preshaping of command inputs, attenuation of a continuous disturbance by means of digital regulation, and "two-way" isolation, are discussed. Motion controllers, i.e. relative and absolute motion controllers, are described in detail.

Control system design specifications are given, followed by a discussion of general control system requirements, such as accuracy, stability, sensitivity, reaction speed, control effort, robustness, observability and controllability. The specifications and general requirements are used to select a suitable controller type. The control system design procedure is described and a detailed exposition of the controller design is given. The design of a suboptimal controller, coupled to a suboptimal observer, is described. These designs are derived from optimal controller and observer designs. Controller characteristics are expressed in terms of state-space models, transfer functions, and closed-loop poles and zeroes. In order to facilitate implementation of the controller, the controller transfer functions are converted to digital filter form.

The test apparatus, test procedure and execution are described. Three controller configurations, i.e. disturbance feedforward, output feedback and feedforward plus feedback configurations, are tested. Test data is processed and the test results are presented. The attenuation factor spectra are shown graphically and RMS attenuation factors are given. The test results are discussed.

The various controller types are discussed in section 6.2, followed by the disturbance attenuation methods in section 6.3. The controller design is described in detail in section 6.4. The test setup is shown in section 6.5 and the test equipment is discussed. A description of the test execution follows in section 6.6. The test results are presented and discussed in section 6.7. Finally, chapter 6 is summarized in section 6.8.

6.2 Summary of various controller types

A concise summary of various controllers is given in this section. The controllers are classified according to type and compared in terms of application, principles of operation, advantages and disadvantages.

A large number of controller types exist. These controllers can broadly be classified in one or more of the following categories: Open-loop feedforward-, closed-loop feedback-, linear-, nonlinear-, output-, state-, optimal-, reduced-order-, tracking controllers and regulators. These categories are discussed in short below.

6.2.1 Open-loop feedforward controllers

The principle of operation of open-loop controllers can be summarized as follows: On the basis of knowledge about the system and of past experience, a prediction is made of what the input should be to give the desired output; the input is adjusted accordingly [Schwarzenbach & Gill, 1986]. The output may, or may not, be measured. A feedforward controller is also known as a prefilter, series compensator, or feedforward compensator.

The purpose of a feedforward controller is to cancel out a significant part of a disturbance before it enters the system. Computation of the control requires a model of the system. The more closely the disturbance can be monitored and the more accurate the system model, the better will be the control [Schwarzenbach & Gill, 1986].

Open-loop controllers can perform well if external disturbances are relatively insignificant [Meirovitch, 1990]. However, the control depends only on the expected system behaviour, and not on the actual behaviour. If some unexpected factor causes the output to deviate from the desired output, there is no way of correcting the deviation.

A vast number of uncertainties, in the form of disturbances or plant variations, may cause the deviations, and every possible uncertainty may require a different design. In order to avoid repetitive design and testing, adaptive controllers can be used to do real-time adjustment of controller characteristics. Adaptive controllers are described in detail by Goodwin & Sin [1984], and will not be discussed any further in this study. Alternatively, open-loop control can be used in combination with closed-loop control, where the feedforward compensator attenuates the disturbance, and the feedback compensator provides the necessary corrective action, stability and robustness.

6.2.2 Closed-loop feedback controllers

In feedback control, the control takes into consideration the actual system behaviour, instead of the expected behaviour [Meirovitch, 1990]. Feedback is used in closed-loop controllers to decrease the sensitivity of the system to plant variations, to enable adjustment of the system transient response, to reject disturbances and to reduce steady-state tracking errors [Bishop, 1993]. Two main types of closed-loop controllers can be distinguished, i.e. output feedback

controllers and state feedback controllers. These two controller types are discussed in short in the next two sections.

6.2.3 Output feedback controllers

Output feedback controllers often used are PID controllers, rate feedback controllers, lead-lag compensators and frequency-shaping filters. The choice of a suitable controller depends on the control objective and the controller characteristic.

If accurate transient behaviour, in terms of overshoot, rise-time, settling-time and DC error is required, a PID controller is normally used. This controller type consists of a parallel combination of a proportional (P)-element, an integral (I)-element and a differential (D)-element, placed in the forward path of the closed-loop, with unity feedback. The P-element gains the output error to increase the control effort, the I-element integrates the error to obtain accurate steady-state behaviour, while the D-element lowers the overshoot peak. Simpler variations of PID controllers include PI- and PD controllers. PID controller design is described in detail by Schwarzenbach & Gill [1986].

In order to eliminate large initial transients that may damage a plant or may cause system malfunctioning, the PID controller discussed above may be removed and replaced by a minor feedback loop, which differentiates the output. This method of feedback control is known as rate feedback, or negative velocity feedback. Since it is not good practice to differentiate the output signal, due to the presence of noise, measurement of the output rate may be directly done, using an output rate sensor [Schwarzenbach & Gill, 1986].

If both control accuracy and high stability margins are essential, a phase compensator, such as a phase-lead-, phase-lag- or lead-lag filter, may be used. A phase lead compensator is a 1^{st} order filter, with high-pass characteristics, which increases the phase of the closed-loop system. The filter numerator and denominator coefficients determine the phase spectrum. Phase-lead compensation generally improves rise-time and reduces the amplitude of transient oscillations, but increases the bandwidth [Schwarzenbach & Gill, 1986].

A phase-lag filter is a 1^{st} order filter with low-pass filtering characteristics. Lag compen-sation reduces overshoot, but at the expense of rise-time. The limitations of lead- and lag filters are partially overcome by lead-lag filters. The lead- and lag elements may be combined into a single filter, or may be placed in series, separated by a buffer [Schwarzen-bach & Gill, 1986].

A frequency-shaping filter can be placed in the feedback loop to obtain the required plant frequency-domain behaviour. This can be achieved by, inter alia, pole assignment and optimal frequency shaping filter design techniques. Optimal frequency shaping is possible with LQG design, by including frequency-shaped weighting matrices in the quadratic cost functional [Meirovitch, 1990]. Pole assignment using output feedback is described by Brogan [1985]. Practically, output controllers can be implemented by placing digital filters between the sensors and plant.

6.2.4 State feedback controllers

In state-feedback control, the plant states are combined, either linearly or nonlinearly, to obtain the control signal. A large variety of state feedback controllers exist. Since it is impossible to discuss all the varieties here, a brief discussion is given on optimal-, static-, dynamic-, full-state feedback- and reduced-order controllers, as well as state feedback controllers using observers.

An optimal state feedback gain matrix can be determined which stabilizes the system, minimizes the control effort and meets the disturbance rejection criterion. Two of the most popular versions of optimal state feedback controllers, are H_2 and H_∞ controllers, the names of which are derived from their respective optimality criteria. Other versions of optimal controllers include bang-bang controllers, and optimal controllers designed by variational methods, as discussed in detail by Kirk [1970] and Meirovitch [1990]. More recently, optimal controllers have also been designed by application of genetic algorithms. A serious limitation of optimal state controllers is that they are seldom robust [Kuo, 1982]. In order to obtain sufficient robustness, modification of the controller design may be required. Robust design will be discussed in short in section 6.4.

State control can be directly done if the output is invertible, i.e. if the states can be obtained by inversion of the linear, or nonlinear, function $y(x)$, that expresses the outputs in terms of the states. This type of state control is known as static state control. The term "static" indicates that the relationship between the output and control is either a constant factor, or a nonlinear function of the output, but is independent of frequency. Static state controllers have no dynamics of their own, which limits their performance in terms of criteria such as optimality, stability and robustness. Static state controller design and stabilization are, however, relatively simple. Stability of the closed-loop system is only determined by its gain and phase margins.

If $y(x)$ is not invertible, for instance if the output matrix is singular, a state observer is required to reconstruct the states from measured outputs. This type of state control is known as dynamic state control, since the observer has its own dynamic behaviour, independent of that of the plant. Observer order is normally equal to, or less than, the plant order. If the observer order is equal to that of the plant, the observer is known as a full-state observer, and the controller is known as a full-state feedback controller. Observability and controllability are conditions for full-state feedback, and will be discussed in short in section 6.4.

In order to avoid interference of the observer with the plant, observer poles can be arbitrarily placed at twice the plant natural frequencies, as a rule-of-thumb. However, if plant natural frequencies are high, high sample rates may be required for accurate control, which may lead to excessively noisy measurement signals. As an alternative, optimal linear quadratic gaussian (LQG) observer design can be done, where both disturbance and output noise energy levels are taken into account to determine the observer gain matrix.

Estimation of all the plant states is impossible if the plant is not observable. However, in general, it is still possible to estimate the observable components of the states of such a plant; if the unobservable components decay extremely rapidly, this partial estimation may be adequate [Anderson & Moore, 1989]. Observers used for this purpose are known as reduced-order observers, the design of which is discussed in more detail by Anderson & Moore [1989]

and Meirovitch [1990]. It will be shown in section 6.4 that the magnetostrictive LOS stabilization system is observable.

Stability of a closed-loop linear state-feedback controlled system is determined by the signs of the real parts of the closed-loop eigenvalues. If the real parts of all the eigenvalues are negative, the system is unconditionally stable. The stability margin of a closed-loop state-controlled system can be obtained by means of the Nyquist criterion.

6.2.5 Linear controllers

A comprehensive range of linear controllers exists; a detailed description of which is beyond the scope of this study. Linear controllers can broadly be classified as linear state- and linear output controllers. The control signal generated by a linear state controller, is a linear combination of the states, while that generated by a linear output controller, is the product of the output and a transfer function with constant coefficients. The number of transfer functions depends on the number of controls and outputs. A single-input-single-output (SISO) controller has only one *TF*. The number of *TF*'s of a multiple-input-multiple-output (MIMO) controller, is the product of the number of output and control variables. For large MIMO systems, state control is generally more powerful than output control.

Linear control is applied to systems whose characteristics stay constant, or vary slightly with changes in states or outputs (e.g. weakly nonlinear systems), over the range of operation. Linear control is particularly popular because system characteristics and behaviour can be analyzed using the well-established linear systems theory.

Linear controllers make use of linear feedback and / or feedforward elements, with constant coefficients, to generate the plant control signal. Linear control design methods are, inter alia, optimal design (H_2 and H_∞) methods, robust design methods, frequency shaping and arbitrary pole placement. Stability of a linear closed-loop system is determined by the eigenvalues of the system coefficient matrix, or poles of the transfer functions.

Disadvantages of linear control arise from the fact that most dynamic systems display some degree of nonlinearity. This characteristic limits the application of linear controllers to weakly nonlinear systems. Where large changes in characteristics are encountered, linear control may lead to instability, unduly high input energy and inaccurate control [Slotine & Li, 1991]. Linear control is therefore not recommended for highly nonlinear systems. Nonlinear controllers are recommended for this purpose.

6.2.6 Nonlinear controllers

In nonlinear control, the control signal may either be a nonlinear function of the outputs, or a nonlinear function of the states. The former is known as nonlinear output control, while the latter is known as nonlinear state control.

Nonlinear control methods include input-output linearization, input-state linearization, sliding mode control, linearization by means of describing functions, nonlinear control using nonlinear

observers, and adaptive control. Nonlinear control design methods are described in detail by Gelb & VanderVelde [1968], Slotine & Li [1991] and Vidyasagar [1978].

If applied to highly nonlinear systems, the advantages of nonlinear control are higher accuracy, better stability and lower control effort. The disadvantages are a higher degree of complication in mathematical analysis and control hardware. One of the most difficult tasks in nonlinear control design is to find a feedback function that will linearize, as well as stabilize, the system. In the case of weakly nonlinear systems, however, linearization is less complicated, and linear control may often be directly applied.

6.2.7 Tracking controllers

Tracking control is defined as follows by Meirovitch [1990]: "The tracking problem is defined as the problem of designing a control input so as to cause the plant state to follow a given reference state. The linear tracking problem is the one in which the control is a linear function of the state".

Tracking control can be applied to this study, by controlling the relative angular acceleration between the base and instrument. The base and instrument accelerations are measured and the relative acceleration is calculated. The tracking error, which is the difference between the relative acceleration and (negative) base acceleration, is driven to zero.

The advantage of using a tracking controller for this application is that the relative acceleration is large, ideally equal in magnitude to the disturbance, and is therefore easily measurable. Sensor noise is comparatively small and therefore does not significantly influence controller performance, as long as the controller is operated outside the sensor noise frequency band.

The disadvantage is that, although control is closed-loop, the relative acceleration, instead of the output acceleration, is controlled. The main objective of LOS stabilization of the optical instrument is to minimize the output. A controller that drives the output to zero, or as close to zero as possible, will therefore be more applicable. This controller type is known as a regulator.

An example of a tracking controller that is of importance to this study, is a state observer. The observer estimates the states from the measured plant output, estimated output and control input. The observer error, which is the difference between the true states and estimated states, is driven to zero. The control is obtained from the estimated states.

More information on tracking controllers is given by Anderson & Moore [1989] and Kirk [1970].

6.2.8 Regulators

The following definition of the regulator problem is given by Meirovitch [1990]: "The regulator problem is defined as the problem of designing a control input so as to drive the plant from some initial state to a constant final state. Another way of defining the regulator problem is as one in which the reference input is constant. Because a simple coordinate transformation can translate the origin of the state-space to any constant point in the space, the regulator problem can be redefined as the problem of designing a control input, so as to drive the plant to the zero state. The linear regulator problem is the one in which the control is a linear function of the state." Since the output of a linear system can be described as a linear combination of the states, a controller that drives the output to zero, can also be classified as a regulator.

The presence of noise may make it difficult to drive the output to zero. For this reason, regulator design is often aimed at minimizing the output, instead of driving it to zero. Generally, regulated systems with low output magnitudes, wide disturbance frequency bands and high system cutoff frequencies, may experience serious noise effects.

The objective of this study is to minimize the output, in the presence of the base disturbance and measurement noise. The output is the angular acceleration of the optical instument, the base disturbance is the base angular acceleration, and the control is the actuator coil voltage. For this application, the aim is to obtain the coil voltage, which will attenuate the effects of the disturbance to such an extent that the output is minimized. Since the required output is significantly smaller than the base disturbance, any regulator considered for attenuation purposes, will therefore also have to be designed to minimize the effects of measurement noise.

6.2.9 Optimal controllers

Optimality of a control system is expressed in terms of a performance measure, the concept of which was originally introduced in classical controller design. Typical performance criteria are system response to a step or ramp input, characterized by rise-time, settling-time, peak overshoot and steady-state accuracy, and the frequency response of the system, characterized by gain and phase margin, peak amplitude and bandwidth [Kirk, 1970].

In modern, or optimal, control, the main goal is to minimize the performance measure, or performance index ("PI"), of a particular system or control problem. Typical optimal control problems are minimum-time, terminal control, minimum control effort, tracking control and regulator problems. (The PI's of each of these problems are given by Kirk [1970]).

Formulation of the PI is necessarily influenced by the control objective. The objective of a regulator, or instance, is to minimize the control effort required to drive the states (for a state regulator), or outputs (for an output regulator), to zero, or as close to zero as possible. Optimization of a regulator therefore requires that both the control and the states (or outputs), be minimized. Weights can be placed on any of the terms in the PI, to emphasize the relative importance of the particular term. For example, an increase in control weight will lower the control effort, while an increase in output weight will lower the output.

The PI may be expressed in linear quadratic (LQ) form, where the squared values of the relevant performance terms are weighed, summed and subsequently integrated over a given time period, which may be definite or indefinite. The value of the PI may be calculated to obtain the relative performance of a system. A low PI indicates better performance than a high PI, for the same plant.

If necessary, constraints can be imposed to limit, or bound, certain system variables or parameters, to ensure that the system operates within its ability. The performance of a constrained system may be the same as, or worse than, that of an unconstrained system. For instance, a regulator with a high output weight, whose control is constrained, may command a control signal in excess of the constraint. The control will be clipped as soon as it reaches the constraint, thereby sacrificing output performance. This may however not happen in the case of a regulator with a lower output weight.

Constraints may also be required to obtain relationships between the individual terms in the PI. An example is the state-space equations of a plant. The state equation provides the relationship between the states and control, while the output equation gives a relationship between the states and outputs.

State feedback gains of LQ optimal linear regulators are obtained from, inter alia, the solution of the steady-state Riccati equation. Derivation of the equation, from the PI and state equations, is described in detail by Anderson & Moore [1989] and Kirk [1970]. The Riccati equation is nonlinear, but can be solved in linear form by Hamiltonian eigenvector decomposition, as described by Meirovitch [1990].

Optimal control design principles are also applied to observer, or estimator design. An optimal observer is also known as a linear quadratic estimator, or Kalman filter. The objective of optimal observer design is to obtain the observer feedback gain matrix that will minimize the effects of input and output noise.

Optimal control is thoroughly described by Anderson & Moore [1989], Brogan [1985], Kirk [1970] and Meirovitch [1990].

6.2.10 Conclusion of section 6.2

Controllers considered for this study are made up of combinations of two or more of the controllers discussed in the foregoing sections. A suitable controller for the magnetostrictive LOS stabilization system will typically be a linear regulator, with sufficient disturbance attenuation, stability, robustness and optimality, for a bounded control voltage. The selection of a suitable type of controller for the LOS stabilization system will be covered in section 6.4.3.

6.3 Principles of disturbance attenuation

In this study, LOS stabilization of the optical instrument can be considered as a disturbance attenuation method. The disturbance is the base motion, which is transmitted to the optical instrument by the plant. The resulting motion of the optical instrument, i.e. the plant output, is the product of the disturbance and uncontrolled transmissibility of the plant.

The objective is to attenuate the effects of the base motion on the LOS accuracy of the optical instrument. To achieve this, the transmitted base motion must be attenuated to reduce the motion of the optical instrument to a significantly low fraction of the base motion. The ratio of the remaining output to the disturbance is known as the attenuation factor.

Base and optical instrument motions may be expressed in terms of variables such as angular displacements, speeds or accelerations. The choice of the most suitable variable will necessarily depend on the sensors used for measuring the motions. Since the sensors used in this study are accelerometers, the base and instrument motions will be expressed in terms of angular accelerations. (Although the sensors can only measure translational accelerations, angular accelerations can be obtained by dividing the difference between the measured signals by the distance between the sensors).

In this section, the attenuation factor is discussed in more detail. The nature of the disturbance is subsequently discussed. Requirements for attenuation of disturbances and noise are given, followed by a description of feedforward compensation of a known disturbance entering a system at a given point. Modern attenuation methods, i.e. optimal attenuation, preshaping of command inputs, digital regulation of continuous disturbances and two-way isolation, are discussed in short.

The application of disturbance attenuation methods is extended to motion controllers of various kinds, the most basic of which are relative and absolute motion controllers, disturbance feedforward (open-loop) controllers and a combination of disturbance feedforward and absolute motion controllers. A simple method for improving the robustness of optimal motion controllers, is discussed.

6.3.1 Attenuation factor

The isolation ability of the system can be expressed in terms of an attenuation factor, which is the ratio of the attenuated output, to the disturbance:

$$\gamma = \frac{y}{d} \qquad \textbf{(6.3.1.1)}$$

where γ is the attenuation factor, y is the attenuated output and d is the disturbance.

In disturbance attenuation, the ultimate goal is to drive the output to zero, in order to achieve total isolation. However, although this may be theoretically feasible, it is practically impossible to achieve. The reason is that the measured disturbance and output signals will almost always be contaminated with noise. As the output is driven to zero, its signal-to-noise

ratio approaches zero, thereby making feedback control extremely difficult. It is therefore more realistic to minimize the output, instead of driving it to zero.

At the other end of the scale, an attenuation factor of unity indicates that all the base motion is transmitted to the optical instrument, i.e. no isolation takes place. This may for instance happen in the trivial case of total absence of a stabilization system. When a stabilization system is present, but is not controlled, the attenuation factor may exceed unity. This will for instance happen if the base excites one or more of the natural frequencies of the plant. In this case, γ represents the transmissibility (TR) of the stabilization system, for zero control input. A properly designed isolation system must be able to attenuate both the disturbance and its dynamic effects on the plant.

The TR magnitude and phase spectra of the LOS stabilization system were shown in figure 5.6.8. From the figure, it can be seen that the TR magnitude is unity at DC and gradually increases with frequency, reaching local maxima at the natural frequencies, and local minima at anit-resonant frequencies. The TR magnitude is approximately unity in the disturbance frequency BW of 0 Hz to 100 Hz.

From the above discussion, it can be seen that a practically achievable goal for γ should be between zero and one:

$$0 \leq \gamma \leq 1 \tag{6.3.1.2}$$

The lower γ, the more effective the isolation.

Mathematical expression of the attenuation factor will depend on the control objective. A number of control objectives can be formulated to suit the need. Firstly, if the objective is to reduce a peak in the time trace of the output to a given fraction of that of the disturbance, γ can be expressed as:

$$\gamma = \frac{|y(t)|_{\max}}{|d(t)|_{\max}} \tag{6.3.1.3}$$

Secondly, if the objective is to attenuate the disturbance at the dominant frequency in the BW, the attenuation factor can be expressed as:

$$\gamma = \frac{Y(j\omega_d)}{D(j\omega_d)} \tag{6.3.1.4}$$

where ω_d is the dominant disturbance frequency.

In the third place, if the objective is to obtain an output whose magnitude is a constant fraction of that of the disturbance at each frequency in the disturbance *BW*, the attenuation factor can be expressed as:

$$\gamma(j\omega) = \frac{Y(j\omega)}{D(j\omega)} = const \qquad \textbf{(6.3.1.5)}$$

To obtain this attenuation factor, an isolation system is required which rejects a constant percentage of the disturbance at all the frequencies in the disturbance *BW*.

Lastly, if the objective is to minimize the ratio of output energy to disturbance energy over a given frequency bandwidth, the attenuation factor can be expressed as the ratio of the *RMS* of the output to that of the disturbance:

$$\gamma = \frac{y_{RMS}}{d_{RMS}} \qquad \textbf{(6.3.1.6)}$$

In this case, the attenuation factor is a constant scalar. It will however not necessarily be constant with frequency and may contain a spectrum of frequencies.

6.3.2 Nature of the disturbance

A disturbance can broadly be classified in terms of its type, whether the disturbance is known, and its position of entering the system. Disturbance types include, inter alia, wide-band random, band-limited random, narrowband, harmonic, transient, and DC disturbances, as well as measurement and system noise.

A distinction is often made between noise and disturbances, since the system characteristics required for disturbance attenuation differ from those required for noise attenuation [Anderson & Moore, 1989]. Disturbance and noise attenuation requirements will be discussed in section 6.3.3. A thorough comparison between different control methods for narrowband disturbance attenuation is given by Sievers & von Flotow [1992]. DC disturbance attenuation is described in detail by Kuo [1982].

A disturbance can be termed a known disturbance if it can be measured before control system design. The disturbance is measured and characterized in terms of parameters such as magnitude and phase spectra, power spectral density and RMS value. These parameters are used to design the controller in order to meet the control objective, e.g. to achieve a required RMS output. The control objective will be met as long as the known disturbance is the only disturbance entering the system. Unknown disturbances are necessarily more difficult to attenuate. To achieve this, sufficient robustness must be supplied by the feedback loop in order to compensate for the uncertainties. Attenuation of a known disturbance entering a system at a given position, by means of feedforward compensation, is described by Schwarzenbach & Gill [1986].

Disturbances may enter the system at the input or output, or may originate inside the system. An example of a disturbance entering the system at the input, is measurement noise

contaminating the reference signal of a tracking controller. An example of a disturbance entering the system at the output, is measurement noise contaiminating the output signal of a regulator. Input noise and output noise mainly originate from sensors and electromagnetic radiation, infiltrating the system through unscreened wires. System noise may originate from loose, rattling or faulty system components.

In the case of the LOS stabilization system, which is the topic of this study, the known disturbance is the angular acceleration of the mounting base of the optical instrument. The disturbance enters the system at the input. The unknown disturbances are base and output measurement noise, as well as seismic motion of the test setup, caused by environmental disturbances such as traffic.

6.3.3 Requirements for disturbance and noise attenuation

The requirements for disturbance and noise attenuation are discussed in short in this section. Sensitivity and complementary sensitivity functions, which provide an indication of the dependence of the tracking error, output and control signals, on the reference, disturbance and noise signals, are defined. The requirements for accurate tracking, disturbance and noise attenuation are expressed in terms of these functions.

The block diagram of a closed-loop controller is shown in figure 6.3.3.1. The reference input, output and tracking error signals are respectively denoted by r, y and e, while the output measurement noise and disturbance signals are represented by n and d. The control signal is denoted by u. The plant and controller transfer functions are represented by $G_p(s)$ and $G_c(s)$. (The TF's may either be vectors or scalars, depending on the number of inputs and outputs).

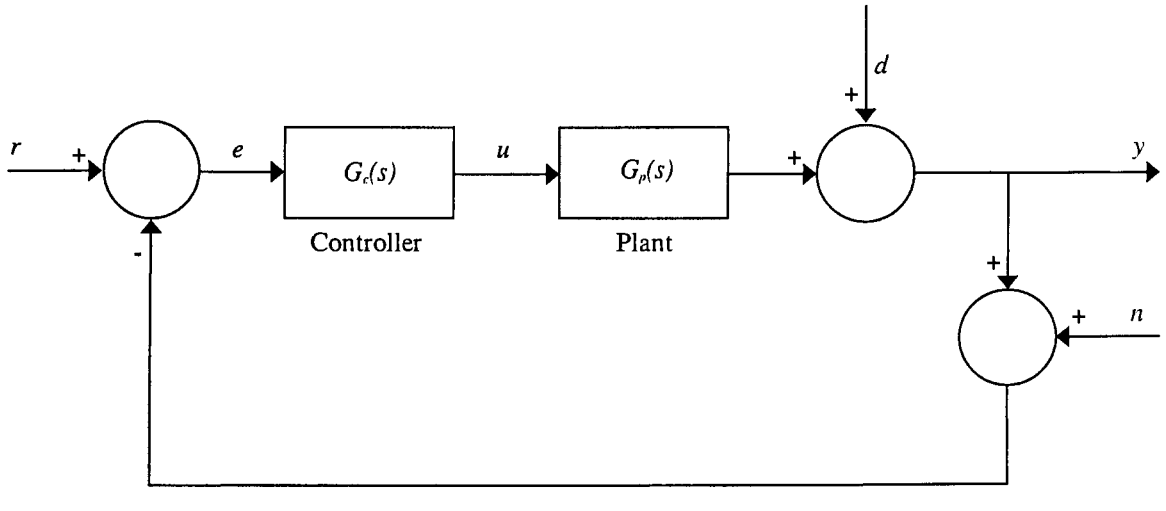

Figure 6.3.3.1: Block diagram of closed-loop controller, with disturbance and noise entering the system at the output [Anderson & Moore, 1989]

The sensitivity function S and complementary sensitivity function T, from Anderson & Moore, [1989], are given by:

$$S = \left(I + G_p G_c\right)^{-1} \tag{6.3.3.1a}$$

$$T = G_p G_c \left(I + G_p G_c\right)^{-1} \tag{6.3.3.1b}$$

where T is the complement of S:

$$S + T = I \tag{6.3.3.2}$$

The plant output y, measured tracking error e and control u can be expressed as follows in terms of S and T (the derivations are not done here, only the results are given):

$$y = T(r - n) + Sd \tag{6.3.3.3a}$$

$$e = S(r - n - d) \tag{6.3.3.3b}$$

$$u = G_c S(r - n - d) \tag{6.3.3.3c}$$

Requirements for accurate tracking, disturbance attenuation and noise attenuation, in terms of the sensitivity and complementary sensitivity functions, are discussed in detail by Anderson & Moore [1989].

The requirement for accurate tracking and good disturbance attenuation is:

$$\overline{\sigma}[S(j\omega)] << 1 \tag{6.3.3.4}$$

where $\overline{\sigma}$ denotes the largest singular value of S.

The requirement for good noise attenuation is:

$$\overline{\sigma}[T(j\omega)] << 1 \tag{6.3.3.5}$$

It can be seen from equations 6.3.3.2, 6.3.3.4 and 6.3.3.5, that there is an inconsistency between the requirements for good tracking and disturbance attenuation on the one hand, and noise attenuation on the other.

6.3.4 Attenuation of a known disturbance entering the system at a given point

A known disturbance entering a system at a given point can be attenuated by means of a feedforward compensator, in conjunction with a unit feedback loop [Schwarzenbach & Gill, 1986]. The disturbance signal is monitored and a control signal is obtained that partially attenuates the disturbance before it affects the system. This attenuation method is particularly applicable to this study, since the disturbance and its position of entering the system, i.e. the angular acceleration of the base, are known in advance.

The block diagram of a feedback controller with feedforward compensation is shown in figure 6.3.4.1.

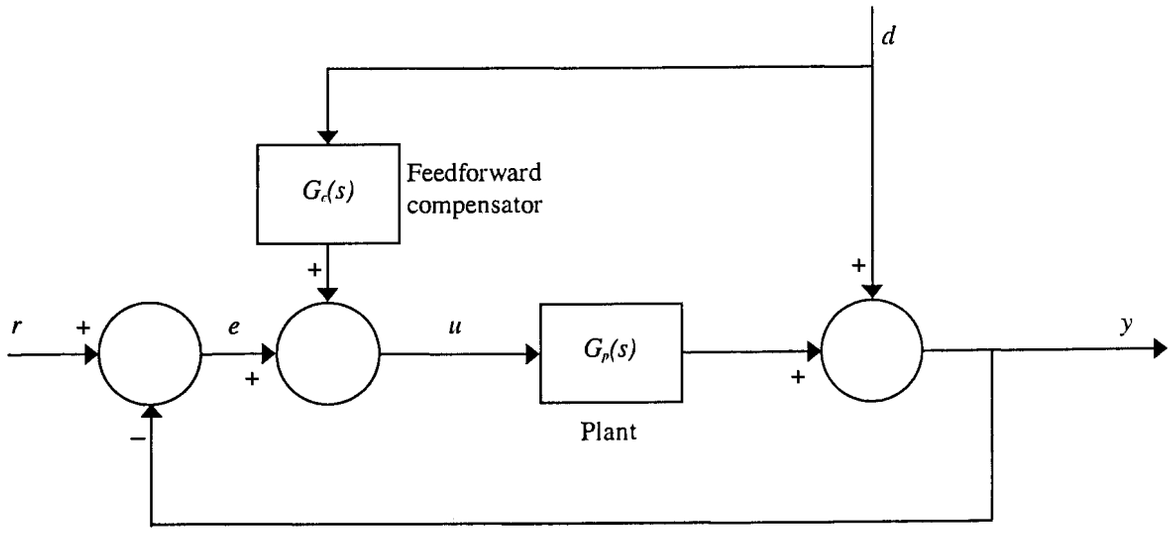

Figure 6.3.4.1: Block diagram of feedback controller with feedforward compensator [Schwarzenbach & Gill, 1986]

The output, tracking error and control are given by:

$$y = G_p u + d \qquad \textbf{(6.3.4.1a)}$$

$$e = r - y \qquad \textbf{(6.3.4.1b)}$$

$$u = e + G_c d \qquad \textbf{(6.3.4.1c)}$$

The output, tracking error and control can be expressed as follows in terms of the reference and disturbance inputs:

$$y = G_p\left(I + G_p\right)^{-1} r + \left(G_p G_c - I\right)\left(I + G_p\right)^{-1} d \qquad \textbf{(6.3.4.2a)}$$

$$e = \left(I + G_p\right)^{-1} r - G_p G_c\left(I + G_p\right)^{-1} d \qquad \textbf{(6.3.4.2b)}$$

$$u = \left(I + G_p\right)^{-1} r + \left(G_c - I\right)\left(I + G_p\right)^{-1} d \qquad \textbf{(6.3.4.2c)}$$

A special case is that of a regulator, whose reference input r is zero. The output of a regulator, in terms of the disturbance, from equation 6.3.4.2a, is given by:

$$y = \left(G_p G_c - I\right)\left(I + G_p\right)^{-1} d \qquad \textbf{(6.3.4.3)}$$

The attenuation factor γ, from equation 6.3.1.1, is given by:

$$\gamma = \frac{y}{d} \qquad \textbf{(6.3.4.4)}$$

Substitution of equation 6.3.4.3 into equation 6.3.4.4 gives:

$$\gamma = \left(G_p G_c - I\right)\left(I + G_p\right)^{-1} \tag{6.3.4.5}$$

For a specified disturbance attenuation factor γ, the required feedforward compensator transfer function G_c is:

$$G_c = \gamma + \left(I + \gamma\right)G_p^{-1} \tag{6.3.4.6}$$

The control u, in terms of the disturbance d and output y, is given by:

$$u = G_c d - y \tag{6.3.4.7}$$

Substitution of equation 6.3.4.6 into equation 6.3.4.7 gives:

$$u = \left[\gamma + \left(I + \gamma\right)G_p^{-1}\right]d - y \tag{6.3.4.8}$$

Equation 6.3.4.8 is only valid for static unit feedback. A similar equation can be derived for an arbitrary dynamic feedback gain $H_c(s)$.

6.3.5 Optimal disturbance attenuation using H_2 and H_∞ optimization techniques

The objective of disturbance attenuation in this study is to make the angular motion of the optical instrument less sensitive to the angular motion of the base. To achieve this, the output of the plant must be minimized.

The control required for this purpose can be obtained in a number of ways, e.g. by classical controller design methods, such as pole placement. However, this method only involves the output, and takes no account of the control effort required to achieve the objective. Necessarily, the output will increase if the control decreases, and vice versa. In order to obtain an efficient controller, the control effort must be weighed against the output. This process is known as optimization.

Various control optimization techniques exist, such as variational optimization and linear quadratic (H_2) optimization. The latter technique is applicable if the disturbance is fixed or has a fixed power spectrum [Doyle et al, 1989]. H_2 optimization is therefore applicable to this study, since the disturbance spectrum is known.

The H_2 performance measure is defined as follows in the frequency domain for a stable transfer function matrix $G(s)$ [Doyle et al, 1989]:

$$\|G\|_2 := \left(\frac{1}{2\pi}\int_{-\infty}^{\infty} trace\left[G(j\omega) * G(j\omega)\right]d\omega\right)^{1/2} \tag{6.3.5.1}$$

Linear quadratic optimization will be discussed in more detail in section 6.4, where the control design will be described in detail.

A modern control optimization technique still under development, which gives better robustness to uncertainties, is H_∞ control. The H_∞ performance measure performance is defined as follows in the frequency domain [Doyle et al, 1989]:

$$\|G\|_\infty := \sup_\omega \sigma_{max}[G(j\omega)] \qquad \textbf{(6.3.5.2)}$$

where σ_{max} is the maximum singular value.

The H_∞ criterion corresponds to designing for the worst disturbance signal [Doyle et al, 1989]. If a full-state feedback controller is used, the feedback gain matrix can be obtained from a solution of a single Riccati equation. State-space solutions to H_∞ control problems and disturbance attenuation by means of H_∞ control, are discussed in detail by Doyle et al [1989], Petersen [1987] and Petersen [1989].

6.3.6 Preshaping of command inputs

Preshaping of command inputs is often used for open-loop disturbance attenuation. The method can however be applied successfully if the input shaping accounts for the dynamic characteristics of the closed-loop plant [Singer & Seering, 1990].

The behaviour of the system to a series of impulses is used to attenuate endpoint vibration. The first impulse excites transient behaviour of the system, which is cancelled by the transient behaviour of subsequent impulses. A short delay, of the order of the period of the first mode of vibration, is incurred. Disturbances other than impulses are expressed as series of impulses.

The impulse amplitude and delay between impulses depend on the frequency and damping factor of the first natural mode. For example, the amplitudes for a two-impulse input are:

$$A_1 = \frac{1}{1+K} \qquad \textbf{(6.3.6.1a)}$$

$$A_2 = \frac{K}{1+K} \qquad \textbf{(6.3.6.1b)}$$

where K is a dimensionless constant, given as follows in terms of the damping factor ζ of the first natural mode of vibration:

$$K = e^{-\zeta\pi/\sqrt{1-\zeta^2}} \qquad \textbf{(6.3.6.2)}$$

The time delay ΔT is given by:

$$\Delta T = \frac{\pi}{\omega_n \sqrt{1-\zeta^2}} \qquad \textbf{(6.3.6.3)}$$

where ω_n is the natural frequency of the first mode of vibration of the system.

6.3.7 Attenuation of a continuous disturbance by means of digital regulation

Digital control is almost universally used in modern control, mainly for its simplicity of implementation and ease of changing control parameters. For these reasons, a digital controller will be used to drive the LOS stabilization system discussed in this study. The principle of operation of the controller is discussed in short below. The system block diagram, from Jacquot [1981], is shown in figure 6.3.7.1.

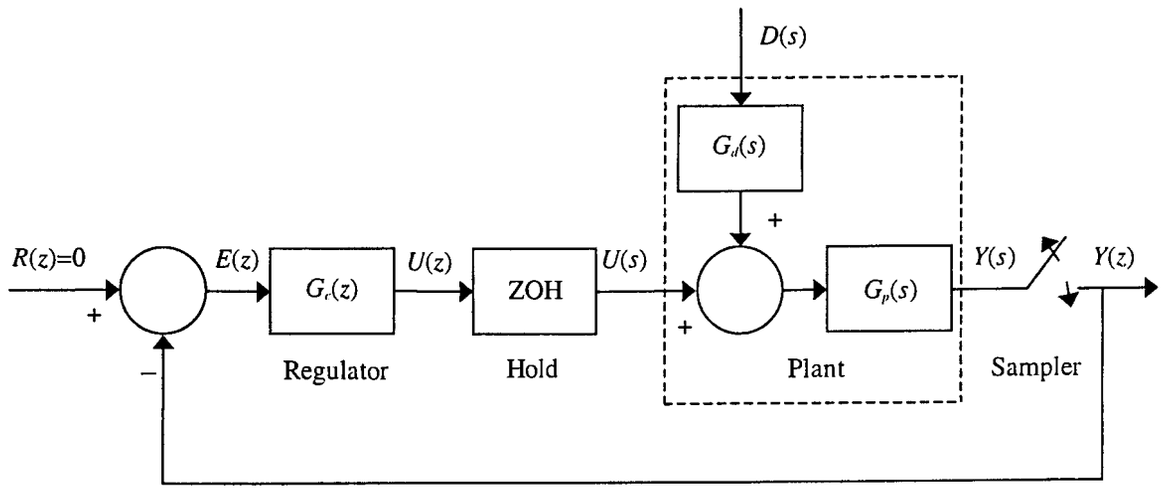

Figure 6.3.7.1: Block diagram of digital regulator for continuous disturbance attenuation [Jacquot, 1981]

A disturbance $D(s)$ enters the plant, with disturbance-to-output and input-to-output transfer functions $G_d(s)$ and $G_p(s)$, at the input. The plant output $Y(s)$ is sampled at a rate T and the sampled output $Y(z)$ is fed back into a digital regulator, with output $U(z)$. A zero order hold is applied to the control to obtain a continuous control signal $U(s)$, which drives the plant to attenuate the disturbance.

6.3.8 Motion controllers

Motion controllers are discussed in this section. A translational SDOF spring-mass-damper system is used to explain the principles of motion control. Although rotational pitch DOF's are of importance in this study, the translational model is used in the interest of simplicity. Analytical equations are obtained which give clear insight into the system characteristics. The principle can easily be extended to a rotational system, such as the LOS stabilization system. This will be done in section 6.4, where the controller design will be covered in detail.

Motion controllers can conveniently be divided into relative motion controllers and absolute motion controllers. A better understanding of the various types of motion controllers is provided with the aid of figure 6.3.8.1. The figure shows a linear spring-mass-damper system, with mass m, spring stiffness k and viscous damping coefficient c, mounted on a moving base with vertical displacement d, speed $\dot{d}$ and acceleration $\ddot{d}$. The vertical displacement, speed and acceleration of the mass are y, $\dot{y}$ and $\ddot{y}$ respectively. The actuator force, which excites the mass to attenuate the transmission of the base motion through the system, is F_a.

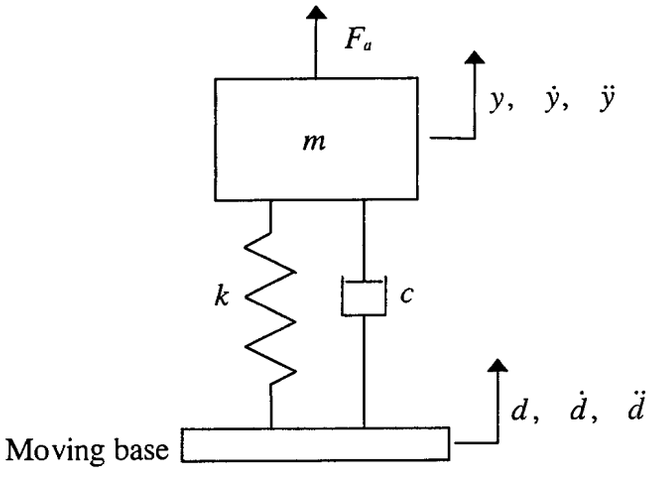

Figure 6.3.8.1 SDOF spring-mass-damper system excited by base motion and actuator force

The motion variable that is controlled depends on the sensor type, e.g. accelerometer, eddy probe (proximity sensor), or linear variable differential transformer (LVDT). In this study, the dynamic motion variables are translational accelerations, measured by means of accelerometers. Transmissibilities of the open-loop and closed-loop systems discussed below will therefore be expressed as ratios of accelerations.

The equation of motion is normally expressed in terms of all the motion variables, i.e. displacement, speed and acceleration. The equation of motion of the system shown in figure 6.3.8.1 is:

$$m\ddot{y} = -c(\dot{y} - \dot{d}) - k(y - d) + F_a \qquad \textbf{(6.3.8.1)}$$

Equation 6.3.8.1 is subsequently used to obtain the open- and closed-loop transmissibilities of the various motion controller types.

6.3.8.1 Relative motion controller

Relative motion control is done by measuring both the base and absolute accelerations, and by feeding back the difference between the two measured signals into the controller, to obtain the actuator force.

In order to derive the equation of motion, consider figure 6.3.8.1 and equation 6.3.8.1. The equation of motion of the SDOF system, for relative motion, is obtained by subtraction of $m\ddot{d}$ on both sides of equation 6.3.8.1:

$$m(\ddot{y} - \ddot{d}) = -c(\dot{y} - \dot{d}) - k(y - d) - m\ddot{d} + F_a \qquad \textbf{(6.3.8.1.1)}$$

Equation 6.3.8.1.1 can be written as:

$$\ddot{y}_r + \frac{c}{m}\dot{y}_r + \frac{k}{m}y_r = -\ddot{d} + \frac{1}{m}F_a \qquad \textbf{(6.3.8.1.2)}$$

where y_r is the relative displacement between the base and mass:

$$y_r = y - d \qquad \textbf{(6.3.8.1.3)}$$

The acceleration of the mass, in terms of the relative and base accelerations, from equation 6.3.8.1.3, is given by:

$$\ddot{y} = \ddot{y}_r + \ddot{d} \qquad \textbf{(6.3.8.1.4)}$$

Selecting the relative displacement and relative speed as states, the base acceleration and actuator force as inputs and the relative acceleration as the output, the state-space equations of the system can be written as:

$$\begin{Bmatrix} \dot{y}_r \\ \ddot{y}_r \end{Bmatrix} = \begin{bmatrix} 0 & 1 \\ -\frac{k}{m} & -\frac{c}{m} \end{bmatrix} \begin{Bmatrix} y_r \\ \dot{y}_r \end{Bmatrix} + \begin{Bmatrix} 0 \\ -1 \end{Bmatrix} \ddot{d} + \begin{Bmatrix} 0 \\ \frac{1}{m} \end{Bmatrix} F_a \qquad \textbf{(6.3.8.1.5a)}$$

$$\ddot{y}_r = \begin{bmatrix} -\frac{k}{m} & -\frac{c}{m} \end{bmatrix} \begin{Bmatrix} y_r \\ \dot{y}_r \end{Bmatrix} - \ddot{d} + \frac{1}{m}F_a \qquad \textbf{(6.3.8.1.5b)}$$

For relative motion control, the actuator force can expressed as follows as a linear combination of the relative displacement and speed:

$$F_a = \begin{bmatrix} -K_1 & -K_2 \end{bmatrix} \begin{Bmatrix} y_r \\ \dot{y}_r \end{Bmatrix} \tag{6.3.8.1.6}$$

where K_1 and K_2 are the relative displacement and relative speed feedback gains respectively. Because the relative displacement and speed are the plant states, the control law given in equation 6.3.8.1.6 describes state feedback control. State control requires that the states be known, either by direct measurement, or by state estimation. Since the output is the relative acceleration, instead of the relative displacement and speed, the states must be reconstructed from the output. This is done as follows, by direct integration of the relative acceleration:

$$y_r = \iint \ddot{y}_r dt dt \tag{6.3.8.1.7a}$$

$$\dot{y}_r = \int \ddot{y}_r dt \tag{6.3.8.1.7b}$$

where $\ddot{y}_r$ is the relative acceleration, which is obtained by subtraction of the measured acceleration of the base, from the measured acceleration of the mass:

$$\ddot{y}_r = \ddot{y} - \ddot{d} \tag{6.3.8.1.8}$$

The closed-loop state-space equations of the system are obtained by substitution of equation 6.3.8.1.6 into equations 6.3.8.1.5a and 6.3.8.1.5b:

$$\begin{Bmatrix} \dot{y}_r \\ \ddot{y}_r \end{Bmatrix} = \begin{bmatrix} 0 & 1 \\ -\dfrac{k+K_1}{m} & -\dfrac{c+K_2}{m} \end{bmatrix} \begin{Bmatrix} y_r \\ \dot{y}_r \end{Bmatrix} + \begin{Bmatrix} 0 \\ -1 \end{Bmatrix} \ddot{d} \tag{6.3.8.1.9a}$$

$$\ddot{y}_r = \begin{bmatrix} -\dfrac{k+K_1}{m} & -\dfrac{c+K_2}{m} \end{bmatrix} \begin{Bmatrix} y_r \\ \dot{y}_r \end{Bmatrix} - \ddot{d} \tag{6.3.8.1.9b}$$

The closed-loop transmissibility of the system, which is the *TF* between the acceleration of the base and the *absolute* accleration of the mass, is obtained from equations 6.3.8.1.4 and 6.3.8.1.9b as:

$$TR = \frac{\ddot{y}}{\ddot{d}} = \frac{\dfrac{c+K_2}{m}s + \dfrac{k+K_1}{m}}{s^2 + \dfrac{c+K_2}{m}s + \dfrac{k+K_1}{m}} \tag{6.3.8.1.10}$$

The poles of the closed-loop system are given by:

$$s = -\frac{c + K_2}{2m} \pm \frac{1}{2}\sqrt{\left(\frac{c + K_2}{m}\right)^2 - 4\frac{k + K_1}{m}} \qquad \textbf{(6.3.8.1.11)}$$

The zero of the closed-loop system is given by:

$$s = -\frac{k + K_1}{c + K_2} \qquad \textbf{(6.3.8.1.12)}$$

The natural frequency f_n and dimensionless damping factor ζ are respectively given by:

$$f_n = \frac{1}{2\pi}\sqrt{\frac{k + K_1}{m}} \qquad \textbf{(6.3.8.1.13a)}$$

$$\zeta = \frac{c + K_2}{2\sqrt{(k + K_1)m}} \qquad \textbf{(6.3.8.1.13b)}$$

The DC transmissibility is unity, and is independent of the feedback gains.

The transmissibility given by equation 6.3.8.1.10 corresponds with the transfer function of a passive low-pass (LP) filter. The filtering characteristic is such that the system will attenuate above $\sqrt{2}$ times the closed-loop natural frequency, i.e. above $f = (1/2\pi)\sqrt{2(k + K_1)/m}$.

Below the attenuation frequency, i.e. in the pass-band, the system will amplify the base motion, in other words, the acceleration of the mass will exceed that of the base. The attenuation band can be widened by reducing the natural frequency. This is achieved by reducing K_1; the lower K_1, the wider the attenuation band.

K_1 can however not be reduced indefinitely, since this will inevitably cause instability. Similarly, instability will result if K_2 is reduced to such an extent that the damping factor becomes negative. The lower limits of K_1 and K_2 are determined by the gain and phase margins of the plant.

In the attenuation band, the *TR* increases with damping, therefore damping is undesirable in this band. However, in the pass-band, the *TR* decreases with damping. In this band, damping must be as high as possible. In order to provide efficient damping in both the attenuation and pass bands, an optimum damping factor is required. For white-noise base motion, the optimum damping factor is 70,7 %.

The controller feedback transfer function $H_c(s)$ between the relative acceleration and actuator force is:

$$H_c(s) = -\frac{K_1}{s^2} - \frac{K_2}{s} \qquad \textbf{(6.3.8.1.14)}$$

The block diagram of the relative motion controller described above, is shown in figure 6.3.8.1.1. The inputs to the plant are the actuator force F_a and base acceleration $\ddot{d}$. The

plant output, which is also the controller input, is the relative acceleration $\ddot{y} - \ddot{d}$. The controller output is the actuator force F_a.

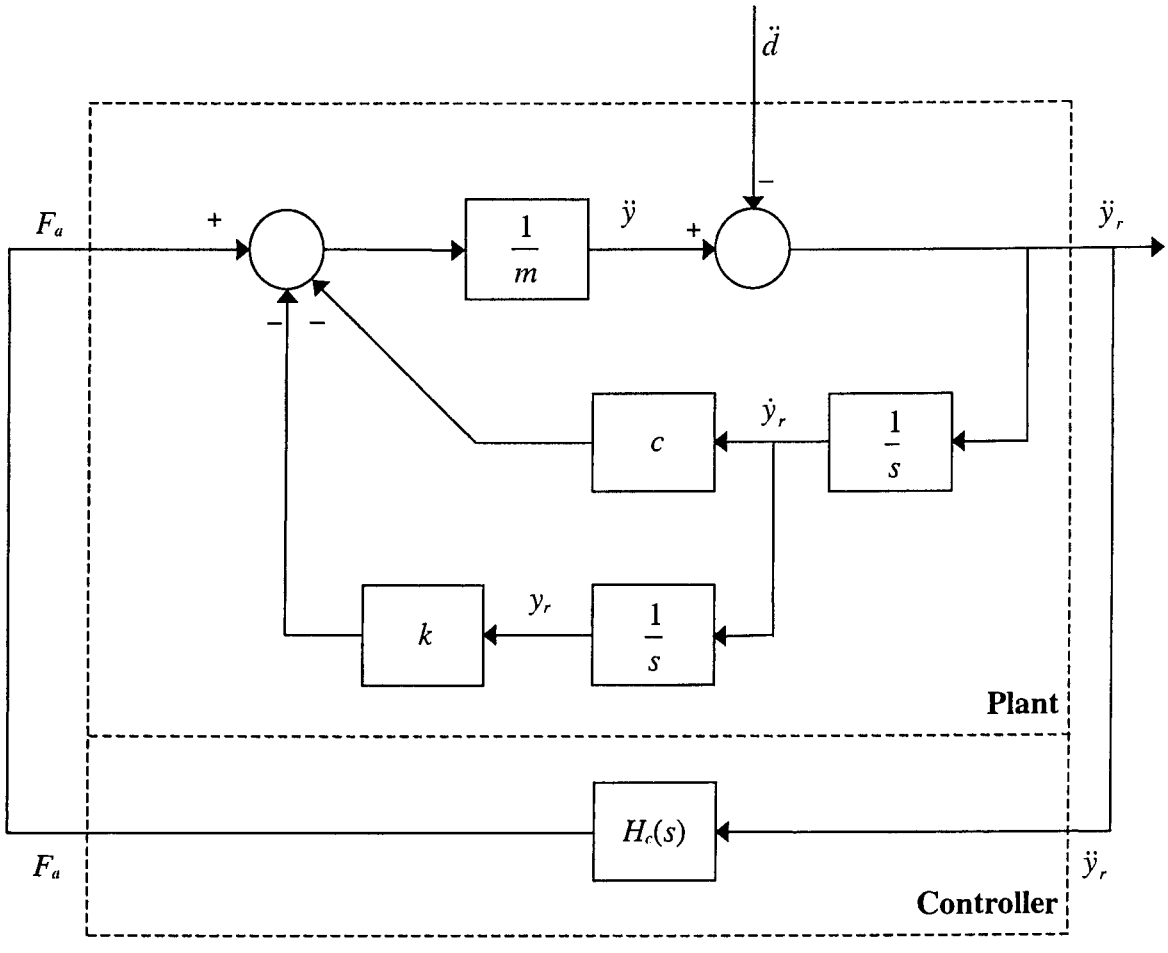

Figure 6.3.8.1.1: Block diagram of relative motion controller

An advantage of the relative motion controller is that it can be implemented passively, and does not require an actuator. The LP characteristics may be desirable from a measurement point of view, since the system can operate at low sample frequencies.

The disadvantages of the system are firstly, that it cannot attenuate at DC. However, depending on the nature of the disturbance, this may not be a necessity, for example where the disturbance does not contain a significant DC component. Secondly, since relative motion, instead of absolute motion, is controlled, the system is incapable of taking any corrective action if the motion of the mass deviates from the required motion. The system is therefore relatively non-robust in comparison with an absolute motion controller.

6.3.8.2 Absolute motion controller

An absolute motion controller measures the acceleration of the mass and feeds this signal back into the controller to obtain the control signal.

In order to derive the equation of motion, consider figure 6.3.8.1. The equation of motion of the system, from equation 6.3.8.1, is:

$$m\ddot{y} + c\dot{y} + ky = c\dot{d} + kd + F_a \qquad \textbf{(6.3.8.2.1)}$$

Equation 6.3.8.2.1 can be written as:

$$m\ddot{y} + c\dot{y} + ky = F_b + F_a \qquad \textbf{(6.3.8.2.2)}$$

where F_b is the equivalent base excitation force, given by:

$$F_b = c\dot{d} + kd \qquad \textbf{(6.3.8.2.3)}$$

The base excitation force is obtained as follows from the base acceleration:

$$F_b = c\int(\ddot{d})dt + k\iint(\ddot{d})dt\,dt \qquad \textbf{(6.3.8.2.4)}$$

The base-excited spring-mass-damper system shown in figure 6.3.8.1 can be replaced with an equivalent base-force excited system, as shown in figure 6.3.8.2.1.

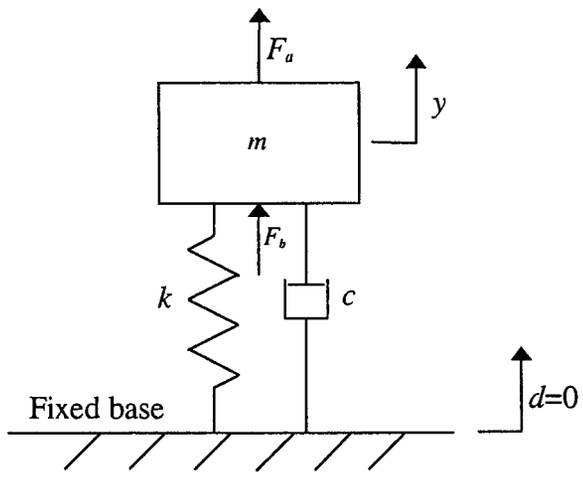

Figure 6.3.8.2.1: Equivalent spring-mass-damper system excited by base and actuator forces

Selecting the absolute displacement and speed of the mass as states, the base excitation and actuator forces as inputs and the acceleration of the mass as the output, the state-space equations of the system can be written as:

$$\begin{Bmatrix} \dot{y} \\ \ddot{y} \end{Bmatrix} = \begin{bmatrix} 0 & 1 \\ -\frac{k}{m} & -\frac{c}{m} \end{bmatrix} \begin{Bmatrix} y \\ \dot{y} \end{Bmatrix} + \begin{Bmatrix} 0 \\ \frac{1}{m} \end{Bmatrix} F_b + \begin{Bmatrix} 0 \\ \frac{1}{m} \end{Bmatrix} F_a \qquad \textbf{(6.3.8.2.5a)}$$

$$\ddot{y} = \begin{bmatrix} -\frac{k}{m} & -\frac{c}{m} \end{bmatrix} \begin{Bmatrix} y \\ \dot{y} \end{Bmatrix} + \frac{1}{m} F_b + \frac{1}{m} F_a \qquad \textbf{(6.3.8.2.5b)}$$

For relative motion control, the actuator force can be expressed as follows as a linear combination of the absolute displacement and speed of the mass:

$$F_a = \begin{bmatrix} -K_1 & -K_2 \end{bmatrix} \begin{Bmatrix} y \\ \dot{y} \end{Bmatrix} \qquad \textbf{(6.3.8.2.6)}$$

where K_1 is the abolute displacement feedback gain and K_2 is the absolute speed feedback gain.

The closed-loop state-space equations are obtained by substitution of equation 6.3.8.2.6 into equations 6.3.8.2.5a and 6.3.8.2.5b:

$$\begin{Bmatrix} \dot{y} \\ \ddot{y} \end{Bmatrix} = \begin{bmatrix} 0 & 1 \\ -\frac{k+K_1}{m} & -\frac{c+K_2}{m} \end{bmatrix} \begin{Bmatrix} y \\ \dot{y} \end{Bmatrix} + \begin{Bmatrix} 0 \\ \frac{1}{m} \end{Bmatrix} F_b \qquad \textbf{(6.3.8.2.7a)}$$

$$\ddot{y} = \begin{bmatrix} -\frac{k+K_1}{m} & -\frac{c+K_2}{m} \end{bmatrix} \begin{Bmatrix} y \\ \dot{y} \end{Bmatrix} + \frac{1}{m} F_b \qquad \textbf{(6.3.8.2.7b)}$$

The transfer function between the base force and output acceleration is:

$$\frac{\ddot{y}}{F_b} = \frac{\frac{1}{m} s^2}{s^2 + \frac{c+K_2}{m} s + \frac{k+K_1}{m}} \qquad \textbf{(6.3.8.2.8)}$$

The transmissibility, which is the transfer function between the base acceleration and absolute acceleration, is obtained from equations 6.3.8.2.3 and 6.3.8.2.8 as:

$$TR = \frac{\ddot{y}}{\ddot{d}} = \frac{\frac{c}{m}s + \frac{k}{m}}{s^2 + \frac{c + K_2}{m}s + \frac{k + K_1}{m}} \qquad \textbf{(6.3.8.2.9)}$$

The poles of the closed-loop system are given by:

$$s = -\frac{c + K_2}{2m} \pm \frac{1}{2}\sqrt{\left(\frac{c + K_2}{m}\right)^2 - 4\frac{k + K_1}{m}} \qquad \textbf{(6.3.8.2.10)}$$

The zero is given by:

$$s = -\frac{k}{c} \qquad \textbf{(6.3.8.2.11)}$$

The natural frequency, damping factor and DC transmissibility of the closed-loop system are respectively given by:

$$f_n = \frac{1}{2\pi}\sqrt{\frac{k + K_1}{m}} \qquad \textbf{(6.3.8.2.12a)}$$

$$\zeta = \frac{c + K_2}{2\sqrt{(k + K_1)m}} \qquad \textbf{(6.3.8.2.12b)}$$

$$TR_{DC} = \frac{k}{k + K_1} \qquad \textbf{(6.3.8.2.12c)}$$

The controller feedback transfer function $H_c(s)$ between the acceleration of the mass and actuator force is:

$$H_c(s) = -\frac{K_1}{s^2} - \frac{K_2}{s} \qquad \textbf{(6.3.8.2.13)}$$

The block diagram of the absolute motion controller is shown in figure 6.3.8.2.1. The controller input is the absolute acceleration of the mass $\ddot{y}$. The controller output is the actuator force F_a. The plant inputs are the actuator and base excitation forces F_a and F_b. The plant output is the absolute acceleration of the mass $\ddot{y}$.

It can be seen from equation 6.3.8.2.9 that only the denominator of the TR is affected by the feedback gains. The numerator is unaffected. The natural frequency increases with an increase in K_1, while the damping factor increases with an increase in K_2. For a positive K_1, k/m is smaller than $(k+K_1)/m$, giving a DC transmissibility of less than unity.

The DC transmissibility and natural frequency are coupled by K_1, i.e. a change in K_1 changes both the DC transmissibility and natural frequency. These two parameters can for instance be separately adjusted by using acceleration feedback in conjunction with displacement and speed feedback. In this case, the feedback law is:

$$F_a = K_1 y + K_2 \dot{y} + K_3 \ddot{y} \qquad \textbf{(6.3.8.2.14)}$$

where K_3 is the acceleration feedback gain.

The closed-loop transmissibility is:

$$\frac{\ddot{y}}{\ddot{d}} = \frac{\frac{c}{m+K_3}s + \frac{k}{m+K_3}}{s^2 + \frac{c+K_2}{m+K_3} + \frac{k+K_1}{m+K_3}} \qquad \textbf{(6.3.8.2.15)}$$

The natural frequency, damping factor and DC transmissibility are respectively given by:

$$f_n = \frac{1}{2\pi}\sqrt{\frac{k+K_1}{m+K_3}} \qquad \textbf{(6.3.8.2.16a)}$$

$$\zeta = \frac{c+K_2}{2\sqrt{(k+K_1)(m+K_3)}} \qquad \textbf{(6.3.8.2.16b)}$$

$$TR_{DC} = \frac{k}{k+K_1} \qquad \textbf{(6.3.8.2.16c)}$$

The transfer function $H_c(s)$ between the acceleration of the mass and actuator force is:

$$H_c(s) = -\frac{K_1}{s^2} - \frac{K_2}{s} - K_3 \qquad \textbf{(6.3.8.2.17)}$$

The block diagram of this controller is shown in figure 6.3.8.2.1.

Advantages of this system type are that the controller is capable of detecting the output, irrespective of what happens at the input. Corrective action can therefore be taken if the output deviates from the required output. Being a feedback controller, the system can be designed to be sufficiently robust. Furthermore, contrary to the relative motion controller, the system can be designed to attenuate at DC.

A disadvantage of this system type is that the control signal, which only depends on the output, may be contaminated by measurement noise. Since the output is a relatively small signal in comparison with the disturbance, the signal-to-noise ratio is low.

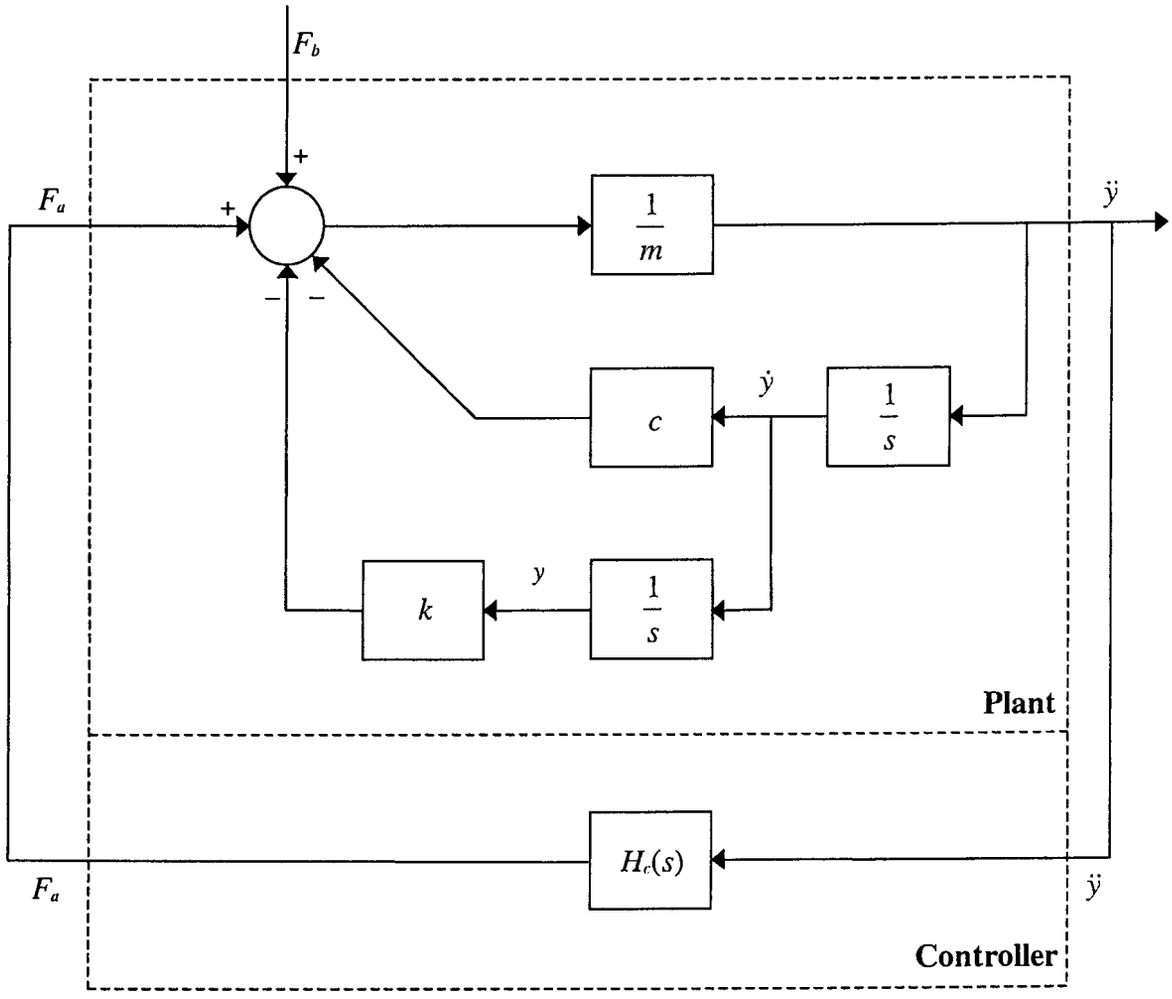

Figure 6.3.8.2.1: Block diagram of absolute motion controller

6.3.8.3 Disturbance feedforward (open-loop) controller

The disturbance feedforward controller measures the acceleration of the base and feeds this signal into the controller to obtain the actuator force.

The actuator force is expressed as follows as a linear combination of the base displacement and speed:

$$F_a = K_1 d + K_2 \dot{d} \qquad \textbf{(6.3.8.3.1)}$$

where K_1 is the base displacement gain and K_2 is the base speed gain.

Substitution of equations and 6.3.8.3.1 into equation 6.3.8.2.1 and simplification of the resulting equation gives the equation of motion as follows:

$$\ddot{y} + \frac{c}{m}\dot{y} + \frac{k}{m}y = \frac{c + K_2}{m}\dot{d} + \frac{k + K_1}{m}d \qquad \textbf{(6.3.8.3.2)}$$

The transmissibility equation of the system is:

$$\frac{\ddot{y}}{\ddot{d}} = \frac{\frac{c + K_2}{m}s + \frac{k + K_1}{m}}{s^2 + \frac{c}{m}s + \frac{k}{m}} \qquad \textbf{(6.3.8.3.3)}$$

The poles of the feedforward-controlled system are given by:

$$s = -\frac{c}{2m} \pm \frac{1}{2}\sqrt{\left(\frac{c}{m}\right)^2 - 4\frac{k}{m}} \qquad \textbf{(6.3.8.3.4)}$$

The zero is given by:

$$s = -\frac{k + K_1}{c + K_2} \qquad \textbf{(6.3.8.3.5)}$$

The natural frequency, damping factor and DC transmissibility are respectively given by:

$$f_n = \frac{1}{2\pi}\sqrt{\frac{k}{m}} \qquad \textbf{(6.3.8.3.6a)}$$

$$\zeta = \frac{c}{2\sqrt{km}} \qquad \textbf{(6.3.8.3.6b)}$$

$$TR_{DC} = 1 + \frac{K_1}{k} \qquad \textbf{(6.3.8.3.6c)}$$

The transfer function $G_c(s)$ between the base acceleration and actuator force is:

$$G_c(s) = \frac{K_1}{s^2} + \frac{K_2}{s} \qquad \textbf{(6.3.8.3.7)}$$

It can be seen from equations 6.3.8.3.6a and 6.3.8.3.6b that the natural frequency and damping factor correspond to those of an uncontrolled SDOF system. The DC transmissibility depends on the base displacement feedforward gain K_1. A DC transmissibility of less than unity can be obtained if K_1 is negative.

The block diagram of the open-loop controller is shown in figure 6.3.8.3.1. The input to the controller is the base acceleration, $\ddot{d}$. The controller output is the actuator force F_a. The plant inputs are the actuator force F_a and the base disturbance force F_b. The plant output is the acceleration of the mass $\ddot{y}$.

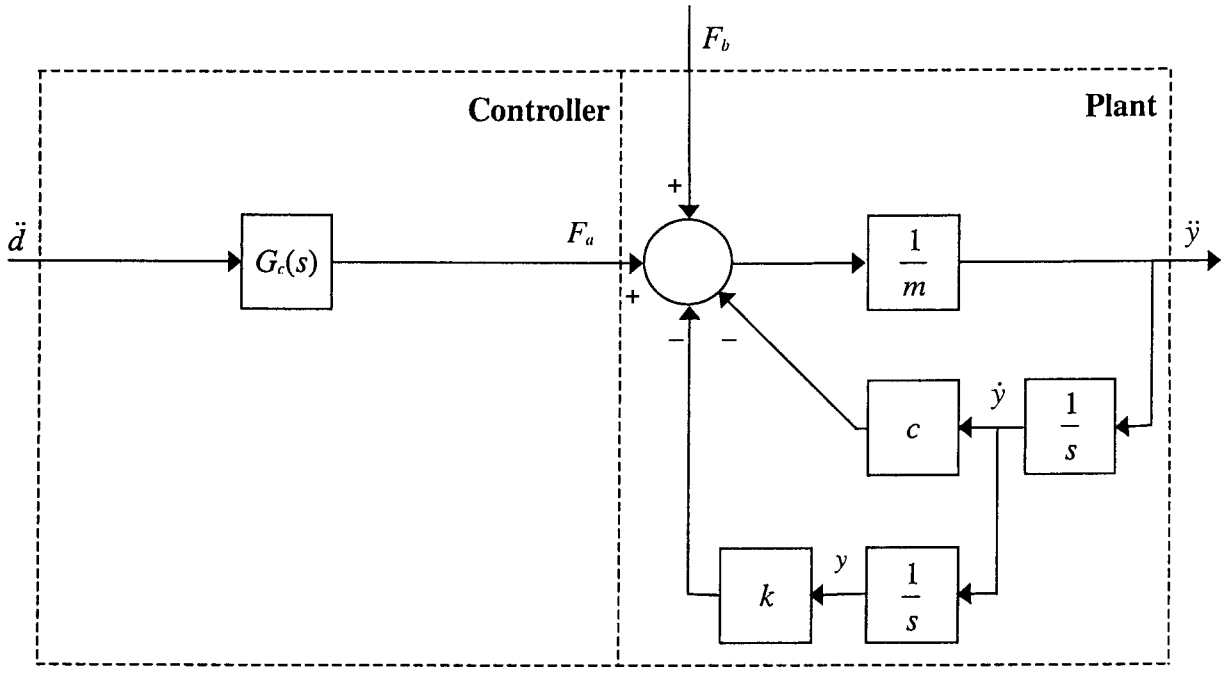

Figure 6.3.8.3.1: Block diagram of disturbance feedforward controller

An advantage of the disturbance feedforward controller is that it is unconditionally stable for any K_1 and K_2. Furthermore, since the base acceleration will be larger than the acceleration of the mass, a higher signal-to-noise ratio will result than in the case of the absolute output controller. This makes it possible to use a relatively high sample rate, which is required for accurate control.

The disadvantage of a disturbance feedforward controller is that there is no feedback loop. The controller can therefore not take any corrective action to compensate for disturbances other than the known base motion. Furthermore, the absence of a feedback loop prevents the system from compensating for shifts of plant poles due to uncertainties.

6.3.8.4 Absolute plus base motion controller

The absolute plus base motion controller measures both the base and mass accelerations and feeds these signals into the controller to obtain the actuator force.

The actuator force is a linear combination of the displacement of the mass, speed of the mass, displacement of the base and speed of the base:

$$F_a = -K_1 y - K_2 \dot{y} + K_3 d + K_4 \dot{d} \qquad \textbf{(6.3.8.4.1)}$$

where K_1 is the absolute displacement gain, K_2 is the absolute speed gain, K_3 is the base displacement gain and K_4 is the base speed gain. K_1 and K_2 are output feedback gains, while K_3 and K_4 are disturbance feedforward gains. This controller is a combination of the absolute acceleration and open-loop controllers, respectively discussed in sections 6.3.8.2 and 6.3.8.3.

Substitution of equations 6.3.8.4.1 into equation 6.3.8.2.1 and simplification of the resulting equation gives the equation of motion as follows:

$$\ddot{y} + \frac{c + K_2}{m}\dot{y} + \frac{k + K_1}{m}y = \frac{c + K_4}{m}\dot{d} + \frac{k + K_3}{m}d \qquad \textbf{(6.3.8.4.2)}$$

The transmissibility equation of the controlled system is:

$$\frac{\ddot{y}}{\ddot{d}} = \frac{\frac{c + K_4}{m}s + \frac{k + K_3}{m}}{s^2 + \frac{c + K_2}{m}s + \frac{k + K_1}{m}} \qquad \textbf{(6.3.8.4.3)}$$

The natural frequency, damping factor and DC transmissibility are respectively given by:

$$f_n = \frac{1}{2\pi}\sqrt{\frac{k + K_1}{m}} \qquad \textbf{(6.3.8.4.4a)}$$

$$\zeta = \frac{c + K_2}{2\sqrt{(k + K_1)m}} \qquad \textbf{(6.3.8.4.4b)}$$

$$TR_{DC} = \frac{k + K_3}{k + K_1} \qquad \textbf{(6.3.8.4.4c)}$$

The feedback transfer function $H_c(s)$ between the absolute acceleration and actuator force is:

$$H_c(s) = -\frac{K_1}{s^2} - \frac{K_2}{s} \qquad \textbf{(6.3.8.4.5)}$$

The feedforward transfer function $G_c(s)$ between the base acceleration and actuator force is:

$$G_c(s) = \frac{K_3}{s^2} + \frac{K_4}{s} \qquad \textbf{(6.3.8.4.6)}$$

It can be seen from equation 6.3.8.4.3 that both the TR numerator and denominator are affected by the controller gains. Poles and zeroes can therefore be shifted independently. Stability of the system only depends on K_1 and K_2, and is independent of K_3 and K_4.

The controller block diagram is shown in figure 6.3.8.4.1. The inputs to the controller are the absolute acceleration of the mass $\ddot{y}$ and the acceleration of the base $\ddot{d}$. The controller output is the actuator force F_a. The inputs to the plant are the actuator force F_a and the base excitation force F_b. The plant output is the absolute acceleration of the mass $\ddot{y}$.

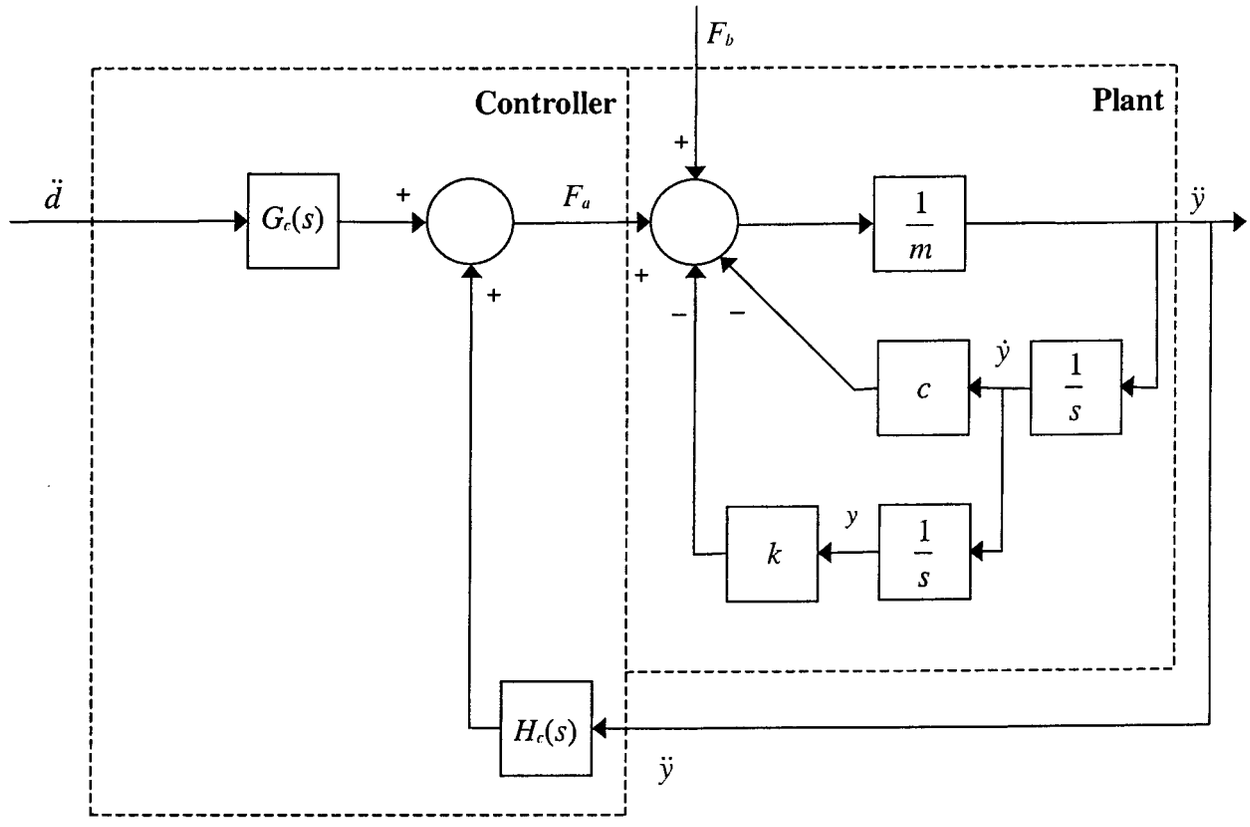

Figure 6.3.8.4.1: Block diagram of disturbance feedforward plus absolute motion controller

A special case of this controller is the relative motion controller discussed previously, which results if $K_3 = K_1$ and $K_4 = K_2$.

The first advantage of this controller type is that its poles and zeroes can be determined independently, since both base motion and absolute motion are used for control. Secondly, as was mentioned in section 6.3.4, a known disturbance may be partially attenuated before entering the system. Thirdly, in the case of a sensor failure, the controller may still operate, albeit at the cost of performance.

A disadvantage of the system is that, because it is not a pure feedback controller, robustness will be lower that that of the absolute motion controller.

6.3.8.5 Robustness improvement

Optimal state controllers are often non-robust. The main reason is that the transmissibilities of optimal controllers are, in many cases, characterized by pole-zero cancellation. The poles will be exactly cancelled by the zeroes, as long as the frequencies and damping factors of the poles and zeroes are constant. This is however not guaranteed, since either the poles or the zeroes may shift, due to, inter alia, plant nonlinearities. If, for instance, the poles shift, but the zeroes

are unaffected, pole-zero cancellation will no longer be effective, resulting in inadequate controller performance. Optimal controllers with low pole damping, in particular, are prone to this problem.

Robustness improvement can be achieved by proper robust feedback design, employing methods such as loop transfer recovery (LTR), as described in detail by Maciejowski [1989], Skogestad & Postlethwaite [1997] and Tsui [1996]. An alternative method of robustness improvement is to place an output integrator in parallel with the state feedback elements [Kuo, 1982, and Anderson & Moore, 1989]. The controller consists of two loops, i.e. an inner state-feedback loop and an outer output integrator loop. This method or robust control is often applied to reject DC disturbances in electric motors [Kuo, 1982].

This control method can also be applied to improve the robustness of motion controllers. A simple example is the absolute motion controller described in section 6.3.8.2. In the case of acceleration output, integral feedback will alter the speed feedback gain, thereby altering the damping factor of the poles.

The actuator force is obtained as follows in terms of the absolute displacement, speed and acceleration of the mass:

$$F_a = \begin{bmatrix} -K_1 & -K_2 \end{bmatrix} \begin{Bmatrix} y \\ \dot{y} \end{Bmatrix} - H_I \int \ddot{y} dt \qquad \textbf{(6.3.8.5.1)}$$

where K_1 and K_2 are the optimal state feedback gains and H_I is the acceleration integral feedback gain.

Simplification of equation 6.3.8.5.1 gives:

$$F_a = -K_1 y - \left(K_2 + H_I\right)\dot{y} \qquad \textbf{(6.3.8.5.2)}$$

Substitution of equation 6.3.8.5.2 into equation 6.3.8.2.1 gives the equation of motion of the closed-loop system as follows:

$$\ddot{y} + \frac{c}{m}\dot{y} + \frac{k}{m}y = -\frac{K_1}{m}y - \frac{\left(K_2 + H_I\right)}{m}\dot{y} + \frac{c}{m}\dot{d} + \frac{k}{m}d \qquad \textbf{(6.3.8.5.3)}$$

The transmissibility equation of the closed-loop system is:

$$\frac{\ddot{y}}{\ddot{d}} = \frac{\frac{c}{m}s + \frac{k}{m}}{s^2 + \frac{c + K_2 + H_I}{m}s + \frac{k + K_1}{m}} \qquad \textbf{(6.3.8.5.4)}$$

The poles are given by:

$$s = -\frac{c + K_2 + H_I}{2m} \pm \frac{1}{2}\sqrt{\left(\frac{c + K_2 + H_I}{m}\right)^2 - 4\left(\frac{k + K_1}{m}\right)} \qquad \textbf{(6.3.8.5.5)}$$

The zero is given by:

$$s = -\frac{k}{c} \qquad \textbf{(6.3.8.5.6)}$$

The natural frequency, damping factor and DC transmissibility are respectively given by:

$$f_n = \frac{1}{2\pi}\sqrt{\frac{k + K_1}{m}} \qquad \textbf{(6.3.8.5.7a)}$$

$$\zeta = \frac{c + K_2 + H_I}{2\sqrt{(k + K_1)m}} \qquad \textbf{(6.3.8.5.7b)}$$

$$TR_{DC} = \frac{k}{k + K_1} \qquad \textbf{(6.3.8.5.7c)}$$

The inner and outer feedback loops can be replaced by a single feedback loop. The transfer function $H_c(s)$ between the acceleration of the mass and the actuator force, from equation 6.3.8.5.2, is:

$$H_c(s) = -\frac{K_1}{s^2} - \frac{K_2 + H_I}{s} \qquad \textbf{(6.3.8.5.8)}$$

Comparison of equation 6.3.8.2.12b with equation 6.3.8.5.7b shows that the relative increase in damping, from the optimal damping, is $H_I/(c + K_2)$.

6.3.9 "Two-way" isolation

The methods discussed so far in section 6.3 are mainly applicable to the attenuation of disturbances exciting a system with a rigid base and mass, through the moving base. This section focusses on the attenuation of disturbances entering the structure at the base and mass, both of which are flexible. The actuator is mounted in between, from where it excites both the base and mass. This attenuation method is appropriately known as "two-way isolation" [Hyde, 1996].

The control system operates on the principle of dual sensor feedback. The absolute motion (speed) of the mass and the actuator force are measured and fed back into the controller, through two control loops, i.e. an inner (unit) force feedback loop and an outer motion feedback loop. The inner feedback loop makes it possible to control the actuator force, as follows. The measured motion signal is gained to give the commanded force signal. The measured actuator force signal is subtracted from the commanded force signal and the

difference is gained and supplied to the actuator. Two-way isolation and dual sensor feedback are described in detail by Hyde [1996].

6.4 Control system design

The design of a controller for the LOS stabilization system is described in this section. Controller specifications are given in section 6.4.1. Factors which influence controller design are mentioned in section 6.4.2. The selection of a suitable controller type is motivated in section 6.4.3. The controller design procedure is described in section 6.4.4. The plant and controller design parameters are given in section 6.4.5.

6.4.1 Control system design specifications

Control system specifications include the particular system performance requirements, and general controller requirements applicable to all types of controllers. Particular performance requirements, applicable to the LOS stabilization system, are the closed-loop attenuation factor, limits to the maximum and minimum values of the control signal, and frequency bandwidth. General requirements, which are almost universal for all types of controllers, are inter alia, stability, robustness and reaction speed. General control system requirements will be given in section 6.4.2.

The required attenuation factor, in terms of RMS of the output, as a fraction of the RMS of the disturbance, is 15%, over a frequency range of 2,5 Hz to 100 Hz. The upper limit of the coil supply voltage is + 28 V. The lower voltage limit is not specified, but 0 V can be accepted as a guide. (This constraint is applied to ensure that the coils are magnetically biased - see section 3.4).

Time-domain performance parameters such as rise-time, settling-time, overshoot and DC error are not specified. Although DC tracking error is not applicable, since the controller required for the LOS stabilization system will be a regulator, a DC voltage of 9,1 V is required to bias the actuator coil.

6.4.2 General control system requirements

General controller requirements are normally expressed in terms of performance factors such as accuracy, stability, sensitivity, reaction speed, control effort, robustness, observability and controllability. These factors are not discussed here. Instead, a summary of each of the factors is given in appendix X.

6.4.3 Selection of a suitable controller type

The controller which is selected for the magnetostrictive LOS stabilization system in this study, is a digital, suboptimal output feedback plus disturbance feedforward regulator, with output integral feedback. The reasons for the choice are as follows: If the advantages and

disadvantages of digital and analogue controllers are compared (see appendix X), the relative ease of implementation and adjustment of control parameters outweigh the cost disadvantage of a digital controller. If a digital controller is available, as it is in this study, it is the logical choice.

Tracking controllers and regulators were respectively discussed in sections 6.2.7 and 6.2.8. The objective in this study is to minimize the output, i.e. the angular acceleration of the optical instrument. This is a regulator objective. Although a tracking controller could also be considered for this application, a relative motion controller would be required, whose control objective would be to drive the relative motion between the base and output to the (negative of the) base motion. An absolute motion controller is however preferred, since it controls the parameter to be minimized, i.e. the absolute angular acceleration of the optical instrument, instead of the relative angular acceleration.

Disturbance feedforward is included because the disturbance is known and enters the system through the base. It can therefore be attenuated to a large extent, before affecting the system.

Optimal feedback controllers are seldom robust. Robustness of optimal controllers can be improved by placing an output integral feedback loop, in parallel with the output feedback loop. (This method of robustness improvement is discussed in appendix X). A disadvantage of this control method is that it slightly complicates the system, since an additional control loop is required. However, a considerable improvement in robustness can be achieved, as will be illustrated in section 6.4.5.

An alternative to the above controller, is a full-state controller. Robustness set aside, state controller design techniques are generally more powerful than *TF* design techniques, especially for systems with large numbers of states, inputs and outputs. State control design techniques also make it possible to convert the dynamic equations of a state controller to analogue *TF* form. Conversion of the continuous *TF*'s to digital filter form (in terms of the discrete delay element $1/z$) is also relatively easy, provided that the frequencies of the closed-loop system poles and zeroes do not exceed the Nyquist frequency.

The advantages of both state and digital controllers will be exploited in the design and implementation of the controller for the LOS stabilization system. The design will be carried out by means of optimal linear quadratic state controller and observer design techniques. The state and output equations will subsequently be written in analogue *TF* form and converted to digital filter form.

The block diagram of the plant and digital regulator is shown in figure 6.4.3.1. The plant inputs are the disturbance d (base angular acceleration) and control u (actuator coil voltage). The plant output y is the absolute angular acceleration of the optical instrument. The regulator inputs are the sampled disturbance $D(z)$ and plant output $Y(z)$. The controller output is the control $U(z)$, supplied to the plant through a zero-order hold ("zoh").

The digital regulator feedforward and feedback filter *TF*'s are $G(z)$ and $H(z)$ respectively. The digital output feedback integrator *TF*, which is the zero-order-hold equivalent of $1/s$, is $T/(z-1)$. The integrator gain is H_I, a constant. The analogue plant disturbance and control input *TF*'s are $G_d(s)$ and $G_u(s)$ respectively.

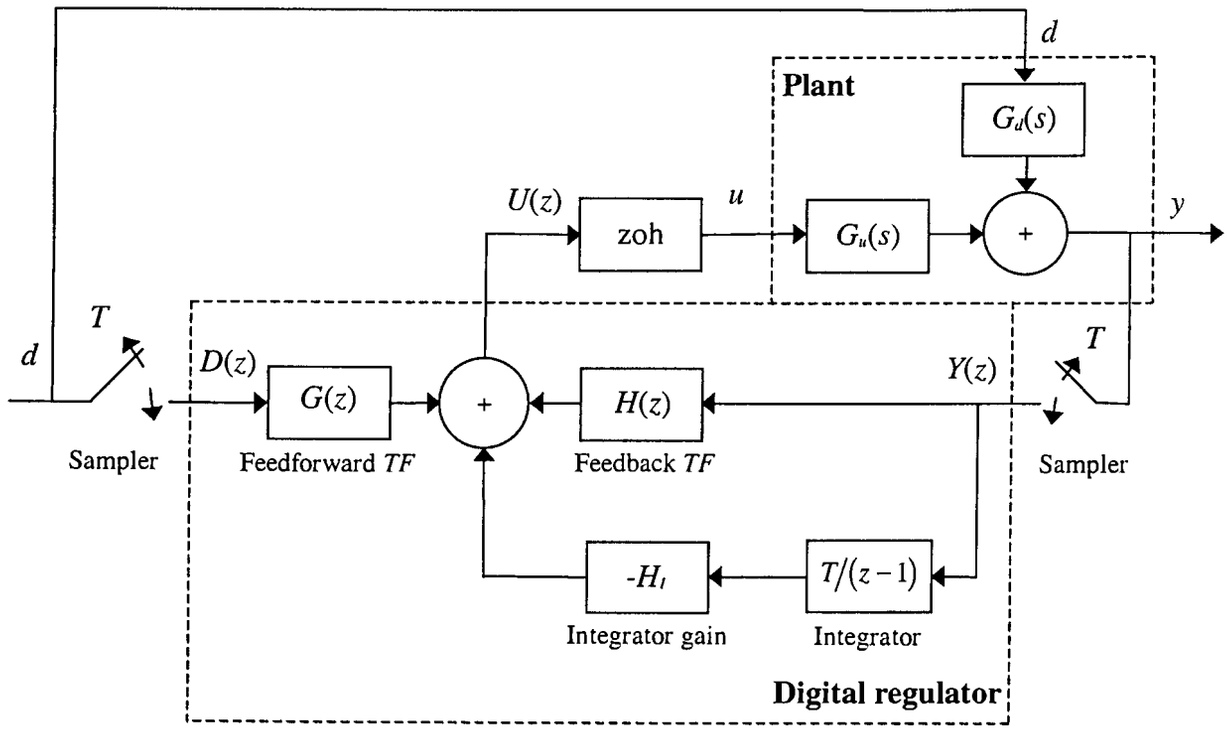

Figure 6.4.3.1: Block diagram of plant and digital regulator

6.4.4 Control system design method

An iterative method is followed in the design of the controller. The process is started by designing an optimal controller and an optimal observer. For the controller design, output and control weights are arbitrarily selected, while MS values of measured disturbance and output noise signals are used as weights for the observer design. Robustness is improved by designing a suboptimal controller and a suboptimal observer. The plant, controller and observer state-space equations are coupled and stability of the closed-loop system is verified. The disturbance-to-control and output-to-control *TF*'s are obtained and converted to digital form. The output integrator gain is arbitrarily selected.

A real-time simulation of the expected closed-loop system behaviour is done, with disturbance and noise signals acting as the extraneous inputs. The RMS-value of the output, in a frequency bandwidth of 0 Hz to 100 Hz, is compared with that of the disturbance. If the output RMS exceeds the specified value, the output weight and integrator feedback gains are adjusted and the process is repeated until the required output RMS is obtained.

The above design method is aimed at attenuating a known disturbance, entering the system through the base. The design is disturbance specific, meaning that the controller will, for example, not be able to reject the disturbance if a harmonic disturbance with the same amplitude as that of the dominating disturbance, i.e. at 96,75 Hz, occurs at 50 Hz.

The magnitude of the disturbance used in the design is 50% of that of the true disturbance, since only one actuator can be controlled. (The reason is that only two power amplifiers are

available for the experimental tests, i.e. one to excite the base and one to drive an actuator coil - see also section 4.3.1).

Detailed description of design procedure

The linear quadratic objective function of the controller is expressed in terms of the control and output. Control and output weights are arbitrarily selected and an optimal linear quadratic regulator (LQR) is designed. The Riccati equation is solved and the optimal feedback gain vector is determined from the Riccati matrix. The closed-loop state-space equations are obtained and converted to *TF* form. The poles and zeroes of the closed-loop transmissibility are determined and graphically displayed on a pole-zero map. It is shown that the optimal controller is characterized by pole-zero cancellation. The frequency spectrum of the closed-loop attenuation factor is shown. The effect of output weight on the attenuation factor is investigated. It is shown that an increase in output weight, reduces the attenuation factor.

A suboptimal controller is subsequently designed. The optimal controller is used as the point of departure. In order to eliminate pole-zero cancellation, the damping factors of most of the zeroes are increased and the frequency of the pole with the lowest frequency is raised. The poles and zeroes of the closed-loop *TR* are shown on a pole-zero map. It is shown that the suboptimal controller *TF* is nonminimum-phase. The frequency spectrum of the closed-loop attenuation factor of the suboptimal controller is shown and compared with that of the optimal controller. It is shown that the suboptimal controller is inferior in terms of attenuation, in comparison with the optimal controller, but is superior in terms of robustness, since it does not display pole-zero cancellation.

An optimal linear quadratic estimator (LQE) is designed. Results obtained from noise measurements are used to determine the disturbance and output weights. The Riccati equation for the optimal observer is solved and the optimal observer driving matrix is determined. The state-space matrices of the optimal observer and suboptimal controller are coupled. The eigenvalues of the coupled system are calculated to verify stability. A pole-zero map of the coupled system is shown. The disturbance to control (*u/d*) and output to control (*u/y*) transfer functions are calculated and their frequency spectra are shown in magnitude and phase form. The plant state-space equations are coupled to the observer and controller equations and stability of the closed-loop system is verified.

It is shown that certain elements of the optimal observer driving matrix are zero, which makes it impossible to control corresponding states from the output. The problem is rectified by designing a suboptimal observer. The zero elements in the driving matrix are replaced by non-zero elements in order to make full-state feedback control possible. The suboptimal observer is coupled to the suboptimal controller and stability of the coupled system is verified.

Equivalent digital filter *TF*'s of the continuous *TF*'s are designed. Poles and zeroes that exceed the Nyquist frequency, are eliminated. The output feedback integrator is replaced by an "equivalent" digital filter, with bounded DC gain. This is done in order to ensure that the control signal is bounded, thereby making it easier to obtain the required DC bias voltage.

Plant, controller and observer state-space, *TF* and digital filter equations

This section gives a summary of the equations required to design the controller. Additional information on different controller types, general controller requirements, configurations and block diagrams, can be found in appendix X.

The plant state and output equations are:

$$\dot{x} = Ax + B_u u + B_d d \qquad \textbf{(6.4.4.1a)}$$

$$y = Cx \qquad \textbf{(6.4.4.1b)}$$

The plant *TF* for the control input, in the absence of the disturbance input, in terms of the state and output matrices, is given by:

$$\frac{Y(s)}{U(s)} = C[sI - A]^{-1} B_u \qquad \textbf{(6.4.4.2)}$$

The plant *TF* for the disturbance input, in the absence of the control input, is given by:

$$\frac{Y(s)}{D(s)} = C[sI - A]^{-1} B_d \qquad \textbf{(6.4.4.3)}$$

The plant eigenvalues are the values of s for which:

$$|sI - A| = 0 \qquad \textbf{(6.4.4.4)}$$

The plant attenuation factor, in the absence of the control input, from equation 6.4.4.3, is:

$$\gamma(s) = C[sI - A]^{-1} B_d \qquad \textbf{(6.4.4.5)}$$

(Equation 6.4.4.5 gives the *uncontrolled* attenuation factor. This term is preferred to "open-loop" attenuation factor, because the latter may also apply to the attenuation factor of a plant controlled by an open-loop controller).

Observability matrix

The plant states are fully observable if the observability matrix

$$\left[C^T \;\vdots\; A^T C^T \;\vdots\; \left(A^T\right)^2 C^T \;\vdots\; \cdots \;\vdots\; \left(A^T\right)^{n-1} C^T\right] \qquad \textbf{(6.4.4.6)}$$

has rank n, where n is the number of plant states.

Controllability matrix

The system is fully controllable if the controllability matrix

$$\left[B \;\vdots\; AB \;\vdots\; A^2B \;\vdots\; \cdots \;\vdots\; A^{n-1}B\right] \tag{6.4.4.7}$$

has rank n.

State and *TF* equations for a state feedback controlled system

For linear state control, the control is a linear combination of the states:

$$u = -Kx \tag{6.4.4.8}$$

where K is the state feedback gain vector.

The closed-loop state space matrices are obtained by substitution of equation 6.4.4.8 into equation 6.4.4.1:

$$\dot{x} = (A - B_u K)x + B_d d \tag{6.4.4.9a}$$

$$y = Cx \tag{6.4.4.9b}$$

The closed-loop eigenvalues are the values of s for which:

$$\left|sI - (A - B_u K)\right| = 0 \tag{6.4.4.10}$$

The closed-loop attenuation factor is given by:

$$\gamma_{cl}(s) = \left.\frac{Y(s)}{D(s)}\right|_{cl} = C\left[sI - (A - B_u K)\right]^{-1} B_d \tag{6.4.4.11}$$

where the subscript *cl* denotes "closed-loop".

Optimal control design equations

The cost function to be minimized, is:

$$J = \int_{t=0}^{t=T} \left[Q_y y^2(t) + Ru^2(t)\right] dt \tag{6.4.4.12}$$

where Q_y and R are the output and control weights, respectively. For a SISO system, both Q_y and R are scalars.

The relationship between the state weight matrix Q_x and Q_y is:

$$Q_x = C^T Q_y C \tag{6.4.4.13}$$

The Riccati equation, in its steady-state version, has to be solved to determine the state feedback gain vector K, which minimizes J for prescribed values of Q_y and R. The steady-state algebraic Riccati equation (ARE), is:

$$Q_x + A^T S_{ss} + S_{ss} A - S_{ss} B_u R^{-1} B_u^T S_{ss} = 0 \tag{6.4.4.14}$$

where S_{ss} is the steady-state solution of the Riccati equation. The optimal state feedback gain matrix is given in terms of the Riccati matrix as:

$$K = R^{-1} B_u^T S_{ss} \tag{6.4.4.15}$$

The optimal state feedback gain matrix gives a linear relationship between the state vector and optimal control.

State-space and *TF* equations of coupled plant, observer and controller

The observer state-space equations are:

$$\dot{\hat{x}} = A\hat{x} + B_u u + B_d d + L(y - \hat{y}) \tag{6.4.4.16a}$$

$$\hat{y} = C\hat{x} \tag{6.4.4.16b}$$

In equation 6.4.4.16a, the observer inputs are the control input u, disturbance d, plant output y and observed output $\hat{y}$.

Substitution of equation 6.4.4.16b into equation 6.4.4.16a gives the observer state equation in the following form:

$$\dot{\hat{x}} = (A - LC)\hat{x} + B_u u + B_d d + Ly \tag{6.4.4.17}$$

In equation 6.4.4.17, the control, disturbance and plant output are the observer inputs. Equation 6.4.4.17 is required to couple the plant, observer, controller and output feedback integrator equations. The coupled equations will be given in the next section.

For state control by means of an observer, the control is a linear combination of the observed states:

$$u = -K\hat{x} \tag{6.4.4.18}$$

Substitution of equation 6.4.4.18 into equation 6.4.4.17, gives the observer state equation in yet another form:

$$\dot{\hat{x}} = (A - B_u K - LC)\hat{x} + B_d d + Ly \tag{6.4.4.19}$$

In equation 6.4.4.19, the disturbance and plant output are the observer inputs.

The coupled plant, observer and controller state-space equations are obtained by combining equations 6.4.4.1, 6.4.4.16b, 6.4.4.18 and 6.4.4.19, as follows:

$$\begin{Bmatrix} \dot{x} \\ \dot{\hat{x}} \end{Bmatrix} = \begin{bmatrix} A & -B_u K \\ LC & A - B_u K - LC \end{bmatrix} \begin{Bmatrix} x \\ \hat{x} \end{Bmatrix} + \begin{bmatrix} B_d \\ B_d \end{bmatrix} d \tag{6.4.4.20a}$$

$$\begin{Bmatrix} y \\ \hat{y} \\ u \end{Bmatrix} = \begin{bmatrix} C & 0 \\ 0 & C \\ 0 & -K \end{bmatrix} \begin{Bmatrix} x \\ \hat{x} \end{Bmatrix} \tag{6.4.4.20b}$$

The closed-loop eigenvalues of the coupled plant, observer and state feedback controller, are the values of s for which:

$$|sI - A_{cl}| = 0 \tag{6.4.4.21}$$

where A_{cl} is the coupled coefficient matrix:

$$A_{cl} = \begin{bmatrix} A & -B_u K \\ LC & A - B_u K - LC \end{bmatrix} \tag{6.4.4.22}$$

The closed-loop attenuation factor is given by:

$$\gamma(s) = [C \quad 0][sI - A_{cl}]^{-1} \begin{bmatrix} B_d \\ B_d \end{bmatrix} \tag{6.4.4.23}$$

The controller *TF*'s, i.e. the disturbance to control and output to control *TF*'s, are given by:

$$\frac{U_f(s)}{D(s)} = -K[sI - (A - B_u K - LC)]^{-1} B_d \tag{6.4.4.24a}$$

$$\frac{U_b(s)}{Y(s)} = -K[sI - (A - B_u K - LC)]^{-1} L \tag{6.4.4.24b}$$

Design equations for LQE optimal observer

A Riccati equation similar to that of the optimal controller (see equation 6.4.4.14) can be written for the optimal LQE observer. The steady-state Riccati equation for the LQE observer is:

$$P_{ss}A^T + AP_{ss} - PC^T R^{-1} CP + B_d Q B_d^T = 0 \qquad \textbf{(6.4.4.25)}$$

where P_{ss} is the steady-state Riccati matrix, A is the plant coefficient matrix, B_d is the plant disturbance input matrix, C is the plant output matrix, and Q and R are the covariances of the uncorrelated process and output noise signals w and v, respectively given by:

$$Q = \frac{1}{T}\int_0^T w^2(t)dt \qquad \textbf{(6.4.4.26a)}$$

$$R = \frac{1}{T}\int_0^T v^2(t)dt \qquad \textbf{(6.4.4.26b)}$$

The observer gain matrix L is obtained as follows from the steady-state Riccati matrix:

$$L = R^{-1} P_{ss} C^T \qquad \textbf{(6.4.4.27)}$$

The LQE observer produces an optimal linear quadratic gaussian (LQG) estimate of the observer state vector $\hat{x}$, for $d = 0$, in equation 6.4.4.16.

State-space and *TF* equations of coupled observer and state plus output integral feedback controller

For linear state plus output integral feedback, the control is given by:

$$u = -K\hat{x} - H_I \int y dt \qquad \textbf{(6.4.4.28)}$$

where H_I is the output integral feedback gain.

Differentiation of equation 6.4.4.28 with respect to time gives:

$$\dot{u} = -K\dot{\hat{x}} - H_I y \qquad \textbf{(6.4.4.29)}$$

Combination of equations 6.4.4.1, 6.4.4.16b, 6.4.4.17 and 6.4.4.29, gives the state-space

equations of the coupled plant, observer and state plus output integral feedback controller, as:

$$\begin{Bmatrix} \dot{x} \\ \dot{\hat{x}} \\ \dot{u} \end{Bmatrix} = \begin{bmatrix} A & 0 & B_u \\ LC & A-LC & B_u \\ -(KL+H_I)C & -K(A-LC) & -KB_u \end{bmatrix} \begin{Bmatrix} x \\ \hat{x} \\ u \end{Bmatrix} + \begin{Bmatrix} B_d \\ B_d \\ -KB_d \end{Bmatrix} d \qquad \textbf{(6.4.4.30a)}$$

$$\begin{Bmatrix} y \\ \hat{y} \\ u \end{Bmatrix} = \begin{bmatrix} C & 0 & 0 \\ 0 & C & 0 \\ 0 & 0 & 1 \end{bmatrix} \begin{Bmatrix} x \\ \hat{x} \\ u \end{Bmatrix} \qquad \textbf{(6.4.4.30b)}$$

The closed-loop eigenvalues of the coupled plant, observer and state plus output integral feedback controller, are the values of s for which:

$$|sI - A_{cl}| = 0 \qquad \textbf{(6.4.4.31)}$$

where A_{cl} is the coupled coefficient matrix:

$$A_{cl} = \begin{bmatrix} A & 0 & B_u \\ LC & A-LC & B_u \\ -(KL+H_I)C & -K(A-LC) & -KB_u \end{bmatrix} \qquad \textbf{(6.4.4.32)}$$

The attenuation factor is given by:

$$\gamma(s) = [C \quad 0 \quad 0][sI - A_{cl}]^{-1} \begin{bmatrix} B_d \\ B_d \\ -KB_d \end{bmatrix} \qquad \textbf{(6.4.4.33)}$$

Equations for the digital filter equivalents of the disturbance to control and output to control *TF*'s are given next.

Digital filter equivalents of continuous *TF*'s

Two methods can be used to obtain the digital equivalents of the continuous *TF*'s. The first is by conversion of the state-space matrices to their discrete equivalents, and by subsequent conversion of the dynamic equations to digital *TF* form. The second is by direct conversion from continuous *TF* form to digital *TF* form. The first method, which is described in detail by Franklin et al [1990], will not be used in this study. The second method can be directly

applied, by transforming the plant poles and zeroes from the s-domain to the z-domain. The transformation equation depends on the type of hold, e.g. zero-order hold ("zoh"), first order hold ("foh") and bilinear transformation (Tustin's method). Application of the "zoh" method is the simplest, and is therefore popular and often used. The method will also be used here. Although other methods may be more accurate for the same sample rate, accuracy can be improved by using higher sample rates.

For a zero-order hold, the discrete domain differential operator z is related to the Laplace-domain differential operator s, by the equation:

$$z = e^{sT} \tag{6.4.4.34}$$

where T is the sample period.

The continuous *TF*'s are written in the following form:

$$G(s) = K_0 \frac{(s-r_1)(s-r_2)\cdots(s-r_m)}{(s-p_1)(s-p_2)\cdots(s-p_n)} \tag{6.4.4.35}$$

where K_0 is the overall gain, r denotes a zero, p denotes a pole and m and n are the *TF* numerator and denominator orders respectively.

By application of equation 6.4.4.34, the discrete equivalent of equation 6.4.4.35, is:

$$G(z) = K_{0z} \frac{(z-e^{r_1 T})(z-e^{r_2 T})\cdots(z-e^{r_m T})}{(z-e^{p_1 T})(z-e^{p_2 T})\cdots(z-e^{p_n T})} \tag{6.4.4.36}$$

The equivalent digital filter equation is obtained by expanding the numerator and denominator terms to obtain polynomials in z, and by subsequent division by the highest power of z of the denominator. The resulting equation is of the form:

$$G(z^{-1}) = \frac{b_0 + b_1 z^{-1} + \cdots + b_m z^{-m}}{a_0 + a_1 z^{-1} + \cdots + a_n z^{-n}} \tag{6.4.4.37}$$

where z^{-1} is the discrete delay.

The discrete equivalents of both the disturbance to control *TF* (as given by equation 6.4.4.24a) and output to control *TF* (as given by equation 6.4.4.24b) are determined by the above method.

Controller design by means of Matlab and Simulink

In this study, design calculations are done with the aid of standard Matlab and Simulink toolboxes. The use of Simulink has a number of advantages, namely that it makes it possible to simulate the behaviour of a continuous plant, controlled by a digital controller. Secondly, the block diagram developed for the simulations requires only minor adjustments, such as the addition of A/D and D/A blocks, to implement the controller and download it onto the DSP. The implementation process will be discussed in section 6.6.2. More information on the use of Matlab for control system analysis, simulation and design is provided by Bishop [1993] and Mathews and Fink [1999].

Real-time simulation of closed-loop system behaviour

After carrying out the above controller design steps, a time-domain simulation of the closed-loop system behaviour is carried out in Simulink. The simulation block diagram is shown in fiigure 6.4.4.1.

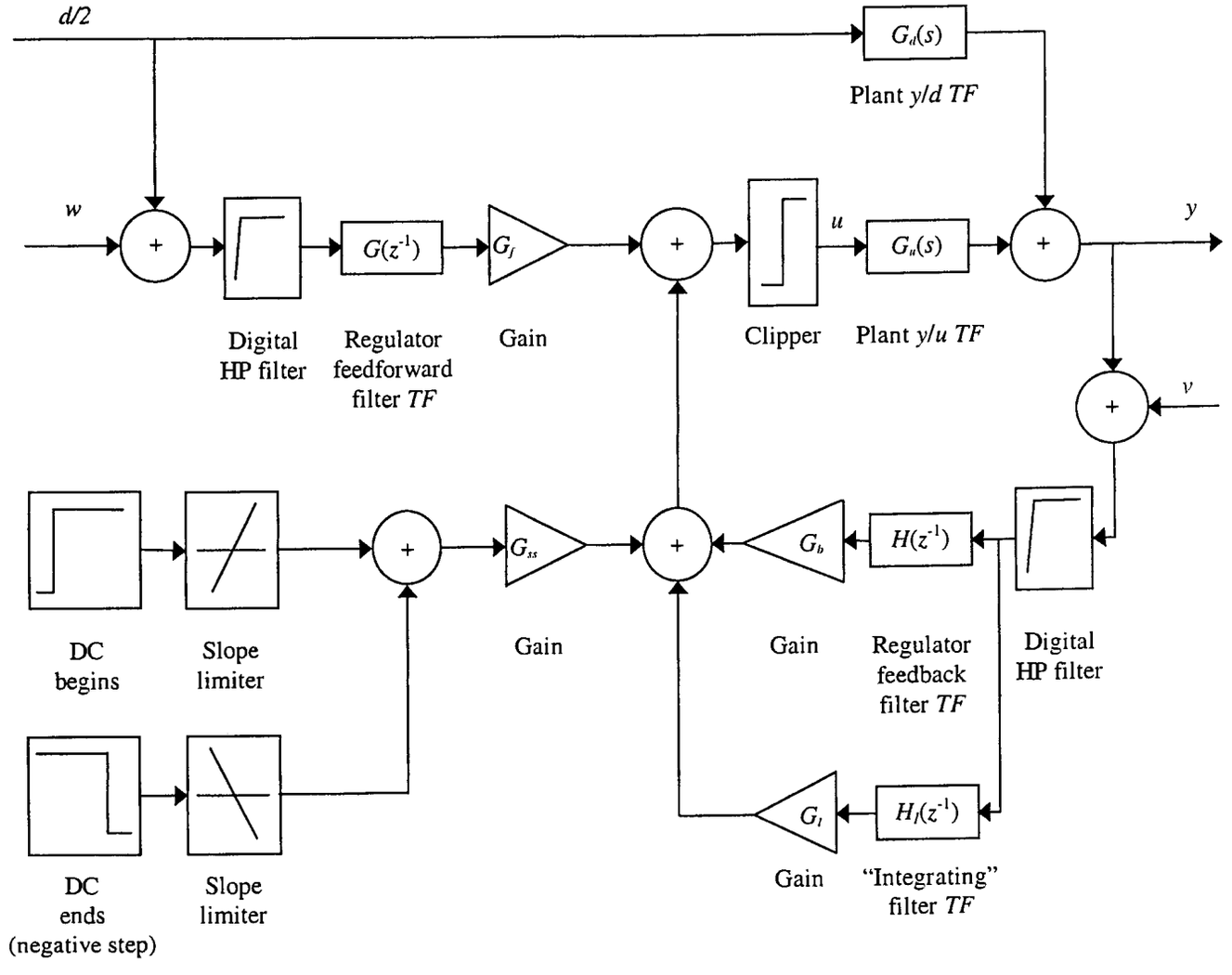

Figure 6.4.4.1: Simulation block diagram of plant and controller, with DC bias

The extraneous inputs are $d/2$, which is 50% of the disturbance, base signal measurement noise w and output signal measurement noise v. The output of the closed-loop system is y.

Third-order, elliptic high-pass (HP) filters are placed in the feedforward and feedback paths in order to demean the disturbance and output signals. Two DC bias blocks, i.e. a positive step to start the DC signal, and a negative step to stop it at the end of the simulation period, are included. The slope limiters ensure that the steps are applied and removed gradually, in order to prevent large transient overshoots. Gain elements are included in the disturbance feedforward, output feedback, output integral feedback and DC bias paths to facilitate controller implementation. Unit feedforward, feedback and DC gains are used for the simulations, while the integral feedback gain is adjustable. A clipper limits the actuator coil supply voltage in order to prevent burnout.

In the interest of high accuracy, a sample period of 4.10^{-4} s, corresponding to a sample frequency of 2,5 kHz, is used. This frequency is 25 times the maximum frequency of the disturbance band of interest (i.e. 100 Hz), 5 times the maximum frequency of the disturbance, including all frequencies (i.e. 500 Hz) and approximately 5 times the maximum measured natural frequency of the plant (476,3 Hz). In order to simulate continuous behaviour of the plant as accurately as possible, the 5^{th} order Runge-Kutta method is used to integrate the dynamic equations. The total duration of the simulation is 4s, which corresponds with that of the known disturbance.

A digital HP filter with the following *TF* is used:

$$G_{filter}\left(z^{-1}\right)=\frac{0{,}9919-2{,}9757z^{-1}+2{,}9757z^{-2}-0{,}9919z^{-3}}{1-2{,}9838z^{-1}+2{,}9677z^{-2}-0{,}9839z^{-3}} \qquad \textbf{(6.4.4.38)}$$

The upper limit of the voltage clipper is set to 28 V and the lower limit to 0 V. The DC bias voltage is 9,1 V (see also table 4.4.5.1). The bias voltage slope limit is 100 V/s.

Design of the disturbance feedforward, output feedback and output integral feedback elements is described in detail in section 6.4.5. The plant characteristics, which were discussed in detail in chapter 5, are repeated in order to provide a better understanding of the controller characteristics.

6.4.5 Plant, controller, observer and closed-loop system parameters

The plant state-space equations are:

$$\dot{x} = Ax + B_u u + B_d d \qquad \textbf{(6.4.5.1a)}$$

$$y = Cx \qquad \textbf{(6.4.5.1b)}$$

where u is the actuator coil voltage, d is the base angular acceleration and y is the optical instrument angular accceleration:

$$u = V \qquad \textbf{(6.4.5.2a)}$$

$$d = \ddot{\theta}_b \qquad \textbf{(6.4.5.2b)}$$

$$y = \ddot{\theta} \qquad \textbf{(6.4.2.5c)}$$

A consists of the following submatrices (see equation 5.6.9a):

$$A = \begin{bmatrix} 0 & I & 0 \\ -\Omega^2 & -2Z\Omega & M^{*-1}\Phi_s^T F_l C_c \\ 0 & 0 & A_c \end{bmatrix} \qquad \textbf{(6.4.5.3)}$$

Numerical values of the elements of the submatrices of A are as follows:

$$\Omega^2 = 1.10^6 \begin{bmatrix} 1{,}481 & & & & \\ & 2{,}093 & & & \\ & & 2{,}469 & & \\ & & & 3{,}588 & \\ & & & & 8{,}959 \end{bmatrix} \qquad \textbf{(6.4.5.4a)}$$

$$2Z\Omega = \begin{bmatrix} 97{,}35 & & & & \\ & 50{,}53 & & & \\ & & 111{,}6 & & \\ & & & 115{,}0 & \\ & & & & 71{,}83 \end{bmatrix} \qquad \textbf{(6.4.5.4b)}$$

$$M^{*-1}\Phi_s^T F_l C_c = \begin{bmatrix} 1{,}47.10^{10} & 3{,}734.10^{6} & 470{,}2 \\ -3{,}179.10^{9} & -8{,}075.10^{5} & -101{,}7 \\ -1{,}204.10^{9} & -3{,}058.10^{5} & -38{,}51 \\ -4{,}379.10^{10} & -1{,}112.10^{7} & -1401 \\ 2{,}723.10^{10} & 6{,}916.10^{6} & 870{,}9 \end{bmatrix} \qquad \textbf{(6.4.5.4c)}$$

$$A_c = \begin{bmatrix} 0 & 1 & 0 \\ 0 & 0 & 1 \\ -1{,}332.10^{9} & -3{,}487.10^{6} & -1817 \end{bmatrix} \qquad \textbf{(6.4.5.4d)}$$

Numerical values of the elements of the driving matrices B_u and B_d are as follows:

$$B_u = [0 \;\; 0 \;\; 0 \;\; 0 \;\; 0 \;\; 0 \;\; 0 \;\; 0 \;\; 0 \;\; 0 \;\; 0 \;\; 0 \;\; 1]^T \qquad \textbf{(6.4.5.5a)}$$

$$B_d = [-9{,}705.10^{-6} \;\; 1{,}5771.0^{-6} \;\; 6{,}437.10^{-6} \;\; 9{,}235.10^{-6} \;\; 0 \;\; 0{,}1476 \;\; -0{,}06532 \;\; -0{,}1424 \;\; -0{,}288 \;\; 0 \;\; 0 \;\; 0 \;\; 0]^T \qquad \textbf{(6.4.5.5b)}$$

Numerical values of the elements of the output matrix C are as follows:

$$C =$$
$$[5{,}14.10^{5} \;\; -3{,}24.10^{6} \;\; -3{,}72.10^{6} \;\; -7{,}94.10^{6} \;\; -1{,}82.10^{6} \;\; 33{,}8 \;\; -78{,}3 \;\; -168 \;\; -255 \;\; -146 \;\; -1{,}14.10^{11} \;\; -2{,}9.10^{7} \;\; -3657] \qquad \textbf{(6.4.5.6)}$$

The plant transfer functions for the control and disturbance inputs are given by:

$$\frac{Y(s)}{U(s)} = C[sI - A]^{-1} B_u \qquad \textbf{(6.4.5.7a)}$$

$$\frac{Y(s)}{D(s)} = C[sI - A]^{-1} B_d \qquad \textbf{(6.4.5.7b)}$$

Numerical values of the plant *TF* numerator and denominator polynomials are obtained by substitution of equations 6.4.5.4 into equation 6.4.5.3, and by subsequent substitution of the resulting equation, as well as equations 6.4.5.5 and 6.4.5.6, into equations 6.4.5.7.

The plant *TF* poles and zeroes, in frequency and damping form, are given in tables 6.4.5.1 to 6.4.5.3.

Table 6.4.5.1: Plant *TF* poles

Undamped frequency (Hz)	Damping factor (%)
74,19	* real pole
193,64	4,00
230,26	1,75
250,09	3,55
269,05	39,95
301,46	3,04
476,37	1,20

* Damping factor not given for real poles and zeroes

Table 6.4.5.2: Plant *TF* zeroes for control input

Undamped frequency (Hz)	Damping factor (%)
0	* real zero
0	* real zero
199,15	3,87
234,23	1,88
251,25	3,52
469,22	1,25
889,88	71,01

Table 6.4.5.3: Plant *TF* zeroes for disturbance input

Undamped frequency (Hz)	Damping factor (%)
74,19	* real zero
196,10	3,94
233,90	1,98
261,96	3,33
269,05	39,95
476,37	1,20

The plant pole-zero maps, for the control and disturbance inputs, are shown in figures 6.4.5.1 and 6.4.5.2 respectively. The units are in rad/s.

The *TF* magnitude and phase spectra for the control and disturbance inputs are shown in figures 6.4.5.3 and 6.4.5.4 respectively.

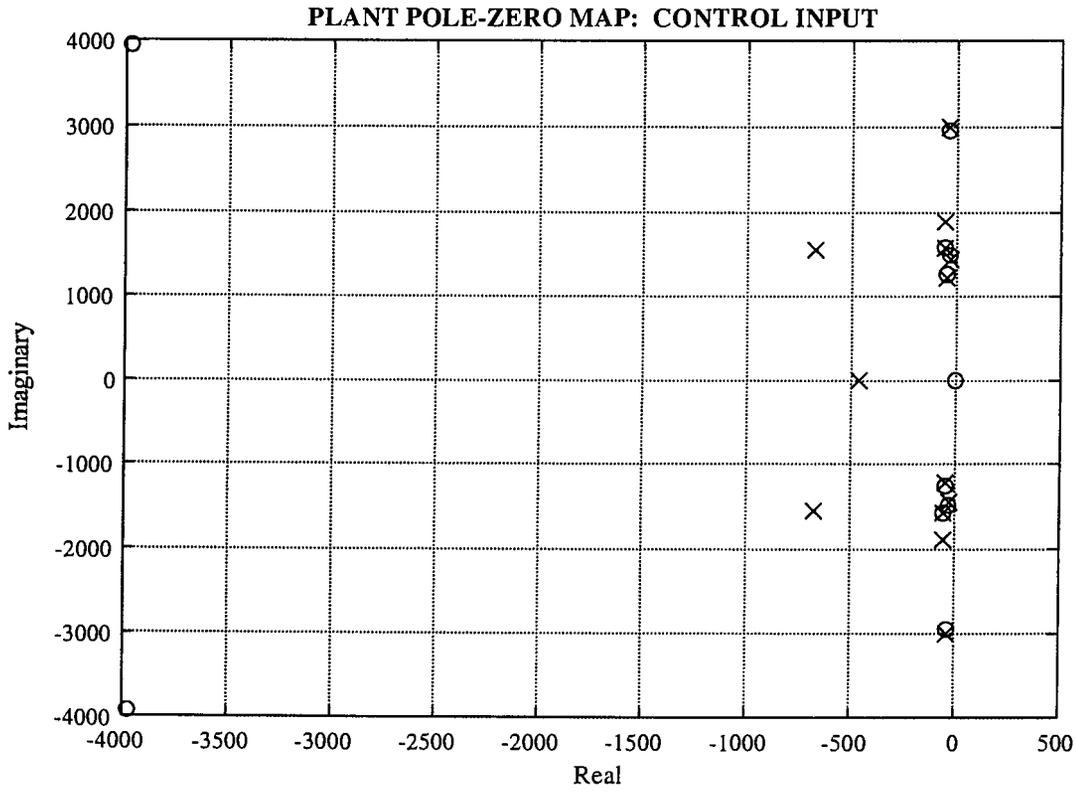

Figure 6.4.5.1: Plant pole-zero map for control input

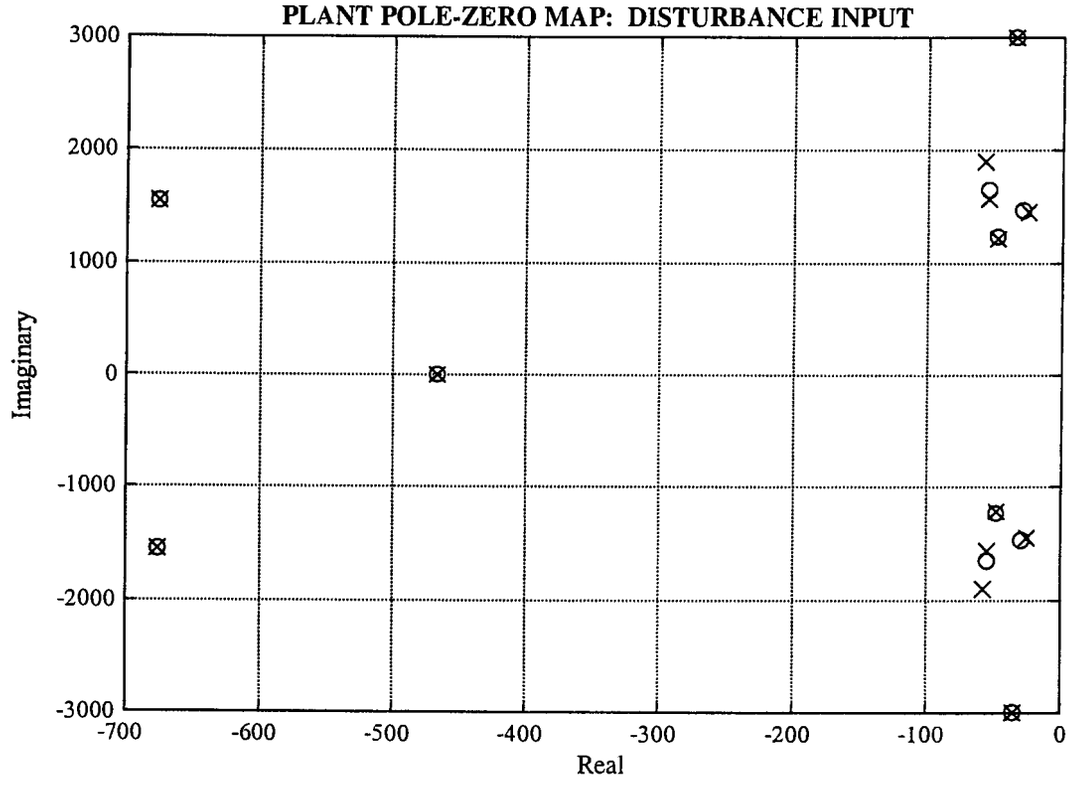

Figure 6.4.5.2: Plant pole-zero map for disturbance input

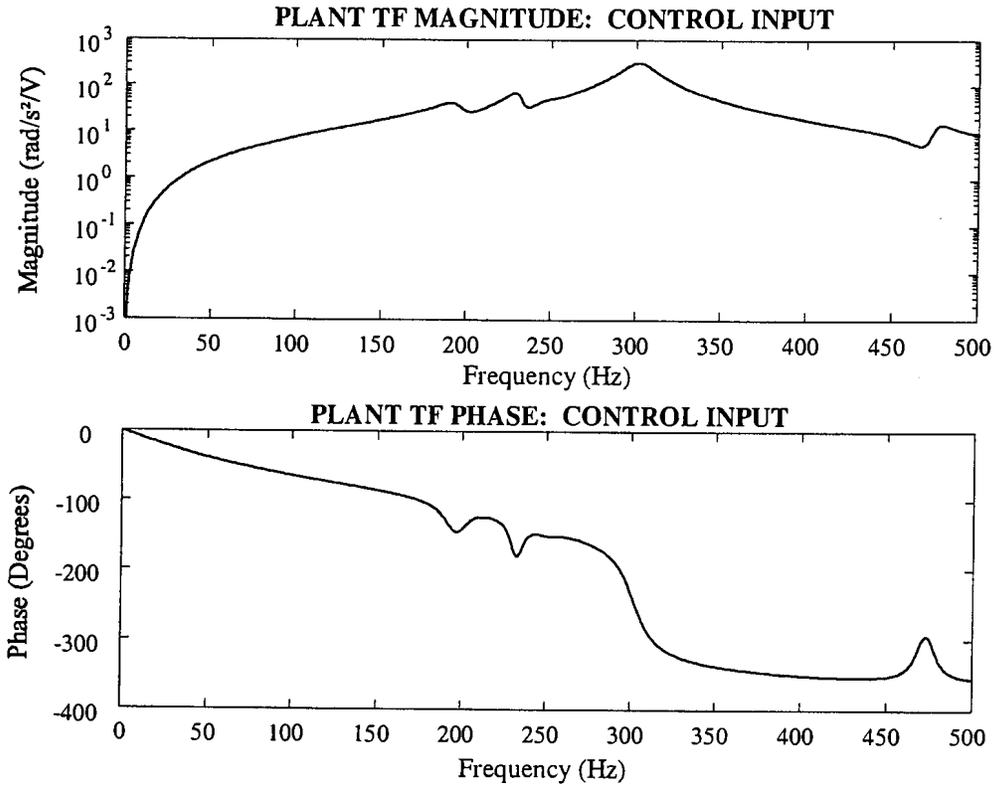

Figure 6.4.5.3: Plant *TF* magnitude and phase spectra for control input

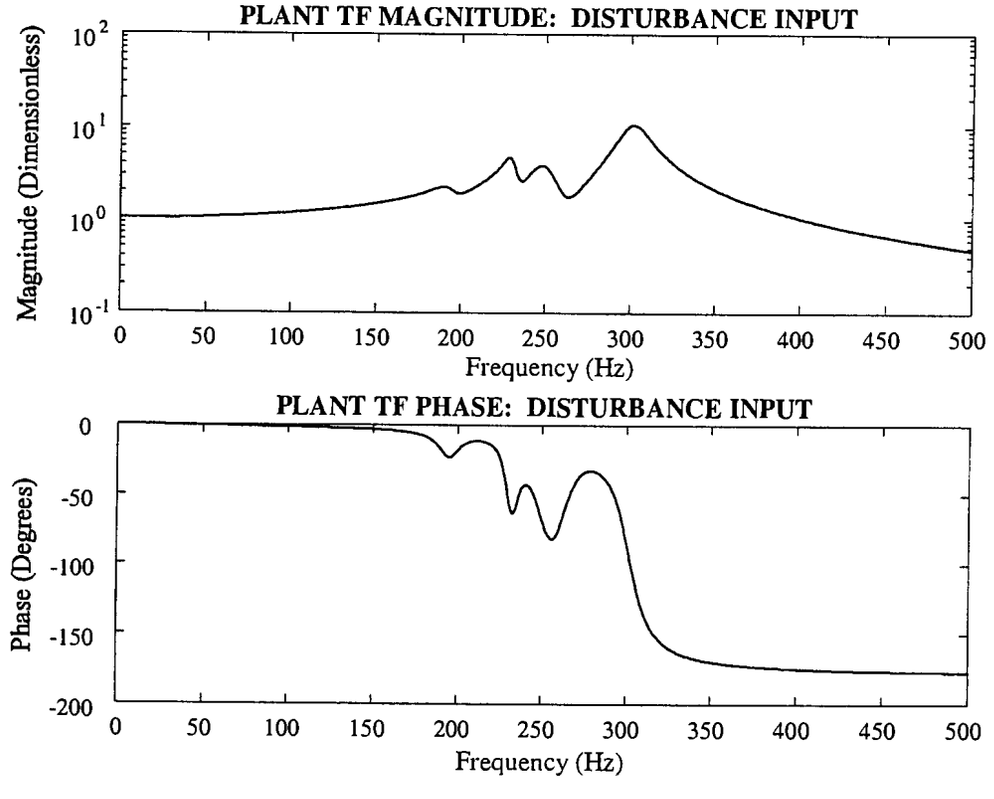

Figure 6.4.5.4: Plant *TF* magnitude and phase spectra for disturbance input

Plant canonical state-space matrices

The plant state-space matrices are expressed as follows in modal canonical form:

$$A = \begin{bmatrix} -48{,}67 & 1216 & & & & & & & & & & & \\ -1216 & -48{,}67 & & & & & & & & & & & \\ & & -25{,}27 & 1447 & & & & & & & & & \\ & & -1447 & -25{,}27 & & & & & & & & & \\ & & & & -55{,}82 & 1570 & & & & & & & \\ & & & & -1570 & -55{,}82 & & & & & & & \\ & & & & & & -57{,}53 & 1893 & & & & & \\ & & & & & & -1893 & -57{,}53 & & & & & \\ & & & & & & & & -35{,}92 & 2993 & & & \\ & & & & & & & & -2993 & -35{,}92 & & & \\ & & & & & & & & & & -466{,}1 & & \\ & & & & & & & & & & & -675{,}3 & 1550 \\ & & & & & & & & & & & -1550 & -675{,}3 \end{bmatrix}$$

(6.4.5.8a)

$$B_{tt} = \{-5{,}534 \quad -0{,}9727 \quad 0{,}2827 \quad 0{,}242 \quad 0{,}5233 \quad -0{,}8961 \quad -8{,}419 \quad 3{,}373 \quad -0{,}05148 \quad 1{,}282 \quad 2{,}550 \quad -10{,}69 \quad -4{,}101\}^T$$

(6.4.5.8b)

$$B_{il} = \{-0{,}005910 \quad 0{,}1476 \quad 0{,}00506 \quad -0{,}1424 \quad -0{,}06529 \quad -0{,}002281 \quad 0{,}2876 \quad 0{,}01749 \quad 0 \quad 0 \quad 0 \quad 0 \quad 0\}^T$$

(6.4.5.8c)

$$C = \{421{,}9 \quad 16{,}89 \quad -2365 \quad -84{,}04 \quad -78{,}25 \quad 2239 \quad 254{,}6 \quad -4186 \quad -607{,}9 \quad -7{,}296 \quad -1003 \quad -2854 \quad 2504\}$$

(6.4.5.8d)

Observability

The rank of the observability matrix in equation 6.4.4.6 is 13, which corresponds with the number of states. The system is therefore observable. (The A matrix is multiplied by a constant factor of 1.10^{-3} to calculate the observability matrix, since the magnitudes of the higher powers of A cause roundoff errors).

Controllability

The rank of the controllability matrix in equation 6.4.4.7 is 13. The system is therefore controllable. (The A matrix is scaled by a factor of 1.10^{-3}, as for the observability matrix).

Selection of output and control weights and calculation of state feedback gains

Output and control weights for use in the optimization cost function (equation 6.4.4.12) are arbitrarily selected and their influence on the closed-loop attenuation factor is investigated. Output weights Q_y of 1000, 2000 and 5000, are selected, together with a unit control weight R. The state weight Q_x is determined for each of the output weights, by application of equation 6.4.4.13. The Riccati equation (6.4.4.14) is solved and the steady state Riccati matrix is obtained, which is used to determine the state feedback gain vectors for each of the above output weights.

The state feedback gain vector K, for $Q_y = 1000$ and $R = 1$, is:

$$K = \{-13325 \quad -126{,}22 \quad 74687 \quad 1285{,}1 \quad 907{,}15 \quad -70794 \quad -6692{,}9 \quad 132290 \quad 19212 \quad 399{,}74 \quad 28390 \quad 87605 \quad -79040\} \tag{6.4.5.9}$$

The state feedback gain vector K, for $Q_y = 2000$ and $R = 1$, is:

$$K = \{-18851 \quad -245{,}34 \quad 105650 \quad 1945{,}3 \quad 1478 \quad -100130 \quad -9384{,}4 \quad 187140 \quad 27176 \quad 437{,}68 \quad 40881 \quad 124390 \quad -112110\} \tag{6.4.5.10}$$

The state feedback gain vector K, for $Q_y = 5000$ and $R = 1$, is:

$$K = \{-29816 \quad -518{,}4 \quad 167100 \quad 3411{,}8 \quad 2772{,}6 \quad -158340 \quad -14951 \quad 295970 \quad 42967 \quad 532{,}1 \quad 65900 \quad 197950 \quad -177640\} \tag{6.4.5.11}$$

Closed-loop attenuation factors for optimal state feedback gains

The closed-loop attenuation factors for each of the above state feedback gain factors are calculated by means of equation 6.4.4.11. The attenuation factors, which are also the magnitude spectra of the closed-loop TR's, are shown in figure 6.4.5.5.

It can be seen from figure 6.4.5.5 that, for the three selected weights, the lowest (i.e. best) attenuation factor is obtained with an output weight of 5000, while the highest (worst) is obtained with a weight of 1000. The suboptimal controller design will be based on the optimal controller, obtained with an output weight of 5000 and a unit control weight.

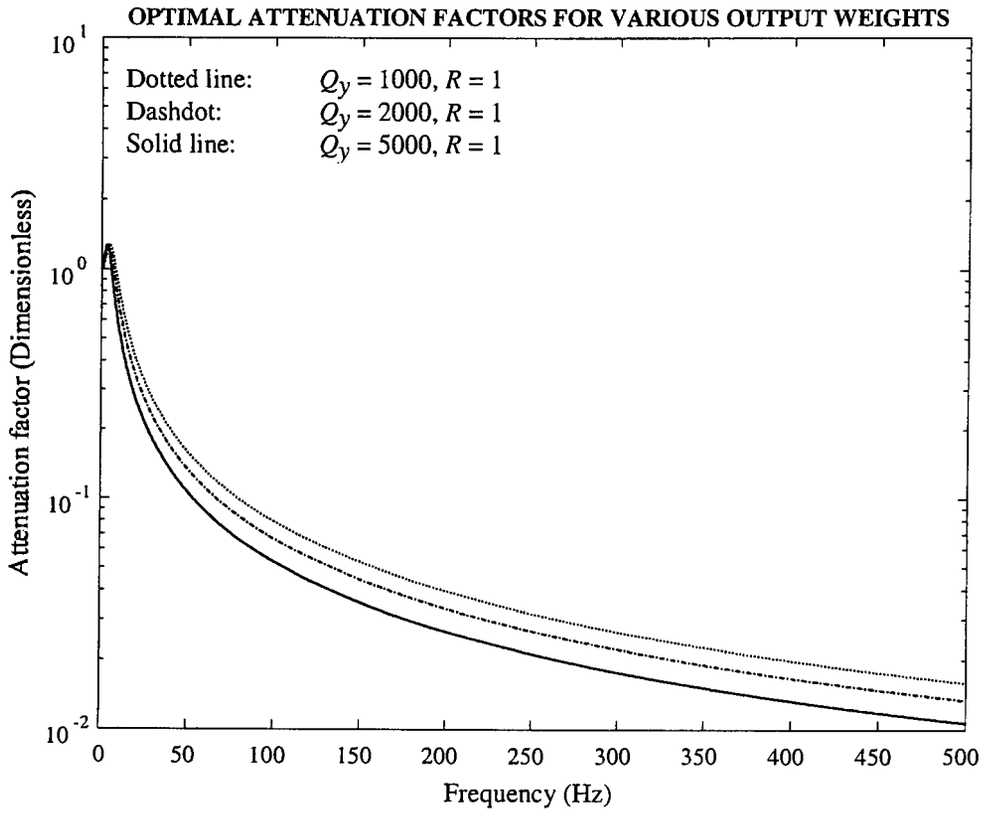

Figure 6.4.5.5: Optimal attenuation factors for Q_y = 1000, 2000 & 5000, with R = 1

The closed-loop poles and zeroes of the optimal controller, for Q_y = 5000 and R = 1, are given in tables 6.4.5.4 and 6.4.5.5 respectively. The closed-loop pole-zero map is shown in figure 6.4.5.6. (The real pole at 41,16 kHz is not shown). From tables 6.4.5.4 and 6.4.5.5, and figure 6.4.5.6, it is clear that almost all of the poles, except for the complex pole pair at 3,74 Hz, are cancelled by zeroes.

Table 6.4.5.4: Closed-loop poles for Q_y = 5000, R =1

Undamped frequency (Hz)	Damping factor (%)
3,74	70,74
199,15	3,87
234,23	1,88
251,35	3,52
469,22	1,25
889,92	71,01
41155	real

Table 6.4.5.5: Closed-loop zeroes for $Q_y = 5000$, $R = 1$

Undamped frequency (Hz)	Damping factor (%)
2,64	real
199,15	3,87
234,23	1,88
251,35	3,52
469,22	1,25
888,35	71,08

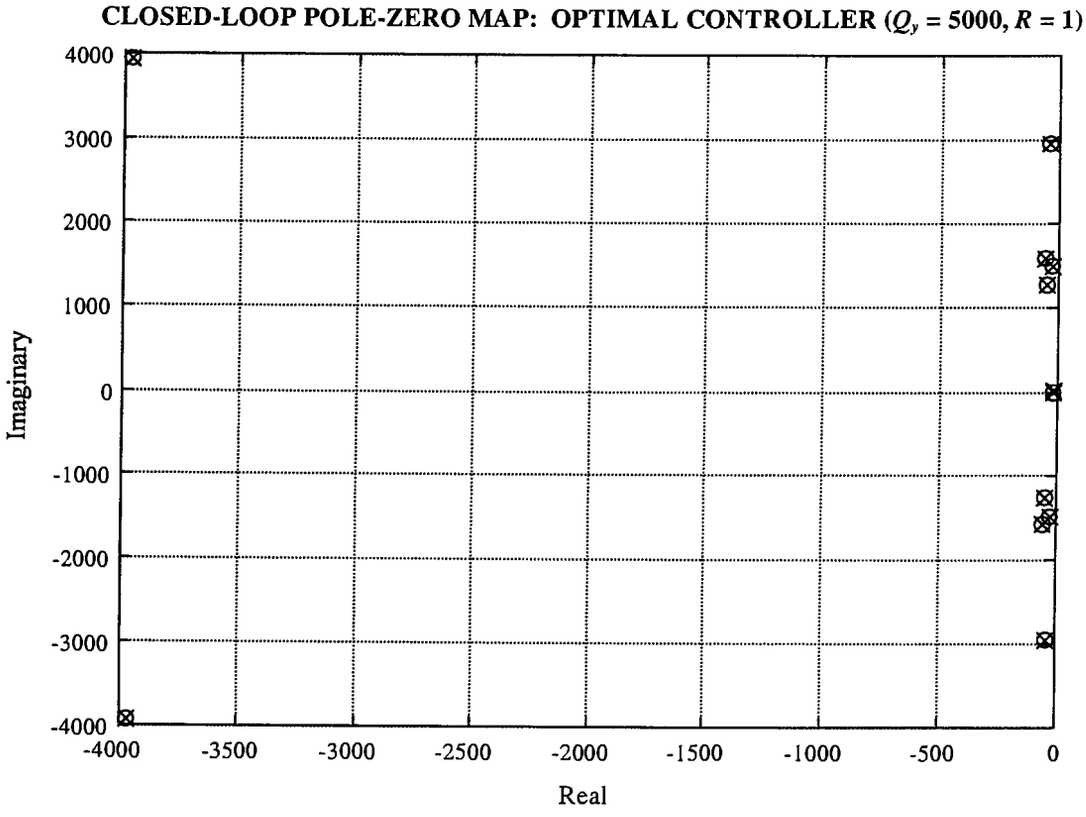

Figure 6.4.5.6: Closed-loop pole-zero map for optimal controller ($Q_y = 5000$, $R = 1$)

The attenuation factor of the optimal controller is compared with the open-loop *TR* magnitude in figure 6.4.5.7. The effect of pole-zero cancellation is clear from the figure.

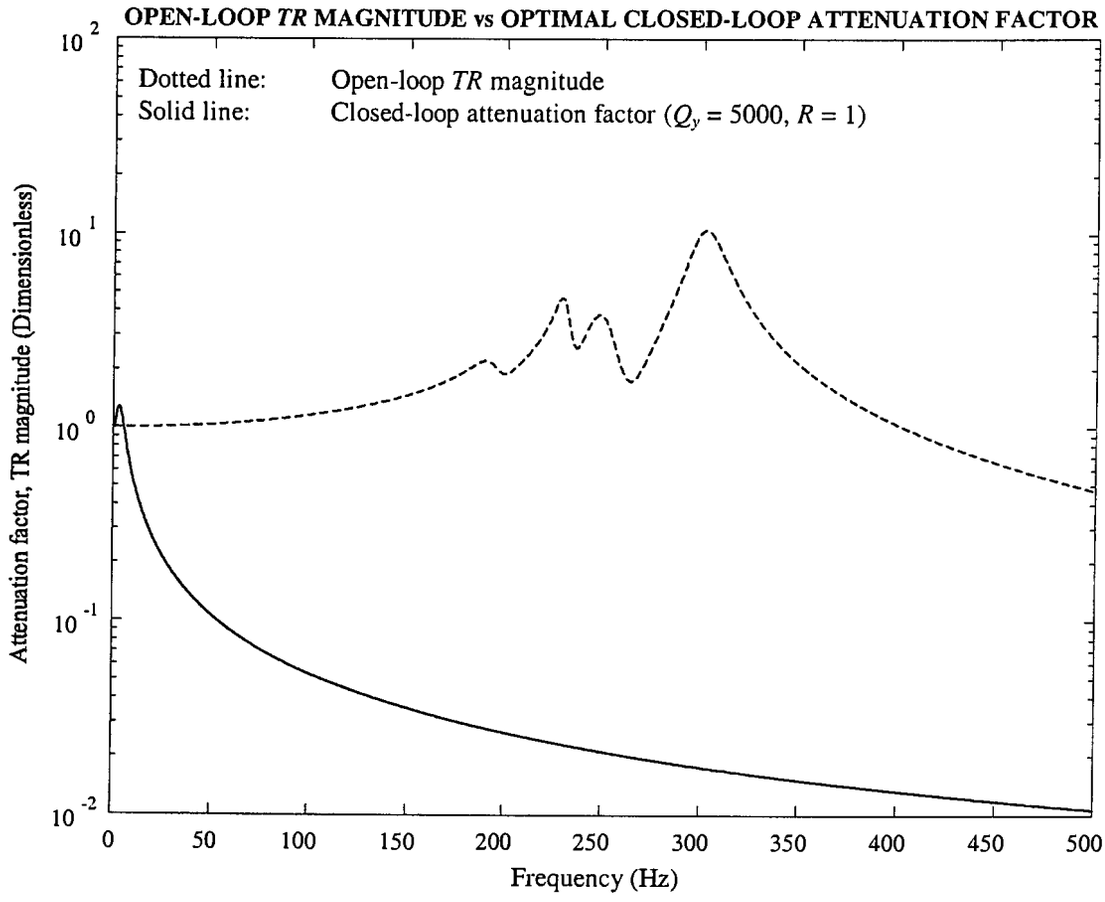

Figure 6.4.5.7: Open-loop *TR* magnitude and optimal closed-loop attenuation factor

The suboptimal control parameters are given next. The design is based on the optimal controller.

Suboptimal state feedback controller

The closed-loop pole with undamped frequency of 3,7 Hz is shifted to 5,6 Hz (i.e. an increase of 50%) and the damping factors of all the zeroes, with the exception of one, are increased to above 5%. Damping of the pole at 234 Hz is lowered from 1,88% to 1,22%. The state feedback gain vector K which places the poles accordingly, is:

$$K=\{-19871 \quad 531{,}5 \quad 107030 \quad 11421 \quad -36570 \quad -92131 \quad -13057 \quad 187250 \quad 29893 \quad 625{,}92 \quad 40340 \quad 126250 \quad -113250\} \tag{6.4.5.12}$$

The poles and zeroes of the suboptimal closed-loop system are given in tables 6.4.5.6 and 6.4.5.7 respectively. The pole-zero map is shown in figure 6.4.5.8. (The real pole at 25,42 kHz is not shown).

Table 6.4.5.6: Poles of suboptimal closed-loop system

Undamped frequency (Hz)	Damping factor (%)
5,63	70,71
199,45	3,87
234,05	1,22
251,33	3,52
468,56	1,25
901,57	71,89
25417	real

Table 6.4.5.7: Zeroes of suboptimal closed-loop system

Undamped frequency (Hz)	Damping factor (%)
3,99	real
199,04	7,41
240,04	1,78 (positive real part)
261,74	7,14
462,60	7,47
879,19	55,03

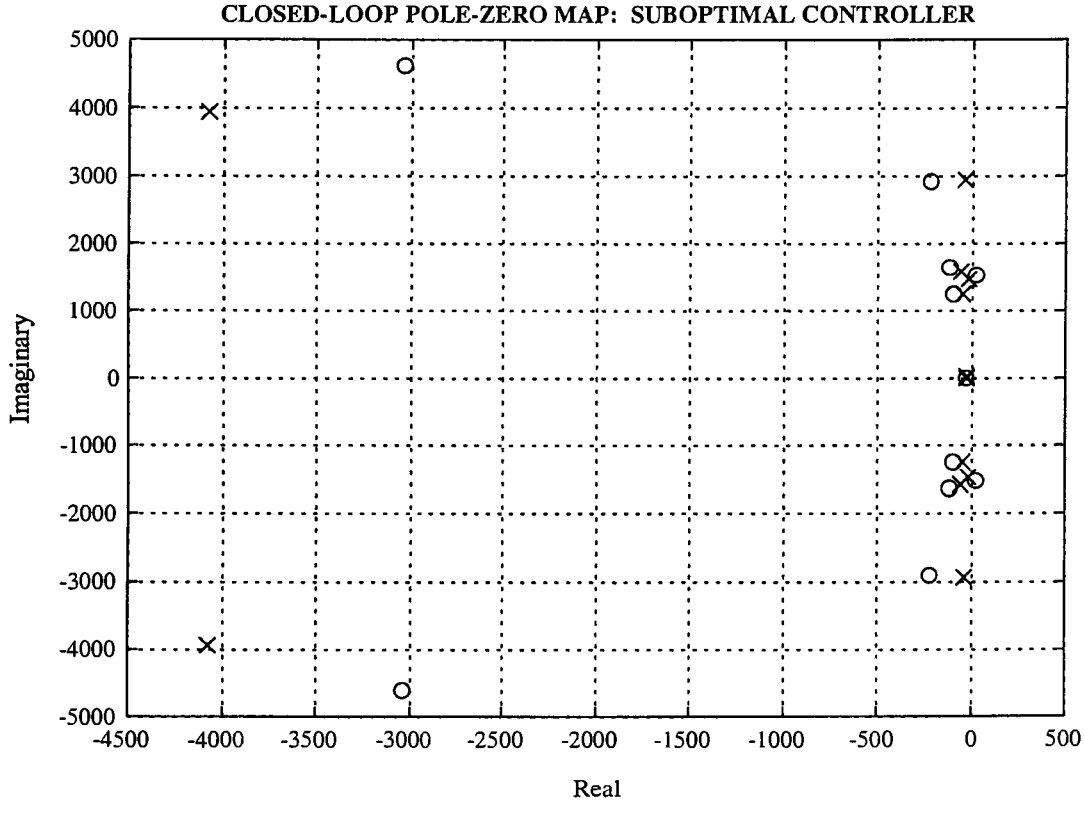

Figure 6.4.5.8: Closed-loop pole-zero map for suboptimal controller

The attenuation factor of the suboptimal controller is compared with the open-loop *TR* magnitude in figure 6.4.5.9.

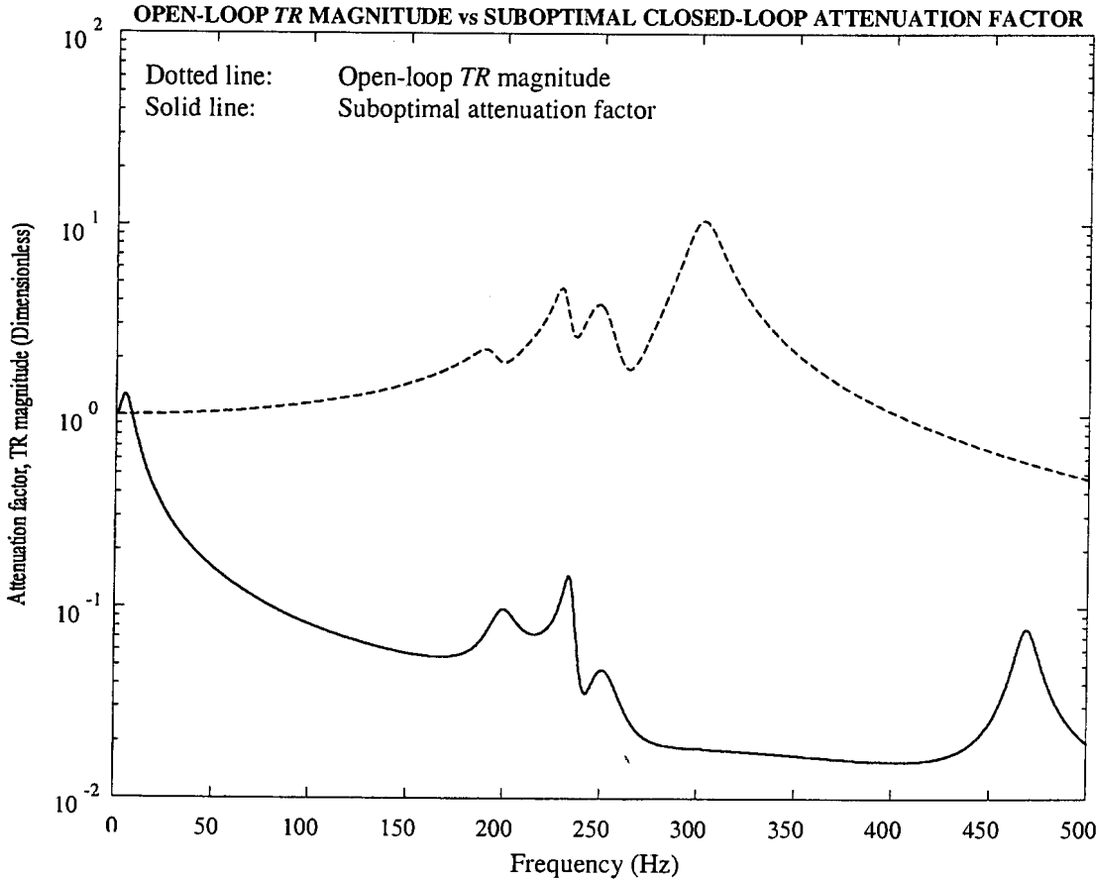

Figure 6.4.5.9: Open-loop *TR* magnitude and suboptimal closed-loop attenuation factor

A comparison between the optimal and suboptimal controller attenuation factors is shown graphically in figure 6.4.5.10. It can be seen from the figure that, unlike in the case of the optimal controller, the suboptimal attenuation factor does not display pole-zero cancellation.

The suboptimal attenuation factor graph displays a resonance peak at 476 Hz, which corresponds with the base natural frequency. The suboptimal controller excites the base mode, while the optimal controller doesn't.

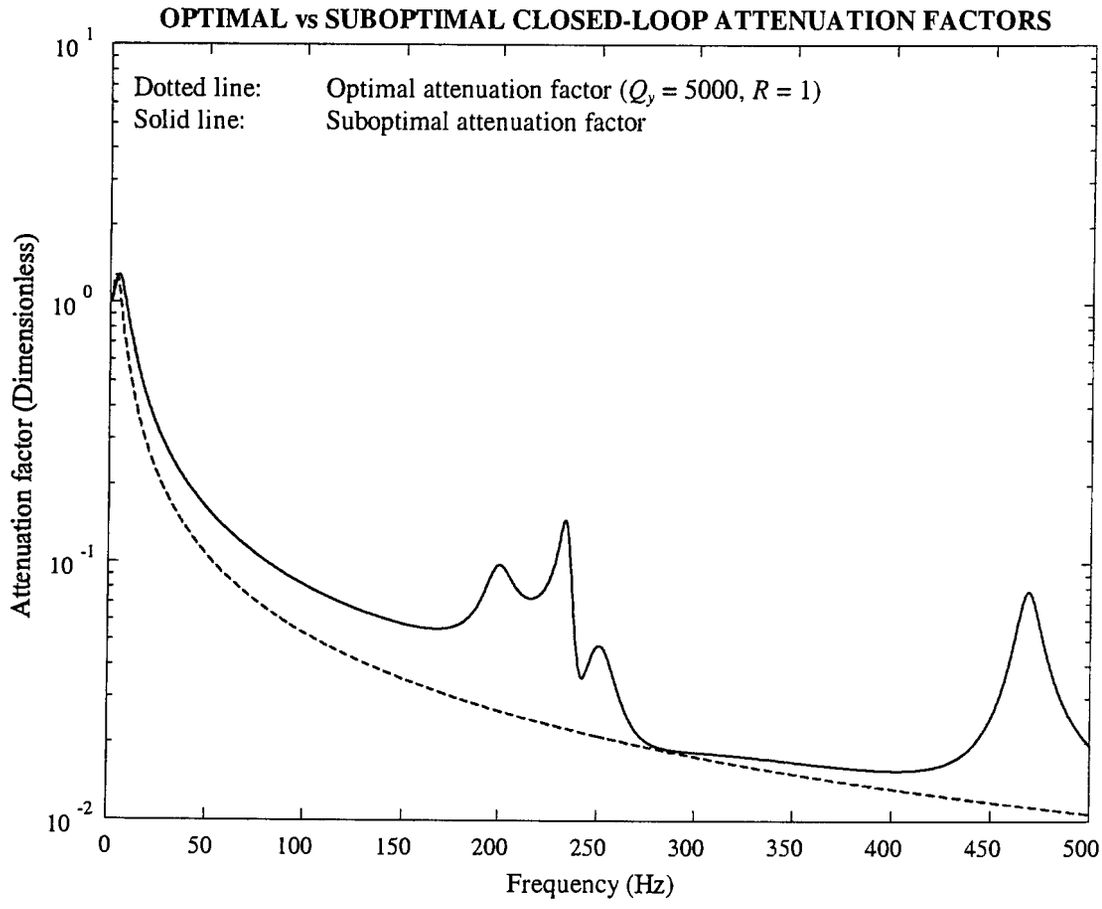

Figure 6.4.5.10: Comparison between optimal and suboptimal closed-loop controller attenuation factors

The optimal linear quadratic observer parameters are given next.

Linear quadratic optimal observer (LQE)

The solution of the optimal observer Riccati equation (6.4.4.25) is determined for measured Q and R values of 0,0103. These values correspond with 15,6% of that of the required output. The solution of the Riccati equation is subtituted into equation 6.4.4.27 to give the optimal observer gain matrix as follows:

$$L = \{0{,}07109 \quad 0{,}1065 \quad -0{,}102 \quad -0{,}0797 \quad -0{,}04247 \quad 0{,}04399 \quad 0{,}09784 \quad -0{,}2468 \quad 0 \quad 0 \quad 0 \quad 0 \quad 0\}^T \tag{6.4.5.13}$$

The disturbance-to-control and output-to-control *TF*'s are obtained by application of equations 6.4.4.24a and 6.4.4.24b. The poles of *U/*D and *U/Y* are given in table 6.4.5.8, while the zeroes of *U/D* and *U/Y* are respectively given in tables 6.4.5.9 and 6.4.5.10.

Table 6.4.5.8: Poles of *U/D* & *U/Y* for optimal observer

Undamped frequency (Hz)	Damping factor (%)
6,66	84,36
199,53	3,98
234,14	1,46
251,63	3,59
468,67	1,36
900,62	71,61
25647	real

Table 6.4.5.9: Zeroes of *U/D* for optimal observer

Undamped frequency (Hz)	Damping factor (%)
74,19	* real
196,16	3,94
233,88	1,78
261,93	3,33
269,05	39,95
476,37	1,20
17681	positive real

Table 6.4.5.10: Zeroes of *U/Y* for optimal observer

Undamped frequency (Hz)	Damping factor (%)
74,19	real
146,95	real
196,62	3,44
234,29	1,02
262,83	2,33
269,05	39,95
476,37	1,20

The pole-zero maps of *U/D* and *U/Y* for the suboptimal controller and optimal observer are shown in figures 6.4.5.11 and 6.4.5.12 respectively. (The real zero of *U/D* at 17,68 kHz is not shown).

The magnitude and phase spectra of *U/D* and *U/Y* are respectively shown in figures 6.4.5.13 and 6.4.5.14.

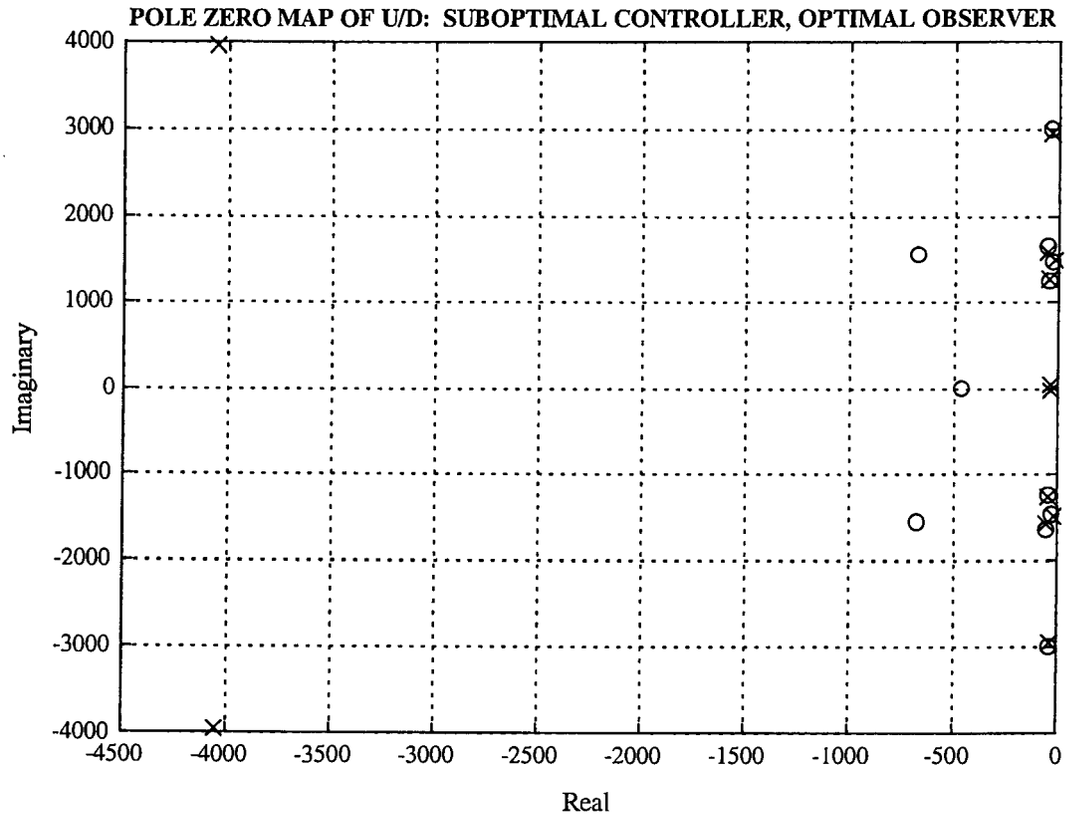

Figure 6.4.5.11: Pole-zero map of *U/D* (suboptimal controller with optimal observer)

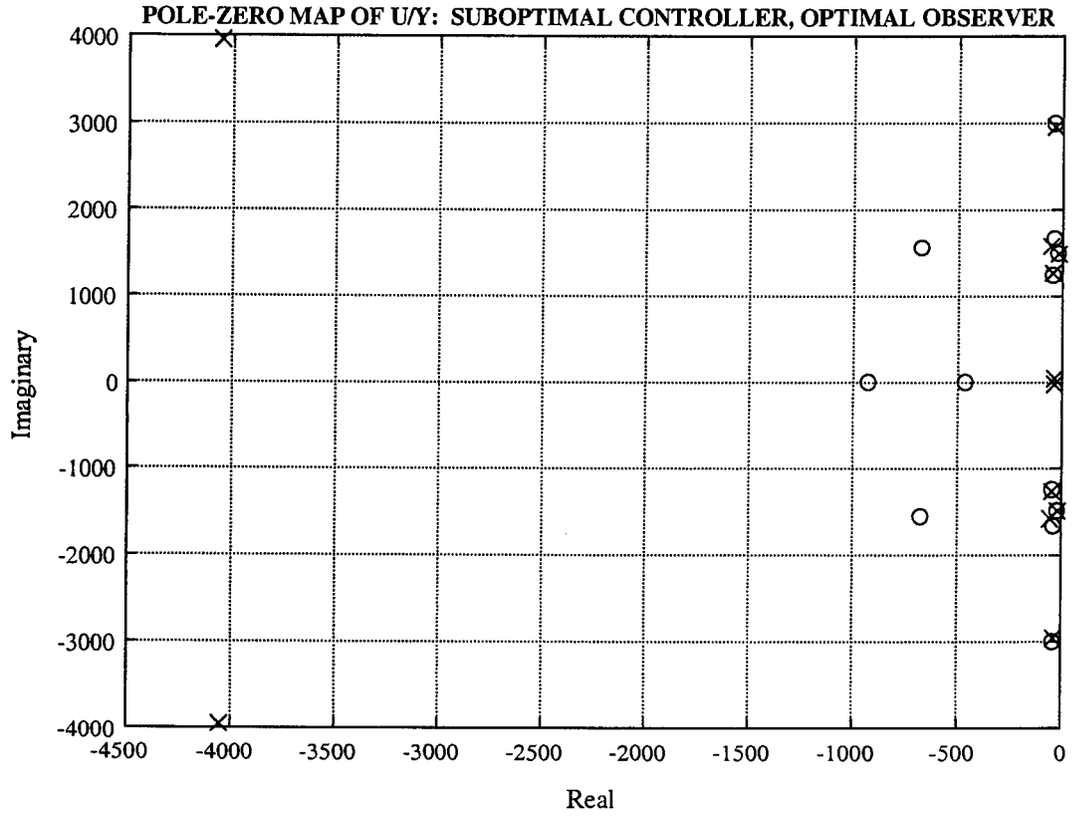

Figure 6.4.5.12: Pole-zero map of *U/Y* (suboptimal controller with optimal observer)

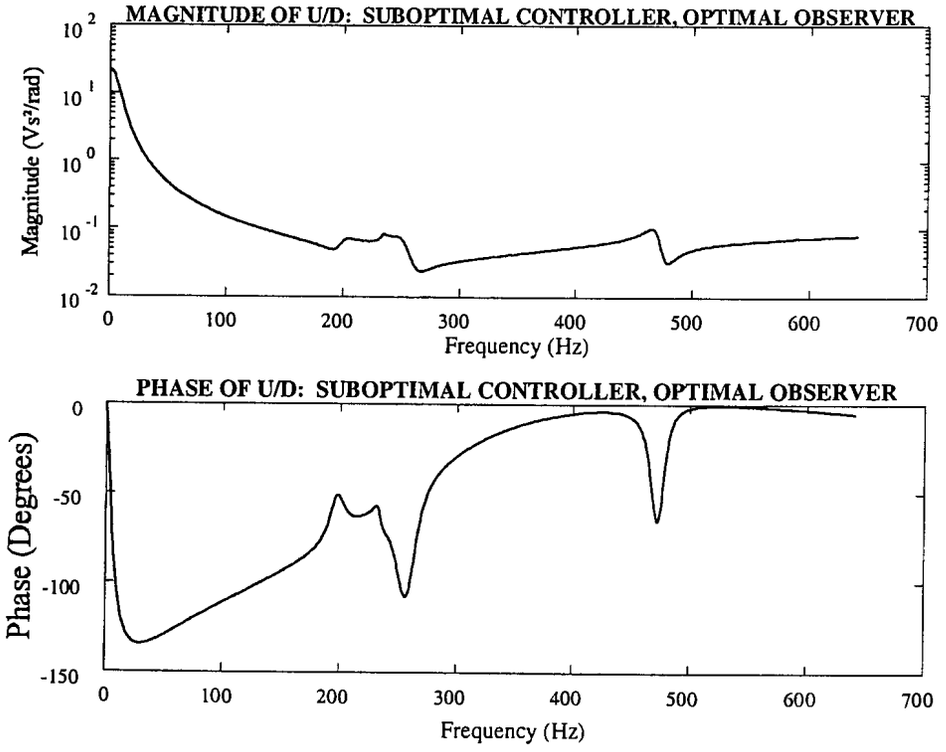

Figure 6.4.5.13: **Disturbance to control *TF* magnitude & phase spectra: Suboptimal controller with LQE optimal observer**

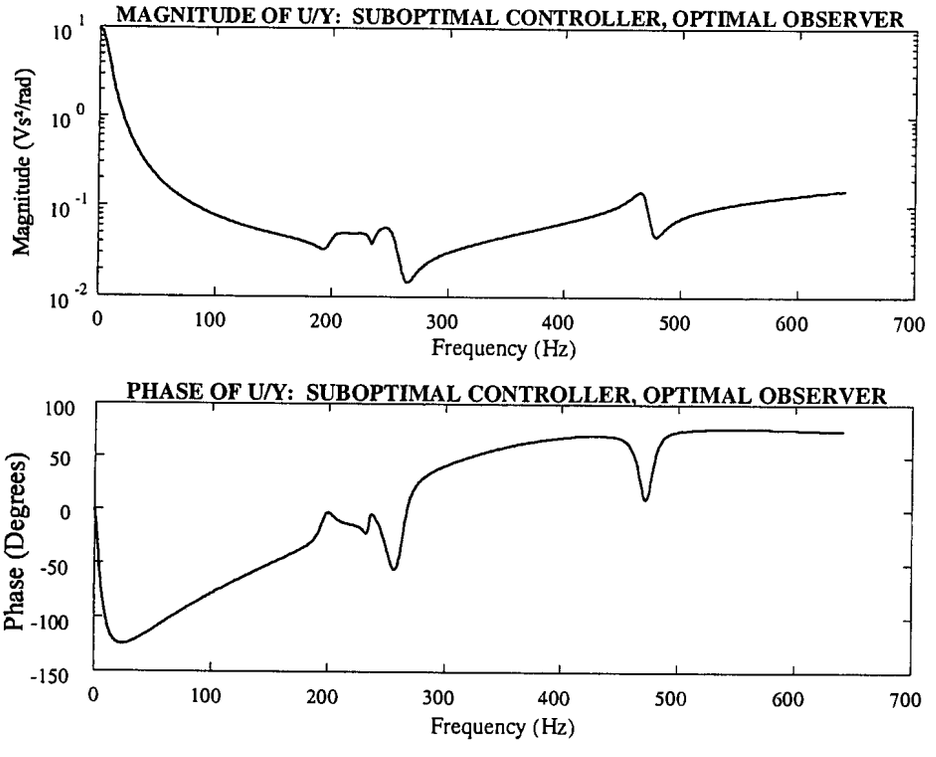

Figure 6.4.5.14: **Output to control *TF* magnitude and phase spectra: Suboptimal controller with LQE optimal observer**

The coupled state and output equations of the closed-loop system, consisting of the plant, suboptimal controller and optimal observer, are given in equations 6.4.4.20. The system is stable.

Suboptimal controller with suboptimal observer

It can be seen from equation 6.4.5.13 that the last five elements of the optimal observer gain matrix are zero. This is a consequence of the fact that the corresponding elements in the disturbance driving matrix B_d (see equation 6.4.5.8c) are zero. Although the plant is fully observable, the controller will not be able to control the last five states, i.e. the two base states and the three coil states, from the output.

In order to control these states, the corresponding elements of the observer gain matrix are changed to nonzero values. Contrary to the design of the suboptimal controller, the purpose is not to alter the frequencies and damping factors of poles and zeroes, but to control all the states. The resulting observer is necessarily suboptimal in terms of the process and output weights Q and R in equations 6.4.4.26.

The suboptimal observer gain matrix is modified as follows:

$$L=\{0{,}07109 \quad 0{,}1065 \quad -0{,}102 \quad -0{,}07697 \quad -0{,}04247 \quad 0{,}04397 \quad 0{,}09784 \quad -0{,}2468 \quad 0{,}05 \quad 0{,}05 \quad 0{,}05 \quad -0{,}02 \quad -0{,}02\}^T \tag{6.4.5.14}$$

The magnitude and phase spectra of U/D and U/Y of the suboptimal controller and suboptimal observer are shown in figures 6.4.5.15 and 6.4.5.16 respectively.

The coupled state and output equations of the closed-loop system, consisting of the plant, suboptimal controller and suboptimal observer, are given in equations 6.4.4.20. The coupled system is stable.

The TF magnitude and phase of U/Y for the suboptimal controller and suboptimal observer are compared with those of the suboptimal controller and optimal observer in figure 6.4.5.17. (The magnitude and phase spectra for U/D are not shown because the differences between the spectra are hardly visible. This is mainly because certain elements of the the L matrix are adjusted, while the B_d matrix is unaffected.)

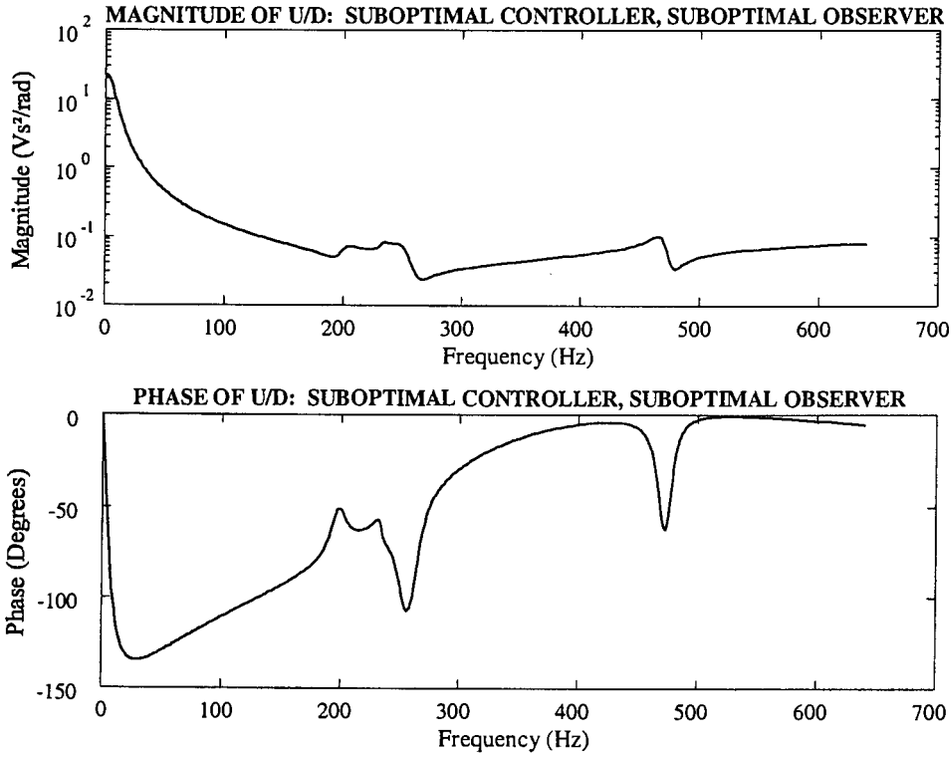

Figure 6.4.5.15: **Disturbance to control *TF* magnitude and phase spectra: Suboptimal controller with suboptimal observer**

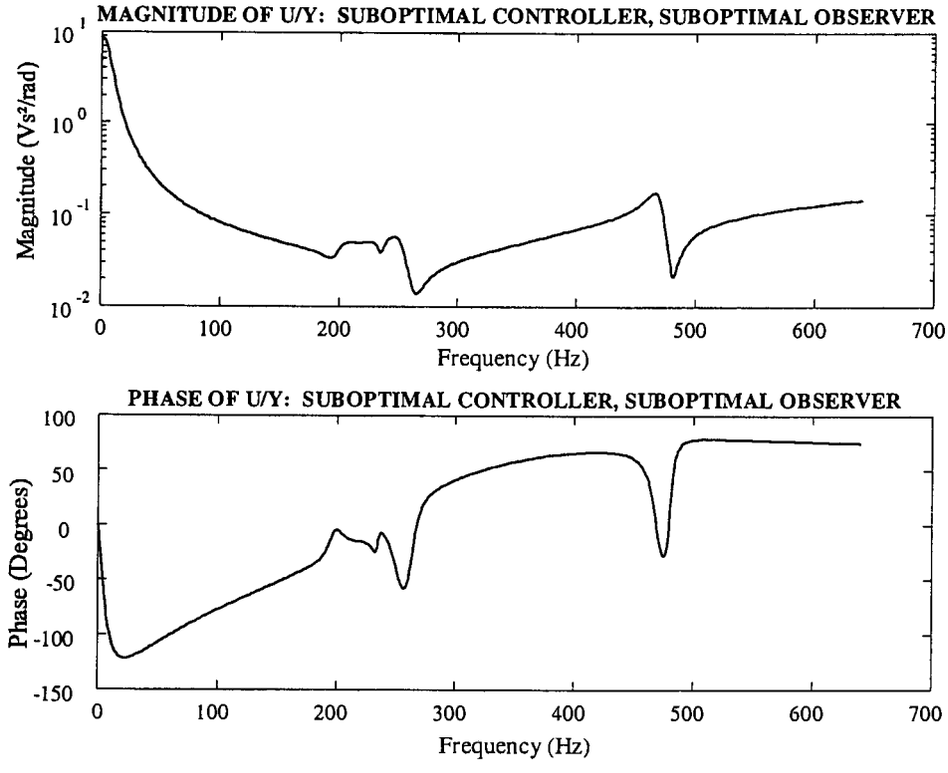

Figure 6.4.5.16: **Output to control *TF* magnitude and phase spectra: Suboptimal controller with suboptimal observer**

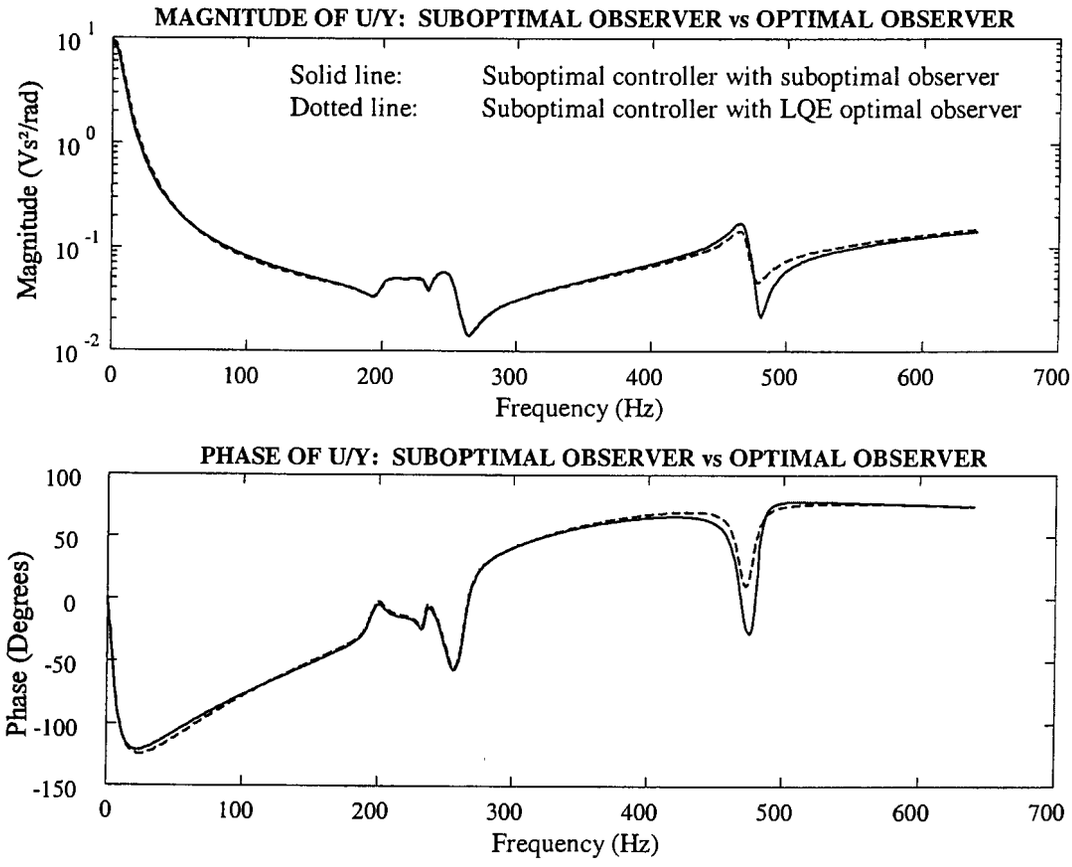

Figure 6.4.5.17: **Output to control *TF* magnitude and phase spectra: Suboptimal controller, suboptimal observer vs optimal observer**

The effect of output integral feedback on the attenuation factor spectra and stability of the closed-loop system are discussed next.

Suboptimal controller with suboptimal observer and output integral feedback

In this study, the optimal integral feedback gain is determined with the aid of simulations. Before the simulation results are given, the effects of the gain on the attenuation factor and closed-loop stability are indicated. The maximum allowable gain at the stability limit, determined by trial-and-error, is 2237. The closed-loop attenuation spectra, for gains of 0, 1000 and -50000, are shown in figure 6.4.5.18. It can be seen that, for the above three gains, the lowest (best) attenuation is achieved with a gain of -50000.

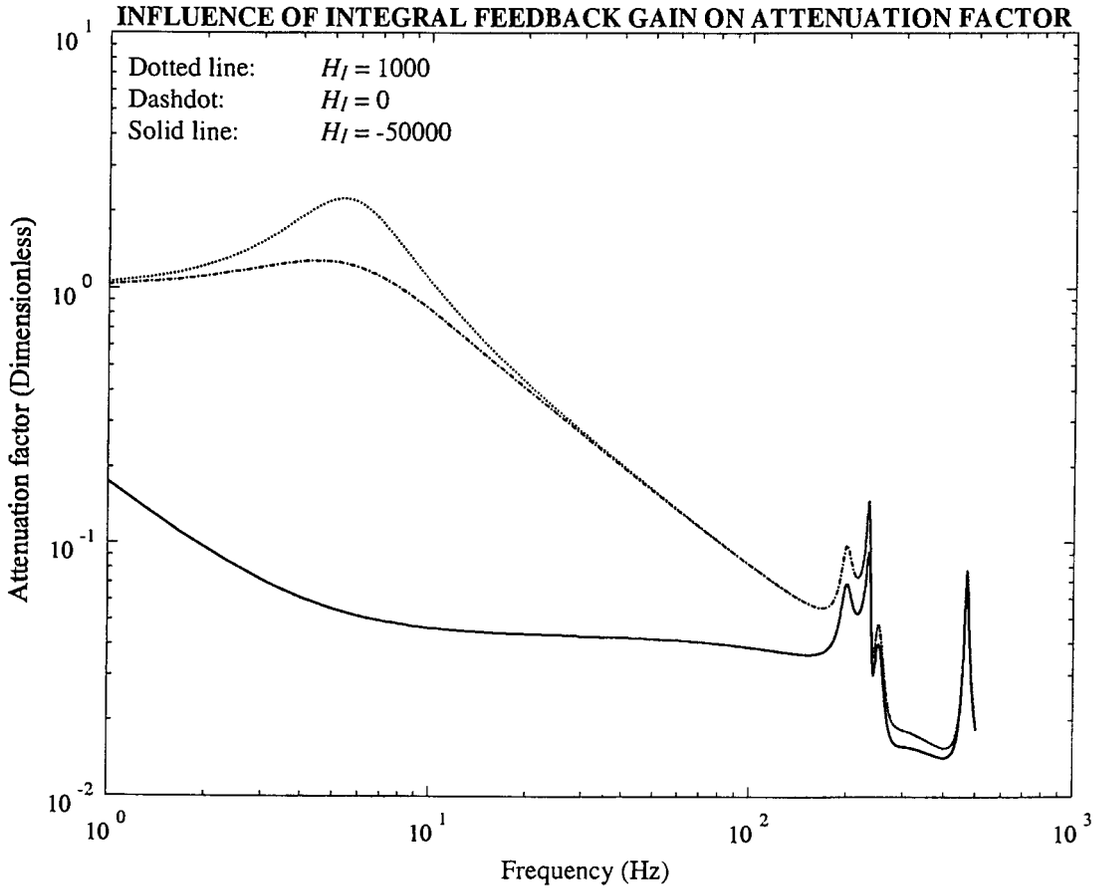

Figure 6.4.5.18: Attenuation factors for suboptimal controller with suboptimal observer and various output integral feedback gains

The design of equivalent digital filters for the disturbance feedforward (*U/D*), output feedback (*U/Y*) and output integral feedback *TF*'s are given next.

Equivalent digital filters

The equivalent digital filters for the disturbance to control and output to control transfer functions *U/D* and *U/Y* are respectively given by:

$$G\left(z^{-1}\right)=\frac{\sum_{i=0}^{12} b_{gi}\left(z^{-1}\right)^{i}}{\sum_{i=0}^{12} a_{gi}\left(z^{-1}\right)^{i}} \qquad \textbf{(6.4.5.15a)}$$

$$H\left(z^{-1}\right)=\frac{\sum_{i=0}^{12} b_{hi}\left(z^{-1}\right)^{i}}{\sum_{i=0}^{12} a_{hi}\left(z^{-1}\right)^{i}} \qquad \textbf{(6.4.5.15b)}$$

The numerator and denominator coefficients of the two digital filters, for a sample frequency of 2,5 kHz, are given in table 6.4.5.11. (Only the first five digits after the decimal point are shown.)

Table 6.4.5.11: Numerator and denominator filter coefficients for $G(z^{-1})$ and $H(z^{-1})$

i	b_{gi}	a_{gi}	b_{hi}	a_{hi}
0	0,05593	1,00000	0,17840	1,00000
1	-0,31316	-6,86194	-1,51049	-7,24684
2	0,69647	21,71518	6,17473	24,48686
3	-0,40650	-40,88123	-16,06805	-50,24938
4	-1,71159	48,39971	29,60721	67,85216
5	5,64420	-32,27825	-40,65931	-59,48195
6	-9,37469	1,15975	42,62427	27,33570
7	10,41497	22,41063	-34,31553	5,90594
8	-8,23882	-25,61932	21,01443	-20,38617
9	4,65344	15,38907	-9,52534	16,49180
10	-1,80623	-5,27795	3,02686	-7,29457
11	0,43651	0,86682	-0,60429	1,76323
12	0,05013	-0,02246	0,05722	-0,17677

In order to determine the coefficients tabled above, the real pole at 25,65 kHz and the real zero of *U/D* at 17,68 kHz, are removed. These frequencies are well in excess of the Nyquist frequency (1,25 kHz). The resulting filter orders are therefore 12, instead of 13. Both filters are the closed-loop system are stable.

Equivalent digital filter for output integrator and filter gain

The feedback integrator is replaced by the following digital filter:

$$H_I\left(z^{-1}\right) = 0{,}0002\frac{1+z^{-1}}{1-0{,}99z^{-1}} \qquad \textbf{(6.4.5.16)}$$

The filter *TF* is compared with that of a pure integrator in figure 6.4.5.19.

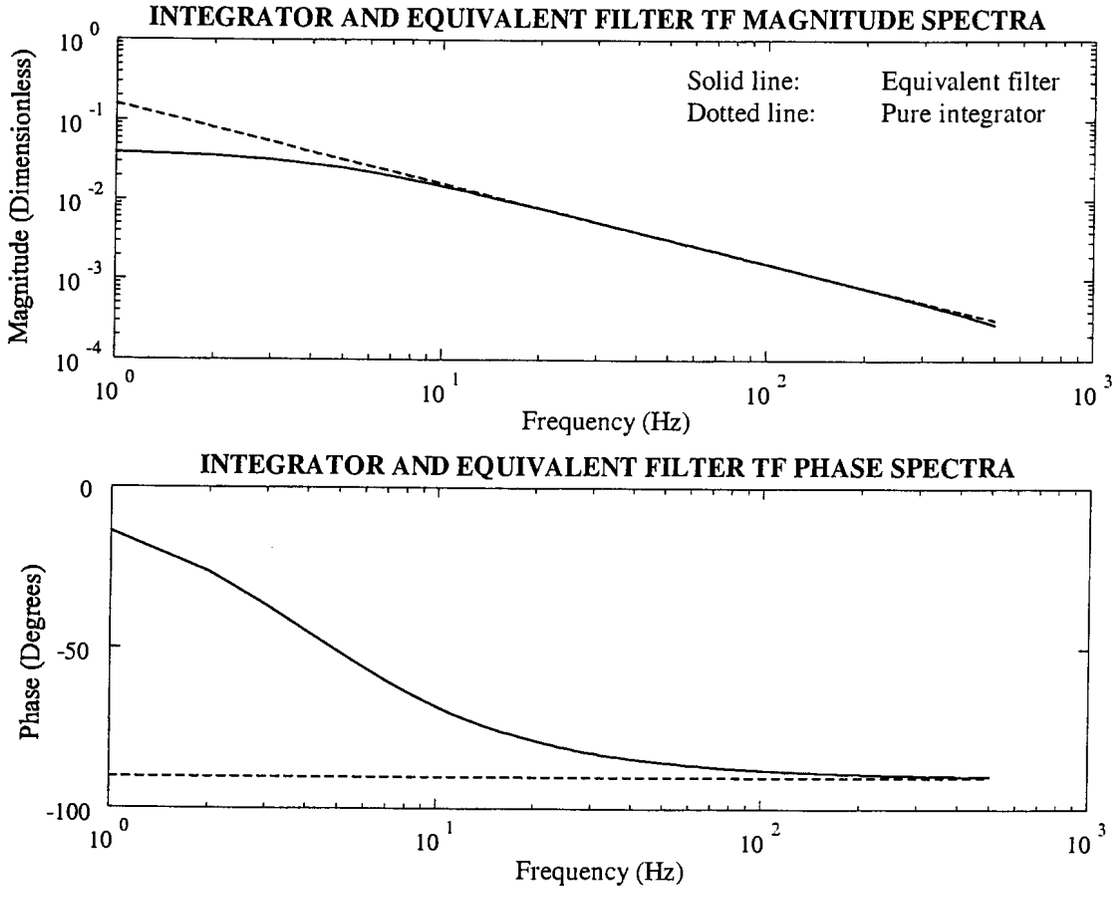

Figure 6.4.5.19: Integrator and equivalent filter magnitude and *TF* phase spectra

The minimum attenuation factor, for a frequency band of 0 Hz to 100 Hz, is achieved with a gain of –61,3.

6.5 Controller test setup and equipment

The controller test setup and test equipment are described in this section. The equipment mainly consists of a test bench, disturbance generation equipment, power amplifiers for the disturbance and control signals, the plant, sensors, sensor signal amplifiers, control equipment and data capturing equipment. A schematic layout of the test setup is shown in figure 6.5.1.

The test bench that was used for characterization of the magnetostrictive LOS stabilization system, as shown in figure 4.3.1.3, is used for testing the controller. The bench serves as a platform for the optical instrument stabilization system and electrodynamic shaker, which excites the base.

The base disturbance signal is generated in Visual Designer, which is a graphical simulation environment, similar to Simulink. The software operates with a low-cost Burr-Brown / Intelligent Instrumentation data card, model PCI 20428-W1, which is normally used for test signal generation and data capturing. Data is generated and captured in buffers, with selectable length, type and sample frequencies. The card is supplied with two D/A and sixteen A/D channels.

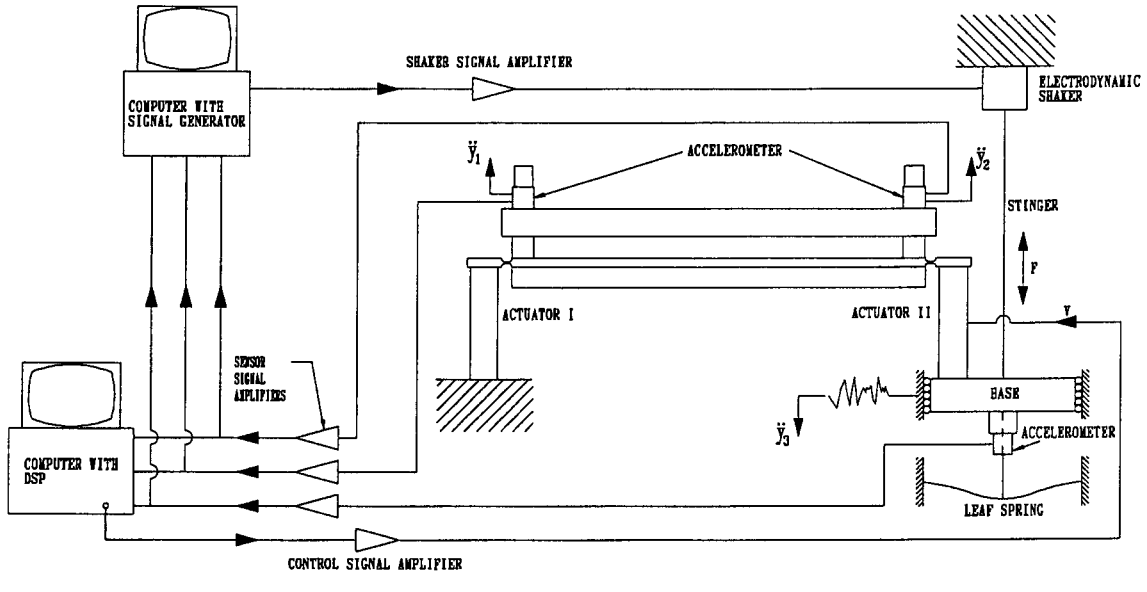

Figure 6.5.1: Controller test setup

The computer communicates with the card through direct memory access (DMA). Processing speed is determined by the computer CPU speed. Contrary to the dSpace card which was used to characterize the plant, this particular Burr-Brown card does not contain a DSP and is not suitable for real-time control, due to excessive throughput lag.

The base disturbance signal is supplied to the electrodynamic shaker via a matched power amplifier. According to the manufacturer, MB Dynamics, frequency bandwidth and maximum power output of the amplifier are 0 Hz to 30 kHz and 750 W respectively.

The shaker excites the base by means of a stinger (a thin steel string). The base is guided by linear bearings, in order to eliminate stick-slip motion, shock feedbacks to the shaker and angular motion of the base. The shaker cannot support the base statically, therefore the latter is suspended by a leaf spring. Spring stiffness and base mass are 7,16 MN/m and 8 kg respectively (see table 5.6.1).

The plant consists of the two actuators, the "dummy" optical instrument and its support structure. Dimensional details of the plant are given in section 4.2, while the dynamic coil and plant characteristics are given in sections 5.4 and 5.6 respectively.

An MB Dynamics SS 250 amplifier, similar to the shaker amplifier, powers the coils of actuator II. The amplifier was discussed in more detail in section 4.3.2. Its TF magnitude and phase spectra, for different output levels and a constant input level, are shown in figure 4.3.2.2.

Three accelerometers are used to measure the base and instrument *translational* motion. Two of the accelerometers are attached to the "dummy" optical instrument, one at each end of the instrument, while the third is placed upside down underneath the base. (A preferred position for accelerometer III would be on top of the base, next to actuator II. However, this space is taken up by the stinger).

Each sensor signal is amplified by a battery-powered amplifier. Amplifier gains are logarithmically adjustable, with gains of 2, 10 or 20, for accelerometers I and II, and gains of 1, 10 or 100 for accelerometer III. The instrument accelerometer amplifiers can also be powered by the main electrical supply, through a transformer, during lengthy test periods.

The amplified signals are captured by a separate PC, which houses the digital signal processor (DSP). The DSP has four analogue input and four analogue output channels. It is timed by a built-in clock, which runs at 40 MHz, and operates independently of the computer CPU clock. The DSP converts the accelerometer signals to digital form, carries out the control calculations, converts the control signal to analogue form and supplies it to the actuator coil via the power amplifier. The software supporting the DSP codes the Simulink block diagram in C, compiles it and loads it onto the DSP. (The DSP was discussed in more detail in section 4.3.2.)

The amplified sensor signals are displayed on a Visual Designer scope and stored in files for later processing.

6.6 Controller implementation and test procedure

Controller implementation and the test procedure are discussed in this section. Excitation of the disturbance is discussed in section 6.6.1, followed by controller implementation in section 6.6.2. The test procedure and test execution are described in sections 6.6.3 and 6.6.4 respectively.

6.6.1 Disturbance excitation

An iterative approach is followed to excite the required disturbance. A description of the procedure is as follows: A filtered random voltage signal excites the base through the electrodynamic shaker (see figure 6.6.1.1 for a diagrammatic representation of the experimental setup). Test duration is 80 s. The base translational acceleration is measured and compared with that of the required disturbance signal. If the RMS-value of the measured signal differs by more than 5% from that of the required signal, the voltage signal amplitude is adjusted and the test is repeated. The procedure is repeated until the RMS-value of the measured signal is within 5% of that of the required signal.

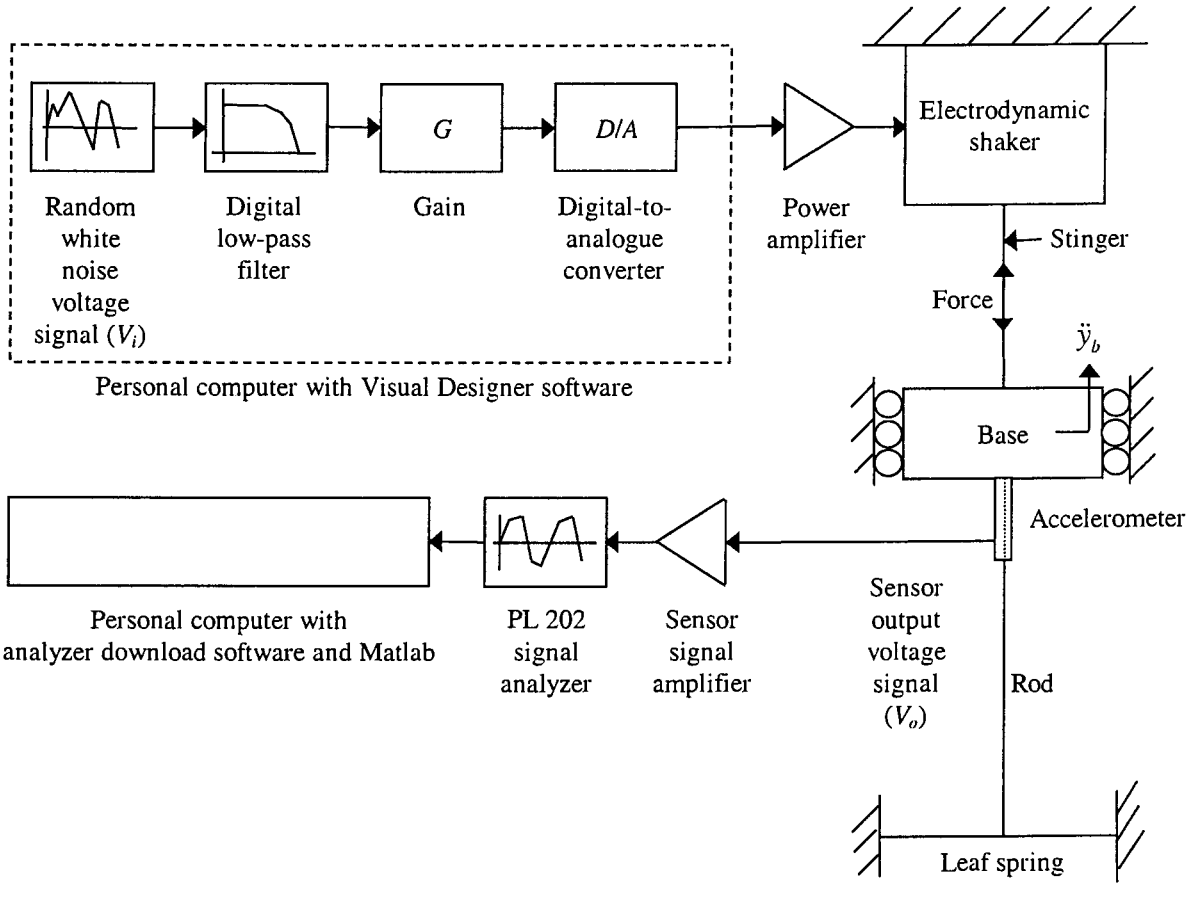

Figue 6.6.1.1: Disturbance excitation experimental setup

The random white-noise signal V_i is generated in Visual Designer. The signal is sampled at 2 kHz, which is 20 times the control bandwidth (100 Hz) and 4 times the maximum frequency of the disturbance signal (500 Hz). The signal is digitally filtered above 500 Hz, by means of a 2nd order low-pass (LP) filter.

The filter *TF* is given by:

$$TF = G(z^{-1}) = 0{,}29289\frac{1+2z^{-1}+1(z^{-1})^2}{1+0.(z^{-1})+0{,}17157.(z^{-1})^2} \qquad \textbf{(6.6.1.1)}$$

where the term z^{-1} represents a single sample-period delay.

Filter *TF* magnitude and phase spectra are shown in figure 6.6.1.2. Filter *TF* magnitude at 500 Hz is 0,707, or -3dB.

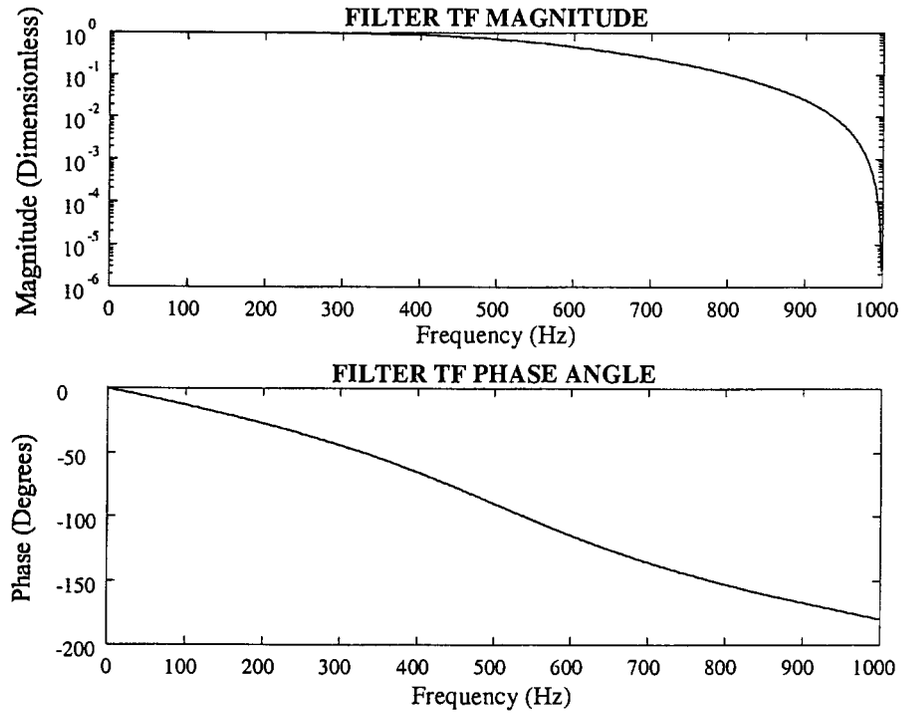

Figure 6.6.1.2: Second order digital LP filter *TF* magnitude and phase spectra

The signal is gained to facilitate amplitude adjustment. The resulting signal is supplied to the shaker through a built-in digital-to-analogue (*D/A*) converter and an external power amplifier, whose gain is held constant. (The amplifier was discussed in more detail in section 4.3.2). The base is excited by the shaker through a steel string, or stinger. Accelerometer output voltage V_o is captured with a PL202 signal analyzer. The captured signal is downloaded to a personal computer and processed in Matlab.

The base translational acceleration $\ddot{y}_b$ is obtained from the accelerometer output voltage signal V_o by means of the following equation:

$$\ddot{y}_b = V_o \times \underbrace{(-1)}_{Factor\,1} \times \underbrace{1000\left(\frac{mV}{V}\right)}_{Factor\,2} \times \underbrace{\frac{1}{10}\left(\frac{mV}{mV}\right)}_{Factor\,3} \times \underbrace{\frac{1}{83{,}1326}\left(\frac{g}{mV}\right)}_{Factor\,4} \times \underbrace{9{,}81\left(\frac{m/s^2}{g}\right)}_{Factor\,5} \qquad \textbf{(6.6.1.2)}$$

Factor 1 compensates for the accelerometer being mounted upside-down. Factor 2 converts the measured accelerometer voltage signal unit from volt to millivolt. This factor is included because the accelerometer calibration factor is given in mV/g. Factor 3 is the inverse of the accelerometer signal amplifier gain factor, i.e. 10. Factor 4 is the inverse of the accelerometer calibration factor, i.e. 83,1326 mV/g. Factor 5 converts the unit of acceleration from g to m/s^2. The resulting conversion factor between the accelerometer output signal V_o and base acceleration $\ddot{y}_b$ in equation 6.6.1.2, is -11,8 $m/s^2/V$.

The base angular acceleration $\ddot{\theta}_b$ is obtained by division of $\ddot{y}_b$ by 0,25m (the base length). The overall conversion factor between the accelerometer output voltage and base angular acceleration, i.e. $\ddot{\theta}_b / V_o$, is therefore -47,2 $rad/s^2/V$.

Once a base angular acceleration with an acceptable RMS-value is achieved, its crest factor, amplitude at 96,75 Hz and percentage energy in the control band, are calculated. If any of these values differ by more than 5% from those of the required acceleration signal, a new voltage signal is generated. The procedure is as follows: The complex Discrete Fourier Transform (*DFT*) of the required acceleration signal is divided by that of the measured signal, at each frequency in the spectrum, and multiplied with that of the random voltage signal:

$$V_{i1}(j\omega_k) = V_{i\,random}(j\omega_k)\frac{\ddot{Y}(j\omega_k)\big|_{required\ signal}}{\ddot{Y}(j\omega_k)\big|_{measured\ signal\ 1}} \qquad \textbf{(6.6.1.3)}$$

where ω_k is the k-th frequency in the spectrum and $\ddot{Y}(j\omega_k)$ is the DFT of $\ddot{y}$ at the k-th frequency. The voltage signal $V_{i1}(t)$ is obtained from the spectrum of voltages $V_{i1}(j\omega_k)$ by means of an inverse Fast Fourier Transform. The test is repeated with $V_{i1}(t)$ as input. Base acceleration is measured and its RMS-value, crest factor, amplitude at 96,75 Hz and percentage energy in the control band, are calculated. If all of these parameters are within 5% of those of the required signal, $V_{i1}(t)$ is the voltage signal which will be used to excite the base.

If not, the base acceleration spectrum is calculated and the *DFT* of V_{i2} is obtained as follows:

$$V_{i2}(j\omega_k) = V_{i1}(j\omega_k)\frac{\ddot{Y}(j\omega_k)\big|_{required\ signal}}{\ddot{Y}(j\omega_k)\big|_{measured\ signal\ 2}} \qquad \textbf{(6.6.1.4)}$$

The voltage signal $V_{i2}(t)$ is obtained from the spectrum of voltages $V_{i2}(j\omega_k)$ by means of an inverse Fast Fourier Transform. The procedure is repeated until the base acceleration RMS-

value, crest factor, amplitude at 96,75 Hz and percentage energy in the control band, are within 5% of those of the required signal.

Parameters of the experimentally generated disturbance signal are compared with those of the required disturbance signal in table 6.6.1.1. The amplitude spectrum of the experimentally generated signal is shown in figure 6.6.1.3.

Table 6.6.1.1: Comparison between measured and required disturbance parameters

Parameter	Required disturbance	Measured disturbance	Relative error
RMS angular acceleration	4,56 rad/s^2	4,59 rad/s^2	0,66 %
Crest factor	2,21	2,14	-3,17 %
Maximum amplitude (@ 96,75 Hz)	4,14 rad/s^2	4,06 rad/s^2	-1,93 %
Percentage energy in control band	91 %	93,7 %	2,97 %

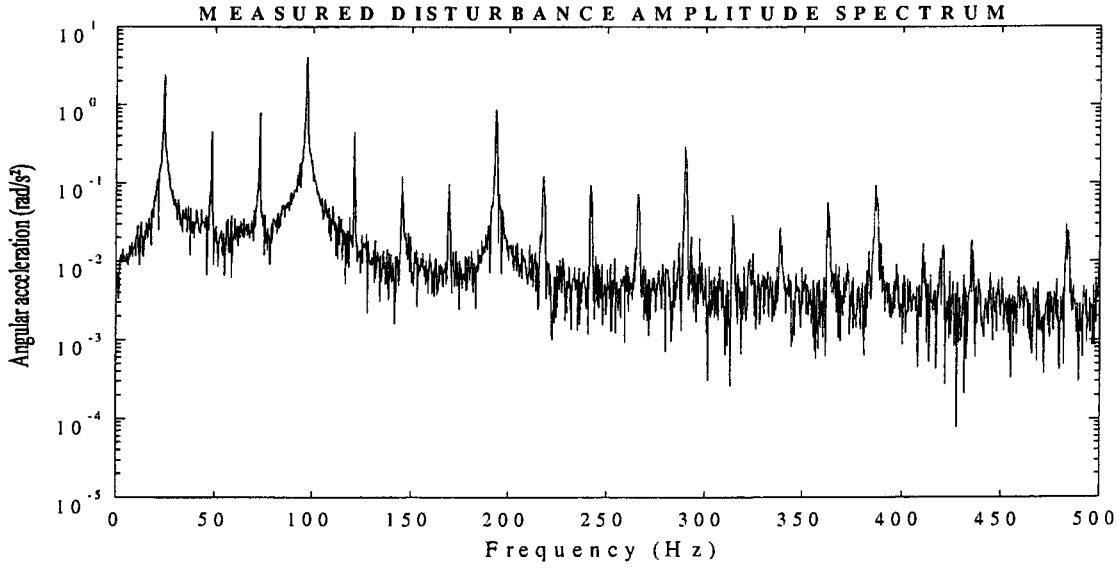

Figure 6.6.1.3: Measured disturbance amplitude spectrum

6.6.2 Controller implementation

The controller block diagram is generated in Simulink, coded in C, compiled and loaded onto the DSP. The block diagram is based on that of the simulated controller, shown in figure 6.4.4.1. For the control experiments, certain elements of the simulated block diagram are retained, some elements are deleted, and a number of elements are added. Elements that are retained, are the high-pass filters, disturbance feedforward and output feedback filter elements, bias signal generation blocks (i.e. step and rate limiter blocks), and gain and summation blocks.

Elements that are deleted, are the plant blocks and noise inputs. During testing, the noise inputs and plant outputs are automatically replaced by the true plant response and measurement noise signals.

Elements that are added, are A/D and D/A converter blocks, overall sensor calibration factor blocks and a "triggering" block, which synchronizes the bias signal with the sensor signals. The latter block is required to force the DSP to cut off the control signal whenever it is unbiased. Synchronization is achieved by multiplication of the bias signal, gained by the inverse of its maximum value, with the control signal.

The resulting experimental block diagram is shown in figure 6.6.2.1. The disturbance sensor signal is V_d and the two output accelerometer signals are V_{a1} for accelerometer I and V_{a2} for accelerometer II. K_{cd}, K_{ca1} and K_{ca2} are the calibration factors for the disturbance and output accelererometers I and II respectively.

Numerical values of the overall sensor calibration factors, DC voltage, rate-of-rise, soft start gain, bias gain, power amplifier gain, clipper limits and DSP card gain are determined. The card gain is unity for throughput signals, i.e. sensor-to-control signals, and 10 for signals generated in Simulink, i.e. the bias signal. The soft start gain and bias gain are scaled accordingly, by dividing the required values by 10. The numerical values used in the block diagram are given in table 6.6.2.1.

Table 6.6.2.1: Constant factors applicable to experimental control block diagram

Constant factor	Value	Unit of measurement
Disturbance accelerometer calibration factor K_{cd}	-45,39	rad/s^2/V
Output accelerometer I calibration factor K_{ca1}	76,27	rad/s^2/V
Output accelerometer II calibration factor K_{caII}	46,37	rad/s^2/V
DC voltage	9,2	V
Rate-of-rise	100	V/s
Soft start gain	0,0927	Dimensionless
Bias gain	0,1087	Dimensionless
Power amplifier gain	1,7	Dimensionless
Clipper limits: Upper; lower	9,9	V
	-9,9	V

Feedforward, feedback and integrator feedback gains are adjustable. The values depend on the controller type to be tested, i.e. open-loop feedforward, closed-loop feedback or feedforward plus feedback. The required values will be given in section 6.6.3, where the controller test procedure will be discussed.

The selected method for integration of the dynamic control equations, i.e. the 5th order Runge-Kutta method, is entered, as well as the integration time-step, i.e. 400μs. The latter is constant, since adaptive time-stepping is not available for real-time implementation of the controller on the DSP (see also section 4.3.2). The block diagram, with its filter, control, bias voltage, gain, clipper and integration parameters, are coded in C, compiled and loaded onto the DSP.

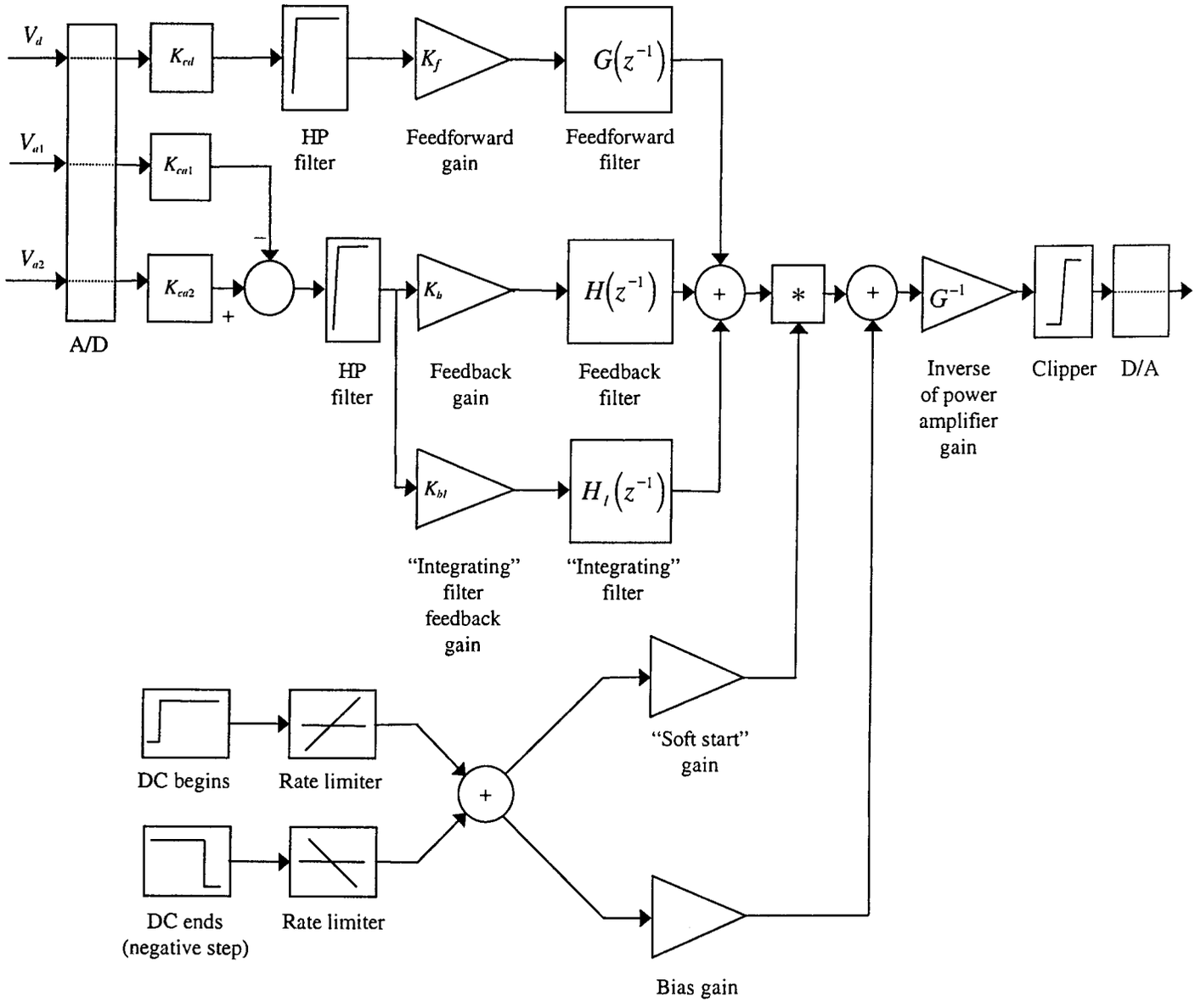

Figure 6.6.2.1: Experimental control block diagram

6.6.3 Test procedure

Three configurations of the controller, i.e. the disturbance feedforward, output feedback and disturbance feedforward plus output feedback configurations, are tested separately. The feedforward controller is tested first. This is to ensure that as large a percentage of the disturbance as possible is removed before the feedback loop is closed.

During the feedforward controller tests, zero output feedback and output integral feedback gains are used. The feedfoward gain is adjusted in increments of 5%, starting at 5%. After incrementing the gain, a test is carried out, the data is captured, processed, and the RMS attenuation factor is calculated. The attenuation factor is compared with that obtained during

the previous test. If an improvement is noticed, the gain is increased and the test is repeated, until no further improvement is achieved. The gain of the last test carried out with this configuration, is the maximum practically achievable feedforward gain.

The feedback loop is subsequently closed. The feedback gain, like the feedforward gain, is adjusted in 5% increments. For this configuration, a zero feedforward gain is used. The output integral feedback gain is initially zero. The feedback gain is increased until the system becomes unstable. The gain at the stability limit, is the maximum feedback gain. The output feedback gain, at the limit, is then held constant and the output integral feedback gain is adjusted in 5% increments, until the system becomes unstable. The gain at the stability limit is the maximum output integral feedback gain.

The disturbance feedfoward plus output feedback controller is subsequently tested. The maximum feedforward gain, output feedback and output integral feedback gains are used during the tests.

6.6.4 Test execution

The disturbance feedforward, output feedback and output integral feedback filter coefficients, sensor calibration factors, feedforward and / or feedback gains, DC voltage, rate limiter slope, clipper limits, sample rate, test duration and integration method are entered into the Simulink block diagram and parameter menu. The block diagram is compiled and loaded onto the DSP. The disturbance signal is excited in Visual Designer and the power amplifier gain is adjusted. An open-loop test is run, the time trace of the disturbance signal is captured and shown on a Visual Designer scope. It is processed and its RMS value is compared with that in table 6.6.1.1. If it differs by more than 5% from that in the table, it is corrected by adjusting the power amplifier gain.

While the disturbance signal is active, the gain of the power amplifier that drives the actuator coils, is adjusted. The DSP, which is inactive at this stage of the test, is activated and the control signal is supplied to the actuator coils, via the power amplifier. The time traces of the base and output signals are captured in Visual Designer and stored in a file for later processing. The time duration of the test corresponds with that of the known disturbance, i.e. 4s. Since this duration is relatively short, the test is repeated 22 times, giving a total duration of 88s for each controller configuration.

Although the same signal analyzer that was used for the characterization tests (as described in section 4.3.3) is available for the tests, it is not used. The reason is that its number of channels is limited to two, and its sample frequencies and window lenghts are only adjustable is fixed increments. The Visual Designer software, on the other hand, gives more flexibility in terms of number of channels, sample frequencies and window lengths. The disadvantage of capturing time traces, however, is that post-processing of the time-domain data is required to obtain the attenuation factor.

6.7 Controller test results

The controller test results are processed, presented and discussed in this section. Processing of the results is described in section 6.7.1. The results are presented in section 6.7.2 and discussed in section 6.7.3.

6.7.1 Processing of test results

The time domain data is processed for each test run of 4s. The captured accelerometer signals are multiplied by their overall calibration factors to obtain the vertical accelerations. The base acceleration signal is divided by the base length to obtain the base angular acceleration. The acceleration measured by accelerometer I is subtracted from that measured by accelerometer II, and divided by the distance between the accelerometers to obtain the output angular acceleration.

The transfer function spectrum of each test is calculated, using the following equation:

$$G(\omega) = \frac{P_{yd}(\omega)}{P_{dd}(\omega)} \qquad \textbf{(6.7.1.1)}$$

where P_{yd} is the cross spectral density between the disturbance and output, and P_{dd} is the disturbance power spectral density. A Hanning window is used to take start- and end effects into account. The frequency resolution is 0,25 Hz, which is the inverse of the test duration of every test, i.e. 4s. The average of the test spectra is calculated for each configuration. The magnitudes of the spectra, i.e. the attenuation factors, are plotted for the disturbance frequency band of 0 Hz to 100 Hz. The attenuation factors at the dominating frequencies in the disturbance spectrum, i.e. at 24 Hz, 48,5 Hz, 72,5 Hz and 96,75 Hz, are tabulated.

The isolation factors, i.e. the complement of the attenuation factors, are calculated at each of the dominating frequencies. The attenuation factors, in terms of the ratio of output RMS to disturbance RMS, in the frequency band of 0 Hz to 100 Hz, are calculated from the time-domain data.

6.7.2 Experimental test results

The maximum feedforward gain achieved during the tests, is 0,76. The maximum feedback and integral feedback gains achieved during the tests are 0,76 and -87,5 respectively. These gains are at the limit of stability.

The experimentally determined attenuation factor of the feedforward controller, for a 0,76 disturbance feedforward gain, zero output feedback gain and zero integral output feedback gain, is shown in figure 6.7.2.1. The frequency range is 0 Hz to 100 Hz, with a resolution of 0,25 Hz. The dashed line indicates a unit attenuation factor accross the spectrum, i.e. the attenuation that would be achieved in the absence of an isolation system. The RMS attenuation for the disturbance feedforward controller, for a frequency bandwidth of 0 Hz to 100 Hz, is 0,44 (-7,06 dB).

The experimentally determined attenuation factor of the feedback controller, for a zero disturbance feedforward gain, output feedback gain of 0,76 and output integral feedback gain of -87,5 is shown in figure 6.7.2.2. The RMS attenuation factor for the feedback controller is 0,7 (-3,1 dB).

The experimentally determined attenuation factor of the feedforward plus feedback controller, for feedforward and feedback gains of 0,76 and an output integral feedback gain of -87,5 is shown in figure 6.7.2.3. The RMS attenuation factor for the disturbance feedforward plus feedback controller is 0,32 (-9,75 dB).

The test results for the three configurations are summarized in table 6.7.2.1.

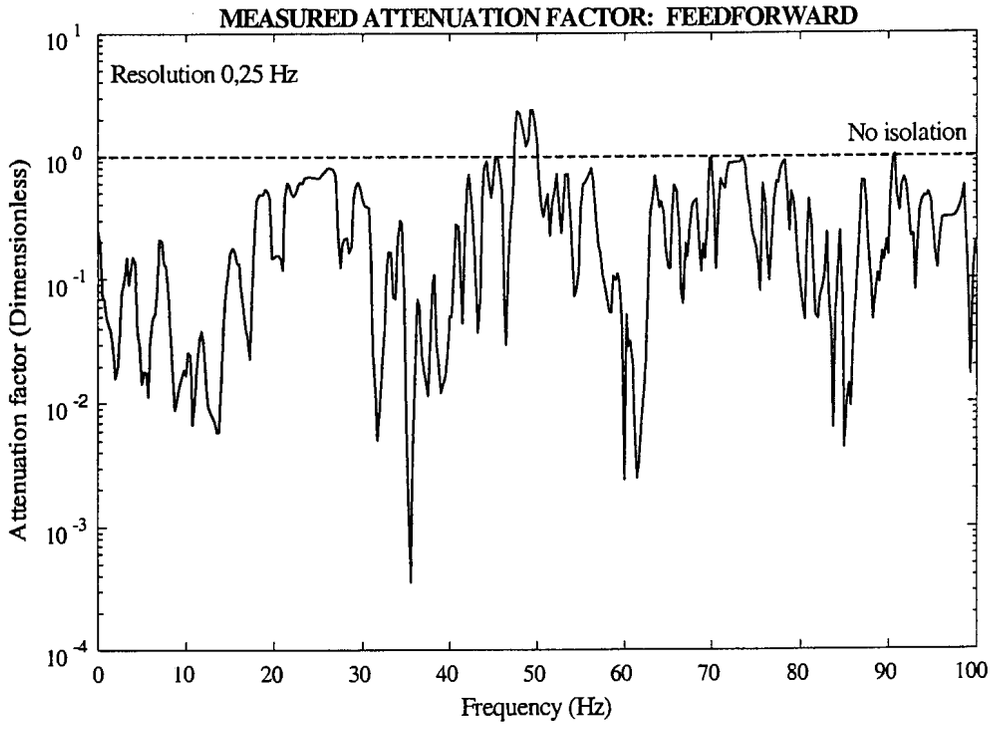

Figure 6.7.2.1: Attenuation factor spectrum for disturbance feedforward controller

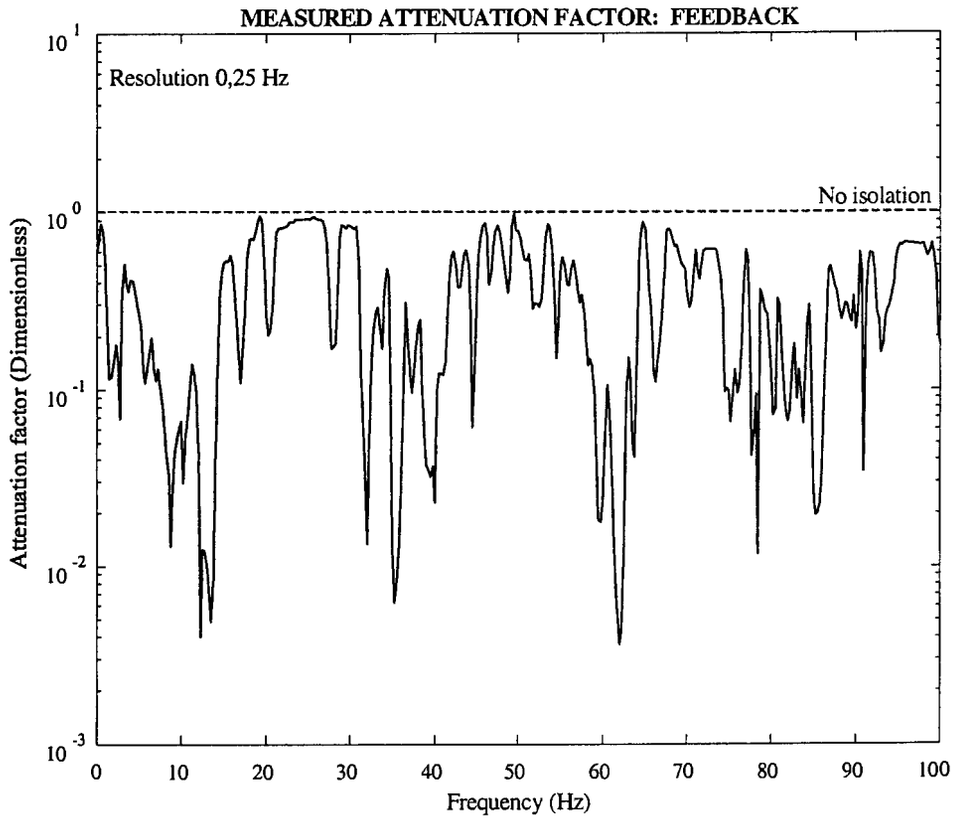

Figure 6.7.2.2: Attenuation factor spectrum for output feedback controller

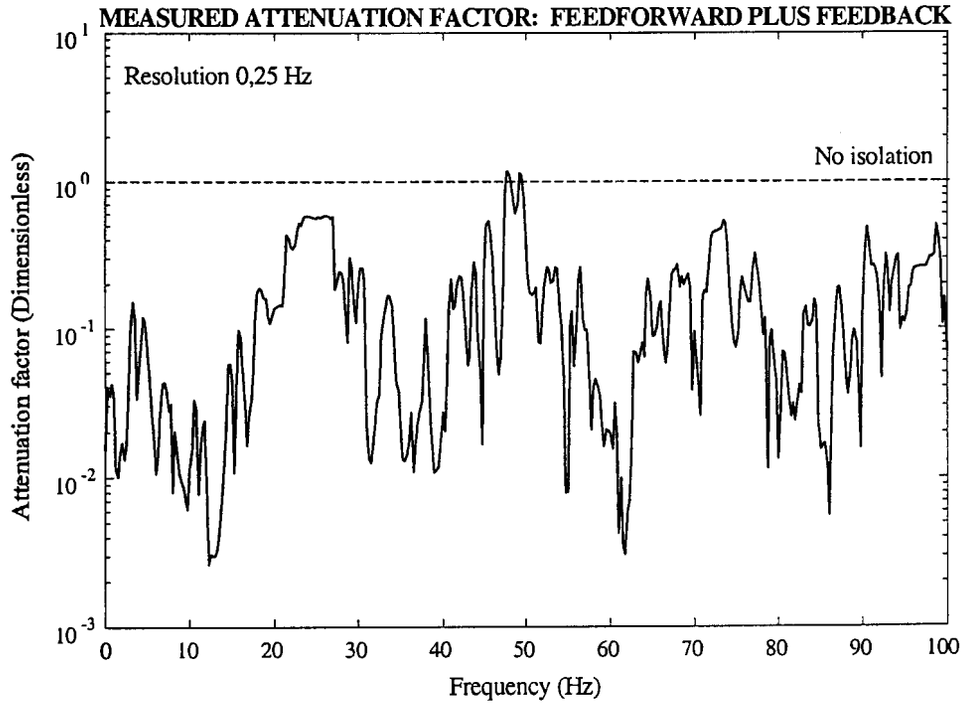

Figure 6.7.2.3: Attenuation factor spectrum for disturbance feedfoward plus output feedback controller

Table 6.7.2.1: Summary of controller test results

Configuration:	Feedforward	Feedback	Feedforward plus feedback
RMS attenuation	0,44	0,70	0,32
Attenuation in dB	-7,06 dB	-3,1 dB	-9,75 dB
Isolation	0,56	0,3	0,68
Target isolation	0,85	0,85	0,85
% of target achieved	66%	35%	80%
dB attenuation at 24 Hz	-3,41	-0,75	-4,73
dB attenuation at 48,5 Hz	3,38	-7,47	-2,58
dB attenuation at 72,5 Hz	-1,11	-4,11	-6,82
dB attenuation at 96,75 Hz *	-10,08	-3,55	-11,66

* Dominant disturbance frequency

A comparison between modelled and experimental transmissibilities of the three controller configurations, at the frequencies where the disturbance peaks (24 Hz, 48,5 Hz, 72,5 Hz and 96,75 Hz) is given in table 6.7.2.2. The tranmissibilities compare favourably at 72,5 Hz for the feedback controller and at 24 Hz for the feedforward plus feedback controller. At the dominant disturbance frequency, i.e. 96,75 Hz, the difference varies from 13,7 % for the feedback controller, to 28,7% for the feedforward controller. The difference is large at 48,5 Hz for all the controllers, and at 72 Hz for the feedforward and feedforward-plus-feedback controllers. Measured and modelled overall attenuations differ by 13,6% for the feedforward controller, -11,4% for the feedback controller and -3,12% for the feedforward plus feedback controller.

Table 6.7.2.2: Comparison between measured and modelled TR's at disturbance peaks

Frequency (Hz):		24	48,5	72,5	96,75#	Overall (RMS)
Feedfoward	Measured (dB):	-3,41	3,38	-1,11	-10,08	0,44
	Modelled (dB):	-2,06	-3,29	-4,53	-7,89	0,5
	***Difference (%):**	**16,8**	**-53,6**	**-32,5**	**28,7**	**13,6**
Feedback	Measured (dB):	-0,75	-7,47	-4,11	-3,55	0,7
	Modelled (dB):	-1,76	-3,31	-4,19	-4,83	0,62
	***Difference (%):**	**-10,99**	**61,44**	**-0,92**	**-13,7**	**-11,4**
Feedforward plus feedback	Measured (dB):	-4,73	-2,58	-6,82	-11,66	0,32
	Modelled (dB):	-5,13	-10,06	-12,65	-13,62	0,31
	***Difference (%):**	**-4,5**	**-57,73**	**-48,89**	**-20,2**	**-3,12**

* Relative to measured transmissibility # Dominant disturbance frequency

Experimental and modelled transmissibilities over the entire disturbance band, for the three controller configurations, are compared in figures 6.7.2.4 to 6.7.2.6. The circles and crosses respectively indicate the measured and modelled transmissibilities at the frequencies where the disturbance peaks. Modelled and measured transmissibilities differ considerably between

peaks, which can be attributed to low signal-to-noise ratios (the disturbance is approximately two orders of magnitude lower between the peaks than at the peaks – see figure 6.6.1.3).

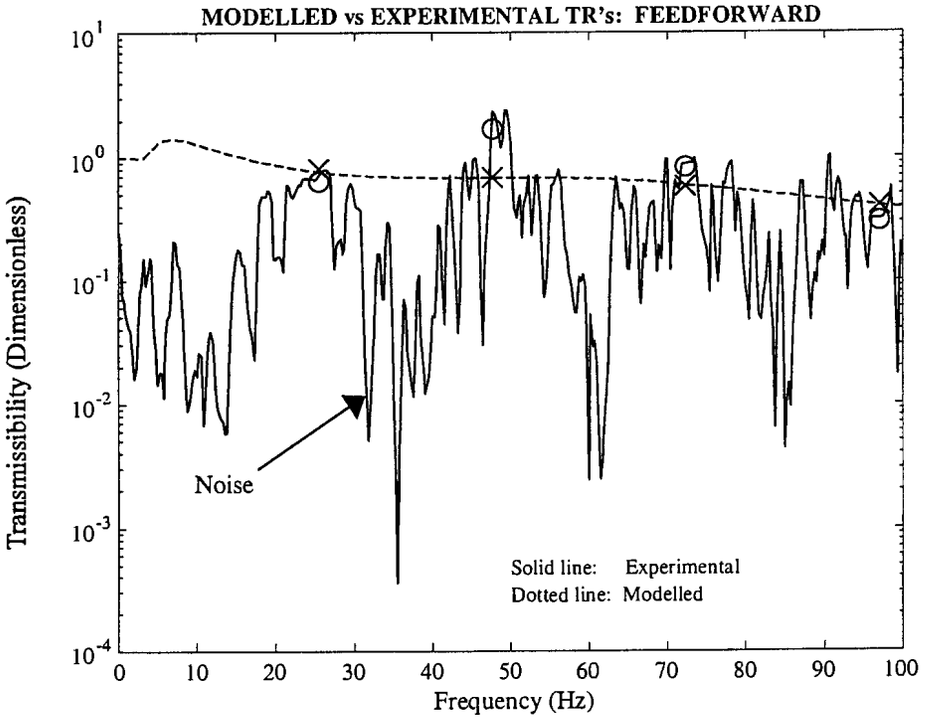

Figure 6.7.2.4: Modelled and measured TR's: Feedforward

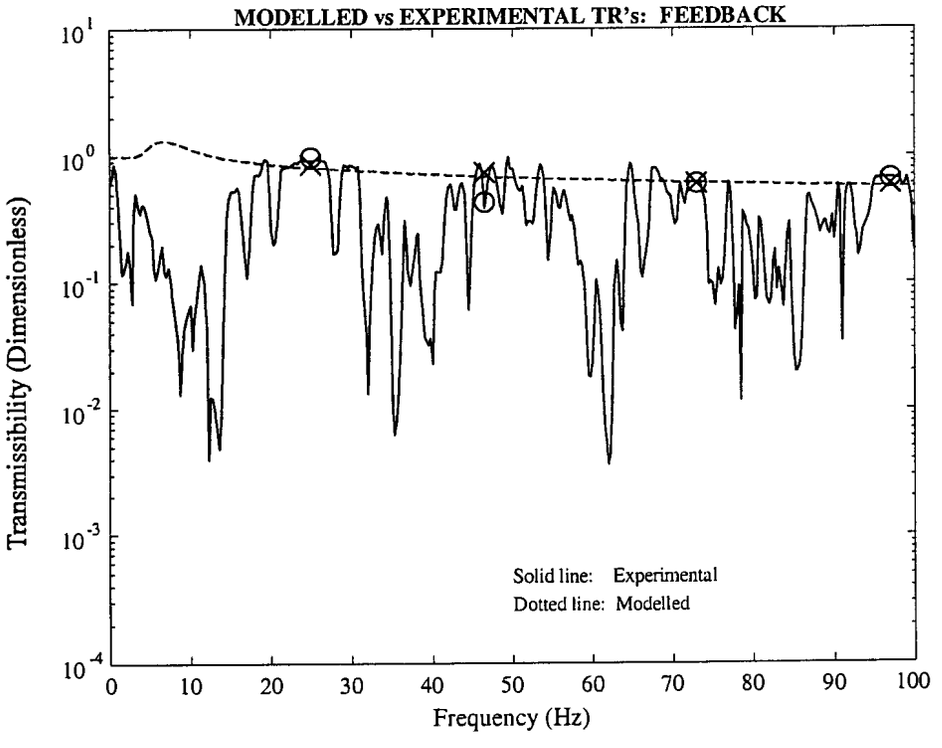

Figure 6.7.2.5: Modelled and measured TR's: Feedback

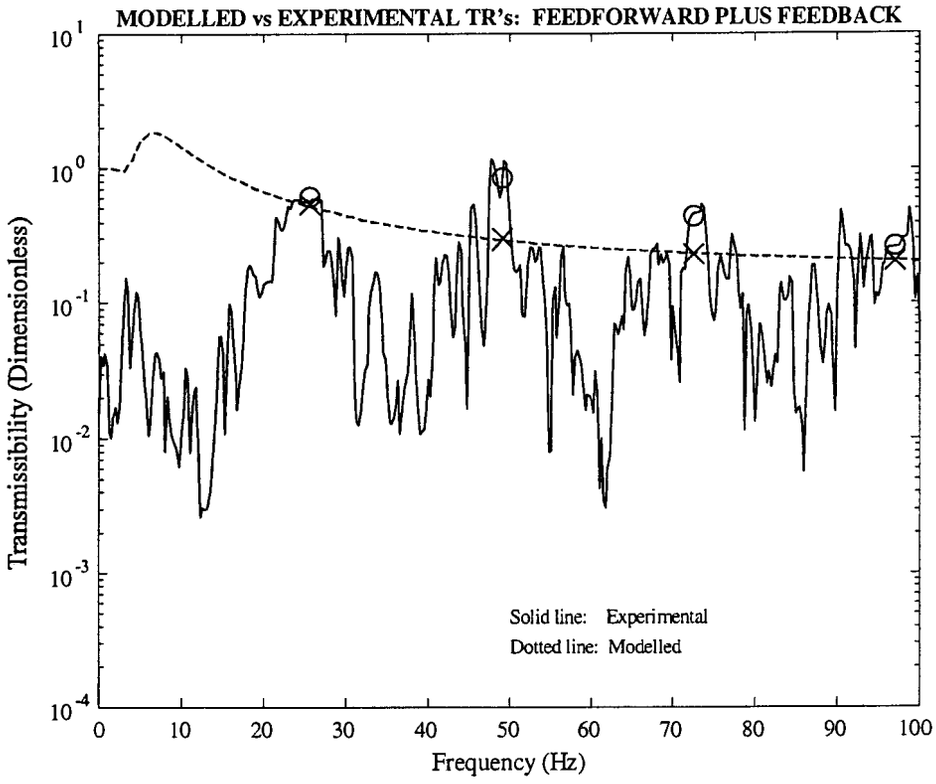

Figure 6.7.2.6: Modelled and measured TR's: Feedforward plus feedback

6.7.3 Discussion of test results

A comparison of the attenuation factor graphs and table 6.7.2.1 show that the best attenuation accross the frequency spectrum is achieved with the disturbance feedforward plus output feedback controller. The RMS attenuation factor achieved with this controller is 80% of the required RMS attenuation. The feedforward controller is ranked second, in terms of RMS attenuation, while the feedback controller is ranked last.

All three controllers display weak performance at 48,5 Hz, which is close to the frequency of the electricity supply network, i.e. 50 Hz. The feedback controller gives the best attenuation at 48,5 Hz, while the feedforward controller amplifies the disturbance. The disturbance feedforward plus output feedback controller attenuates at this frequency, but amplifies slightly in the vicinity of 50 Hz.

A logical choice of the best controller, in terms of overall performance, is the disturbance feedforward plus output feedback controller. Although it slightly amplifies the disturbance at 48,5 Hz, its performance across the rest of the frequency band is acceptable. Furthermore, it is doubtful if the problem at 48,5 Hz will ever be experienced on a vehicle, where the frequency of the power supply varies with engine speed.

Possible reasons for the differences between modelled and experimental results are as follows: Firstly, controller design was based on measured open-loop transfer functions, obtained using a white-noise drive signal, LP-filtered at 130 Hz (see section 4.4.5). This signal did not correspond with the closed-loop drive signal. Secondly, due to the LP filter, open-loop drive signal magnitude above 130 Hz decreased with frequency, resulting in a noisy signal and possibly an inaccurate transfer function magnitude at the dominant plant natural frequency, i.e. 301 Hz. Thirdly, the differences at 47,5 Hz are attributed to (unsuppressed) noise caused by the electricity supply network. Lastly, while feedforward and feedback gains of unity could be achieved during the modelling stage (see section 6.4.4), this was not possible during experimental testing, possibly due to plant nonlinearities.

To summarize, a stable, linear disturbance feedforward plus output feedback controller was tested, which gave an RMS attenuaton of 80% of the target attenuation, in a frequency band of 0 Hz to 100 Hz.

6.8 Summary of chapter 6

The design, implementation and experimental evaluation of a controller for the LOS stabilization system were described in this chapter. A background on various basic controller types was given, followed by a more detailed description of disturbance attenuation methods.

The design of a suitable controller was described in detail. General requirements of controllers were discussed, followed by a specification of the controller performance. The requirements and specification were used to select a suitable controller, i.e. a linear disturbance feedforward plus output feedback regulator, with output integral feedback.

A linear quadratic optimal regulator was subsequently designed. Robustness of the regulator was improved by increasing the lowest natural frequency and damping factors of the attenuation factor zeroes. A suboptimal controller was thus obtained. An optimal state regulator was designed next. The regulator was coupled to the plant and controller. The disturbance-to-control and output-to-control *TF*'s were determined. Zero elements in the observer gain matrix were replaced by nonzero elements. The resulting suboptimal observer was coupled to the plant and suboptimal controller. The integral feedback gain was determined with the aid of simulations of the closed-loop system behaviour. The integrator gain which produced the minimum attenuation factor, was thereby obtained. The disturbance to control and output to control *TF*'s were converted to digital filter form. An "equivalent" digital filter was designed to replace the output feedback integrator.

The control apparatus and test procedure were described. Three configurations of the controller were tested, i.e. disturbance feedforward, output feedback, and disturbance feedforward plus output feedback. The test results were processed and presented. It was found that the disturbance feedforward plus output feedback controller gave the best overall performance in terms of RMS attenuation over the frequency band of 0 Hz to 100 Hz. The controller achieved an RMS attenuation of -9,75 dB in this frequency band. A weak point of the controller is the fact that it does not perform well in the vicinity of 50 Hz, which may be attributed to the electricity supply.

Chapter 7
Summary, conclusions and recommendations

This study covered the line of sight stabilization of an optical instrument by means of gained magnetostrictive actuators. The stabilization system was modelled, designed, manufactured and tested. Modelled and experimental results were compared and inaccuracies of the model were discussed and explained. The model was updated, using the experimental results. A control system was modelled, designed, implemented and tested.

This chapter gives a summary of the work done, conclusions that can be drawn from the results and contributions made by the study, problems encountered and recommendations for future work in the field. The summary is given in section 7.1. Conclusions and contributions are discussed in section 7.2, followed by the problems experienced, in section 7.3. Finally, recommendations for future study are made in section 7.4.

7.1 Summary

Magnetostrictive active LOS stabilization of an optical instrument, excited by a known base disturbance, was motivated in chapter 1. The differences between passive and active isolation methods were discussed and the advantages of active isolation were given. Different actuation methods, i.e. hydraulic, electrodynamic, piezoelectric and magnetostrictive actuation, were compared. Magnetostrictive actuation was selected as the most appropriate isolation method for this study. The cost advantage of magnetostrictive actuators over conventional stabilization devices, e.g. gyroscopes, was pointed out. The limitation of magnetostrictive active isolation, i.e. that a gain mechanism would be required to enhance actuator stroke length, was mentioned. A literature survey of the theory and applications of magnetostriction, and the "giant" magnetostrictive material Terfenol-D, was given.

An analytical model of the magnetostrictive active isolation system was derived in chapter 2. Material characteristics, as obtained from the literature, were used for this purpose. The model would firstly serve as a design aid, and secondly, as a theoretical basis to obtain an accurate, updated model from experimentally determined transfer functions.

The nonlinear and linear magnetostrictive and magnetization characteristics of Terfenol-D were discussed. Strain was modelled as a function of applied mechanical stress and magnetic field strength. Special attention was paid to the two most important nonlinearities, i.e. saturation and hysteresis. The nonlinearities were modelled as range-dependent linearities, in order to facilitate system characterization.

A nonlinear state-space model of a magnetostrictive actuator was derived. The model consisted of an SDOF (2^{nd} order) mechanical subsystem model, coupled to a 1^{st} order electrical coil model. The actuator model was subsequently linearized and coupled to an MDOF structural model of the optical instrument and its support structure. For this purpose, a number of system modelling techniques were evaluated, i.e. the Galerkin, Finite Element, Finite Difference and Rayleigh-Ritz methods. The latter method was selected as the most

suitable modelling technique. The system model was obtained in state-space and transfer function forms. System natural frequencies, normal mode shapes, damping factors, frequency bandwidth and modal forces were obtained from the model.

System design was described in chapter 3. The required system performance parameters, i.e. actuator stroke length and force, system bandwidth and coil resistance to inductance ratio, were calculated from the results obtained in chapter 2. Design concepts for the system components were discussed and evaluated and the most suitable design concepts were selected. An octagonal flexural gain mechanism was selected in favour of resonance spring, hydraulic and elliptical structure mechanisms. Electrodynamic field biasing was considered to be more suitable than permanent magnet biasing, while coil springs were selected in favour of Belleville washers for rod prestressing. Actuator and system concepts were presented.

A detailed system design followed. The required rod lengths, rod diameters and gain factors were calculated and practical design aspects were discussed. The gain mechanisms, field coils, prestress springs and support structure were designed. Detailed drawings of the system components and an assembly drawing of the system, were included. Static and dynamic buckling of the rods, as well as eddy current losses, were checked. The manufacturing procedure was described in short.

Experimental testing of the actuators and LOS stabilization system was dicsussed in chapter 4. The objective of the tests was to obtain quasi-static and dynamic system characteristics. A summary of the most important technical details of the test specimens, i.e. the two actuators and system, was given. These details were required to develop a test procedure and to specify the test equipment.

Two test setups were described, i.e. one for quasi-static characterization of the actuators, and one for dynamic characterization of the system. The quasi-static tests served two purposes, i.e. to ascertain that the actuator stroke lenghts would be sufficient to reject the disturbance, and to determine the most suitable bias voltage for the dynamic tests. The quasi-static test equipment was described in short. The tests were designed and executed and the results were processed. An iterative procedure was followed to obtain the required rod prestress. Graphs of deflection versus coil voltage were obtained for the two actuators. The most suitable bias voltage was calculated.

Different types of dynamic test signals were evaluated and compared and the appropriate signal type was selected. Two dynamic test setups, i.e. and "ideal" and an "available" setup were presented. The latter was chosen by necessity. The tests were designed and executed and the results were processed. The coil voltage to angular acceleration transfer function of the system, for a frequency bandwidth of 0 Hz to 500 Hz, was obtained. It was shown that the modelled results given in chapter 2, differed significantly form the experimentally determined results. Possible reasons for the differences were given and updating of the model was motivated.

Chapter 5 was devoted to updating the model. Identification theory was discussed in short and the most suitable identification technique, i.e. linear, frequency domain identification, was selected and described. An accurate nonparametric transfer function model was identified from the experimentally determined results. The model was adequate for control purposes,

but failed to provide insight into the system dynamic characteristics. To overcome this limitation, a parametric model was derived.

Parametric modelling was facilitated by separating the electrical and mechanical subsystem models. A 3rd order coil model was obtained in state-space and transfer function forms. A mechanical subsystem model, consisting of two 2DOF actuator models, an MDOF model for the optical instrument and support structure, and an SDOF model for the elastically mounted base, was subsequently derived.

The 2DOF actuator models differed from the original SDOF models derived in chapter 2, while the original MDOF model of the optical instrument, was retained. The actuator, base and instrument models were coupled by means of the component mode synthesis method. The mechanical subsystem model was subsequently written in state-space form and coupled to the coil model. The updated system state-space model was converted to transfer function form. The transfer function magnitude and phase spectra of this model compared favourably with the experimentally determined spectra. System natural frequencies, normal mode shapes, damping factors, frequency bandwidth, modal forces and open-loop transmissibility were obtained.

Chapter 6 described the analysis, modelling, simulation, design and experimental evaluation of the control system. General control theory was given as a background. Various controller types, i.e. feedforward, output and state feedback feedback controllers, linear and nonlinear controllers, tracking controllers, regulators and optimal controllers, were discussed in short.

Principles of disturbance attenuation were discussed in more detail. The attenuation factor was defined and the nature of the disturbance was discussed. Requirements for disturbance and noise attenuation were given. An attenuation method for a known disturbance entering a system at a given point, was described. A short summary of optimal control, in terms of H_2 and H_∞ optimal criteria, was given. Other modern disturbance attenuation techniques, such as preshaping of command inputs, attenuation of a continuous disturbance by means of digital regulation, and "two-way" isolation, were discussed. Motion controllers, i.e. relative and absolute motion controllers, were described in detail.

Control system design specifications were given, followed by a discussion of general control system requirements, such as accuracy, stability, sensitivity, reaction speed, control effort, robustness, observability and controllability. The specifications and general requirements were used to select a suitable controller type. A linear, disturbance feedforward plus output feedback controller, with output integral feedback, was selected. The control system design procedure was described and a detailed exposition of the controller design was given. The design of a suboptimal controller, coupled to a suboptimal observer, was described. The controller and observer designs were derived from optimal controller and observer designs. Controller characteristics were expressed in terms of state-space parameters, transfer functions, and closed-loop poles and zeroes. In order to facilitate implementation of the controller, the controller transfer functions were converted to digital filter form.

The test apparatus, test procedure and execution were described. Three controller configurations, i.e. disturbance feedforward, output feedback and feedforward plus feedback configurations, were tested. Test data was processed and the test results were presented and discussed. The attenuation factor spectra were shown graphically and RMS attenuation factors were given. It was shown that the linear disturbance feedforward plus output feedback

controller, with output integral feedback, could achieve 80% of the target attenuation in a disturbance band of 0 Hz to 100 Hz.

7.2 Contributions and conclusions

Firstly, it is possible to stabilize the line of sight of the given optical instrument, over a disturbance frequency bandwidth of 0 to 100 Hz, using gained magnetostrictive actuators. This result shows that magnetostrictive stabilization is a feasible alternative to the more expensive gyroscopic systems normally used for LOS stabilization. Due to the relatively large magnetostrictive strains of 1400 $\mu\varepsilon$ obtainable with Terfenol-D rods, a relatively small displacement gain of 2,7 was sufficient to produce the required actuator stroke length of 75 μm. By comparison, piezoelectric materials, with maximum strains of 200 $\mu\varepsilon$, would require significantly larger gain factors. This, in turn, would result in excessive gain mechanism stresses and an insufficient isolation frequency bandwidth.

Due to the low frequency response of the magnetostrictive LOS stabilization system (as low as 0 Hz), it is superior to electrodynamic systems for low frequency isolation. On the other side of the frequency scale, the high frequency response of the magnetostrictive system (well in excess of 100 Hz – see figure 5.6.7), makes it more suitable than hydraulic isolation for this application. A practical consequence is that hydraulic pumps and valves are eliminated, with an accompanying reduction in maintenance cost.

Secondly, an updated model, based on experimental system identification, must be employed. Since the theoretical model is too inaccurate for controller design purposes (figure 4.5.4.3), it should be combined with the updated model to compose an accurate plant system representation for control design.

Model updating is facilitated by separately modelling the mechanical and electrical subsystems. The mechanical subsystem model, consisting of simple linear lumped mass and stiffness actuator models, coupled to the original distributed optical instrument model, can be obtained using component mode synthesis (section 5.5). The system state-space and transfer function model, which couples the updated mechanical subsystem model to the coil model (section 5.6), gives physically interpretable characteristics, i.e. normal mode shapes, natural frequencies, damping factors and forces, coil DC resistance, voltage to current transfer function and -3dB cutoff frequency. Compared with the experimentally-determined transfer function, the updated model is sufficiently accurate for control design (figure 5.6.4).

Thirdly, reasonable attenuation can be achieved with a linear regulator, in spite of the highly nonlinear saturation and hysteresis characteristics of Terfenol-D. The controller, which consists of a suboptimal disturbance feedforward plus output feedback regulator, with output integral feedback to improve robustness, can be designed using linear state control theory (see section 6.4.4). The tedious work required to construct input-versus-state functions, to linearize and stabilize nonlinear state feedback controllers, is thus eliminated, thereby significantly simplifying controller design. In addition, the regulator employed in this study is relatively easily implemented digitally and can be run on a commercial DSP, using standard Simulink block diagram elements (figures 6.4.4.1 and 6.6.2.1).

In the fourth place, it was experimentally shown (table 6.7.2.1) that the magnetostrictive active LOS stabilization system developed in this study, achieves an attenuation of -9,75 dB, i.e. 80% of the target isolation, in a frequency band of 0 Hz to 100 Hz. This is an indication of the effectiveness of the system.

Lastly, a theoretical model, though inaccurate, can be derived from first principles, to serve as an input to actuator design. The lumped mass and stiffness models of the actuators, coil resistance and inductance equations derived in chapter 2, are a useful design aid. The model makes it possible to calculate the required Terfenol-D rod length and diameter, displacement gain factor, actuator stroke length, rod prestress, number of coil windings, coil resistance to inductance ratio and system isolation frequency bandwidth.

As a final comment: The LOS stabilization system was specifically developed to isolate a lightweight video camera with a mass of 1 kg and length of 250 mm, against a random base disturbance with a frequency bandwidth of 0 to 100 Hz, encountered on a military tank. The given disturbance spectrum (figure 1.1.3) is unique to tracked vehicles and will normally not be encountered in other vehicle types.

Alternative applications of the LOS stabilization system are not the topic of discussion in this thesis. However, extensions to the application are possible under certain circumstances, provided the system bandwidth of 199 Hz and actuator stroke of 75 μm are not exceeded. Applications which may require alterations to the plant and controller, are as follows: An increase in instrument length, for example, will necessitate actuators with longer stroke lengths, since the angular displacement of the isolation system will decrease. If the disturbance frequency spectrum deviates from that of the given disturbance, the controller may have to be redesigned. A change in instrument mass will change the system natural frequencies and isolation bandwidth, but small increases in mass will not decrease the bandwidth to below 100 Hz. Pole and zero shifts due to mass changes must necessarily be accounted for in the control design.

7.3 Problems encountered

A number of problems were experienced in this study. In the first place, design of the gain mechanisms proved problematic and a "worse-than-average" solution had to be accepted. Secondly, the measured -3dB coil cutoff frequency was lower than the required frequency (84 Hz versus 100 Hz). Lastly, an additional personal computer and signal processing board had to be acquired to generate the base motion. These problems are discussed in more detail below.

Design of octagonal gain mechanisms

The octagonal gain mechanisms used in the actuators, are supplied with notched flexures in the corners, in order to allow translational deflection (see figure 3.4.1.5). Although the flexures are sufficiently soft to allow translational deflection, they are too soft to prevent rotational deflection. If the normal mode shapes of a single actuator, in the absence of the optical instrument and other actuator, are analyzed, it is found that the first normal mode

shape is an undesirable rocking mode. (The actuator normal mode shapes were not discussed in this study). Rocking modes place the Terfenol-D rods under fluctuating bending moments, which can cause breakages.

An alternative gain mechanism, with slotted flexures, instead of notched flexures, was originally considered in this study. The mechanism prevents rocking motion and only allows translational motion. A quarter model of the gain mechanism is shown in figure 7.3.1. The forces and bending moment acting on the mechanism, are indicated.

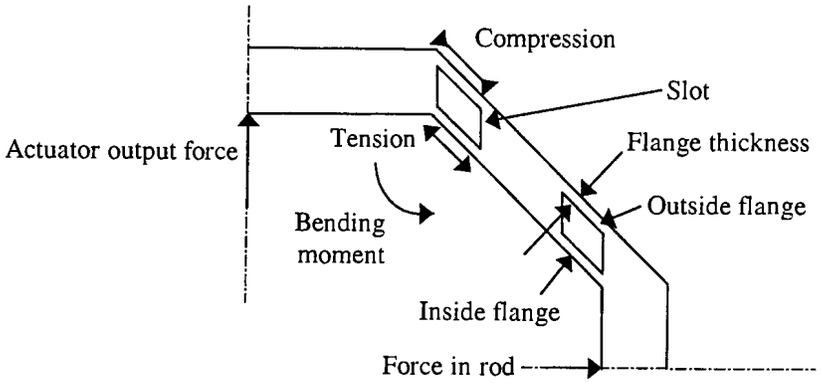

Figure 7.3.1: Quarter model of gain mechanism with slotted flexures

The bending moment causes a tensile force in the inside flange of the flexure and a compressive force in the outside flange. During evaluation of the design concepts, a finite element analysis revealed that the compressive force in the outside flange would exceed the critical buckling force. An effort was made to increase the critical buckling force, by increasing flange thickness and by decreasing flange length, while maintaining the required bending stiffness. Unfortunately, the efforts were unsuccessful and the concept was shelved.

Coil design

One of the design objectives was to obtain a coil with a –3dB cutoff frequency of more than 100 Hz, that could be matched to amplifiers with often-used input impedances of 4 Ω or 8 Ω (see section 3.5.2). The design was based on magnetostrictive and magnetization characteristics of Terfenol-D, as published in the literature. In order to allow a margin of error in the design, the target cutoff frequency was set at 150 Hz, which exceeded the required frequency by 50%.

Initially, a coil with an 8 Ω impedance was selected in favour of a 4 Ω coil, since this measure would make it easier to obtain a sufficiently high cutoff frequency. The higher impedance could be obtained in two ways, i.e. by means of a longer wire, or by means of a wire with a smaller diameter. The longer wire was preferred, since the thinner wire would be too fragile.

The resulting coil was however too heavy and didn't produce the minimum required cutoff frequency of 100 Hz. (The design of the 8 Ω coil is not included in this study).

In order to obtain a lighter coil, with a relatively strong wire, and which could be matched to the available amplifier, it was decided to design an entirely new coil with a 4 Ω impedance, at the cutoff frequency of 100 Hz. The lower impedance was achieved with a shorter and thinner wire, resulting in a significantly smaller and lighter coil. The design of the coil was explained in detail in section 3.5.2.

Experimental identification of the system revealed that the coil cutoff frequency was 84 Hz (see section 5.4.2). This frequency differed from the design cutoff frequency of 150 Hz and the minimum required cutoff frequency of 100 Hz. The differences were attributed to differences between the modelled and true Terfenol-D characteristics. It was mentioned in section 2.7.3 that especially hysteresis characteristics would be difficult to model. The initial hysteresis model was derived from published quasi-static magnetostrictive and magnetization characteristics (see section 2.3), while experimental characterization of the actuators and optical instrument was done dynamically (see section 4.4).

However, although the coil –3dB bandwidth was lower than 100 Hz, the system –3dB bandwidth was sufficient (see section 5.6). The low-pass filtering effect of the coil was to a certain extent cancelled by the mechanical characteristics of the system, due to resonance at frequencies above the disturbance band (see also figure 5.6.7).

Excitation of base motion

Excitation of the disturbance required an additional personal computer and signal processing board (see section 6.6). A more convenient solution would be to generate the signal digitally, e.g. on a computer with signal generation software and D/A converters (as in section 4.3.2), record the signal with an analogue data recorder and save it on a magnetic tape. During controller tests, the base could be excited by playing back the recorded signal through a power amplifier, and by supplying it to the electrodynamic shaker. The suggested procedure is schematically shown in figure 7.3.2.

The abovementioned setup would make it possible to repeat controller tests as many times as required without the need of an additional computer or signal processing board. Unfortunately, a data tape recorder was not available for this purpose.

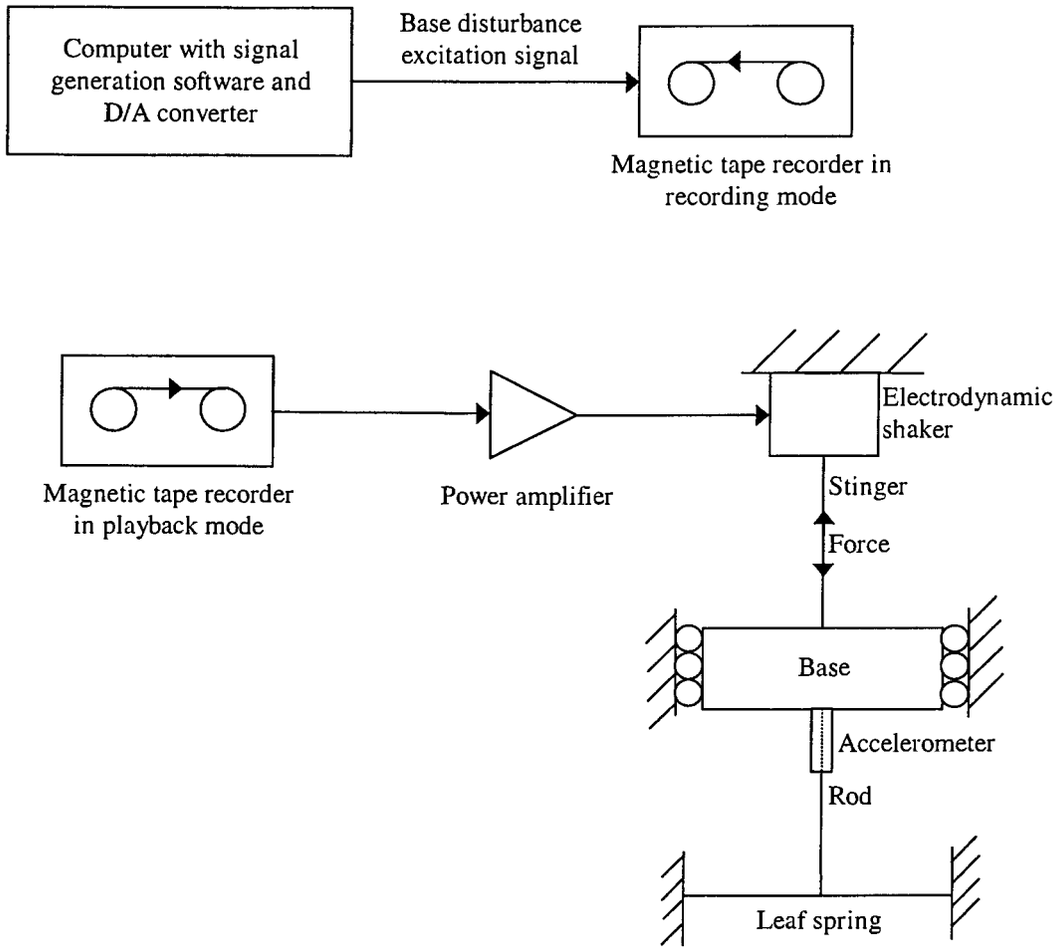

Figure 7.3.2: Suggested disturbance excitation procedure

7.4 Recommendations for future work

A number of recommendations can be made for future work in the field. Firstly, excitation of the optical instrument with both actuators, instead of one, should be considered. This would make it possible to obtain the required output angular acceleration, when exciting the system with the full base angular acceleration.

Secondly, simultaneous translational and rotational isolation of the instrument would both stabilize the line of sight, and isolate the instrument against vertical vibrations that could damage the instrument. In the third place, optimization of the plant and controller during the design phase would make it possible to obtain the optimal plant parameters, before manufacture. Parameters which could be optimized, include, inter alia, plant mechanical and electrical characteristics, sensor types and positions, control inputs and plant outputs.

In the fourth place, more powerful control methods, such as two-way isolation and nonlinear control, could be implemented. A fifth recommendation is to apply permanent magnet biasing, instead of electrodynamic baising. This measure would significantly reduce coil input power

and would eliminate the need for additional biasing signals. A last recommendation is to do away with the mechanical biasing springs altogether and to adjust prestress in the Terfenol-D rods by means of the prestress bolts.

References

Abbundi, R., Clark, A.E., & Koon, N.C., "Temperature dependence of the magnetostriction and magnetization in single crystal $HoFe_2$," Journal of Applied Physics, Volume 50, Number 3, pp. 1671-1673, March 1979.

Adly, A.A., Mayergoyz, I.D., & Bergqvist, A., "Preisach modelling of magnetostrictive hysteresis," Journal of Applied Physics, Volume 69, Number 8, pp. 5777-5779, 15 April 1991.

Anderson, B.D.O., & Moore, J.B., "Optimal Control - Linear Quadratic Methods," Prentice-Hall, Englewood Cliffs, NJ, 1989.

Ashley, S., "Magnetostrictive actuators," Mechanical Engineering, pp. 68 – 70, June 1998.

Atalik, T.S., & Utku, S., "Stochastic Linearization of Multi-Degree-of-Freedom Non-Linear Systems," Earthquake Engineering and Structural Dynamics, Volume 4, pp. 411-420, 1976.

Bartkowiak, R.A., "Electric Circuits," Intext Educational Publishers, New York, 1973.

Bathe, K-J., "Finite Element Procedures in Engineering Analysis," Prentice-Hall, Englewood Cliffs, NJ, 1982.

Bednarck, S., "The giant magnetostriction in ferromagnetic composites within an elastomer matrix," Applied Physics A - Materials Science & Processing, Volume 68, Number 1, pp. 63 – 67, January, 1999.

Béliveau, J.-G., & Soucy, Y., "Damping Synthesis Using Complex Substructure Modes and a Hermitian System Representation," AIAA Journal, Vol. 23, No. 12, pp. 1952-1956, December 1985.

Benfield, W.A., & Hruda, R.F., "Vibration Analysis of Structures by Component Mode Substitution, AIAA Journal, Vol. 9, No. 7, pp. 1255-1261, July 1971.

Bergqvist, A., & Engdahl, G., "A Stress-dependent Magnetic Preisach Hysteresis Model," IEEE Transactions on Magnetics, Volume 27, Number 6, pp. 4796-4798, November 1991.

Billings, S.A., Tsang, K.M., & Tomlinson, G.R., "Application of the NARMAX Method to Nonlinear Frequency Response Estimation," Proceedings of the 6th International Modal Analysis Conference, Kissimmee, FL, pp. 1433-1438, 1988.

Bishop, R.H., "Modern Control Systems Analysis and Design Using MATLAB," Addison Wesley, Reading, MA, 1993.

Bittanti, S., Campi, M., & Lorito, F., "ICSS: A program for the identification and control of time varying systems," Proceedings of the European Simulation Multiconference, pp. 588-592, 1992.

Bozic, S.M., "Digital and Kalman Filtering," Edward Arnold, London, 1990.

Braun, S.G., & Ram, Y.M., "Structural Parameter Identification in the Frequency Domain: The Use of Overdetermined Systems," Transactions of the American Society of Mechanical Engineers, Journal of Dynamic Systems, Measurement and Control, Volume 109, pp. 120-123, June 1987.

Besbes, M., Ren, Z., & Razek, A., "Finite Element Analysis of Magneto-Mechanical Coupled Phenomena in Magnetostrictive Materials," IEEE Transactions on Magnetics, Volume 32, Number 3, pp. 1058-1061, May 1996.

Broch, J.T., "Mechanical Vibration and Shock Measurements," Bruel & Kjær, Glostrup, Denmark, April 1984.

Brogan, W.L., "Modern Control Theory," Second edition, Prentice-Hall, Englewood Cliffs, NJ, 1985.

Bryant, M.D., "Bond Graph Models for Linear Motion Magnetostrictive Actuators," Transactions of the American Society of Mechanical Engineers, Journal of Dynamic Systems, Measurement, and Control, Volume 118, pp. 161-167, March 1996.

Bryant, M.D., Fernández, B., Wang, N., Murty, V.V., Vadlamani, V., and West, T.S., "Active Vibration Control in Structures Using Magnetostrictive Terfenol with Feedback and/or Neural Network Controllers," Journal of Intelligent Material Systems and Structures, Volume 4, pp. 484-489, 1993.

Budgor, A.B., Lindenberg, K., & Shuler, K.E., "Studies in Nonlinear Stochastic Processes. II. The Duffing Oscillator Revisited," Journal of Statistical Physics, Volume 15, Number 5, pp. 375-391, 1976.

Burden, R.L., & Faires, J.D., "Numerical analysis," Third edition, Prindle, Weber & Schmidt, Boston, MA, 1985.

Butler, J.L., "Application Manual for the Design of Etrema Terfenol-D Magnetostrictive Transducers," Edge Technologies Inc., Ames, Iowa, February 1988.

Butler, J.L., Butler, A.L., & Butler, C.L., "Hybrid magnetostrictive / piezoelectric Tonpilz transducer," Journal of the Acoustical Society of America, Volume 94, Number 2, Part 1, pp. 636-641, August 1993.

Butler, J.L., & Lizza, N.L., "Eddy current loss factor series for magnetostrictive rods," Journal of the Acoustical Society of America, Volume 82, Number 1, p. 378, July 1987.

Chapra, S.C., & Canale, R.P., "Numerical Methods for Engineers - with Personal Computer Applications," McGraw-Hill, New York, 1985.

Chen, S., Billings, S.A., & Luo, W., "Orthogonal least squares methods and their application to non-linear system identification," International Journal of Control, Volume 50, Number 5, pp. 1873-1896, 1989.

Clark, A.E., "High Power Rare Earth Magnetostrictive Materials," Journal of Intelligent Material Systems and Structures, Volume 4, Number 1, pp. 70-75, January 1993.

Clark, A.E., & Savage, H.T., "Magnetostriction of Rare Earth-Fe_2 Compounds under Compressive Stress," Journal of Magnetism and Magnetic Materials 31-34, pp. 849-851, 1983.

Clark, A.E., Spano, M.L., & Savage, H.T., "Effect of Stress on the Magnetostriction and Magnetization of Rare Earth-$Re_{1.95}$ Alloys," IEEE Transactions on Magnetics, Volume MAG-19, Number 5, pp. 1964-1966, September 1983.

Clark, A.E., Teter, J.P., Wun-Fogle, M., Moffett, M., & Lindberg, J., "Magnetomechanical coupling in Bridgman-grown $Tb_{0.3}Dy_{0.7}Fe_{1.9}$ at high drive levels," Journal of Applied Physics, Volume 67, Number 9, pp. 5007-5009, 1 May 1990.

Clough, R.W., & Penzien, J., "Dynamics of Structures," McGraw-Hill Kogakusha, Tokyo, 1982.

Conte, S.D., & de Boor, C., "Elementary Numerical Analysis," Second edition, McGraw-Hill Kogakusha, Tokyo, 1972.

Cooper, J.E., "Comparison of Some Time-Domain-System Identification Techniques Using Approximate Data Correlations," Journal of Modal Analysis, pp. 51-57, April 1989.

Cooper, W.D., & Helfrick, A.D., "Electronic Instrumentation and Measurement Techniques," Third edition, Prentice-Hall, Englewood Cliffs, NJ, 1985.

Cowan, C.F.N., & Grant, P.M., "Adaptive Filters," Prentice-Hall Signal Processing Series, Englewood Cliffs, NJ, 1985.

Craig, R.R. (jr.), "Structural Dynamics - An Introduction to Computer Methods," John Wiley & Sons, New York, 1981.

Craig, R.R. (jr.), & Bampton, M.C.C., "Coupling of Substructures for Dynamic Analyses," AIAA Journal, Vol. 6, No. 7, pp. 1313-1319, July 1968.

Crawley, E.F., & Hall, S.R., "The Dynamics of Controlled Structures, 1991 Notes," Massachusetts Institute of Technology Space Engineering Research Center, Cambridge, MA, July 1991.

D'Azzo, J.J., & Houpis, C.H., "Linear Control System Analysis and Design – Conventional and Modern," Second edition, McGraw-Hill, Singapore, 1986.

Dimas, D.J., & Pardoen, G.C., "Extrapolation of Modal-Analysis Techniques to Nonlinear Damped Systems," The International Journal of Analytical and Experimental Modal Analysis, Volume 3, Number 3, pp. 81-88, July 1988.

Doong, T., & Mayergoyz, I.D., "On Numerical Implementation of Hysteresis Models," IEEE Transactions on Magnetics, Volume MAG-21, Number 5, pp. 1853-1855, September 1985.

Doyle, J.C., Glover, K., Khargonekar, P.P., & Francis, B.A., "State-Space Solutions to Standard H_2 and H_∞ Control Problems," IEEE Transactions on Automatic Control, Volume 34, Number 8, pp. 831-847, August 1989.

Dyberg, J., "Magnetostrictive Rods in Mechanical Applications," Presented at The First Conference on Giant Magnetostrictive Alloys and Their Impact on Actuator and Sensor Technology, Marbella, Spain, 7-9 March 1986.

ElMadany, M.M., & Dokainish, M.A., "Articulated Vehicle Dynamic Analyses Using Equivalent Linearization Technique," SAE Paper 801421, SAE/SP-80/475, pp. 75-86, 1980.

Ewins, D.J., "Modal Testing: Theory and Practice," Research Studies Press Ltd, Taunton, Somerset, England, 1991.

Franklin, G.F., Powell, J.D., & Workman, M.L., "Digital Control of Dynamic Systems," Second edition, Addison Wesley, Reading, MA, 1990.

Füllekrug, U., "Structural-Dynamics Identification in the Time-Domain, Estimation of Modal Parameters Based on Forced Vibrations," Journal of Modal Analysis, pp. 58-67, April 1989.

Gerald, C.F., & Wheatley, P.O., "Applied Numerical Analysis," Third edition, Addison-Wesley, Reading, MA, 1984.

Gelb, A., & Vander Velde, W.E., "Multiple-Input Describing Functions and Nonlinear System Design," McGraw-Hill, 1968.

Goodwin, G.C., & Sin, K.S., "Adaptive Filtering Prediction and Control," Prentice Hall, Englewood Cliffs, NJ, 1984.

Hall, D.L., & Flatau, A.B., "Non-linearities, Harmonics and Trends in Dynamic Applications of Terfenol-D," Proceedings of the North American Conference on Smart Structures and Materials, SPIE, volume 1917-86, 1993.

Harris, C.M., "Shock and Vibration Handbook," Third edition, McGraw-Hill, New York, 1988.

Hayes, J.G., "Numerical Approximation to Functions and Data," The Athlone Press, University of London, 1970.

Hiller, M.W., Bryant, M.D., & Umegaki, J., "Attenuation and Transformation of Vibration Through Active Control of Magnetostrictive Terfenol," Journal of Sound and Vibration, Volume 134, Number 3, pp. 507-519, 1989.

Hintz, R.M., "Analytical Methods in Component Modal Synthesis," AIAA Journal, Vol. 13, No. 8, pp. 1007-1016, August 1975.

Hyde, T.T., "Active Vibration Isolation for Precision Space Structures," PhD Thesis, Department of Aeronautics and Astronautics, Massachusetts Institute of Technology, January 1996.

Ibrahim, R.A., "Response Analysis of Nonlinear Systems using Functional-Perturbation Type Approach," Proceedings of the 6th International Modal Analysis Conference, Kissimmee, FL, pp. 1480-1488, 1988.

Jacobson, D.H., "Extensions of Linear-Quadratic Control, Optimization and Matrix Theory," Academic Press, London, 1977.

Jacquot, R.G., "Modern Digital Control Systems," Dekker, New York, 1981.

Jiles, D.C., "Introduction to Magnetism and Magnetic Materials," Chapman & Hall, 1991.

Joshi, C.H., "Compact Magnetostrictive Actuators and Linear Motors," Paper presented at Actuator 2000 Conference, Bremen, Germany, June 2000.

Karnopp, D.C., & Trikha, A.K., "Comparative Study of Optimization Techniques for Shock and Vibration Isolation, Transactions of the American Society of Mechanical Engineers, Journal of Engineering for Industry, pp. 1128-1132, November 1969.

Kashyap, R.L., & Rao, A.R., "Dynamic Stochastic Models from Empirical Data," Academic Press, New York, 1976.

Khargonekar, P.P., Petersen, I.R., & Rotea, M.A., "H_∞ Optimal Control with State-Feedback, IEEE Transactions on Automatic Control, Volume 33, Number 8, pp. 786-788, August 1988.

Kim, B., "Dual-Loop DPLL Gear-Shifting Algorithm for Fast Synchronization," IEEE Transactions on Circuits and Systems – II: Analog and Digital Signal Processing, Volume 44, Number 7, pp. 577-586, July 1997.

Kirk, D.E., "Optimal Control Theory - An introduction," Prentice-Hall, Englewood Cliffs, NJ, 1970.

Klein, L.R., & Dowell, E.H., "Analysis of Modal Damping by Component Modes Using Lagrange Multipliers," Transactions of the American Society of Mechanical Engineers, Journal of Applied Mechanics, pp. 527-528, June 1974.

Kubomura, K., "Component Mode Synthesis for Damped Structures," AIAA Journal, Vol. 25, No. 5, pp. 740-745, May 1987.

Kubomura, K., "A Theory of Substructure Modal Synthesis," Transactions of the American Society of Mechanical Engineers, Journal of Applied Mechanics, Volume 49, pp. 903-909, December 1982.

Kuo, B.C., "Automatic Control Systems," Fourth edition, Prentice-Hall, Englewood Cliffs, NJ, 1982.

Kvarnsjö, L., "On Characterization, Modelling and Application of Highly Magnetostrictive Materials," PhD Thesis, Royal Institute of Technology, Electric Power Research Centre, Department of Electrical Plant Engineering, Stockholm, Sweden, 1993.

Kwakernaak, H., & Sivan, R., "Linear Optimal Control Systems," Wiley-Interscience, New York, 1972.

Leonard, P.J., Rodger, D., Karagular, T., & Coles, P.C., "Finite Element Modelling of Hysteresis," IEEE Transactions on Magnetics, Volume 31, Number 3, pp. 1801-1804, May 1995.

Likhachev, A.A., & Ullakko, K., "Quantitative model of large magnetostrain effect in ferromagnetic shape memory alloys," The European Physical Journal B, Volume 14, Number 2, pp. 263 – 257, March 2000.

Liu, K., & Miller, D.W., "Time Domain State-Space Identification of Structural Systems," Transactions of the American Society of Mechanical Engineers, Journal of Dynamic Systems, Measurement, and Control, Volume 117, pp. 608-618, December 1995.

Liu, K., Jacques, R.N., & Miller, D.W., "Frequency Domain Structural System Identification by Observability Range Space Extraction, Transactions of the American Society of Mechanical Engineers, Journal of Dynamic Systems, Measurement, and Control, Volume 118, pp. 211-220, June 1996.

Machine Design, "Cabin Noise Squelched with Antivibes," p.25, April 4, 1994.

Maciejowski, J.M., "Multivariable Feedback Design," Addison Wesley, Wokingham, England, 1989.

Masri, S.F., Chassiakos, A.G., & Caughey, T.K., "Identification of Nonlinear Dynamic Systems Using Neural Networks," Transactions of the American Society of Mechanical Engineers, Journal of Applied Mechanics, Volume 60, pp. 123-133, March 1993.

Masri, S.F., Chassiakos, A.G., & Caughey, T.K., "Structure-unknown non-linear dynamic systems: identification through neural networks," Smart Materials and Structures, Volume 1, pp. 45-56, 1992.

Masters, B.P., & Crawley, E.F., & van Schoor, M.C., "Global Structure Modeling Using Force-State Component Identification," AIAA Journal of Guidance, Control and Dynamics, Volume 19, Number 1, pp. 198-206, January/February 1996.

Mathews, J.H, & Fink, K.D., "Numerical Methods Using Matlab," Third edition, Prentice-Hall, Upper Saddle River, NJ, 1999.

McCaig, M., & Clegg, A.G., "Permanent Magnets in Theory and Practice," Second edition, Pentech, London, 1987.

Meeks, S.W., & Timme, R.W., "Rare earth iron magnetostrictive underwater sound transducer," Journal of the Acoustical Society of America, Volume 62, Number 5, pp. 1158-1164, November 1977.

Meirovitch, L., "Dynamics and Control of Structures," John Wiley & Sons, New York, 1990.

Ossart, F., Davidson, R., & Charap, S.H., "A 3D Moving Vector Preisach Hysteresis Model," IEEE Transactions on Magnetics, Volume 31, Number 3, pp. 1785-1788, May 1995.

Petersen, I.R., "Disturbance Attenuation and H^{∞} Optimization: A Design Method Based on the Algebraic Riccati Equation," IEEE Transactions on Automatic Control, Volume AC-32, Number 5, pp. 427-429, May 1987.

Petersen, I.R., "Complete Results for a Class of State Feedback Disturbance Attenuation Problems," IEEE Transactions on Automatic Control, Volume 34, Number 11, pp. 1196-1199, November 1989.

Pinches, M.J., & Ashby, J.G., "Power Hydraulics," Prentice Hall International, UK, 1989.

Pratt, J., "Design and analysis of a self-sensing Terfenol-D magnetostrictive actuator," MS Thesis, Department of Aerospace Engineering and Engineering Mechanics, Iowa State University, Ames, Iowa, 1993.

Press, W.H., Teukolsky, S.A., Vetterling, W.T., & Flannery, B.P., "Numerical Recipes in FORTRAN - The Art of Scientific Computing," Second edition, Cambridge University Press, New York, 1992.

Raath, A.D., "Dynamic System Identification," Project Report VLG\90\050, Centre for Structural Mechanics, Laboratory for Advanced Engineering, 5 April 1990.

Randall, R.B., "Frequency Analysis," Third edition, Bruel & Kjær, Glostrup, Denmark, September 1987.

Rao, S.S., "The Finite Element Method in Engineering," Second edition, Pergamon Press, Elmsford, NY, 1989.

Reed, R.S., "Shock isolation using an active magnetostrictive element," Proceedings from 59th Shock and Vibration Symposium, Volume 4, Sandia National Laboratories, Albuquerque, NM, October 1988.

Reed, R.S., "Active Vibration Isolation Using a Magnetostrictive Actuator," Technical Paper, System Engineering Department, U.S. Naval Academy at Annapolis, 1989.

Restorff, J.B., Savage, H.T., Clark, A.E., & Wun-Fogle, M., "Preisach modelling of hysteresis in Terfenol," Journal of Applied Physics, Volume 67, Number 9, pp. 5016-5018, 1 May 1990.

Rizzoli, V., & Masotti, D., "General-Purpose Analysis of Nonlinear Circuits Containing Saturating / Hysteretic Inductors by the Harmonic-Balance Technique," IEEE Transactions on Magnetics, Volume 31, Number 3, pp. 2290-2303, May 1995.

Roark, R.J., & Young, W.C., "Formulas for Stress and Strain," Fifth edition, McGraw-Hill, Tokyo, 1983.

Rubin, S., "Improved Component-Mode Representation for Structural Dynamic Analysis," AIAA Journal, Vol. 13, No. 8, pp. 995-1006, August 1975.

Sablik, M.J., & Jiles, D.C., "A model for hysteresis in magnetostriction," Journal of Applied Physics, Volume 64, Number 10, pp. 5402-5404, 15 November 1988.

Schoukens, J. & Pintelon, R., "Identification of Linear Systems – A Practical Guideline to Accurate Modelling," Pergamon Press, Oxford, 1991.

Schulze, M.P., Greenough, R.D., & Galloway, R.D., "The Stress Dependence of k_{33}, d_{33}, λ and μ in $Tb_{0.3}Dy_{0.7}Fe_{1.95}$," IEEE Transactions on Magnetics, Volume 28, Number 5, pp. 3159-3161, September 1992.

Schwarzenbach, J. & Gill, K.F., "System Modelling and Control," Second edition, Edward Arnold, London, 1986.

Sears, F.W., & Zemansky, M.W., "University Physics," Fourth edition, Addison Wesley, Reading, MA, 1975.

Sewell, J, & Kuhn, P., "Comparison of Magnetic Biasing Techniques for Terfenol D," in Proceedings of Second International Conference on Giant Magnetostrictive and Amorphous Alloys for Actuators and Sensors, C. Tyrén, Ed., Marbella, Spain, October 1988.

Shigley, J.E., "Mechanical Engineering Design," Third edition, McGraw-Hill Kogakusha, Tokyo, 1977.

Sievers, L.A., & von Flotow, A.H., "Comparison and Extensions of Control Methods for Narrow-Band Disturbance Rejection," IEEE Transactions on Signal Processing, Volume 40, Number 10, pp. 2377-2391, October 1992.

Simon, M., & Tomlinson, G.R., "Use of Hilbert Transform in Modal Analysis of Linear and Nonlinear Structures," Journal of Sound and Vibration, Volume 96, Number 4, pp. 421-436, 1984.

Singer, N.C., & Seering, W.P., "Preshaping Command Inputs to Reduce System Vibration," Transactions of the American Society of Mechanical Engineers, Journal of Dynamic Systems, Measurement, and Control, Volume 112, pp. 76-82, March 1990.

Sinha, N.K., & Kuszta, B., "Modelling and Identification of Dynamic Systems," Van Nostrand Reinhold Electrical / Computer Science and Engineering Series, New York, 1983.

Skogestad, S., & Postlethwaite, I., Multivariable Feedback Control – Analysis and Design, John Wiley & Sons, Chichester, England, November 1997.

Slotine, J-J.E., & Li, W., "Applied Nonlinear Control," Prentice Hall, Englewood Cliffs, NJ, 1991.

Spiegel, M.R., "Mathematical Handbook of Formulas and Tables," Schaum's Outline Series in Mathematics, McGraw-Hill, New York, 1968.

Spring Design Manual, Part 2, "Design and Application of Helical and Spiral Springs," Society of Automotive Engineers, SAE HS 795, 1990.

Stockum, L.A., & Carroll, G.R., "Precision stabilized platforms for shipboard electro-optical systems," SPIE Volume 493, The National Symposium and Workshop on Optical Platforms, pp. 414-425, 1984.

Thomson, W.T., "Theory of Vibration with Applications," Fourth edition, Chapman & Hall, Englewood Cliffs, NJ, 1993.

Tomlinson, G.R., "Detection, Identification and Quantification of Nonlinearity in Modal Analysis – A Review," Proceedings of the 4th International Modal Analysis Conference, Los Angeles, CA, Volume 2, pp. 837-843, 1986.

Tse, F.S., Morse, I.E., & Hinkle, R.T., "Mechanical Vibrations - Theory and Applications," Second edition, Allyn & Bacon, Boston, MA, 1978.

Tsui, C-C., "Robust Control System Design – Advanced State-space Techniques," Marcel Dekker, New York, 1996.

Vajda, F., & Della Torre, E., "Modelling Δm Curves Using the Complete-Moving-Hysteresis Model," IEEE Transactions on Magnetics, Volume 31, Number 3, pp. 1809-1812, May 1995.

Van Schoor, M.C., "The Coupled Nonlinear Dynamics of Spacecraft with Fluids in Tanks of Arbitrary Geometry," PhD Thesis, Department of Aeronautics and Astronautics, Massachusetts Institute of Technology, March 1989.

Van Schoor, M.C., & Bester, C.R., "The Development of a Magnetostrictive-Hydraulically Gained Actuator," Project Report, Laboratory for Advanced Engineering, Department of Mechanical Engineering, Universtiy of Pretoria, Pretoria, RSA, 1992.

Van Schoor, M.C., Masters, B.P., & Rodgers, J., "Smart Materials: Opportunities for Competitive Products," Course presented at the University of Pretoria, South Africa, 28 – 30 June, 1999.

Vidyasagar, M., "Nonlinear System Analysis," Prentice-Hall, Englewood Cliffs, NJ, 1978.

Vinh, T., Haoui, A., & Chevalier, Y., "Extension of Modal Analysis to Nonlinear Structure," Proceedings of the 2nd International Modal Analysis Conference, Orlando, FL, pp. 852-857, 1984.

Wakiwaka, H., Umezawa, T., Yamada, H., Kobayashi, K., & Yoshikawa, T., "Improvement of Flux Density Uniformity in Giant Magnetostrictive Material for Acoustic Vibration Element," IEEE Transactions on Magnetics, Volume 29, Number 6, pp. 2443-2445, November 1993.

Weaver, W., & Johnston, P.R., "Finite Elements for Structural Analysis," Prentice-Hall, Englewood Cliffs, NJ, 1984.

Widrow, B., & Stearns, S.D., "Adaptive Signal Processing," Prentice-Hall, Englewood Cliffs, NJ, 1985.

Wen, Y.K., "Equivalent Linearization for Hysteretic Systems Under Random Excitation," Transactions of the ASME, Journal of Applied Mechanics, Volume 47, pp. 150-154, March 1980.

Worden, K., Stansby, P.K., & Tomlinson, G.R., "Identification of Nonlinear Wave Forces," Journal of Fluids and Structures, Volume 8, pp. 19-71, 1994.

Worden, K., & Tomlinson, G.R., "Developments in Force-State Mapping for Nonlinear Systems," Proceedings of the 6th International Modal Analysis Conference, Kissimmee, FL, pp. 1471-1479, 1988.

Wright, J.R., & Al-Haddid, M.A., "Sensitivity of the Force-State Mapping Approach to Measurement Errors," The International Journal of Analytical and Experimental Modal Analysis, Volume 6, Number 2, pp. 89-103, April 1991.

Zienkiewicz, O.C., "The Finite Element Method," Third edition, McGraw-Hill, London, 1977.

APPENDICES

Appendix A
Complex Laplace-domain transfer functions from state-space equations

Consider the state and output equations of an LTI system (equations 2.5.1.19):

$$\dot{x} = Ax + Bu \tag{A.1a}$$
$$y = Cx + Du \tag{A.1b}$$

The Laplace-transform of equation A.1a is:

$$sX(s) - x(0) = AX(s) + BU(s) \tag{A.2}$$

For $x(0) = 0$, equation A.2 becomes:

$$sX(s) = AX(s) + BU(s) \tag{A.3}$$

Solving equation A.3 for $X(s)$ gives:

$$X(s) = [sI - A]^{-1} BU(s) \tag{A.4}$$

The Laplace-transform of equation A.1b is:

$$Y(s) = CX(s) + DU(s) \tag{A.5}$$

Substitution of equation A.4 into equation A.5 gives:

$$Y(s) = \left(C[sI - A]^{-1} B + D\right)U(s) \tag{A.6}$$

The transfer function $G(s)$ is the ratio of the output $Y(s)$ to the input $U(s)$:

$$G(s) = \frac{Y(s)}{U(s)} = C[sI - A]^{-1} B + D \tag{A.7}$$

Appendix B
Exact solution methods for equations of motion of nonlinear systems

Consider the equation of motion for natural behaviour of an undamped SDOF system with a general, nonlinear restoring force $g(y)$, as governed by the DE:

$$m\ddot{y} + \kappa g(y) = 0 \tag{B.1}$$

where m is the mass, κ is a constant, y and $\ddot{y}$ are the mass displacement and acceleration respectively.

Equation B.1 can be written as:

$$\frac{d(\dot{y}^2)}{dy} + 2\frac{\kappa}{m} g(y) = 0 \tag{B.2}$$

The *time versus displacement* relationship is obtained by integrating equation B.2 twice:

$$t - t_0 = \frac{1}{\sqrt{2\frac{\kappa}{m}}} \int_0^y \frac{d\chi_2}{\sqrt{\int_{\chi_2}^{Y} g(\chi_1) d\chi_1}} \tag{B.3}$$

where t is time, t_0 corresponds to the time when $y = 0$, Y is the displacement when $\dot{y} = 0$ and χ_1 and χ_2 are integration variables. The *displacement versus time* relationship may be obtained by inverting equation B.3.

For an odd nonlinear restoring force, i.e. $g(-y) = -g(y)$, the natural period of vibration τ_n is given by:

$$\tau_n = \frac{4}{\sqrt{2\frac{\kappa}{m}}} \int_0^Y \frac{d\chi_2}{\sqrt{\int_{\chi_2}^{Y} g(\chi_1) d\chi_1}} \tag{B.4}$$

Exact solutions can be obtained in all cases where the integrals in equation B.4 can be explicitly expressed in terms of Y. For pure powers of displacement $g(y) = y^n$, τ_n is given by:

$$\tau_n = \frac{4}{\sqrt{\frac{\kappa}{m} Y^{n-1}}} \psi(n) \tag{B.5}$$

where $\psi(n)$ is a function whose values are given in table B.1, for n ranging from 0 to 7.

Table B.1: Values of the function $\psi(n)$ [Harris, 1988]

n	$\psi(n)$
0	1,4142
1	1,5708
2	1,7157
3	1,8541
4	1,9818
5	2,1035
6	2,2186
7	2,3282

Solutions for polynomials of displacement and velocity-squared damping are given by Harris [1988]. Exact solutions for forced vibration of nonlinear systems are virtually nonexistent, except if the system can be represented in a stepwise linear manner [Harris, 1988].

Appendix C
The perturbation method

Consider the following equation of motion for natural behaviour of a weakly nonlinear SDOF system:

$$\underbrace{\ddot{y}+\omega_0^2 y}_{linear}+\underbrace{\frac{\kappa}{m}g(\dot{y},y)}_{nonlinear}=0 \qquad \textbf{(C.1)}$$

where ω_0 is the linear system natural frequency, κ is a small parameter and g is a nonlinear function of speed $\dot{y}$ and displacement y. The first two terms on the left hand side of equation C.1 describe the behaviour of the linear part of the system, while the third, or perturbation term, accounts for the effects of the weak nonlinearity.

A solution of the following form is assumed for y [Gelb & VanderVelde, 1968]:

$$y(t)=y_0(t)+\frac{\kappa}{m}y_1(t)+\left(\frac{\kappa}{m}\right)^2 y_2(t)+\cdots+ \qquad \textbf{(C.2)}$$

where y_0, y_1, y_2, $\cdots$, are displacement functions of time. These functions are obtained by solving the following system of linear, non-homogeneous, 2nd order DE's:

$$\ddot{y}_0+\omega_0^2 y_0=0 \qquad \textbf{(C.3a)}$$

$$\ddot{y}_1+\omega_0^2 y_1=-g(\dot{y}_0,y_0) \qquad \textbf{(C.3b)}$$

$$\ddot{y}_2+\omega_0^2 y_2=-\frac{\partial g}{\partial y}(\dot{y}_0,y_0)y_1-\frac{\partial g}{\partial \dot{y}}(\dot{y}_0,y_0)\dot{y}_1 \qquad \textbf{(C.3c)}$$

$$\vdots \qquad \vdots \qquad \vdots \qquad \vdots$$

Equations C.3a to C.3b are solved recursively. The first equation (C.3a) is solved for y_0 and $\dot{y}_0$. With y_0 and $\dot{y}_0$ known, g, $\partial g/\partial y$ and $\partial g/\partial \dot{y}$ are obtained. Equation C.3b is subsequently solved for y_1 and $\dot{y}_1$, whereafter equation C.3c is solved for y_2 and $\dot{y}_2$. The solutions of y_0, y_1 and y_2 are substituted into equation C.2 to obtain $y(t)$. The procedure can be repeated as many times as the number of terms required in the series expansion in equation C.2.

Appendix D
The method of slowly varying amplitude and phase

Consider the following equation of motion for natural behaviour of a weakly nonlinear SDOF system:

$$\underbrace{\ddot{y}+\omega_0^2 y}_{linear}+\underbrace{\frac{\kappa}{m}g(\dot{y},y)}_{nonlinear}=0 \qquad \textbf{(D.1)}$$

where ω_0 is the linear system natural frequency, κ is a small parameter and g is a nonlinear function of speed $\dot{y}$ displacement y.

A solution of the following form is assumed for y [Gelb & VanderVelde, 1968]:

$$y(t)=A\sin\psi \qquad \textbf{(D.2)}$$

where A and ψ are functions of time, given by:

$$A=A(t) \qquad \textbf{(D.3a)}$$
$$\psi=\omega_0 t+\theta(t) \qquad \textbf{(D.3b)}$$

The following set of approximate DE's in A and θ can be derived [Gelb & VanderVelde, 1968]:

$$\dot{A}\approx-\frac{1}{2\pi\omega_0}\int_0^{2\pi}\mu g(A\sin\psi,A\omega_0\cos\psi)\cos\psi d\psi \qquad \textbf{(D.4a)}$$

$$\dot{\theta}\approx\frac{1}{2\pi\omega_0}\int_0^{2\pi}\frac{1}{A}\mu g(A\sin\psi,A\omega_0\cos\psi)\cos\psi d\psi \qquad \textbf{(D.4b)}$$

Equations D.4 are solved as follows: The right hand side of equation D.4 a is integrated with respect to ψ, resulting in a 1st order separable DE in A. This DE is solved and its solution $A=\underline{A}$ is obtained. Subsequently, the right hand side of equation D.4b is integrated with respect to ψ and another 1st order DE is obtained. Replacing A by $\underline{A}$, the latter DE is solved to obtain its solution $\theta=\underline{\theta}$.

The solution of equation D.1 is then:

$$y(t)=\underline{A}(t)\sin[\omega_0 t+\underline{\theta}(t)] \qquad \textbf{(D.5)}$$

Appendix E
Statistical linearization

Consider a general nonlinear SDOF system with an equation of motion of the form

$$g(\ddot{y},\dot{y},y)=f(t) \tag{E.1}$$

where g is the total internal force and f is the stationary gaussian random excitation force with zero mean. It is assumed that a stationary solution to equation E.1 exists.

The linear equivalent of equation E.1 is:

$$m\ddot{y}+c\dot{y}+ky=f(t) \tag{E.2}$$

where m, c and k are the mass, damping coefficient and spring stiffness to be determined, such that the solution of equation E.2 will give an approximate solution to equation E.1.

In approximating a nonlinear system by a linear system, an error will be made. The error may be defined as the difference between the solutions of the two systems, an can be written as:

$$e=g(\ddot{y},\dot{y},y)-m\ddot{y}-c\dot{y}-ky \tag{E.3}$$

The mass, damping coefficient and stiffness are determined by setting the mean square (MS) error equal to zero, resulting in:

$$m=E\left[\frac{\partial g(\ddot{y},\dot{y},y)}{\partial \ddot{y}}\right] \tag{E.4a}$$

$$c=E\left[\frac{\partial g(\ddot{y},\dot{y},y)}{\partial \dot{y}}\right] \tag{E.4b}$$

$$k=E\left[\frac{\partial g(\ddot{y},\dot{y},y)}{\partial y}\right] \tag{E.4c}$$

where $E[\ ]$ is the expected value of the term in brackets.

The method of equivalent linearization can be applied to a large variety of nonlinear system types. Examples are systems with cubic stiffening characteristics [Atalik & Utku, 1976], nonlinear damping characteristics [Atalik & Utku, 1976], hysteretic restoring forces [Wen, 1980], the Duffing oscillator [Budgor et al, 1976] and equations of motion of articulated vehicles [ElMadany & Dokainish , 1980]. Application of the method to a system with hysteretic restoring forces, as described by Wen [1980], is discussed next.

Statistical linearization applied to a system with hysteretic restoring forces

Consider a system whose equation of motion is of the form

$$m\ddot{\bar{y}} + g(\dot{\bar{y}}, \bar{y}) + z(\bar{y}) = \bar{f}(t) \tag{E.5}$$

where $\bar{y}$ is the dimensionless displacement and $\bar{f}$ is the dimensionless force:

$$\bar{y} = \frac{y}{Y} \tag{E.6a}$$

$$\bar{f} = \frac{f}{F_y} \tag{E.6b}$$

In equation E.5, g is the nonhysteretic component of the restoring force, while z is the hysteretic component.

The relationship between z and y is given by the following 1st order nonlinear DE:

$$\dot{z} = -\gamma|\dot{y}|.z.|z|^{n-1} - \beta\dot{y}|z|^n + G\dot{y} \tag{E.7}$$

where γ and β are parameters which control the shape of the hysteresis loop, G is the restoring force amplitude and n is an exponent which describes the smoothness of transition from elastic to plastic response.

From Wen [1980], equations E.5 and E.7 can be written in linear state-space form as

$$\dot{x} = Ax + Bu \tag{E.8}$$

where x and u are the state vector and input respectively:

$$x = \{\bar{y}, \quad z, \quad \dot{\bar{y}}\}^T \tag{E.9a}$$

$$u = \bar{f}(t) \tag{E.9b}$$

A and B are the coefficient and driving matrices respectively, given by:

$$A = \begin{bmatrix} 0 & 0 & 0 \\ 0 & -k_h & -c_h \\ -\alpha\omega_0^2 & -(1-\alpha)\omega_0^2 & -2\zeta_0\omega_0 \end{bmatrix} \tag{E.10a}$$

$$B = [0, \quad 0, \quad 1/m]^T \tag{E.10b}$$

In equation E.10a, α is the post-to pre-yielding stiffness ratio, ζ_0 is the viscous damping ratio

and ω_0 is the pre-yielding natural frequency:

$$\omega_0 = \sqrt{\frac{F_Y}{mY}} \tag{E.11}$$

k_h and c_h are the linearized hysteresis stiffness and damping coefficient. Both k_h and c_h depend on n. For the special case of $n = 1$, k_h and c_h are given by:

$$k_h = \gamma E\left[|\dot{y}|\right] + \beta E\left[\dot{y}\frac{\partial |z|}{\partial z}\right] \tag{E.12a}$$

$$c_h = \gamma E\left[z\frac{\partial |\dot{y}|}{\partial y}\right] + \beta E\left[|z|\right] - G \tag{E.12b}$$

It can be seen that the highly nonlinear system, as described by equations E.5 and E.7, is replaced by the equivalent linear system, as represented by equations E.8 to E.12. By comparison, the linear equations are considerably easier to solve than the nonlinear equations. Linear solutions of the above hysteretic system to gaussian inputs are given by Wen [1980].

Appendix F
The Describing Function (DF) method

Consider a nonlinear system driven by a harmonic input of the form

$$u(t) = U \sin \omega t \tag{F.1}$$

where u is the input as a function of time and U is the input amplitude.

The output $y(t)$, which is generally non-sinusoidal, can be expressed as follows by means of a Fourier series:

$$y(t) = \frac{a_0}{2} + \sum_{i=1}^{\infty} [a_i \cos(i\omega t) + b_i \sin(i\omega t)] \tag{F.2}$$

where the Fourier coefficients are a_i and b_i are functions of U and ω, determined by:

$$a_0 = \frac{1}{\pi} \int_{-\pi}^{\pi} y(t) d(\omega t) \tag{F.3a}$$

$$a_i = \frac{1}{\pi} \int_{-\pi}^{\pi} y(t) \cos(i\omega t) d(\omega t) \tag{F.3b}$$

$$b_i = \frac{1}{\pi} \int_{-\pi}^{\pi} y(t) \sin(i\omega t) d(\omega t) \tag{F.3c}$$

For an odd nonlinearity, the coefficient a_0 is zero:

$$a_0 = 0 \tag{F.4}$$

In harmonic DF analysis, only the fundamental frequency is considered. Therefore, *y(t)* can be approximated by:

$$y(t) \approx y_1(t) = a_1 \cos \omega t + b_1 \sin \omega t \tag{F.5}$$

The output *y(t)* is written in terms of the output amplitude and phase of the fundamental frequency as:

$$y_1(t) = Y \sin(\omega t + \phi) \tag{F.6}$$

where Y are the output amplitude and phase respectively, as functions of input amplitude and frequency:

$$Y = Y(U, \omega) \tag{F.7a}$$

$$\phi = \phi(U, \omega) \tag{F.7b}$$

In terms of the fundamental Fourier coefficients, Y and ϕ are:

$$Y = \sqrt{a_1^2 + b_1^2} \tag{F.8a}$$

$$\phi = \tan^{-1}\left(\frac{a_1}{b_1}\right) \tag{F.8b}$$

In complex representation, y_1 can be written as:

$$y_1 = Ye^{j(\omega t+\phi)} \tag{F.9}$$

The describing function N of a nonlinear system is the ratio of the fundamental component of the output, to the input:

$$N = \frac{Ye^{j(\omega t+\phi)}}{Ue^{j\omega t}} \tag{F.10}$$

where N is a function of the input amplitude and frequency:

$$N = N(U,\omega) \tag{F.11}$$

In rectangular coordinates, N can be written as:

$$N(U,\omega) = \frac{1}{U}(b_1 + ja_1) \tag{F.12}$$

The above derivation is only applicable to harmonically excited nonlinear systems. The DF method can also be extended to analyze nonlinear system behaviour to non-harmonic inputs, like two-sinusoid inputs, dual-inputs (e.g. DC plus sinusoid), transient and random inputs. N is tabled for a vast range of nonlinearities, for each of the above input types, by Gelb & Vander Velde [1968]. Examples of nonlinearities applicable to the analysis of Terfenol-D characteristics, are saturation and hysteresis. The DF's of these nonlinearities can be found in Gelb & Vander Velde [1968].

Appendix G
Fifth order Runge-Kutta (R-K) method

In the R-K methods, the states and outputs are obtained in the time domain by direct integration of the state equations. The solution of each state equation is approximated by a polynomial. The order of the polynomial can vary from 1st order to 5th order and higher. The higher the order, the more accurate the solution for the same computational effort [Chapra & Canale, 1985]. For this reason, higher order methods are often preferred to lower order methods.

The R-K methods are discussed in detail by Burden & Faires [1985], Chapra & Canale [1985], Conte & de Boor [1972], Gerald & Wheatley [1984] and Press et al [1992]. A short description of the 5th order method, also known as Butcher's method, is given below.

Consider a nonlinear time-invariant system, whose state and output equations are of the following form (see equations 2.5.1.2a and 2.5.1.2b):

$$\dot{x} = f(x,u) \qquad \textbf{(G.1a)}$$
$$y = g(x,u) \qquad \textbf{(G.1b)}$$

Equations G.1a and G.1b are solved by dividing time into finite intervals, and by recursively calculating the states and outputs for successive intervals using simple algebra.

Time at the beginning of the i-th time step is denoted by t_i. The state and output equations corresponding to t_i are:

$$\dot{x}_i = f(x_i,u_i) \qquad \textbf{(G.2a)}$$
$$y_i = g(x_i,u_i) \qquad \textbf{(G.2b)}$$

where x_i, u_i and y_i respectively represent the state vector, input and output at the beginning of the i-th time step.

The state vector x_{i+1}, at the beginning of the i+1-th time step, is obtained by the following equation:

$$x_{i+1} = x_i + \frac{\Delta t}{90}(7k_1 + 32k_3 + 12k_4 + 32k_5 + 7k_6) \qquad \textbf{(G.3)}$$

where Δt is the time step, given by:

$$\Delta t = t_{i+1} - t_i \qquad \textbf{(G.4)}$$

Δt may be constant, or may be adjusted during simulation to accommodate changing stiffness of the system. Generally, the smaller Δt, the more accurate the solutions.

Variables k_1 to k_6 in equation G.3 represent the derivatives of the state vector at intermediate

intervals between t_i and t_{i+1}. Note that k_2 does not appear in equation G.3. It is a "dummy" variable, which is only used to determine k_3, k_4 and k_6.

Variables k_1 to k_6 are determined recursively by means of the following equations:

$$k_1 = f(t_i, \quad x_i) \tag{G.5a}$$

$$k_2 = f\left(t_i + \frac{\Delta t}{4}, \quad x_i + \frac{\Delta t}{4}k_1\right) \tag{G.5b}$$

$$k_3 = f\left(t_i + \frac{\Delta t}{4}, \quad x_i + \frac{\Delta t}{8}k_1 + \frac{\Delta t}{8}k_2\right) \tag{G.5c}$$

$$k_4 = f\left(t_i + \frac{\Delta t}{2}, \quad x_i - \frac{\Delta t}{2}k_2 + (\Delta t)k_3\right) \tag{G.5d}$$

$$k_5 = f\left(t_i + \frac{3\Delta t}{4}, \quad x_i + \frac{3\Delta t}{16}k_1 + \frac{9\Delta t}{16}k_4\right) \tag{G.5e}$$

$$k_6 = f\left(t_i + \Delta t, \quad x_i - \frac{3\Delta t}{7}k_1 + \frac{2\Delta t}{7}k_2 + \frac{12\Delta t}{7}k_3 - \frac{12\Delta t}{7}k_4 + \frac{8\Delta t}{7}k_5\right) \tag{G.5f}$$

The output y_{i+1} for the i+1-th time step is given by:

$$y_{i+1} = g(x_{i+1}, u_{i+1}) \tag{G.6}$$

Appendix H
Actuator nonlinear dehysterized transfer functions

In order to obtain the nonlinear, dehysterized *TF's*, three sets of simulations are done, one for each of the input RMS values, i.e. 2,18 V, 1,63 V and 1,09 V. The nonlinear state equations (equations 2.5.1.11 and 2.5.1.12) are solved in the time-domain by means of the 5th order Runge-Kutta method. The states are the actuator displacement x_a, speed $\dot{x}_a$ and coil current I (see equation 2.5.1.4). The input is the coil voltage V. The input with the highest RMS value, i.e. 2,18 V, is applied first. The initial values of the states are set equal to zero.

For each time-step, stress and field are calculated from the states, using equations 2.4.4 and 2.4.10. The magnetostrictive and magnetization parameters, i.e. permeability μ^σ, Young's modulus E, piezomagnetic cross-coupling constant d^σ and strain constant d^H, are calculated from stress and field, using equations 2.5.1.10a to 2.5.1.10d. The state equations are integrated using equations G.3 and G.5a to G.5f (see appendix G), thereby obtaining the state vector at the end of each time step. The outputs are calculated in terms of the states at the end of each time step, using equation G.6. At the beginning of a new time-step, input voltage is updated and the procedure as set out in this paragraph, is repeated. At the end of the simulation, outputs for all the time steps are stored. The procedure is repeated for the 1,63 V and 1,09 V RMS inputs.

The nonlinear dehysterized transfer functions for the three coil input voltages, in terms of the inputs and outputs, are obtained by means of the following equation:

$$G(j\omega)=\frac{P_{xy}}{P_{xx}} \qquad \textbf{(H.1)}$$

where $G(j\omega)$ is the transfer function between the coil input voltage and actuator displacement output, P_{xy} is the cross-spectral density (CSD) between the input and output and P_{xx} is the power spectral density (PSD) of the input. Since the displacement signal is a simulation output, no measurement noise is present, resulting in high coherence.

$G(j\omega)$ in equation H.1 is complex, with a frequency-dependent magnitude and phase angle. The transfer function magnitude and phase, for a 2,18 V RMS coil input voltage, are shown in figure H.1.

The DC magnitude is 13,57 μm/V. The resonance frequency is 375 Hz. The maximum magnitude, at resonance, is 21,88 μm/V. The ratio between the maximum and DC magnitudes is 1,61. The -3dB bandwidth, i.e. where the magnitude is 70,7% of the DC value, is 482 Hz. The *TF* phase decreases linearly from 0 Hz to approximately 300 Hz. This reduction in phase can be attributed to coil inductance. At 375 Hz, phase decreases more rapidly with frequency. This phase decrease is due to resonance. Above 482 Hz, the actuator is operated in its filtering range, where the slope of the phase is approximately equal to that for frequencies below 300 Hz.

Similar *TF* spectra to figure H.1, exist for the 1,63 V and 1,09 V RMS coil input voltages. These spectra will however not be shown because they correspond almost exactly with the *TF* shown in figure H.1. Instead, the maximum and static magnitudes and their ratio, resonance frequency and -3 dB bandwidth for the three input voltages, are given in table H.1.

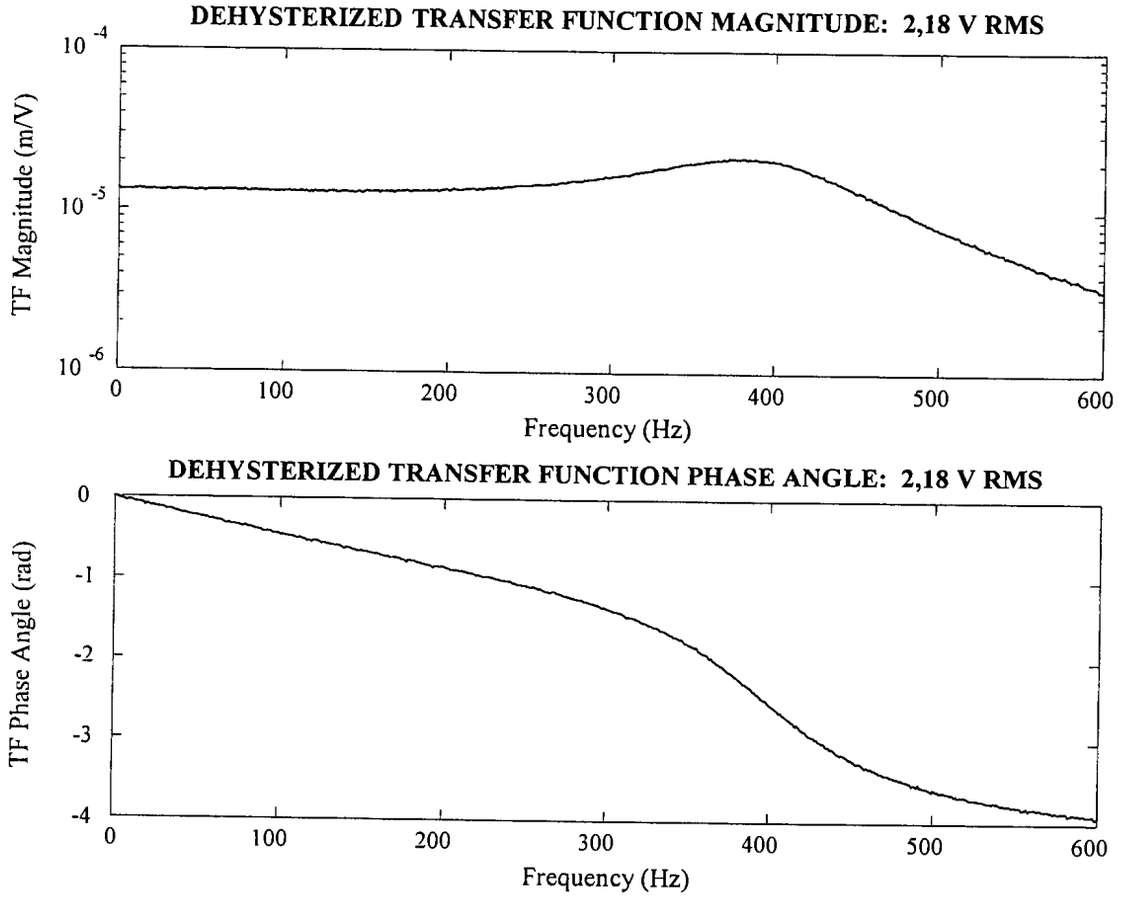

Figure H.1: Dehysterized transfer function for a 2,18 V RMS coil input voltage

Table H.1: Nonlinear dehysterized static & dynamic transfer function parameters

Parameter	2,18 V	1,63 V	1,09 V
Static magnitude (TF_S):	13,57 μm/V	13,68 μm/V	13,76 μm/V
Maximum magnitude (TF_R):	21,88 μm/V	21,95 μm/V	21,99 μm/V
TF_R/TF_S:	1,61	1,60	1,60
Resonance frequency:	375 Hz	375 Hz	375 Hz
-3 dB bandwidth:	483 Hz	482 Hz	481 Hz

It can be seen from table H.1 that the static and dynamic parameters are, for all practical purposes, independent of input voltage. The dehysterized characteristics can therefore be considered linear and can be expressed in terms of constant magnetostrictive and magnetization parameters, i.e. μ^{σ}, E, d^{σ} and d^{H}. The conclusion can be drawn that, for the

voltage inputs used in the simulations, the actuator is excited inside its linear range, i.e. outside its saturation range (see figure 2.2.1.6). The linear parameters are calculated in appendix J and their effects on the linear *TF* are discussed.

Appendix J
Actuator linear dehysterized characteristics

An equivalent linear *TF* of the actuator, using constant magnetostrictive and magnetization parameters, is obtained in this section. The linear *TF* magnitude and phase are calculated from the average parameters and compared with the nonlinear *TF* magnitude and phase. It is shown that the linear phase spectra closely match the nonlinear spectra, but that the magnitude spectra differ, especially for frequencies above the resonance frequency.

The average values of μ^σ, E, d^σ and d^H are calculated as follows from the nonlinear time-domain simulation outputs:

$$\mu^\sigma = \mu_m^\sigma = \frac{1}{T}\int_{t=0}^{t=T} \mu^\sigma(t)dt \qquad \textbf{(J.1a)}$$

$$E = E_m = \frac{1}{T}\int_{t=0}^{t=T} E(t)dt \qquad \textbf{(J.1b)}$$

$$d^\sigma = d_m^\sigma = \frac{1}{T}\int_{t=0}^{t=T} d^\sigma(t)dt \qquad \textbf{(J.1c)}$$

$$d^H = d_m^H = \frac{1}{T}\int_{t=0}^{t=T} d^H(t)dt \qquad \textbf{(J.1d)}$$

where t is time, T is the maximum time and the subscript m denotes the average value of the particular parameter.

The average parameters for the three coil input voltages, using equations J.1a to J.1d, with $T = 40$ s, are given in table J.1.

Table J.1: Average linear dehysterized magnetostrictive & magnetization parameters

Parameter	2,18 V RMS	1,63 V RMS	1,09 V RMS
Permeability μ^σ:	6,962 μTm/A	6,969 μTm/A	6,977 μTm/A
Young's modulus E:	23,46 GPa	23,36 GPa	23,28 GPa
Piezomagnetic cross-coupling constant d^σ:	1,088.10^{-8} m/A	1,089.10^{-8} m/A	1,09.10^{-8} m/A
Strain constant d^H:	1,204.10^{-8} m/A	1,208.10^{-8} m/A	1,21.10^{-8} m/A

The parameters tabled above and the actuator parameters (m_a, G, R_c, N, l_T and A_T, from table 2.7.3.1), are used to calculate k_a and ω_n (equations 2.4.22 and 2.4.23) and L_f, cf and L_0 (equations 2.4.45 to 2.4.47). For the dehysterized characteristics, zero damping is used. The Laplace-domain transfer functions are calculated from equations 2.5.2.1 to 2.5.2.3. The frequency-domain transfer function magnitude and phase angle are calculated from equation 2.5.3.6a and 2.5.3.6b respectively.

The linear dehysterized *TF* magnitude and phase, for a 2,18 V RMS coil input voltage, are shown in figure J.1. For comparison purposes, the nonlinear *TF* magnitude and phase are also shown. It can be seen from figure J.1 that the *TF* phase obtained from the linear average parameters is virtually identical to that obtained from the nonlinear simulations. The linear and nonlinear *TF* magnitudes compare well for frequencies below approximately 300 Hz. However, for frequencies above 300 Hz, the magnitudes differ. The difference increases with an increase in frequency.

The difference in magnitudes can be attributed to the fact that the *TF* calculated from average parameters does not include the effects of superharmonics. The result would be the same if the harmonic balance technique were used. The nonlinear *TF*, on the other hand, was obtained using the 5^{th} order Runge-Kutta method. Using this method, at least one superharmonic for all frequencies, up to 50% of the Nyquist frequency, is included in the output (see section 2.7.1).

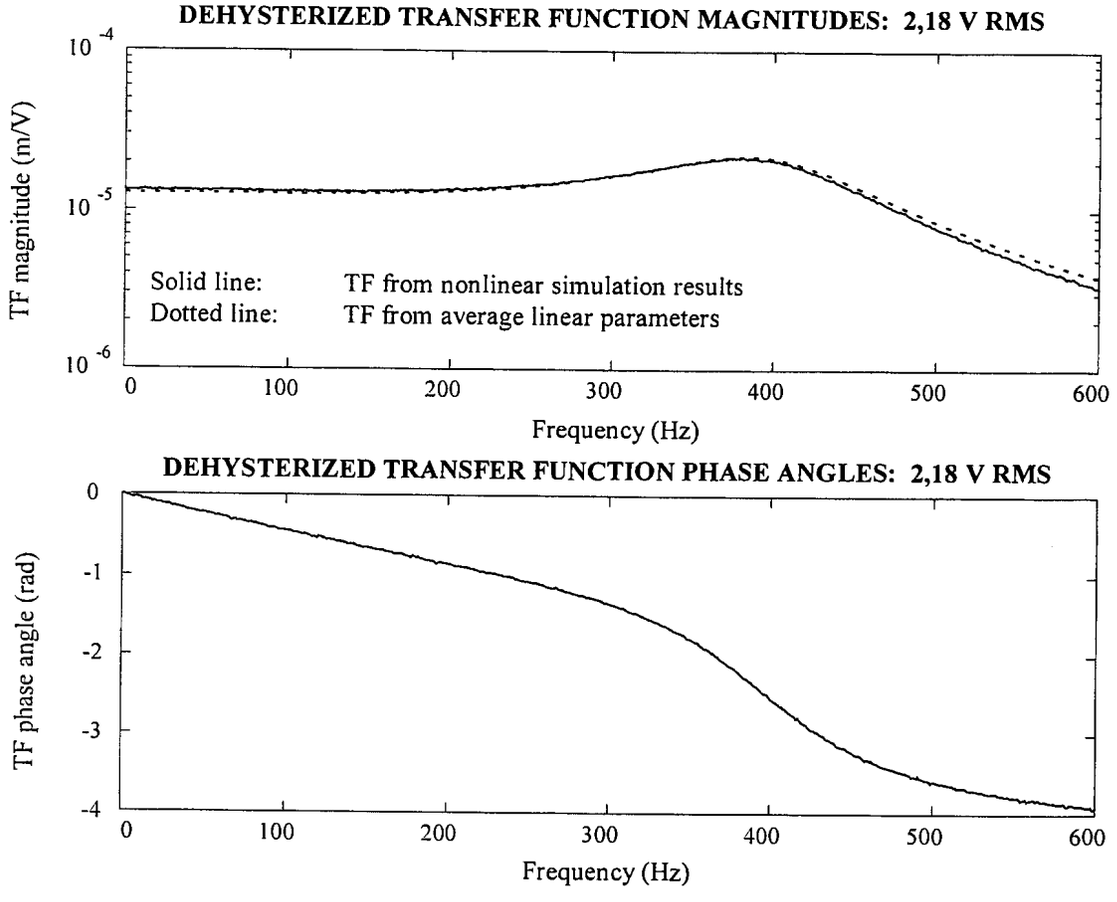

Figure J.1: Linear and nonlinear dehysterized *TF*'s for a 2,18 V RMS input

The linear, dehysterized *TF* parameters for an input voltage of 2,18 V RMS, using the average values of μ^{σ}, E, d^{σ} and d^{H} in table J.1, are given in table J.2. For comparison purposes, the nonlinear *TF* parameters, from table H.1, are also given.

Table J.2: Linear and nonlinear *TF* characteristics for a 2,18 V RMS input

Parameter	Nonlinear	Linear
Static magnitude (TF_S):	13,57 μm/V	13,00 μm/V
Maximum magnitude (TF_R):	21,88 μm/V	23,52 μm/V
TF_R/TF_S:	1,61	1,81
Resonance frequency:	375 Hz	385 Hz
-3 dB bandwidth:	483 Hz	500 Hz

A comprehensive list of the linear characteristics, for each input voltage, is given in table J.3.

Table J.3: Linear characteristics for 2,18 V, 1,63 V and 1,09 V RMS input voltages

Parameter	2,18 V RMS	1,63 V RMS	1,09 V RMS
p_0	$1{,}400.10^5$	$1{,}397.10^5$	$1{,}392.10^5$
q_0	$1{,}077.10^{10}$	$1{,}071.10^{10}$	$1{,}065.10^{10}$
q_1	$7{,}754.10^6$	$7{,}715.10^6$	$7{,}683.10^6$
q_2	2486	2482	2476
q_3	1	1	1
μ^σ	$6{,}962.10^{-6}$ Tm/A	$6{,}969.10^{-6}$ Tm/A	$6{,}977.10^{-6}$ Tm/A
E	23,46 GPa	23,36 GPa	23,28 GPa
d^σ	$1{,}088.10^{-8}$ A/m	$1{,}089.10^{-8}$ A/m	$1{,}090.10^{-8}$ A/m
d^H	$1{,}204.10^{-8}$ A/m	$1{,}208.10^{-8}$ A/m	$1{,}210.10^{-8}$ A/m
f_n	331,3 Hz	330,6 Hz	330,0 Hz
f_{deff}	397,6 Hz	396,6 Hz	395,8 Hz
ζ_{eff}	15,9%	15,9%	15,8%
L_f	2,304 mH	2,306 mH	2,309 mH
cf	0,6643	0,6640	0,6635
L_o	1,287 mH	1,289 mH	1,292 mH
R_c/L_o	395,7 Hz	395,0 Hz	394,12 Hz
F_I	27,03 N/A	27,01 N/A	26,98 N/A

Note that the effective damped natural frequency of the actuator *exceeds* the undamped natural frequency. The reason is that f_n is the uncoupled (mechanical) natural frequency of the actuator, as given by equation 2.4.22, while f_{deff} is the imaginary part of the complex pole of the coupled *TF* (see equations 2.6.11 and 2.6.12a).

Table J.3 shows that the dehysterized parameters vary slightly for different RMS inputs. This is however not the case if hysteresis effects are taken into account (see appendix K).

Appendix K
Actuator linear characteristics, including hysteresis effects

Actuator linear characteristics, including hysteresis effects, are calculated using the iterative harmonic balance technique. The technique is explained in more detail in section 2.7.2. The permeability μ^σ, strain constant d^H and damping coefficient c, as well as the static and dynamic parameters, are input voltage- and frequency-dependent. The effects of hysteresis on E and d^σ are insignificant in comparison with its effect on μ^σ and d^H (see section 2.3) and are therefore neglected.

Harmonic voltages, whose RMS-values correspond with those of the random voltage inputs used in the time-domain simulations, are used as inputs. This is done to allow a direct comparison between the dehysterized and hysteresis characteristics. For each voltage amplitude and frequency, the field amplitude H_A, permeability μ^σ, strain constant d^H and damping coefficient c, are calculated. The values of E and d^σ, for the appropriate voltage input, are obtained from table J.3 (see appendix J).

The frequency band is 0,01 Hz to 600 Hz. Frequency resolution varies according to the slope of the magnitude curve with respect to frequency. At low frequency, where the slope is low, a low resolution is used. As the slope increases, resolution is increased.

μ^σ, E, d^σ and d^H, together with m_a, G, R_c, N, l_T and A_T (from table 2.7.3.1), are used to calculate k_a and ω_n (equations 2.4.22 and 2.4.23), L_f, cf and L_0 (equations 2.4.45 to 2.4.47). The dimensionless damping factor ζ is obtained from equation 2.4.25. The TF numerator and denominator polynomial coefficients are calculated by means of equation 2.5.2.4, table 2.5.2.1 and equations 2.5.2.5. The transfer function magnitude and phase for each frequency are calculated from equation 2.5.3.6a and 2.5.3.6b respectively.

The field strength frequency spectrum for a 2,18 V RMS input is shown in figure K.1. The field amplitude at 0,01 Hz is 17,62 kA/m. From 0,01 Hz to 328 Hz, field amplitude decreases. At 328 Hz, a gap appears in the spectrum, where the iterative harmonic balance technique fails to give convergence. The frequency range of non-convergence is 328 Hz to 332 Hz. The gap is situated at the minimum field amplitude (4156 A/m). For frequencies above 332 Hz, field increases until a local peak is reached at 440 Hz. From 440 Hz to 600 Hz, field amplitude decreases with an increase in frequency.

Similar spectra can be shown for the 1,63 V RMS and 1,09 V RMS inputs. The ranges of non-convergence for these inputs are 327 Hz to 331 Hz and 324 Hz to 331 Hz respectively.

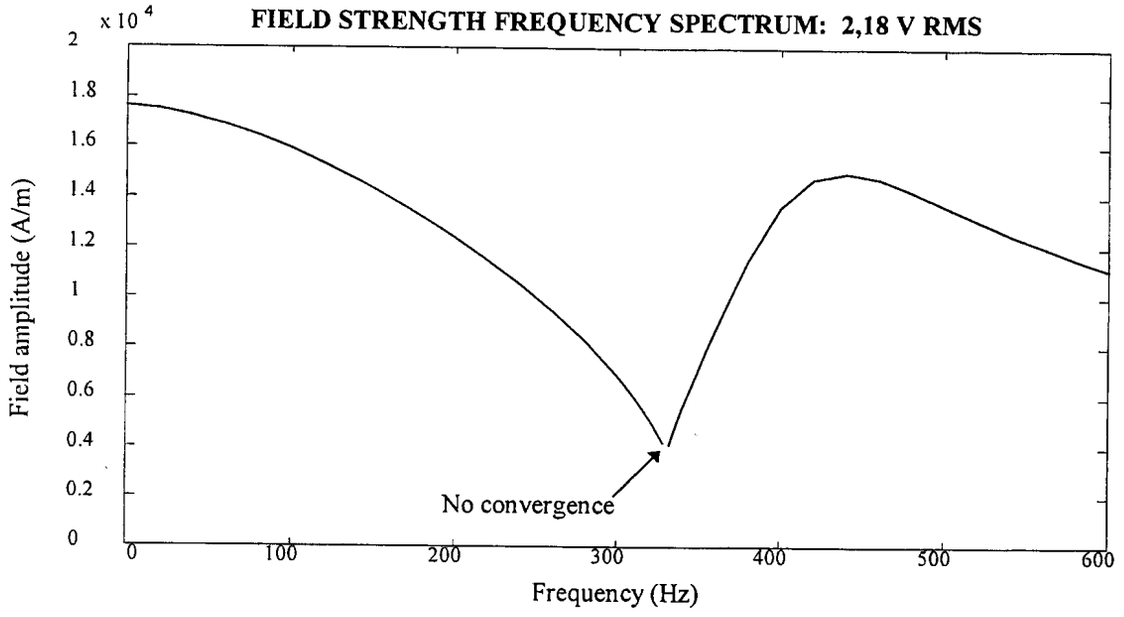

Figure K.1: Field strength frequency spectrum, including hysteresis: 2,18 V RMS

The frequency spectrum of permeability, including hysteresis, for a 2,18 V RMS input voltage, is shown in figure K.2. The permeability at 0,01 Hz is 5,57 μTm/A. Permeability decreases from 0,01 Hz to 328 Hz, where μ^{σ} is 0,62 μTm/A. For frequencies from 328 Hz to 332 Hz, permeability cannot be calculated, due to the convergence problem explained above. Above 332 Hz, permeability increases with frequency until a local peak is reached at 440 Hz. For frequencies above 440 Hz, permeability decreases with an increase in frequency.

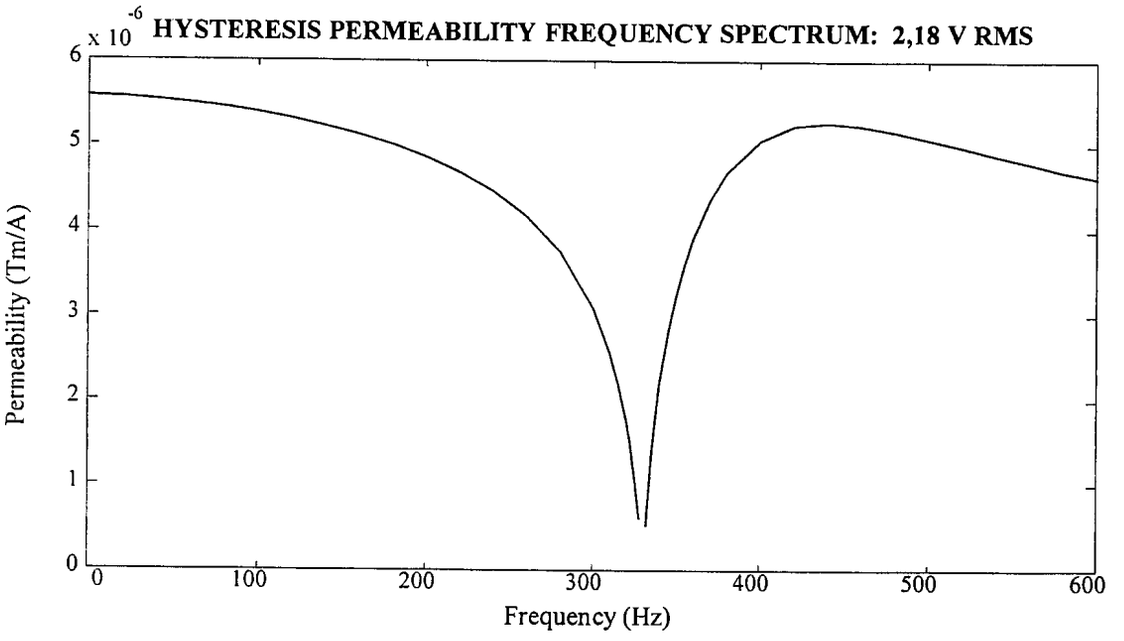

Figure K.2: Permeability frequency spectrum, including hysteresis: 2,18 V RMS

The frequency spectrum of the strain constant, including hysteresis, for a 2,18 V RMS input voltage, is shown in figure K.3. The strain constant at 0,01 Hz is $9{,}52.10^{-9}$ m/A. Strain constant decreases from 0,01 Hz to 328 Hz, where d^H is $1{,}27.10^{-9}$ m/A. Above 332 Hz, strain constant increases until a local peak is reached at 440 Hz. For frequencies above 440 Hz, strain constant decreases with an increase in frequency.

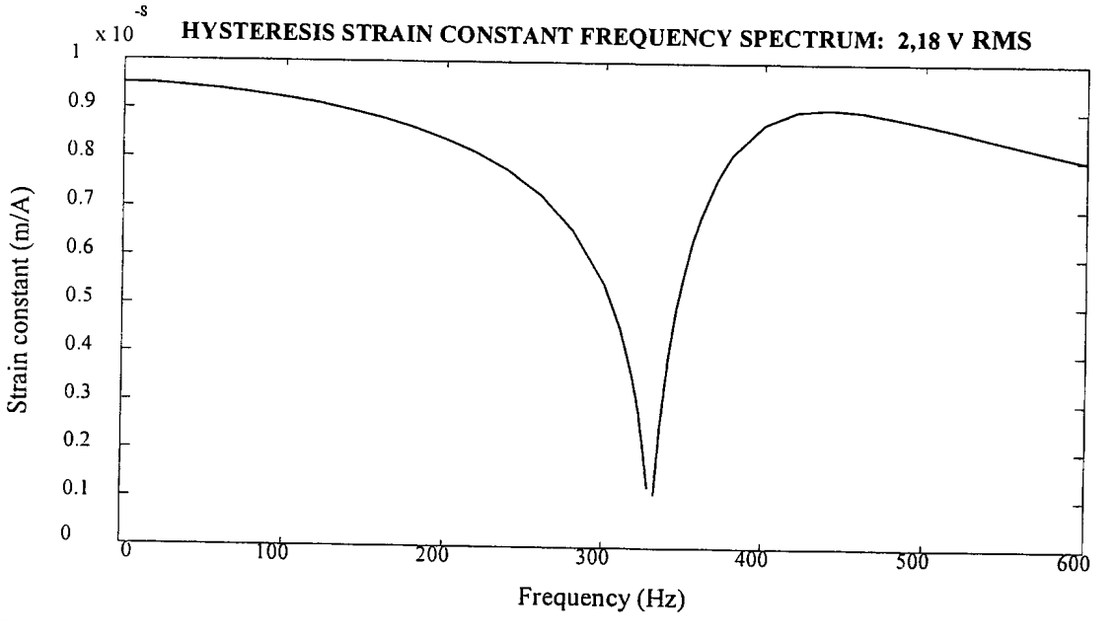

Figure K.3: Strain constant frequency spectrum, including hysteresis: 2,18 V RMS

For comparison purposes, the spectra of the strain constants for 1,63 V RMS and 1,09 V RMS inputs are shown together with that of the 2,18 V RMS input (see figure K.4). It can be seen that strain constant increases with an increase in input voltage.

The frequency spectrum of the damping coefficient, for a 2,18 V RMS input voltage, is shown in figure K.5. The damping coefficient at 0,01 Hz is $1{,}31.10^{6}$ Ns/m. A sharp notch appears between 328 Hz and 332 Hz. At the latter frequency, the damping coefficient is 4,59 Ns/m. For a frequency range of 0,01 Hz to approximately 200 Hz, damping coefficient varies hyperbolically with frequency. In this range, the mathematical relationship between frequency and damping coefficient is:

$$c(f) = \frac{13076}{f} \qquad \textbf{(K.1)}$$

where f is frequency and c is damping coefficient.

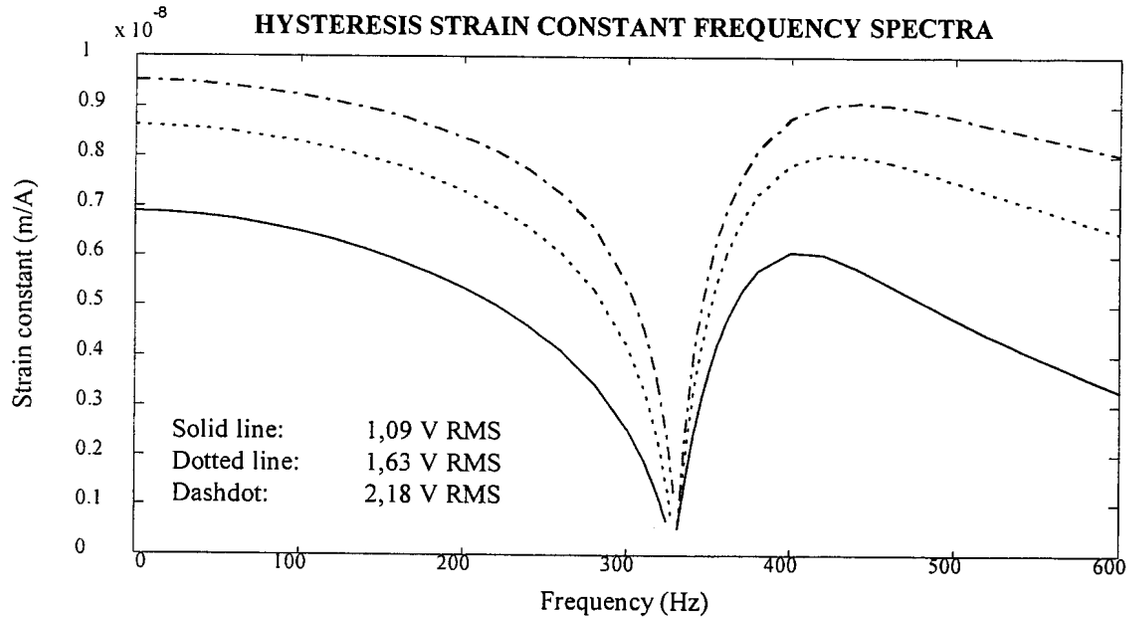

Figure K.4: **Strain constant frequency spectra, including hysteresis, for 2,18 V, 1,63 V and 1,09 V RMS coil input voltages**

The hyperbolic relationship between damping coefficient and frequency was discussed in section 2.3, where hysteresis models of Terfenol-D were derived (see also equation 2.3.15). On a logarithmic scale, the damping coefficient characteristic between 0,01 Hz and 200 Hz is a straight line, as shown in figure K.5.

The magnitude and phase of the transfer function for a 2,18 V RMS input, including hysteresis, are shown in figure K.6, together with the dehysterized magnitude and phase.

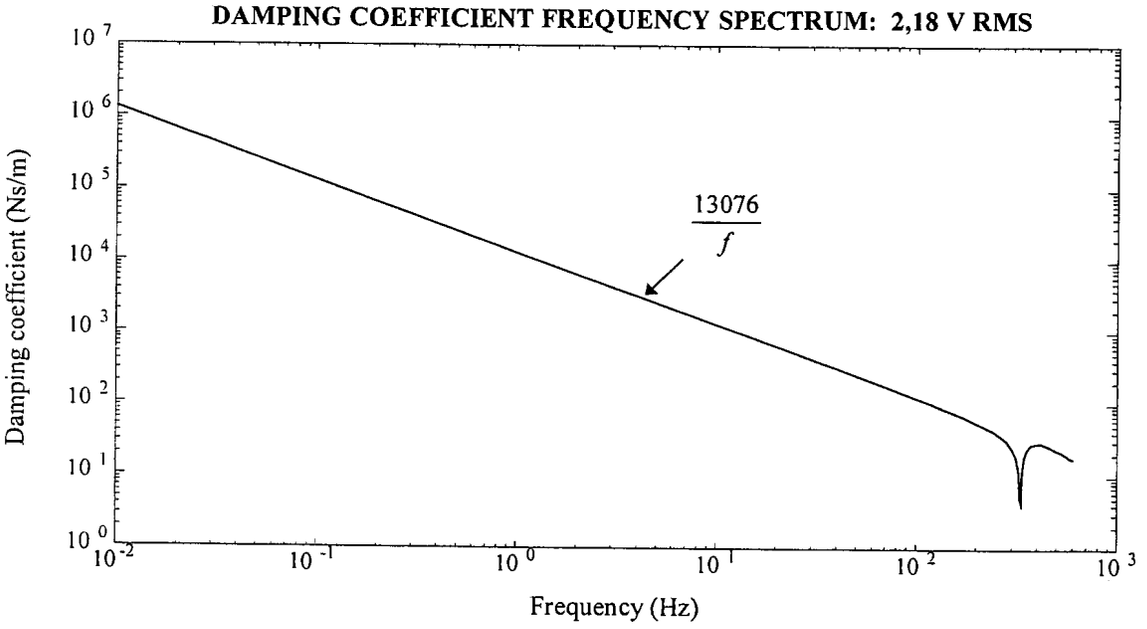

Figure K.5: **Damping coefficient frequency spectrum for 2,18 V RMS input**

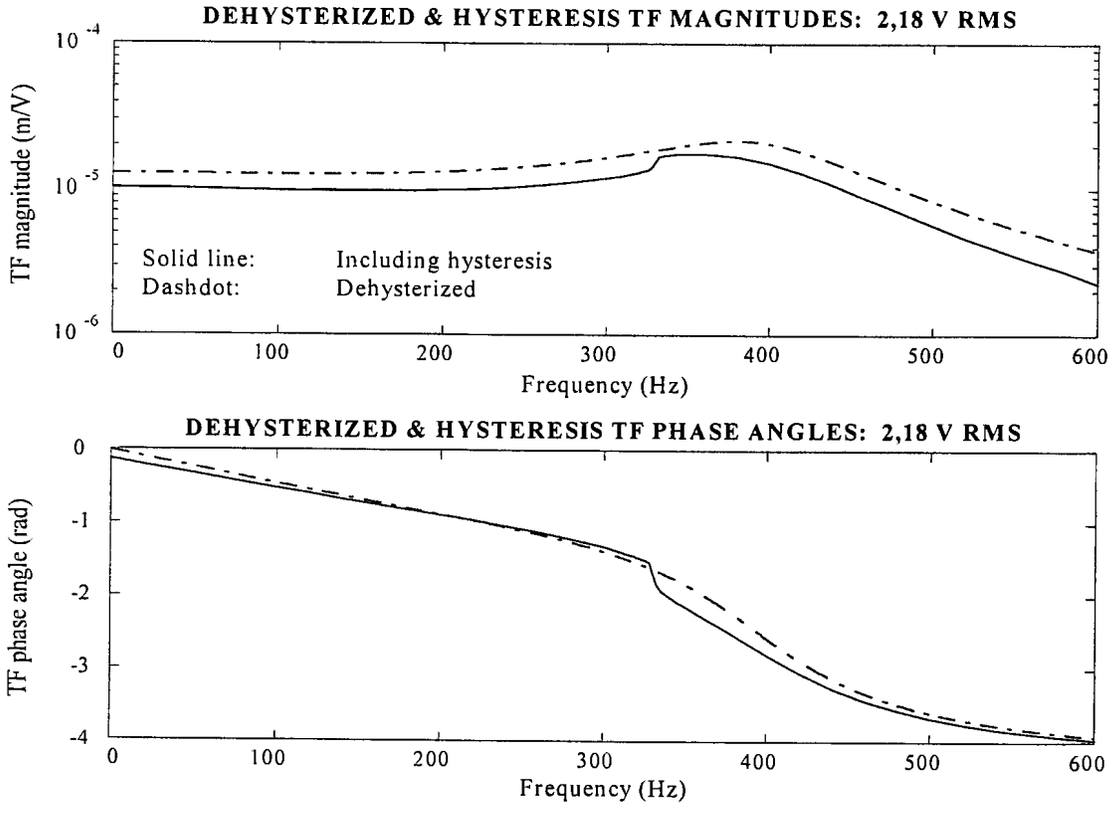

Figure K.6: Dehysterized and hysteresis transfer functions for a 2,18 V RMS input

At 0,01 Hz, the magnitude for hysteresis behaviour is 10,2 μm/V, compared with 13,57 μm/V for dehysterized behaviour (see table H.1). The resonance frequency and maximum magnitude for the hysteresis *TF* are 355 Hz and 17,7 μm/V respectively, compared with 375 Hz and 21,88 μm/V for the dehysterized *TF*. The inclusion of hysteresis effects therefore reduces magnitude at 0,01 Hz by 24,8%, resonance frequency by 5,3% and maximum magnitude by 19,1%.

Magnitude decreases slightly from 0,01 Hz to approximately 190 Hz, which can be attributed to coil inductance. At approximately 250 Hz, magnitude gradually increases with frequency. Between 328 Hz and 332 Hz, magnitude rises sharply with frequency. From 328 Hz to 370 Hz, magnitude is almost constant. Above 370 Hz, a gradual reduction in magnitude sets in. The -3 dB bandwidth is 475 Hz, which is 1,5% lower than in the dehysterized case.

The phase angle displays a peculiar characteristic, especially at low frequencies. At 0,01 Hz, phase is considerably lower that in the dehysterized case. The reason is the extremely high damping coefficient, i.e. $1{,}31.10^6$ Ns/m, at 0,01 Hz (see also figure K.5). This phase characteristic is typical of hysteretic systems.

For frequencies from 0,01 Hz to 328 Hz, the slope of the phase, with respect to frequency, is lower than in the dehysterized case. Between 328 Hz and 332 Hz, phase decreases sharply. At 332 Hz, the phase is considerably lower than in the dehysterized case. Above 332 Hz, a

gradual phase reduction sets in, until 600 Hz, where the phases of the dehysterized and hysteresis *TF's* are approximately equal.

A summary of the most important hysteresis characteristics at 0,01 Hz and resonance, for a 2,18 V RMS input, is given in table K.1.

Table K.1: Hysteresis characteristics at 0,01 Hz and resonance for a 2,18 V RMS input

Parameter	0,01 Hz	Resonance (355 Hz)
Field amplitude H_A	17618 A/m	7946 A/m
Permeability μ^σ	$5{,}57.10^{-6}$ Tm/A	$3{,}63.10^{-6}$ Tm/A
Young's modulus E	23,46 GPa	23,46 GPa
Piezomagnetic cross-coupling constant d^σ	$1{,}088.10^{-8}$ m/A	$1{,}088.10^{-8}$ m/A
Strain constant d^H	$9{,}522.10^{-9}$ m/A	$6{,}338.10^{-9}$ m/A
Damping coefficient c	$1{,}31.10^{6}$ Ns/m	24,31 Ns/m
TF magnitude	10,2 μm/V	17,7 μm/V
TF phase	-0,1263 rad	-2,205 rad
Stroke length (17,5 V p-p)	178,5 μm	309,8 μm

The transfer function spectra for 1,63 V and 1,09 V RMS inputs are shown in figures K.7 and K.8 respectively. For a 1,63 V RMS input, the magnitude at 0,01 Hz is 9,27 μm/V, which is 32,2% lower than in the dehysterized case. The maximum magnitude of 17,9 μm/V occurs at 345 Hz, a reduction of 18,5% in maximum magnitude and 8% in resonance frequency, in comparison with the dehysterized case. The -3 dB bandwidth is 470 Hz, which is 2,5% lower than in the dehysterized case.

For a 1,09 V RMS input, the magnitude at 0,01 Hz is 7,42 μm/V, which is 46% lower than in the dehysterized case. The maximum magnitude of 18,1 μm/V occurs at 340 Hz, a reduction of 17,7% in maximum magnitude and 9,3% in resonance frequency, in comparison with the dehysterized case. The -3 dB bandwidth is 445 Hz, which is 7,5% lower than in the dehysterized case.

A graphical comparison between the hysteresis transfer functions for the 2,18 V, 1,63 V and 1,09 V RMS inputs, is shown in figure K.9. The effect of input voltage on the *TF* spectra, as discussed above, is clearly visible. Furthermore, a typical nonlinear softening characteristic is displayed. This is due to the voltage dependence of the strain constant, as shown in figure K.4.

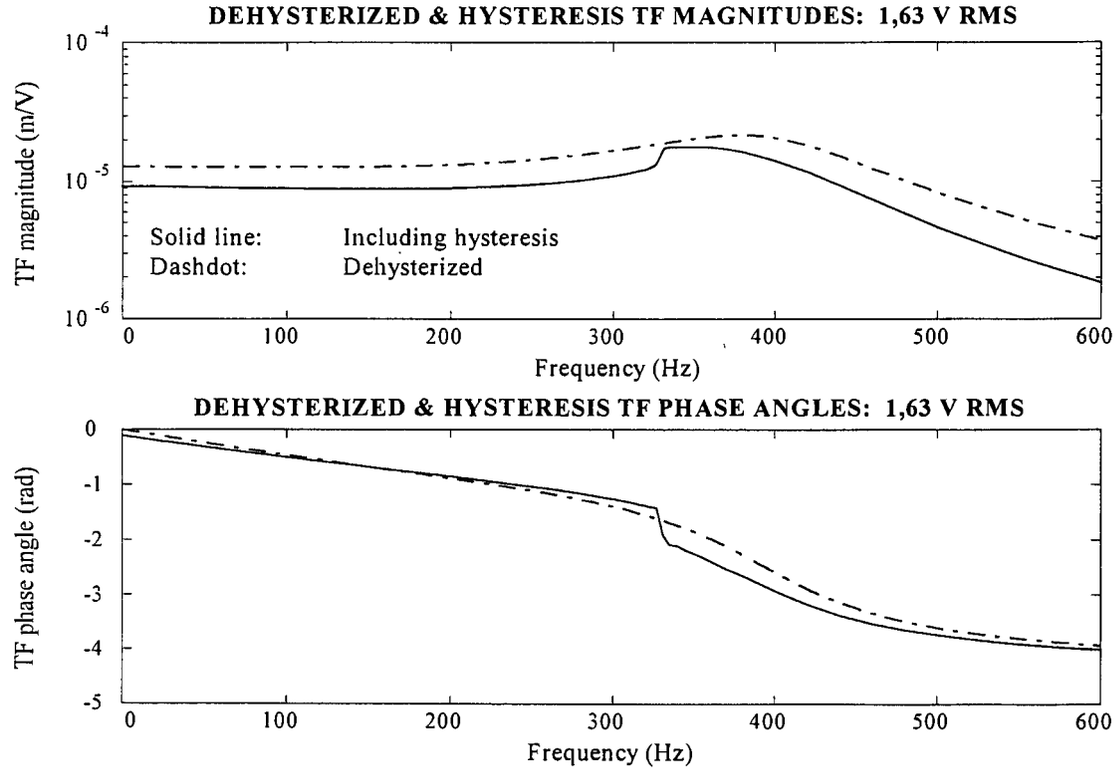

Figure K.7: Dehysterized and hysteresis transfer functions for a 1,63 V RMS input

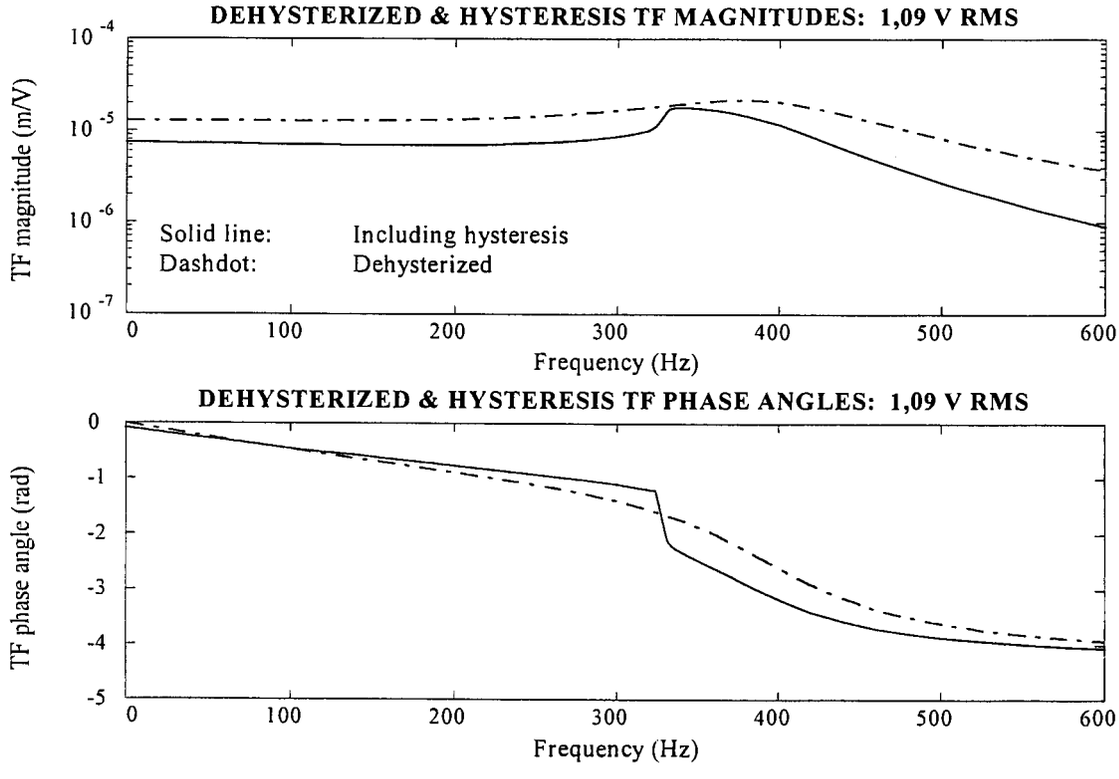

Figure K.8: Dehysterized and hysteresis transfer functions for a 1,09 V RMS input

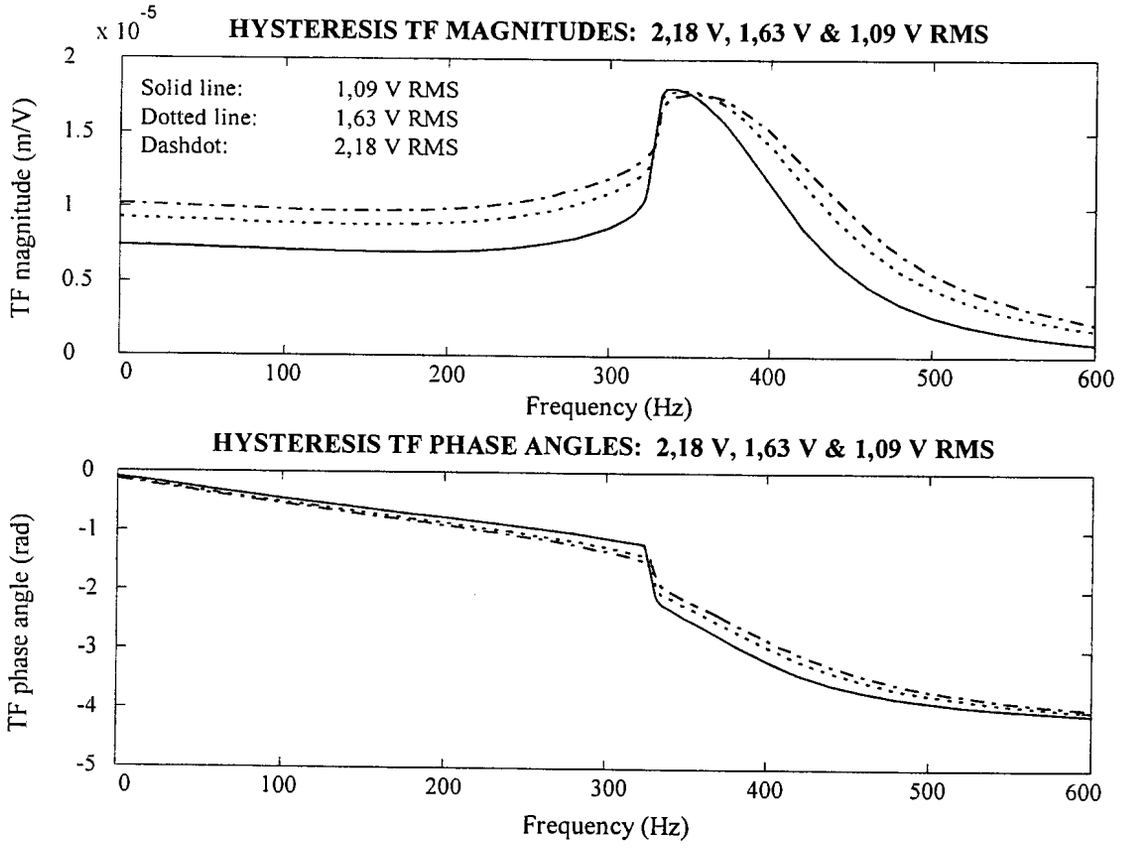

Figure K.9: Hysteresis transfer functions for 2,18 V, 1,63 V and 1,09 V RMS inputs

Appendix L
Exact separation of variables method

Consider equation 2.8.2.1:

$$\underbrace{\rho_s A_s \frac{\partial^2 w}{\partial t^2}}_{mass\ \ term} + \underbrace{E_s I_s \frac{\partial^4 w}{\partial x^4}}_{stiffness\ \ term} = P \qquad \textbf{(L.1)}$$

Using separation of variables, the exact solution to equation L.1 is expressed as:

$$w(x,t) = \sum_{i=1}^{\infty} \phi_i(x) q_i(t) \qquad \textbf{(L.2)}$$

where $\phi_i(x)$ is the i-th normal mode shape of the beam at a position x on the beam and $q_i(t)$ is the i-th modal amplitude at time t.

The equation of motion for natural behaviour of the beam, from equation L.1, is:

$$\underbrace{\rho_s A_s \frac{\partial^2 w}{\partial t^2}}_{mass\ \ term} + \underbrace{E_s I_s \frac{\partial^4 w}{\partial x^4}}_{stiffness\ \ term} = 0 \qquad \textbf{(L.3)}$$

For natural behaviour, q_i is a harmonic function of time:

$$q_i = \sin \omega_i t \qquad \textbf{(L.4)}$$

where ω_i is the i-th angular natural frequency. The differential equation describing the i-th normal mode shape, is

$$\frac{d^4 \Phi_i}{dx^4} - \beta_i^4 \Phi_i = 0 \qquad \textbf{(L.5)}$$

where β_i is the i-th eigenvalue, given by:

$$\beta_i = \left(\frac{\rho_s A_s}{E_s I_s} \omega_i^2 \right)^{\frac{1}{4}} \qquad \textbf{(L.6)}$$

The general solution of equation L.5 is:

$$\Phi_i(x) = A_i \cos \beta_i x + B_i \sin \beta_i x + C_i \cosh \beta_i x + D_i \sinh \beta_i x \qquad \textbf{(L.7)}$$

The values of β_i depend on the beam supports. Tabulated values of β_i for cantilever, simply-supported, clamped-clamped and clamped-free beams, are given by Harris [1988], Thomson [1993] and Tse et al [1978]. In most of these references, only the first four to six eigenvalues are given.

Appendix M
Derivation of system state-space model

The forced modal equation of motion of the system (equation 2.8.5.1) is:

$$M^*\ddot{q} + C^*\dot{q} + K^*q = Q \tag{M.1}$$

where M^*, C^* and K^* are normal mode mass, damping and stiffness matrices respectively and Q is the modal excitation force vector, given by:

$$Q = \int_{x=0}^{x=l} \Phi^T(x) F(x,t)\,dx \tag{M.2}$$

F is the excitation force at any point x, at time t:

$$F = F(x,t) \tag{M.3}$$

In a more concise matrix form, equation M.2 can be written as:

$$Q = \Phi^T F \tag{M.4}$$

The coordinates x_{a1} and x_{a2} of the actuator attachment points are:

$$x_{a1} = 0 \tag{M.5a}$$
$$x_{a2} = l \tag{M.5b}$$

Substitution of equations M.5 into equation M.2 and writing the resulting equation in the form of equation M.4, gives:

$$Q = \left[\Phi^T(0) \quad \Phi^T(l)\right] \begin{Bmatrix} F_{a1} \\ F_{a2} \end{Bmatrix} \tag{M.6}$$

F_{a1} and F_{a2} are the actuator excitation forces, which (from section 2.4) can be expressed as:

$$F_{a1} = \frac{A_T E N d^H}{G l_T} I_1 \tag{M.7a}$$

$$F_{a2} = \frac{A_T E N d^H}{G l_T} I_2 \tag{M.7b}$$

where I_1 and I_2 are the two actuator coil currents.

The modal equation of motion is obtained by substitution of equations M.7a and M.7b into

equation M.6 and by subsequent substitution of the resulting equation into equation M.1:

$$\ddot{q} + 2Z\Omega\dot{q} + \Omega^2 q = \frac{A_T E N d^H}{G l_T} M^{*-1}\left[\Phi^T(0) \quad \Phi^T(l)\right]\begin{Bmatrix} I_1 \\ I_2 \end{Bmatrix} \tag{M.8}$$

where Z is the diagonal modal damping matrix, whose elements are given as follows in terms of the damping coefficient C_{ii}^*, mass M_{ii}^* and natural frequency Ω_{ii} of the *i*-th normal mode:

$$Z_{ii} = \frac{C_{ii}^*}{2M_{ii}^*\Omega_{ii}} \tag{M.9}$$

The coil current equations are:

$$\dot{I}_1 = -\frac{A_T E N d^\sigma}{G l_T L_0}\dot{w}(0,t) - \frac{R_c}{L_0} I_1 + \frac{1}{L_0} V_1 \tag{M.10a}$$

$$\dot{I}_2 = -\frac{A_T E N d^\sigma}{G l_T L_0}\dot{w}(l,t) - \frac{R_c}{L_0} I_2 + \frac{1}{L_0} V_2 \tag{M.10b}$$

where V_1 and V_2 are the coil input voltages and $\dot{w}(0,t)$ and $\dot{w}(l,t)$ are the vertical translational speeds at the actuator attachment points, given by:

$$\dot{w}(0,t) = \Phi(0)\dot{q}(t) \tag{M.11a}$$

$$\dot{w}(l,t) = \Phi(l)\dot{q}(t) \tag{M.11b}$$

Substitution of equations M.11 into equations M.10 gives:

$$\begin{Bmatrix} \dot{I}_1 \\ \dot{I}_2 \end{Bmatrix} = -\frac{A_T E N d^\sigma}{G l_T L_0}\begin{bmatrix} \Phi(0) \\ \Phi(l) \end{bmatrix}\dot{q} - \frac{R_c}{L_0}\begin{bmatrix} 1 & 0 \\ 0 & 1 \end{bmatrix}\begin{Bmatrix} I_1 \\ I_2 \end{Bmatrix} + \frac{1}{L_0}\begin{bmatrix} 1 & 0 \\ 0 & 1 \end{bmatrix}\begin{Bmatrix} V_1 \\ V_2 \end{Bmatrix} \tag{M.12}$$

Combining equations M.8 and M.12 and writing the resulting system of equations in state-space form, gives:

$$\begin{Bmatrix} \{\dot{q}\} \\ \{\ddot{q}\} \\ \begin{Bmatrix} \dot{I}_1 \\ \dot{I}_2 \end{Bmatrix} \end{Bmatrix} = \begin{bmatrix} 0 & I & 0 \\ -\Omega^2 & -2Z\Omega & \frac{A_T E N d^H}{G l_T} M^{*-1}\left[\Phi^T(0) \quad \Phi^T(l)\right] \\ 0 & -\frac{A_T E N d^\sigma}{G l_T L_0}\begin{bmatrix} \Phi(0) \\ \Phi(l) \end{bmatrix} & -\frac{R_c}{L_0}\begin{bmatrix} 1 & 0 \\ 0 & 1 \end{bmatrix} \end{bmatrix}\begin{Bmatrix} \{q\} \\ \{\dot{q}\} \\ \begin{Bmatrix} I_1 \\ I_2 \end{Bmatrix} \end{Bmatrix} + \begin{bmatrix} 0 & 0 \\ 0 & 0 \\ \frac{1}{L_0}\begin{bmatrix} 1 & 0 \\ 0 & 1 \end{bmatrix} \end{bmatrix}\begin{Bmatrix} V_1 \\ V_2 \end{Bmatrix} \tag{M.13}$$

The outputs can be chosen to be the translational and rotational displacements of the instrument. The rotational displacement, which is equal to the LOS angle θ, is of prime importance. The translational displacement is not required, since it does not determine LOS accuracy. Two other outputs, which are of importance, are the vertical displacements w_1 and w_2 at the instrument attachment points x_1 and x_2 on the support structure. The difference between these two outputs, divided by the instrument length, gives the LOS angle θ.

Displacement w_1 is given by:

$$w_1 = w(x_1, t) = \Phi(x_1) q(t) \tag{M.14}$$

Displacement w_2 is given by:

$$w_2 = w(x_2, t) = \Phi(x_2) q(t) \tag{M.15}$$

The angular displacement θ of the optical instrument is:

$$\theta(t) = \frac{1}{l}(w_2 - w_1) \tag{M.16}$$

Substitution of equations M.14 and M.15 into equation M.16 gives:

$$\theta(t) = \frac{1}{l}\left(\Phi(x_2) - \Phi(x_1)\right) q(t) \tag{M.17}$$

Equations M.14, M.15 and M.17 are combined as follows in one output equation:

$$\begin{Bmatrix} w_1 \\ w_2 \\ \theta \end{Bmatrix} = \begin{bmatrix} \{\Phi(x_1)\} & \{0\} & \{0 \quad 0\} \\ \{\Phi(x_2)\} & \{0\} & \{0 \quad 0\} \\ \left\{\frac{1}{l}\left(\Phi(x_2) - \Phi(x_1)\right)\right\} & \{0\} & \{0 \quad 0\} \end{bmatrix} \begin{Bmatrix} \{q\} \\ \{\dot{q}\} \\ \begin{Bmatrix} I_1 \\ I_2 \end{Bmatrix} \end{Bmatrix} \tag{M.18}$$

Appendix N
Derivation of the complex Laplace-domain transfer function of a hydraulically-gained magnetostrictive actuator

A hydraulically-gained Terfenol-D actuator is schematically shown in figure N.1. Its equivalent mechanical model is shown in figure N.2.

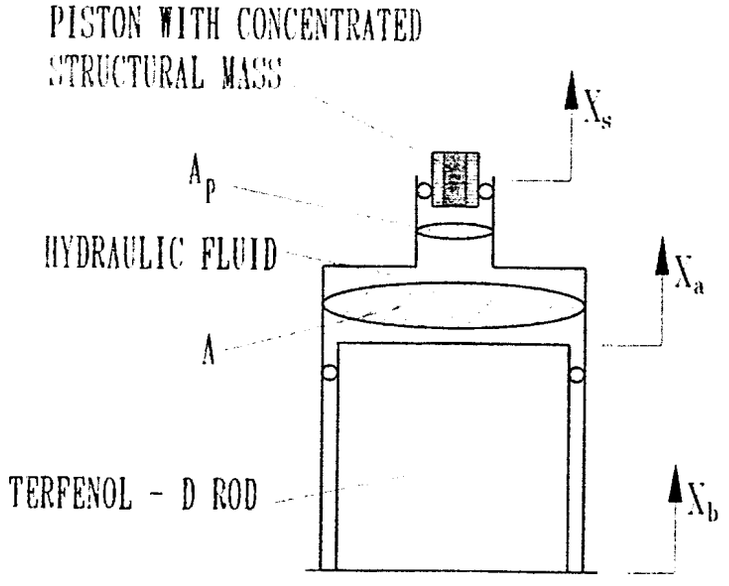

Figure N.1: Hydraulically-gained magnetostrictive actuator

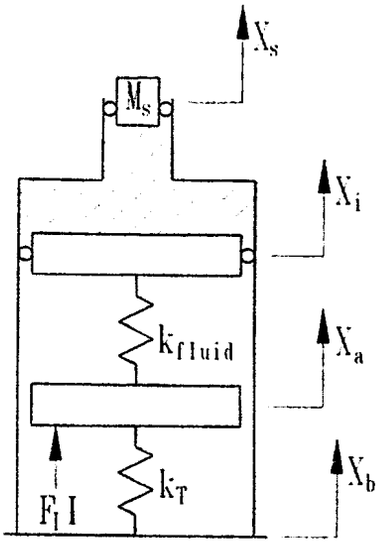

Figure N2: Equivalent mechanical model of the hydraulically-gained actuator

The derivation that follows, will be done for a static base, i.e. $x_b = 0$.

Bulk modulus and equivalent linear liquid stiffness

The bulk modulus K_B of a fluid is defined as the ratio of the change in pressure dP, to the change in volume dV per unit volume V:

$$K_B = \frac{dP}{\left(\frac{dV}{V}\right)} \tag{N.1}$$

which gives:

$$dP = \frac{K_B}{V} dV \tag{N.2}$$

Multiplication of equation N.2 with the Terfenol-D rod cross-sectional area A gives:

$$AdP = \frac{AK_B}{V} dV \tag{N.3}$$

The infinitesimal change in the force transmitted by the fluid dF_{fluid} is given by:

$$dF_{fluid} = AdP \tag{N.4}$$

The infinitesimal change in fluid volume is given by:

$$dV = Ad\left(x_a - x_i\right) \tag{N.5}$$

Substitution of equations N.4 and N.5 into equation N.3 and rewriting the resulting equation gives:

$$\frac{dF_{fluid}}{d\left(x_a - x_i\right)} = \frac{A^2 K_B}{V} \tag{N.6}$$

It can be seen from equation N.6 that the rate of change of the force transmitted by the fluid, with respect to the deflection of the rod, is directly proportional to the rod area squared, directly proportional to the fluid bulk modulus and inversely proportional to the fluid volume. A and K_B are constant, while V is not. Equation N.6 is therefore nonlinear. In order to obtain a linear force-deflection characteristic, equation N.6 must be linearized. This is done below.

During excitation of the actuator, the fluid volume will contain a DC, or reference component V_{ref} and a fluctuating component ΔV:

$$V = V_{ref} + \Delta V \tag{N.7}$$

Substitution of equation N.7 into equation N.6 gives:

$$\frac{dF_{fluid}}{d(x_a - x_i)} = \frac{A^2 K_\beta}{V_{ref} + \Delta V} \tag{N.8}$$

Dividing both the numerator and denominator of the right hand side of equation N.8 by V_{ref} gives:

$$\frac{dF_{fluid}}{d(x_a - x_i)} = \frac{\frac{A^2 K_\beta}{V_{ref}}}{1 + \frac{\Delta V}{V_{ref}}} \tag{N.9}$$

Most hydraulic fluids have high bulk moduli. $\Delta V/V_{ref}$ is therefore relatively small for most hydraulic fluids, so that the numerator on the right hand side of equation N.9 can be approximated by:

$$1 + \frac{\Delta V}{V_{ref}} \approx 1 \tag{N.10}$$

Substitution of equation N.10 into equation N.9 gives:

$$\frac{dF_{fluid}}{d(x_a - x_i)} = \frac{A^2 K_\beta}{V_{ref}} \tag{N.11}$$

It can be seen from equation N.11 that the equivalent linear liquid stiffness k_{fluid} is given by:

$$k_{fluid} = \frac{A^2 K_\beta}{V_{ref}} \tag{N.12}$$

Deflection of the Terfenol-D rod

Consider figure N.2. The deflection x_a of the rod is determined by the force balance equation:

$$k_{fluid}(x_i - x_a) - k_T x_a + F_I I = 0 \tag{N.13}$$

where I is the coil current, F_I is the force per unit current and k_T is the rod stiffness. F_I and k_T are respectively given by:

$$F_I = \frac{AENd^H}{l_T} \tag{N.14a}$$

$$k_T = \frac{AE}{l_T} \tag{N.14b}$$

Rewriting equation N.13 gives:

$$x_a = \frac{k_{fluid}}{k_{fluid} + k_T} x_i + \frac{F_l}{k_{fluid} + k_T} I \qquad \textbf{(N.15)}$$

The displacement gain is given as follows in terms of x_s and x_i:

$$G = \frac{x_s}{x_i} \qquad \textbf{(N.16)}$$

Substitution of equation N.16 into equation N.15 gives the deflection of the rod as follows in terms of x_s and I:

$$x_a = \frac{k_{fluid}}{k_{fluid} + k_T} \frac{x_s}{G} + \frac{F_l}{k_{fluid} + k_T} I \qquad \textbf{(N.17)}$$

Equation of motion

The equation of motion of the piston is:

$$\ddot{x}_s = \frac{PA_p}{m_s} + \ddot{x}_i \qquad \textbf{(N.18)}$$

where P is the fluid pressure and A_p is the piston cross-sectional area.

The displacement gain factor, in terms of the piston and rod areas, is given by:

$$G = \frac{A}{A_p} \qquad \textbf{(N.19)}$$

Substitution of equation N.19 into equation N.18 gives:

$$\ddot{x}_s = \frac{PA}{m_s G} + \ddot{x}_i \qquad \textbf{(N.20)}$$

Substitution of equation N.16 into equation N.20 and simplification of the resulting equation gives:

$$\ddot{x}_s = \frac{PA}{m_s (G - 1)} \qquad \textbf{(N.21)}$$

The force exerted by the rod on the fluid, is given by:

$$PA = k_{fluid} (x_a - x_i) \qquad \textbf{(N.22)}$$

Substitution of equation N.22 into equation N.21 gives:

$$\ddot{x}_s = \frac{k_{fluid}}{m_s(G-1)}(x_a - x_i) \tag{N.23}$$

Substitution of equation N.16 into equation N.23 and simplification of the resulting equation gives:

$$\ddot{x}_s + \frac{k_{fluid}}{m_s G(G-1)} x_s = \frac{k_{fluid}}{m_s(G-1)} x_a \tag{N.24}$$

Substitution of equation N.17 into equation N.24 gives:

$$\ddot{x}_s + \frac{k_{fluid}}{m_s G(G-1)} x_s = \frac{k_{fluid}}{m_s(G-1)}\left(\frac{k_{fluid}}{k_{fluid}+k_T}\frac{x_s}{G} + \frac{F_l}{k_{fluid}+k_T} I\right) \tag{N.25}$$

Collecting terms containing x_s on the left hand side gives:

$$\ddot{x}_s + \frac{k_{fluid}}{m_s G(G-1)}\left(1 - \frac{k_{fluid}}{k_{fluid}+k_T}\right) x_s = \frac{F_l}{m_s(G-1)}\left(\frac{k_{fluid}}{k_{fluid}+k_T}\right) I \tag{N.26}$$

Simplification of equation N.26 gives the equation of motion as follows in terms of x_s and I:

$$\ddot{x}_s + \frac{k_T}{m_s G(G-1)}\left(\frac{k_{fluid}}{k_{fluid}+k_T}\right) x_s = \frac{F_l}{m_s(G-1)}\left(\frac{k_{fluid}}{k_{fluid}+k_T}\right) I \tag{N.27}$$

Coil current equation

The coil current equation of an ungained magnetostrictive actuator is given by:

$$\dot{I} = -\frac{AENd^{\sigma}}{l_T L_0}\dot{x}_a - \frac{R_c}{L_0} I + \frac{1}{L_0} V \tag{N.28}$$

Substitution of equation N.17 into equation N.28 gives:

$$\dot{I} = -\frac{AENd^{\sigma}}{l_T L_0}\left(\frac{k_{fluid}}{k_{fluid}+k_T}\frac{\dot{x}_s}{G} + \frac{F_l}{k_{fluid}+k_T}\dot{I}\right) - \frac{R_c}{L_0} I + \frac{1}{L_0} V \tag{N.29}$$

Collecting terms containing $\dot{I}$ on the left hand side gives:

$$\left[1+\left(\frac{k_T}{k_{fluid}+k_T}\right)\frac{F_I N d^\sigma}{L_0}\right]\dot{I}=-\left(\frac{k_{fluid}}{k_{fluid}+k_T}\right)\frac{k_T N d^\sigma}{G L_0}\dot{x}_s-\frac{R_c}{L_0}I+\frac{1}{L_0}V \qquad \textbf{(N.30)}$$

The term $k_T/\left(k_{fluid}+k_T\right)$ is expressed as:

$$\frac{k_T}{k_{fluid}+k_T}=1-\frac{k_{fluid}}{k_{fluid}+k_T} \qquad \textbf{(N.31)}$$

Substitution of equation N.31 into equation N.30 gives the coil current equation as follows in terms of x_s and I:

$$\left[1+\left(1-\frac{k_{fluid}}{k_{fluid}+k_T}\right)\frac{F_I N d^\sigma}{L_0}\right]\dot{I}=-\left(\frac{k_{fluid}}{k_{fluid}+k_T}\right)\frac{k_T N d^\sigma}{G L_0}\dot{x}_s-\frac{R_c}{L_0}I+\frac{1}{L_0}V \qquad \textbf{(N.32)}$$

State-space equations

The equation of motion (N.27) and coil current equation (N.32) are simplified by defining the following two constant parameters α and β:

$$\alpha=\frac{k_{fluid}}{k_{fluid}+k_T} \qquad \textbf{(N.33a)}$$

$$\beta=1+(1-\alpha)\frac{F_I N d^\sigma}{L_0} \qquad \textbf{(N.33b)}$$

Substitution of equation N.33a into equation N.27 gives the equation of motion as:

$$\ddot{x}_s+\alpha\frac{k_T}{m_s G(G-1)}x_s=\alpha\frac{F_I}{m_s(G-1)}I \qquad \textbf{(N.34)}$$

Substitution of equations N.33 into equation N.32 and dividing both sides of the resulting equation by β gives the coil current equation as:

$$\dot{I}=-\frac{\alpha}{\beta}\frac{k_T N d^\sigma}{G L_0}\dot{x}_s-\frac{R_c}{\beta L_0}I+\frac{1}{\beta L_0}V \qquad \textbf{(N.35)}$$

The equation of motion (N.34) and coil current equation (N.35) are combined into a single set of state-space equations, in the following familiar form:

$$\dot{x} = Ax + Bu \tag{N.36a}$$
$$y = Cx + Du \tag{N.36b}$$

where

$$x = \left\{ x_s, \quad \dot{x}_s, \quad I \right\}^T \tag{N.37}$$

is the state vector,

$$u = V \tag{N.38}$$

is the coil voltage input,

$$y = x_s \tag{N.39}$$

is the actuator displacement output,

$$A = \begin{bmatrix} 0 & 1 & 0 \\ -\alpha \dfrac{k_T}{m_s G(G-1)} & 0 & \alpha \dfrac{F_l}{m_s (G-1)} \\ 0 & -\dfrac{\alpha}{\beta} \dfrac{k_T N d^{\sigma}}{G L_0} & -\dfrac{1}{\beta} \dfrac{R_c}{L_0} \end{bmatrix} \tag{N.40}$$

is the coefficient matrix,

$$B = \begin{bmatrix} 0 \\ 0 \\ \dfrac{1}{\beta L_0} \end{bmatrix}^T \tag{N.41}$$

is the driving matrix,

$$C = \begin{bmatrix} 1 & 0 & 0 \end{bmatrix} \tag{N.42}$$

is the output matrix and

$$D = 0 \tag{N.43}$$

is the transmission matrix.

Coil voltage to displacement *TF*

The coil voltage input to displacement output *TF* is obtained from:

$$\frac{X_s(s)}{U(s)} = C[sI - A]^{-1} B + D \qquad \textbf{(N.44)}$$

Substitution of equations N.40 to N.43 into equation N.44, and using the relationships for k_T and F_l in equations N.14, gives the *TF* as:

$$\frac{X_s(s)}{V(s)} = \frac{\dfrac{\alpha}{\beta}\dfrac{AENd^H}{m_s(G-1)l_T L_0}}{s^3 + \dfrac{1}{\beta}\dfrac{R_c}{L_0}s^2 + \left[\alpha\dfrac{AE}{m_s G(G-1)l_T} + \dfrac{\alpha^2}{\beta}\left(\dfrac{AEN}{l_T}\right)^2 \dfrac{d^\sigma d^H}{m_s G(G-1)L_0}\right]s + \dfrac{\alpha}{\beta}\dfrac{AE}{m_s G(G-1)l_T}\dfrac{R_c}{L_0}} \qquad \textbf{(N.45)}$$

Appendix P
Displacement gain factor for elliptical gain mechanism

Consider figure 3.4.1.4. The undeformed lengths of the major and minor axes of the ellipse are given by b and a, respectively. The displacement gain factor G is the ratio of the change in length Δa of the minor axis, to the change in length Δb of the major axis:

$$G = \frac{\Delta a}{\Delta b} \tag{P.1}$$

It is however more convenient to obtain an equation for the gain factor in terms of the change in length of the major axis only, since this will make it possible to obtain the output displacement of the gain mechanism for a given input displacement. The derivation of this equation is done as follows. Exact and approximate equations for the perimeter of an ellipse are given and compared. It will be shown that the approximate equation is reasonably accurate for a/b ratios ranging from 0,1 to 1. The approximate equation is then used to derive an expression for Δa in terms of a, b and Δb. The latter equation is substituted into equation P.1 to give the gain factor.

The exact equation for the perimeter of an ellipse, from Spiegel [1968], is:

$$P_e = 4b \int_0^{\pi/2} \sqrt{1 - k^2 \sin^2 \theta}\, d\theta \tag{P.2}$$

where P_e is the perimeter, θ is a dummy variable, which ranges from zero to the included angle between the major and minor axes, i.e. $\pi/2$, and k is a dimensionless constant, which depends on the lengths of the major and minor axes:

$$k = \frac{\sqrt{b^2 - a^2}}{b} \tag{P.3}$$

Division of equation P.2 by b, gives the ratio of the exact perimeter, to the length of the major axis:

$$\frac{P_e}{b} = 4 \int_0^{\pi/2} \sqrt{1 - k^2 \sin^2 \theta}\, d\theta \tag{P.4}$$

The integral in equation P.4 is an incomplete elliptical integral of the second kind and does not have a closed-form solution. The solution can be obtained numerically.

As an alternative, the following approximate equation can be used [Spiegel, 1968]:

$$P_e \approx 2\pi \sqrt{\frac{1}{2}\left(a^2 + b^2\right)} \tag{P.5}$$

From equation P.5, the ratio of the approximate perimeter to the length of the major axis, is obtained as:

$$\frac{P_e}{b} \approx 2\pi\sqrt{\frac{1}{2}\left[\left(\frac{a}{b}\right)^2 + 1\right]} \qquad \textbf{(P.6)}$$

The approximate and exact P_e/b ratios, for a/b ratios from 0,1 to 1, together with the percentage error of the approximate P_e/b ratio, are given in table P.1.

Table P.1: Approximate and exact P_e/b ratios for different a/b ratios

a/b	Approximate P_e/b (Equation P.6)	Exact P_e/b (Equation P.4)	% Error
0,10	4,4650	4,0574	10,05
0,20	4,5309	4,2052	7,74
0,30	4,6385	4,3910	5,64
0,40	4,7851	4,5993	4,04
0,50	4,9673	4,8444	2,54
0,60	5,1812	5,1065	1,46
0,70	5,4232	5,3817	0,77
0,80	5,6897	5,6725	0,30
0,90	5,9773	5,9732	0,07
1,00 (circle)	6,2832	6,2832	0,00

It can be seen from table P.1 that the aproximate P_e/b ratio, as obtained from equation P.6, is acceptably accurate for the given range of a/b ratios.

Equation P.6 is subsequently used to derive an equation for G in terms of a, b and Δb. It is assumed that the perimeter P_e stays constant, irrepective of Δb.

Replacing the approximate equation P.6 with an equation, squaring both sides, and rewriting gives:

$$\frac{P_e^2}{2\pi^2} = a^2 + b^2 \qquad \textbf{(P.7)}$$

For a constant perimeter, b can be increased to $b+\Delta b$, and a can be simultaneously decreased to $a-\Delta a$, without affecting the left hand side of equation P.7. Replacing a with $a-\Delta a$ and b with $b+\Delta b$ in equation P.7, gives:

$$\frac{P_e^2}{2\pi^2} = (a - \Delta a)^2 + (b + \Delta b)^2 \qquad \textbf{(P.8)}$$

Equations P.7 and P.8 are equal, therefore:

$$(a-\Delta a)^2+(b+\Delta b)^2=a^2+b^2 \qquad \textbf{(P.9)}$$

Simplification of equation P.9 gives the following quadratic equation in Δa:

$$(\Delta a)^2-2a(\Delta a)+\left[2b\Delta b+(\Delta b)^2\right]=0 \qquad \textbf{(P.10)}$$

The roots of equation P.10 are:

$$\Delta a=a\pm\sqrt{a^2-2b\Delta b+(\Delta b)^2} \qquad \textbf{(P.11)}$$

Rejection of the largest root in equation P.11 gives Δa as follows in terms of a, b and Δb:

$$\Delta a=a-\sqrt{a^2-2b\Delta b+(\Delta b)^2} \qquad \textbf{(P.12)}$$

Substitution of equation P.12 into equation P.1, gives the following expression for G in terms of a, b and Δb:

$$G=\frac{a-\sqrt{a^2-2b\Delta b+(\Delta b)^2}}{\Delta b} \qquad \textbf{(P.13)}$$

Appendix Q
Exact and approximate gain factors for octagonal flexural gain mechanism

Consider figure 3.4.1.5. The displacement gain factor is the ratio of the change in height of the octagonal gain mechanism to the elongation of the rod:

$$G = \frac{x_s}{x_a} \tag{Q.1}$$

where x_a is the product of the strain ε in the rod and the rod length l_T:

$$x_a = \varepsilon l_T \tag{Q.2}$$

and x_s is given by:

$$x_s = 2(h_0 - h) \tag{Q.3}$$

The initial height h_0 of the slanted beam is given by:

$$h_0 = r\sin\theta_0 \tag{Q.4}$$

and the final height h is given by:

$$h = \sqrt{r^2 - \left(r\cos\theta_0 + \frac{x_a}{2}\right)^2} \tag{Q.5}$$

The final height is obtained in terms of the rod strain and length, by substitution of equation Q.2 into equation Q.5:

$$h = \sqrt{r^2 - \left(r\cos\theta_0 + \frac{\varepsilon l_T}{2}\right)^2} \tag{Q.6}$$

Substitution of equations Q.4 and Q.6 into equation Q.3 gives x_s as follows:

$$x_s = 2\left(r\sin\theta_0 - \sqrt{r^2 - \left(r\cos\theta_0 + \frac{\varepsilon l_T}{2}\right)^2}\right) \tag{Q.7}$$

The exact gain factor is obtained by substitution of equations Q.7 and Q.2 into equation Q.1:

$$G = 2\frac{r\sin\theta_0 - \sqrt{r^2 - \left(r\cos\theta_0 + \frac{\varepsilon l_T}{2}\right)^2}}{\varepsilon l_T} \tag{Q.8}$$

Approximate gain factor

An approximate equation for the displacement gain, in terms of θ_0, is subsequently derived.

From equation Q.8:

$$\frac{G\varepsilon l_T}{2} - r\sin\theta_0 = -\sqrt{r^2 - \left(r\cos\theta_0 + \frac{\varepsilon l_T}{2}\right)^2} \qquad \textbf{(Q.9)}$$

Squaring both sides of equation Q.9 gives:

$$\left(\frac{G\varepsilon l_T}{2} - r\sin\theta_0\right)^2 = r^2 - \left(r\cos\theta_0 + \frac{\varepsilon l_T}{2}\right)^2 \qquad \textbf{(Q.10)}$$

Expanding terms on both sides of equation Q.10 gives:

$$\left(\frac{G\varepsilon l_T}{2}\right)^2 - G\varepsilon l_T r\sin\theta_0 + r^2\sin^2\theta_0 = r^2 - r^2\cos^2\theta_0 - \varepsilon l_T r\cos\theta_0 - \left(\frac{\varepsilon l_T}{2}\right)^2 \qquad \textbf{(Q.11)}$$

Neglecting 2nd order terms and noting that $\sin^2\theta_0 + \cos^2\theta_0 \equiv 1$, equation Q.11 reduces to:

$$-G\varepsilon l_T r\sin\theta_0 \approx -\varepsilon l_T r\cos\theta_0 \qquad \textbf{(Q.12)}$$

From equation Q.12, the following approximate equation for G, in terms of θ_0, results:

$$G \approx \cot\theta_0 \qquad \textbf{(Q.13)}$$

A graphical comparison between the gain factors calculated with equations Q.8 and Q.13, for initial angles ranging from 5° to 30°, an active rod length of 35 mm, strain of 1000 $\mu\varepsilon$ and slanted beam radius of 19 mm, is shown in figure Q.1.

The error of the approximate gain factor, relative to the exact gain factor, is shown in figure Q.2. It can be seen that the approximate gain factor is sufficiently accurate for initial angles ranging from 5° to 30°, i.e. for gains ranging from 1,7 to 11,4. The error is less than 5% for angles larger than 5,8° and less than 1° for angles larger than 12,8°.

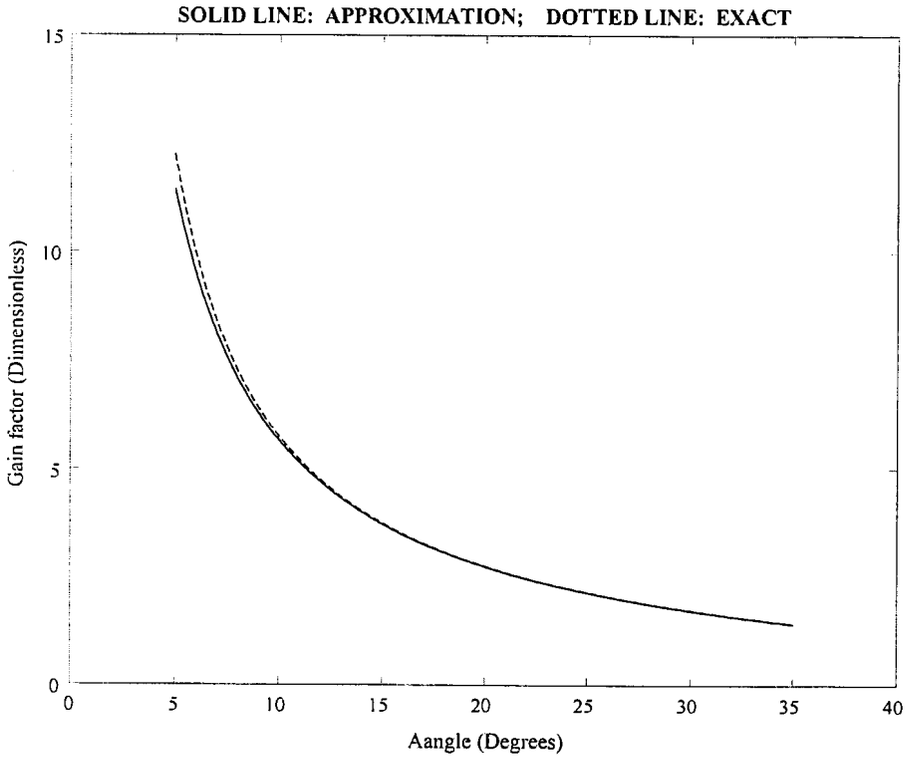

Figure Q.1: Approximate and exact gain factors versus initial angle of slanted beam

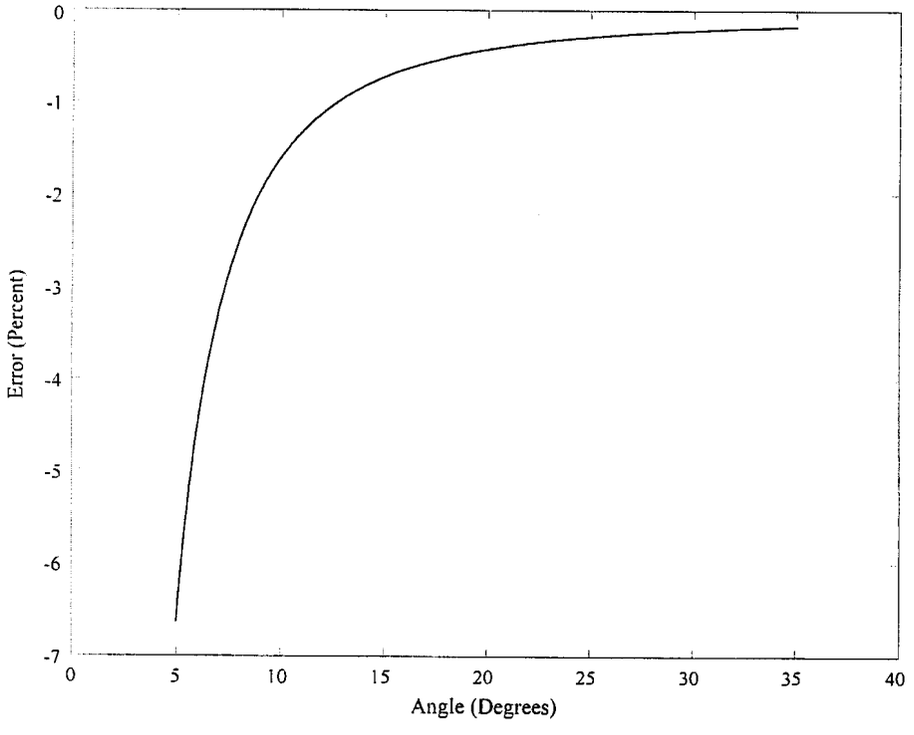

Figure Q.2: Error of approximate gain factor versus initial angle of slanted beam

Appendix R
Volume of a permanent magnet

Consider figure 3.4.2.1. The fluxes in the magnet, Terfenol-D rod and air gap between the end caps and magnet, are respectively given by:

$$\phi_m = B_m A_m \quad \textbf{(R.1a)}$$
$$\phi_T = B_T A_T \quad \textbf{(R.1b)}$$
$$\phi_g = B_g A_g \quad \textbf{(R.1c)}$$

where ϕ_m, ϕ_T and ϕ_g are the fluxes in the magnet, rod and air gap respectively. B_m, B_T and B_g are the flux densities in the magnet, rod and air gap respectively. A_m, A_T and A_g are the cross-sectional areas of the magnet, rod and air gap respectively.

The flux in the magnet is equal to the flux in the rod and the flux in the air gap:

$$\phi_m = \phi_T = \phi_g \quad \textbf{(R.2)}$$

Substitution of equations R.1a to R.1c into equation R.2 gives:

$$B_g = \frac{B_T A_T}{A_g} \quad \textbf{(R.3a)}$$

$$B_m = \frac{B_T A_T}{A_m} \quad \textbf{(R.3b)}$$

The total magnetomotive force in the loop is zero:

$$H_m l_m + H_T l_T + H_g l_g = 0 \quad \textbf{(R.4)}$$

where H_m is the demagnetizing force in the magnet and H_T and H_g are the field in the rod and the field in the gap respectively. l_m, l_T and l_g are the magnet, rod and gap lengths respectively.

In equation R.4, it is assumed that the permeability of the end caps is infinite. The assumption is justifiable, for two reasons. In the first place, the end caps are made of steel, which has a relatively high permeability. Secondly, the end caps are relatively thin in comparison with the rod length.

Equation R.4 can be written as:

$$H_m l_m = -H_T l_T - H_g l_g \quad \textbf{(R.5)}$$

The field in the gap is given by:

$$H_g = \frac{B_g}{\mu_0} \tag{R.6}$$

where $\mu_0 = 4\pi.10^{-7}\ Tm/A$ is the permeability of free space.

Substitution of equation R.6 into equation R.3a gives:

$$H_g = \frac{B_T A_T}{\mu_0 A_g} \tag{R.7}$$

Subsequent substitution of equation R.7 into equation R.5 gives:

$$H_m l_m = -\frac{B_T A_T l_g}{\mu_0 A_g} - H_T l_T \tag{R.8}$$

H_m is obtained as follows from equation R.8:

$$H_m = -\frac{1}{l_m}\left(\frac{B_T A_T l_g}{\mu_0 A_g} - H_T l_T\right) \tag{R.9}$$

Multiplying equation R.3b with equation R.9 gives:

$$B_m H_m = -\frac{B_T A_T}{A_m l_m}\left(\frac{B_T A_T l_g}{\mu_0 A_g} - H_T l_T\right) \tag{R.10}$$

The magnet volume V_m is given by:

$$V_m = A_m l_m \tag{R.11}$$

Substitution of equation R.11 into equation R.10 gives:

$$B_m H_m = -\frac{B_T A_T}{V_m}\left(\frac{B_T A_T l_g}{\mu_0 A_g} - H_T l_T\right) \tag{R.12}$$

Rewriting equation R.12 gives:

$$V_m = \frac{B_T A_T}{B_m H_m}\left(H_T l_T - \frac{B_T A_T l_g}{\mu_0 A_g}\right) \tag{R.13}$$

The flux density in the rod is a function of the field in the rod:

$$B_T = B_T(H_T) \tag{R.14}$$

The required field in the rod is equal to the bias field:

$$H_T = H_b \tag{R.15}$$

Substitution of equation R.15 into equation R.14 gives the flux density in the rod in terms of the bias field:

$$B_T = B_T(H_b) \tag{R.16}$$

Substitution of equations R.15 and R.16 into equation R.13 gives:

$$V_m = \frac{B_T(H_b)A_T}{B_m H_m}\left(H_b l_T - \frac{B_T(H_b)A_T l_g}{\mu_0 A_g}\right) \tag{R.17}$$

Appendix S
Maximum coil power for electromagnetic field biasing

The coil current, in terms of the magnetic field, is given by (see equation 3.4.2.7):

$$I = \frac{l_T}{N} H \tag{S.1}$$

The coil voltage, in terms of the field, is given by (see equation 3.4.2.10):

$$V = \frac{l_T}{N} \sqrt{R_c^2 + \omega^2 L_0^2}\, H \tag{S.2}$$

The coil power is the product of the coil voltage and coil current:

$$P = VI \tag{S.3}$$

Substitution of equations S.1 and S.2 into equation S.3 gives the following equation for coil power in terms of magnetic field:

$$P = \left(\frac{l_T}{N}\right)^2 \sqrt{R_c^2 + \omega^2 L_0^2}\, H^2 \tag{S.4}$$

Parameters which are of particular importance in the analysis of the electromagnetic field biasing, are the maxima of the coil current, voltage and power. For excitation frequencies that are considerably lower than the coil R_c/L_0 ratio, the phase angle of the coil can be ignored. It can therefore be assumed that the maximum voltage and current coincide with the maximum field. By sustitution of $H = H_{max}$ into equations S.1, S.2 and S.4, the maximum current, voltage and power are given by:

$$I_{max} = \frac{l_T}{N} H_{max} \tag{S.5a}$$

$$V_{max} = \frac{l_T}{N} \sqrt{R_c^2 + \omega^2 L_0^2}\, H_{max} \tag{S.5b}$$

$$P_{max} = \left(\frac{l_T}{N}\right)^2 \sqrt{R_c^2 + \omega^2 L_0^2}\, H_{max}^2 \tag{S.5c}$$

In equations S.5, the maximum field is the sum of the bias field H_b and the amplitude H_A of the AC component of the field:

$$H_{max} = H_b + H_A \tag{S.6}$$

By substitution of equation S.6 into equations S.5, the maximum coil current, voltage and power are expressed as follows:

$$I_{\max} = \frac{l_T}{N}\left(H_b + H_A\right) \tag{S.7a}$$

$$V_{\max} = \frac{l_T}{N}\sqrt{R_c^2 + \omega^2 L_0^2}\left(H_b + H_A\right) \tag{S.7b}$$

$$P_{\max} = \left(\frac{l_T}{N}\right)^2 \sqrt{R_c^2 + \omega^2 L_0^2}\left(H_b + H_A\right)^2 \tag{S.7c}$$

Appendix T
Fundamental natural frequency of a simply-supported beam with a concentrated mass attached at the centre and which is subjected to a compressive axial force

The fundamental natural frequency of a beam with a concentrated mass at the centre, and which is subjected to an axial force acting at the beam ends, is analyzed in the following steps. The fundamental natural frequency of a simply-supported, uniform beam is first analyzed in the absence of any concentrated mass or axial force. The effect of the concentrated mass is then added. For the purpose of simplifying the analysis, the concentrated mass is expressed in terms of an equivalent density, which is added to the beam material density to give the total distributed beam density.

The next step will be to write the fundamental natural frequency of a uniform beam, which is subjected to an axial force. The frequency is then adjusted by replacing the beam material density with the total distributed density, to include the effect of the concentrated mass.

The fundamental angular natural frequency ω_1 of a simply-supported uniform beam, in the absence of any concentrated mass, can be obtained from the following equation:

$$\omega_1^2 = \left(\frac{\pi}{l_T}\right)^4 \frac{EI}{\rho A_T} \qquad \textbf{(T.1)}$$

where E is Young's modulus of the rods, I is the second moment of area of the rod cross-section, ρ is the density of the rod material, A_T is the rod cross-sectional area and l_T is the rod length.

The relationship between the natural frequency f_1 and the angular natural frequency ω_1 is:

$$f_1 = \frac{1}{2\pi}\omega_1 \qquad \textbf{(T.2)}$$

By taking the square root of the terms on both sides of equation T.1, and substitution of the resulting equation into equation T.2, the fundamental natural frequency is obtained as:

$$f_1 = \frac{1}{2\pi}\left(\frac{\pi}{l_T}\right)^2 \sqrt{\frac{EI}{\rho A_T}} \qquad \textbf{(T.3)}$$

An equation of the same form as equation T.3, for the fundamental natural frequency of a beam with a concentrated mass attached at the centre, is required. This will facilitate inclusion of the effect of the axial force. To this end, the concentrated mass is first expressed in terms of an equivalent density. The equivalent density is then added to the beam material density to give the distributed density of the beam.

The equivalent density ρ_{eq} is given by the following equation:

$$\rho_{eq} = \frac{2m_c}{A_T l_T} \tag{T.4}$$

where m_c is the concentrated mass.

The distributed density ρ_{distr} is the sum of the beam material density and the equivalent density:

$$\rho_{distr} = \rho + \rho_{eq} \tag{T.5}$$

Substitution of equation T.4 into equation T.5 gives the distributed density as follows in terms of the beam material density and concentrated mass:

$$\rho_{distr} = \rho\left(1 + \frac{2m_c}{\rho A_T l_T}\right) \tag{T.6}$$

The fundamental natural frequency of the beam with a mass attached at the centre, is expressed as follows in the form of equation T.3:

$$f_1 = \frac{1}{2\pi}\left(\frac{\pi}{l_T}\right)^2 \sqrt{\frac{EI}{\rho_{distr} A_T}} \tag{T.7}$$

where ρ_{distr} is given by equation T.6.

Substitution of equation T.6 into equation T.7 gives the fundamental natural frequency of a simply-supported beam with a concentrated mass at the centre, as:

$$f_1 = \frac{1}{2\pi\sqrt{1 + 2\,m_c/(\rho A_T l_T)}}\left(\frac{\pi}{l_T}\right)^2 \sqrt{\frac{EI}{\rho A_T}} \tag{T.8}$$

It can be seen from equation T.8 that the addition of a concentrated mass at the beam centre lowers the fundamental natural frequency.

The effect of the axial force on the fundamental natural frequency of the beam can now be included. The fundamental natural frequency of a uniform, simply-supported beam subjected to an axial compressive force F_b acting at the ends, can be obtained from the following equation [Tse et al, 1978]:

$$\omega_1^2 = \left(\frac{\pi}{l_T}\right)^4 \frac{EI}{\rho A_T} - \left(\frac{\pi}{l_T}\right)^2 \frac{F_b}{\rho A_T} \tag{T.9}$$

The first term on the right hand side represents the natural frequency of the uniform beam, as given by equation T.2, and the second term corrects for the axial force. Note that the second term is negative for a compressive force, implying that a compressive force lowers the beam natural frequency. By substitution of equation T.2 into equation T.9 and taking the square root on both sides of the resulting equation, the fundamental natural frequency of a uniform beam subjected to an axial force at the ends, is given by:

$$f_1 = \frac{1}{2\pi}\sqrt{\left(\frac{\pi}{l_T}\right)^4 \frac{EI}{\rho A_T} - \left(\frac{\pi}{l_T}\right)^2 \frac{F_b}{\rho A_T}} \qquad \textbf{(T.10)}$$

In order to include the effect of the concentrated mass on the natural frequency, the material density ρ in equation T.10 is replaced with the distributed density ρ_{distr}:

$$f_1 = \frac{1}{2\pi}\sqrt{\left(\frac{\pi}{l_T}\right)^4 \frac{EI}{\rho_{distr} A_T} - \left(\frac{\pi}{l_T}\right)^2 \frac{F_b}{\rho_{distr} A_T}} \qquad \textbf{(T.11)}$$

Finally, by substitution of equation T.6 into equation T.11, the fundamental natural frequency of a simply-supported beam with a concentrated mass attached at the centre and which is subjected to compressive axial force, is given by:

$$f_1 = \frac{1}{2\pi}\sqrt{\left(\frac{\pi}{l_T}\right)^4 \frac{EI}{\rho(1+2m_c/\rho A_T l_T)A_T} - \left(\frac{\pi}{l_T}\right)^2 \frac{F_b}{\rho(1+2m_c/\rho A_T l_T)A_T}} \qquad \textbf{(T.12)}$$

Appendix U
Linear and nonlinear system identification models and techniques

U.1 Linear system identification models and techniques

The objective of linear identification is to obtain a system in transfer function or state-space form from measured data. Different models have been developed for this purpose, such as the following: AR (Auto Regressive), MA (Moving Average), ARX (Auto Regressive with eXogenous inputs), ARMA (Auto Regressive Moving Average), ARMAX (Auto Regressive Moving Average with eXogenous inputs) and ARIMA (Auto Regressive Integrated Moving Average). In mechanical system identification terminology, "exogenous inputs" refers to measurement noise.

The ARMA model is widely used for discrete time-domain identification of linear systems. The model is a combination of the AR and MA models. Output at the current time step is expressed in terms of previous outputs, previous inputs and the current input, using the discrete delay element z^{-1}. The current output is given by:

$$Y(z) = Y(z)\sum_{k=1}^{N} a_k z^{-k} + U(z)\sum_{k=0}^{M} b_k z^{-k} \qquad \textbf{(U.1.1)}$$

where $Y(z)$ is the z-domain output, $U(z)$ is the z-domain input, a_k is the k-th output delay gain and b_k is the k-th input delay gain. N is the number of output delay elements used in the model and M is the number of input delays. The z-domain TF is given by:

$$G(z) = \frac{Y(z)}{U(z)} = \frac{\sum_{k=0}^{M} b_k z^{-k}}{1 - \sum_{k=1}^{N} a_k z^{-k}} \qquad \textbf{(U.1.2)}$$

Regression methods are used to determine the gains. Regression methods will be discussed in short later.

Time-domain model from free-decay system response

The method used for obtaining system parameters from free-decay response is known as the complex exponential method. The output is written as a linear series of exponentially decaying functions in complex conjugate pairs. Each function is represented by a modal amplitude and an eigenvalue. A number of methods for determining the amplitudes and eigenvalues exist, such as the Prony and Ibrahim time-domain (ITD) methods [Ewins, 1991]. The Prony method is limited in its application by the fact that the number of poles contained in the response data must be known in advance and the data must be noise-free. Many techniques have been developed to improve the performance of the method, two of which are based on singular value decomposition (SVD) and oversized eigenmatrix methods.

Identification models for time-varying systems

Various model types may be used to represent characteristics and behaviour of time-dependent systems, such a discrete-time and state-space models. In both model types, characteristics vary with time. In discrete-time models, the a_k's and b_k's in equation U.1.2 are functions of time. Identification of time-varying systems is described in more detail by Bittanti et al [1992] and Kashyap & Rao [1976]. The difference between time-invariant and time-dependent state-space models was discussed in short in section 2.5 (see equations 2.5.1.1 to 2.5.1.3). In linear time-dependent state-space systems, state and output matrices are of the form $A = A(t)$, $B = B(t)$, $C = C(t)$ and $D = D(t)$. If a discrete-time model of the system is known, state and output matrices can be obtained from the coefficients a_k and b_k.

Regression techniques

Regression techniques are used to determine system model coefficients. Least-squares (LS) models are generally used for off-line identification of parameters. This method of identification may however be time-consuming.

In order to speed up the process, real-time identification tools, such as exponentially-weighted recursive least-squares (RLS) algorithms, have been developed. RLS identification is described by, inter alia, Goodwin & Sin [1984], Kim [1997] and Schoukens & Pintelon [1991]. The least-square error is given by Cowan & Grant [1985] as:

$$E_{n+1} = \sum_{i=1}^{n+1} w^{n+1-i} \left| \hat{y} - y \right|^2 \qquad \textbf{(U.1.3)}$$

where E is the identification model error and w is an exponential weighting function of time, such that $0 \leq w \leq 1$. $\hat{y}$ is the modelled output and y is the measured output. E is a function of the coefficient, or parameter vector, C:

$$E = E(C) \qquad \textbf{(U.1.4)}$$

where $C = \{a_1, a_2, \ldots, a_N \quad b_0, b_1, \ldots, b_M\}^T$. The parameter vector is determined in real-time.

For off-line identification, the weighting function is unity. The parameter vector is obtained by setting the partial derivatives of E with respect to each of the parameters, equal to zero:

$$\frac{\partial E}{\partial C_l} = 0, \quad l = 1, 2, \cdots, N + M + 1 \qquad \textbf{(U.1.5)}$$

where C_l the l-th element of the coefficient vector.

For linear-in-the-parameters models, the solution of equation U.1.5 can be obtained using orthogonal, linear LS solution techniques. For nonlinear-in-the-parameters models, the

Gauss-Newton and Newton-Raphson methods are generally used. The Gauss-Newton method is described in appendix V.

Laplace- and frequency domain *TF* models from discrete time-domain models

The complex Laplace-domain *TF* of a system whose time-domain *TF* is known, is obtained by substitution of z with e^{sT} in equation U.1.2:

$$z = e^{sT} \tag{U.1.6}$$

where s is the complex Laplace-domain differential operator and T is sample time. The transfer function $G(s)$ can be written in the form:

$$G(s) = \frac{\sum_{k=0}^{M} p_k s^k}{\sum_{l=0}^{N} q_l s^l} \tag{U.1.7}$$

where the p_k's and q_l's are the numerator and denominator polynomial coefficients respectively.

The complex ω-domain *TF* of a system whose time-domain *TF* is known, is obtained by substitution of z with $e^{j\omega T}$ in equation U.1.2:

$$z = e^{j\omega T} \tag{U.1.8}$$

The transfer function $G(j\omega)$ can be written in the following form:

$$G(j\omega) = \frac{\sum_{k=0}^{M} p_k (j\omega)^k}{\sum_{l=0}^{N} q_l (j\omega)^l} \tag{U.1.9}$$

where the p_k's and q_l's are the numerator and denominator polynomial coefficients respectively, which are equal to those in equation U.1.7.

The polynomial coefficients can be determined if the a_k's and b_k's in equation U.1.2 are known. If not, the *TF* model must be available in some other form, such as measured spectra.

Frequency-domain models from measured *TF* spectra

The objective is to obtain system *TF* spectra that match the experimentally measured spectra as closely as possible. A vast number of ω domain identification techniques exist. The technique used will mainly depend on system characteristics, e.g. linearity and number of degrees of freedom. Linear frequency-domain identification techniques can broadly be classified as SDOF and MDOF identification techniques.

Frequency-domain identification of an SDOF system can be done by means of the peak-amplitude method, circle fit method and the so-called inverse method [Ewins, 1991]. Receptance properties are used in the peak amplitude and circle fit methods to determine system characteristics, while inverse receptance properties are used in the "inverse method".

The receptance curve (*X/F*) of an SDOF system displays, inter alia, a peak amplitude and two frequencies where the amplitudes are 70,7% of the peak amplitude. The frequency where the peak occurs, is the natural frequency f_n. The two frequencies where the amplitudes are 70,7% of the peak amplitude, are the half-power points. The half-power bandwidth is denoted by Δf. The dimensionless damping factor ζ is given by the equation $\zeta = 2\Delta f / f_n$. This identification method is known as the peak amplitude method. Stiffness and mass are respectively given by:

$$k = \left[(X/F)\big|_{f=0} \right]^{-1} \qquad \textbf{(U.1.10a)}$$

$$m = k/(2\pi f_n)^2 \qquad \textbf{(U.1.10b)}$$

The Nyquist plot of the receptance of an SDOF system is a circle in the complex plane. This circle is known as the modal circle. Natural frequency, damping factor and modal amplitude can be calculated from the circle properties. The procedure is not given here, but is described in full by Ewins [1991]. This method is known as the circle-fit method and is widely used for frequency-domain identification of SDOF systems.

An alternative to the circle-fit method, is the "inverse" method. In the complex plane, the inverse receptance curve (*F/X*) produces a horizontal straight line. The maximum real value of *F/X* is *k*, the spring constant. The intercept of the line with the imaginary axis gives the damping $c\omega$ directly. The frequency at the origin of the graph, i.e. where the real and imaginary axes cross, is the natural frequency.

Three types of MDOF frequency-domain identification techniques are discussed here. The first type is the circle-fit method, which is an extension of the SDOF circle-fit method. The method is described by Ewins [1991]. The method cannot be used if the modes are closely-coupled or if damping is extremely light. (Closely coupled modes occur in systems where the natural frequencies are closely-spaced or where damping is high, or both).

A more general approach to multi-mode curve-fitting is an LS data fit to measured *TF* frequency spectra in complex form. Depending on reliability of measured data and system characteristics, more accurate data fits are generally obtained than with the circle fit method. One disadvantage of the method is that the LS problem is nonlinear, which requires iterative solution techniques, such as the Newton-Raphson and Gauss-Newton methods. As is the

case with all iterative techniques, starting values in the range of convergence of the numerical system, are required. Furthermore, poles of the fitted *TF* may be unstable, even for globally stable plants. The LS method for frequency-domain identification is discussed in short by Ewins [1991].

The third method is identification using overdetermined systems, as described by Braun & Ram [1987]. Model order is assumed higher than that of the physical system. The method was developed to overcome the problem of specifying model order in the presence of noise. Singular value decomposition is used to solve the LS data fitting problem.

State-space identification of linear systems

State-space identification techniques can broadly be classified as direct and indirect techniques. Indirect techniques are applied to convert existing time-, frequency- or Laplace-domain models to state-space models. Direct models are used to obtain state-space models from measured spectra without intermediate steps.

Conversion of *s*-domain models to state-space models is described by Schwarzenbach & Gill [1986]. The *TF* (*Y*/*U*) is written as the product of two functions in *s*:

$$\frac{Y(s)}{U(s)} = \frac{Y(s)}{V(s)} \frac{V(s)}{U(s)} \qquad \textbf{(U.1.11)}$$

where $Y(s)/V(s)$ is the numerator, divided by the highest power of *s*, and $V(s)/U(s)$ is the denominator, divided by the highest power of *s*. *V*/*U* is written as a linear DE and expressed in canonical state-space form. The output is expressed in terms of the state vector and input, in the form of equation 2.5.1.3b.

A similar technique can be used to convert discrete-time models to discrete state-space form if the a_k and b_k coefficients in equation U.1.2 are known. The state and output equations of a linear discrete system are:

$$x(k+1) = \Phi x(k) + \Gamma u(k) \qquad \textbf{(U.1.12a)}$$

$$y(k) = Hx(k) + Ju(k) \qquad \textbf{(U.1.12b)}$$

where $x(k)$, $u(k)$ and $y(k)$ are the *k*-th state vector, input and output respectively. Φ, Γ, *H* and *J* are the coefficient-, driving-, output- and transmission matrix, respectively.

The discrete state and output matrices are related to their respective continuous equivalents by means of the following equations [Franklin et al, 1990] and [Liu & Miller, 1995]:

$$\Phi = e^{AT} \tag{U.1.13a}$$

$$\Gamma = \int_0^T e^{A\eta} B d\eta \tag{U.1.13b}$$

$$H = C \tag{U.1.13c}$$

$$J = D \tag{U.1.13d}$$

where T is the sample period and η is an integration variable.

State-space models can be directly obtained from measured spectra, using, for instance, the Frequency domain Observability Range Space Extraction (FORSE) algorithm. The algorithm is explained in detail by Liu et al [1996]. It uses proper state-space parameterization and Singular Value Decomposition (SVD) to ensure good numerical properties for multivariable and high dimensional structural systems. It achieves high accuracy in the frequency domain by overparameterizing the model. The FORSE algorithm is an extension of the ORSE time-domain identification algorithm [Liu & Miller, 1995].

U.2 Nonlinear system identification models and techniques

Techniques for determining the parameters of nonlinear systems from measured data can broadly be classified as time-domain techniques, frequency-domain techniques, force-state component identification and identification using neural networks.

Time-domain identification techniques for nonlinear systems

Similar models to the linear time-invariant models have been developed for time-domain identification of nonlinear systems. Two of the most popular models are as the NARX (Nonlinear Auto Regressive with eXogenous inputs) and NARMAX (Nonlinear Auto Regressive Moving Average with eXogenous inputs) models. The NARX model is a special case of the NARMAX model. The NARMAX model is described by Chen et al [1989] and Worden et al [1994]. Othogonal LS data fit techniques, such as the classical Gram-Schmidt (CGS) and modified Gram-Schmidt (MGS) schemes, Householder transformation and Givens method can be used to determine model parameters [Chen et al, 1989].

Force-state component identification

Force-state component identification is done to obtain the restoring force f in a component or structure in terms of the state vector x and its derivative with respect to time, $\dot{x}$.

The equation of motion is written in the following form:

$$m\ddot{x} + f(x,\dot{x}) = p(t) \qquad \textbf{(U.2.1)}$$

where $p(t)$ is the load vector.

f can be determined for a large variety of nonlinearities, e.g. nonlinear spring and nonlinear damping characteristics, nonlinearities with memory and combinations of linear and nonlinear stiffness and damping.

Characteristics may be represented mathematically, i.e. by $f(x,\dot{x})$, or graphically, by a 3-dimensional force-state map. Force-state component identification is described in more detail by Masters et al [1996], Worden & Tomlinson [1988] and Wright & Al Haddid [1991].

Frequency-domain identification of nonlinear systems

Nonlinear frequency-domain identification can broadly be classified as SDOF identification, modal analysis (for MDOF systems), and identification using time-domain inputs. The SDOF and modal analysis identification techniques are, in essence, extensions of linear system identification methods. Two SDOF identification techniques are the circle fit method, as described by Ewins [1991] and the use of response-surface plots, as explained by Dimas & Pardoen [1988].

Modal analysis identification methods for MDOF systems include the Hilbert transform method, the use of functional series (Volterra method) and range-dependent linear identification. The Hilbert transform method is a well-known linearization technique in the fields of numerical signal processing of filters, acoustics and physics. It is extended to MDOF mechanical system identification by Vinh et al [1984] and Simon & Tomlinson [1984]. The frequency response function (*FRF*) of an MDOF system, for a sinusoidal input, is expressed in terms of an equivalent linear *TF*. The method can be applied to systems with strong nonlinearities and no a priori assumption of the nonlinearities is required. The disadvantage, however, is that the method is more difficult to apply to identification procedures where random excitation is used.

The Volterra system model consists of two parts, i.e. a linear system model and a nonlinear extension to the model, using higher order terms. In the ω-domain, the linear term is expressed by a classical Fourier transform of the *TF*. The nonlinear terms are written as multiple convolutions, using Volterra kernels. The ω-domain representation of the nonlinear part is obtained by taking the multi-dimensional Fourier transform of the higher order terms. Two difficulties associated with the method are the number of terms required for accurate

modelling and efficient methods of computing multi-dimensional Fourier transforms (MDFT's). The Volterra method is explained in more detail by Tomlinson [1986].

A third method is range-dependent linearization. The system is assumed linear for a given input energy level. Linear identification is done for each input energy level, using linear MDOF techniques. The effects of nonlinearities on the ω-domain *FRF* for a constant input energy level are ignored. This method is applicable if the system is weakly nonlinear or if the nonlinearity only has a significant influence outside the frequency band of interest. The disadvantage is that characterization tests must be done for each input energy level in order to determine the effect of the nonlinearity on the *FRF*.

Nonlinear frequency-domain identification is often done from measured time-domain inputs and responses, using methods such as the NARMAX method. Application of the NARMAX method to nonlinear frequency response estimation is described by Billings et al [1988]. The NARMAX method is a convenient method of expressing inputs and outputs as higher order series. The model is validated in the time domain and transformed to the frequency-domain. The procedure is as follows: The input is first assumed to be harmonic. The input is substituted in the NARMAX model and the output amplitude at the given frequency is calculated, using harmonic balance. A second harmonic is added to the input. The output amplitude is calculated as a function of the two input frequencies. The procedure is repeated until the amplitudes of all the desired frequencies have been obtained.

Identification using neural networks

Neural network identification makes use of parallel distributed processing to identify the internal forces of structure-unknown nonlinear dynamic systems typically encountered in the field of applied mechanics [Masri et al, 1992]. Identification of the restoring force of an SDOF system is described by Masri et al [1993]. The restoring force $g(y,\dot{y})$ is written in terms of the measured input $u(t)$, acceleration $\ddot{y}(t)$ and mass m as:

$$g(y,\dot{y}) = u(t) - m\ddot{y}(t) \qquad \textbf{(U.2.2)}$$

Measured signals are discretized and fed into the neural network. Network output is an approximate restoring force $\hat{g}(y,\dot{y})$. The identification procedure consists of two phases, i.e. the network learning phase and the evaluation phase. The procedure is described in detail by Masri et al [1993].

Appendix V
Gauss-Newton method applied to LS identification in the frequency domain

The difference between the modelled *TF* and experimentally-determined *TF* is known as the estimation error and is given by:

$$e = G - \hat{G} \tag{V.1}$$

where e is the error, $\hat{G}$ is the modelled *TF* and G is the experimentally-determined *TF*. G is known at discrete frequencies, thus the error can only be evaluated at these frequencies. The error e_r at the r-th frequency is:

$$e_r = G_r - \hat{G}_r \tag{V.2}$$

where G_r and $\hat{G}_r$ are the measured *TF* and approximate *TF* at the r-th frequency, given by:

$$G_r = G(j\omega_r) \tag{V.3a}$$
$$\hat{G}_r = \hat{G}(j\omega_r) \tag{V.3b}$$

It can be seen from equations V.2 and V.3 that the error varies with frequency. As a globally accurate model is required, the error squared is summed and minimized over the frequency band. The global error is given by:

$$E = \sum_{r=1}^{R} e_r^2 \tag{V.4}$$

where E is the global error and of the model and R is the number of discrete frequencies.

Both G and $\hat{G}$ are complex (see equations V.3). The global error can therefore be expressed as the sum of the error of the real term squared, plus the error of the imaginary term squared [Schoukens & Pintelon, 1991]:

$$E = \sum_{r=1}^{R}\left[\left(\mathrm{Re}\{G_r\} - \mathrm{Re}\{\hat{G}_r\}\right)^2 + \left(\mathrm{Im}\{G_r\} - \mathrm{Im}\{\hat{G}_r\}\right)^2\right] \tag{V.5}$$

E is a nonlinear function of the polynomial coefficient vector C:

$$E = E(C) \tag{V.6}$$

C is given as follows in terms of the TF numerator and denominator polynomial coefficients:

$$C = \{p_0, p_1, \cdots, p_M, \quad q_0, q_1, \cdots, q_N\}^T \tag{V.7}$$

where M and N are the numerator and denominator polynomial orders respectively.

From equation V.4, E can be expressed in matrix notation as:

$$E = e^T e \tag{V.8}$$

Substitution of equation V.1 into equation V.8 gives:

$$E = \left(G - \hat{G}\right)^T \left(G - \hat{G}\right) \tag{V.9}$$

where G and $\hat{G}$ are R x 1 vectors and E is a 1 x 1 scalar.

The objective of LS identification is to determine the parameter vector C, which minimizes E. C is obtained by setting the partial derivatives of E with respect to each of the parameters C_l, equal to zero and by solving for C_l:

$$\frac{\partial E}{\partial C_l} = 0, \quad l = 1, 2, \cdots, N + M + 2 \tag{V.10}$$

where C_l is the l-th element of the coefficient vector.

The solution of equation V.10 is determined iteratively. An initial estimate of C is made, which will not necessarily satisfy equation V.10. The initial estimate is known as the starting value. Using the estimated C, the error gradient $\partial E/\partial C$ is calculated, from which the change ΔC in the parameter vector is obtained. C is added to ΔC to obtain an updated parameter vector. The updated C is subsequently used to calculate $\partial E/\partial C$. If the error gradient is sufficiently close to zero, the procedure is stopped. This condition is known as the stopping criterion. If the stopping criterion is not met, ΔC, C and $\partial E/\partial C$ are updated and the procedure is repeated until the stopping criterion is met.

The starting value must be selected within a limited range, known as the system range of convergence. If the starting value is selected outside this range, the method will diverge. If the starting value is selected inside the range of convergence, the method will either converge to a local minimum, or to the global minimum. The selection of starting values of a system with unknown coefficients is generally difficult. The method suggested by Schoukens & Pintelon [1991] is to linearize equation V.4, in order to obtain the linear solution to equation V.10 and to use this solution as a starting value. With a known starting value, ΔC can be calculated, using the procedure set out below.

For a small increment ΔC in equation V.6, the estimation error can be written as follows, using a Taylor series expansion:

$$E(C+\Delta C)=E(C)+(\Delta C)^T\frac{\partial E}{\partial C}+\frac{1}{2}(\Delta C)^T\frac{\partial^2 E}{\partial C^2}\Delta C+\cdots+ \qquad \textbf{(V.11)}$$

where C and $\partial E/\partial C$ are (N+M+2) x 1 vectors. $\partial^2 E/\partial C^2$ is an (N+M+2) x (N+M+2) matrix.

The partial derivative of equation V.11 with respect to ΔC is:

$$\frac{\partial E(C+\Delta C)}{\partial \Delta C}=\frac{\partial E(C)}{\partial \Delta C}+\frac{\partial E}{\partial C}+\frac{\partial^2 E}{\partial C^2}\Delta C+\cdots+ \qquad \textbf{(V.12)}$$

For E to be a minimum, the partial derivative of $E(C+\Delta C)$ with respect to ΔC must be zero:

$$\frac{\partial E(C+\Delta C)}{\partial \Delta C}=0 \qquad \textbf{(V.13)}$$

The first term on the right hand side of equation V.11 is constant, therefore:

$$\frac{\partial E(C)}{\partial \Delta C}=0 \qquad \textbf{(V.14)}$$

Substitution of equations V.13 and V.14 into equation V.12 gives:

$$\frac{\partial E}{\partial C}=-\frac{\partial^2 E}{\partial C^2}\Delta C \qquad \textbf{(V.15)}$$

ΔC is obtained from equation V.15 as:

$$\Delta C=-\left(\frac{\partial^2 E}{\partial C^2}\right)^{-1}\frac{\partial E}{\partial C} \qquad \textbf{(V.16)}$$

It can be seen from equation V.16 that ΔC depends on both 1st order and 2nd order derivatives of E with respect to C. It is however more convenient to express ΔC in terms of the 1st order derivative only. This is done with the aid of equation V.9.

The 1st order partial derivative of E with respect to C, from equation V.9, is given by:

$$\frac{\partial E}{\partial C}=-2\left(\frac{\partial \hat{G}}{\partial C}\right)^T\left(G-\hat{G}\right) \qquad \textbf{(V.17)}$$

where $\partial\hat{G}/\partial C$ is an R x (N+M+2) matrix.

$\partial^2 E/\partial C^2$ is obtained by partial differentiation of equation V.17 with respect to C. For a small error, $\partial^2 E/\partial C^2$ is given by:

$$\frac{\partial^2 E}{\partial C^2} = 2\left(\frac{\partial \hat{G}}{\partial C}\right)^T\left(\frac{\partial \hat{G}}{\partial C}\right) \qquad \textbf{(V.18)}$$

Substitution of equationsV.17 and V.18 into equation V.16 gives:

$$\Delta C = \left[\left(\frac{\partial \hat{G}}{\partial C}\right)^T\left(\frac{\partial \hat{G}}{\partial C}\right)\right]^{-1}\left(\frac{\partial \hat{G}}{\partial C}\right)^T\left(G - \hat{G}\right) \qquad \textbf{(V.19)}$$

Methods of determining the stopping criterion are explained by Schoukens & Pintelon [1991]. For the purpose of this study, the stopping criterion can either be a relatively small change in E, or a negligible increment ΔC in the parameter vector. The former stopping criterion may be mathematically expressed as:

$$\frac{E(C + \Delta C)}{E(C)} \leq \alpha \qquad \textbf{(V.20)}$$

where α is an arbitrarily selected factor, e.g. 0,1%.

If system sensitivity to parameter variations is low, equation V.20 will not necessarily guarantee a negligible ΔC. For systems of this type, the following stopping criterion is recommended:

$$\frac{\Delta C_l}{C_l} \leq \alpha \qquad \textbf{(V.21)}$$

The stopping criterion given in equation V.21 is generally stricter than that in equation V.20, since the latter may give a parameter vector whose elements do not satisfy equation V.21.

Appendix W
Derivation of system transmissibility and two-input model

System transmissibility (*TR*) can be expressed in terms of transfer functions such as the input force to output force *TF*, base angular displacement to output angular displacement *TF* (θ/θ_b), base angular velocity to output angular velocity *TF* ($\dot{\theta}/\dot{\theta}_b$) and base angular acceleration to output angular acceleration *TF* ($\ddot{\theta}/\ddot{\theta}_b$). The most appropriate transfer function is mainly determined by the sensors used for system characterization and control.

Accelerometers were used for dynamic system characterization in chapter 4. The measured vertical accelerations were subsequently used to calculate the base and output angular accelerations (see section 4.5.1). Accelerometers will also be used as sensors during testing of the control system. It is therefore appropriate to express the *TR* as the transfer function between base angular acceleration and output angular acceleration ($\ddot{\theta}/\ddot{\theta}_b$).

The transmissibility is required in terms of system characteristics, such as state and output parameters, natural frequencies, damping factors and normal mode shapes. A derivation of the *TR* follows below. In order to simplify the derivation, an assumption is made that the *TR* is independent of sensor dynamics. The consequence of this assumption is that the transfer functions, θ/θ_b, $\dot{\theta}/\dot{\theta}_b$ and $\ddot{\theta}/\ddot{\theta}_b$, are equal over a wide frequency bandwidth. This makes it possible to derive the transfer function θ/θ_b and set it equal to $\ddot{\theta}/\ddot{\theta}_b$:

$$TR = \frac{\ddot{\theta}}{\ddot{\theta}_b} = \frac{-\omega^2\theta}{-\omega^2\theta_b} = \frac{\theta}{\theta_b} \qquad \textbf{(W.1)}$$

Consider figure 5.5.1. The displacement of the moving base is denoted by y_b. The base mass, stiffness and excitation force, are respectively denoted by k_b, m_b and F_b.

In this derivation, y_b is a known signal, i.e. the disturbance signal. For a known base displacement, the system displacement vector is given by:

$$y = \left\{ \{y_{a1}\} \quad w_s(x) \quad \{y_{a2}\} \right\}^T \qquad \textbf{(W.2)}$$

The equation of motion of actuator II, for a base *translational* displacement input y_b, is:

$$\begin{bmatrix} m_{a21} & 0 \\ 0 & m_{a22} \end{bmatrix} \begin{Bmatrix} \ddot{y}_{a21} \\ \ddot{y}_{a22} \end{Bmatrix} + \begin{bmatrix} k_{211}+k_{212} & -k_{212} \\ -k_{212} & k_{212}+k_{222} \end{bmatrix} \begin{Bmatrix} y_{a21} \\ y_{a22} \end{Bmatrix} = \begin{Bmatrix} k_{211} \\ k_{222} \end{Bmatrix} y_b \qquad \textbf{(W.3)}$$

The equation of motion, for a base *angular* displacement input θ_b, is:

$$\begin{bmatrix} m_{a21} & 0 \\ 0 & m_{a22} \end{bmatrix} \begin{Bmatrix} \ddot{y}_{a21} \\ \ddot{y}_{a22} \end{Bmatrix} + \begin{bmatrix} k_{211}+k_{212} & -k_{212} \\ -k_{212} & k_{212}+k_{222} \end{bmatrix} \begin{Bmatrix} y_{a21} \\ y_{a22} \end{Bmatrix} = l \begin{Bmatrix} k_{211} \\ k_{222} \end{Bmatrix} \theta_b \qquad \textbf{(W.4)}$$

where l is the horizontal distance between the two actuators.

The equation of motion of motion of actuator II, in modal coordinates, is:

$$M_{a1} \begin{Bmatrix} \ddot{q}_{a21} \\ \ddot{q}_{a22} \end{Bmatrix} + K_{a1} \begin{Bmatrix} q_{a21} \\ q_{a22} \end{Bmatrix} = \{F_{a2}\} \qquad \textbf{(W.5)}$$

where $\{F_{a2}\}$ is the modal excitation force vector, given by:

$$\{F_{a2}\} = l \psi_{a2}^T \begin{Bmatrix} k_{211} \\ k_{222} \end{Bmatrix} \theta_b \qquad \textbf{(W.6)}$$

The system equation of motion, in component modal coordinates, is:

$$M\ddot{q} + Kq = F \qquad \textbf{(W.7)}$$

where F is the modal base excitation force.

M, K, q and F are respectively given by:

$$M = \begin{bmatrix} [M_{a1}] & & \\ & [M_s] & \\ & & [M_{a2}] \end{bmatrix} \qquad \textbf{(W.8a)}$$

$$K = \begin{bmatrix} [K_{a1}] & & \\ & [K_s] & \\ & & [K_{a2}] \end{bmatrix} \qquad \textbf{(W.8b)}$$

$$q = \begin{Bmatrix} \{q_{a1}\} \\ \{q_s\} \\ \{q_{a2}\} \end{Bmatrix} \qquad \textbf{(W.8c)}$$

$$F = \begin{Bmatrix} \{0\} \\ \{0\} \\ \{F_{a2}\} \end{Bmatrix} \qquad \textbf{(W.8d)}$$

The sizes of M and K are 14 x 14 each, while those of q and F are 14 x 1 each.

The equations of motion of the actuators and structure are currently uncoupled. Coupling is done by means of the modal coupling equation:

$$q = Cq_r \tag{W.9}$$

where q_r is the coupled modal displacement vector and C is the coupling matrix, given by:

$$C = \begin{bmatrix} 1 & \{0\} & 0 \\ 1 & -\{\psi_s(0)\} & 0 \\ \{0\} & [I] & \{0\} \\ 0 & \{0\} & 1 \\ 0 & -\{\psi_s(l)\} & 1 \end{bmatrix} \tag{W.10}$$

The sizes of C and q_r are 14 x 12 and is 12 x 1 respectively. The coupling matrix given above, is the C-matrix given in equation 5.5.38, whose last row and last column are deleted.

The coupled system modal equation of motion is:

$$M_r\ddot{q}_r + K_r q_r = F_r \tag{W.11}$$

where M_r and K_r are given by equations 5.5.41 and F_r is given by:

$$F_r = C^T F \tag{W.12}$$

The reduced coordinate vector q_r is written as follows in terms of the eigenvector U and the normal mode displacement vector q_n (see equation 5.5.42):

$$q_r = Uq_n \tag{W.13}$$

The sizes of U and q_n are 12 x 12 and 12 x 1 respectively.

Substitution of equation W.13 into equation W.11 and premultiplication of the resulting equation with U^T, gives:

$$M^*\ddot{q}_n + K^* q_n = Q \tag{W.14}$$

where M^* and K^* are the normal mode mass and stiffness matrices respectively, as given by equations 5.5.48. Q is the modal excitation force vector, given by:

$$Q = U^T C^T F \tag{W.15}$$

Premultiplication of equation W.14 with M^{*-1} gives the normal mode equation of motion in the following form:

$$\ddot{q}_n + \Omega^2 q_n = M^{*-1} Q \tag{W.16}$$

where Ω is the diagonal natural frequency matrix.

Adding modal damping terms to equation W.16 gives:

$$\ddot{q}_n + 2Z\Omega\dot{q}_n + \Omega^2 q_n = M^{*-1}Q \qquad \textbf{(W.17)}$$

The modal state and output equations can be written as follows:

$$\dot{x} = A_h x + B_h \theta_h \qquad \textbf{(W.18a)}$$
$$\theta = C_h x + D_h \theta_h \qquad \textbf{(W.18b)}$$

The state vector x is:

$$x = \begin{Bmatrix} q_n \\ \dot{q}_n \end{Bmatrix} \qquad \textbf{(W.19)}$$

A_h, B_h, C_h and D_h are respectively given by:

$$A_h = \begin{bmatrix} 0 & I \\ -\Omega^2 & -2Z\Omega \end{bmatrix} \qquad \textbf{(W.20a)}$$

$$B_h = \begin{Bmatrix} \{0\} \\ M^{*-1}U^T C^T \begin{Bmatrix} \{0\} \\ \{0\} \\ l\psi_{a2}^T \begin{Bmatrix} k_{211} \\ k_{222} \end{Bmatrix} \end{Bmatrix} \end{Bmatrix} \qquad \textbf{(W.20b)}$$

$$C_h = \begin{Bmatrix} \dfrac{\Phi_s(x_2) - \Phi_s(x_1)}{x_2 - x_1} & \{0\} \end{Bmatrix} \qquad \textbf{(W.20c)}$$

$$D_h = 0 \qquad \textbf{(W.20d)}$$

The sizes of A_h, B_h, C_h and D_h are 24 x 24, 24 x 1, 1 x 24 and 1 x 1 respectively.

Combining equations W.18 to W.20 gives:

$$\begin{Bmatrix} \dot{q}_n \\ \ddot{q}_n \end{Bmatrix} = \begin{bmatrix} 0 & I \\ -\Omega^2 & -2Z\Omega \end{bmatrix} \begin{Bmatrix} q_n \\ \dot{q}_n \end{Bmatrix} + \begin{Bmatrix} \{0\} \\ M^{*-1} U^T C^T \begin{Bmatrix} \{0\} \\ \{0\} \\ l\psi_{a2}^T \begin{Bmatrix} k_{211} \\ k_{222} \end{Bmatrix} \end{Bmatrix} \end{Bmatrix} \theta_b \qquad \textbf{(W.21a)}$$

$$\theta = \begin{bmatrix} \dfrac{\Phi_s(x_2) - \Phi_s(x_1)}{x_2 - x_1} & \{0\} \end{bmatrix} \begin{Bmatrix} q_n \\ \dot{q}_n \end{Bmatrix} \qquad \textbf{(W.21b)}$$

The system transmissibility is the *TF* between θ_b and θ is given by:

$$\frac{\theta}{\theta_b} = C_b [sI - A_b]^{-1} B_b \qquad \textbf{(W.22)}$$

By application of equation W.1, the *TR*, i.e. the *TF* between $\ddot{\theta}_b$ and $\ddot{\theta}$, is given by:

$$\frac{\ddot{\theta}}{\ddot{\theta}_b} = C_b [sI - A_b]^{-1} B_b \qquad \textbf{(W.23)}$$

The number of state equations, for the selected number of actuator and optical instrument assumed modes, is 24. The system as described by equations W.21 has 24 eigenvalues in complex conjugate pairs. However, many of the eigenvalues occur at high frequencies, well above the bandwidth, and have no significant effect on system performance inside the band. States corresponding with these frequencies, can therefore be eliminated. This was also done for the coil voltage input, where, apart from the three coil states, only the first ten mechanical subsystem states were retained. For the base input, the 5th and 10th states (corresponding with the 5th normal mode) are eliminated, while the 1st to 4th and 6th to 9th states (corresponding with the first four normal modes) are retained.

The transmissibility magnitude and phase spectra, for a frequency bandwidth of 0 to 500 Hz, are shown in figure W.1.

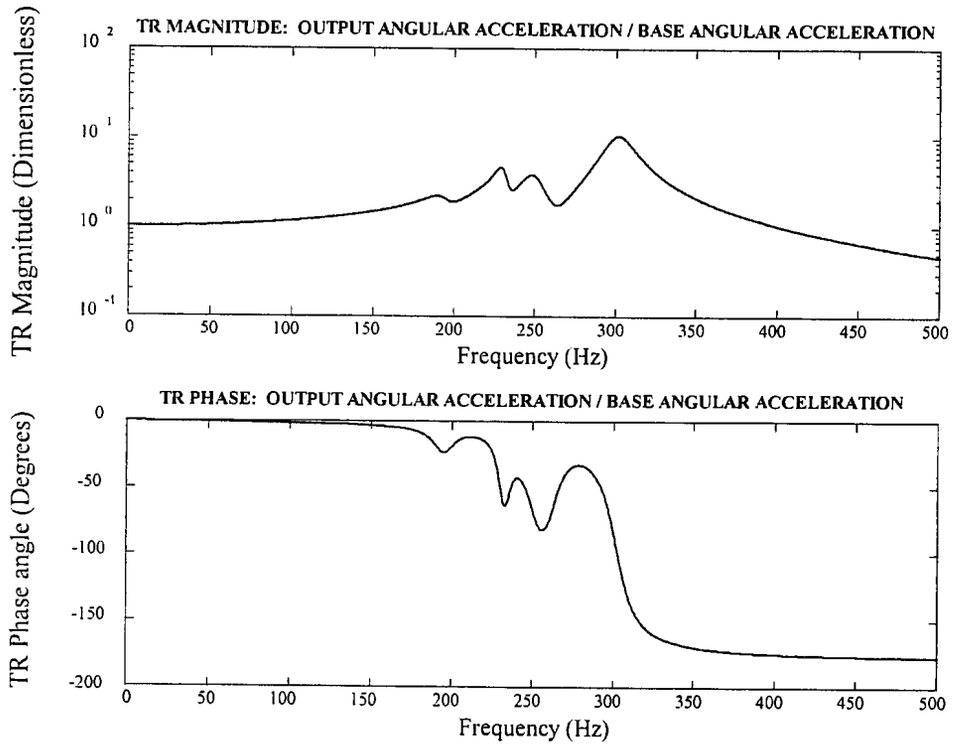

Figure W.1: System base to output transmissibility spectra

Two-input state-space model for control system analysis and design purposes

The state-space model of the system currently consists of two separate state models, one for the coil voltage input, given by equations 5.6.6 to 5.6.9, and one for the base angular acceleration input, given by equations W.18 to W.23. For the purpose of analyzing and designing the control system, it is convenient to combine the two state models into a single state model, with two simultaneous inputs, i.e. coil voltage and base angular acceleration. The coil voltage is the controllable input, while the base motion is the disturbance. The state and output equations, for these two inputs, are:

$$\dot{x} = Ax + B\begin{Bmatrix} V \\ \ddot{\theta}_b \end{Bmatrix} \qquad \textbf{(W.24a)}$$

$$\ddot{\theta} = Cx + D\begin{Bmatrix} V \\ \ddot{\theta}_b \end{Bmatrix} \qquad \textbf{(W.24b)}$$

The state vector, from equation 5.6.6, is:

$$x = \begin{Bmatrix} q_n \\ \dot{q}_n \\ x_c \end{Bmatrix} \qquad \textbf{(W.25)}$$

A is the system coefficient matrix, given in equation 5.6.9a:

$$A = \begin{bmatrix} [0] & [I] & [0] \\ -\Omega^2 & -2Z\Omega & M^{*-1}\Phi_s^T F_l C_c \\ [0] & [0] & A_c \end{bmatrix} \qquad \textbf{(W.26)}$$

The first ten rows and columns of A correspond with A_h in equation equation W.20a.

B is a matrix with two vector columns:

$$B = [B_V \quad B_{\ddot{\theta}h}] \qquad \textbf{(W.27)}$$

B_V is given by equation 5.6.9b:

$$B_V = \begin{Bmatrix} \{0\} \\ \{0\} \\ B_c \end{Bmatrix} \qquad \textbf{(W.28a)}$$

For the first four normal modes, $B_{\ddot{\theta}h}$ is given by:

$$B_{\ddot{\theta}h} = \begin{Bmatrix} \{B_h\}_{rows\,1-4} \\ 0 \\ \{B_h\}_{rows\,13-16} \\ 0 \\ \begin{Bmatrix} 0 \\ 0 \\ 0 \end{Bmatrix} \end{Bmatrix} \qquad \textbf{(W.28b)}$$

C is the output matrix given in equation 5.6.9c:

$$C = \frac{\Phi_s(x_2) - \Phi_s(x_1)}{x_2 - x_1}\left[-\Omega^2 \quad -2Z\Omega \quad M^{*-1}\Phi_s^T F_l C_c\right] \qquad \textbf{(W.29)}$$

D is a row vector with two zero elements:

$$D = \{0 \quad 0\} \qquad \textbf{(W.30)}$$

Note that the C-matrix in equation W.29 corresponds with the C-matrix in equation 5.6.9c. However, this C-matrix does not correspond with C_h in equation W.20c. In order to obtain a C-matrix, which is valid for both inputs, the elements of $B_{\ddot{\theta}h}$ are modified as explained next.

The procedure is as follows: Equations W.21 are written in canonical form, whereby uncoupled state and output equations for each normal mode are obtained. Each modal state equation is then written as follows in *TF* form, using equation W.1:

$$\left(\frac{\ddot{\theta}}{\ddot{\theta}_h}\right)_i = \left(\frac{\theta}{\theta_h}\right)_i = C_i\left[sI - A_i\right]^{-1} B_i \qquad \textbf{(W.31)}$$

where the subscript i denotes the i-th normal mode. The sizes of A_i, B_i, C_i and D_i are respectively 2 x 2, 2 x 1, 1 x 2 and 1 x 1.

Equation W.31 is written as follows for the i-th mode:

$$\left(\frac{\ddot{\theta}}{\ddot{\theta}_h}\right)_i = \{C_1 \quad C_2\}_i \begin{bmatrix} \dfrac{s - A_{22}}{s^2 - (A_{11} + A_{22})s + A_{11}A_{22} - A_{21}A_{12}} & \dfrac{A_{12}}{s^2 - (A_{11} + A_{22})s + A_{11}A_{22} - A_{21}A_{12}} \\ \dfrac{A_{21}}{s^2 - (A_{11} + A_{22})s + A_{11}A_{22} - A_{21}A_{12}} & \dfrac{s - A_{11}}{s^2 - (A_{11} + A_{22})s + A_{11}A_{22} - A_{21}A_{12}} \end{bmatrix}_i \begin{Bmatrix} B_1 \\ B_2 \end{Bmatrix}_i$$

(W.32)

Expanding equation W.32 gives:

$$\left(\frac{\ddot{\theta}}{\ddot{\theta}_h}\right)_i = \left(\frac{p_1 s + p_0}{s^2 + q_1 s + q_0}\right)_i \qquad \textbf{(W.33)}$$

where:

$$p_{0i} = \left(-A_{11}B_2C_2 + A_{12}B_2C_1 + A_{21}B_1C_2 - A_{22}B_1C_1\right)_i \qquad \textbf{(W.34a)}$$

$$p_{1i} = \left(B_1C_1 + B_2C_2\right)_i \qquad \textbf{(W.34b)}$$

$$q_{0i} = \left(A_{11}A_{22} - A_{12}A_{21}\right)_i \qquad \textbf{(W.34c)}$$

$$q_{1i} = \left(-A_{11} - A_{22}\right)_i \qquad \textbf{(W.34d)}$$

The input voltage to angular acceleration *TF* is subsequently written in canonical form to obtain an uncoupled state and output equation for each of the first four normal modes. The modal state equation for the i-th mode is then written as follows, in the *TF* form of equation W.33:

$$\left(\frac{\ddot{\theta}}{V}\right)_i = C_i\left[sI - A_i\right]^{-1} B_i \qquad \textbf{(W.35)}$$

Equations W.34a and W.34b are written in matrix form as:

$$\begin{bmatrix} C_1 & C_2 \\ A_{21}C_2 - A_{22}C_1 & A_{12}C_1 - A_{11}C_2 \end{bmatrix}_i \begin{Bmatrix} B_1 \\ B_2 \end{Bmatrix}_i = \begin{Bmatrix} p_1 \\ p_0 \end{Bmatrix}_i \qquad \textbf{(W.36)}$$

where C_{1i} and C_{2i} are the elements of C_i in equation W.35. From equation W.36, B_{1i} and B_{2i} are determined as follows:

$$\begin{Bmatrix} B_1 \\ B_2 \end{Bmatrix}_i = \begin{bmatrix} C_1 & C_2 \\ A_{21}C_2 - A_{22}C_1 & A_{12}C_1 - A_{11}C_2 \end{bmatrix}_i^{-1} \begin{Bmatrix} p_1 \\ p_0 \end{Bmatrix}_i \qquad \textbf{(W.37)}$$

The resulting $B_{\ddot{\theta}h}$ -vector, is:

$$B_{\ddot{\theta}h} = \{(B_1)_{i=1} \quad (B_1)_{i=2} \quad (B_1)_{i=3} \quad (B_1)_{i=4} \quad 0 \quad (B_2)_{i=1} \quad (B_2)_{i=2} \quad (B_2)_{i=3} \quad (B_2)_{i=4} \quad 0 \quad 0 \quad 0 \quad 0\}^T \qquad \textbf{(W.38)}$$

Equations W.24 therefore become:

$$\begin{Bmatrix} \dot{q}_n \\ \ddot{q}_n \\ \dot{x}_c \end{Bmatrix} = \begin{bmatrix} [0] & [I] & [0] \\ -\Omega^2 & -2Z\Omega & M^{*-1}\Phi_s^T F_l C_c \\ [0] & [0] & A_c \end{bmatrix} \begin{Bmatrix} q_n \\ \dot{q}_n \\ x_c \end{Bmatrix} + \begin{bmatrix} B_V & B_{\ddot{\theta}h} \end{bmatrix} \begin{Bmatrix} V \\ \ddot{\theta}_h \end{Bmatrix} \qquad \textbf{(W.39a)}$$

$$\ddot{\theta} = \frac{\Phi_s(x_2) - \Phi_s(x_1)}{x_2 - x_1} \begin{bmatrix} -\Omega^2 & -2Z\Omega & M^{*-1}\Phi_s^T F_l C_c \end{bmatrix} \begin{Bmatrix} q_n \\ \dot{q}_n \\ x_c \end{Bmatrix} \qquad \textbf{(W.39b)}$$

Appendix X
General control system requirements

General controller requirements are normally expresessed in terms of performance factors such as accuracy, stability, sensitivity, reaction speed, control effort, robustness, observability and controllability. These factors are discussed in short below, together with methods to meet the requirements.

X.1 Accuracy

Control accuracy is influenced by parameters such as transient overshoot, settling time, DC error, tracking error and disturbance attenuation over a given bandwidth. Excessive transient overshoot may damage the plant and must therefore be reduced to within a safe range. Two simple methods of transient overshoot control, are rate feedback and PID-control [Schwarzenbach & Gill, 1986]. Differentiation of the error signal, by means of a differentiator (D) element, in parallel with the P and I elements, will lower the overshoot peak. The higher the D-element gain, the lower the overshoot. However, the higher the D-element gain, the longer the transient rise time.

Rate feedback is accomplished by placing a differentiator in parallel with the output feedback elements. A disadvantage of rate feedback is that it may drive the plant unstable if control is non-collocated.

Settling time is the time it takes the system output to reach and stay within 5% of the steady-state value, during step excitation [Schwarzenbach & Gill, 1986]. The settling time T of a system with distinct, complex poles, can be obtained from the following approximate equation:

$$T \approx \frac{5}{\zeta_1 \omega_1} \qquad \textbf{(X.1.1)}$$

where ω_1 is the lowest angular natural frequency and ζ_1 is the corresponding damping factor.

DC error is the deviation of the system output from the setpoint, after the settling time has elapsed. A simple method of eliminating DC error is to integrate the error signal, by means of an integrator element, placed in parallel with the proportional element. The disadvantage of this measure is that it will lower the damping required to limit transient overshoot [Schwarzenbach & Gill, 1986].

Tracking error is the relative error between the reference signal and output. It is, as the name indicates, only applicable to tracking controllers. Tracking error may depend on a variety of factors, such as the transient phenomena discussed above, system frequency bandwidth, nonlinearities, measurement noise, control hardware throughput delay, as well as sensor range, resolution and bandwidth. All of these factors must necesssarily be addressed during the design of a tracking controller. This is, however, beyond the scope of this study.

Disturbance attenuation, on the other hand, is important in this study. The plant must provide the necessary filtering characteristics to reject the base disturbance, in order to obtain a sufficiently low output angular acceleration. Due to noise and unmodelled plant characteristics, such as nonlinearities, it will be extremely difficult to totally reject the disturbance. Instead, the remaining output must be minimized. The ratio of the remaining output to the base disturbance, is known as the attenuation factor. This factor is a measure of determining the performance of the system. The attenuation factor was discussed in more detail in section 6.3.1.

Control accuracy may also be affected by the control system type. It may for instance be attractive, from a cost point of view, to use an analogue controller, instead of a digital controller. Simple analogue controllers, although outdated, do not require digital signal processing equipment, analogue-to-digital (A/D) and digital-to-analogue (D/A) converters.

The limitation of an analogue controller, however, is that the required feedforward and feedback characteristics may be difficult to obtain. If the controller does not perform as originally anticipated during the design, certain parameters may have to be changed. Whereas this is easily accomplished with digital controllers, it may be extremely difficult with analogue controllers. The reason is that analogue equipment such as resistors, capacitors and inductors, may not have the required range of adjustment. While rheostats have been around for a long time, adjustable capacitances are currently only available in capacitors with relatively small capacitances.

X.2 Stability

Stability, together with accuracy, is probably the most important requirement of a control system. Stability of a linear time invariant (LTI) system is determined by the real parts of its eigenvalues: An LTI system is unconditionally stable if the real parts of all its eigenvalues are negative.

This statement must, however, be qualified for a *linearized* system. Linear systems analysis applied to a nonlinear system, may only be accurate over a limited working range. This phenomenon was discussed in detail in section 2.7. The equivalent linear range will depend on the nature of the nonlinearity. A weakly nonlinear system may have a fairly large linear range of operation and may therefore be accurately represented by a linear model. Linear stability (gain and phase) margins of the linearized system will closely approximate those of the nonlinear system. This system type can be relatively easily stabilized by a linear controller.

On the other hand, a strongly nonlinear system may have relatively small linear ranges of operation, also known as regions of local stability. If the system is operated inside any of these regions, it will be stable. If operated outside these regions, it will be unstable. Such a system is globally unstable. Local and global stability are discussed in more detail by Slotine & Li [1991].

Nonlinear systems may be accurately controlled and stabilized by nonlinear controllers. The design and implementation of nonlinear controllers is however beyond the scope of this study.

Alternatively, a nonlinear plant may be controlled by a linear controller, with sufficient robustness to compensate for changes in characteristics (e.g. DC gains, natural frequencies and damping factors), without sacrificing other important performance parameters (e.g. accuracy). Techniques of improving system robustness will be discussed in section X.6.

X.3 Sensitivity

Sensitivity of a control system depends on two factors, i.e. parameter sensitivity and sensor sensitivity. Parameter sensitivity can be described as the "inverse phenomenon" of robustness, i.e. a more robust system is less sensitive to a change in the value of a specific parameter. Robustness will be discussed in short in section X.6. More detailed discussions on the subject are provided by D'Azzo & Houpis [1986], Maciejowski [1989], Skogestad & Postlethwaite [1997], Slotine & Li [1991] and Tsui [1996].

Sensor sensitivity mainly depends on sensor resolution and sensor calibration factor. Sensor resolution is the smallest increment in a measured signal to which a sensor will respond [Cooper & Helfrick, 1985]. The smaller the increment, the better the resolution. Sensor resolution is an important parameter in vibration isolation applications. The objective of vibration isolation is to obtain output signals with low magnitudes, in comparison with the disturbances. In order to measure and control accurately, sensors must be able to respond to small changes in outputs.

Calibration factor is the ratio of the sensor output signal to the measured variable [Cooper & Helfrick, 1985]. The calibration factor of an accelerometer, for instance, is the ratio of the output voltage to the measured acceleration, and is normally expressed in mV/g. The most suitable calibration factor is determined by the full-scale range of the data acquisition equipment. It is preferable that this range correspond to the output range of the sensor, as it will eliminate the need for unduly high control signal gains. (In section 4.3.3, for example, it was mentioned that the coil voltage exceeded the signal analyzer range, and had to be scaled by means of a voltage divider, before it could be measured).

X.4 Reaction speed

Reaction speed is determined by two main factors, i.e. controller frequency bandwidth and throughput lag. The required frequency bandwidth can be obtained during the design phase, by calculation of the controller feedforward and feedback parameters. Optimal and pole-placement design techniques are often used for this purpose. The cutoff frequency of the controlled system can be verified by comparing it with the required cutoff-frequency.

Throughput lag is the time it takes to execute the A/D conversion of sensor signals, apply digital control (e.g. by feedforward and feedback compensation, digital filtering, frequency shaping, addition, subtraction, gaining and clipping of signals) and convert the signals back to analogue form. The lag is often also expressed in terms of data buffer length or number of samples.

The lag depends, inter alia, on the control hardware configuration. If the controller runs on its own processor (DSP), the DSP does the A/D and D/A conversion, as well as the control calculations. The processor must be specifically programmed for this purpose. Programming is normally done externally, in languages like Assembler, C, Pascal, Quick Basic, or Visual Basic, whereafter the program is compiled and loaded onto the processor. Some processors may be programmed and compiled from graphic environments like Simulink (see section 4.4). Processing speed mainly depends on the DSP clock speed. Compiling of the program necessarily improves throughput speed.

X.5 Control effort

Control effort is the input required to drive the plant to its desirable output. In the case of the magnetostrictive LOS stabilization system, coil voltage is the input, and the optical instrument angular acceleration is the output. The objective is to minimize the output. While this is an important goal, it must be achieved with as little control effort as possible. Both the output and control effort must therefore be minimized. This process is known as optimization. A type of controller which simultaneously minimizes output and control input, is an optimal regulator.

The optimal feedforward and feedback control parameters are determined mathematically, by application of methods such as variational optimization and linear quadratic optimal regulator (LQR) design. In order to obtain a criterion which can be used to evaluate system optimality, and which can be expressed in terms of a single numerical value, an objective function is defined. This function, also known as the cost function, must be minimized to obtain the optimal control parameters.

The linear quadratic (LQ) optimal cost function for the regulator problem under discussion, is:

$$J = \int_{t=0}^{t=T} \left[y^2(t) + u^2(t) \right] dt \qquad \textbf{(X.5.1)}$$

where J is the cost function.

In equation X.5.1, the output and control are equally weighed. The output and control can be separately weighed, as follows:

$$J = \int_{t=0}^{t=T} \left[Q_y y^2(t) + R u^2(t) \right] dt \qquad \textbf{(X.5.2)}$$

where Q_y and R are the output and control weights, respectively.

The cost function is more conveniently expressed in matrix form, where y and u are vectors:

$$J = y^T Q_y y + u^T R u \qquad \textbf{(X.5.3)}$$

The cost function can be extended to include a term which contains the product of the input and output:

$$J = \int_{t=0}^{t=T} \left[Q_y y^2(t) + Ru^2(t) + Ny(t)u(t) \right] dt \qquad \textbf{(X.5.4)}$$

where N is the weight of the product yu. Inclusion of this term may result in a cost function which cannot strictly be termed "linear quadratic", as yu will only be positive for all t if u and y are in phase. This is however not the case with the magnetostrictive active vibration isolation system (see figure 4.5.2.3). For this reason, the yu-term will henceforth not be included in the cost function.

Optimization can either be unconstrained or constrained. Unconstrained optimization means that neither y nor u is bounded. An example of an unconstrained optimization equation is given by equation X.5.2. The equation does not supply sufficient information to minimize J, since there is no relationship between u and y. The required relationship is supplied by the state and output equations, which are the constraint equations for the LQR state regulation problem under discussion:

$$\dot{x} = Ax + B_u u + B_d d \qquad \textbf{(X.5.5a)}$$

$$y = Cx \qquad \textbf{(X.5.5b)}$$

Equations X.5.5 may not necessarily be the only constraint equations. Constraints can be added to suit the problem. Although the input is accounted for in the cost function, it may exceed the available supply. To avoid this, an additional constraint, i.e. available source voltage (+28 V for the magnetostrictive active isolation system) can be added. Another constraint, which can be added in the interest of robustness, is minimum damping.

A relationship between the states and control, which satisfies equations X.5.3 and X.5.5 above, is required. In a state-controlled linear system, the control is a linear combination of the states:

$$u = -Kx \qquad \textbf{(X.5.6)}$$

where K is the optimal state feedback gain, or "state feedback control law". A necessary condition for equation X.5.6 is that all the states be known from measured outputs. This property, which is known as observability, will be discussed later.

The elements of K can be determined in a number of ways, e.g. by variational optimization methods and by solving the algebraic Riccati equation (ARE). The Riccati equation, in its steady state form, is:

$$Q_x + A^T S_{ss} + S_{ss} A - S_{ss} B_u R^{-1} B_u^T S_{ss} = 0 \qquad \textbf{(X.5.7)}$$

where S_{ss} is the steady-state Riccati matrix and Q_x is the state weight, related to Q_y by:

$$Q_x = C^T Q_y C \qquad \textbf{(X.5.8)}$$

Equation X.5.7 must be solved to obtain the steady-state Riccati matrix. A solution method often used, is Hamiltonian eigenvector decomposition, which is described in detail by Meirovitch [1990].

The optimal feedback gain matrix K is given in terms of the Riccati matrix as:

$$K = R^{-1} B_u^T S_{ss} \qquad \textbf{(X.5.9)}$$

The closed-loop state and output equations are obtained by substitution of equation X.5.6 into equation X.5.5:

$$\dot{x} = (A - B_u K)x + B_d d \qquad \textbf{(X.5.10a)}$$

$$y = Cx \qquad \textbf{(X.5.10b)}$$

It can be seen from equation X.5.10a that the only input to the closed-loop regulator, is the disturbance d.

The closed-loop eigenvalues are the values of s for which:

$$\left| sI - (A - B_u K) \right| = 0 \qquad \textbf{(X.5.11)}$$

The block diagram of the plant and state feedback regulator, with state and control equations given by equations X.5.5 and X.5.6 respectively, is shown in figure X.5.1.

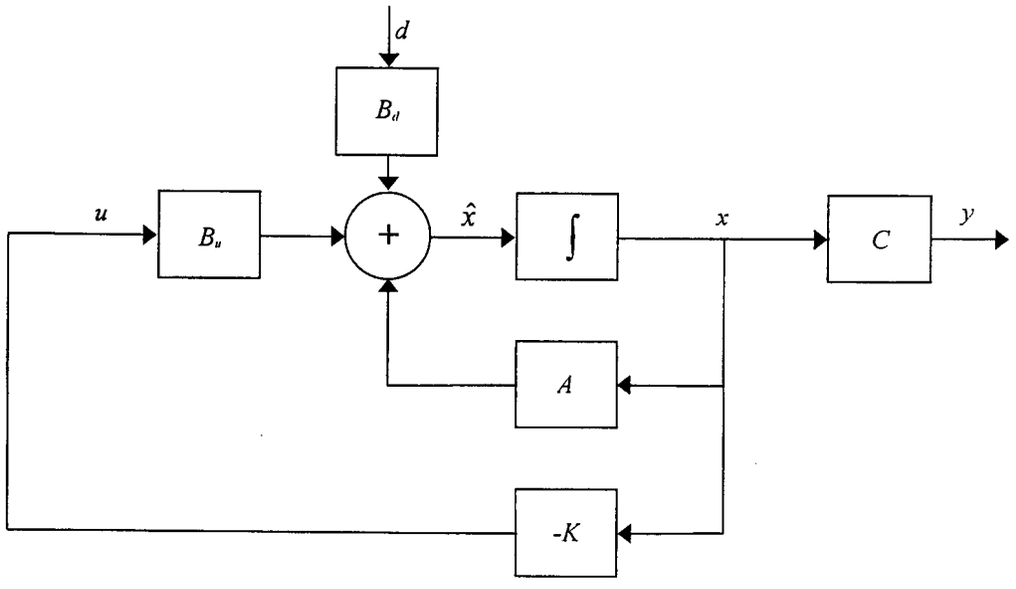

Figure X.5.1: State feedback regulator block diagram

More thorough discussions on optimal control can be found in Anderson & Moore [1989], Brogan [1985], D'Azzo & Houpis [1986], Kirk [1970], Kuo [1982] and Meirovitch [1990].

X.6 Robustness

The ability of a controller to meet its performance criteria in the presence of plant, input, disturbance and measurement noise uncertainties, is known as robustness. An example of a plant uncertainty is a nonlinearity, which may cause the plant to display different characteristics at different excitation levels. Depending on the nature of the nonlinearity, a robust controller will partly or fully compensate for the changes in characteristics.

Examples of input and disturbance uncertainties are DC offsets, which may be attributed to unmodelled sensor characteristics. A typical example is the DC characteristic of an accelerometer. Theoretically, an accelerometer has a zero DC output, but practically, the output voltage may contain a DC component. Resistive accelerometers, in particular, display this characteristic. Noise uncertainties may include input and output sensor noise, noise generated by measurement equipment, such as amplifiers, and electromagnetic noise in unscreened cables.

Linear quadratic (LQ) optimal state feedback controllers are seldom robust [Kuo, 1982]. The reason is that these controllers often operate on the principle of pole-zero cancellation, i.e. the frequency and damping factor of a *TF* pole coincide with those of a *TF* zero. When the plant is excited at the design drive level, the zero will exactly cancel the pole. If, however, the drive level is slightly altered, phenomena such as nonlinear plant behaviour may cause the frequency and damping factor of the pole to shift, to such an extent that it may no longer coincide with those of the zero. The pole may not be cancelled at all, with the result that transmissibility of the closed-loop system may be worse than that of a system without vibration isolation.

A number of solutions exist to improve robustness, three of which are as follows: Firstly, pole damping may be increased, using pole-placement techniques. If the pole shifts within a narrow frequency band, it will still be partly cancelled by the zero. Although performance, in terms of attenuation, will not match that of the LQ optimal controller, robustness will improve.

Secondly, the optimality constraints (see equations X.5.5) may be expanded to include minimum closed-loop damping factors. Although this measure may complicate the solution of the Riccati equation, the optimal feedback gain may be obtained by application of alternative optimization methods, such as variational methods.

Thirdly, a solution suggested by Kuo [1982], is to place an output integrator, with gain H_I, in parallel with the state feedback matrix, as shown in figure X.6.1. The effect of this method on improving the robustness of an absolute motion controller was discussed in section 6.3.8.5.

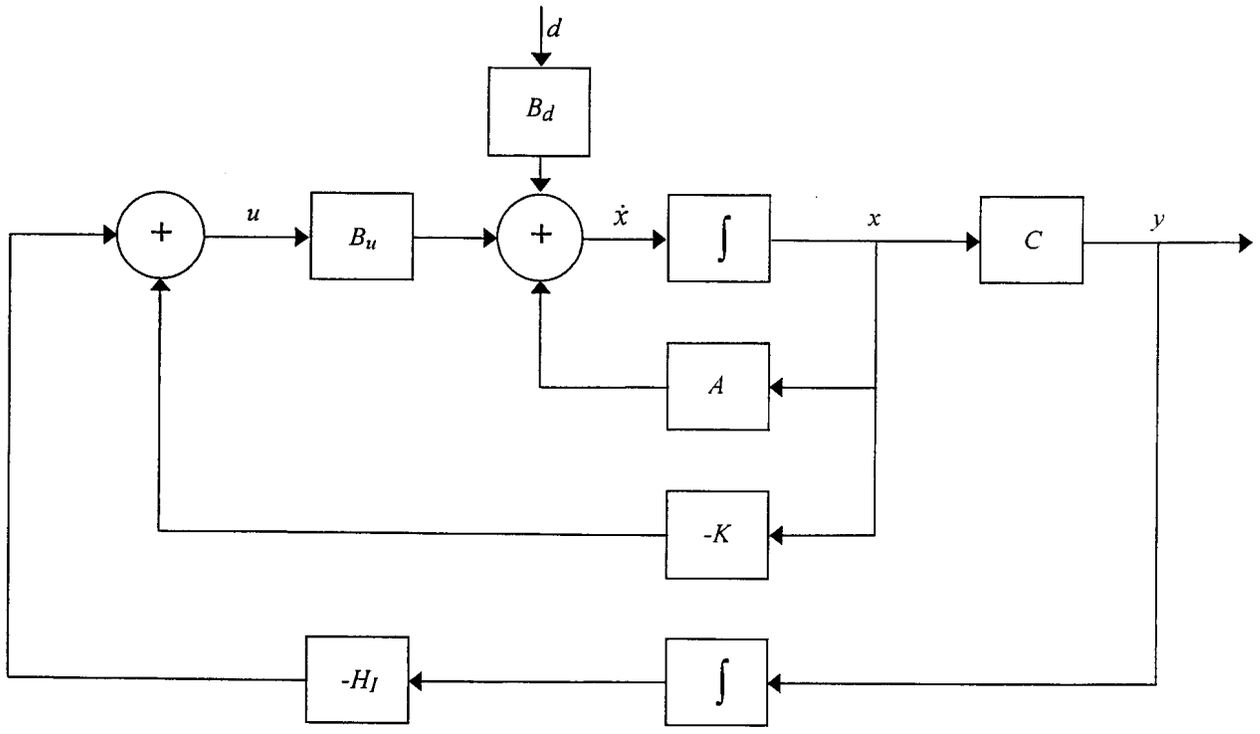

Figure X.6.1: State plus output integral feedback regulator block diagram

The control law is of the following form:

$$u = -Kx - H_I \int y dt \qquad \textbf{(X.6.1)}$$

Differentiation of equation X.6.1 with respect to time, gives:

$$\dot{u} = -K\dot{x} - H_I y \qquad \textbf{(X.6.2)}$$

Substitution of equations X.5.5 into equation X.6.2 and simplification of the resulting equation gives:

$$\dot{u} = -\left(KA + H_I C\right)x - KB_u u - KB_d d \qquad \textbf{(X.6.3)}$$

Equation X.6.3 is the controller state equation. The term $KA + H_I C$ couples the plant and controller state equations.

Combination of the plant and controller state and output equations X.5.5 and X.6.3 gives the closed-loop system state-space equations as follows:

$$\dot{x}_{cl} = A_{cl}x_{cl} + B_{cl}d \qquad \textbf{(X.6.4a)}$$

$$y_{cl} = C_{cl}x_{cl} \qquad \textbf{(X.6.4b)}$$

where x_{cl} is the closed-loop state vector, given by:

$$x_{cl} = \begin{Bmatrix} x \\ u \end{Bmatrix} \qquad \textbf{(X.6.5)}$$

A_{cl}, B_{cl} and C_{cl} are the closed-loop coefficient, driving and output matrices, respectively given by:

$$A_{cl} = \begin{bmatrix} A & B_u \\ -(KA + H_f C) & -KB_u \end{bmatrix} \qquad \textbf{(X.6.6a)}$$

$$B_{cl} = \begin{bmatrix} B_d \\ -KB_d \end{bmatrix} \qquad \textbf{(X.6.6b)}$$

$$C_{cl} = \begin{bmatrix} C & 0 \end{bmatrix} \qquad \textbf{(X.6.6c)}$$

The eigenvalues of the closed-loop system are the values of s for which:

$$|sI - A_{cl}| = 0 \qquad \textbf{(X.6.7)}$$

The integrator raises the DC and low-frequency content of the control signal, thereby making the system more sensitive to feedback at low frequencies and less sensitive at high frequencies. A typical application is DC disturbance rejection in electric motor control, as explained by Kuo [1982].

The method can also be applied to improve low-frequency behaviour of the magnetostrictive LOS stabilization system, which is the topic of this study. All but one of the plant poles are well in excess of the disturbance band (see table 5.3.2), therefore an integrator will make the system less sensitive to feedback at most of the plant natural frequencies.

However, a disadvantage of this method, is that an integrator in the feedback loop may drive the control to infinity, although the output may be bounded. A cure to the problem is to high-pass filter the control signal. If the filter cutoff frequency is sufficiently low, the DC component will be eliminated, but the desirable low-frequency characteristics will be retained.

More sophisticated robust control methods include loop transfer recovery (LTR), as discussed by Maciejowski [1989], Skogestad & Postlethwaite [1997] and Tsui [1996].

X.7 Observability

State feedback is a powerful control method, especially for high-order systems. A condition for state control is that the states be observable from output measurements. If all the states can be reconstructed from the output, a system is said to be completely observable, or simply, observable.

Mathematically, the *n*-th order LTI system, whose state and output equations are given by

$$\dot{x} = Ax + Bu \qquad \textbf{(X.7.1a)}$$

$$y = Cx \qquad \textbf{(X.7.1b)}$$

is observable if and only if the matrix

$$\left[C^T \;\vdots\; A^TC^T \;\vdots\; \left(A^T\right)^2C^T \;\vdots\; \cdots \;\vdots\; \left(A^T\right)^{n-1}C^T\right] \qquad \textbf{(X.7.2)}$$

has rank *n* [Kirk, 1970].

Observability makes it possible to observe the states by means of a state observer, or estimator. State observer dynamics can be described by means of observer state and output equations. The inputs to the observer depend on the controller configuration. For an absolute motion controller, i.e. for pure output feedback (see section 6.3.8.2), the observer input is the plant output. For a relative motion controller and an absolute plus base motion controller (see sections 6.3.8.1 and 6.3.8.4), the observer inputs are the plant output and disturbance.

The observer state-space equations, for an absolute plus base motion controller, are:

$$\dot{\hat{x}} = A\hat{x} + B_u u + B_d d + L\left(y - \hat{y}\right) \qquad \textbf{(X.7.3a)}$$

$$\hat{y} = C\hat{x} \qquad \textbf{(X.7.3b)}$$

where $\hat{x}$ is the observed state vector, which differs from the true plant state vector, A is the plant coefficient matrix, B_u is the plant driving matrix for the controllable input u, B_d is the plant driving matrix for the disturbance input, y is the plant output, $\hat{y}$ is the observed output and L is the observer driving matrix. The observer state equation for a pure output feedback controller is given by equation X.7.3a, with a zero disturbance driving matrix B_d.

For full-state feedback control, the control is a linear combination of the observed states:

$$u = -K\hat{x} \qquad \textbf{(X.7.4)}$$

where K is the state feedback gain matrix.

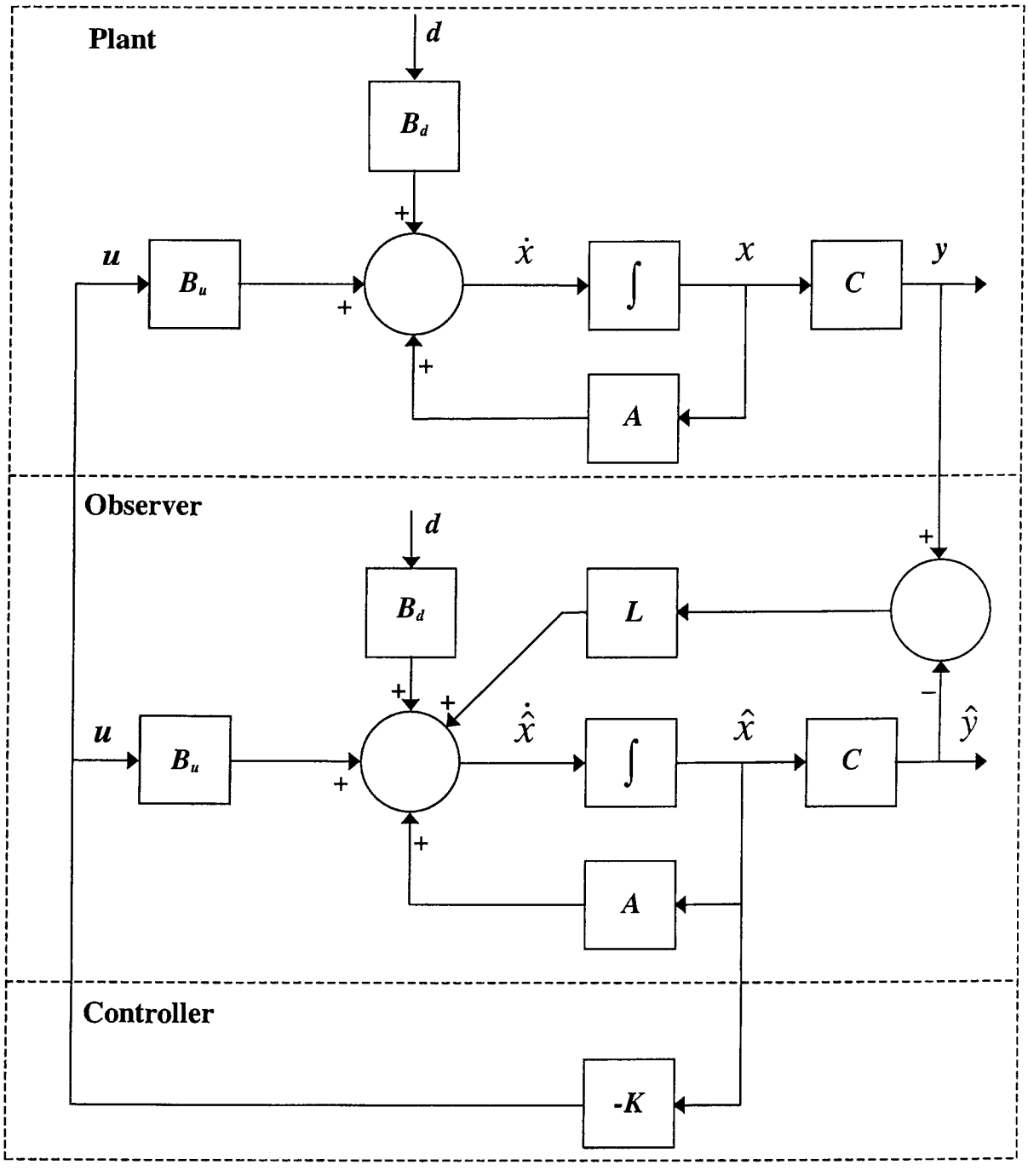

Figure X.7.1: Block diagram of plant, state observer and state feedback controller

To conclude, if the system is non-observable, the observable states may still be estimated, by means of a reduced-order observer. Reduced-order observers are described in more detail by Anderson & Moore [1989], Franklin et al [1990] and Kwakernaak & Sivan [1972].

X.8 Controllability

A system is said to be completely controllable if every state variable can be controlled to reach a certain objective in finite time by some unconstrained control u [Kuo, 1982]. The physical interpretation of controllability is that, if any one of the state variables is independent of the control u, driving this particular state to a desired state in finite time by means of u will be impossible. This state is said to be uncontrollable, which means that the system is not completely controllable, or simply uncontrollable [Kuo, 1982].

Controllability can be expressed as follows in terms of the plant state matrices A and B. Mathematically, the n-th order LTI system, whose state and output equations are given by

$$\dot{x} = Ax + Bu \qquad \textbf{(X.8.1a)}$$

$$y = Cx \qquad \textbf{(X.8.1b)}$$

is controllable if and only if the matrix

$$\left[B \;\vdots\; AB \;\vdots\; A^2B \;\vdots\; \cdots \;\vdots\; A^{n-1}B\right] \qquad \textbf{(X.8.2)}$$

has rank n [Kirk, 1970].

Alternative practical methods of testing controllability of a system are discussed by Kuo [1982].